Optical 3D imaging of subcellular dynamics in biological cultures and tissues : applications to ophthalmology and neuroscience

Olivier Thouvenin

université PARIS DIDEROT PARIS 7 — Institut Langevin ONDES ET IMAGES — ESPCI PARIS — Frontières du Vivant — SORBONNE PARIS CITÉ

THÈSE DE DOCTORAT
DE L'UNIVERSITÉ SORBONNE PARIS CITÉ

Spécialité

Imagerie

(ED 474 - Frontières du Vivant)

Préparée à l'Institut Langevin - Ondes et Images

Présentée par

Olivier THOUVENIN

sous la direction de

Mathias FINK et Claude BOCCARA

Sujet de la thèse :

Optical 3D imaging of subcellular dynamics in biological cultures and tissues: Applications to ophthalmology and neuroscience

Soutenue le 07 Juillet 2017

devant le jury composé de :

Mr.	BOURDIEU	Laurent	Rapporteur	DR CNRS
Mr.	MARQUET	Pierre	Rapporteur	M.D/Ph.D Laval University
Ms.	VILLARD	Catherine	Examinateur	DR CNRS
Ms.	EMILIANI	Valentina	Présidente du jury	DR CNRS
Mr.	PAQUES	Michel	Examinateur	PU-PH UMPC
Mr.	FORT	Emmanuel	Examinateur	Prof. ESPCI
Mr.	FINK	Mathias	Directeur de thèse	Prof. ESPCI
Mr.	BOCCARA	Claude	Membre invité	Emeritus Prof. ESPCI

Remerciements

Evidemment, cette thèse n'aurait pas pu converger vers quelque chose de vaguement présentable sans l'aide essentielle dont j'ai pu bénéficier au cours de ces dernières années. Bien que ces remerciements ne tiennent qu'en quelques lignes, je tiens à préciser que le ratio entre la taille des remerciements et la taille du manuscrit n'est évidemment pas comparable à l'importance de la contribution de toutes ces personnes, mais afin de ne pas écrire des remerciements de plusieurs centaines de pages, j'espère que le lecteur indulgent s'en contentera !
Traditionnellement, j'aimerais commencer ces remerciements par m'excuser par avance pour les personnes que je vais oublier probablement dans les lignes qui suivent (mais que je remercie ici), ainsi que pour l'absence d'un fil conducteur agréable au lecteur dans ces remerciements.

Traditionnellement encore, j'aimerais aussi commencer en remerciant les deux personnes sans qui cette thèse n'aurait littéralement pas pu avoir lieu : Claude et Mathias ! Un grand merci pour m'avoir accepté au sein du laboratoire, et m'avoir accordé une confiance et une autonomie (presque) sans limite ! Bien que ce fût parfois difficile de comprendre les raisons de votre optimisme à mon égard dans les moments où rien ne marchait, j'ai vraiment apprécié nos discussions et votre enthousiasme permanent pour la science de manière générale (et même la biologie de temps en temps !). C'est réellement une belle source d'inspiration qui est source de motivation à poursuivre en recherche académique. J'adresse une mention spéciale à Claude, avec qui j'ai eu plus souvent l'occasion de discuter et de venir me plaindre des petits problèmes que la vie de doctorant souvent impose. Ton sens de l'écoute et de la patience ont, j'imagine parfois, été mis à rude épreuve, mais tu l'as toujours affronté avec un entrain remarquable. Combien de fois suis-je venu dans ton bureau en pensant avoir une idée géniale... et combien de fois m'as-tu expliqué pourquoi ça ne marchait évidemment pas ! Mais je m'en sortais souvent avec une belle leçon de physique, et généralement avec une petite anecdote sur ton enfance en cadeau au passage !
Toujours en parlant d'encadrant et de mentor scientifique, humain, voire même spirituel, j'aimerais souligner la présence et l'apport considérable de Kate et de Claire pour leur gentillesse, motivation, sourire de tous les instants, et leur activité constante.

J'aimerais également adresser un énorme merci aux membres de mon jury, avec une pensée particulière pour les rapporteurs. J'imagine qu'en acceptant de faire parti du jury, vous ne vous attendiez pas à vous retrouver avec un manuscrit de 300 pages... Et pourtant, vous avez tous pris le temps de le lire en détail, et j'ai apprécié les nombreux commentaires que vous avez pu faire, souvent d'une grande justesse et pertinence. J'espère que nos chemins se recroiseront! J'en profite pour également mettre en avant la contribution de Catherine et Ivan, membres de mon comité de thèse, et dont j'ai pu bénéficier du retour et de la sympathie chaque année.

Je veux aussi remercier ici Kate, Claude, Amir et mon père pour les relectures et corrections du manuscrit que ce soit sur le plan scientifique et syntaxique, et sans qui ce manuscrit serait probablement illisible.

J'en arrive aux nombreux collaborateurs que j'aie pu rencontrer au cours de ma thèse, et que je n'aie malheureusement pas tous choyés autant que je l'aurais dû, et qu'ils le méritent. Comme vous pourrez le voir, j'ai voulu tester beaucoup (trop ?) de choses, et dans de nombreux domaines variés, ce que je n'aurais pu réaliser sans l'aide de tous. Merci donc pour votre aide, votre temps, et les discussions d'un grand intérêt scientifique. Dans l'ordre historique des collaborations, je tiens à remercier Pamela Rodriguez et Alain Bessis de l'IBENS, pour les premières cultures de neurones et pour avoir été les premiers biologistes à être intrigués par nos théories électromécaniques. Un grand merci à l'équipe de Catherine Villard, successivement à l'institut Curie puis à l'IPGG, et notamment à Céline et Floriane, pour avoir pris la suite sur les préparations d'échantillon biologiques avec grande expertise. J'aimerais également souligner la contribution du groupe de Zsolt Lenkei à l'ESPCI, avec l'aide principalement de Diana, Julie et Maureen pour notre rendez-vous hebdomadaire de récupération stratégique de divers échantillons (cultures, tissus, drogues, etc...) et nos longues discussions associées. Un autre côté majeur de ma thèse a été la collaboration fructueuse avec l'Institut de la vision, au sein de l'ERC Synergy, et particulièrement avec Kate. Je tiens à aussi y remercier Abishek, Djida, Nacim, Kristina, et Valérie pour les différents échantillons et discussions. Au cours de ma thèse, j'ai pu réaliser l'imagerie de quelques poissons in vivo grâce à l'interaction experte de l'équipe de Claire à l'ICM, que je suis ravi de rejoindre pour la suite du chemin. Un merci aussi à Jenna, Yasmine et les autres ! La dernière grosse collaboration dans laquelle j'ai eu la chance d'évoluer est celle sur l'exclusion de fluorescence avec les groupes de Mathieu et Catherine à l'IPGG. J'aimerais surtout remercier Clotilde et Céline, mais également Larisa pour les expériences et retours à ce sujet. Enfin, j'aimerais également exprimer ma gratitude à Fabien, Ralitza et Violaine de l'institut Curie, David de l'institut Jacques Monod, Laurent, Jean François de l'IBENS et l'équipe LLTEch, pour diverses collaborations.

Pour rester sur un plan scientifique, ce travail de thèse s'est inséré dans l'équipe formidable qu'est l'équipe OCT de l'institut Langevin, et je voudrais remercier principalement Amir, Clément A., Charles-Edouard, Jean Marie, et Mai, pour les nombreuses manips réalisées ensemble et tous les échanges scientifiques. J'adresse aussi mes chaleureux remerciements au reste de l'équipe et assimilés, notamment Amaury, Clément (Gastaud), Daria, Egidijus, Ignacio, Peng, Romain, Slava, Victor, et Yasmina pour les nombreuses discussions et aides autour de l'OCT et autres. J'en profite pour insister sur la qualité exceptionnelle de l'environnement dans lequel cette équipe évolue, à savoir au sein de l'Institut Langevin. Pour moi, ce labo n'a pas son pareil que ce soit en terme de qualité scientifique, d'échanges entre les différentes personnes et différents groupes, aussi bien entre doctorants qu'avec les chefs. J'aimerais ajouter des remerciements spéciaux aux équipes techniques et de gestion qui permettent de rendre possible le travail de tous : Abdel, Christelle, Emmanuel, Johnny, Laurine, Lorraine, Marjolaine, et Patricia notamment. Merci à tous pour votre aide précieuse, et votre expertise pour régler mes problèmes administratifs persistants !
Ces remerciements sont aussi l'occasion d'adresser mon amitié à toute l'équipe du CRI, et notamment à mon école doctorale Frontières du vivant et en particulier à mes co-docotrants de son cru 2014-2017, qui a su former un formidable esprit communautaire et singulier dans le paysage de la recherche et de l'éducation française.

Si les remerciements *scientifiques* touchent à leur fin, je n'ai là décrit qu'une partie du travail du doctorant, en laissant de côté, jusqu'à maintenant, l'aspect développement personnel et intellectuel propre à la thèse. J'aimerais passer le reste de ces remerciements à rendre leurs lauriers aux

différents acteurs de ces développements, à ces gens, que l'imaginaire collectif associe à ces experts de la machine à café ou du comptoir, toujours très prompts à refaire le monde. Dans cette idée, j'aimerais insister sur la qualité humaine des individus que j'ai eu la chance de pouvoir côtoyer à l'institut Langevin, et où j'ai pu me lier d'amitié avec nombre de ces membres. J'aimerais ici remercier les membres de la randonnée de l'extrême : François B., Gauthier, Justine, Laurine, Marion, Nikos. Ma thèse a été aussi rythmée par les échanges musclés avec les membres de la team Squash Langevin : Clotilde, François, Laura, Vincent, et Jérôme notre maitre à tous. De manière générale, je remercie les gens de l'Institut Langevin, pour les bons moments passés ensemble, que ce soit au séminaire de l'EPOM en crête, au cours des soirées apéros terrasse et autres folles soirées de la montagne Ste Geneviève. Mais comment pourrais-je parler de l'Institut Langevin sans mentionner le fameux bureau R31, et ses membres éminents. Que ce fusse pour sortir de donjons médiévaux (10 minutes plus tôt que le R32 soit dit en passant), pour inventer des modèles scientifiques collaboratifs (pour partir en conf à l'autre bout du monde), pour tester des sucreries à l'aspect pas toujours optimal, pour pratiquer l'hypnose sur doctorant ou autres techniques de modificateurs quantiques d'états fonctionnels, ou encore pour commenter ou vivre des compétitions sportives intenses, ce bureau fût le théâtre d'une activité intense, et presque studieuse de temps en temps. J'aurais même entendu dire qu'il faisait parti du top 10 des meilleurs bureaux de Paris. A visiter absolument ! Enfin bref, j'aimerais en remercier ses locataires illustres : Amir, Papamir pour les intimes, sauveur de demoiselles en détresse, et amateur de Long Islands à la mode d'Hemingway, Aurélien, futur fondateur de la BBBC (Baelde Bullshit Business Corporation), Baptiste, grand joueur de Ukulélé contrôlé par Arduino, Clément D., conseiller littéraire et créateur de jeux divers et d'entropie procrastinatoire, Jean-Baptiste, qui a bien compris que rien ne servait de courir, il suffisait de partir à temps. Mais reste t-il encore à partir parfois... Je remercie également Marion, pour beaucoup de choses, mais pas pour les surnoms qu'elle invente, ni pour ses cours d'optique. Je remercie aussi Peng, notamment pour ne pas avoir manipé avec mes yeux au cours de sa thèse, Yann, grand commentateur sportif et grand expérimentateur bulleur, et Vincent, pour la traduction en 12 langues de mon résumé de thèse, les discussion sur la nature de l'univers remplis de démons de Loschmidt, et pour avoir fait vivre les pharmacies du 05 ème. En vrac, et pour finir sur le R31, je remercie les anciens et nouveaux membres : Fabien, Slava, Florian, Sanders, Kammel, et je n'oublie pas le ficus évidemment !
En dehors du Langevin, j'ai passé pas mal de temps à poser des questions stupides de biologie et médecine et à mendier des cellules et autres échantillons bios aux amis de PSB : Anaëlle, Andreas, Clotilde, Fabien, Charlène et Romain. Je passais le reste de mon temps à me plaindre de nos conditions de thésards respectifs avec eux, ainsi qu'avec mes amis de Lyon, avec mention spéciale pour les expats Arthur, Cyril et Sarah.

Tant qu'à faire, j'aimerais profiter de ces remerciements déjà d'une longueur certaine pour assurer ma considération profonde aux hommes politiques français (avec grand prix remportés par JLM, et EM, toute ressemblance avec des personnalités existantes étant évidemment fortuite) pour avoir involontairement participé à ma procrastination de rédaction de thèse. Ma rédaction ayant correspondu à peu près à la période chaude de la campagne présidentielle et ayant donc grandement bénéficié des débats politiques sous-jacents au sein du laboratoire...

Enfin, plus sérieusement, j'aimerais remercier infiniment mes parents, mes deux frangins, ma famille en général, ainsi que Marine, pour m'avoir encouragé sans condition et tout en n'ayant qu'une vague idée de ce que je faisais, et pour leur support affectif, logistique et psychologique.

Enfin bref, un grand merci à tous pour votre présence et aides diverses!

Résumé

Cette thèse a pour objectif l'étude d'un lien effectif potentiel entre la motilité cellulaire, la mécanique cellulaire, et l'activité biochimique de ces mêmes cellules. Ce couplage a été étudié dans divers systèmes biologiques, et aussi bien dans des cultures de cellules qu'à l'intérieur de tissus plus complexes. Notamment, nous avons particulièrement cherché à détecter un couplage *électromécanique* dans des neurones qui pourrait être impliqué dans la propagation du message nerveux. Pour ce faire, nous avons dû développer deux microscopes optiques à la sensibilité extrême. Ces microscopes se composent de deux parties principales. La première sert à détecter des mouvements axiaux plus petits que la longueur d'onde optique, soit en dessous de 100 nanomètres. La deuxième partie permet la détection d'un signal de fluorescence, offrant la possibilité de suivre l'évolution biochimique de la cellule. Avec ces deux microscopes multimodaux, il est donc possible de suivre de manière simultanée un contraste de motilité, un contraste mécanique, un contraste structurel et un contraste biochimique. Si l'un de ces systèmes est basé sur la tomographie de cohérence optique plein champ et permet de faire de telles mesures en 3-D et en profondeur dans les tissus biologiques, le second ne permet que des mesures dans des cultures de cellules, mais est bien plus robuste au bruit mécanique. Dans ce manuscrit, nous allons essentiellement décrire le développement de ces deux appareils, et préciser les contrastes auxquels ils sont sensibles spécifiquement. Nous développerons également deux des applications principales de ces microscopes que nous avons étudié dans le détail au cours de cette thèse. La première application développe l'intérêt d'un de nos microscopes pour la détection sans marquage des principaux composants cellulaires et structuraux de la cornée et de la rétine. La seconde application tend à détecter et à suivre des ondes électromécaniques dans des neurones de mammifères.

Keywords: Imagerie Biomédicale, Neurophotonique, Tomographie à cohérence optique plein champ, Imagerie de phase quantitative, Interférométrie, Fluorescence, Microscopie à illumination structurée, Motilité, Ophtalmologie

Abstract

This PhD project aims to explore the relationship that might exist between the dynamic motility and mechanical behavior of different biological systems and their biochemical activity. In particular, we were interested in detecting the electromechanical coupling that may happen in active neurons, and may assist in the propagation of the action potential. With this goal in mind, we have developed two highly sensitive optical microscopes that combine one modality that detects sub-wavelength axial displacements using optical phase imaging and another modality that uses a fluorescence path. Therefore, these multimodal microscopes can combine a motility, a mechanical, a structural and a biochemical contrast at the same time. One of this system is based on a multimodal combination of full-field optical coherence tomography (FF-OCT) and allows the observation of such contrast inside thick and scattering biological tissues. The other setup provides a higher displacement sensitivity, but is limited to measurements in cell cultures. In this manuscript, we mainly discuss the development of both systems and describe the various contrasts they can reveal. Finally, we have largely used our systems to investigate diverse functions of the eye and to look for electromechanical waves in cell cultures. The thorough description of both biological applications is also provided in the manuscript.

Keywords: Biomedical imaging, Neurophotonics, Full-field optical coherence tomography, Quantitative phase imaging, Interferometry, Fluorescence, Structure illumination microscopy, Motility, Ophthalmology

A head full of waves. *Reproduction of* ***the wave*** *by* ***Hokusai*** *focusing onto a brain as an illustration of my project initial objective. It aims to detect the role of mechanical waves and mechanical activity in neuroscience.*

Contents

Introduction **1**

I Following nanometric deformations in cell cultures 9

1 Optical detection of nanometric deformations in cell cultures: Quantitative Phase Imaging 15

1.1 First experiments in Phase Imaging . . . 16
1.2 Quantitative phase imaging (QPI) today . . . 18
1.3 Sensitivity in QPI . . . 23
1.3.1 Spatial averaging and phase sensitivity . . . 24
1.3.2 Phase sensitivity and noise behavior . . . 25
1.3.3 Transmission versus reflection interferometry . . . 29
1.4 Decoupling refractive index variations from height changes . . . 31
1.4.1 General decoupling procedures . . . 33
1.4.2 Measuring the refractive index of the external medium . . . 34
1.4.3 Dry Mass measurement . . . 34
1.5 QPI main biological applications . . . 36
1.6 A new tool for refractive index/height decoupling: Fluorescence exclusion . . . 38
1.6.1 Physically constrained fluorescence exclusion . . . 40
1.6.2 FxM theoretical framework . . . 45
1.6.3 FxM numerical model . . . 47
1.6.4 Measuring refractive index maps . . . 50
1.6.5 Future developments in fluorescence exclusion . . . 50

2 Custom built QPI systems 55

2.1 From Michelson to Linnik interferometry . . . 57
2.2 Amplitude and phase separation: Different phase-stepping schemes . . . 57
2.2.1 Fixed phase-stepping . . . 59
2.2.2 Integrative phase-stepping . . . 61
2.2.3 Increasing the acquisition speed using sliding windows . . . 63
2.2.4 Hilbert transform for single shot phase recovery . . . 64
2.3 Phase unwrapping: From phase maps to 3-D optical path maps . . . 64
2.4 Linnik interferometer and simultaneous fluorescence measurement . . . 67
2.5 Mechanical and thermal stability: Common-path interferometer . . . 68
2.6 Wide-angle differential interference contrast microscopy . . . 69
2.6.1 Wollaston & Nomarski prism . . . 70
2.6.2 Interest for wide-angle Nomarski prisms . . . 71
2.6.3 Phase Modulator and phase-stepping in Wa-DIC . . . 72
2.6.4 Changing the shear angle . . . 74

2.7 Wa-DIC reflection microscope in practice . . . 75
2.7.1 Quantitative phase imaging . . . 75
2.7.2 Deconvolution of the phase image . . . 77
2.7.3 Birefringence measurement . . . 78
2.8 Simultaneous QPI and fluorescence measurement with Wa-DIC configuration . . . 79

II From cell culture to tissue imaging: Phase imaging using Optical Coherence Tomography 83

3 Extending optical phase measurements to thick tissues: Optical Coherence Tomography (OCT) 87
3.1 Quantitative phase imaging in thick tissues . . . 88
3.1.1 Problems arising in thick tissues . . . 88
3.1.2 Other 3-D phase imaging systems . . . 92
3.2 Low-coherence interferometry . . . 93
3.2.1 Low temporal coherence . . . 93
3.2.2 Low Spatial Coherence . . . 97
3.2.3 Combining low spatial and low temporal coherence . . . 101
3.3 Optical Coherence Tomography (OCT) . . . 101
3.3.1 Principle of time domain Optical Coherence Tomography . . . 102
3.3.2 Spectral domain and swept-source OCT . . . 103
3.4 Phase imaging using OCT . . . 105
3.4.1 Recovery of quantitative phase differences . . . 105
3.4.2 Doppler and Functional OCT . . . 106
3.4.3 Optical elastography with OCT . . . 108

4 Full-Field Optical Coherence Tomography 113
4.1 Full-Field Optical Coherence Tomography . . . 114
4.1.1 Basic layout and interest . . . 114
4.1.2 Layouts of our different systems . . . 118
4.2 Reasons for using a spatially incoherent illumination . . . 122
4.3 Full-Field OCT versus scanning OCT . . . 123
4.4 FF-OCT performance . . . 124
4.5 FF-OCT for histology . . . 129
4.6 A quick word about swept source FF-OCT . . . 132
4.7 Label-free *In situ* vesicle imaging in zebrafish larvae . . . 133

5 Development of new multimodal Full-Field OCT systems 137
5.1 Simultaneous FF-OCT and SIM microscope . . . 138
5.1.1 Structured Illumination Fluorescence Microscopy . . . 139
5.1.2 Multimodal system optical design . . . 143
5.1.3 Static association of FF-OCT and SIM . . . 148
5.1.4 Mechanical wave observation . . . 149
5.2 Dynamic FF-OCT . . . 152
5.2.1 Principle of D-FF-OCT . . . 152
5.2.2 Motility contrast in cells . . . 156
5.2.3 Separation between amplitude and phase . . . 158

5.2.4 Origin of the phase fluctuations and optical sectioning in D-FF-OCT . . . 161
5.2.5 Phase fluctuation signal analysis . . . 164
5.2.6 D-FF-OCT for histology and to reveal various sample features . . . 171
5.2.7 D-FF-OCT signal variation under different conditions . . . 174
5.2.8 *In vivo* D-FF-OCT . . . 177

III Biological applications 183

6 FF-OCT measurements in the eye 187
6.1 Organization of the eye . . . 189
6.1.1 Cellular organization of the cornea . . . 190
6.1.2 Cellular organization of the retina . . . 191
6.2 Static and dynamic FF-OCT imaging of the cornea . . . 196
6.2.1 Evidence of the stem cell niche in the cornea . . . 196
6.2.2 Another interest for static FF-OCT and fluorescence in the cornea . . . 197
6.2.3 Dynamic FF-OCT in the cornea . . . 199
6.3 Static and dynamic FF-OCT imaging of the retina . . . 199
6.3.1 High-resolution imaging of the retina layer by layer . . . 204
6.3.2 D-FF-OCT to assess local cell viability . . . 207
6.4 Conclusion and future developments . . . 207

7 Activity-dependent phase changes in neurons and electromechanical coupling 213
7.1 Classical theory of electrical activity propagation in neurons . . . 214
7.1.1 Brief history of the ionic hypothesis of action potentials . . . 215
7.1.2 The passive properties of the cellular membrane . . . 217
7.1.3 Ion channels and the cell resting potential . . . 222
7.1.4 The Hodgkin & Huxley model . . . 226
7.2 Beyond the Hodgkin & Huxley theory . . . 231
7.3 Alternative electrical models . . . 236
7.3.1 The pressure pulse model . . . 237
7.3.2 The action waves model . . . 238
7.3.3 The soliton model . . . 240
7.4 Measurement of dynamic phase changes in neuron cultures . . . 244
7.5 Measurement of activity dependent phase changes in tissues . . . 246

Conclusions and perspectives 251

8 Résumé substantiel (FR) 253
8.1 Objectifs, contexte, et organisation de la thèse . . . 254
8.2 Chapitre 1 : L'imagerie de phase quantitative et la détection de déformations axiales sub-longueur d'onde. . . . 255
8.3 Chapitre 2: Interféromètres développés au cours de cette thèse . . . 256
8.4 Chapitre 3 : Imagerie dans les tissus . . . 259
8.5 Chapitre 4 : Tomographie à cohérence optique plein champ . . . 261
8.6 Chapitre 5 : Approches multimodales de la tomographie à cohérence optique plein champ . . . 261
8.7 Chapitre 6 : Applications sur l'imagerie de l'oeil . . . 265

8.8 Chapitre 7 : Mesure de changements biophysiques de cellules actives électriquement 265

A Introduction to optical imaging in biological media 271
A.1 A few principles of geometrical optics . . . 271
A.2 Wave optics, diffraction limit and PSF . . . 271
A.3 Optical detectors . . . 271
A.4 Optical response: The complex refractive index . . . 271
A.5 Light scattering . . . 271
A.6 Imaging of cells . . . 272
A.7 Imaging of tissues . . . 272

B Procedure for axial scanning in high NA FF-OCT 273
B.1 Axial scanning procedure . . . 273
B.2 Reminder on numerical aperture . . . 275
B.3 Calculation of the defocus . . . 275
B.3.1 Defocus in a homogeneous sample . . . 275
B.3.2 Defocus in a medium of varying refractive index . . . 277
B.4 Calculation of the reference arm correction . . . 278
B.5 Measurement of the refractive index . . . 279
B.6 Possible corrections . . . 279

C Mechanical contrast in optical phase systems 281
C.1 Cellular mechanics . . . 281
C.2 Tissue Mechanics . . . 282
C.2.1 Mechanical contrast: Elastography . . . 282
C.2.2 Towards passive elastography. . . . 284

D Scientific contributions 287

References 289

List of abbreviations

- **DHM**: Digital Holography Microscope
- **DIC**: Differential Interference Contrast
- **Wa-DIC**: Wide-angle Differential Interference Contrast
- **FWC**: Fluorescence eXclusion Method
- **FWC**: Full Well Capacity
- **FWHM**: Full Width Half Maximum
- **NA**: Numerical Aperture
- **OCT**: Optical Coherence Tomography
- **FF-OCT**: Full-Field Optical Coherence Tomography
- **D-FF-OCT**: Dynamic Full-Field Optical Coherence Tomography
- **PCA**: Principal Component Analysis
- **PDMS**: PolyDiMethylSiloxane
- **PSF**: Point Spread Function
- **QPI**: Quantitative Phase Imaging
- **RBC**: Red Blood Cell
- **SIM**: Structure Illumination Microscopy
- **STD**: STandard Deviation
- **SVD**: Singular Value Decomposition

Introduction

Life is literally defined as the existence of a soul, or an *anima* in Latin, which shares the same root as animal (defined as a multicellular, usually mobile, with cells not embedded in a rigid wall) and animate (that possesses the ability of motion). These definitions highlight how deeply intricate the notion of life is with the notion of motion and mechanics. In contrast to minerals, living organisms possess the ability to move or to create motion via the action of self-generated forces, in contrast to external forces. If the smallest biological objects such as bacteria and viruses importantly rely on random motions and external forces to explore their space, they all contain a complex inner machinery whose interaction and functioning are deeply regulated by self-generated physical forces. If the molecular motors generating active displacements have been largely characterized in terms of biochemistry, the importance of physical forces for regulating biological activity is probably still underestimated today although it is a very active field of Biology and becomes increasingly popular. The field of biomechanics is closely associated to it since mechanics aims to explain how a cell or how a tissue respond on average to (and propagate) a physical deformation, or displacement.

The spatial and temporal scales of biological displacements are extremely variable from a few hundred picometers to several meters and from the microsecond to several years. At the organism level, nature is full of examples illustrating the extreme variety of spatiotemporal scales, like between the Mayflies that can explore several kilometers squared for the few minutes of their existence to the walking palm tree of the rain forests that moves of a few centimeters a year. At the microscopic level, cells are capable of generating and sustaining millimetric displacements using biochemical energy but are also capable of generating and measuring displacements as vanishingly small as 100 picometers, and integrate them into a biochemical response. The biomechanical forces associated with these displacements are highly spectacular in some specialized organs, such as the high synchronicity of heartbeat, the large amplitude of the muscle contraction, or the impressive sensitivity of the ears. Furthermore, biomechanical forces play a pivotal role in many other aspects of life, such as tissue and tumors development, adhesion, inflammatory response [1], and might also be involved in the transmission of the nervous signal. Not surprisingly, the dysfunction of the transduction of these biomechanical forces is a source of a number of diseases. Obviously, such a large panel of spatial and temporal scales is extremely hard to capture in their entire complexity and explains why the role of biomechanical forces is still under intense investigation. Especially, displacements of a few nanometers and displacements faster than the millisecond are still challenging to accurately track with modern equipment.

At the nanoscopic scale, electron microscopy displays a nanometric resolution but requires

working with fixed static samples. Atomic force microscope (AFM) can detect biologically relevant displacements but are invasive, can only measure axial displacements at a single position at a given time, and cannot penetrate cells. At the opposite scale, Ultrasound and magnetic resonance imaging (MRI) can image rapid large-scale propagation of micron-size mechanical deformations and can penetrate in depth inside tissues [2, 3]. However, they display low transverse resolution and obtain a signal averaged over thousands of cells so that they cannot access cell biomechanics. As a compromise, optical imaging provides cellular and subcellular resolution and image field of views that allows visualizing a few cells in their close environment. Optical imaging can provide label-free or dye-enhanced contrast in cell cultures, transparent organisms, or close to thick tissue surface. It can hardly penetrate deeper than one millimeter inside thick tissues. It offers a good transverse resolution of about a few hundred nanometers, which is still *a priori* not sufficient to image the smallest displacements of the human body. Ultimately, the ideal experimental device to investigate the relationship between biomechanics and biological activity would be able to measure to measure simultaneously a biomechanical information and a biochemical information. In this context, optical imaging is also particularly interesting as several chemical dyes have recently been engineered to record diverse biochemical signals and can measure concentration ratios of various molecules inside the cells. In this manuscript, I will explain how recent optical tools including ours have the ability to study infinitesimal displacements in cells and in tissues down to the nanometric scale, using optical phase information instead of intensity measurements only. I will show that thanks to this phase measurement, optical microscopes can measure displacements in cells of a few nanometers only at several hundred frames per second. Nevertheless, due to optical diffraction limit, the measured displacements are averaged over a volume on the order of 1 μm^3 so that only collective displacements can be observed. Eventually, this information gives a number of biologically-relevant features, such as membrane displacement, tissue elasticity, or a global motility contrast of the cell. In this manuscript, I will mainly describe one microscope we have built that combines optical phase imaging in both cells and tissues to measure structural and biomechanical cues and fluorescence microscopy to measure biochemical cues.

This manuscript is divided into three mainly distinct part. The first part aims to introduce quantitative phase imaging both in terms of optical systems and of biological applications. The principle of the measurement of the optical phase, not directly accessible with light detectors, will be described. The information one can get with the optical phase measurement will also be covered. Among other, the optical phase measures either fluctuations of subcellular refractive index (linked to the protein and lipid density), or height fluctuations. Given the typical values of refractive index of biological systems (around 1.36-1.38), optical phase imaging systems can measure axial displacements of a few nanometers and can even detect subnanometric axial displacements if the signal can be averaged either temporally or spatially. Chapter 1 principal objective is to give an overview of the history and the current development, applications, and limitations of the field called quantitative phase imaging (QPI). Then, the end of chapter 1 and chapter 2 describe three original optical systems that can detect sub-wavelength axial displacements and to the development of which I have participated. Chapter 2 particularly focuses on two interferomters coupled to a fluorescence path we have built during this PhD project. The first one is a full-field optical coherence tomography (FF-OCT) system and is based on a low coherence Linnik interferometer while the second interferometer, we named, wide-angle differential interference contrast (Wa-DIC) microscope, uses a lateral shearing between the two light polarization states. I will emphasize that despite their apparent simplicity both ystems exhibit technical characteristics close to state of the art QPI systems. The next two parts then mainly focuses on experiments we have performed with

FF-OCT. The second part of this manuscript demonstrates how it is possible to extend the 2-D measurement of the optical phase in cell cultures to the more biologically-relevant (and especially mechanically-relevant) case of 3-D imaging in thick and more complex biological tissues. Although the QPI community and the interferometric tissue imaging (essentially OCT imaging) community are mostly independent and separated, chapter 3 tries to bridge these 2 communities and emphasize the resemblances and differences of both communities favorite techniques. Chapter 3 develops a few startegies and some pitfalls to perform quantitaitve phase measurements in thick tissues. It also presents a few classical examples of phase-sensitive applications to perform elasticity, blood flow, and functional imaging. Interestingly enough, FF-OCT appears as an ideal bridge between QPI and OCT communities since it provides a superior lateral resolution in contrast to most of OCT microscopes. Alternatively, the second part of this manuscript has also been written so that it can also be read as an independent part aiming to describe a multimodal optical platform based on FF-OCT that we have developed during this project. Chapter 4 gives yet another description of FF-OCT, more thorough and tissue-oriented. Besides, it compares technological performances and differences between FF-OCT and usual OCT microscopes. Chapter 4 shows that FF-OCT can advantageously detect subcellular details in tissues and appears as a promising tool to increase performances and simplify histology procedures. Then, chapter 5 describes two additional modalities that we have combined to FF-OCT. The first one is a fluorescence path in a structured illumination microscopy (SIM) configuration that allows for a cellular identification and for a dynamical biochemical information measurement. The third modality is a newly developed technique, named dynamic FF-OCT, that takes advantage of the higher concentration of active molecular displacements in cells in contrast to the extracellular space to emphasize the signal from cells and also obtain a motility-dependent signal. Furthermore, the third and last part of this manuscript is dedicated to two biological applications we have particularly targeted during my project. Chapter 6 aims to describe the eye functioning and to show that the combination of static and dynamic FF-OCT is particularly effective to detect most key features of both the cornea and retina. The very last chapter, chapter 7, aims to describe recent theories of electromechanical propagation of the nervous signal and illustrates how dynamic phase measurements can help verifying such theories. Chapter 7 also presents how quantitative phase imaging, including the systems we have developed, can detect fast optical changes associated with neuronal electrical activity and can ultimately provide a label-free detection tool for neuronal activity.

Behind the scenes: Organization of the manuscript and story of the project

This small section is dedicated to help a reader in the rush to direct his efforts on the essential parts of this quite long manuscript (for the length of which I apologize). The variety of subjects I have been involved in and my (pathological) will to understand everything (and to explain everything!) might have lengthened this manuscript and might distract the reader from whatever is the goal of a PhD manuscript. I also tried to make this manuscript understandable and insightful for scientists of different fields, including optical imaging, acoustics, biomechanics, and neurosciences so that some parts of the manuscript might seem obvious to a few readers. Finally, in this section, I also wanted to add a brief story of the project in order to justify the way I built this manuscript storyline.

Initially, this research project aimed to investigate the existence and the eventual coupling between action potentials and a mechanical wave in active neurons or nerves. For several reasons

described in this manuscript, we believe that action potentials can generate mechanical waves that can co-propagate with them but also that mechanical waves can generate action potentials and neuronal activity. Nevertheless, if the propagation of a mechanical wave along the neurite of a mammalian neuron has been postulated for a long time, it has yet never been observed. Indeed, the amplitude of such mechanical wave is expected to be in the order of 0.1 nanometer. The objective of my thesis was to build a quantitative phase microscope that would be able to detect such mechanical waves and then to try to generate neuronal activity from diverse mechanical stimuli in neuron cultures. After 4 years, I have spent most of my time building optical systems but we have yet not succeed to detect a mechanical displacement in a mammalian neuron (which was supposed to be the very first step of the project!....). We also wanted to push forward the ability to detect mechanical waves in tissues as tissues mechanical parameters are significantly different and we might also expect the detection of a more significant mechanical wave that would be created by a collective effect by thousands of active neurons. To be honest, we also pushed forward the tissue measurements because it is the main specialty of the lab. In any case, in order to have the versatility to work in both cultures and tissues, we have developed an interferometric microscope in a low coherence and in a reflection configuration. We then chose to detect electrical activity from fluorescence probes in order to avoid mechanical contact of patch clamp and therefore to avoid created mechanical artifacts. In short, we have built a multimodal platform combining a low coherence Linnik interferometer (FF-OCT) and structured illumination fluorescence microscopy (SIM). However, if the system is performing well in tissues and in cell cultures, its mechanical and thermal stability is not optimal. For this reason, we decided to build a second, common-path, interferometer we called wide-angle differential interference contrast microscope. Unfortunately, we have not been able to image active neuronal cell cultures with it. In the meantime, we have been quite excited by the development of dynamic FF-OCT in the lab these past years and I have participated actively to its development. Dynamic FF-OCT permits to reveal metabolically-active cells inside a tissue based on the motion of their intracellular scatterers. Especially, the multimodal system I have built was interesting for its superior transverse resolution, which allows to collect more signal and to observe finer dynamics, and for its combination with fluorescence microscopy that enabled us to validate the new contrast seen in dynamic FF-OCT. Alternatively, I have been involved in several other collaborations I will be describing throughout the manuscript, including an important collaboration focusing on the imaging of the eye.

At the end of these intense four years, we have not been able to progress that much on our initial goal but we have explored many other directions. For this reason, I have decided to center my manuscript on the optical detection of sub-wavelength motions in cells, then in tissues and finally introduce a few applications, eventually including our attempts to detect electromechanical waves in neurons and the theoretical models predicting them. Therefore, this thesis and this manuscript have mainly focused on technological development rather than on biological fundamental questions, although I have tried to introduce several biological applications.

To summarize my manuscript in a few sentences, I have mainly develop one microscope, described in chapter 5 that I used for phase measurements in both cell cultures (See chapter 2) and inside tissues (See chapters 4 and 5). Additionally, I have developed two other microscopes to detect sub-wavelength axial displacements that are respectively presented at the end of chapter 1 and at the end of chapter 2. Chapter 1 and chapter 3 mainly present literature reviews of quantitative phase imaging and of optical coherence tomography respectively. In an attempt to control the length of this manuscript, I decided to sweep the traditional introductory chapter on optical

imaging to appendix A. Finally, chapter 6 presents the functioning of the eye and the imaging of it with our multimodal microscope and chapter 7 focuses on the functioning of neurons and the possible existence of electromechanical waves to propagate the action potentials.

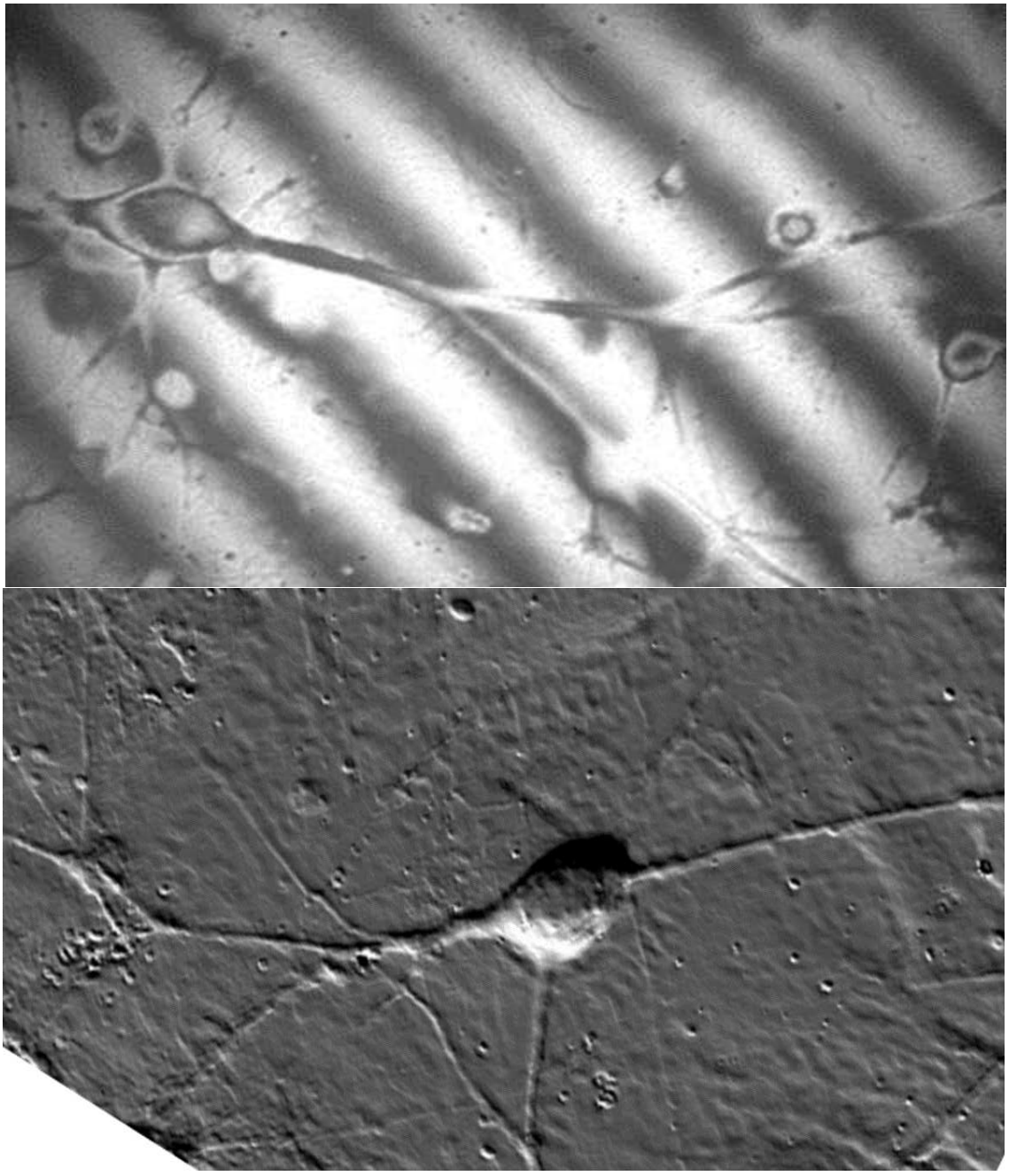

Phase imaging of neurons. *The two images show hippocampal neuron cultures as captured with quantitative phase microscopes we have designed*

Part I

Following nanometric deformations in cell cultures: Quantitative Phase Imaging

As discussed in this manuscript introduction, optical imaging seems to be the most promising technique to dynamically observe subcellular displacements in cells in their close environment. Nevertheless, the diffraction limit imposes a resolution on the order of the optical wavelengths, between 400 nm and 1μm, which is often insufficient to detect most of the subcellular displacements. If several super-resolution techniques have been developed and have become very popular these past few years, they often impose making a compromise between resolution and acquisition speed. The most sensitive techniques also require the use of external fluorophores and the use of high-intensity illuminations. In a different approach, quantitative phase imaging (QPI) aims to measure the optical phase variation caused by the delay the light encounters when going through a cell.

As illustrated in figure 1, a quantitative phase measurement can be thought as a time measurement in which the time lag between a reference beam and a sample beam (passing through a cell for example) produces an intensity difference. The time lag is often expressed as a difference of optical path between the two beams. The optical path represents the product between the refractive index, *i.e.* inversely proportional the relative speed of light in the medium, with the propagation distance in this medium.

$$\delta = n * d_{\text{propagation}} = \frac{c}{v_{\text{milieu}}} * d_{\text{propagation}} \tag{1}$$

The principle of phase imaging is to measure sub-wavelength variations in optical path length via the intensity variations. Indeed, optical detectors are sensitive to the square root of the field amplitude and not to the complex field (in contrast to other imaging modalities like acoustics). As it will be discussed in chapter 1, QPI can easily access sub-wavelength axial sensitivity, even though the phase is averaged over a diffraction-limited pixel (as illustrated by figure 1 C and D) Interestingly, phase measurements are also used in ultrasound and MRI (but are named time-of-flight measurements) to recover an axial information with more accuracy that which could be obtained with the diffraction limit.

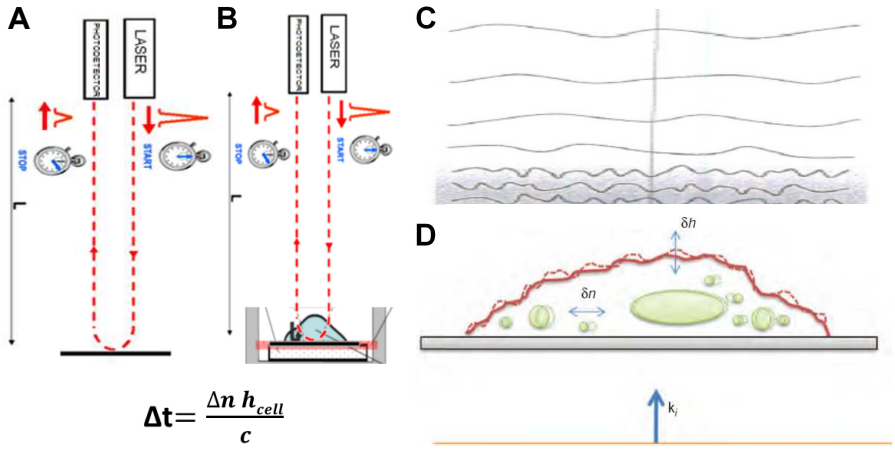

Figure 1 – Principle of quantitative phase imaging. Panel A and B illustrate the time-of-flight equivalent of QPI. It measures the phase difference or time-of-flight difference between a beam that is simply reflected on the mirror and a beam that goes through an object before being reflected. The time difference depends on the object height and the refractive index difference between the object and the surrounding medium. **Panel C and D** show the wavefront distortion in the near-field caused by the local variations of the cellular refractive index. Nevertheless, when imaged in the far-field, the high frequencies of wavefront distortion are averaged out so that the phase measurement is finally diffraction limited.

Nevertheless, phase imaging is particularly complicated in optics because light travels at extreme speed and the refractive index is usually below 0.1. For example, for a cell of 10 μm and refractive index difference of 0.1, the time-of-flight difference is 3.10^{-15}s, a difference that is far too small to be measured by any current photodetector. To be able to record such small time differences, one requires a conversion process, which in the present case is optical interference and is a nonlinear process that generates some issues that will be developed in chapter 1. The first part of this manuscript will begin by introducing the history and the main systems and applications of QPI systems in chapter 1. In this chapter, I will also discuss the ultimate sensitivity of QPI and discuss different configurations, as well as decoupling procedures to extract a height or a refractive index information from the phase signal. Next, in chapter 2, I will illustrate the QPI procedure from the direct image acquisition to the final phase image and I will present two multimodal QPI systems that we have developed during my thesis. Each of the systems performances will be demonstrated with several examples captured over the years of my project on cell cultures. Applications of our QPI systems, especially on activity-related phase changes in neuronal cultures will be presented in chapter 7.

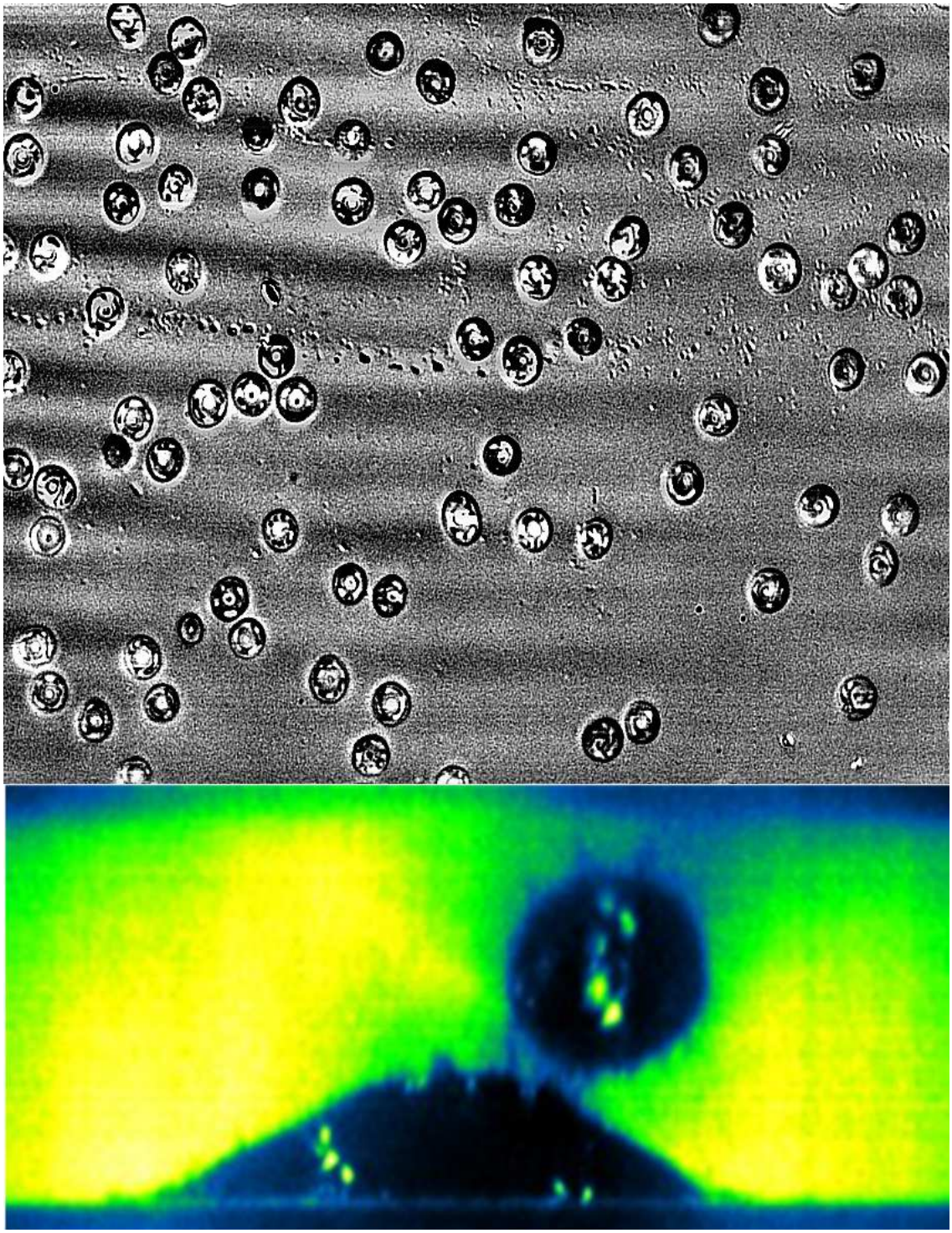

This is my blood. *The top image is a quantitative phase image of my own red blood cells. The bottom image illustrates the last part of chapter 1 presenting fluorescence exclusion microscopy.*

CHAPTER 1

Optical detection of nanometric deformations in cell cultures: Quantitative Phase Imaging

Table of contents

1.1 First experiments in Phase Imaging **16**
1.2 Quantitative phase imaging (QPI) today **18**
1.3 Sensitivity in QPI **23**
1.3.1 Spatial averaging and phase sensitivity 24
1.3.2 Phase sensitivity and noise behavior 25
1.3.3 Transmission versus reflection interferometry 29
1.4 Decoupling refractive index variations from height changes **31**
1.4.1 General decoupling procedures 33
1.4.2 Measuring the refractive index of the external medium 34
1.4.3 Dry Mass measurement 34
1.5 QPI main biological applications **36**
1.6 A new tool for refractive index/height decoupling: Fluorescence exclusion . . . **38**
1.6.1 Physically constrained fluorescence exclusion 40
Basic principle 40
Expected sensitivity 42
1.6.2 FxM theoretical framework 45
1.6.3 FxM numerical model 47
1.6.4 Measuring refractive index maps 50
1.6.5 Future developments in fluorescence exclusion 50

In this chapter, I will first introduce the history of phase imaging, and some of the most popular systems, as well as more modern systems, current challenges, and applications. I will then derive the ultimate phase sensitivity of quantitative phase imaging systems in a unique and general manner. I will also introduce some decoupling procedures to extract the height information from the phase signal. Finally, I will introduce a new technique named fluorescence exclusion microscopy that is similar to quantitative phase measurement. It also allows an independent accurate height measurement that can be used in parallel with a QPI system in order to provide a measurement of refractive index maps. Except for the last part, this chapter will essentially serve as an introduction to the next chapter, in which I describes two original QPI systems that I developed during my PhD. Additional applications of QPI will be found in chapter 7, in which I will return to our initial idea of tracking neuronal activity using mechanical deformations.

1.1 First experiments in Phase Imaging

As noted in the introduction and in appendix A, optical detectors can only measure intensity differences so that an object of complex transmittance $t_{obj}(x,y)e^{i\phi_{obj}(x,y)}$ gives an intensity transmission $T = |t_{obj}|^2$. This coefficient mainly depends on the object scattering and absorbing properties. For weakly scattering or weakly absorbing samples, which is often the case of single cell layers, a small signal decrease has to be detected over a large high intensity and low-frequency background, which provides a low contrast. Nevertheless, a quite typical way of enhancing the contrast is to remove background intensity. It has been applied to microscopy as early as the 1850s, either using *oblique* illumination or dark field microscopy [4], which blocks the incoming light to only look at the light scattered by the sample. It is quite intuitive since this *oblique* illumination is directly inspired by astronomy, in which the moon and the planets can be observed at night as they reflect light from the sun. Albeit, direct sunlight during the day would have prevented reflected light to be detected. In a quite general manner, the light scattered by a sample is the product between its scatterers cross-section and the Fresnel coefficient calculated either in transmission or reflection. Therefore, the total scattered intensity scales at best as $(\frac{n_{obj}-n_{medium}}{n_{obj}+n_{medium}})^2$. As expected it is quite weak for most biological objects that display refractive indices in the 1.35-1.38 range. Therefore *oblique* or dark field microscopy has to be performed with cameras that are sensitive to a small number of photons and might be complicated to implement in practice.

On the other hand, an imaging strategy based on the optical phase measurement would give a linear dependency of the signal with the refractive index difference and might exhibit small variations while an intensity-based measurement would produce a negligible signal. A first approach to create a phase-based contrast is not surprisingly known as phase contrast microscopy. It was developed by *F. Zernike* in the late 1930s [5] using the interference-based image formation theory, developed by *E. Abbe* between 1873 and 1910 [6]. In this theory, and under coherent illumination, the image formation can be written as the interference between the spatial average of the field U_0,

and its spatial fluctuation component U_1 (coming from light scattering and absorption) [7]:

$$I(x,y) = |U(x,y)|^2 = |U_0|^2 + |U_1(x,y)|^2 + 2|U_0|.|U_1(x,y)|.cos(\Delta\phi(x,y)) \tag{1.1}$$

Where $|U_0|^2$ is largely dominant in brightfield microscopy and is blocked in dark field microscopy. From equation 1.1, we can foresee another issue, which is that the cosinus of the phase difference is not sensitive to small phase variations. To emphasize the interference term and the small phase variations, F. Zernike had the brilliant idea to replace the illumination blocker of dark field microscopy (which lies in the objective back focal plane) by a thin metal film that not only attenuates the zero-order component of the field by t, but also creates a phase variation α. In the case of a weakly scattering object, a medium zero-order attenuation a and a $-\frac{\pi}{2}$ phase shift (*i.e.* optimal operating conditions in phase contrast microscopy), the total intensity becomes:

$$I(x,y) = I_{Ill}.(a^2 - 2a.t_{obj}(x,y)sin(\Delta\phi(x,y))) \simeq I_{Ill}.(a^2 - 2a.t_{obj}(x,y).\Delta\phi(x,y)) \tag{1.2}$$

which creates a linear dependency with phase variation in the case of small phase variations. Nevertheless, phase contrast microscopy is not *quantitative*, since the sinus function is only linear in a small region of small phase variations, which is more or less valid on small structures such as axons or dendrites, but starts to fail on cell somas.

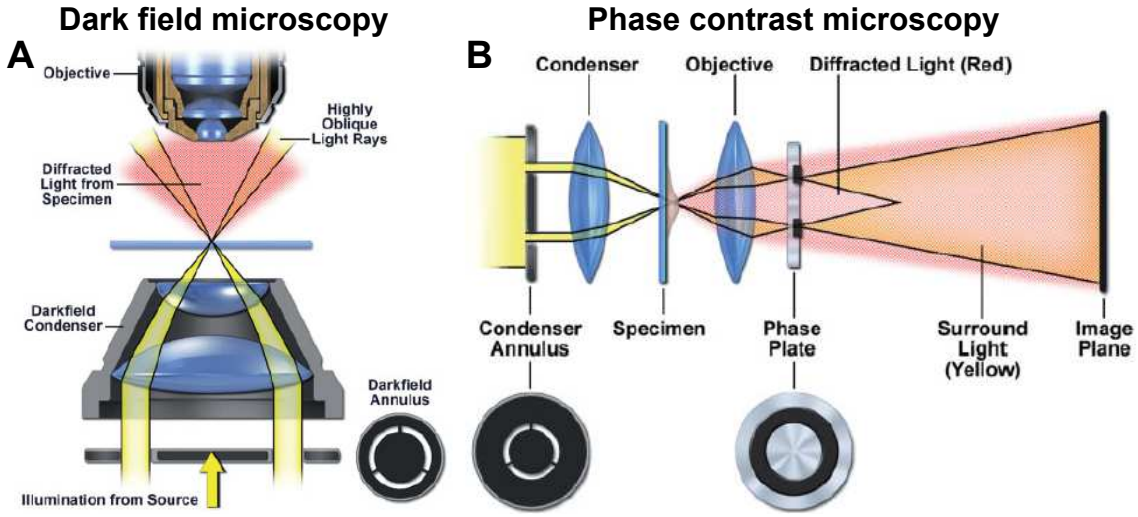

Figure 1.1 – Principle of dark field and phase contrast microscopies. Panel A illustrates the principle of dark field or oblique microscopies, in which the sample is illuminated by a light that can not be captured by the detection objective so that only scattered light can be imaged on the detector. **Panel B** shows the strategy of Phase contrast microscopy. In this case, the sample is also illuminated by a side beam, that can here be captured by the detection objective. Instead of rejecting the incident beam, a conjugate phase mask is inserted in the detection objective back focal plane, in order to attenuate and shift the phase of the incident beam. Therefore, the detector captures the interference between the incident and scattered intensity with a linear phase dependency for small phase shifts. Both panels have been taken from chapter 7 of *D.Murphy*'s book [8].

The second historical and common solution to generate a phase contrast is known as differential interference contrast (DIC) and was developed by *G. Nomarski* in 1952 (Patent in 1952, and first associated publication in 1955) [9, 10]. Its principle is to separate the incident light into two polarizations, to create a small transverse spatial shift between the two polarizations, and recombine

them so that they interfere with a phase difference corresponding to the spatial phase derivative along the axis of the shift. If we neglect polarization effects, *e.g.* polarization dependency of the scattering coefficient, or of refractive index, and if we assume a homogeneous separation between the two polarizations, we can record the following intensity:

$$I(x,y) = 2|U_0|^2(1 + cos(\frac{\partial\phi}{\partial x}.h)) \tag{1.3}$$

with h, the local thickness of the object. Similarly to phase contrast microscopy, the optimal sensitivity to small phase (and small phase derivative) variations is obtained by shifting the phase by an additional $\frac{\pi}{2}$. For this reason, modern DIC commercial systems are often equipped by a *De Sernamont* compensator which consists of adding a polarizer, a quarter wavelength retardation plate, and an analyzer [10, 11]. It allows cancellation of the zero-order background (filtered by the analyzer) and adds a constant $\frac{\pi}{2}$ phase shift between the two polarizations. Therefore, the intensity can be written as:

$$I(x,y) = 2|U_0|^2 sin(\frac{\partial\phi}{\partial x}.h) \simeq 2|U_0|^2\frac{\partial\phi}{\partial x}.h \tag{1.4}$$

in the small phase gradient approximation, assuming the spatial shift has been introduced along the x direction. Nevertheless, DIC is only linear over a small bandwidth of phase derivatives. It can only access phase gradient along one direction and it is sensitive to polarization artifacts. More details on DIC microscopy can be found in the next chapter, as one of the interferometers we have developed is quite similar to DIC.

So far, we have seen two optical techniques that can reveal a contrast based on the object phase map. They both had a large impact in biology as they authorized the visualization of multiple small transparent objects without the need for an external probe. Nevertheless, these techniques are not quantitative in the sense that the relationship linking the intensity and the phase map is not linear and can not be inverted for most of the phase values. The next section is dedicated to the history of development and characterization of microscopes that can provide such a quantitative phase map measurement.

1.2 Quantitative phase imaging (QPI) today

Although many optical interferometers have been developed since the 1950s [9, 12] and have been followed by the development of holography that also accesses the phase [13], these systems have mainly been used for revealing biological objects or for assessment of surface flatness. To my knowledge, the first quantitative phase measurement of biological objects was proposed as early as 1951-1952, with the pioneering work of *Davies & Wilkins* [14] and followed by *R.Barer* [15] to measure cell thickness, dry mass and volume. They measured the phase change created by a cell and by measuring the small phase difference that occurs when the cell is exposed to a different solution [16]. Interestingly, phase measurements as accurate as a few nanometers were already available using visual color determination in white light DIC microscopes for example [17]. Nevertheless, the term quantitative phase imaging emerged at the beginning of the 1990s with the development of digital cameras that can accurately record small intensity differences and accurately measure phase difference from intensity changes. Here also, quantitative phase systems have mainly been used for metrology [18] and biomedical purposes [19]. Some of the first quantitative phase microscopes for biomedical imaging were developed in low coherence and scanning configurations, probably inspired by techniques developed for the rapidly growing field

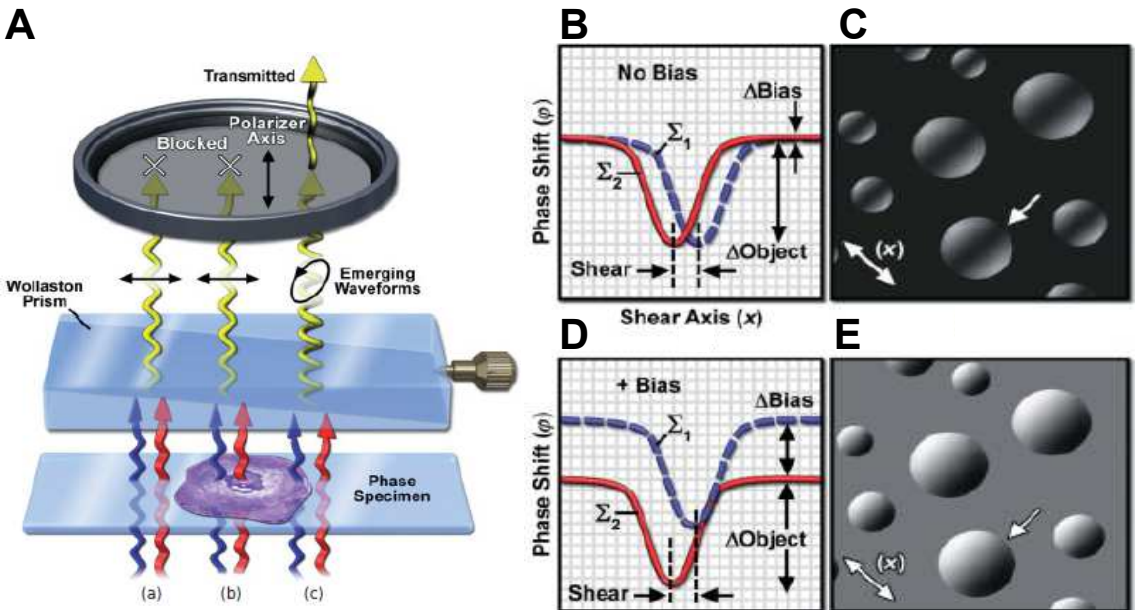

Figure 1.2 – Differential Interference Contrast (DIC) microscopy principle. Panel A shows the principle of the technique. A first Wollaston prism in the linearly polarized illumination path splits the illumination into two adjacent beams of orthogonal polarization. In the detection path, a second Wollaston prism recombines the two beams into a beam with the initial linear polarization unless of the two polarizations have been retarded by passing through a phase object, creating an elliptical beam that can go through the analyzer and be detected by the camera. **Panels B to E** illustrate the interest of adding a quarter-wave plate in the detection path (panels D and E), to shift the phase difference of $\frac{\pi}{2}$, and become linear to small phase gradients. Panels C and E represent DIC images of oil droplets with or without the quarter-wave plate, and panels B and D the profile along the shear axis and along the droplet. All images have been adapted from chapter 10 of *D. Murphy*'s book [8].

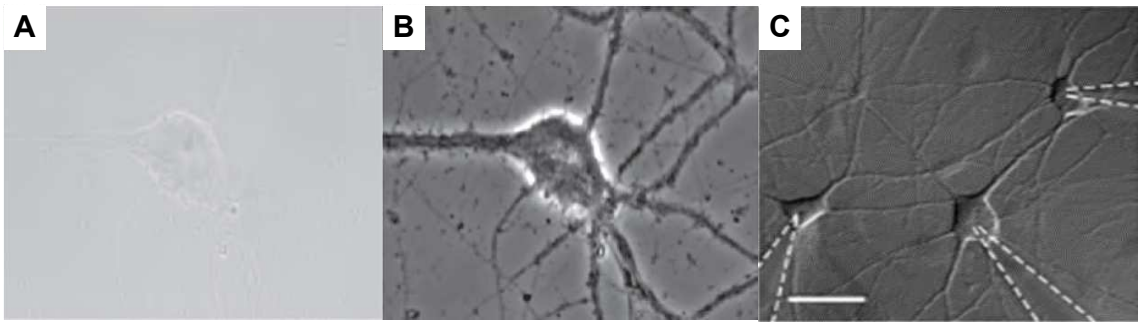

Figure 1.3 – Different phase contrast strategies for label-free neuron imaging. Panel A shows a bright field image of a neuron, while **panel B** shows its corresponding Zernike phase contrast and **panel C** its differential interference contrast (DIC) image. These images have been adapted from *G. Popescu* 's book [7].

of Optical Coherence Tomography (OCT) [20, 21] and were later applied to cell imaging [22, 23]. In the meantime, full-field quantitative phase microscopes were developed using an introduced defocus [24] or by linearizing phase maps obtained with standard phase microscopes such as DIC [25]. Quantitative phase imaging really became popular in application to biological measurements around 2005 with the development of digital holography microscopy [26], Fourier phase microscopy [27] and all the associated techniques. Nowadays, dozens of QPI techniques have been developed

and hundreds to thousands of articles have been published on the subject, that I can obviously not all describe here. The mainstream in the QPI field is to use full field QPI microscopes in which the entire field of view is acquired at the same time. Nevertheless, whatever other characteristics each of them might have, the ultimate phase sensitivity of any QPI system at a given pixel is ultimately controlled by the number of interfering photons, which is quite similar from one system to another. Additionally, in an attempt to compare the different existing systems, *Gabriel Popescu and colleagues* have defined four main performances and classified full-field QPI systems into four corresponding categories [7], while an optimal QPI system combines all of the four main abilities:

- **Off-axis interferometry** represents the main class of QPI systems that enables single shot phase acquisition and therefore present the interest of displaying an optimized acquisition rate, only limited by the camera frame rate. Off-axis interferometry includes off-axis digital holography (DHM) [26], heterodyne digital holography [28], Hilbert Phase Microscopy [29] or any system exhibiting a high spatial frequency of its fringe patterns. Off-axis measurements allow for single shot extraction of both amplitude and phase maps using adequate processing in the Fourier space. The off-axis configuration mainly enables the shift of an incoherent low-frequency noise from a high frequency coherent signal (due to the presence of interference fringes) in the Fourier space. This large shift permits the accurate separation of the interference signal from the background noise but also allows for the amplitude and phase separation [30]. Recently, it has been additionally demonstrated that off-axis geometry can perform super-resolution imaging [31] by rotating the angle between the two beams to fill a higher part of the Fourier space than what is normally allowed by the diffraction limit (similarly to structured illumination microscopy as it will be presented in chapter 5).

- **Phase shifting interferometry** represents the class of systems that require several frames to measure a phase map by successively changing the optical path difference by a controlled amount. Here again, it will be extensively presented in the next chapter, as the two interferometers I built are phase-shifting systems. The optical path difference can be easily modulated with phase modulators in polarization interferometers [32,33] or in an OCT configuration, in which the reference arm position can be translated by a piezo [20,21]. Phase shifting interferometers are logically slower than single shot interferometers but usually offer higher spatial resolution, since no operation in Fourier space is required. Indeed, in Fourier space, the high spatial frequencies usually have low SNR, and can, therefore, be averaged out using numerical treatments. In the case of off-axis digital holography, phase shifting is often performed to accurately clean the zero order component, and recover the full extension of spatial frequencies in the first order [28].

- **Common path interferometry** represents the class of QPI systems in which the reference and sample arms propagate within approximately the same physical path. It can be performed using polarization interferometers in which the two arms are simply the two orthogonal polarizations (like DIC microscopy). Another solution is to use low NA interferometers with the reference arm role played by the glass coverslip above or below the sample [22]. Finally, classic common path QPI systems can be obtained by separating the zero and first order of a signal simply diffracted by the object and shifting one of the two, as in Fourier Phase Microscopy [27] and Diffraction Phase Microscopy [34]. Common path interferometry is really important to eliminate mechanical noise or any other external noise. Because QPI systems are very sensitive to optical path variations, they are also very sensitive to any sort of noise, such as temperature fluctuations (which modulate the refractive index)

or mechanical vibrations (that elongate one arm with respect to the other) so that the phase signal fluctuates a lot over time, reducing the actual sensitivity of the interferometers. In contrast, common path interferometers, are temporally stable since these fluctuations have similar effects on both arms and do not account for phase difference variations.

- **Low coherence interferometry** represents the class of QPI systems operated in a low coherence configuration, such as white light interferometry [35, 36]. In the context of phase measurements in cell cultures, the low coherence configuration allows for the suppression of speckle noise (originating from all the light reflections inside the setup) that creates a random phase fluctuation between adjacent pixels, which prevents detection of spatial correlations in the measurements or at least adds some spatial noise between adjacent pixels. The low coherence can be either temporal using spectrally-extended sources or spatial using spatially-extended sources. However, the low coherence imposes a high number of modes, so that simple filtering becomes complicated. For example, phase contrast microscopes and most off-axis digital holography microscopes require coherent light to efficiently filter the zero order component. I will discuss in the next part different configurations of low coherence interferometry, which is also used to create optical sectioning in the depth of a scattering tissue and is at the basis of OCT technology.

In addition to these four categories, we can mention two other popular categories of systems that, as for me, do not fit in any of these previous four classes. The first category includes the non or self-interferometric QPI systems based on a local wavefront measurement. If a plane wave is incident on a cell, the local wavefront is deformed accordingly to the shape of the cell. This modification of the wavefront can also be interpreted as an angular shift, with an initial wave vector being transformed into several wave vectors tilted from the original one, whose angle depends on the phase delay, and more precisely on the phase gradients. Phase gradient maps from weakly scattering objects have been successfully measured from these local wavefront distortions using several strategies. The first phase gradient measurement based on wavefront estimation was performed by voluntarily applying a defocus above and below an object to measure its axial phase gradient [24,38] obtaining 3 images (one without defocus). In this case, the transport-of-intensity equation states that the axial derivative of the intensity depends on the phase gradient, which can mathematically calculated. Alternatively, a 2-D high-resolution wavefront sensor can be directly used instead of a camera to emphasize the mutual interference between the nonscattered field and the scattered field (quadriwave lateral shearing interferometry [39]). Finally, a quatrefoil (or partitioned) tube lens can be used to split the image into four different parts on the camera. It allows measuring lateral shifts in the tube lens plane (conjugated to the sample or camera plane) corresponding to an angular shifts in the sample plane. The lateral shift is estimated by gauging the intensity balance between the 4 sub images (partitioned detection aperture [40]). Many other similar techniques could be cited to illustrate gradient-based phase measurement using angular shift detection, including the ones allowing measurements in thick scattering tissues [41, 42]. All these techniques can only compute phase gradient maps [1], but all are common path, single shot and can usually be performed in low coherence design. Nevertheless, features like lateral resolution or the field of view (or both), have to be sacrificed in favor of the single shot ability.

Finally, the sixth and last category of QPI systems represents tomographic QPI systems. The basic idea is to use reconstruction algorithms similar to the ones used in X-ray or MRI imaging

[1] Note that phase maps can be numerically computed from 2-D phase gradient maps and one reference point by integration, in the Fourier domain for example [25]

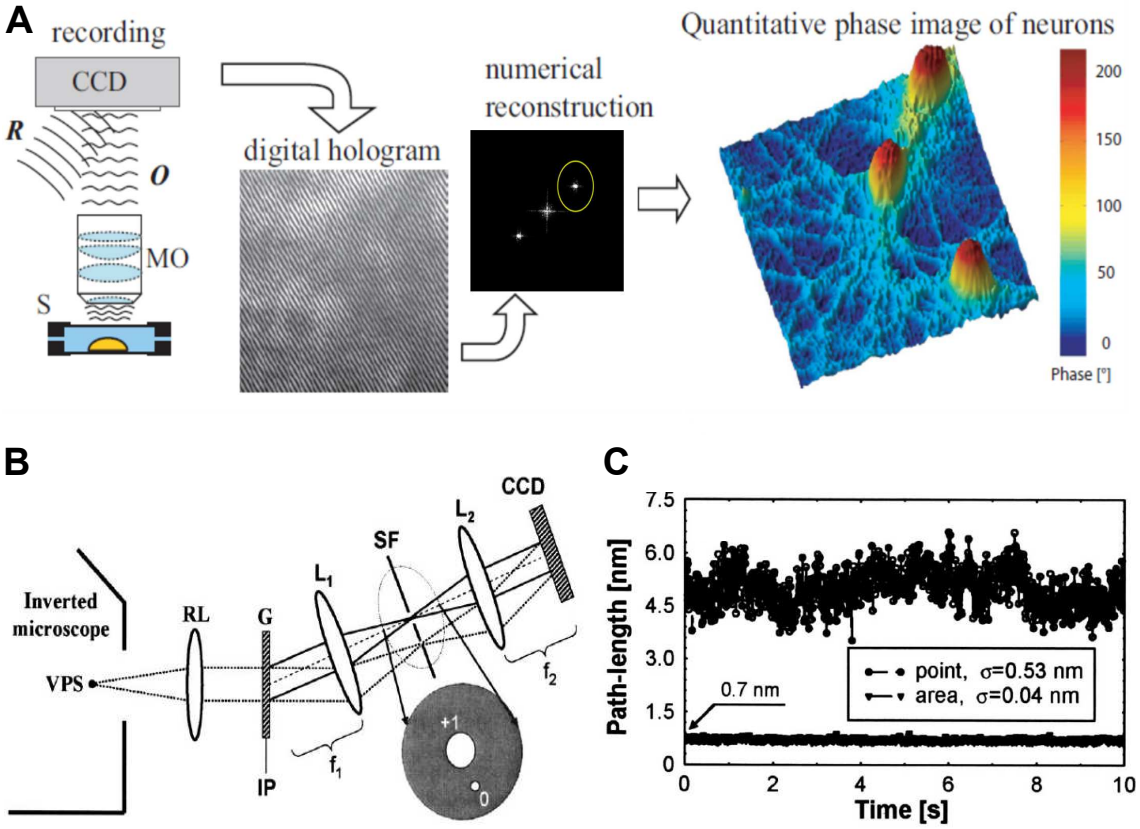

Figure 1.4 – Example of two modern QPI strategies. Panel A presents the principle of digital holography microscopy (DHM). A numerical hologram (or interferogram) between a sample arm phase shifted by an object and a tilted reference arm is recorded on a 2-D camera [26,30] at a controlled distance from the object plane. The phase can be numerically reconstructed by selecting the $+1$ order within the Fourier transform of the signal, and by propagating the signal in the Fresnel approximation [30]. Panel A has been modified from [37]. **Panel B** presents the principle of diffraction phase microscopy [34]. The signal from a standard widefield transmission microscope illuminates a transmission grating placed in the object plane that diffracts the scattered light in the first diffraction order (high spatial frequencies) and the unscattered light (low spatial frequency) in the zeroth order. An additional physical spatial filter is added in the grating Fourier plane to filter out out-of-focus light and the multiple orders of diffraction. Finally, the first and zeroth order interfere in an off-axis configuration enabling the single shot reconstruction enabled by Hilbert transform [29] or similar algorithms to those used in DHM [30]. **Panel C** illustrates the extreme phase stability in common-path interferometers (diffraction phase microscopy here [34]) either in a single shot or on a homogeneous sample free region.

that use similar angles to reconstruct a 3-D view of a sample, in this case, named optical diffraction tomography. By acquiring several 2-D phase maps of the sample under different angles, it similarly becomes possible to reconstruct the 3-D refractive index distribution of the sample, as illustrated in figures 1.5 C and D. In mathematical terms, the imaging process can only access limited frequencies in the direction of the light propagation (see Annex A), which prevents the objects localization in 3-D. Nevertheless, by changing the direction of the light propagation (or the object orientation), the k-space can be filled in all directions and axial localization can be performed. The first intuitive possibility to change the angle is to physically rotate the sample by rotating the holder [43] or the cell using an optical trap [44]. Interestingly, it can be shown that it is equivalent to changing the illumination angle, although only a more limited extension of angles is accessible, which offers a much more practical configuration [45, 46]. Optical diffraction tomography can be extended from the cases of the weak phase approximation (not valid for cells larger than a few microns) using the

Rytov approximation valid in the low phase gradient approximation and is independent from the sample thickness [47]. Finally, phase tomographic imaging can be performed in weakly scattering thick samples using low coherence systems by integrating the phase while changing the focus from one side of the sample to another [48].

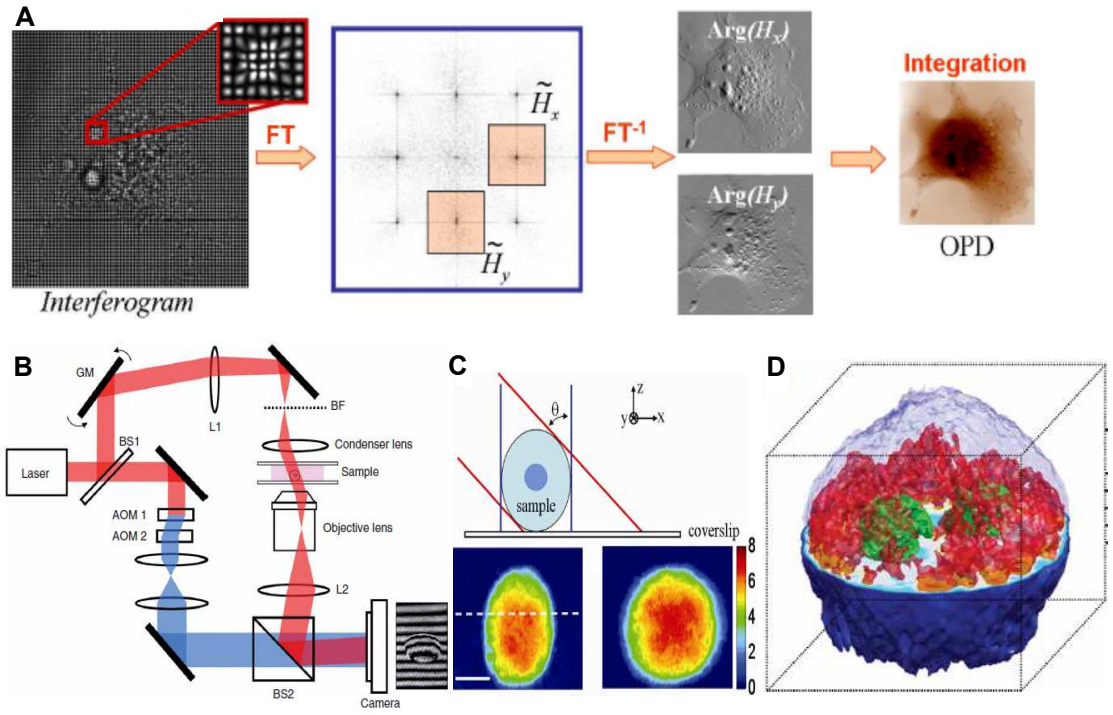

Figure 1.5 – Two other examples of modern QPI systems. Panel A presents the principle of quadriwave lateral shearing interferometry based on high-resolution measurement of the wavefront in the sample plane using a modified Shack-Hartman [39]. When Fourier transformed, two spatial components of the wavefront measurement can be extracted and inverse Fourier transformed to recover the phase gradients along the two transverse dimensions. An additional integration step from a phase reference point enables the reconstruction of the sample phase map [39]. **Panels B to D** present an example of a tomographic QPI system, called tomographic phase microscopy [45]. The setup consists in a Mach-Zehnder interferometer with the camera placed in the sample plane with a varying sample beam orientation controlled by a galvanometric mirror (Panel B). The phase is measured for each different incident angle (Panel C, from the supplementary data of *W.Choi et al.* [45]) and corresponds to the projection along these different angles. A numerical reconstruction based on the inverse Radon transform allows the reconstruction of the 3-D refractive index map of the sample [45], here of a HeLa cell (Panel D).

To summarize these two sections on the various phase imaging and quantitative phase imaging systems that exist, we have seen how diverse they are, and how competitive this field has become. So far, biological applications of QPI have been voluntarily omitted but they will be described in section 1.5. As I will show in the next section, sensitivity of full field QPI systems mainly depends on camera performance showing that the system design is not the most important feature at the end.

1.3 Sensitivity in QPI

If phase imaging has mainly been developed to create a contrast in cells with low absorption and low scattering, it also exhibits an extremely high axial resolution. Indeed, phase imaging aims

to transform axial information into an intensity measurement, which, thanks to highly sensitive detectors, can provide sub-wavelength axial sensitivity, ultimately down to a precision of a few picometers. To my knowledge, sensitivity of all QPI systems is similar or at least controlled by similar parameters. In this section, I will derive the phase sensitivity of phase imaging systems, and give main parameters to be controlled to increase it. I will discuss the notion of phase sensitivity in terms of corresponding motion, and will finally compare reflection and transmission interferometers in terms of axial sensitivity to displacement. Ultimately, I will demonstrate that QPI systems are limited by the number of interfering photons that are averaged to produce a given measurement. Before going further down, we can notice that even if we focus here on microscopy, the theory of quantitative phase imaging is largely scalable, and the same physics principle is in play in large interferometers such as VIRGO and LIGO, which aim to detect gravitational waves. For a popularization physics conference, I created a graph to roughly compare experimental sensitivities of our microscopic interferometers with the VIRGO interferometer, as illustrated in figure 1.6.

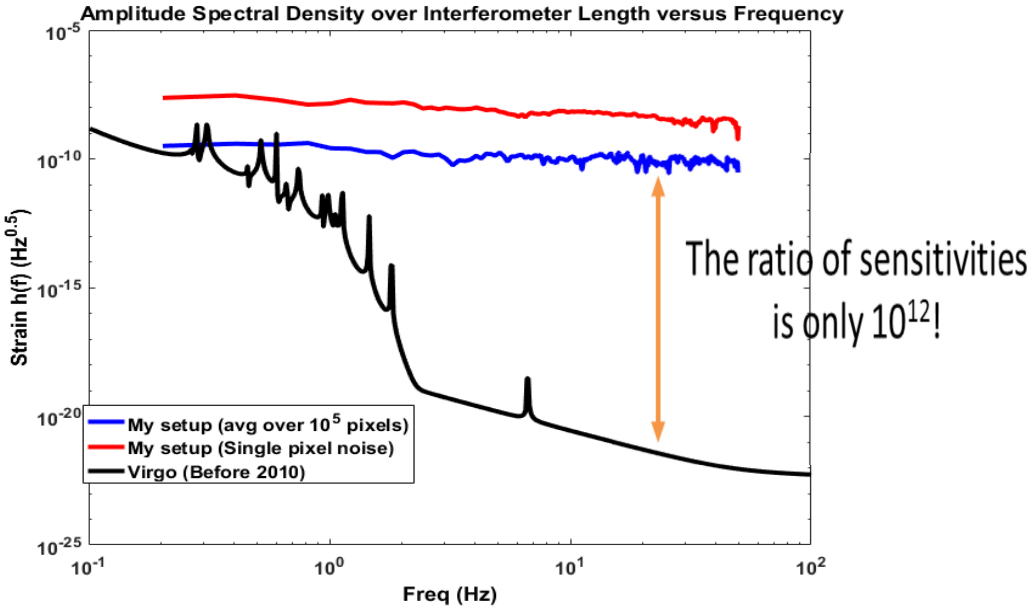

Figure 1.6 – Comparison between VIRGO's and our systems' sensitivities. The strain calculated as the square root of the power spectral density divided by the length of the interferometer arms is plotted in the case of one typical QPI system (without spatial average in red, and with an average over 10^5 pixels in blue) and in the case of the VIRGO experiment (black line).

While not being a flattering comparison for my QPI systems, all these experiments are shot-noise limited, although the number of interfering photons is tremendously high in large-scale interferometers giving access to much higher sensitivities, that are increased further by complex processing. Indeed, QPI systems are limited by the maximum power that can be sent onto the cell, and by intrinsic mechanical and temperature fluctuations that arise from live cell imaging. Nevertheless, we can expect common-path QPI system sensitivity to be fairly constant over frequency, which is not true for the VIRGO experiment that does exhibit similar sensitivity to QPI systems at low temporal frequencies.

1.3.1 Spatial averaging and phase sensitivity

On first encountering QPI, it might be quite confusing to hear about picometer axial sensitivity, when the size of an atomic bond is on the order of 150 pm. The aim of this subsection is to give

a qualitative understanding of the physical meaning of QPI phase sensitivity and to demonstrate that QPI systems are not that powerful to measure the fluctuations of electronic bonds. First, QPI measurements are often expressed in terms of the optical path difference that corresponds to $\Delta n \Delta h$, with Δn around 5.10^{-2} for most biological objects, so that sensitivity to height changes is reduced to a few nanometers single shot[2]. However, caution has to be taken as it corresponds to height sensitivity and not to axial resolution. First, phase measurements correspond to the phase average over one voxel size, which is ultimately controlled by the diffraction limit in all three dimensions. Additionally, the phase measurement can possibly be modified by any phase object in the light path between the illumination objective and the detection objective, even though its influence is convolved by the system PSF and therefore attenuates as these objects are further away from the image plane. Finally, as it will be detailed within the next subsection, the phase sensitivity directly depends on the square root of the number of detected photons, so that accurate phase measurements can only be performed when billions of photons arrive at the detector during one exposure time. It is quite logical that a single photon cannot reach an axial phase sensitivity lower than the wavelength and the diffraction limit, even with a perfect detector. Nevertheless, by sending and detecting many photons, the average position of the object can be localized with a much higher accuracy[3]. Therefore, picometer sensitivities can be reached because they correspond to a transverse spatial average measurement and to the probing of many different electronic states of a metallic network within optical detectors' exposure times (which are much slower than typical oscillation times of electron clouds).

1.3.2 Phase sensitivity and noise behavior

In this subsection, I will calculate the phase sensitivity as a function of the camera parameters and as a function of the noise in a quite general form. Although a few similar phase noise calculations can be found [18, 49, 50], I will try to estimate the phase noise for perfect but also nonperfect imaging conditions, and with as few approximations as possible, which I could not find properly written in any article. Interestingly, the phase noise I calculate here is general enough to be valid both in QPI and phase-sensitive phase imaging. First, let us define the intensity and the contrast of an interferogram:

$$I = I_{Ref} + I_{Sample} + I_{inc} + 2\sqrt{I_{Ref}.I_{Sample}}cos(\phi) \tag{1.5}$$

which we can rewrite with incoming intensity I_0, arriving onto the interferometer beamsplitter, and reflection coefficients R_{Ref}, R_{sample} and R_{inc}, respectively standing for reference mirror reflectivity, backscattering coefficient coming from the interfering part of the sample, and for the sum of all non-interfering reflections coming from either optical elements, or non-interfering parts in the sample arms.

$$I = I_0.(R_{Ref} + R_{sample} + R_{inc}) + 2.I_0.\sqrt{R_{sample}R_{Ref}}.cos(\phi) \tag{1.6}$$

[2]Nevertheless, if we consider fluctuations at the surface of an object around a central value, the optical path difference is proportional to $n_{medium}.\Delta h$. Similarly, if we consider spatial or temporal averaging, a direct height sensitivity below a few hundred picometers can be measured.

[3]Note that it could be compared to super-localization in fluorescence microscopy, with the PSF maximum that can be localized with an accuracy depending on the square root of the number of photons.

Therefore, we can calculate the contrast of the interferogram:

$$C = \frac{I_{max} - I_{min}}{I_{max} + I_{min}} = \frac{4.I_0.\sqrt{R_{sample}R_{Ref}}}{2.I_0.(R_{Ref} + R_{sample} + R_{inc})} \tag{1.7}$$

Equation 1.7 helps us to rewrite equation 1.6 as a function of the mean intensity and of the contrast:

$$I = I_0.(R_{Ref} + R_{sample} + R_{inc}).(1 + C.cos(\phi)) \tag{1.8}$$

With $I_0.(R_{Ref} + R_{sample} + R_{inc}) = I_{mean}$, the mean intensity captured by the detector. We can also calculate the maximum intensity, that we choose to be as close as camera saturation as possible:

$$I_{max} = I_{mean}.(1 + C) \tag{1.9}$$

so that we can write the intensity as a function of I_{max} and the contrast:

$$I = I_{max}.\frac{1 + C.cos(\phi)}{1 + C} \tag{1.10}$$

In the case of a shot-noise limited experiment, the standard deviation σ_I of the intensity can be written, assuming the contrast is low enough so that even minimum intensity variation is shot-noise limited:

$$\sigma_I = \sqrt{FWC}.\sqrt{\frac{1 + C.cos(\phi)}{1 + C}} \tag{1.11}$$

where FWC is the camera full well capacity, which is the maximum number of photons a pixel can capture in a single exposure time without saturating. σ_I depends on the phase map. At this point, we can try to derive the standard deviation of the phase accessible using only direct intensity, which is equivalent to the estimation of the intensity standard deviation increase due to a phase change. We can first write:

$$cos(\phi) = \frac{I(1 + C) - I_{max}}{C} \tag{1.12}$$

From equation 1.12, we can use the propagation of uncertainties [51], which states that the variance of a function of independent Gaussian variables (in this case, the shot-noise limited intensity, which may be approximated as a Gaussian) can be expressed as the sum of the partial derivatives of the function over the different variables multiplied by their variance. Standard deviation is then calculated by taking the square root. Applied to the case of a cosine, we obtain the phase standard deviation σ_ϕ:

$$\sigma_\phi.|sin(\phi)| = \sigma_I.\frac{1 + C}{C} \tag{1.13}$$

We can see that, without phase modulation, the standard deviation of either the phase or the intensity depends on the local phase, and is therefore spatially inhomogeneous, which can be intuitively understood. Indeed, since the shot noise is proportional to the intensity, the intensity standard deviation will be more important close to maxima and less important in the vicinity of minima. On the other hand, we expect the intensity standard deviation variation to a phase change to be more intense in the linear part of the cosine, and almost negligible close to the maxima and minima. Therefore, we expect a random phase variation to create an intensity standard deviation which depends on a sinusoidal pattern with a doubled frequency, which can be provided by the

$|sin(\phi)|$ of the above equation.

Now, we expect that phase shifting will enable the calculation of a phase map and of an amplitude map that are homogeneous within the field of view. We will derive the calculation in the case of a 4 phase algorithm to estimate the phase sensitivity of our systems, as it will be described in chapter 2. In this case, the phase map can be calculated as:

$$\phi = atan(\frac{I_4 - I_2}{I_1 - I_3}) \tag{1.14}$$

where ϕ is the local phase, which depends on spatial position (x,y), and on time, which we have not displayed for the sake of readability. Intensities $I_{I=1..4}$ respectively correspond to the intensity calculated with an external phase shift of respectively 0, $\frac{\pi}{2}$, π, and $\frac{3\pi}{2}$. We will neglect for now the sample phase variation happening during the 4 phase modulation, even though an overview of the artifacts it will create will be presented in section 5.2.3. From equation 1.10, we can write the two intensity difference terms:

$$I_4 - I_2 = 2I_{max}\frac{C}{1+C}sin(\phi) \tag{1.15}$$

And,

$$I_1 - I_3 = 2I_{max}\frac{C}{1+C}cos(\phi) \tag{1.16}$$

By using the propagation of uncertainties again [51], and noticing that the derivative of the arctangent function is: $atan(x)' = \frac{1}{1+x^2}$, we can write:

$$\begin{aligned}\sigma_\phi &= \sigma(\frac{I_4 - I_2}{I_1 - I_3}).\frac{1}{1+(\frac{I_4-I_2}{I_1-I_3})^2} \\ &= \sigma(\frac{I_4 - I_2}{I_1 - I_3}).\frac{1}{1+tan(\phi)^2}\end{aligned} \tag{1.17}$$

Moreover, assuming all the measurements to have independent noise (which is supposed to be the case for shot noise), the covariance of two intensity measurements is equal to 0, and we can write:

$$\sigma(\frac{I_4 - I_2}{I_1 - I_3})^2 = (\frac{I_4 - I_2}{I_1 - I_3})^2.(\frac{\sigma^2(I_4 - I_2)}{(I_4 - I_2)^2} + \frac{\sigma^2(I_1 - I_3)}{(I_1 - I_3)^2}) \tag{1.18}$$

And,

$$\sigma^2(I_4 - I_2) = \sigma^2(I_4) + \sigma^2(I_2) \tag{1.19}$$

$$\sigma^2(I_1 - I_3) = \sigma^2(I_1) + \sigma^2(I_3) \tag{1.20}$$

Finally, we can express the different intensities standard deviation, in the shot noise approximation as:

$$\sigma^2(I_1) = I_1 = I_{max}.\frac{1 + C.cos(\phi)}{1+C} \tag{1.21}$$

and so on for the different intensities, so that we obtain:

$$\frac{\sigma^2(I_4 - I_2)}{(I_4 - I_2)^2} = \frac{I_{max}.\frac{2}{1+C}}{4I_{max}^2(\frac{C}{1+C})^2 sin^2(\phi)} \tag{1.22}$$

$$\frac{\sigma^2(I_1 - I_3)}{(I_1 - I_3)^2} = \frac{I_{max}.\frac{2}{1+C}}{4I_{max}^2(\frac{C}{1+C})^2 cos^2(\phi)} \tag{1.23}$$

Hopefully, this calculation is soon coming to an end. By injecting the above equations back into equation 1.18, we obtain:

$$\sigma^2(\frac{I_4 - I_2}{I_1 - I_3}) = \frac{2}{I_{max}}.\frac{1+C}{C^2}.\frac{1}{4}.(\frac{1}{sin^2(\phi)} + \frac{1}{cos^2(\phi)}) \tag{1.24}$$

with:

$$\frac{1}{4}.(\frac{1}{sin^2(\phi)} + \frac{1}{cos^2(\phi)}) = \frac{1}{4sin^2(\phi)cos^2(\phi)} = \frac{1}{sin^2(2\phi)} \tag{1.25}$$

Coming back to equation 1.17, and calculating the square root of equation 1.24, we obtain:

$$\sigma_\phi = \frac{1}{1+tan^2(\phi)}.\sqrt{\frac{2.tan^2(\phi)}{sin^2(2\phi)}}.\frac{1}{\sqrt{FWC}}.\frac{\sqrt{1+C}}{C} \tag{1.26}$$

Noting that $\frac{1}{1+tan^2(\phi)} = cos^2(\phi)$, that we can inject in the square root to reach the following equation:

$$\frac{1}{1+tan^2(\phi)}.\sqrt{\frac{tan^2(\phi)}{sin^2(2\phi)}} = \sqrt{\frac{cos^2(phi)sin^2(phi)}{sin^2(2\phi)}} = \frac{1}{2} \tag{1.27}$$

Finally, the phase noise can be written as a rather simple equation:

$$\sigma_\phi = \frac{1}{\sqrt{2}}.\frac{\sqrt{1+C}}{C}.\frac{1}{\sqrt{FWC}} \tag{1.28}$$

with no further dependency of the initial phase map, as illustrated in figure 1.7.

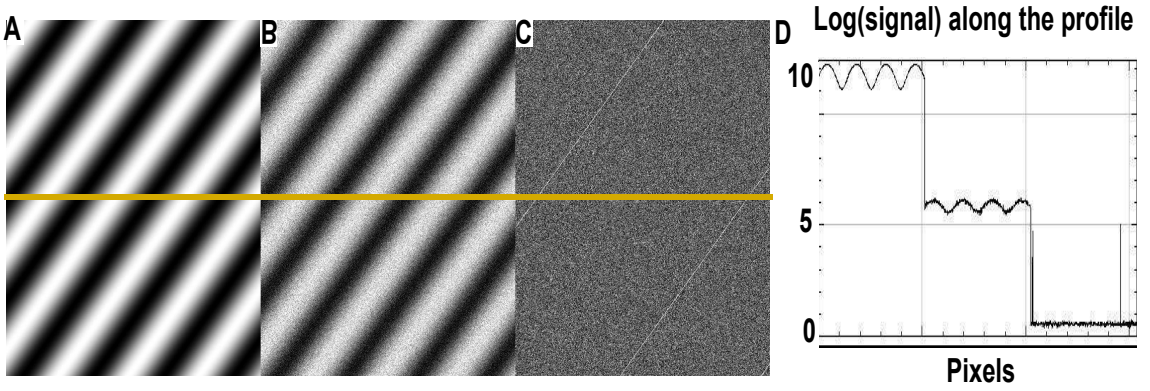

Figure 1.7 – Shot noise effect in QPI measurement. Panels A and B show a typical simulated fringe pattern that could be obtained in one shot in a QPI system (panel A), and its corresponding standard deviation due to shot noise (panel B). The standard deviation of the intensity depends on the initial phase map since the shot noise depends on the square root of the intensity. **Panel C** shows the standard deviation of the phase map reconstructed from a 4 phases process, with the same number of images, showing no dependency on the initial phase map, as predicted by equation 1.28. Except for high noise lines caused by phase wrapping (wherever the phase shifts from 2π to 0), the phase noise is extremely low, as illustrated by **panel D** that plots the log of the intensity along the yellow line crossing the 3 different images.

Additionally, we can write the standard deviation of the optical path:

$$\sigma_\delta = \frac{\lambda_0}{2\sqrt{2}\pi}.\frac{\sqrt{1+C}}{C}.\frac{1}{\sqrt{FWC}} \tag{1.29}$$

which we plotted in figure 1.8. For a contrast of 0.5 and an FWC of 1,600,000 electrons, the noise on the optical path is as low as $\frac{\lambda}{4000}$, corresponding to 136 pm in only 4 acquisitions. Interestingly, because these measurements are shot noise limited, the only limitation to consider is the total number of photons that are averaged to produce a given measurement. This number can be increased by averaging either temporally or spatially, and the noise will decrease accordingly with the square of the number of measurements. In summary, we can write:

$$\sigma_\delta = \frac{\lambda_0}{2\sqrt{2}\pi}.\frac{\sqrt{1+C}}{C}.\frac{1}{\sqrt{N_{pixels}FWC}} \tag{1.30}$$

with N_{pixels}, the number of averaged pixels, either spatially or temporally. Note that a single picometer resolution can then be obtained by spatially averaging over a 10x10 pixel area, and by temporally averaging over 10 images, still under the assumption of no spatial or temporal inhomogeneity.

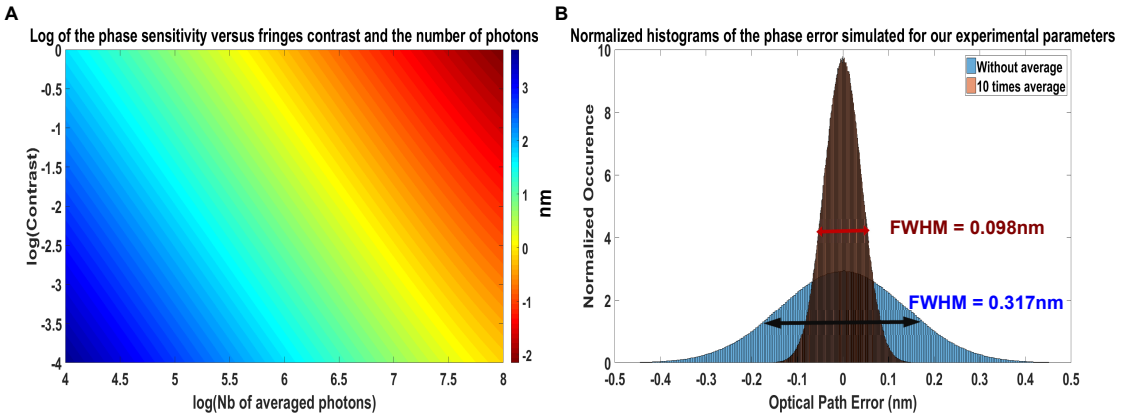

Figure 1.8 – Phase sensitivity versus contrast and the number of captured photons. Panel A is a 3-D plot representing the logarithm of the numerically calculated optical path sensitivity due to shot noise calculated on intensity images in a 4 phase process versus the fringe contrast in the vertical axis and the number of captured photons in the horizontal axis. The optical path sensitivity ranges from 1μm for a low contrast of 10^{-4} and low FWC of 10^4 to 10 pm for a high contrast close to 1, and a high effective FWC (10^6 photoelectrons with a 100 hundred pixels average for example). **Panel B** shows the optical path histogram for a similar simulation with a contrast of 0.5, and an FWC of 10^6 in single (four frames) shot (blue histogram), and a 10 pixels average (red histogram). The full width half maximum (FWHM) of the blue histogram is calculated to 317 pm, leading to the standard deviation of the Gaussian process of 135 pm, remarkably close to the value theoretically calculated above. Additionally, the red histogram FWHM is measured at 98 pm, about $\sqrt{10}$ lower than the blue histogram FWHM, as predicted by equation 1.30.

1.3.3 Transmission versus reflection interferometry

While most QPI systems work in transmission, the two interferometers we have developed have the originality of working in reflection. We chose this configuration for its compactness, and for versatility to work either in cells or in scattering samples if operated in low coherence configuration. Additionally, when working with cell cultures, reflection interferometers still offer the possibility

to work either in transmission-like mode, mainly capturing the light reflected by the coverslip, or in reflection mode, isolating the backscattering signal coming from the cell scatterers [52], as illustrated in figure 1.9. The transmission configuration has the advantage of having a high reflection coefficient in comparison to the low backscattered signal from the cells. Ideally, the transmission configuration authorizes to match the reflectivity of the reference and sample arms. We have grown cell cultures on the same silicon wafers that we used in the reference so that we have observed high interference fringes contrast up to 0.6. Nevertheless, the transmission configuration can only measure an integrated phase information, as light has traversed the entire cell height[4]. On the other hand, the reflection configuration enables the measurement of 3-D information of the scatterer positions inside the cells. It can especially measure cell topography, but measures much smaller signals from the sample arm. The phase sensitivity is supposedly smaller. However, in the reflection configuration, phase changes directly measure axial displacements, while refractive index changes alter the backscattered amplitude. In contrast, the transmission configuration measures the optical path of the cell, and the axial displacement is multiplied by the refractive index difference, which is often small. Therefore, in terms of axial sensitivity, it is not obvious to find which configuration is better. Such an estimation is the aim of this subsection.

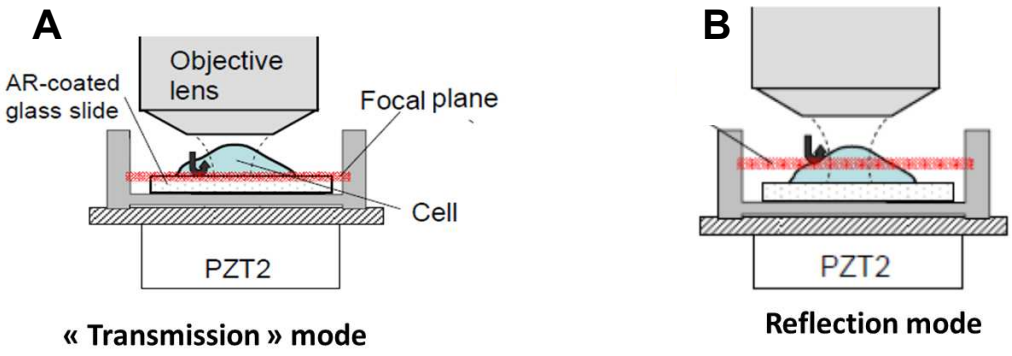

Figure 1.9 – Imaging possibilities for a reflection microscope. **Panel A** illustrates the transmission-like configuration in which the focal plane lies on the glass coverslip on which the cells have grown [52]. This configuration integrates the phase twice over the entire cell, in a local way only if the depth of field is larger than the cell. **Panel B** shows the classic reflection mode where the signal backscattered by the cell is measured.

Let us first consider the transmission-like configuration, since we can easily estimate axial sensitivity:

$$\sigma_{h,Trans} = \frac{1}{2}.\frac{\sigma_\delta}{\Delta n} \tag{1.31}$$

Using equation 1.28, axial sensitivity can be derived further:

$$\sigma_{h,Trans} = \frac{\lambda_0}{4\sqrt{2}\pi}.\frac{\sqrt{1.6}}{0.6}\frac{1}{\Delta n\sqrt{FWC}} \tag{1.32}$$

Let us now look at the sensitivity in the reflection configuration:

$$\sigma_{h,Refl} = \frac{1}{2}.\frac{\sigma_\delta}{n} \tag{1.33}$$

[4]We should add that the transmission configuration is locally sensitive only to phase changes happening within the depth of focus. For large cells, the phase fluctuations coming from depths above the depth of field are integrated on sections larger than a single pixel size.

This time, however, contrast is supposedly much smaller than 0.6 and should depend on the refractive index difference. To estimate the contrast, we will take a simple case of the reflection at the surface of the cell, neglecting the thin lipidic membrane, and simply estimating the back reflection caused as the light goes from a medium of index n_{medium} to the intracellular medium n_{Cell}. Therefore, we can estimate the reflection coefficient at the cell surface from the Fresnel coefficients under the approximation of small angles and without considering polarization effects:

$$R_{Cell} = |\frac{n_{Cell} - n_{medium}}{n_{Cell} + n_{medium}}|^2 = (\frac{\Delta n}{n_{medium} + 0.5\Delta n})^2 \tag{1.34}$$

Now trying to estimate contrast from the reflection coefficients, we can write:

$$C = \frac{I_{max} - I_{min}}{I_{max} + I_{min}} = 2\sqrt{R_{Cell}.R_{Ref}}R_{Cell} + R_{Ref} + R_{inc} \tag{1.35}$$

again for the sake of simplicity, we first estimate that the dominant intensity, and therefore the dominant reflection coefficient, comes from the reference, so that we neglect the reflection from the cell, which is often a decent approximation, but also the reflection on all the optical elements, and the camera noise, which we will discuss further on. In this case, we can write the contrast as:

$$C = 2.\frac{R_{Cell}}{R_{Ref}} \tag{1.36}$$

With $R_{Ref} \simeq 23\%$ in our experiments, using a silicon wafer in the reference arm. Because Δn is weak, on the order of 3.10^{-2} to 5.10^{-2}, R_{Cell} is on the order of 0.1%, and C on the order of 0.1, so that we can approximate $\frac{\sqrt{1+C}}{C}$ by $\frac{1}{C}$. The contrast formula can finally be written:

$$C \simeq |\frac{\Delta n}{n_{medium} + 0.5\Delta n}| \tag{1.37}$$

Finally, the axial sensitivity in reflectivity can be expressed as:

$$\sigma_{h,Refl} = \frac{\lambda_0}{4\sqrt{2}\pi}.\frac{n_{medium} + 0.5\Delta n}{\Delta n}.\frac{1}{n_{medium}\sqrt{FWC}} \tag{1.38}$$

And,

$$\sigma_{h,Refl} \simeq \frac{\lambda_0}{4\sqrt{2}\pi}.\frac{1}{\Delta n.\sqrt{FWC}} \tag{1.39}$$

This is slightly better than transmission but quite similar. However, reflection from the surface below the cell adds a 4% coefficient in the incoherent signal that lowers the useful FWC, and the corresponding height sensitivity. Finally, it does not impact too much the final sensitivity when the same reflecting surface is used in both the reference arm and the sample arm in transmission-like configuration. For most of our experiments, we used the transmission-like configuration with cells growing on silicon wafers.

1.4 Decoupling refractive index variations from height changes

Phase imaging can be extremely sensitive to measure a time delay of some fraction of the light versus another part. However, it is hard to know whether this time delay comes from a large

change in the local speed of light on a small path, or from a smaller change in the speed of light, but happening on a longer path. For example, a visible light beam will propagate for the same period of time in 1.33 mm of air and in about 1 mm of water. Yet, it is of major importance to carefully separate these two variables in order to characterize the biological importance of physical changes imaged with QPI. A local change in the speed of light, measured with the refractive index, will tend to be related to the propagation through an aggregate of variable density of proteins or lipids. For example, it can reveal a transiting vesicle, organelles, denser parts of a cell, or even membrane reorganizations. Conversely, if the refractive index remains constant, a phase change relates to a height change of the imaged object. For example, it can reveal membrane flickering in red blood cells [53] or a direct mechanical compression [54]. Finally, a phase change may originate from a change of both properties, that sometimes evolve in opposite directions. For example, cell swelling, which, in the case of hypotonic shock, consists of water uptake to balance the cell osmolarity, is characterized by a volume increase and by a refractive index decrease (due to the intracellular material dilution) [55]. In total, the cell phase signal decreases during a water uptake, since the refractive index change is more important than the height change [5].

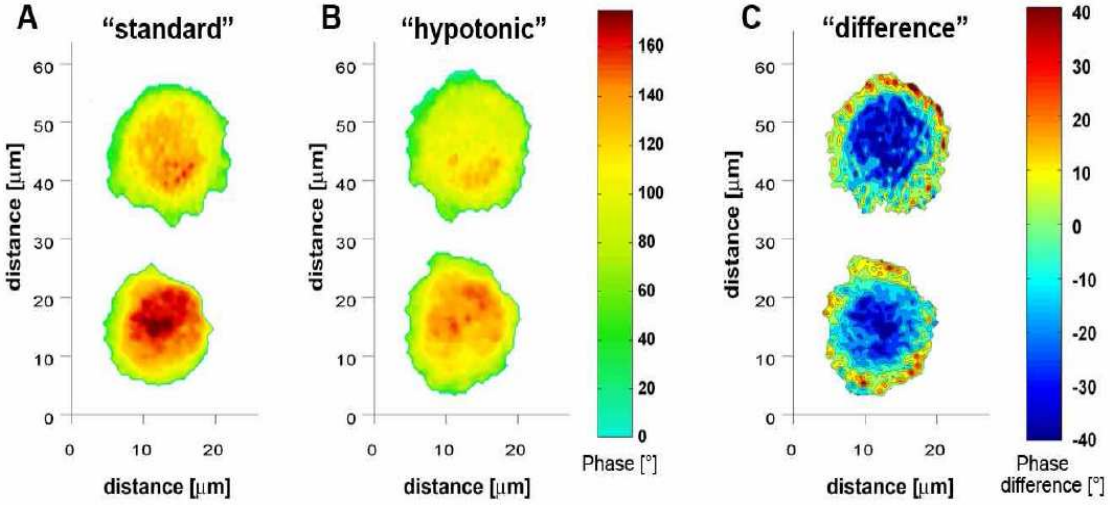

Figure 1.10 – Phase imaging of cell swelling. Panels A and B show phase maps of two neuron cell bodies acquired with digital holographic microscopy before (panel A) and after (panel B) a hypotonic shock [55]. **Panel C** emphasizes the phase difference between panel B and A, and illustrates that the cell swelling has increased the cell volume (area at least, with positive phase difference at the cell edges), while the total phase has decreased, indicating a refractive index decrease, which has also been validated using a decoupling procedure [55].

To be able to unambiguously decouple the refractive index difference, *i.e.* the difference in the speed of light, from the length of the medium light has traveled trough, two independent measurements of varying heights or refractive indices are required. Many strategies have been imagined over the years, even though they often impose heavy constraints. In the following section, I present some of the most popular decoupling procedures and, finally, I detail one of these techniques we contributed to the development of during this project. Next, to quantitatively measure the local refractive index of a cell, the careful measurement of the refractive index of the medium should be performed, and I will provide a brief description of how we accomplished it.

[5] Indeed, we can expect the refractive index to depend on the total volume of water that went through the cell, while the height should depend on the volume to the power of one third.

I will also emphasize the use of dry mass measurements, which corresponds to the intracellular mass of everything but water and can be obtained without a decoupling procedure.

1.4.1 General decoupling procedures

In QPI, the phase difference $\Delta\phi$ is measured, imposing a coupling between the local refractive index difference and the local height [6]:

$$\Delta\phi(x,y,t) = \frac{2\pi}{\lambda_0}.(n_{Cell}(x,y,t) - n_{medium}).h_{Cell}(x,y,t) \tag{1.41}$$

From equation 1.41, we can imagine different strategies to decouple the refractive index difference from the height. The first quite intuitive possibility that has been developed in 2005 is to perform a rough independent height measurement using confocal fluorescence microscopy in parallel with the phase measurement [56]. A similar approach consists of determining the height of a cell in suspension by measuring its diameter and assuming a spherical shape [57]. A second different approach is to perform two independent phase measurements, by replacing the extracellular medium by another medium of the same osmolarity but of different refractive index [55]. If we note $OPL_1 = \frac{2\pi\phi_1}{\lambda_0}$ and OPL_2 the two optical path length difference measurements performed with the extracellular media of refractive index n_{medium} and $n_{medium} + \delta n$, we can write [55]:

$$n_{Cell} = \frac{\delta n.OPL_1}{(OPL_1 - OPL_2)} + n_{medium} \tag{1.42}$$

And,

$$h_{Cell} = \frac{(OPL_1 - OPL_2)}{\delta n} \tag{1.43}$$

We can also mention an ingenious development of this technique preventing the need of the extracellular medium change, and permitting real-time live cell decoupling measurements. The group of *P.Marquet* has developed a dual-wavelength digital holography microscope, and an approach that consists of adding an absorbing dye to the extracellular medium so that the refractive index is also drastically modified at the vicinity of the absorption peak of the dye [7] [58]. Therefore, the phase measured at both wavelengths allows probing two significantly different extracellular medium refractive indices and using a similar reconstruction (as the one shown in equation 1.43) of both cell height and cell refractive index.

Finally, a more recent and more popular approach has been the development of 3-D QPI systems enabling direct calculation of the refractive index tomography of a cell, using numerical reconstruction after measuring the object phase under several angles, as discussed in section 1.2 [43,45]. Using such approaches, it becomes possible to reconstruct a 3-D volume with local variations of refractive index difference and with local height of the cell.

[6] We can add here that the variation of $\Delta\phi$ over time (or its spatial variation as well) enable eliminating the medium refractive index measurement:

$$\frac{\partial\Delta\phi}{\partial t} = \frac{2\pi}{\lambda_0}.\frac{\partial n_{Cell}}{\partial t}.h_{Cell} + n_{Cell}.\frac{\partial h_{Cell}}{\partial t} \tag{1.40}$$

[7] When deriving refractive index from Maxwell's equations, and when considering resonances to explain absorption peak, there is a theoretical and experimental coupling between the increase of the imaginary part of the refractive index (absorption), and its real part(leading to a phase change).

1.4.2 Measuring the refractive index of the external medium

Most of decoupling procedures cited above require careful measurement of the extracellular medium refractive index, which is not trivial, even though many commercial refractometers can be found nowadays [59][8]. Unfortunately, having no such commercial system at the Institute, nor the money to buy a 10 k$ system, we extracted an old *Pulfrich refractometer* (designed in the 1930s) out of one of the ESPCI darkest rooms, as illustrated in figure 1.11. The Pulfrich refractometer principle is fairly simple and based on the total reflection angle measurement at the interface between a liquid medium of an unknown refractive index and a cubic glass prism of a precisely pre-calibrated refractive index. The illumination is parallel to the glass prism so that the maximal output angle corresponds to the angle of the light illuminated by the critical angle θ_{crit} for which:

$$sin(\theta_{crit}) = \frac{n_{medium}}{n_{glass}} \tag{1.44}$$

The output light beam then reaches the side face of the prism with an angle $\theta_{crit} + \frac{\pi}{2}$, and exits in air towards the detector through the angle θ_{exit}:

$$sin(\theta_{crit} + \frac{\pi}{2}) = cos(\theta_{crit}) = \frac{sin(\theta_{exit})}{n_{glass}} \tag{1.45}$$

Combining the two equations 1.44 and 1.45 squared, we obtain the medium refractive index:

$$n_{medium} = \sqrt{n_{glass}^2 - sin^2(\theta_{exit})} \tag{1.46}$$

The output angle can be measured using a rotating telescope, and a Vernier scale to reach a sub-milliradian angle precision, permitting the measurement of refractive index on the order of 10^{-3}. Of course, the accuracy depends on the precision of the parallelism of the incoming light beam, which is performed by illuminating the medium with a divergent beam (using a standard LED in our case), so that many illumination angles reached the samples. The output angle θ_{exit} is therefore measured by taking the first angle at which the light becomes detectable. Calibration steps and measured values are voluntarily not displayed here, but the measured refractive index values have been used for the refractive index calculation performed in the next section.

1.4.3 Dry Mass measurement

In addition to the decoupling procedure, QPI measurement can directly access a physical property of the cell, known as dry mass, which more or less corresponds to the mass of everything but water (such as lipids, DNA, RNA, proteins) in a cell. It has been demonstrated that QPI measurements can estimate the dry mass of an object by calculating the integral of the phase signal over the entire cell area [60]. As introduced in appendix A, a mammalian cell mass is mainly controlled by its water content (about 70% of the total cell mass). When confluent cells are dried up to a point (generally 130°) where there is no water left, the mass of the cell has, quite logically, decreased to the dry mass. Obviously, such a method is quite invasive, and tracking the evolution of dry mass, over time and notably over cell cycles had remained a very challenging task before the development of QPI-based dry mass measurements [60, 61]. For more information about live cell mass profiling, using either QPI, or micro-resonator channels, the thorough review from *T.Zangle and M. Teitell* can be consulted [62]. To my knowledge, the first dry mass measurement using

[8]Interestingly, it was mainly pushed forward by the alcohol industry to control sugar concentration and fermentation process non-invasively

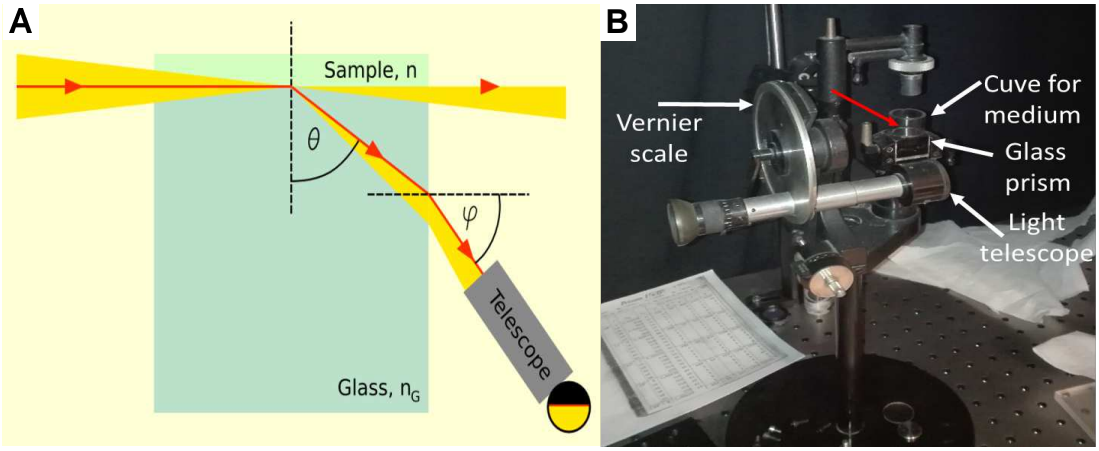

Figure 1.11 – Principle of Pulfrich refractometer. Panel A illustrates its principle. A parallel light beam illuminates an interface between a sample of unknown refractive index and a glass prism of calibrated refractive index. The minimum angle at which light becomes detectable corresponds to the critical angle from which the medium refractive index can be computed. **Panel B** shows the Pullfrich refractometer we found in the lab.

modern QPI systems has been performed by *G.Popescu and colleagues* [60], who were inspired by the pioneering work from *R.Barer* [15] and *Davies & Wilkins* [14] in 1952. Such measurements rely on the assumption that cells are a homogeneous mix of only water and a homogenous mix with a refractive index depending on dry mass concentration inside the cell. Therefore, using the Maxwell-Garnett theory permitting the derivation of a mean cellular refractive index dependent on the mass concentration of nonaqueous material inside the cell

$$\mathrm{n_{eff}} = (\mathrm{n_{DM}} - \mathrm{n_{medium}}).\frac{V}{V + V_0} + \mathrm{n_{medium}} \tag{1.47}$$

With V, the volume of non-aqueous material, and (V + $\mathrm{V_0}$), the total cell volume. By introducing a coefficient α, equal to the refractive index evolution with the dry mass concentration $\frac{dn}{dC}$, and assuming that change in refractive index due to nonaqueous material is mainly controlled by lipids, it becomes possible to rewrite the equation 1.47 as a linear relationship between the refractive index difference and the dry mass concentration C:

$$\mathrm{n_{eff}} = \mathrm{n_{medium}} + \alpha.\mathrm{C} \tag{1.48}$$

Dry mass concentration only relates to an average measurement and might be inaccurate for example with an increase of nucleic acid concentration [62] or with a change of the lipid organization. Neverthless, dry mass measurements advantageously benefit from several extensive accurate measurements of the coefficient α, representing the linear coefficient linking a refractive index increase with a protein refractive index. Interestingly, and over many thousand proteins [63], the protein refractive index increment (α) distribution is a nice Gaussian curve exhibiting a low standard deviation [9]. The average α is 0.19, and less than 1% of the proteins have α coefficient below 0.18, or above 0.20. Measurements of the whole cell α coefficient give values around 0.19 $(g.m^{-3})^{-1}$ [62,65]. By further calculating the integral of the phase shift over the entire surface of a cell, and using equations 1 and 1.48 gives:

[9] It has been demonstrated that the far-field optical response of proteins does not depend on the 3-D structure of the protein, but mainly depends on its amino acid composition [63,64], which is relatively similar from one protein to another, explaining the gaussian curve and the low standard deviation.

$$\int_A \Delta\Phi.\mathrm{d}S = \frac{2\pi}{\lambda}.\int_A \Delta n(x,y)h(x,y)\mathrm{d}S = \frac{2\pi}{\lambda}.\int_A \alpha C(x,y).h(x,y)\mathrm{d}S \tag{1.49}$$

This last integral being the definition of the total dry mass of a cell, this quantity can be directly calculated from a phase map:

$$\mathrm{m_{Cell}} = \frac{\lambda}{2\pi\alpha}\int_A \Delta\Phi\mathrm{d}S \tag{1.50}$$

We can also add, that a local mass parameter σ, named dry mass surface density, can also be easily locally computed on subregions inside the cell. The interest of both of these parameters will be emphasized in the next section that focuses on the biological applications of QPI.

1.5 QPI main biological applications

If phase contrast and DIC microscopies have revolutionized the label-free detection of cells and intracellular details, QPI is expected to revolutionize label-free cellular biological detection as well, since it enhances the detection of finer subcellular structures and detect their 3-D (re-)organization over time while it can also detect many physical parameters out of the phase signal, such as dry mass, biomechanical properties, or transmembrane water movements. As a label-free technique, QPI is nonspecific, which makes any specific signal of interest hard to extract from global complex biological fluctuations happening at various time and space scales. On the other hand, QPI presents no photobleaching, and low phototoxicity, authorizing imaging times ranging from millisecond to weeks [61, 66, 67]. Moreover, QPI can access sub-wavelength information with a transverse resolution ranging from a few hundred nanometers to a few centimeters [31, 68, 69]. Therefore, QPI is able to track the evolution of hundreds of cells in parallel for days [66]. Many biological parameters and studies have been conducted at the interface between optical labs and biology labs. Nevertheless, these techniques have yet hardly been transferred to biology labs and hospitals, despite their promising results being accumulated for about 15 years. This section aims at reviewing some of the most popular and most promising biological applications of QPI, which here again summarizes hundreds of papers that I can not all describe. More details about biological applications can be found in extensive QPI reviews and books ([7, 70, 71] for example):

- **Red blood cell membrane (RBC) fluctuations:** It is by far the most studied system in QPI with several potential biological and medical applications that have been found. The red blood cell membrane fluctuations, often referred to as membrane flickering, are an important subject of interest in biophysics, and have been quite well characterized over the years. The interest for QPI is that the amplitude of fluctuations are on the order of 10 to 100 nm, which is small enough to require the sub-wavelength sensitivity of QPI but which is large enough to produce an easily detectable phase signal. As a first approach to RBC membrane fluctuations, it was simply considered as a thermal fluctuation of the membrane layer, *i.e.* a sort of Brownian motion of a geometrically constrained layer [72]. The amplitude of membrane fluctuations are particularly high in the red blood cells, as their cytoskeleton is less rigid than other mammalian cells, and their membrane can fluctuate more freely. In fact, and as a further refinement, the influence of RBC cytoskeleton has proved to be nonnegligible on the membrane fluctuations, and RBCs have proved to be a model system for low-order interaction between cytoskeleton and membrane mechanics [53, 73, 74]. Interestingly, QPI analysis of membrane fluctuations have permitted the measurement RBC mechanical parameters such as their shear modulus or viscosity [75, 76] (More information

can be found in appendix C) and to detect RBC membrane fluctuation changes linked to RBC age [77], diseases like sickle cell anemia (and predict it) [78], diabetes [79], or even parasite infections causing malaria [76].

- **Measurement of the cellular content:** The refractive index dependency of phase measurements can be used to characterize the intracellular content. The first example is through the estimation of dry mass, described above, which gives some idea about the protein and lipidic content of a cell. The evolution of dry mass and dry mass density have been thoroughly studied during cell growth [80, 81] and cell mitosis [61]. Interestingly, the hemoglobin content of RBC has been successfully measured using the intracellular refractive index of the RBC [82]. [10]

- **Cell and structures characterization:** Because QPI techniques can access several physical parameters of the cell, in 2-D and 3-D [83], they can be useful to automatically identify tissue regions, cell types, and organelles (including the nucleus, and nucleolus) type and relative positions. Such physical parameters include the absolute volume, the refractive index, the cellular content (as described above), or more complex dynamic parameters, such as the fractal dimension, diffusion coefficients, or light scattering parameters. To pick-up a few concrete examples, we can start evoking the sorting of circulating tumor cells, whose concentration is a good indicator of the patient survival rate, that present higher dry mass, higher volumes and lower dry mass density than leukocytes, naturally present in blood [84]. *F. Merola et. al.* have combined DHM and optical trapping to automatically identify and measure sperm morphology and content in order to sort the healthy ones and eventually perform a sex-selection [44]. Finally, the measurement of light scattering parameters [85] and fractal dimension [86] of thin pieces of tissues can help to diagnose tumors in a sample.

- **Sub-wavelength cellular movement:** The sub-wavelength accuracy of QPI systems is very interesting for the detection of nanometric axial displacements like in the RBC membrane fluctuations we have already mentioned above. Interestingly, electrically-induced displacements have been detected using QPI systems. A first validation has been performed in detecting low amplitude cardiomyocyte displacements, which is a well-characterized coupling between electrical activity and mechanical forces [22]. From measured amplitudes, QPI would be able to measure a long-range mechanical communication between cardiac cells [89]. Another impressive result has been the demonstration of a voltage-induced membrane deformation in HEK cells excited by electrophysiology [90]. I will give more details on the detection of electrically-induced deformations in chapter 7. Additionally, QPI systems can accurately track cell migration, cytoskeleton [91], collagen fiber and protrusion displacements (emphasized in polarization-sensitive QPI systems [92]) or follow vesicle transport [93, 94], which allows following most of the mass transport inside the cell, and can be used to measure diffusion coefficients and active transport components inside the cell.

- **Measurement of Transmembrane water movements:** Finally, the group of *P. Marquet* has carefully investigated QPI ability to measure transmembrane water movements as a physical parameter, and has been able to successfully link phase changes to the transmembrane electrical current [70, 95, 96]. It provides another way to detect meaningful electrical

[10] It means that a deoxyhemoglobin/hemoglobin ratio could eventually be calculated from a single wavelength measurement, either using phase measurement in a confined environment or using all cell phase statistics or even by measuring a scattering ratio.

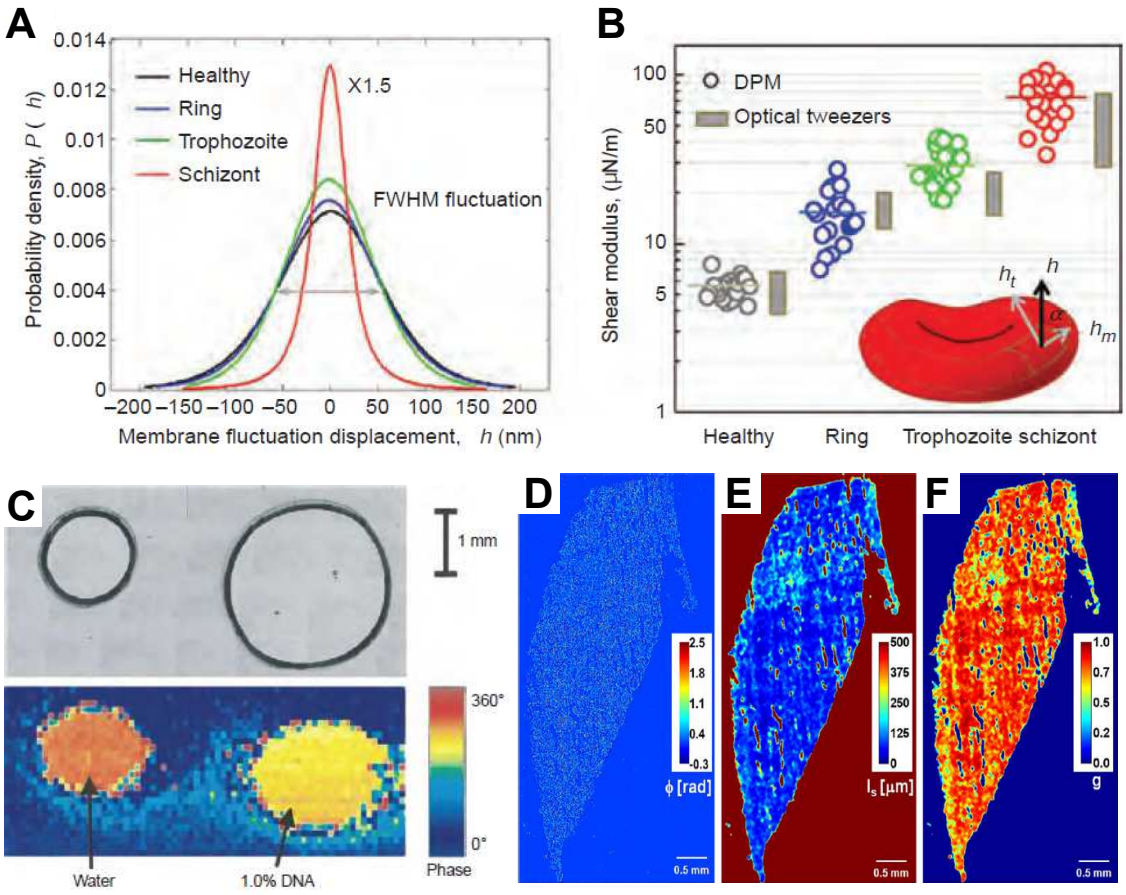

Figure 1.12 – Biological applications of QPI. Panel A shows the characteristic RBC membrane fluctuations in healthy RBCs and in Malaria parasite-infected RBC at three different stages (Ring, Trophozoite and Schizont stages at increasing stages of the disease development) [7, 76]. It directly enables the calculation of the mechanical shear moduli of the RBCs at different stages, as illustrated in **panel B**, which are in good agreement with shear modulus measurement using optical tweezers. Panels A and B illustrate QPI ability to characterize cell states from their mechanical performances. **Panel C** illustrates QPI ability to differentiate two objects based on their refractive index composition by measuring a phase difference between a water droplet and a water plus 1% DNA droplet [87]. Finally, **panels D to F** illustrate QPI ability to characterize a sample (here a histological thin tissue) based on its optical property. The phase heterogeneity enables the calculation of the tissue mean free path (l_s in panel E) and the scattering anisotropy factor (g, in panel F) [85] that are known to be modified in some tumorous samples [88].

activity from quantitative phase measurements, as these long-standing detected currents are involved in long-term potentiation and differentiation. Coupled with super-resolution performances of DHM and its ability to reveal dendritic spines [31], it is thought to allow for the label-free detection of long-term potentiation and might lead to the development of new biomarkers for neuronal disorders such as psychiatric disorders [70].

1.6 A new tool for refractive index/height decoupling: Fluorescence exclusion

Looking for simple, versatile, though powerful, techniques to decouple the height from the refractive index for our QPI measurements, and unambiguously detect axial changes, I discussed

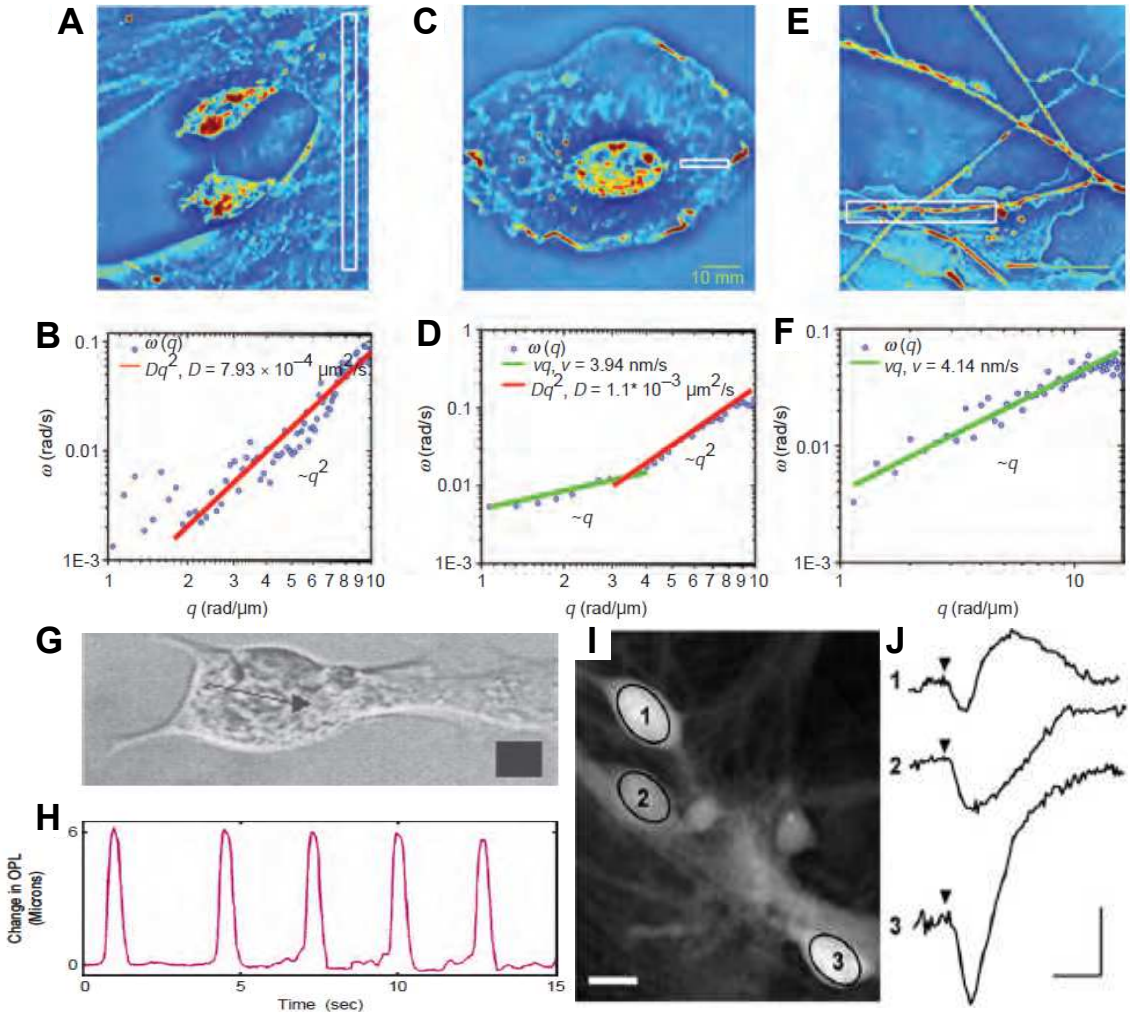

Figure 1.13 – Some more biological applications of QPI. Panels A to F are examples of intracellular transport using QPI [93], and the corresponding dispersion curves. Panels A and B correspond to a zone inside a microglial cell, with a majority of passive transport, panels C and D to an area inside a glial cell exhibiting both active and passive transport. Panels E and F correspond to a region inside an hippocampal neuron dendrite, with mostly active transport within. **Panels G and H** present an example of the detection of sub-wavelength mechanical motion in cardiomyocyte [22]. **Panels I and J** illustrate 3 different characteristic phase responses to a glutamate shock in a culture of cortical neurons (scale bars represent 10μm in panel I, and 2 minutes and 5° in panel J) [96].

with people from two research groups from the Institut Curie and the Institut Pierre-Gilles de Genes: The group of Matthieu Piel, interested in understanding cell volume regulation during mitosis and the group of Catherine Villard aiming to understand volume changes during neurite development. Both teams were using a technique named fluorescence exclusion method (FxM) to estimate cell volumes, through fluorescence decrease due to the exclusion from the cell volume in the constrained environment of a microfluidic chamber. I collaborated with them to try to better characterize this technique and understand its limitations. I developed a simple theoretical model that showed the ability of fluorescence exclusion to measure cell volumes in most of experimental conditions, even though the height measurement might sometimes be inaccurate. Despite its apparent simplicity, Fluorescence exclusion can reach impressive resolution, if correctly operated, and can be competitive with several QPI techniques in terms of height measurement. Interestingly for me (and I hope for this manuscript also), the essence of FxM and QPI appears similar to me.

They fundamentally consist of finding a strategy to transform an axial information into an intensity information, so that a 3-D map can be computed from a single 2-D measurement of an optical signal. Obviously, the two strategies are significantly different, as QPI measurements can only access an axial information coupled to a composition (through the refractive index) information, while FxM directly measures the cell height. When combined, these two techniques can additionally perform a decoupling of the phase signal to measure the refractive index map of a sample. At the end of this section, I will show a few examples of refractive index map reconstruction and will present several ideas that we are now validating to increase FxM performances.

1.6.1 Physically constrained fluorescence exclusion

In this subsection, I will introduce the concept of fluorescence exclusion microscopy and show a few limitations in a rather qualitative manner. I will finally give an estimation of the sensitivity of FxM, and different potential sources of error.

Basic principle

The basic principle of fluorescence exclusion method (FxM) is quite simple. It consists of measuring the distribution of fluorescence intensity in a microfluidic chamber filled with a fluorescent dye and seeded with cells. Without cells, the fluorescence signal depends on the concentration of fluorophores, and on the volume of the chamber. In presence of cells, assuming that fluorophores are physically excluded from cells, the fluorescence signal decreases depending on the volume occupied by the cells in the chamber. When using a simple widefield fluorescence microscope, we can demonstrate that the fluorescence signal drop varies linearly with the cell volumes [97, 98], offering a simple way to measure cell volumes. Interestingly, since FxM is based on a simple widefield microscope, dynamic, large-field or high transverse resolution measurements of cell volumes can be performed. Intuitively, the sensitivity in volume will be controlled by the sensitivity in intensity of the fluorescence microscope and will depend on some ratio between the cell volume and the microfluidic chamber height. In some conditions that I will further discuss, the local cell volume, and even cellular height averaged on a single pixel can be computed, as illustrated in figure 1.14 Despite its apparent simplicity in terms of optics, I mainly used this technique to optimize its sensitivity its image interpretation. On purpose, I will not discuss in details the design of the microfluidic chamber, or the selection of fluorophores that can not penetrate the cells, which was our collaborators' main expertise. In brief, they designed several microfluidic PDMS chambers of height ranging from 3μm to 25 μm, with PDMS pillars within the chamber that offer a reference signal, as it will be discussed later. The size of the microfluidic chamber is often chosen as a compromise between resolution and invasiveness (keeping invasiveness low requires the chamber to be high enough to prevent any mechanical and volume constraints on the cells). Additionally, careful design of the microfluidic chambers allows performing long time acquisitions with a high cell survival rate after several days. On fluorophores selection, the *ideal* fluorophore has to be totally excluded from as many cell lines as possible, which often depends on the fluorophore size and its interaction with the cell membrane. Ideally, these fluorophores are to be cost-effective, since fluorophores have to occupy the entire volume of the chamber. After experimenting several fluorophores and quantum dots, *C. Cadart* found that only 70 kDa Dextran with Alexia488 (green fluorophore), or 10 kDa Dextran with Texas-red (red fluorophore) presented low internalization and low toxicity. For more information about these two parameters, I refer to the following method paper about fluorescence exclusion [98], as well as the PhD manuscripts of *C. Cadart* and *C. Braini* [99, 100].

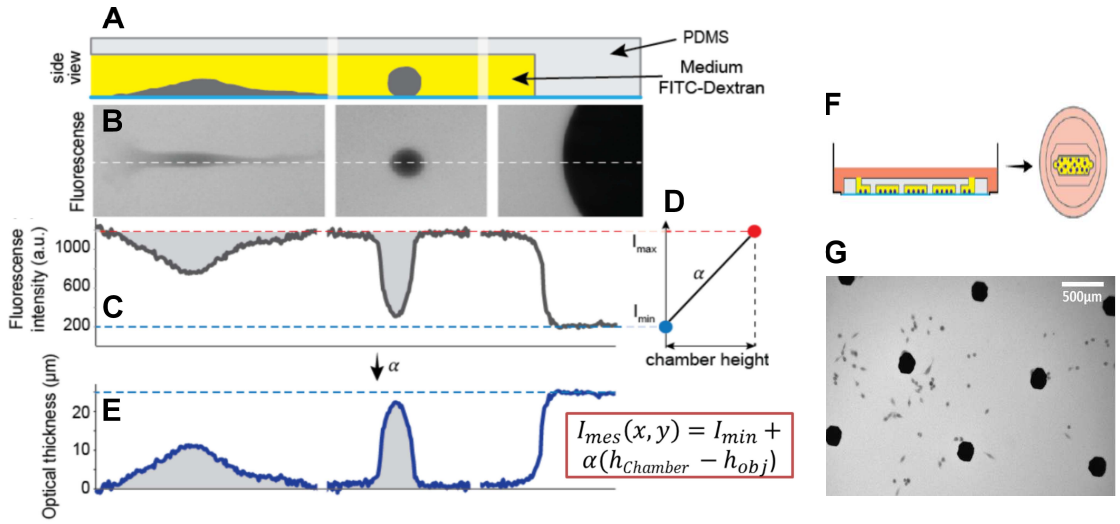

Figure 1.14 – Principle of fluorescence exclusion microscopy (FxM). Panels A to E illustrate the successive steps of FxM to recover a local height measurement. A microfluidic chamber of controlled height is seeded with cells and filled with a fluorescence medium, that can not penetrate inside the cells (panel A). When imaged with a widefield fluorescence microscope (panel B), the fluorescence signal is maximal in the chamber outside the cells and decreases with the object height (From left to right, a flat epithelial cell, a spherical cell, and a PDMS pillar). A linear relationship can be found between the measured intensity (panel C) and the object height (panel D). Knowing the chamber height and the minimal intensity (measured at the pillar) allows the calculation of the linear coefficient and the local height computation (panel E). Finally, **panel F** shows the microfluidic chamber organization, and **panel G** shows a typical large field FxM measurement with a 10X, 0.3 NA objective. Panels A to F have been adapted from *C. Cadart et. al.* [98].

The major assumption here has been to consider a linear relationship between the measured fluorescence intensity, and the cell volumes in the case of widefield microscopy. It simply derives from the assumptions that, first, fluorophores concentration is spatially homogeneous in the chamber and is null inside the cells. Second, we assume that, at camera frame rates, the fluorescence intensity emission is homogeneous in time. Therefore, the emitted fluorophore intensity I_{emit} from a given volume V is simply proportional to this volume times the local concentration and is proportional to the illumination intensity. It can be generally written as:

$$I_{emit}(x,y) = I_{Ill}.F_{Convert}.C(x,y).V \tag{1.51}$$

with $C(x,y)$, the local fluorophore concentration within the volume V, I_{Ill}, the illumination intensity, supposedly locally constant in a transmission widefield microscope, and $F_{Convert}$ the single fluorophore conversion factor, which is the ratio between the number of re-emitted photons versus incoming photons. It probably depends on the fluorophore quantum yield, absorption, and cross section. Under the previous assumption of homogeneous concentration of fluorophores equal to C_0 outside the cell, and outside the chamber, and equal to 0 anywhere else, the emitted intensity becomes:

$$I_{emit}(x,y) = I_{Ill}.F_{Convert}.C_0(V - V_{Cell}) \tag{1.52}$$

with V the local microfluidic chamber volume around a cell of interest. The potential value of the minimal volume V for a given cell geometry will be discussed in the next subsection. Keeping it

simple, we can assume that the entire microfluidic chamber lies within the depth of focus of the objective, so that each camera pixel intensity only depends on the local information at a given voxel in the sample plane. Therefore, we can write the local volume as the product between the pixel section and the height of the chamber. We can rewrite the measured intensity using equation 1.52 for a single pixel, using a proportionality coefficient $\alpha = F_{Convert}.C_0.S_{Pixel}$, that is supposed to be constant over time and over the field of view:

$$\mathrm{I_{mes}}(x,y) = \mathrm{I}_{min} + \alpha.(\mathrm{h_{Chamber}} - \mathrm{h}(x,y)) \tag{1.53}$$

with I_{min}, the minimal intensity captured by the camera, and equal to camera noise in an ideal case. α can henceforward be calculated as:

$$\alpha = \frac{\mathrm{I}_{max} - \mathrm{I}_{min}}{\mathrm{h_{Chamber}}} \tag{1.54}$$

Here, we consider I_{min}, I_{max}, and $\mathrm{h_{Chamber}}$ to be spatially constant, which is a good approximation if the illumination is reasonably even. Otherwise, the linear coefficient α has to be modified as a local value, and needs to be computed locally, or extrapolated. From equation 1.53, it is also convenient to write the formula that computes the local height from the measured intensity:

$$\mathrm{h}(x,y) = \mathrm{h_{Chamber}}.\frac{\mathrm{I}_{max} - \mathrm{I_{mes}}(x,y)}{\mathrm{I}_{max} - \mathrm{I}_{min}} \tag{1.55}$$

We can note that if we neglect camera noise in the first instance, FxM can interestingly measure the total cell volume including all the small cellular elements such as nanometric cell protrusions which participate in the fluorescence exclusion, even though these structures cannot be resolved, either because they are too small, or because they are out-of-focus. Nevertheless, besides the cellular volume, it can be interesting in measuring the local cell height, and eventually height fluctuations. It was a sufficient motivation to extend FxM measurements to higher numerical aperture (NA) measurements, trying to map cell heights with higher transverse resolution. Additionally, a naive observation is that the smallest NA objective provided in commercial widefield microscopes is often around 0.3. It means that even at relatively low resolution, a part of the cells and of the microfluidic chambers are usually out-of-focus, which invalidates the main assumption leading to equation 1.53. In this case, the local height computed by equation 1.53 is an average of the height over the imaging cone, as illustrated in figure 1.15. The higher the NA, or the higher the depth of field versus the size of the microfluidic chamber, the more inaccurate the local height becomes, as it is more and more coupled with the adjacent pixels. Finally, it is understandable as the measured intensity is the convolution between the local height and the system PSF. I will describe it in the next subsection in order to estimate the conditions for accurate height and volume measurements.

Expected sensitivity

In this subsection, I will discuss the expected sensitivity in fluorescence exclusion, and diverse sources of noise. Going back to the fundamental equation of fluorescence exclusion 1.53, let's now take into account potential spatial inhomogeneities:

$$\mathrm{I_{mes}}(x,y) = \mathrm{I}_{min}(x,y) + \alpha(x,y).(\mathrm{h_{Chamber}}(x,y) - \mathrm{h}(x,y)) \tag{1.56}$$

From equation 1.56, it becomes easier to identify a few potential sources of noise in the calculation of the local height. Errors in such calculation can arise from intensity fluctuations, from local misestimation of the coefficient α, or from the chamber height. In this subsection, I will

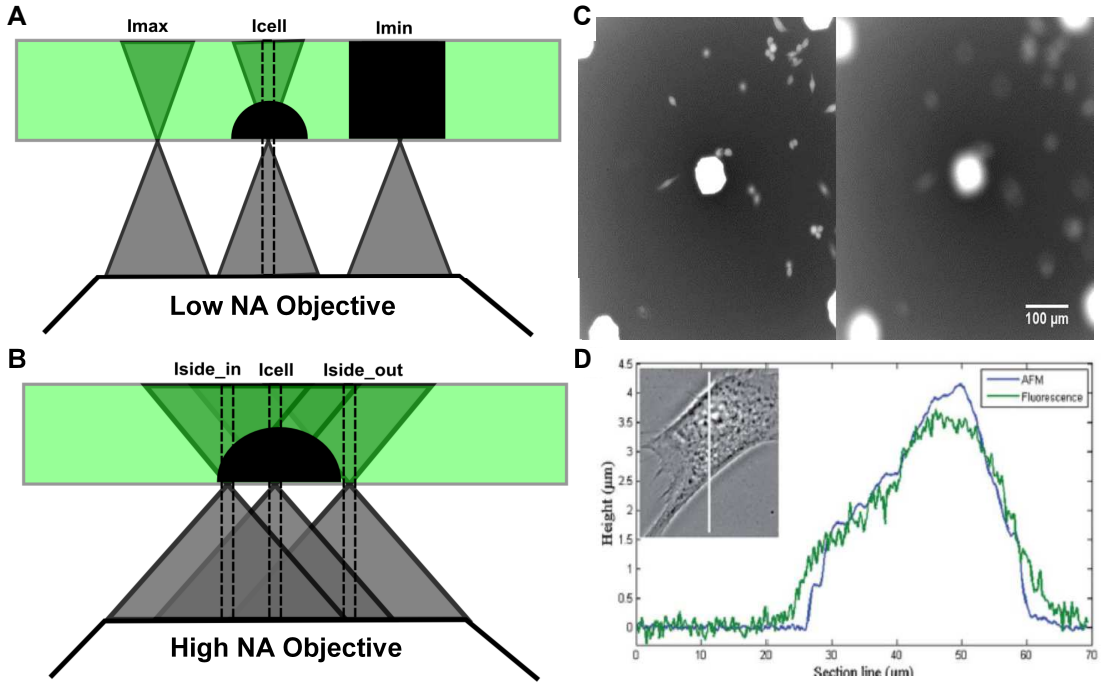

Figure 1.15 – FxM height measurement accuracy versus objective NA and versus defocus. Panels A and B illustrate the photon collection in FxM in the case of a low NA (panel A) and a high NA (panel B) microscope objective. In the case of the maximal and minimal intensity measurement (around a pillar excluding fluorescence), there is little error because the fluorophore concentration is locally homogeneous over the entire beam collection area (dark green cones). However, when imaging a cell larger than the depth of focus, the calculated local height measurement is averaged over the imaging cone and would appear smaller at the top of a hemispherical cell, and larger on its side (panel B). The error importance obviously depends on the objective NA which controls the imaging angular distribution, but also on the focal plane (not shown here, but optimal at half the local cell height ideally). **Panel C** is the experimental validation of a height measurement difference between the in-focus (left image) and the out-of-focus (right image) foci. **Panel D** is a comparison between FxM height (green) and AFM height (blue) measurements found in *C.Bottier et al.* [97] that illustrates a reasonable height calculation but also illustrates the height underestimation on the top of the cell, and the height overestimation on its edges.

mainly discuss the case of the height sensitivity controlled by the fluorescence intensity noise, in a similar way to that which was performed in section 1.3. Nevertheless, on top of this *ideal* noise, there are two other important sources of noise. The first one may come from a misestimation of the local linear coefficient, which can originate from either intensity measurements errors(of I_{min} and I_{max}), or from local fluctuations of the chamber height. The local extrema intensities can be misestimated due to illumination field inhomogeneity (the illumination field often has a Gaussian shape, which can be numerically corrected for more accurate measurements [98]), or from a pollution of the chamber (fluorophores that penetrate the PDMS or dirt inside the chamber reducing maximal intensity). Local fluctuations of the chamber height can be the result of the chamber fabrication process. We note that pillars that are used for the minimal intensity measurements are also an important feature of the chamber to ensure roof flatness. The second potential large source of error comes from the assumption of homogeneous fluorophore concentration C_0 in the chamber and 0 outside the chamber or inside the cells. This approximation fails in case of local

photobleaching (with inhomogeneous illumination), or in case of fluorophore uptake by the cells. As previously explained, the choice of an adequate fluorophore is thus an important parameter for the success of a FxM measurement.

Even in the case of a perfect experiment with no other experimental sources of noise, the technique sensitivity is ultimately limited by the intensity noise as discussed in appendix A and in section 1.3. In the case of FxM, we often work with a high number of photons, generated by the choice of bright and relatively concentrated fluorophores that we choose. As I will explain, fluorescence exclusion sensitivity is higher when operated as close to camera saturation as possible, in the shot noise regime similarly to phase imaging. To give a rough idea of the number of photons involved in fluorescence exclusion, we will take the case of the sCMOS camera PCO edge 5.1 that I installed on my systems: Its full well capacity is 30,000 electrons, conversion factor 0.46 electrons per count, and its dark current and readout noise are less than 10 electrons per pixel per second. Therefore, close to saturation, every pixel of the camera can receive about 65,000 photons with the camera noise generating a few dozen photons in worst cases. In this configuration, the shot noise represents about 250 photons, 10 times more photons that the camera noise. Limitation by the camera noise arises when the shot noise comes around a few dozen photons, corresponding to 1 % to 5% of camera saturation, or ultimately to objects with local heights between 95 to 100% of the chamber height. Therefore, we will mainly discuss the situation where the intensity noise comes from the shot noise. Below is calculated the noise it creates on the object height. This should give the ultimate sensitivity of fluorescence exclusion in optimal conditions. Let us first relate the height variation Δh corresponding to a given intensity variation ΔI. We extend equation 1.55 to:

$$\mathrm{h} + \Delta\mathrm{h} = \mathrm{h_{Chamber}}.\frac{\mathrm{I}_{max} - \mathrm{I} - \Delta(\mathrm{I})}{\mathrm{I}_{max} - \mathrm{I}_{min}} \tag{1.57}$$

$$\mathrm{h} + \Delta\mathrm{h} = \mathrm{h_{Chamber}}.\frac{\mathrm{I}_{max} - \mathrm{I}}{\mathrm{I}_{max} - \mathrm{I}_{min}} - \mathrm{h_{Chamber}}.\frac{\Delta\mathrm{I}}{\mathrm{I}_{max} - \mathrm{I}_{min}} \tag{1.58}$$

The first term is in fact the local height h (equation 1.55). Hence,

$$|\Delta\mathrm{h}| = \mathrm{h_{Chamber}}.\frac{|\Delta\mathrm{I}|}{\mathrm{I}_{max} - \mathrm{I}_{min}} \tag{1.59}$$

In good optical conditions, we can assume that I_{min} is negligible with respect to I_{max}, and that I_{max} is close to the camera saturation level, and that the experiment is shot-noise limited with $\frac{\Delta\mathrm{I}}{\mathrm{I}_{max}} = \sqrt{\frac{1}{FWC}}$, with FWC, the camera Full Well Capacity. Hence, equation 1.59 reduces to:

$$|\sigma_\mathrm{h}| \simeq \frac{\mathrm{h_{Chamber}}}{\sqrt{FWC}} \tag{1.60}$$

In optimal imaging conditions, the height sensitivity only depends on the microfluidic chamber height and on the camera FWC (or reduced FWC, if the imaging is performed further from camera saturation), and can be as low as 30 nm for a 3 μm high chamber, and a camera reduced FWC of 10,000 photoelectrons, as illustrated in figure 1.16. Recalling equation 1.29 about the optical path sensitivity in QPI, we can note that the chamber height is replaced by $\frac{\lambda}{2\pi}$ in QPI, which corresponds to an equivalent chamber of about 100 nm. Obviously, QPI permits much higher optical path sensitivity than FxM height sensitivity. Indeed, optical wavelengths are much smaller than typical chamber heights and FWC in QPI are often much higher than in fluorescence imaging. Nevertheless, it is worth remembering that FxM directly measures local heights, and its height sensitivity is not divided by a low refractive index difference, meaning that height

sensitivities are almost similar in both QPI and FxM in most cell types. Finally, FxM is often criticized for its low sensitivity, but I feel this is mainly because it is often used far from its optimal operating range.

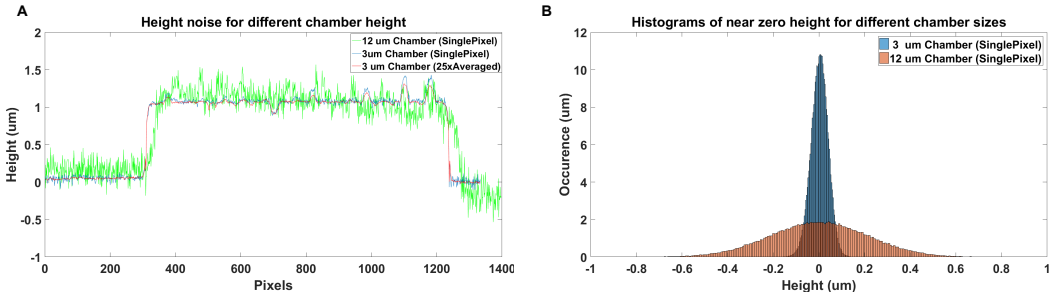

Figure 1.16 – Height sensitivity in FxM. Panel A shows an FxM experimental height sensitivity measurement on a 1.17μm high (externally measured with a profilometer) long stripe in 12μm (green plot) and 3μm chamber (red and blue lines), showing the decreasing noise with the height chamber. The red line has been calculated by spatially averaging along the width of the stripe (25 pixels) and exhibits smaller variations as predicted. **Panel B** shows the histograms of a similar object-free region, calculated for a 12μm (red histogram) and 3μm (blue histogram) chambers showing a noise standard deviation around 200 nm and 50 nm respectively, with a four-fold ratio, as predicted by equation 1.60.

1.6.2 FxM theoretical framework

In the two following subsections, I will describe the simple theoretical and numerical framework I have developed to understand and optimize fluorescence exclusion microscopy. For the sake of simplicity, I will mainly discuss the case of a widefield transmission microscope, which is the easiest but also the most accurate setup to perform fluorescence exclusion in my opinion. Let us first try to understand the physical origin of the technique, and explain how the fluorescence intensity can be linear with the height of the chamber, independently of the imaging parameters. If the influence of the imaging parameters is relatively easy in conventional microscopy, it was harder to get an intuitive notion of FxM since we are looking at *negatives* of the objects we want to image (the fluorophores are outside the cells). One important result that came out from the next two subsections is that we can consider that FxM acts as a *normal* imaging system for the cell, as long as there is no spatial heterogeneity in the emitted intensity of fluorophores outside the cells.

Let us first refer to appendix A, in which we introduce the concept of the Point Spread Function (PSF) of an imaging system. In the detector plane, the intensity can be classically written as the convolution between the detection system PSF and the emitted intensity $\mathrm{I_{emit}}$. In such a microscope configuration, we can assume homogeneous illumination coming from a low NA condenser, usually illuminating a large field of view that would limit the vignetting artifacts.

The intensity at the detector plane can be written:

$$\mathrm{I_{det}}(\vec{\rho}, z) = \mathrm{I_{emit}} * PSF_{\mathrm{det}} = \int\int\int \mathrm{I_{emit}}(\vec{\rho}_0, z_0).PSF_{\mathrm{det}}(\vec{\rho} - \vec{\rho}_0, z - z_0)\mathrm{d}\vec{\rho}_0\mathrm{d}z_0 \tag{1.61}$$

The emitted fluorescence intensity $\mathrm{I_{emit}}$ in a voxel of volume dV depends on the incident intensity, on the number of fluorophore particles in this voxel, or the fluorescence concentration, and on a single fluorophore cross section, and quantum yield. For a given experiment, we assume the

fluorophore properties to be constant, and its concentration to be locally homogenous. We name α_0 the constant term gathering the fluorophore properties and geometrical terms. Therefore, we can write the emitted fluorescence intensity as:

$$\mathrm{I_{emit}}(\vec{\rho}_0, z_0) = \alpha_0.\mathrm{I_{inc}}(\vec{\rho}_0, z_0).\mathrm{C_{fluo}}(\vec{\rho}_0, z_0) \tag{1.62}$$

In the case of a widefield microscope with homogeneous illumination, we can reduce the problem complexity as spatial dependence of the emitted fluorescence intensity only depends on the local concentration of fluorophores. The detected intensity therefore is:

$$\mathrm{I_{det}}(\vec{\rho}, z) = \alpha_0.\mathrm{I_{inc}} \int\int\int \mathrm{C_{fluo}}(\vec{\rho}_0, z_0).PSF_{\mathrm{det}}(\vec{\rho} - \vec{\rho}_0, z - z_0)\mathrm{d}\vec{\rho}_0\mathrm{d}z_0 \tag{1.63}$$

Additionally, we can use a property of nonaberrated PSFs that originates from the lossless axial propagation of intensity and states that the integral of the PSF over each transverse cross section is constant:

$$\int\int PSF(\vec{\rho}, z)\mathrm{d}\vec{\rho} = Cst \tag{1.64}$$

When combining this equation with a fluorophore concentration of either zeros inside cells and outside the microfluidic chamber, and ones elsewhere, we can write:

$$\begin{aligned}\mathrm{I_{det}}(\vec{\rho}, z) = \alpha_0.\mathrm{I_{inc}}(&\int\int\int_{V_{Chamber}} PSF_{\mathrm{det}}(\vec{\rho} - \vec{\rho}_0, z - z_0)\mathrm{d}\vec{\rho}_0\mathrm{d}z_0 \\ &- \int\int\int_{V_{Cell}} PSF_{\mathrm{det}}(\vec{\rho} - \vec{\rho}_0, z - z_0)\mathrm{d}\vec{\rho}_0\mathrm{d}z_0)\end{aligned} \tag{1.65}$$

With $V_{Chamber}$ the minimal volume of the chamber around a cell so that the entire cell can be imaged in this volume. Finally, to image the entire cell volume, the detected intensity has to be integrated into an area A_{Cell} corresponding to the pixels that feel the influence of a given cell. Using equation 1.64, we can finally write:

$$\int\int_{A_{Cell}} \mathrm{I_{det}}(\vec{\rho}, z_{focus})\mathrm{d}\vec{\rho} = \alpha_0.(A_{Cell}.h_{Chamber} - V_{Cell}) \tag{1.66}$$

Note that the spatial dependence of the PSF is only included inside the integration area A_{Cell}, which means that it will have to be chosen larger when the cell (or a part of the cell) is out-of-focus. Interestingly, a quick calculation with geometrical optics enables the estimation of the minimal integration area that needs to be taken into account to accurately measure the entire cell volume, assuming the focus is made within the chamber. To account for the asymmetric cell surface, I express an integration radius R_{int} instead of an integration area:

$$R_{int} = R_{Cell} + \frac{1}{\sqrt{(\frac{n}{NA})^2 - 1}} \tag{1.67}$$

with R_{Cell}, the real cell radius along one direction. Obviously, the final volume measurement will be accurate only if there is only one cell in the integration volume (integration area times the chamber height), and no other spatial heterogeneities.

From equation1.65, the local height measurement can be obtained under the assumption that

the entire cell lies within the depth of focus, inside which:

$$PSF_{\text{det}}(\vec{\rho} - \vec{\rho}_0, z - z_0) \simeq \delta(\vec{\rho}_0, z_0) \tag{1.68}$$

where δ is the delta function, implying a pixel to pixel correspondence between the image plane and the camera plane. Using equation 1.64, equation 1.65 taken with the detector conjugated with the image plane therefore becomes:

$$\mathrm{I}_{\text{det}}(\vec{\rho}, z_0) = \alpha'.(h_{Chamber} - h_{Cell}) \tag{1.69}$$

Note that this equation only depends on the assumption that the cell (and only the cell) lies inside the depth of focus and on the spatial homogeneity of the fluorophore concentration. It means that the local height measurement can be correct even in the case of a chamber higher than the depth of focus, as long as the cell is smaller than the depth of focus.

1.6.3 FxM numerical model

In order to validate the theoretical framework, a numerical model has been developed. It consists in calculating the convolution between a fluorophore concentration and a 3-D system PSF, as illustrated in figure 1.17. To reduce computation time, we only performed 2-D simulations in the XZ plane. It corresponds to the integration of the PSF in the third dimension (Y) that is equivalent to only considering infinite objects and chambers in this direction. Such an approximation will be discussed at the end of the results subsection. Finally, we used a final assumption that we made from the beginning of this section, *i.e.* fluorophore concentration is homogeneous in the entire microfluidic channel and equal to C_0, and is equal to 0 inside the cells, and outside the chamber. Therefore, we can define a binary function C' that is equal to 0 inside the cells and outside the chamber, and equal to 1 inside. We chose the camera position to be conjugated with the perfect focus. The result of the convolution will thus correspond to a variation of the focal plane inside the chamber, but it might also correspond to a change of the camera plane. Hence, the simulation runs as follow:

1. **Definition of the chamber organization.** It consists of defining the 2-D matrix C' with zeros corresponding to pixels outside the chambers, inside the cells and pillars, and with ones corresponding to the free medium inside the chamber. In practice, we start the creation of the object matrix by defining the boundaries of the microfluidic chamber. We can easily change the chamber height, but we always simulate an infinite chamber in the transverse dimensions, which is often the case in experiments. Then, we can add a pillar of different height and width. We can either simulate a single pillar having the height of the entire chamber, similarly to experiments described in [98], or 3 pillars of different heights, to simulate experiments described in [61] supplementary materials. Since this is a simulation we can also decide not to have pillars as we can easily control our level of noise, and easily find a location where the absence of signal caused by a cell is negligible. Finally, we define one or many cells in the chamber of different shapes. So far, we only simulate cells with shapes that could be easily analytically calculated, such as circles, ellipses, or rectangles, and combinations of such objects. For example, we created round objects in the middle of the chamber, to simulate detached circular cells, in the beginning of mitosis. We also simulated neurons with a central soma and one neurite on each side of the soma, by assuming a central half disk, and a long thin rectangle crossing the somas, as illustrated in figure 1.17.

2. **PSF calculation depending on the imaging parameters.** Accurate calculation of a system 3-D PSF, depending on the emission wavelength, and the numerical aperture of the lenses is a complex, though well-studied problem [38]. To simulate theoretical PSFs expected for our microscope configuration, we used a Java software named PSF Generator, developed by H.Krisner and Daniel Sage, from the Biomedical Imaging Group at EPFL [101–103]. We used it to simulate perfect theoretical PSFs, using Born & Wolf 3-D PSF Model [38] of a single point emitter in perfect imaging conditions. We also calculated aberrated PSFs, accounting for aberrations coming from the refractive index mismatches arising at the objective medium to coverslip interface, and at the coverslip to imaging medium interface. To perform such a calculation, PSF Generator used the Gibson&Lanni PSF model [104].

   The software allows the calculation of PSFs with different levels of accuracy, rising with computation time. In our case, it is crucial to simulate theoretical PSFs using the best possible resolution, since we integrate the 3-D PSF along one transverse dimension, to only use a 2-D "X-Z" PSF. With average accuracy calculations, the residuals far from focus sum up in the integration process (especially since intensity values can only be positive), leading to inaccurate 2-D PSFs. With the best accuracy possible, the 3-D PSF calculation lasts about 30 minutes. However, such a calculation is only required once for each optical configuration (objective NA, immersion medium, and magnification), and does not depend on the microfluidic chamber organization. I only simulated about 10 PSF files that I reused for many different simulations.

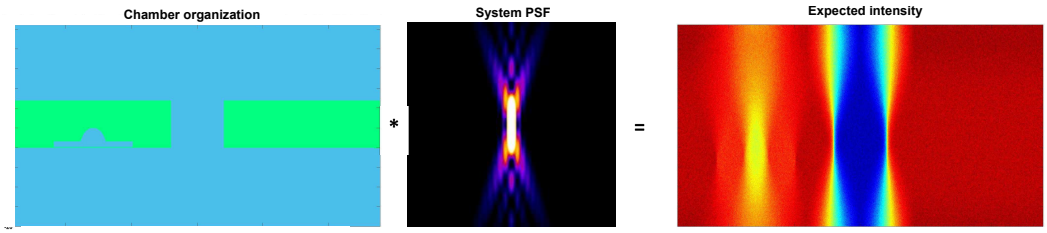

Figure 1.17 – FxM Numerical model. A 2-D microfluidic chamber with a neuron-like shaped surface and a pillar surface excluding fluorescence inside the chamber is numerically designed (**panel A**). The corresponding matrix is convolved with a PSF file corresponding to the experimental imaging parameters (**panel B**). **Panel C** illustrates the result of the convolution giving the expected detected intensity by the detector, to which Gaussian noise can be added.

4. **Intensity calculation.** The detected intensity corresponds to the convolution between the C' matrix and the PSF matrix. The convolution is performed by calculating the Fourier transform of the two previous matrices, to multiply them, and then calculate the inverse Fourier transform. Let me insist on the fact that the object matrix that we will create here has to have the same dimensions as the PSF file that is calculated, otherwise the calculation of the convolution might be misleading. An additive noise can also be added to simulate the effect of the shot noise or of the camera noise.

5. **Height and volume calculation.** Using equation 1.55, the local height of a cell can be calculated, and the corresponding volume (or surface in 2-D) by integrating over an arbitrarily chosen area.

With such a simulation, we have been able to demonstrate the height measurement failure when imaging cells higher than the depth of focus as well as the accurate volume calculation in all cases (if the integration area chosen is large enough). These results are presented in figure 1.18 and in *C.Cadart et. al.* [98].

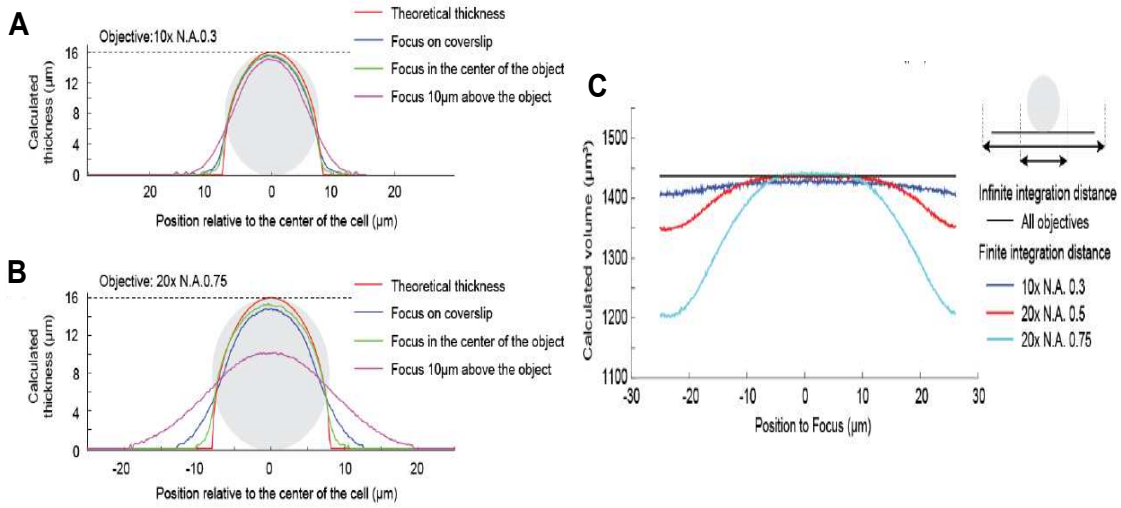

Figure 1.18 – Height and volume measurement accuracy using FxM numerical model. Panels A and B show the calculated local thickness as a result of a simulation of a 16 μm spherical cell in a 25μm high chamber at different foci. With a 10X 0.3 NA objective (panel A) with a depth of focus around 12μm, the height measurement is quite accurate for every pixel along the cell, and starts to become less accurate when the focus is placed on the coverslip or 10 μm above the cell (respectively blue and pink lines). With a 20X 0.75 NA objective and a corresponding depth of field around 3μm, the height measurement is strongly impacted and is even more inaccurate for larger defocus. **Panel C** shows the result of a similar simulation but in terms of calculated volume. If the integration area is large compared to the cell (black curve), the calculated volume becomes equal to the theoretical cell volume for all objectives and all defoci. Nevertheless, the volume measurement can be inaccurate if a smaller integration area is chosen, with an error that now depends on the imaging parameters.

Even if this simulation has a good qualitative predictive power, and helped us to realize several features of fluorescence exclusion, its results have to be interpreted with caution. Indeed, the finite third dimension will probably increase the effect of defocus on the accuracy of the measurement, and the effect will likely be squared and more important. In these 2-D simulations, the calculated thickness can be fairly accurate even for objects four to five times higher than the depth of focus (see figure 1.18 B for example) while I expect a much faster accuracy decrease in a 3-D configuration. Additionally, I did not take into account the intensity cross section decrease due to the finite size of the objective's front physical aperture, which will result in the loss of signal, and possibly a nonlinearity with the cell volume, at large defocus with respect to the depth of focus. To look deeper into the possibilities and limitations of FxM, this simulation could be extended to the case of aberrated PSFs (as they can be simulated with PSFGenerator [101], or experimentally measured), or to the case of an absorbing medium to study the influence of Phenol Red on the measurement accuracy for example. Also, we could extend it to other configurations, such as scanning configuration in which the illumination intensity is not homogeneous but depends on an illumination PSF or extend it to other fluorescence microscopes. Finally, we should also take care of light scattering in a future model, although cells are weakly scattering, scattering might alter the ultimate sensitivity of this technique. Nevertheless, in a similar way as for out-of-focus light,

we expect the diffusion to average-out for volume measurements on large areas.

1.6.4 Measuring refractive index maps

Despite fluorescence exclusion similarities with quantitative phase imaging, we initially wanted to combine it with a QPI measurement in order to decouple the height and the refractive index of phase measurements. Using the Linnik interferometer I will present in the next chapter and chambers prepared by *C. Cadart* and *C. Braini*, we could perform such decoupling procedure in HeLa cells and in neurons. For these measurements, chambers of height between 3 μm up to 20.8 μm have been imaged simultaneously with a fluorescence path and a QPI path. The fluorescence path allows the measurement of the cell volumes, while the QPI path measures the change in the optical path caused by the cell. The phase information can be averaged on the entire cell area to obtain an estimation of the product between the cell volume and the cellular mean refractive index. The fluorescence image is then overlaid to the phase image and the calculated cell volume is divided to the cell *phase volume*, which gives an estimation of the mean cell refractive index. As illustrated in figure 1.19, these proof-of-concept experiments allowed us to measure average refractive index between 1.36 and 1.37, which is consistent with typical values of cell refractive indices found in the literature [56]. Additionally, we could verify our measurements by computing the refractive index of a PDMS pillar in the chamber and found a value of 1.41, also consistent with PDMS refractive index. Nevertheless, the local refractive index cannot properly reconstructed here because the imaged cells are larger than our system depth-of-field and not symmetric enough to estimate their 3-D shape. Furthemore, as it could be observed in figure 1.19 A, the fluorescence background is quite heterogeneous, probably due to the existence of significant aberrations. Indeed, our system configuration (reflection configuration) imposes to cross 2 mm of PDMS before reaching the chamber. The background heterogeneity lowers the sensitivity and the accuracy of the reconstruction so that we did not want to compute a local refractive index since local fluctuations might be caused by noise and not necessarily by intracellular signal. Nonetheless, we expect that these fluctuations average out at the cellular scale, giving correct estimations of the mean cellular refractive index, as might be validated by the values we measured.

1.6.5 Future developments in fluorescence exclusion

As I got more and more into the details of fluorescence exclusion, I felt like this technique could be much more powerful that what its current use authorizes. To emphasize this potential, we recently tried or imagined several experiments that I describe here as a perspective on fluorescence exclusion since I will not speak again of this technique in the rest of the manuscript. To emphasize the similar axial sensitivity of FxM and QPI, a first idea would be to demonstrate the ability of FxM to measure RBC membrane flickering similarly to QPI by investigating the local fluctuations of the fluorescence intensity. At this point, we have successfully imaged red blood cells (See figure at the beginning of this chapter) in a 10 μm chamber but are currently still processing the data.

Furthermore, we have demonstrated that FxM-based height measurements are ultimately controlled by the detection system PSF, it should be possible to apply a deconvolution algorithm to FxM measurements, using theoretical PSF (it is unlikely that the PSF would be aberrated in a transmission widefield transmission microscope). The idea is then to use a similar calculation than the one performed in the numerical model, although in this case the Fourier transform of the height measurement will be divided by the Fourier transform of the PSF to obtain an accurate

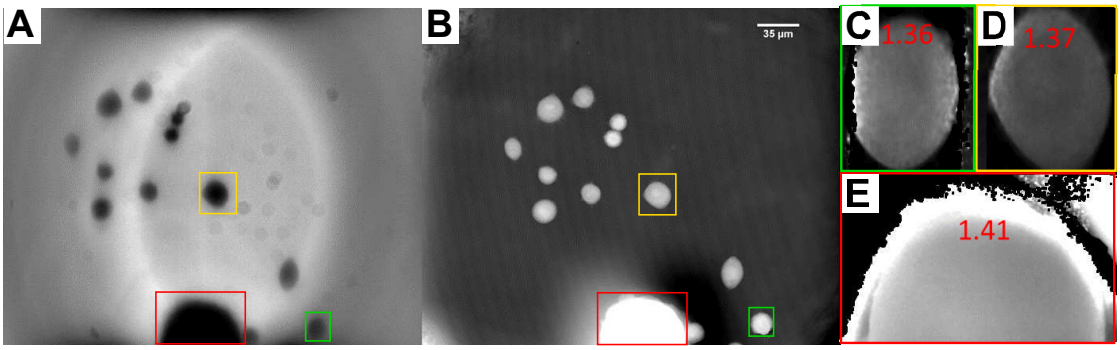

Figure 1.19 – Principle of refractive index measurement using fluorescence exclusion combined with quantitative phase imaging. Panel A and B respectively show the fluorescence intensity map and the corresponding phase imaging map of a HeLa cells culture in a 20.8 μm high PDMS chamber. The fluorescence image in panel A has been spatially high-pass filtered to homogenize the background. Nevertheless, high spatial frequency inhomogeneities of the illumination background can still be observed because the light path crosses more than 2 mm of PDMS of refractive index 1.41 which creates significant aberrations. **Panels C to E** show the refractive index reconstruction and the average refractive index calculated from associated regions. Panels C and D show 2 different cells, in which the refractive index locally varies between 1.35 and 1.38. A darker region (lower refractive index) at the center of the cell in panel D might correspond to the cell nucleus. Panel E shows that the refractive index reconstruction seems effective on average in the PDMS pillar displayed in the panel and whose refractive index is measured around 1.41.

height measurement in most conditions. It should allow the measurement to become truly independent of the cell geometry. Nevertheless, the division by the system PSF can be complicated in practice as the zeros of the PSF will create infinite noise values in high-frequency domains of the image. Hopefully, this is again a well-studied problem and many solutions have been investigated. Some of these strategies for low-noise deconvolution procedures will be mentioned in the next chapter to recover the phase difference in the wide-angle DIC we have built.

Finally, I would like to emphasize one last technique we have been trying to develop lately. The main constraint of FxM probably comes from the microfluidic chamber, which requires an experience and material for developing microfluidic chips, and can limit its use. In order to eliminate this constraint, a potential option is to create a virtual optical chamber instead of the microfluidic physical chamber. For example, any fluorescence microscope that is enabled to perform optical sectioning would be able to create such a virtual chamber with no or a negligible number of detected photons from outside the chamber. Ideally, and because the contrast varies with the dimension of the chamber, the ideal setup would be able to adjust its optical section to the cell height, eventually varying it over time to work as close as the optimal contrast at any time. Towards that goal, it seems that confocal microscopy or structured illumination microscopy would be efficient as their optical sections can easily be modified either by changing the rejection pinhole size or by changing the grid frequency. Nevertheless, if everything seems to work well in principle, it is not obvious in practice since one of the key characteristics of confocal microscopy is to filter out-of-focus light. As a consequence, the intensity cross-section decreases with the defocus as $(z - z_{focus})^{-2}$ (as illustrated in figure 1.20 A) so that linearity between recorded intensity and cell volume is not ensured. However, we could show that such linearity is a good approximation if the

pinhole size is chosen correctly, as illustrated in figure 1.20 B. We could calculate the conditions for which this approximation is correct, and we could perform the first experimental evidence for confocal based FxM measurements, giving a rough idea of beads volume. We still have a few problems to resolve such as determining the actual focus with respect to the bottom (which is critical to know the correct height of the virtual chamber) before being able to use it for biology experiments. Finally, by eliminating the microfluidic chamber, it seems to be possible to make a volume measurement using confocal microscopy, but the technique would probably become more complicated to operate and less accurate.

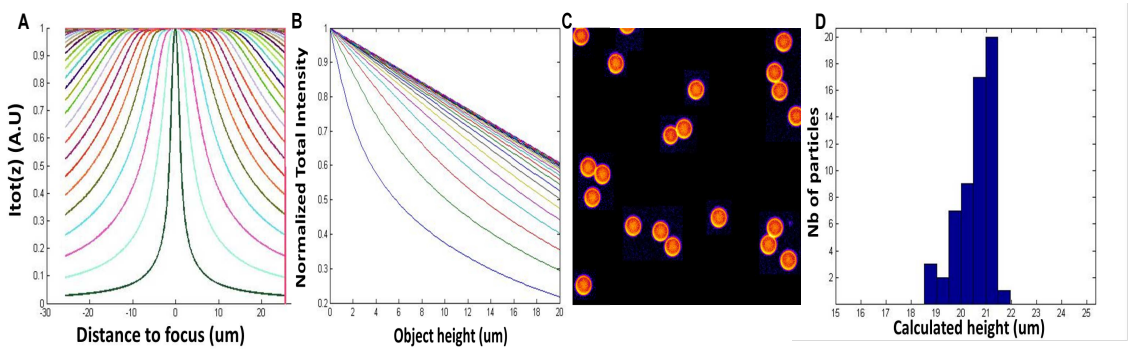

Figure 1.20 – Confocal-based FxM measurements. **Panel A** illustrates the defocus dependence of the intensity cross section which explains the confocal ability to perform optical sectioning. The different colors correspond to different aperture sizes. **Panel B** shows the result of a numerical simulation plotting the measured intensity versus the height of a large object at a focus corresponding to half the size of the object, and showing the linearity between intensity measurement and the object height for large enough pinholes. **Panels C and D** respectively show height map and volume histograms experimentally measured with confocal-based FxM on 20μm beads, showing a good reproducibility of the measurement and an acceptable accuracy, even though it seems to be a small fixed error in the measurement (mean diameter above 20.5 μm instead of 20μm).

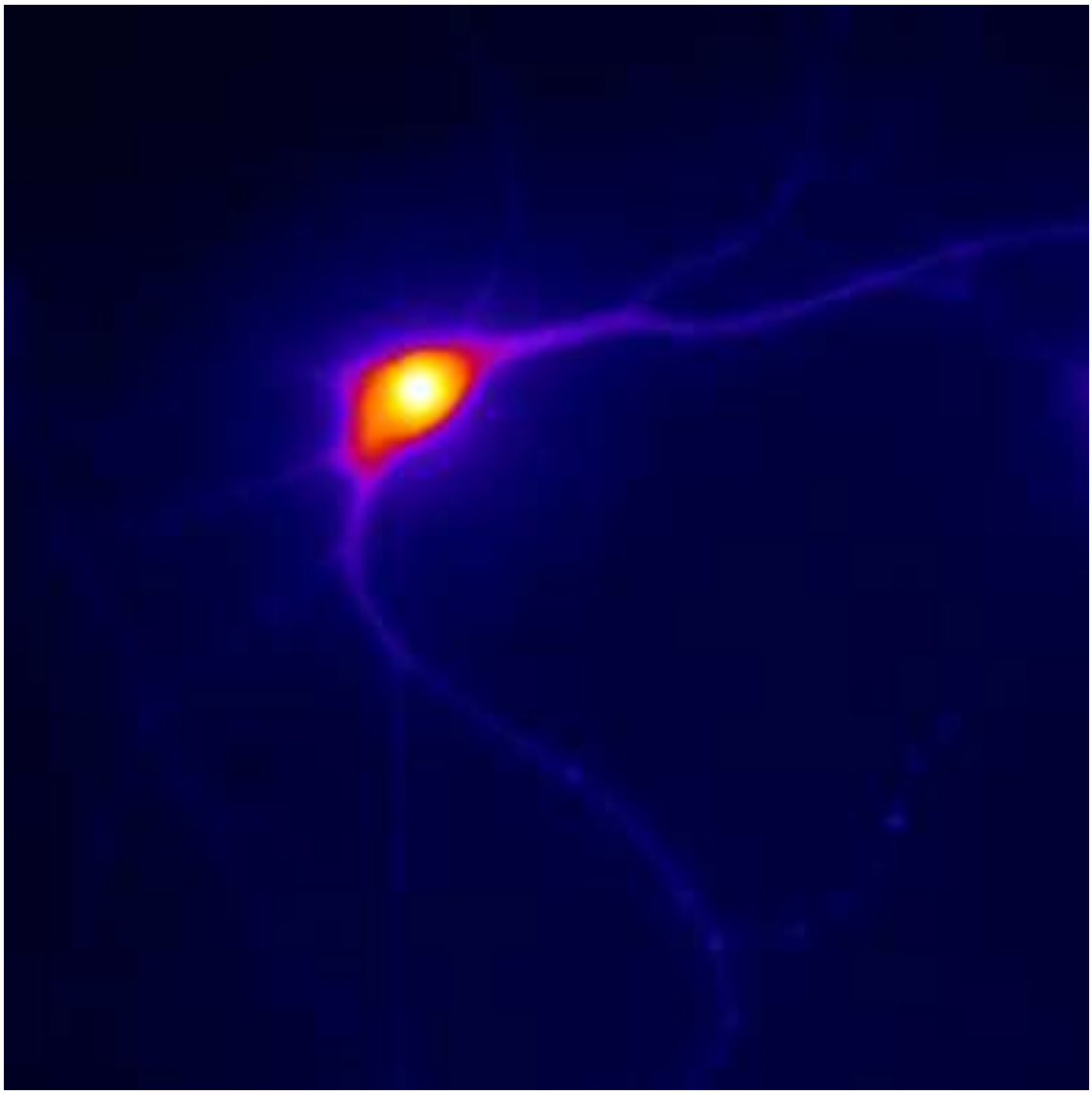

Neuron glowing in the dark. *The image presents a fluorescence (calcium-indicator) view of a cultured neuron, as acquired in parallel to a quantitative phase image in the multimodal microscope presented in this chapter.*

CHAPTER 2

Custom built QPI systems

Table of contents

2.1 From Michelson to Linnik interferometry **57**
2.2 Amplitude and phase separation: Different phase-stepping schemes **57**
2.2.1 Fixed phase-stepping 59
2.2.2 Integrative phase-stepping 61
2.2.3 Increasing the acquisition speed using sliding windows 63
2.2.4 Hilbert transform for single shot phase recovery 64
2.3 Phase unwrapping: From phase maps to 3-D optical path maps **64**
2.4 Linnik interferometer and simultaneous fluorescence measurement **67**
2.5 Mechanical and thermal stability: Common-path interferometer **68**
2.6 Wide-angle differential interference contrast microscopy **69**
2.6.1 Wollaston & Nomarski prism 70
2.6.2 Interest for wide-angle Nomarski prisms 71
2.6.3 Phase Modulator and phase-stepping in Wa-DIC 72
2.6.4 Changing the shear angle 74
2.7 Wa-DIC reflection microscope in practice **75**
2.7.1 Quantitative phase imaging 75
2.7.2 Deconvolution of the phase image 77
2.7.3 Birefringence measurement 78
2.8 Simultaneous QPI and fluorescence measurement with Wa-DIC configuration . **79**

Following the long introduction on QPI, this chapter will be dedicated to present my humble contribution to this field. As a reminder, we started building QPI systems to use their extreme axial sensitivity to detect propagation of activity-dependent mechanical displacements in neurons and especially neurites, probably of sub-nanometric amplitude and of timescale around 1 ms. To our knowledge, there is no available commercial system that meets these requirements, so we started to build our own QPI systems. However, *C.Boccara* 's team have invented and developed full-field optical coherence tomography (FF-OCT), a white light interferometer mainly used in tissues, which will be mainly described in the second part of this manuscript. Our first approach was therefore to adapt the existing FF-OCT systems in the lab to perform QPI measurements in neuronal cultures. FF-OCT is based on a Linnik interferometer, that I will first briefly describe in this chapter, and can be used as a phase shifting white light QPI system. The first setup configuration we have operated used a fast camera that could acquire up to 30,000 frames per second with which, we would hope to follow the action potential propagation. Nevertheless, due to its low FWC and therefore low phase sensitivity and due to its complexity to interface with an independent electrical measurement, we decided to build another FF-OCT system that would simultaneously combine a FF-OCT and a fluorescence path [105] that can detect the electrical activity of the neurons. For the course of this manuscript, I decided to leave all considerations related to the elaboration of this system in chapters 4 and 5 since its main interest is the ability to also perform measurements in thick scattering tissues. In this chapter, I will simply describe Linnik interferometers in comparison with Michelson interferometers and I will describe the full procedure to go from a direct interferogram to the measurement of a quantitative phase map in cell cultures. Nevertheless, we soon realized that FF-OCT configuration was not always optimal to detect sub-nanometric variations due to mechanical and thermal noise limiting the sensitivity above the camera shot noise. To recover the shot noise limited sensitivity, we developed another QPI microscope in a common-path configuration so that the mechanical and thermal phase variations would be felt the same way in both arms and the measured phase difference would be therefore robust to these vibrations. The interferometer is based on polarization separation of beams using Wollaston or Nomarski prisms, and is quite similar to a reflection Differential Interference Contrast (DIC) microscope in its design. However, in the configuration we have developed, we decided to largely spatially separate the polarized beams and to add a polarization modulator in order to obtain a quantitative phase measurement of small objects. This microscope was inspired by past work done at the LOP at the Institut Langevin [18] from the teams of *J. P. Roger* and *C. Boccara*, although, to my knowledge, it was the first time such configuration was used for biological measurements. We also enriched this microscope with a fluorescence path, with the same idea of simultaneously measuring an electrical activity. Therefore, a second part of this chapter will be dedicated to the description of this technique and to its potential. This chapter mainly aims to describe the technological developments of these two systems, while their applications to neuronal cultures will be further detailed in chapter 7.

2.1 From Michelson to Linnik interferometry

The first QPI system I have developed during this project is based on the setup of full-field optical coherence tomography (FF-OCT) that is simply a Linnik interferometer in a low coherence configuration similar to the setup described in *Yamauchi et. al.* [52]. The FF-OCT configuration will be largely detailed in chapter 4 so I will only present it briefly here. In essence, the Linnik interferometer consists in the better-known Michelson interferometer but is better adapted to biological imaging at micron scale. Linnik interferometer distinguishes from Michelson interferometer by the addition of two identical microscope objectives in the two arms of the interferometer, as illustrated in figure 2.1. A 2-D detector is conjugated with the objective focal plane so that the phase information is acquired simultaneously on all the camera pixels. In this configuration and similarly to the Michelson configuration with tilted mirrors, parallel interference fringes can be observed in the camera plane with a fringe distance inversely proportional to the angle between the two mirrors corresponding to a tilted wavefront[1]. The imaging configuration of the Linnik interferometer offers a high transverse resolution limited by diffraction hence by the objectives NA. Microscope objectives are preferred to imaging lenses to reduce optical aberrations and the two same objectives are used to reduce uncontrolled optical path variations between both paths. Note that the magnification of the objective also affects angles (with the same factor) so that it is quite hard to have exactly the same average angle in both arms and to eliminate the interference fringes. As mentioned, the interferometer is operated in a low coherence configuration, which is not crucial for QPI measurements but is mandatory for tissue imaging, as it will be discussed in chapter 3. The important point for this chapter is that our systems are operated with LEDs both spatially and temporally incoherent, which cancels the speckle formation in a transmission-like configuration, as previously discussed. The Linnik configuration offers a phase shifting low coherence QPI configuration and can eventually be slightly off-axis to recover a phase map in two acquisitions [106], or even in a single shot[2]. Phase shifting in this configuration is simply performed by mechanical translation of the reference mirror mounted on a piezoelectric actuator.

2.2 Amplitude and phase separation: Different phase-stepping schemes

In the previous chapter, we have seen that 4 phases shifting authorizes the homogenization of the intensity and phase noise of interferograms. In this section, I will recall the interest for phase shifting in interferometry, and present several strategies we have been using in our 2 QPI phase shifting systems and also in our measurements in biological tissues that will be presented in the next part. Obviously, phase shifting algorithms have been widely studied in various interferometer configurations and all of them allow the calculation of an amplitude and a phase map. However, it is important to carefully select the phase shifting algorithm adapted to the interferometer and imaging parameters. Otherwise, amplitude and phase separation will be only partial and it can add an important noise to the phase measurement, preventing shot noise limited experiments. In this section, we will express the interference pattern as an incoherent combination of light that does not interfere (coming from the reflections on the optics, out-of-focus light,...) and some

[1] We can note that circular fringes or distorted fringes can be observed in presence of optical aberrations but this barely affects the transverse resolution of the phase image as it will be further detailed in chapter 4.

[2] see strategies reviewed in [107] chapter 7 or using a blazed grating [108] or a retroreflector as the reference mirror [109], which tilts the spatial wavevectors but not the coherence volume [110]. Note that if these strategies are efficient when imaging a cell culture, they often less perform in tissues.

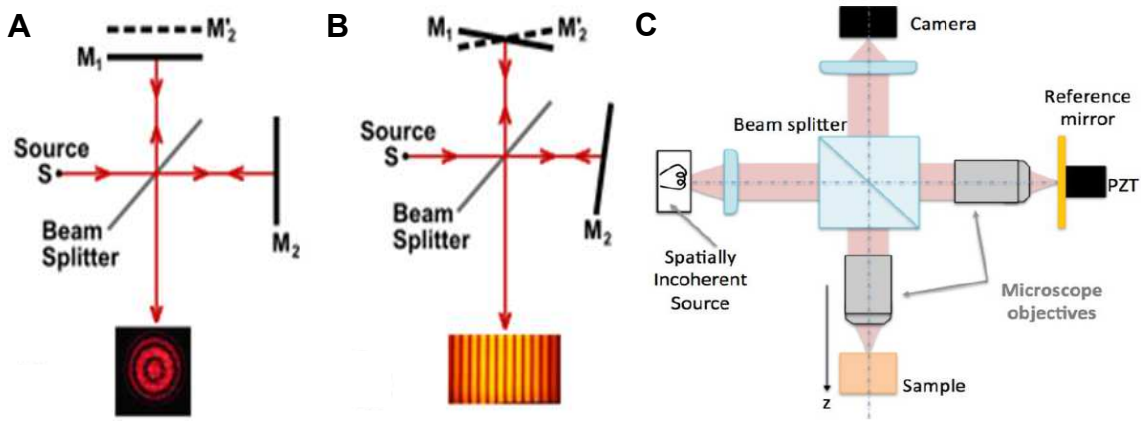

Figure 2.1 – From Michelson to Linnik configuration. Panels A and B present the well-known Michelson interferometer in its parallel (panel A) and tilted (panel B) configurations. **Panel C** presents the Linnik configuration in comparison, which differs from the Michelson interferometer by the addition of two microscope objectives and a tube lens to conjugate the imaged plane with a 2-D sensor.

coherent light that interferes:

$$\mathrm{I_{detector}(x,y,t)} = \mathrm{I_{inc}} + \mathrm{I_{coh}(x,y,t)} * cos(\phi_{\mathrm{sample}}(\mathrm{x,y,t})) \tag{2.1}$$

From this equation, it is apparent that producing interference patterns is not enough to quantitatively measure the phase. Indeed, it is impossible to know whether an intensity change is caused by an amplitude change ($\sqrt{\mathrm{I_{sample}}}$) or by a phase change that modulates the cosinus. Plus, the nonlinearity and periodicity of the cosinus make difficult the interpretation of an intensity change into a quantitative phase difference. Regardless of the characteristics of the phase system that is used, the goal of a quantitative phase system is first to extract the interference term out of the total intensity, and then to separate the amplitude information from the phase information, and to linearize the phase term. It corresponds to perform a fitting of a cosinus in the intensity fluctuation, or to the fitting of a circle in the phase space, eventually in presence of noise as illustrated in figure 2.2. To perform a more accurate fitting, strategies consisting in accumulating data with the same four steps, or in calculating a higher number of phase steps can be developed, however at the cost of the acquisition speed. The different phase-stepping algorithms can fall into two main categories: fixed steps and integrative steps. In the first case, phase-stepping is easy to implement, as a phase shift is introduced into a number of fixed steps. It requires the modulation to stabilize around an averaged constant value on a timescale faster than the frame time minus the exposure time, which then limits the exposure time. Alternatively, Integrative phase steps strategies measure the average phase during a constantly moving phase scan and imposes on working with an exposure time as close as the frame time as possible. Finally, I will also introduce a 5 phases integrative steps algorithm, which is supposed to be more robust in white light configuration, as illustrated in figure 2.3. All these modulation schemes are available on the various versions of the home-made user interface software I have developed to control my experiments. On a final general note, all the phase-stepping algorithms presented below are accurate only assuming the amplitude and the phase difference are not changing over timescales smaller than the time required for the multiple phase calculation. Some effect of phase variations faster than 4 phases calculation will be presented in chapter 5.

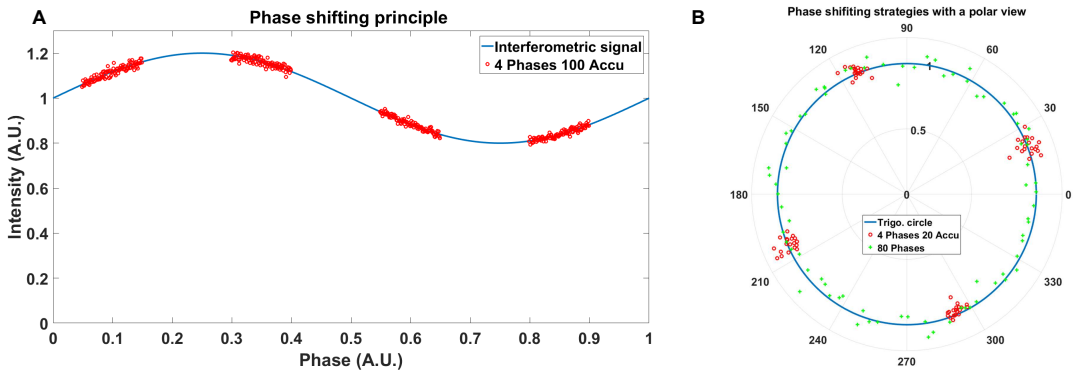

Figure 2.2 – Phase shifting principle. Panel A illustrates the phase shifting strategy from the point of view of the interferometric signal. From 4 phases, an accurate fitting of the cosinus can be performed, which enables the measurement of the incoherent intensity, the interference term amplitude, and the initial phase. In presence of noise on both the amplitude and the phase, the fitting accuracy can be increased by accumulating several frames around the same 4 phases, and average the estimated amplitude and phase values. **Panel B** presents the same strategy in the phase space, in which the fitting consisting in finding the radius of the circle. It additionally compares a strategy of 4 phases with 20 accumulations (red circles) and a strategy of 80 phases (green crosses).

2.2.1 Fixed phase-stepping

Again, the principle of fixed phase-stepping is to produce fixed phase shifts between each image acquisition, which is performed using the displacement of a piezoelectric on which is mounted the reference arm in our case. The piezo mechanical displacement ultimately limits the acquisition speed but also limits the exposure time since the piezo has to stabilize before the measurement can be started. Obviously, the stabilization time increases with the acquisition speed and with the amplitude of displacement. In the case of the piezo we are using, the stabilization time is usually around 1 ms, while the acquisition speed can go up to 700 Hz and therefore imposes on working with short exposure times to avoid artifacts, or to decrease the acquisition speed. Nevertheless, fixed phase-stepping is mainly used for its simplicity to implement. Indeed, the piezo displacement being linear with the applied voltage, we can either use calibration curve to calculate the voltage that corresponds to a $\frac{\pi}{2}$ phase shift and then multiply this voltage for the corresponding required phase shifts. The calibration can also be easily performed by calculating the 4 phases amplitude signal for various voltages on a fringe pattern. The fringe pattern contrast in the amplitude image reaches a minimum for a voltage corresponding to a phase shift of $\frac{\pi}{2}$. In this subsection, I will further shortly present 2 phases, 4 phases, and N phases schemes that we implemented in our microscopes.

- **2 Phases:** To optimize the temporal frequencies bandwidth, while maintaining a good contrast in the interference signal, a first approach is to record only 2 images with a phase difference of π. It allows to remove all the incoherent light that often hides the coherent interfering signal, especially in scattering samples. From equation 2.1, we can calculate intensity difference after a phase shift of π that transforms the cosinus into minus the cosinus:

$$\Delta \mathrm{I} = 2\mathrm{I}_{\mathrm{coh}} cos(\phi_{\mathrm{sample}}) \tag{2.2}$$

  The intensity difference here couples the amplitude and the phase term but advantageously remove the incoherent light, which has proven to be useful to better extract the signal

amplitude using Hilbert transform [106] or the phase difference signal in dynamic FF-OCT [111] that I will develop further in this manuscript.

- **4 Phases:** If only three phases are required to separate the phase and the amplitude, we often use a 4 phase steps scheme that allows an easier and more robust calculation of both terms. This scheme consists in calculating four successive images ($I_{1..4}$) with a respective phase difference of $\frac{3*\pi}{2}$, π, $\frac{\pi}{2}$, and 0. The $\frac{pi}{2}$ transforms a cosinus into a sinus, and equation 2.2 can be used twice to obtain:

$$\mathrm{I}_4 - \mathrm{I}_2 = 2\mathrm{I}_{\mathrm{coh}} cos(\phi_{\mathrm{sample}}) \tag{2.3}$$

And,

$$\mathrm{I}_1 - \mathrm{I}_3 = 2\mathrm{I}_{\mathrm{coh}} sin(\phi_{\mathrm{sample}}) \tag{2.4}$$

The interference signal amplitude can therefore be calculated as:

$$A = \frac{1}{2}\sqrt{(\mathrm{I}_4 - \mathrm{I}_2)^2 + (\mathrm{I}_1 - \mathrm{I}_3)^2} \tag{2.5}$$

Note that we call this term the signal amplitude, while it is still an intensity corresponding to twice the reference arm amplitude times the sample arm amplitude, as we often consider the reference signal to be spatially constant so that the interference signal *amplitude* is proportional to the sample arm amplitude. Additionally, the phase can be calculated as:

$$\phi_{\mathrm{sample}} = atan(\frac{\mathrm{I}_1 - \mathrm{I}_3}{\mathrm{I}_4 - \mathrm{I}_2}) \tag{2.6}$$

Here also, note that, in Matlab, it is often more stable to calculate the phase of the complex signal $(A.(cos(\phi_{\mathrm{sample}}) + isin(\phi_{\mathrm{sample}}))$ than calculating the arctangent of the ratio between the sinus and the cosinus, which is only defined between $-\frac{\pi}{2}$ and $\frac{\pi}{2}$ and is highly sensitive to noise close to the zeros of the cosinus.
In biological scattering tissues, we are almost exclusively using 4 phases modulation to extract the amplitude signal and can accumulate the measurement to increase the SNR as the square root of the number of accumulations similarly to what was calculated in the previous chapter on phase sensitivity.

- **N Phases:** To further increase the accuracy of the amplitude and phase calculation, a final strategy using any number (above 4) of phases is also possible to implement [112, 113]. For N measurements $I_{k=1..N}$ with a phase shift between 0 and 2π, $\delta\phi_k = 2\pi\frac{k-1}{N}$, the phase can be accurately calculated as:

$$\phi_{\mathrm{sample}} = -atan(\frac{\Sigma_{k=1}^{N} \mathrm{I}_k sin(\frac{2\pi k}{N})}{\Sigma_{k=1}^{N} \mathrm{I}_k cos(\frac{2\pi k}{N})}) \tag{2.7}$$

Qualitatively, we can compare this strategy with $N = 4n$ with n corresponding to the number of accumulations in a 4 phases strategy. Instead of accumulating the four same measurements the N phases strategy distributes its measurements all around the phase space, as illustrated in figure 2.2 B. The N phases strategy presented above is probably easier to compute and to implement with a mechanical modulation, but another N phases strategy may consist in a random (but controlled) phase modulation with which the intensity signal can be cross-correlated and is supposed to be the optimal way to eliminate random noise (such as shot

noise) [114]. To compare N phases and 4 phases schemes, my intuition[3] is that the N phases strategy will give a higher accuracy in the case where both the amplitude and the phase change over time, while both techniques would perform similarly if only the phase is changing over time or in the case of shot noise intensity fluctuations.

2.2.2 Integrative phase-stepping

The second family of phase-stepping techniques is based on integrative, or *heterodyne*, techniques consisting in imposing a continuous modulation of the phase difference. The main advantage of this class of techniques is that the exposure time can be (and in fact has to be) as high as the frame time (equal to the inverse of the acquisition rate). Additionally, in the case of a mechanical displacement, the smoother displacement allows for higher scanning frequencies and therefore higher acquisition rates. In integrative phase schemes, the phase measured in a single image is the average of the phase difference over the course of the phase change. For example, in the case of a linear phase increase, the measured phase will be the middle phase. In this subsection, I will present the two techniques we have been using in our experiments, either sinusoidal 4 phases modulation or triangular 5 phases modulation

- **Sinusoidal 4 Phases:** In this configuration, the reference mirror position is sinusoidally modulated at a frequency equal to the fourth of the acquisition speed. The main interest of this modulation scheme is to increase the frequency and have been particularly useful in the high-speed system we have been using. A full calculation as well as an error estimation can be found in a paper from *A.Dubois* in 2001 [115], which consists in calculating two terms:

$$\Sigma_s = -I_1 + I_2 + I_3 - I_4 = \frac{1}{f_{cam}\pi}\Gamma_s A sin(\phi_{\text{sample}}) \tag{2.8}$$

$$\Sigma_c = -I_1 + I_2 - I_3 + I_4 = \frac{1}{f_{cam}\pi}\Gamma_c A cos(\phi_{\text{sample}}) \tag{2.9}$$

  with f_{cam} the camera frequency, and Γ_s and Γ_c, two constants that depend on the relative time delay between the camera and the sinusoidal modulation and on the modulation amplitude. From these two terms, the amplitude and the phase can be calculated if $\Gamma_s = \Gamma_c$, which can be accurate only after a careful calibration of both the modulation amplitude and the time delay. Briefly, the calibration consists of two steps [115]. First, the time delay is adjusted to its zero value[4] for which $\Sigma_s^2 + \Sigma_c^2$ is equal to 0 (or to a minimal value) for all modulation amplitudes. Then, the time delay is set to its optimal value corresponding to a phase shift of 0.98 rad, and the modulation amplitude can be optimized. Its optimal value is found when the fringes pattern visibility reaches a minimum, similarly to the 4 phases steps calibration strategy.

- **Triangular 5 Phases:** Finally, we recently adopted a phase-stepping integrative approach consisting in modulating the reference mirror position in triangles with a frequency equal to the tenth of the camera frequency (from which we extract two phase images) [69]. The amplitude and phase can be calculated as:

[3] Unfortunately, I could not find any articles comparing the N phases and 4 phases accumulated strategies and I could not find the time to make the calculation...

[4] This requires a calibration since a jitter between the camera trigger and the acquisition can exist.

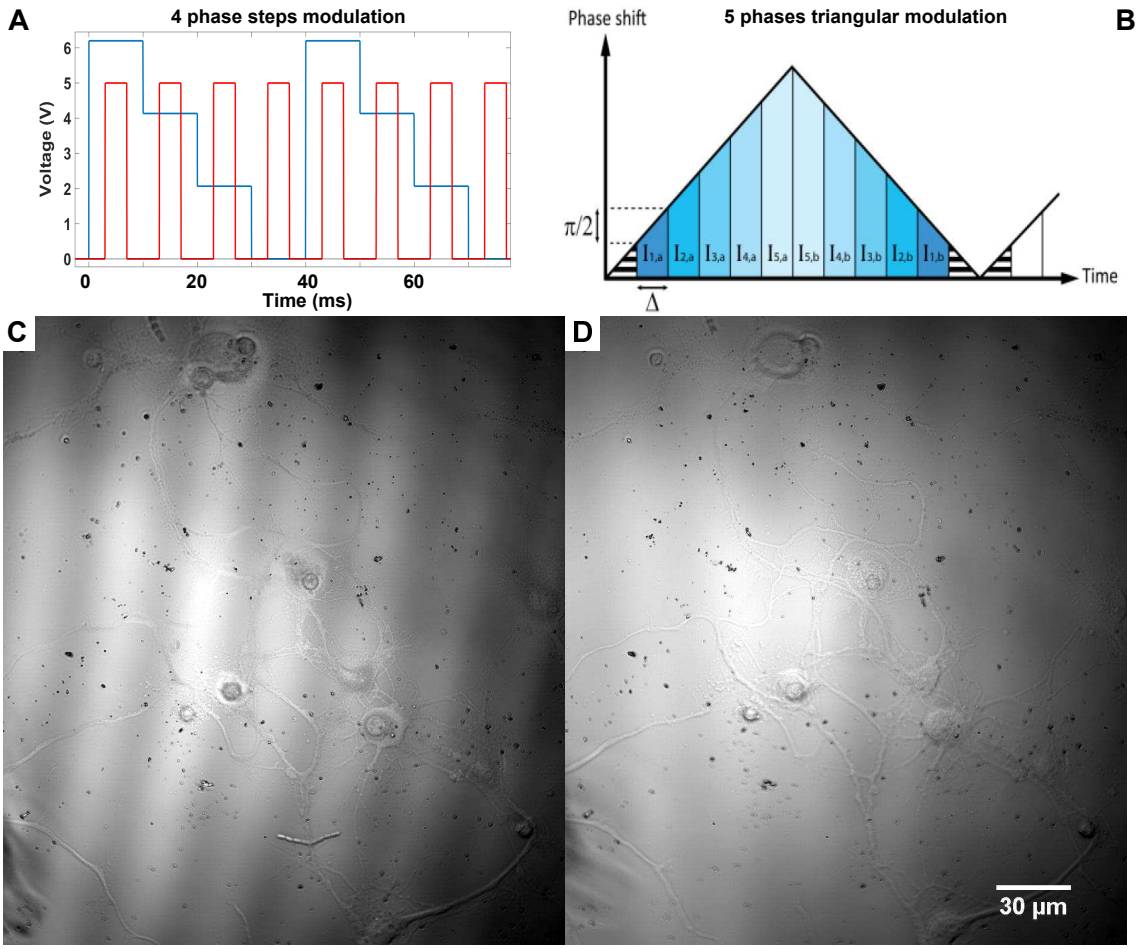

Figure 2.3 – Comparison between 4 phases and 5 phases scheme. Panels A and B present the modulation pattern to perform a 4 phases steps (panel A) or triangular 5 phases (panel B from 2.11. In panel A, the blue line represents the piezo modulation, while the red line shows the camera trigger. In triangular modulation (panel B), the camera exposure time is Δ corresponding to a phase increase of $\frac{\pi}{2}$. **Panels C and D** illustrate the respective accuracy of the amplitude reconstruction for the 4 phases (panel C) and 5 phases (panel D) strategies. The 4 phases strategy displays a higher coupling between the amplitude and phase maps which prevent the good visualization of cells giving an optical path difference higher than 2π due to phase wrapping in the amplitude map. The phase map has almost disappeared from the amplitude map in the 5 phases configuration. When the phase maps are compared (not shown, the phase noise is higher in 4 phases than with a 5 phases modulation.

$$A = \sqrt{4(I_2 - I_4)^2 + (I_1 - 2.I_3 - I_5)^2} \tag{2.10}$$

$$\phi_{\text{sample}} = -atan(\frac{2(I_2 - I_4)}{(I_1 - 2.I_3 - I_5)}) \tag{2.11}$$

Amplitude and phase maps can be calculated during the ascending part of the triangle, and during the descending part as well by changing the order of the images (In the descending part, I_5 corresponds to the first image, and so on...). This phase-stepping strategy main interest is its ability to measure an amplitude and phase map for any phase shift between two consecutive images (in comparison to 4 phases schemes for which a $\frac{\pi}{2}$ phase shift is mandatory), although the SNR can be increased for a $\frac{\pi}{2}$ modulation. Nevertheless, it is of critical importance when using broadband interferometers. Indeed, from the beginning of this section, I have mentioned phase shifts induced by a given displacement of a mirror. But

the phase shift is equal to $\frac{\pi}{2}$ only for the light central frequency, while it corresponds to different phase shifts for the other wavelengths, which may introduce a strong noise in the phase calculation at the end. As another consequence, 4 phases algorithms couple the phase and amplitude maps, which is not (or less) the case with a 5 phases modulation strategy, as illustrated in figure 2.3. Additionally, the phase calculation is more stable for incoherent light, since the denominator is not a single intensity difference and would not diverge for a very small amplitude of the interference term; Phase noise can here also be avoided. The calibration of this technique is quite simple, as it can use the calibration of the 4 phases steps to find the voltage to apply for a $\frac{\pi}{2}$ modulation. An additional time delay has to be added so that the edge of the triangle is exactly at the end of the fifth image, otherwise the phase in the ascending and descending phases will be different.

2.2.3 Increasing the acquisition speed using sliding windows

Obviously, the more phases are acquired to reconstruct the phase information, the more limited is the frequency bandwidth. However, in this subsection, we would like to make a comment on the real loss in temporal resolution. Especially, when imaging a fast and high SNR phase change, we can preserve the temporal resolution, by reconstructing the phase using a sliding window. Let's take the example of 4 phases imaging to illustrate such scheme. Instead of calculating a phase image every 4 images, a sliding window allows to calculate N-3 phase images for N intensity images acquired, as illustrated in Figure 2.4. The first phase frame is calculated with 4 phases, as usual. Then, the next phase image is calculated with the fifth intensity image replacing the first intensity image. Then, the third phase image is calculated with the fifth and sixth intensity images respectively replacing the first and second intensity images, and so on and so forth. The measured phase signal being the time average of the object phase over the total time of the 4 phases acquisition, it can effectively not detect frequency below the acquisition frequency divided by 4, but it can follow the average phase change associated with a transient process (which is notably the case for a propagating neuronal signal!) up to the camera acquisition rate.

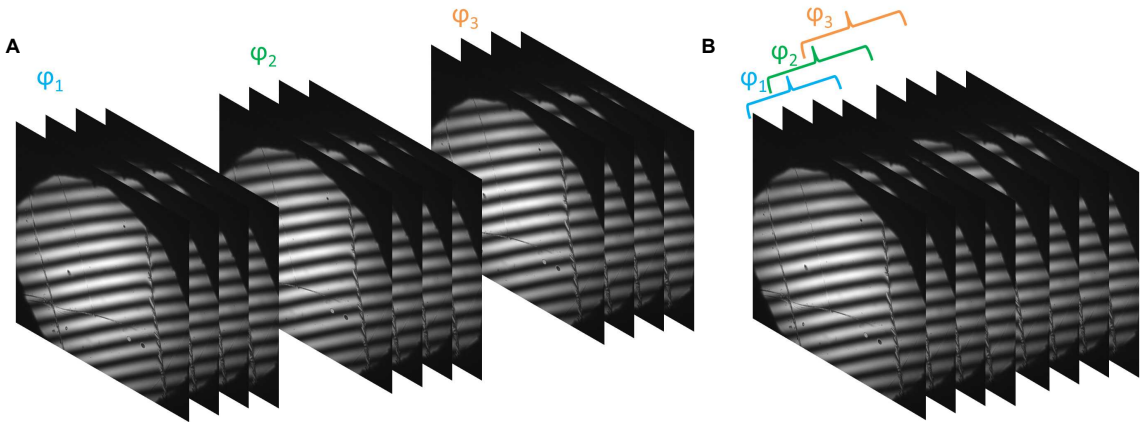

Figure 2.4 – Principle of sliding window acquisition. Panel A illustrates the image combination in a standard 4 phases process that calculates an amplitude and a phase map for every set of 4 images. **Panel B** illustrates the principle of sliding window acquisition that produces a phase and amplitude image at the camera frequency acquisition. The first phase image is calculated using the 4 first images, but the next phase images are calculated using only one new frame and three frames already used.

2.2.4 Hilbert transform for single shot phase recovery

In this subsection, I will briefly describe the use of Hilbert transform to recover the phase signal in a single shot. It is worth noticing that our phase maps look like phases maps used in Hilbert phase microscopy to recover the object phase without the need for phase shifting [7, 29]. It requires the imaging of several interference fringes in the field of view even if they start being attenuated due to the system low coherence but it does not require especially high fringes spatial frequency as used in Digital Holography. In low coherence systems (used for reducing the speckle noise and the spatial phase heterogeneities), a high-frequency fringe pattern would be attenuated after a few periods and would drastically reduce the field of view[5]. In our systems, we have investigated the use of Hilbert transform in order to increase the speed. Interestingly, our systems exhibit with this ability respectively 3 and 4 of the 4 properties of full field QPI systems as defined by *G. Popescu* [7] and are among the most versatile QPI systems. In phase shifting interferometry, the amplitude and the phase are separated by calculating a complex term and taking either its modulus or its phase. In fact, this complex term can be instantaneously calculated using the analytic representation of the real interference intensity measurement. The analytic representation is simply calculated by removing the negative frequency components of the Fourier transform of the real signal (that are redundant anyway due to the Hermitian symmetry of real functions) [116]. The resulting analytic signal is complex and can be used to measure the instantaneous amplitude and phase of the signal. The amplitude term would mainly correspond to the low-frequency variations (such as an amplitude decrease due to low coherence) while the phase would integrate most of the high frequencies. With several interference fringes, the instantaneous phase can be calculated as long as the object is weakly scattering and that it does not perturb the amplitude too much. Finally, the concept of negative frequency is not trivial in multiple dimensions and needs to choose an arbitrary direction that separates the Fourier space in two regions from the origin.

In practice, an initial high-pass filter is applied to remove the incoherent low-frequency signal and only isolate the interference signal. Then the analytic signal is calculated by using the fringes direction as the arbitrary direction and numerically canceling all the pixels below the orthogonal line in the Fourier space and going back to the real space. The resulting analytic (complex) signal displays the instantaneous amplitude as its modulus and the instantaneous phase as its phase. If this procedure works efficiently on flat coverslips, it introduces several artifacts when objects with high spatial frequencies are images as illustrated in figure 2.5. Nevertheless, it might be a reasonable price to pay to increase the acquisition speed in some cases.

2.3 Phase unwrapping: From phase maps to 3-D optical path maps

From 2-D phase maps obtained with phase shifting algorithm (see figure 2.6A for example), the quantitative phase map of the object yet can not be easily calculated. The first issue is that the measured phase is the sum of the object phase map with the local phase associated with the fringe pattern. The other more important issue is the phase measurement 2π periodicity, *a priori* preventing the phase reconstruction for phase differences higher than 2 π, which is often the case around cell somas. This complex problem of *phase unwrapping* has been known for a long time and has been extensively studied [117], even though most solutions have been developed for the case of off-axis holography while relying on a clear separation of the fringe pattern from the

[5] unless a blazed grating is used in the reference arm, as explained in the introduction of this chapter.

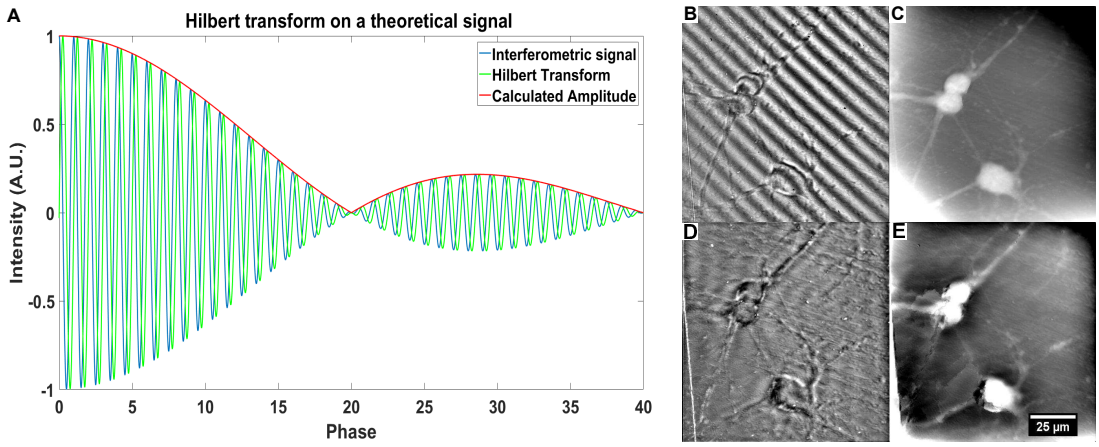

Figure 2.5 – Principle of single-shot phase recovery using the Hilbert transform. Panel A illustrates the principle of the Hilbert transform. An interferometric signal (blue line) is composed of a high-frequency cosinus term damped by a carrier signal. The Hilbert transform (green signal) allows to isolate the high-frequency signal and multiply it by i in the Fourier space, which transforms a cosinus into a sinus. From the cosinus and the sinus, the local amplitude and phase can be computed similarly to other phase shifting algorithms. **Panels B to E** show a practical implementation of a single shot phase recovery using a Hilbert transform on a hippocampal neuron culture. Panel B shows a direct interferogram acquired with our Linnik interferometer, and panel C shows the corresponding phase map calculated with a 4 phases steps algorithm. Panels D and E respectively show an amplitude and phase maps recovered in a single shot from the image displayed in panel B. It allows for a correct reconstruction but adds a few artifacts.

object in the Fourier space but can not be used in our low coherence case. Phase unwrapping is an important issue because, if performed inaccurately, it can add a large phase noise in the QPI measurements. In the next part, in chapter 3, I will present another approach to prevent the need for phase unwrapping that recovers the phase difference between two consecutive frames in time that is often smaller than 2π. Nevertheless, if the phase map of an object needs to be observed, phase unwrapping algorithms are a critical point. Briefly, if one-dimensional unwrapping problem is easy, it becomes more complex in multiple dimensions, especially in presence of noise. The most natural approach is to perform unwrapping on either the lines or the columns of the image but, in presence of noise, it is hard to get a continuous phase in the perpendicular direction of the unwrapping process. Complex strategies have been implemented to correct and minimize the discontinuities but are often computationally intense. During this work, we have mainly used two different standard 2-D unwrapping algorithms, namely *2-D SRNCP* (sorting by reliability using noncontinuous path) [118] and *Volkov* or phase gradients algorithms [119]. The first approach consists in performing a 1D unwrapping algorithm but on a 2-D path chosen so that the error is minimized. All pixels are sorted in order of the minimization of their phase difference with their first and second order neighbors. The unwrapping path choses the next pixel as being the least variant including the pixels in diagonal. Once this path arrives at some point where all the phase gradients are important, the path can start from another location (noncontinuous path) so that at the end all pixels with smooth phase gradient have been unwrapped. Finally, the regions with high phase gradients are unwrapped in order to minimize the error with multiple unwrapped pixels surrounding these regions. The *Volkov* algorithm consists in calculating the phase gradient which cancels the 2π constant phase jumps. The phase map has then to be calculated from its gradient, which can be performed in the Fourier space. For both strategies, we adapted available C or Matlab routines that can be performed in a short amount of time (below one second for a 2M pixels image). For the many different algorithms we could try, the most satisfying one for

our cell culture measurements is a combined strategy. First, it uses the 2-D SRNCP algorithm to reconstruct an unwrapped phase, which is the sum of the unwrapped fringes and the object phase, as illustrated in figure 2.6 B. Then, to remove the low-frequency component, it uses a home-made Matlab code that consists in selecting manually the areas where the cells or phase artifacts are in order to remove them and in applying a Gaussian filter to the processed image. It gives a good approximation of the local phase induced by the fringe pattern, which is then subtracted to the original unwrapped phase image. It authorizes to isolate the phase difference induced by the object only, as illustrated in figure 2.6 C, and gives a phase map that is quite homogeneous in the center of the field, as illustrated in figure 2.7 B. Nevertheless, in some cases, the *Volkov* procedure performs better but usually provides phase maps with a less homogeneous background that lowers the contrast, as illustrated in figure 2.7 A. Indeed, when performing the Fourier transform, the *Volkov* algorithm tend to apply a high pass filter and to remove the fringes phase but less accurately than using the linear regression combined with the 2-D SRNCP algorithm. I have to admit that I could not identify any pattern to predict which algorithm will better perform for a given phase map so I usually tried with the 2-D SRNCP algorithm first and switch to the *Volkov* procedure if I was not satisfied, in a totally empirical manner. In the future, it could be worth spending more time and energy to optimize this unwrapping procedure.

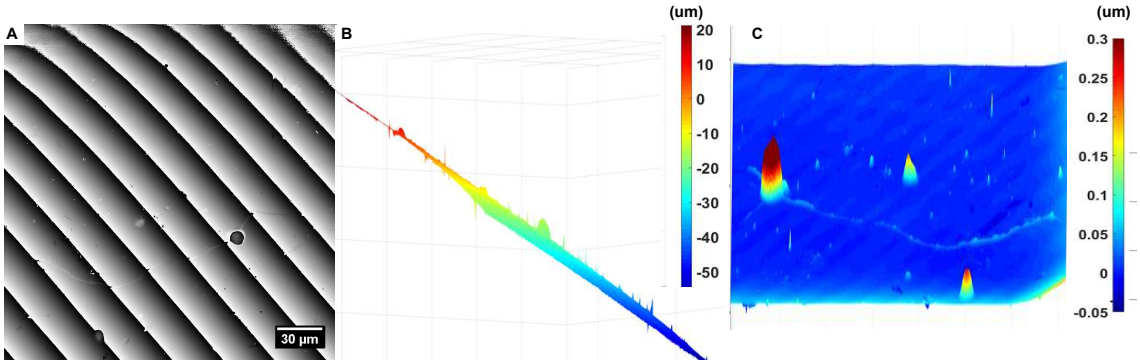

Figure 2.6 – Phase unwrapping principle. Panel A shows a typical phase image with a 2π periodicity, in which the neuron optical path is hardly measurable. **Panel B** shows the phase map obtained after having applied a phase unwrapping algorithm. The neuron optical path is here also complicated to apprehend because the fringes phase pattern is not spatially homogeneous. **Panel C** shows the final quantitative optical path map after subtracting the fringes phase pattern (using an averaged linear regression for example), showing a background around zero and an optical path increase around the neuron.

Once the object phase map is obtained, a number of additional filters can be used to obtain various pieces of information about the biological objects [7]. An interesting example is to calculate the phase derivative to obtain a DIC-like image as illustrated in figure 2.7 C. Calculating this derivative is not only interesting to provide a DIC-like display but can be understood as a robust spatial high-pass filter. Interestingly, having access to the real phase map, higher order derivatives can be calculated such as the phase Laplacian that allows for an artifact-free (without any preferential direction) high-pass filter. Nevertheless, the higher-order the filter becomes, the lower the SNR becomes. If such spatial derivatives can nicely emphasize small neurites, cellular protrusions or any other sub-wavelength object, they are not necessarily efficient to detect an activity-dependent phase change as it is expected to have a large spatial extension due to the propagation velocity.

We can finally add that similarly to the case of fluorescence exclusion in the previous chapter,

the measured phase is a spatial average of the field over the system PSF[6] so that when imaging cells larger than the depth-of-focus, the phase information about the top of the cell is spatially averaged around adjacent pixels, and an adequate deconvolution might be beneficial to perform.

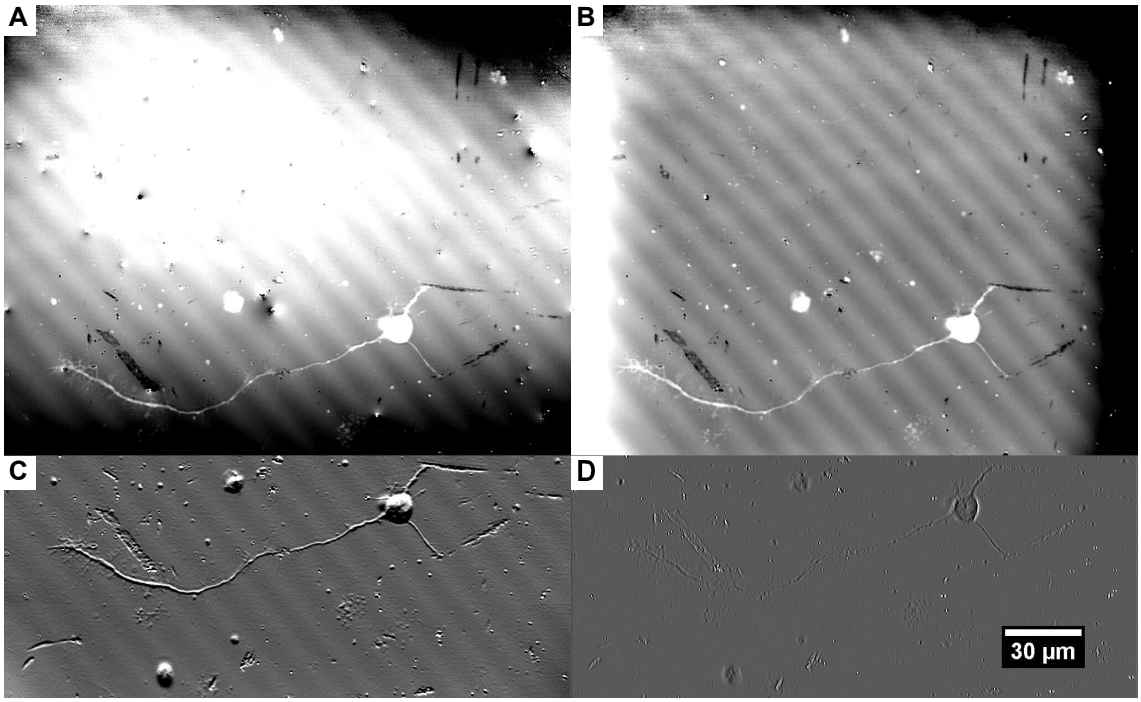

Figure 2.7 – Mathematical filtering of the quantitative phase image. Panels A and B show the same quantitative phase map calculated either with a Volkov unwrapping algorithm (panel A) or with an SRNCP algorithm (panel B). The latter shows a much better estimation in the central part of the image which seems to be consistent over many images. **Panel C** shows the phase derivative along the columns of panel B phase map. It approximately corresponds to the application of a highpass filter and logically looks like a DIC image with an identifiable shear axis. **Panel D** shows the Laplacian of the phase map, which sacrifices a part of the image SNR (2nd order highpass filter) to remove the preferential shear axis of the DIC-like image.

2.4 Linnik interferometer and simultaneous fluorescence measurement

Finally, one crucial point to detect an activity-dependent phase change is to measure not only the phase but also the neuron culture electrical activity with a sub-millisecond synchronization. To achieve this objective, the interest of our first QPI system is its coupling with a fluorescence path that allows to capture the electrical activity using calcium [120, 121] or voltage-dependent probes [122]. Ultimately, it can also measure several other dynamic cellular features related with its activity such as its ATP content [123] or the position of its mitochondria [124]. Below is a simple outcome report allowed by this multimodal setup, however the description of the complete original setup will be performed in chapter 5 [105]. The phase measurement can be performed simultaneously to the fluorescence measurement with a 10 μs accuracy (limited by the electronic controller, but it might be easily increased) . With such setup, we could investigate phase changes associated with spontaneous electrical activity of an old neuron culture. Figure 2.8 presents an

[6]Except that the phase equivalent of PSF might not be the same as the intensity PSF, on which I could not find or calculate any satisfying answer.

example of such parallel detection in which the phase measurement is too noisy to correlate with the measured electrical activity detected with a calcium indicator. More successful experiments will be presented in chapter 7.

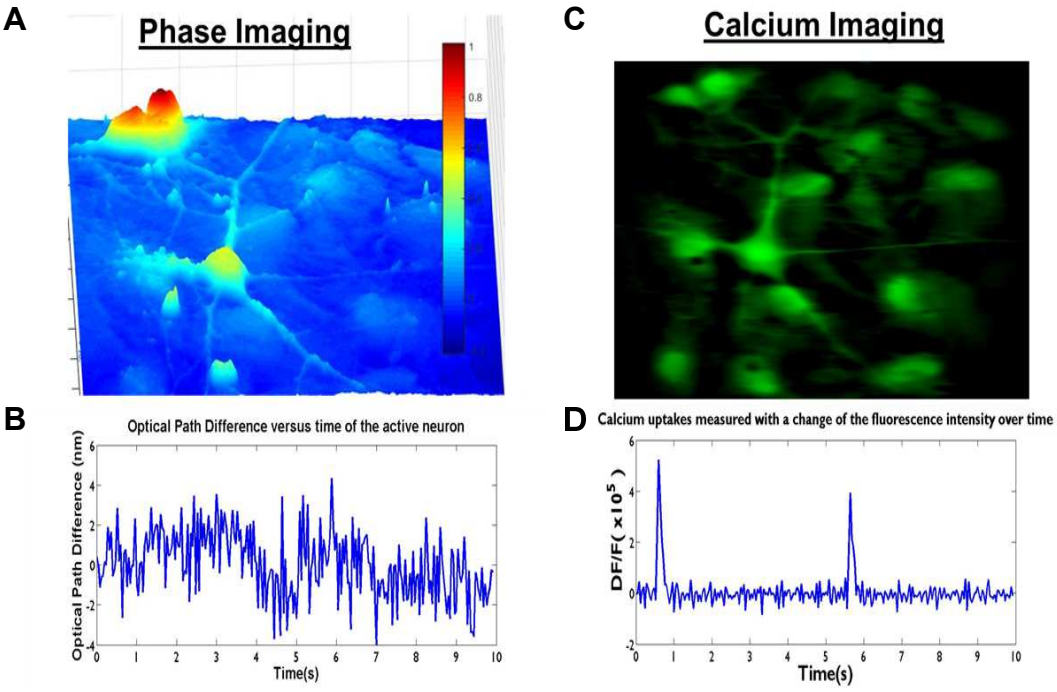

Figure 2.8 – Quantitative Phase Image and simultaneous recording of the calcium concentration in a neuron culture. Panel A shows a quantitative optical path map of a 2 weeks hippocampal neuron culture (with glial cells) and **panel B** represents a plot of the optical path measurement versus time at the soma of the top left neuron (within the red area). **Panel C** shows the corresponding simultaneous fluorescence map of Fluo-4, a calcium indicator. **Panel D** represents the differential fluorescence signal plot over time within the same area than panel B and illustrates a typical spontaneous activity of the neuronal network. In this figure, the optical path signal is too noisy to get any signal out of the noise but is far from the shot noise.

In this experiment, the phase measurement is quite noisy and is far from the shot noise limit, which is unlikely to be related to a biological activity and is probably due to either mechanical vibrations or temperature fluctuations. Despite our efforts to mechanically stabilize the setup and mechanically couple both arms of the interferometer, we have always measured additional phase noise higher than shot noise even though we have been able to make a few experiments close to shot noise when the environment is quieter. To reach ultimate performances, it motivated us to build another QPI system that would be based on a common-path configuration in order to eliminate such mechanical and temperature fluctuations that will be described until the end of the chapter.

2.5 Mechanical and thermal stability: Common-path interferometer

In fact, the attempt to obtain shot noise limited phase measurements is again a well known problem in QPI. Several techniques have been developed to mechanically isolate the interferometer and to stabilize the temperature. Nevertheless, maintaining the phase noise below 1 mrad becomes technically challenging, especially in conditions suitable for biological measurements. Interestingly, this issue has been faced from the beginning of interferometry and we can refer to the famous

Michelson & Morley experiment trying and failing to verify the existence of aether. Michelson and Morley really tried hard to push forward the sensitivity of their experiment as they notably mounted their interferometer on a 2 tons granite table floating on a mercury bath to absorb most of the mechanical vibrations. Despite these precautions, their sensitivity was probably around 50 mrad [125]. Another interesting value is the sensitivity reached in giant interferometers, such as VIRGO or LIGO, developed for detecting gravitational waves and mentioned briefly in the previous chapter. Latest developments permitted them to reach amazing sensitivities below 10^{-12} rad. However, working in the vacuum, with million dollars equipment and at several meters below the ground surface is little compatible with an ideal microscope that you want to put on the corner of a table to image living objects in a lab in the center of any city. To reach the shot noise limit, an easier solution is the development of common-path interferometers, in which both arms are spatially combined so that they both feel mechanical and temperature fluctuations the same way. Therefore, the optical path variation stays unchanged and the experiment can easily reach shot noise. In figure 2.9, we compare the experimental phase noise and phase noise frequency obtained with the Linnik interferometer (during good experimental conditions) and with our common-path interferometer that we named wide angle DIC microscope (Wa-DIC) and that I will be presenting in the next few chapters. It shows our ability to reach the shot noise limit with this new interferometer.

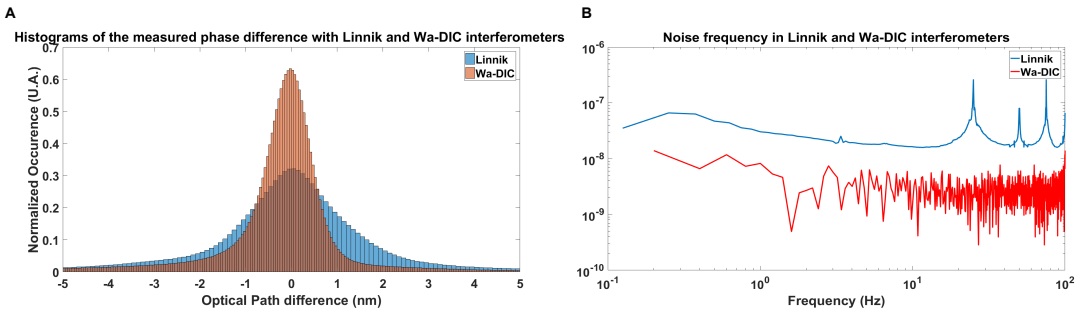

Figure 2.9 – Comparison of phase noise between a Linnik and Wa-DIC (common-path) interferometers. Panel A shows the comparison in the experimental optical path difference histograms of a Linnik and a common-path interferometer in the same experimental conditions (same camera and similar contrast). If the common-path interferometer is shot noise limited (standard deviation around 400 pm for a 200,000 FWC camera), the Linnik interferometer is less sensitive (standard deviation around 1 nm) due to mechanical noise. **Panel B** plots the noise frequency for the two same experiments, exhibiting a low-frequency component as well as large peaks around 25 and 50 Hz in the Linnik noise spectrum, while the Wa-DIC noise spectrum looks like a random noise frequency spectrum.

2.6 Wide-angle differential interference contrast microscopy

In the previous chapter, we have seen the principle of DIC microscopy, a white light common-path interferometer, which can only access a contrast based on the phase gradient. Inspired by DIC microscopy, and by previous work developed at the Institut Langevin during the early 1990s [18], we have developed a QPI system we named Wide-angle differential interference contrast microscopy (Wa-DIC) that can directly measure the phase of objects of small spatial extension and can give a birefringence-like measurement. Its common-path configuration allows for a high temporal stability as demonstrated in the previous section. Additionally, our Wa-DIC microscope is performed in low coherence, in a phase shifting and slightly off-axis configuration at the crossing point between the four categories defined by *G.Popescu* [7]. Recently, a similar setup in transmission has been

published by the group of *Y. Park* as a simple add-on to simply add in front of the camera [33]. We believe our configuration is both compact and easy to set, but we acknowledge that image interpretation has yet to be improved. In this section, I will successively describe the principle of Wollaston and Nomarski prism, emphasize the choice of a wide angle Nomarski prism that allows to measure the phase instead of the phase gradient and demonstrate how to perform phase shifting to perform a quantitative phase measurement. The description of the setup scheme, as well as its extension to provide an additional fluorescence measurement, will be detailed in the next sections.

2.6.1 Wollaston & Nomarski prism

The principle of DIC as well as Wa-DIC microscopes relies on the separation of an incoming linearly polarized beam into two beams of orthogonal polarizations. This is usually performed using either Wollaston or Nomarski prisms, the principle of which this subsection aims to explain. Shortly, such prisms use two similar wedges of birefringent uniaxial crystals in two different orientations and cemented together. The orientation of an uniaxial crystal gives the direction along which the light propagates with an extraordinary refractive index n_e, while it propagates with an ordinary refractive index n_o along the two other directions. The birefringence property of the crystal has two effects on a linearly polarized wave. First, because of the difference in refractive index, the relative phase between the two polarizations will change. Second, if the crystal birefringence orientation is not along the direction of the beam polarization, the beam will separate into two beams of different angles [12]. An intuitive case is illustrated in figures 2.10 A and B when a light passes through a Wollaston prism. At the separation between the two wedges, the angle between the light propagation direction and the second wedge surface causes the light to be refracted depending on the refractive index, accordingly to the Snell-Descartes law. In the case of the Wollaston prism, the first wedge is oriented along the light ordinary polarization while the second one is oriented along the extraordinary polarization so that at the separation, the ordinary ray changes from a refractive index n_e to n_o and the extraordinary ray from n_o to n_e. Therefore, they are refracted in different directions and the angular divergence comes from this tilted separation between the two wedges. It can be easily shown that for small angular divergences α, the latter is given by:

$$\alpha = 2(n_e - n_o)tan(\theta) \tag{2.12}$$

with θ, the angle between the entrance surface of the prism and the plane of wedges separation. Similarly, the path difference between the two polarizations is given by [12]:

$$\Delta\delta = \alpha x \tag{2.13}$$

with x the distance between the beam entrance and the center of the entrance surface. Logically, if the beam enters the prism close to a corner it will mainly propagate in one wedge and little in the other, introducing a larger path difference between the two polarizations. This property is interesting because it allows the scanning of the optical path difference by transversely translating the prism with respect to the center of the optical beam. Classically, interference fringes can only be observed when the two polarized beam converge into the same plane, often named *interference plane* [8]. The interference plane can also be understood as the plane where the two polarizations have no transverse shift between each other. If this interference is conjugated with the back focal plane of an objective, the two polarized beams will focus onto the sample with a similar angular distribution. It corresponds to the formation of interference fringes of very large spatial extension, often higher than the field of view, which is the usual configuration of DIC microscopes. On

the contrary, the further the interference plane is from the back focal plane of the objective, the higher the tilt between the two beams will become, which produces interference fringes of smaller spatial extension down to a point where the interference pattern is rapidly attenuated in white light. In Wollaston prism, the interference plane lies inside the prism, which makes it complicated to conjugate with objective back focal planes that are often at the back surface of the microscope objectives.

In practice, most of the polarization interferometers (such as DIC microscopes) use Nomarski prisms instead of Wollaston prisms that shift the position of the interference plane outside the prism, which makes it easier to conjugate with the objective back focal plane [8, 12, 126]. In contrast with Wollaston prism, Nomarski prisms use a first wedge with a tilted orientation (see figure 2.10 D). At the entrance of this first wedge, the extraordinary ray (with the polarization perpendicular to the plane) is supposed to keep its direction. On the contrary, the ordinary ray changes direction because a part of it travels at the speed $\frac{c}{n_e}$ and another part at $\frac{c}{n_o}$. If we call β, the angle between the first wedge orientation and the entrance surface, and α', the first angular shift between the two polarization, we can easily calculate:

$$tan(\alpha') = \frac{n_o}{n_e}\frac{cos(\beta)}{sin(\beta)} \tag{2.14}$$

After similar refraction at the wedges separation similarly to what happens with the Wollaston prism, it allows for the two rays to cross outside the Nomarski prisms. Apart from this feature, Nomarski prisms exhibit similar properties to Wollaston prisms.

2.6.2 Interest for wide-angle Nomarski prisms

As its name lets guess, the main difference between DIC and wide angle DIC is the use of a wide angle Nomarski prism. In an imaging configuration, the angle divergence leads the two rays to focalize at two separate locations as illustrated in figure 2.11 (or better explained in Annex A). Obviously, the transverse shift depends on the angular divergence and can be easily calculated for small angular divergence:

$$d_{trans} = f_{obj}.\alpha \tag{2.15}$$

with f_{obj}, the focal length of the microscope objective. In DIC, the Nomarski is chosen so that the beam divergence is extremely low (on the order of 10^{-5} rad) and the two beams are shifted of a few dozen nanometers, a distance smaller than the diffraction limit. Therefore, the transverse shift can not be imaged but the phase difference can be considered as the phase gradient along the shear direction. In wide-angle DIC microscopy, we chose to work with a larger beam divergence and therefore a larger transverse shift of a few microns, as illustrated infigure 2.11. In the case of a single small object, one polarization goes through the object before being reflected, while the other polarization does not cross any object a few microns apart so that it can serve as a phase reference. Therefore, the phase of the object can be directly measured instead of the phase gradient. Note that, thanks to the spatial multiplexing offered by the microscope objective and the full-field configuration, the objects are imaged twice, once with a first polarization and a second time with the other polarization, as it will be illustrated in the next section. This configuration is supposed to be particularly effective to provide quantitative phase imaging of neurites that are only a few microns large in diameter and can be easily separated into two distinct objects. Nevertheless, the phase image interpretation becomes more complicated for larger objects or dense cultures because the second beam also passes through an object of an uncontrolled refractive index. If

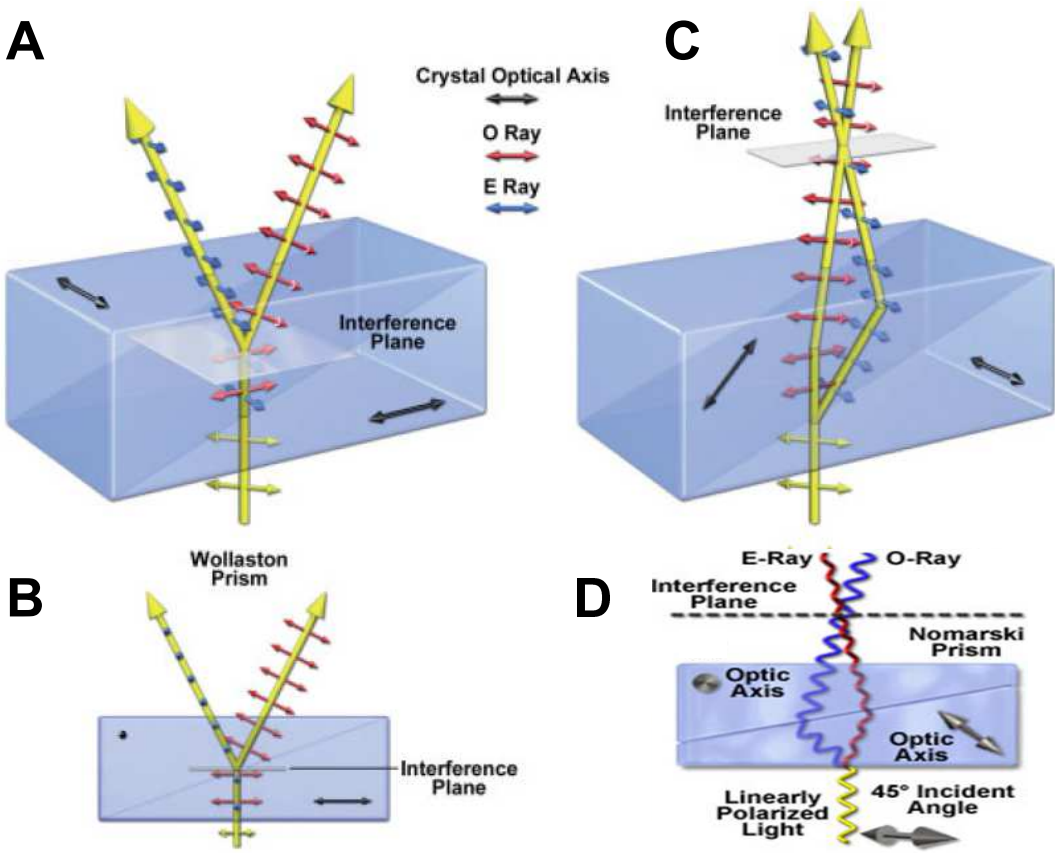

Figure 2.10 – Principle of Wollaston and Nomarski prisms. Panels A and B show a 3-D and 2-D views of a Wollaston prism illustrating the angular divergence between the two polarizations and the localization of the interference plane at the wedges separation. **Panel C** shows a 3-D view of one configuration of Nomarski prisms illustrating the shift of the interference plane outside the prism. The 3 images have been reproduced from [8]. **Panel D** shows a 2-D view of a Nomarski prism in a different configuration than Panel C. In this configuration, the wedge with a tilted orientation is the entrance wedge, which gives a more intuitive notion of Nomarski prisms in my opinion. Pay attention that the color code between the ordinary and extraordinary beams are inverted compared to the previous panels. The tilted orientation in Nomarski prism causes the ordinary ray to be deflected at the entrance of the prism, which shifts the interference plane. Panel D has been extracted from Olympus website [126].

more complicated, we will show in the next section that it is theoretically possible to reconstruct a quantitative phase image even for large objects.

2.6.3 Phase Modulator and phase-stepping in Wa-DIC

Compared to regular DIC microscopes, our Wa-DIC microscope can also measure quantitative phase measurements using a liquid crystal phase modulator. On the contrary to the Linnik interferometer that has two independent arms making it easy to mechanically modulate the optical path length difference, it is more complicated in a common-path interferometer. Nevertheless, in polarization interferometers, it is possible to modulate the optical path difference using phase modulators that will increase the optical path of only one polarization [32]. In practice, we used a liquid crystal phase retarder. Its principle relies on a small layer of a liquid crystal solution in its nematic phase with a preferential orientation. In presence of an electric field, the molecules tend to align along the field with an order degree controlled by the amplitude of the electric field. When no voltage is applied, the orientation of the molecules is parallel to the largest surface and perpendicular to the light propagation so that the medium is birefringent with an axis oriented in

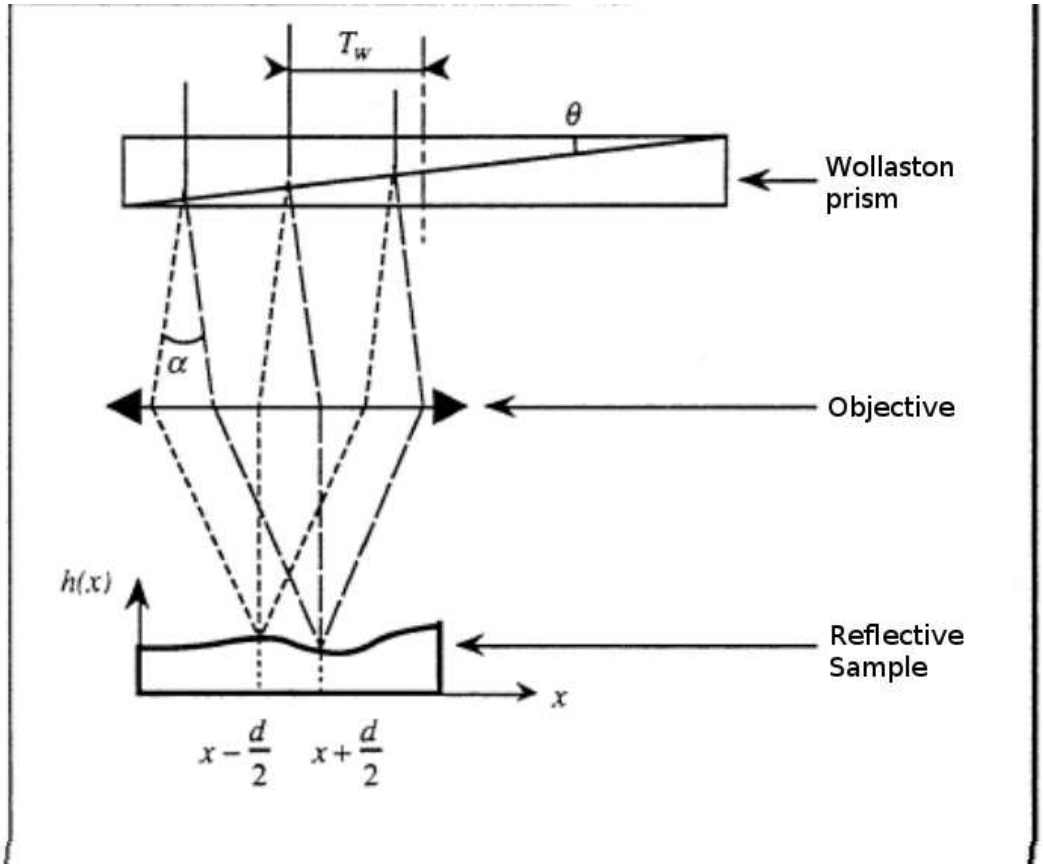

Figure 2.11 – Principle of Wollaston microscope. The Wollaston or Nomarski prism divides the beam into two beams of diverging angles and of perpendicular polarizations. Coming on the back focal plane of the objective with two different angles, the two beams focus at different transverse positions in the sample arm. Being reflected back and recombined by the objective and Wollaston prism on the way back, the final intensity at one given pixel depends on the interference between the two beams, hence on the phase difference between two transverse positions inside the sample. This image has been taken from the PhD manuscript of P.Gleyzes [18].

the plane and perpendicular to the light propagation. In presence of a high electric field applied in the direction of the light propagation, the molecules become oriented in the direction of the light propagation so that no birefringence is measured by the light. We can note that the liquid crystal retarder often use a compensator to reach no retardance between the two polarizations because the order in presence of a voltage is not perfect and a remaining birefringence can be observed even at maximal voltage [127]. The maximal amount of retardance is controlled by the thickness of the liquid crystal as well as by the birefringence of the molecules used, but is often a fixed value. Liquid crystal phase retarders are useful tools to modulate the optical path difference in polarization microscopes, although they usually offer medium speed performances, as illustrated in figure 2.12 D. If switching time from two different polarized states is quite short to go from high retardance to a low retardance, it becomes much slower to perform the inverse process [127][7]. In practice, we performed 4 phases steps measurement from the high retardance state to the low retardance state that allows to minimize the switching time to return to the high retardance state with a maximal voltage difference[8]. We could perform acquisitions to up to 100 Hz (phase image

[7]It is not surprising to understand that the molecules quickly follow the electric field, but require more time to go back to the polarized orientation at low voltages with only low forces applied to the molecules.

[8]If someone needs to use this liquid crystal retarder, attention needs to be paid so that the signal is continuously modulated with a 2 kHz square pattern and the applied voltage corresponds to the amplitude of the steps. A sinusoidal or triangular modulation can be performed by multiplying the 2 kHz signal with a carrier signal with

at 25 Hz) with a 2 ms exposure time triggered at the end of each phase step.

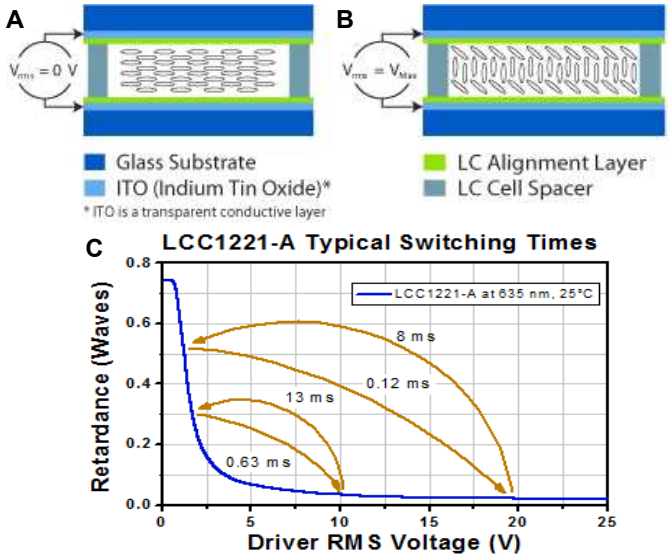

Figure 2.12 – Principle of liquid crystal phase retarder. Panels A and B illustrate the liquid crystal orientation in different voltage conditions, respectively 0 V and 25 V. Without any electric field, the molecules are oriented perpendicularly to the smallest dimension, while they follow the electric field orientation when applied. The degree of longitudinal orientation varies from 1 without electric field toa few percents at 25 V. **Panel C** shows the typical switching times of our liquid crystal retarder, enabling a maximal modulation frequency between 100 Hz and 50 Hz.

2.6.4 Changing the shear angle

One common problem of DIC microscopes, including Wa-DIC microscope, is that they provide a preferential direction which might not be adequate to the sample orientation. It can be especially dramatic when imaging neurites that are small in diameter but can be very long. If the neurite grows along the shear direction, the wide angle strategy would obviously fail, and the phase gradient in DIC microscopy would be smaller. To prevent this effect, we mounted the Nomarski prism on a rotation mount so that the shear angle can be easily modified and manually chosen to be optimal with respect to the object. Note that it would be similar to rotate the object in the transverse plane and that the rotation mount would permit to carefully choose the shear directions. An image independent of any shear direction could be theoretically reconstructed from 3 shear directions with an increasing angle of 120°. We also emphasize that an ideal similar setup could be obtained by replacing the Nomarski prism by a phase SLM *(spatial light modulator)*. SLM often works with a single polarization so that the perpendicular polarization is not affected by the phase mask of the SLM, while the other polarization can be deflected by adding a linear phase delay on the SLM (or a phase grating). Advantageously, the SLM would directly give the possibility to modulate the phase by adding a continuous phase to the SLM pattern, and would directly allow to change the shear angle without any mechanical part.

the desired modulation.

2.7 Wa-DIC reflection microscope in practice

This section aims at describing the practical implementation of the Wa-DIC reflection microscope and aims to illustrate the different features offered by this microscope. If the setup configuration is apparently simple and compact, its complexity comes from the phase image interpretation. Indeed, the phase image is the sum of the phase difference obtained with one polarization minus the phase difference obtained with the other with a given transverse shift. Our initial interest was to study neurites that are in the order of 1 to 2 μm in diameter so that the two phase images do not overlap and the object phase can directly be measured. The first subsection will illustrate some examples of phase images that can be obtained with the Wa-DIC microscope and will show that the phase difference is not well defined in larger objects. To recover a real phase information, it corresponds to a single mathematical operation that can be reversed in some sort of deconvolution process that I will present in a second subsection. Finally, I will illustrate another interest of the Wa-DIC microscope that can provide a local birefringence measurement for small objects with an interferometric sensitivity.

2.7.1 Quantitative phase imaging

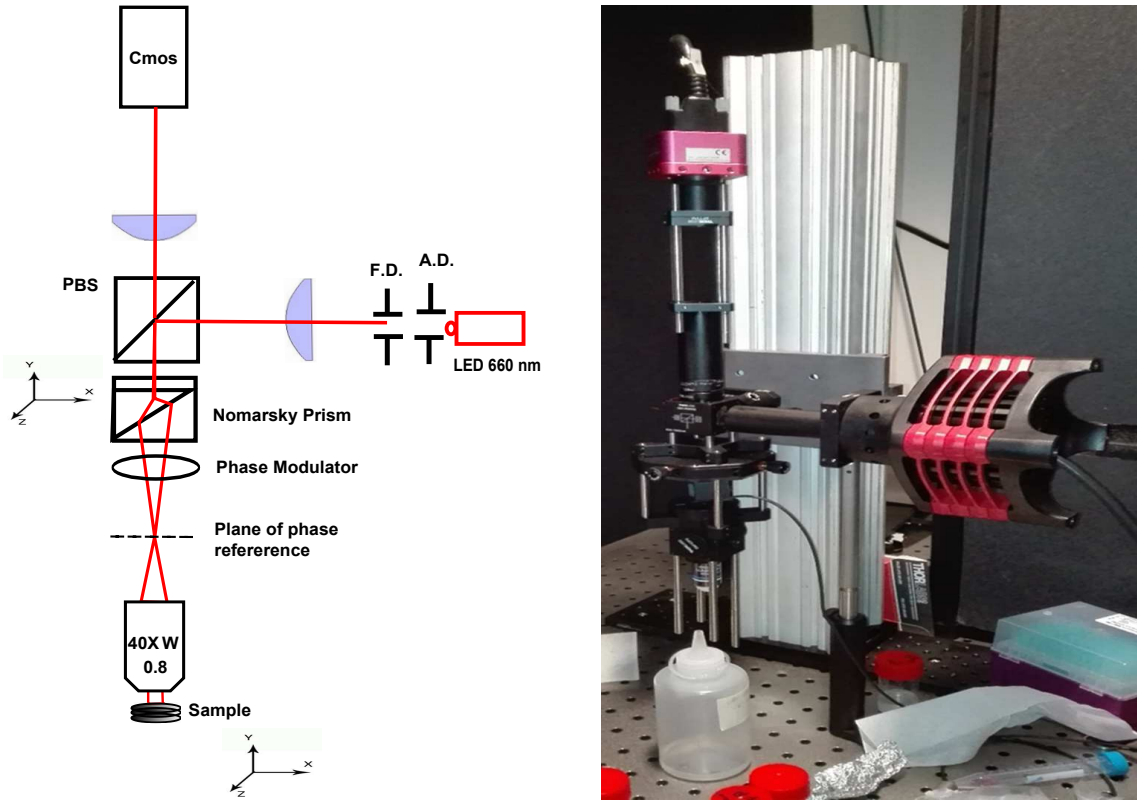

Figure 2.13 – Scheme and photograph of the WaDIC setup, the description of which can be found in the main text.

The Wa-DIC microscope consists in using a classical reflection microscope and inserting a Nomarski prism and a phase modulator in between the microscope objective and the illumination and detection path. A spectrally extended LED illuminates a polarizing beamsplitter in a Kohler-like illumination. The polarizing beamsplitter acts as a linear polarizer and as a beam deflector for the light to reach the microscope objective. The light beam then reaches a Nomarski prism that splits the light into two beams of different polarizations and different angle that further pass through

a liquid crystal phase modulator (Half-wave liquid crystal retarder LCC1221-A, Thorlabs) that can introduce a variable phase shift between the two beams of different polarization. The two beams then reach the microscope objective (Olympus, 40X 0.8 NA) back focal plane with different angles and at different positions. This will respectively lead the beam to focalize at two different positions in the object plane and will introduce an angular shift between the two beams, which will create interference fringes. The Nomarski prism introduces an angular shift of 10^{-3} rad[9] that induces a transverse shift of 4.5 μm between the two beams, corresponding to about 15 times the transverse resolution. The light is then reflected by the glass or silicon coverslip and back travels through the phase modulator, is recombined by the Nomarski prism, and is linearly polarized again through the polarizing beam splitter. It is then focused onto a CMOS camera by a tube lens of 250 mm of focal length. Note that the phase modulator is crossed twice so that a half-wave retarder is enough to modulate the phase difference to up to 2π. The Nomarski prism is mounted on a 2" XY translation stage to adjust carefully its center in the center of the beam, which permits to have the zero path difference at the center of the field, being of critical importance when using a spectrally extended light source. Its relative axial position to the microscope objective can be manually changed to adjust fringes spacing, which is maximal when the back focal plane of the objective lies in the plane of phase reference (whose position is characteristics to the Nomarski prism). The Nomarski prism is finally attached to a rotation mount to allow for a quick manual change of the shear direction and to choose the most advantageous one depending on the sample. Compared to transmission DIC microscope, this reflection configuration offers the advantage of using a single objective, a single Nomarski prism, and to be easy to align. The microscope scheme of the Wa-DIC microscope is presented in figure 2.13.

The Wa-DIC microscope measures the interference between the two recombined beams at the camera plane. The interference term can be isolated using a phase-stepping algorithm as described in section 2.2 by modulating the phase difference with the phase modulator. Generally, the phase difference is the sum of a fringe pattern controlled by the position of the microscope objective and the phase of the object. In order to estimate it, we will further consider the shear direction along the x-axis only, but the result would be identical for any shear direction. At a single pixel of the camera corresponding to the pixel at the position (x,y), the measured phase difference can be written as:

$$\phi(\mathrm{x,y}) = \phi_{\mathrm{fringes}}(\mathrm{x,y}) + \frac{2\pi}{\lambda_0}.(n_e(x+\frac{d}{2},y).h_{\mathrm{object}}(x+\frac{d}{2},y) - n_o(x-\frac{d}{2},y).h_{\mathrm{object}}(x-\frac{d}{2},y))) \quad (2.16)$$

with n_e and n_o being respectively the refractive index of the object for extraordinary and ordinary directions, h_{object}, the object height at a given position, and d the transverse shift caused by the shear. In the case of a small object only surrounded by the external medium, the phase image of the image is split in two with a first positive phase measured with the extraordinary polarization in ($x_{\mathrm{object}} - \frac{d}{2}$,y) and a negative phase map measured with the ordinary polarization in ($x_{\mathrm{object}} + \frac{d}{2}$,y), as illustrated in figure 2.14. In practice, for small phase differences, it can be convenient to work with the microscope objective in the plane of phase reference and with a phase shift of $\frac{pi}{2}$ so that the intensity change is directly proportional to small phase differences. Interestingly, the $\frac{pi}{2}$ phase shift can be simply obtained by transversely translating the Nomarski prism without the need for the liquid crystal retarder once and for all[10]. Nevertheless, when looking at higher phase difference, a phase shifting algorithm can be applied. In practice, I noticed that

[9] where the typical Nomarski prisms used in DIC introduce an angular shift around 10^{-5} rad

[10] More generally, the liquid crystal retarder could be replaced by a motorized translation stage of the Nomarski

phase unwrapping algorithms were performing better when the two beams were slightly off axis producing a fringe pattern with a few fringes in the field of view but I have no physical argument to support this claim. Fringes are obtained by translating the microscope objective further from the Nomarski, which will be a requirement for inserting a dichroic mirror and add a fluorescence path that I will describe in section 2.8.

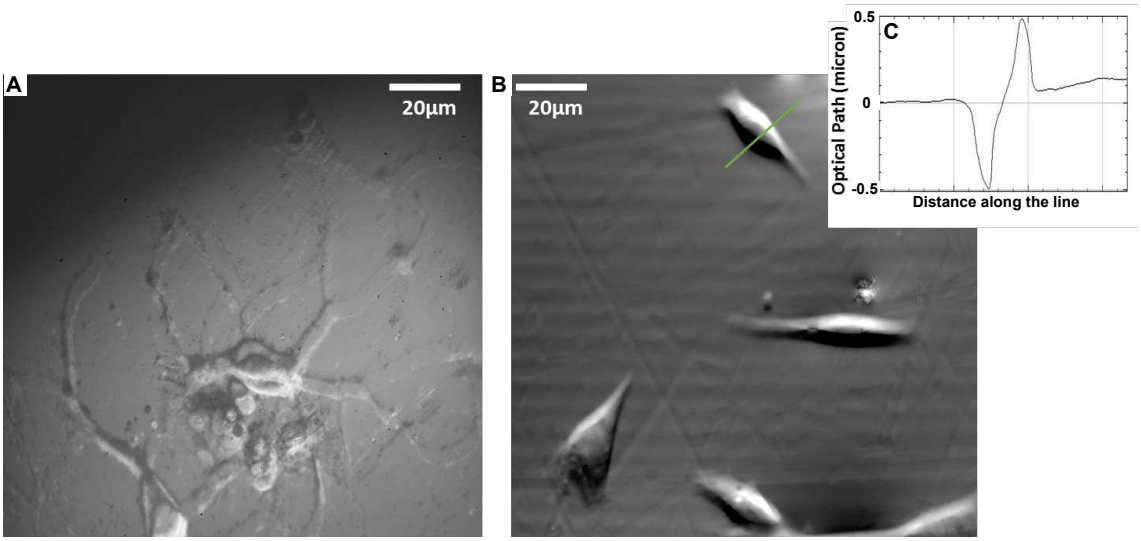

Figure 2.14 – Wa-DIC images of cell cultures. Panel A shows a direct intensity image obtained with the Wa-DIC image on a neuron culture with the objective back focal plane close to the phase reference plane (interference fringes larger than the field of view). It produces a doubled image, composed of the extraordinary phase of the objects superimposed to minus its ordinary phase transversely shifted. If the neurites are well separated, the phase difference around the cell somas is more complex. **Panel B** shows a phase map measured on a 3t3 (fibroblast cell line) cell culture and **panel C** plots the phase profile along the green line. It shows that Wa-DIC microscope can access two phase maps obtained with the different polarizations shifted along the shear direction.

2.7.2 Deconvolution of the phase image

With the Wa-DIC microscope, we can either directly measure the phase evolution of a small object or try to reconstruct a phase map of extended objects. In fact, equation 2.16 of the phase difference in Wa-DIC corresponds to a single convolution with a Dirac difference, as I will show it in this subsection. Therefore, passing to the Fourier plane, the effect of such convolution can be theoretically canceled to recover the local object phase map. In this subsection, I will go through the maths of this deconvolution and will show a first practical attempt of it and discuss the experimental problems of deconvolution.
In order to reconstruct the physical phase of the object at its real position, we first neglect the potential object birefringence in order to obtain:

$$\phi(\mathrm{x,y}) \simeq \frac{2\pi}{\lambda_0}.(n(x+\frac{d}{2},y).h_{\mathrm{object}}(x+\frac{d}{2},y) - n(x-\frac{d}{2},y).h_{\mathrm{object}}(x-\frac{d}{2},y)) \qquad (2.17)$$

This equation can easily be rewritten as a convolution between the physical phase of the object at the position (x,y) with a difference between two diracs centered at the two shifted positions:

prism. Nevertheless, because of its size and weight, it is easier, more robust and faster to work with such liquid crystal retarder.

$$\phi(\text{x,y}) \simeq \frac{2\pi}{\lambda_0}.n(x,y).h_{\text{object}}(x,y) * (\delta(x+\frac{d}{2},y) - \delta(x-\frac{d}{2},y)) \tag{2.18}$$

To simplify this equation, it is possible to express its equivalent in the Fourier space, taking advantage of the fact that the Fourier transform of a convolution is the dot product of the Fourier transforms. Additionally:

$$\begin{aligned} FT((\delta(x+\frac{d}{2},y) - \delta(x-\frac{d}{2},y))) &= e^{-2ik_x\pi\frac{d}{2}} - e^{2ik_x\pi\frac{d}{2}} && (2.19)\\ &= -2i.sin(\pi k_x d) && (2.20) \end{aligned}$$

From equations 2.18 and 2.20, and going back to the real space, the physical phase at the position (x,y) can be expressed as:

$$\phi(\text{x,y}) \simeq FT^{-1}(-\frac{FT(\phi_{mes}(k_x,k_y))}{2isin(\pi k_x d)}) \tag{2.21}$$

Equation 2.21 states that, in theory, at least, the physical phase map can be reconstructed by calculating the inverse Fourier transform of the ratio between the Fourier transform of the measured phase map and 2i times a sinus depending on the transverse shift. We can add that for a given shear direction, the argument of the sinus becomes: $\pi(k_x d_x + k_y d_y)$.

However, this deconvolution is complex to realize in practice due to the real nature of the measurement. In theory, the Fourier transform of the measured phase should have periodic true zeros, corresponding to the zeros of the sine function. In practice, because of the noise, the amplitude of the Fourier transform is not exactly zero at the expected zeros. Therefore, at these positions, the division by the sinus corresponds to a division by zero, which amplifies the noise at these positions in the Fourier space. Back to the real space, it creates artifacts, creating ghost replicates of the objects, as illustrated in figure 2.15. Nevertheless, with more time, we could have used similar algorithms to the ones used for deconvolution or phase integration, which have been widely studied. For the deconvolution process, we used a Wiener filter, inspired by discussions with *C. Demene* from the Institut Langevin [128] which consists in dividing the signal in the Fourier space by the sum of the sinus and the noise power spectral density (PSD_{noise}) instead of the sinus only:

$$\phi(\text{x,y}) \simeq FT^{-1}(-\frac{FT(\phi_{mes}(k_x,k_y))}{2isin(\pi k_x d) + PSD_{noise}(k_x,k_y))}) \tag{2.22}$$

It is known to partly remove the noise artifacts close to the zeros of the sinus. With such a filter, we could obtain real phase maps of the objects, even though some ghost images can still be observed, as shown in figure 2.15[11].

2.7.3 Birefringence measurement

Coming back to equation 2.16, we can also directly measure the phase without deconvolution for small objects and for both polarizations giving access to a birefringence parameter. Indeed, if there is no other object at a distance d, we obtain:

$$\phi(x+\frac{d}{2},y) = \frac{2\pi}{\lambda_0}.(n_{medium} - n_o(x,y)).h_{\text{object}}(x,y) \tag{2.23}$$

[11]Nevertheless, such ghost images can also be found in most of the deconvolution strategies and seem to be a common artifact.

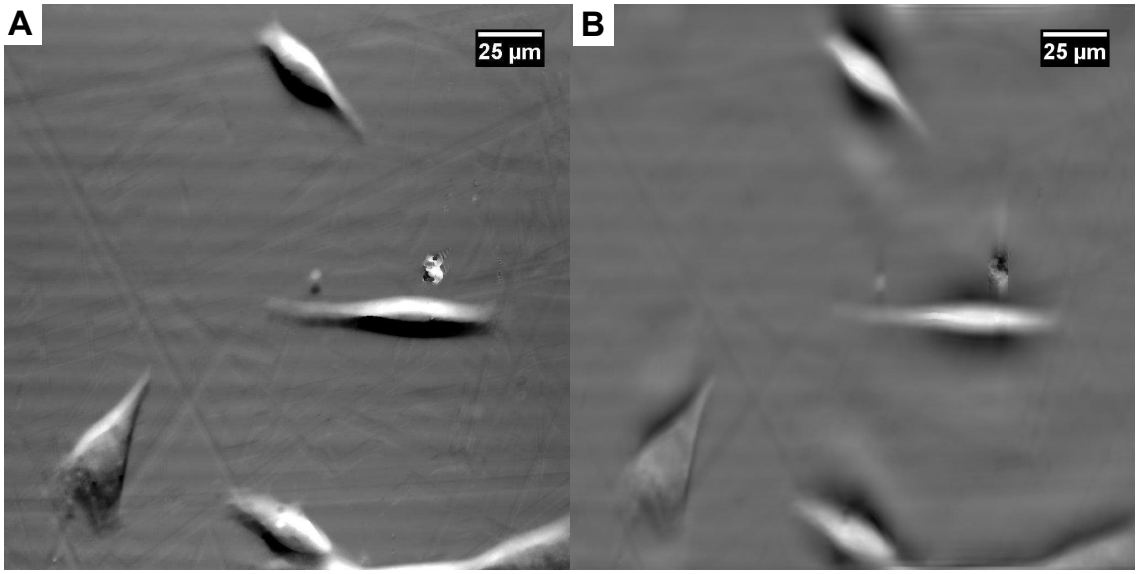

Figure 2.15 – Wa-DIC deconvolution process. The object is retrieved, but several ghost images appeared.

And,

$$\phi(x - \frac{d}{2}, y) = \frac{2\pi}{\lambda_0}.(n_e(x,y) - n_{medium}).h_{\text{object}}(x,y) \tag{2.24}$$

From these two equations, we can calculate a relative birefringence change by subtracting equations 2.24 and 2.23 and by dividing by equation 2.24

$$\frac{n_e - n_o}{n_e - n_{medium}} = \frac{\phi_e - \phi_o}{\phi_e} \tag{2.25}$$

This can be of particular importance to compare a phase change to a birefringence change. Indeed, as will be described in section 7, both birefringence and optical path are expected to change during the propagation of an action potential in a nerve. Here, with a single setup, we expect to be able to follow both effects simultaneously to see whether a similar deformation can be observed in single mammalian neurons.

2.8 Simultaneous QPI and fluorescence measurement with Wa-DIC configuration

Keeping the idea to follow activity-related phase (and birefringence) changes in neuron cultures, the next step is to couple the Wa-DIC setup with a fluorescence path similarly to what has been described for the Linnik interferometer. As a reminder, the fluorescence path can be used for the optical recording of electrical activity of neuron cultures or for providing an independent height measurement using Fluorescence exclusion. The configuration of the Wa-DIC microscope allows a simple coupling with a fluorescence path as presented in figure 2.16. Indeed, thanks to the common-path configuration, any non-birefringent object can be inserted in the light path. In practice, we add a simple dichroic filter in between the liquid crystal phase modulator and the microscope objective to optimize the fluorescence collection. In addition to this dichroic filter, a block containing an illumination path and a detection path is attached to the system. The only constraint of this configuration is that the objective has to be moved further from the Nomarski prism and the plane of phase reference can not be conjugated with the objective back focal

plane. Nevertheless, in the current configuration the distance between the Nomarski prism and the objective is small enough to generate only a few interference fringes in the field of view with little amplitude decrease over the entire field, as illustrated in figure 2.16. Interestingly, we could use the same cameras and the same software to synchronize the phase and fluorescence imaging as the one developed for the Linnik interferometer. Additionally, the fluorescence information might have another interest. It might be interesting to use the *a priori* information on the position and the shape of the object obtained by a fluorescence measurement to optimize the Wa-DIC deconvolution procedure. However, if similar algorithms using *a priori* information are quite popular, it would have required to spend some time to write or to adapt a proper deconvolution algorithm, which might be an interesting future development.

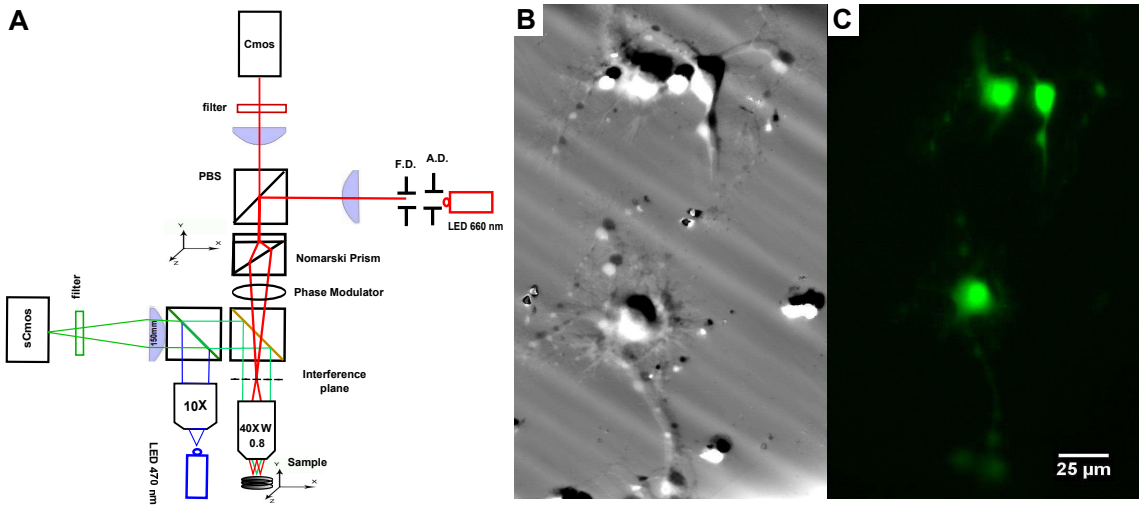

Figure 2.16 – Multimodal setup combining Wa-DIC and fluorescence microscopy. Panel A presents a scheme of the setup. Compared with the Wa-DIC setup in figure 2.13, a simple dichroic filter has been inserted in between the phase modulator and the microscope objective. It does not change the path difference because the filter is not birefringent but prevents the matching of the interference plane and the objective back focal plane, leading to the formation of interference fringes. **Panels B and C** respectively show a phase image in a 3 days neuronal rat hippocampal neuron culture and the corresponding fluorescence image (Fluo-4) acquired simultaneously.

Intermediate conclusion

In this first part of the manuscript, we have introduced quantitative phase microscopy, a set of label-free optical techniques that can measure sub-nanometric optical path fluctuations inside cells. It can access mechanical displacements, mass transport and can track subcellular dynamics in various cell types and extended time and spatial scales. In chapter 1, I have reviewed many quantitative phase strategies and showed that they can be of great interest in various biological and medical applications. In a second chapter, I described two quantitative phase microscopes we have developed during my PhD with the idea of measuring an activity-dependent phase variation in neuronal cultures, which will be the object of the last chapter of this manuscript. Interestingly, both systems integrate a fluorescence path that may offer the possibility to follow electrical dynamics of the neurons simultaneously to the phase measurement. Finally, we have introduced a third optical technique named Fluorescence exclusion in chapter 1 that we also contributed to developing. This technique provides an independent volume measurement that permits to separate the height from the refractive index in a QPI measurement. But, more importantly, we have emphasized the similarity in terms of principles and performances between this technique and quantitative phase systems. In this first part, I have demonstrated the strength of the optical approach consisting in transforming an axial information into an intensity information, which allows for a sub-wavelength axial sensitivity. We have proposed a quite general framework and set of calculations of the axial sensitivity offered by such a strategy in various optical conditions. Interestingly, we will show in the next part that quantitative phase imaging can be extended to scattering tissues using low-coherence interferometry. Finally, a few applications to cellular phase imaging will be detailed in chapter 7 as well as some theories describing the activity-dependent phase changes I have been aiming at detecting.

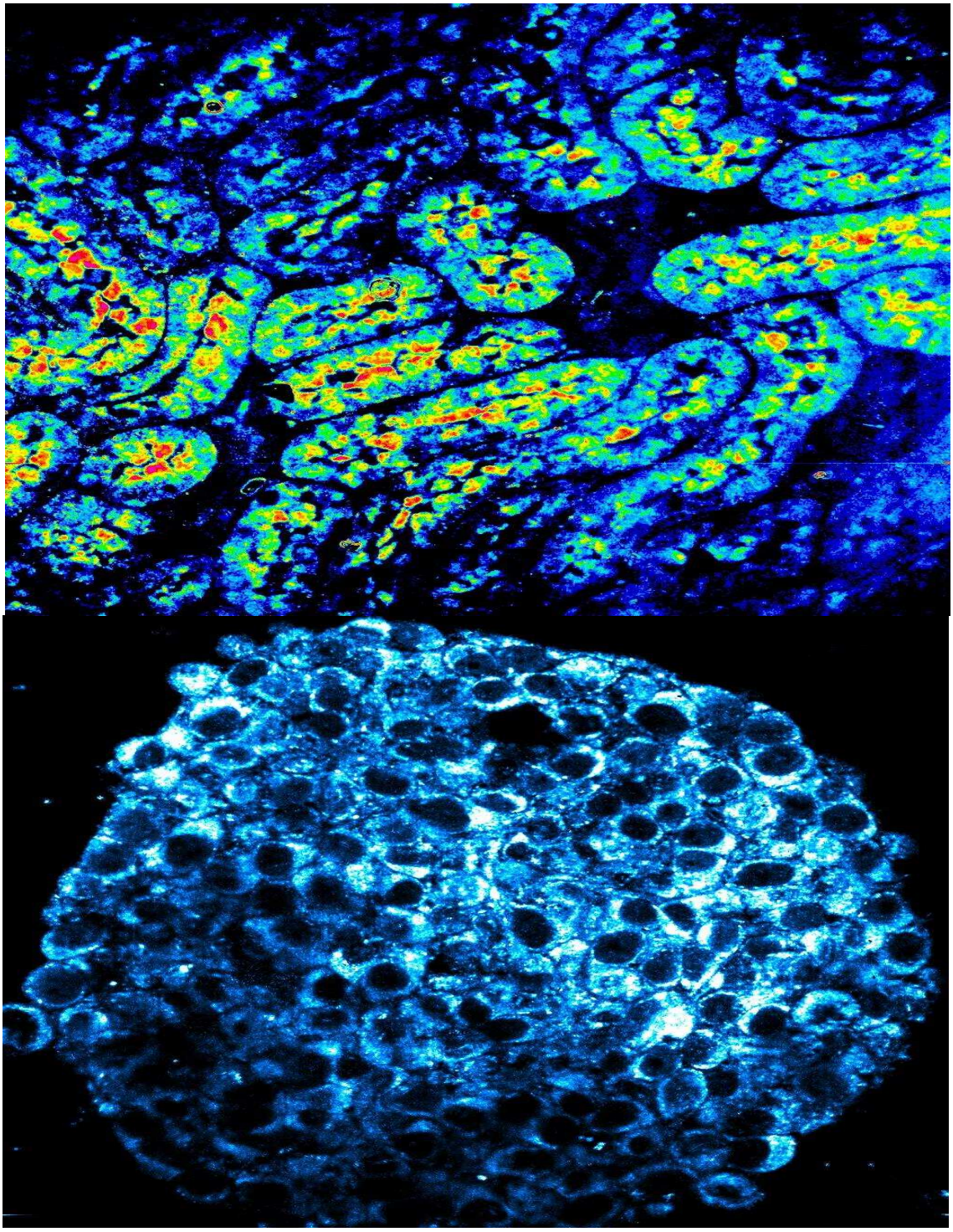

Tissue imaging with full-field optical coherence tomography (FF-OCT). *The top image shows a high-resolution en face view of a kidney and the image at the bottom presents a spheroid of tumorous cells as imaged with dynamic FF-OCT presented in chapter 5.*

Part II

Optical Coherence Tomography

So far, we have seen how to optically measure sub-wavelength mechanical deformations and intracellular motion in single cells. Nevertheless, it is often of critical importance to be able to characterize any observation in tissues in a second step, maybe more importantly when looking at mechanical cues. In terms of mechanics, we can particularly mention the important difference between the Young's Modulus, *i.e.* mechanical deformability, of tissues and the Young's modulus of glass coverslips, while cells behavior usually depend on their mechanical environment [1]. Moreover, tissues are usually much more compact cellular environments than cell cultures, which might also impact the local mechanics of the cells. At this point, we can add that QPI would probably fail at measuring phase variations in cultures grown on tissue mimicking polymers, or on pillars, as it would probably create small local phase fluctuations, since these supports are not flat at all, requiring QPI systems to be adapted to these configurations in order to be effective. Therefore, we felt it would be more interesting in moving directly to optical systems that can operate tissues measurement. However, it can be easily imagined that many additional difficulties may arise from the extension of such measurements in thick samples and *in vivo*. In this part, I will first show some of those issues, and present of few systems that enable phase measurements in thick samples. I will particularly emphasize the development of Optical Coherence Tomography (OCT), which is probably the first and the most common class of low-coherence interferometric optical microscopes. If most of applications of OCT rely on measuring of the tissue morphology by simply measuring the backscattered amplitude of the different tissue structures, I will highlight some more recent developments of OCT that measure the phase variations to extract a sub-wavelength motion information. Then, in chapter 4, I will present Full-Field OCT, an OCT-derived technique based on the same Linnik interferometer presented in chapter 2 and used for phase imaging in cell cultures. FF-OCT, invented and developed at the Institut Langevin 19 years ago by the group of Claude Boccara, is the main technique I have used during my thesis. Interestingly, I will show that FF-OCT provides a very versatile phase imaging approach, as it can work both in cultures and in thick scattering samples. Its versatility comes from the reflection configuration, and the ability to have high intensities in the reference arm to enhance weak sample backscattering signals in tissues by homodyne detection. Finally, chapter 5 will mainly focus on our development of two novel multimodal FF-OCT systems, associating respectively Dynamic FF-OCT and Structured Illumination Microscopy (SIM) to the standard FF-OCT system. Thanks to these systems, the usual structural contrast of FF-OCT can be enriched by motility contrast and molecular contrast. The development of these systems enabled us to answer a few specific biological questions, that will be further described within the next and last part III.

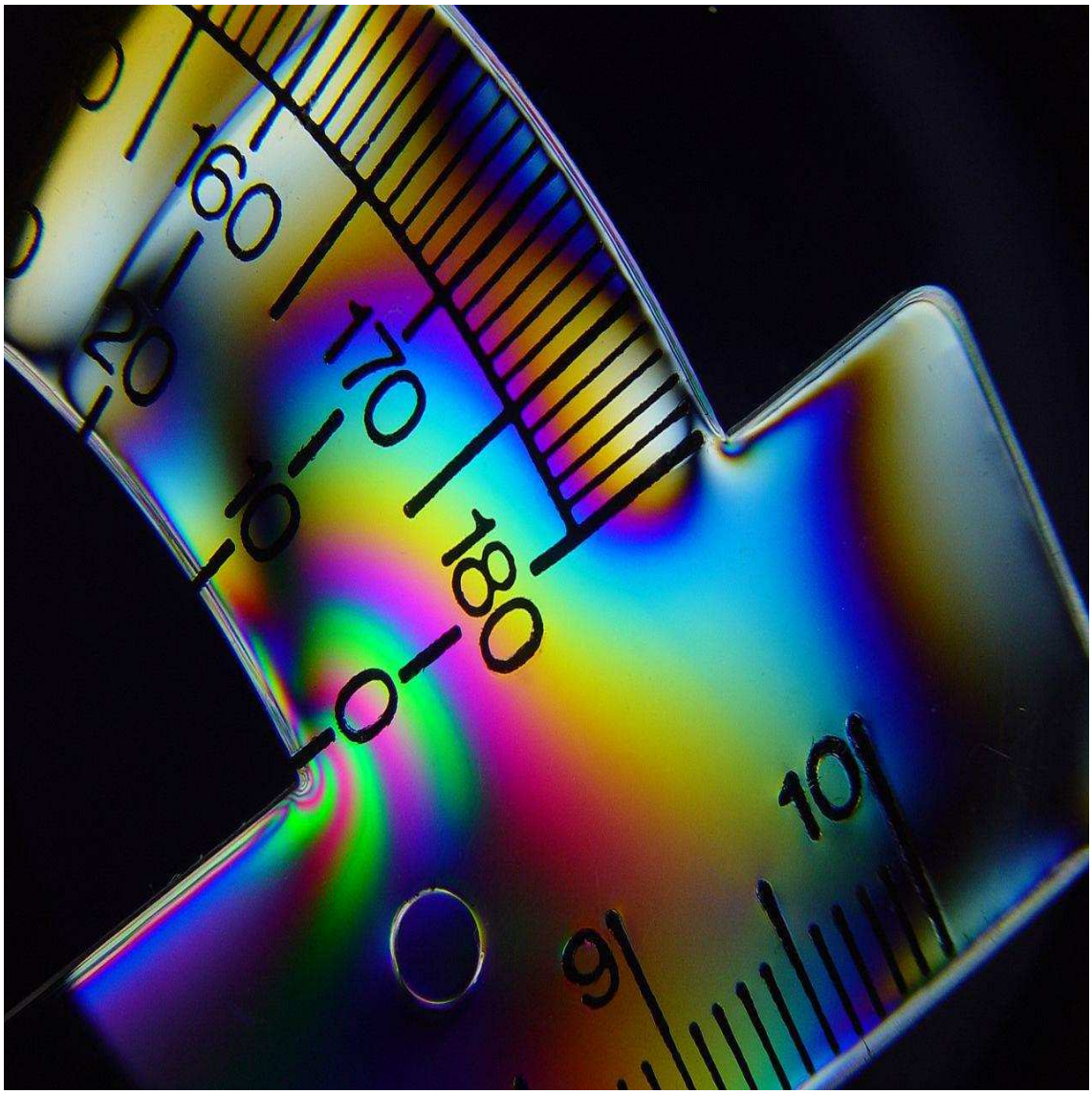

Imaging phase changes with low-coherence interferometry. *The image presents a perfect illustration of the goal of this chapter. It aims at detecting angular (phase) changes with low-coherence interferences that account for the irridescent coloration of the plastic under compression.*

CHAPTER 3

Extending optical phase measurements to thick tissues: Optical Coherence Tomography (OCT)

Table of contents

3.1 Quantitative phase imaging in thick tissues **88**
3.1.1 Problems arising in thick tissues 88
Tissue and structures scattering properties 89
Absence of a phase reference 89
Out-of-focus phase changes 91
3.1.2 Other 3-D phase imaging systems 92
3.2 Low-coherence interferometry **93**
3.2.1 Low temporal coherence 93
3.2.2 Low Spatial Coherence 97
3.2.3 Combining low spatial and low temporal coherence 101
3.3 Optical Coherence Tomography (OCT) **101**
3.3.1 Principle of time domain Optical Coherence Tomography 102
3.3.2 Spectral domain and swept-source OCT 103
3.4 Phase imaging using OCT **105**
3.4.1 Recovery of quantitative phase differences 105
3.4.2 Doppler and Functional OCT 106
3.4.3 Optical elastography with OCT 108

In this chapter, I will first illustrate some obstacles of imaging thick samples with quantitative phase imaging. However, I will show that low-coherence interferometry offers an optical sectioning that allows to localize the phase measurement at a single depth. Quantitative phase measurements can therefore be retrieved, especially temporal variations of the phase. Then, I will present the most common versions of Optical Coherence Tomography (OCT), a technique that relies on low-coherence interferometry and can access quantitative phase variations at optically important depths in thick samples. I will finally highlight the phase sensitivity of OCT through two recent techniques that measure sub-wavelength motions in biological tissues, either caused by blood flow, or by shear waves propagation. Most of the notions introduced here will be used in the two next chapters, in which I will describe more specifically the work we have been doing in the team for the past few years, including mine. Indeed, the techniques we developed are based on FF-OCT, which is nothing but one of the many variants of OCT.

3.1 Quantitative phase imaging in thick tissues

As previously discussed in chapter 1, the phase information can be understood as the optical time required for the object wave to propagate to a given depth and then to arrive at the detector. If we keep on using this analogy, we can illustrate most of the constraints arising from measurements in thick scattering samples. In this section, I will highlight some of these issues. Throughout the rest of the chapter, I will focus on Optical Coherence Tomography (OCT), which is at the core of the techniques we have been developing during my thesis, and that I will describe in the next two chapters.

3.1.1 Problems arising in thick tissues

The objective of this subsection is to introduce some of the most important pitfalls when trying to perform QPI measurements inside scattering samples. We will mainly consider here the case of a reflection QPI system because it seems more relevant to perform measurements in thick tissues where light can not penetrate easily through or to perform *in vivo* measurements. We also make this assumption, as FF-OCT is mounted in a reflection configuration. However, to my knowledge, apart from OCT measurements that I will further describe, most of the other QPI systems used in tissues are operated in transmission through very thin samples, or in transmission-like configuration [48, 85]. Compared to the case of a reflection QPI system in cell cultures, the sample light is no longer reflected by a mirror but is backscattered by the tissues structures. Not only does it reduce the contrast but it does also prevent having a flat phase reference often required to perform a nice unwrapping process. Finally, an important point to consider in tissues is that except at the tissue surface, there might be potentially moving objects everywhere between the front aperture of the microscope objective and the focal point so that measured phase changes could theoretically originate from anywhere between the surface and the imaging depth.

Tissue and structures scattering properties

As stated above, the first important difference is the typical low reflectivity of biological structures in comparison to the previously used metallic or dielectric mirror in the sample arm. Figure 3.1 illustrates different processes to bring back the light to the photodetector. As mentioned in appendix A, and depending on the size of the microstructure, light can be more or less backscattered to the detector. As a general rule of thumb and reminder, the apparent reflectivities of small particles increase with their size and with their refractive index difference with the surrounding medium as illustrated in figure 3.1 (D to F). Therefore, lower reflectivity lowers contrast, which causes the phase sensitivity to decrease. Indeed, as described in chapter 1, the phase sensitivity for small contrasts can be written as:

$$\sigma_\Phi = \frac{1}{\sqrt{2}C}.\frac{1}{\sqrt{FWC}} \tag{3.1}$$

A simple solution would therefore be to choose a low reflectivity mirror in the reference arm to match reflectivities of the two arms and restore the contrast. However, in practice, sample reflectivities are 2 to 5 orders of magnitude smaller than usual silicon wafers that we used for our QPI experiments. If the reference mirror is chosen so that its reflectivity matches the sample reflectivity, we first would not be able to fill the camera full well capacity without significantly increasing the light intensity, at the risk of heating, even burning, the sample. Plus, because a tissue is composed of plenty of scatterers that all contribute for a small part to the final intensity, but their contributions add up and result in a significant incoherent signal. Since the camera would still capture these photons, it would limit the useful full well capacity of the camera and limit the SNR accordingly. Finally, if signals from reference and sample arms are weak, and the power is increased, the few percent of reflection occurring at each optical elements (Beamsplitter, Lenses and microscope objectives) start to become significant and also contribute to decreasing the useful FWC. In practice, we choose to use the same silicon wafer mirror in the reference arm with a relatively high reflectivity, so that the interference signal $\sqrt{I_{ref}I_{sample}}$ is *amplified* by the reference arm and the contribution of incoherent light from either sample or optical elements is reduced. This is an important feature of interferometric microscopes compared to confocal reflectance microscopes that require using much higher power to be able to detect low reflectivity structures. Nevertheless, because the SNR depends on the ratio $\sqrt{\frac{R_{ref}}{R_{sample}}}$, it is significantly lower in tissue than in cultures. In practice, it is hard to be sensitive to phase variations smaller than 50 nm in tissues. Additionally, we should add that the phase sensitivity is also lowered by naturally occurring phase variations of the sample.

Absence of a phase reference

In chapter 1, we have seen the importance for a QPI system to have a flat reference surface, especially to perform phase unwrapping. We have also seen that phase unwrapping algorithms often fail in too dense cell cultures, in which the spatial phase fluctuations are too important. We can add that common-path systems, like the Wa-DIC interferometer presented in chapter 2, will particularly fail at measuring phase if there is no single reference point. Not surprisingly, the case of tissue imaging is therefore complicated as we are no longer looking at light reflected from a single flat surface. Because objects within the tissue can be both in-focus and separated by an axial distance of a few wavelengths, it means that the relative phase between two neighboring objects can be random, as it depends on the 3-D position of objects in *a priori* random positions, as illustrated in figure 3.2. It results in a so-called speckle-like image of *apparently random* intensity fluctuations

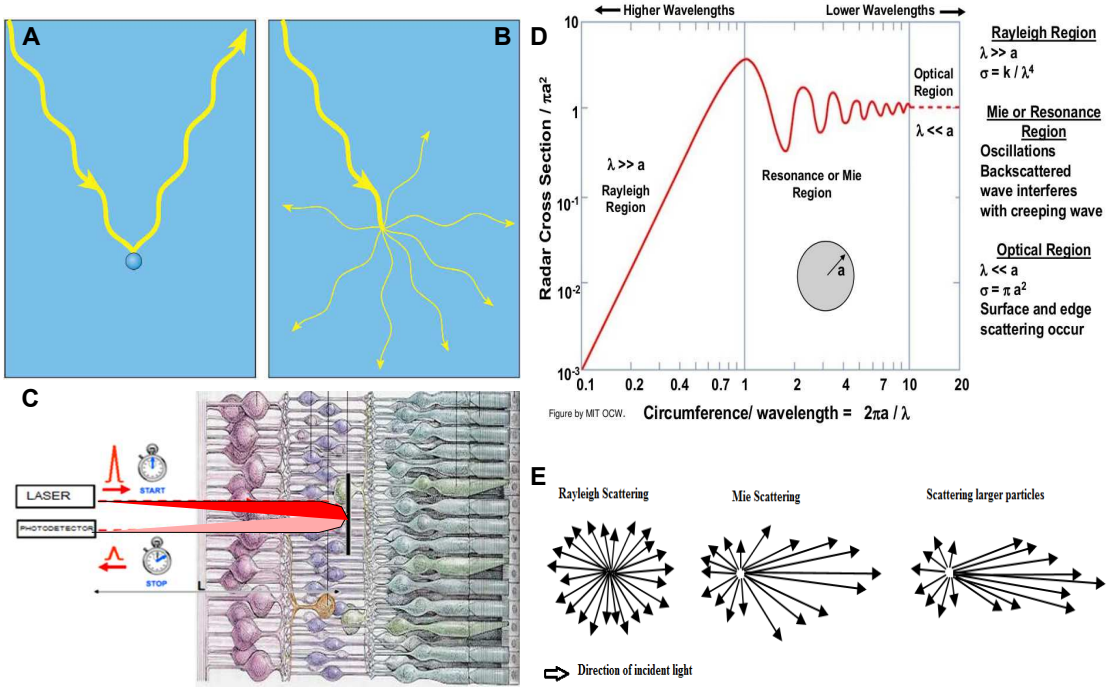

Figure 3.1 – Scattering regimes and backscattering amplitude in tissues. Panels A and B illustrate two scattering regimes. For particles much larger than visible wavelengths (about 5 to 10 μm), the object can be considered as a local low reflectivity mirror that simply partially reflects light, as illustrated in **A**. However, for smaller particles, the light is first only partially scattered. Plus, it is scattered in many directions, following either Mie or Rayleigh scattering, so that the backscattered intensity coming back to the detector is significantly attenuated. **Panel C** is an illustration of an attempt to perform a QPI measurement (somehow equivalent to the measurement of the light propagation time) inside a tissue. It illustrates the attenuation of the signal coming back to the detector, which lowers the SNR, and therefore the accuracy of the phase measurement. Addition SNR deterioration comes from backscattering of incoherent signal from layers above the imaging depth, as illustrated by the addition of weak signal that tends to blur the direct signal close to the photodetector. **Panels D and E** present a more mathematical vision of the different optical scattering regimes. **Panel D** shows the evolution of a particle cross-section with its size and the corresponding scattering regimes. Even though the total scattered intensity remains roughly within the same order of magnitude in the Mie regime, **panel E** shows that as the particle size increases, the forward scattering becomes more and more important, which would decrease the apparent reflectivity of the particle.

caused by an *apparently random* phase fluctuation between adjacent pixels. I named these images speckle-like images because usual speckle maps are generated from the collective interference between several wavevectors and are mainly arising from random multiple scattering in biological samples. These usual speckle maps also result in a random phase map. In reflection interferometry, the random phase maps can come from a combination of the random scatterer positions inside a single voxel, from one voxel to its neighboring pixel, and from multiple scattering. Nevertheless, we can add that for large structures, such as nuclei, or myelin fibers, close from the sample surface, interference fringes can be detected along these structures. Interestingly, fringes spacing can be ingeniously used to determine the angle of fibers with respect to the focal plane [129].

Anyway, in a general case, the phase is apparently random spatially so that no phase unwrapping algorithm could even find the phase difference associated with a single depth inside the sample. Hopefully, if the object positions are apparently random at a given plane and time, their position

should be fairly constant between 2 successive image acquisition. In other words, the acquired random phase map should be quite static over time, or at least should change continuously, at least if the frame rate is important enough. Therefore, if direct quantitative phase imaging is not possible in scattering samples, phase imaging systems can still measure quantitative phase differences. From this, two options are then available. One can either look at phase difference over time at a single position, as it will be further described in this chapter with the Doppler OCT, and in chapter 5 with the development of dynamic FF-OCT. The second option is to calculate the phase difference at two successive close axial positions. As it will be detailed in chapter 5, it authorizes the reconstruction of the phase of a single tissue layer.

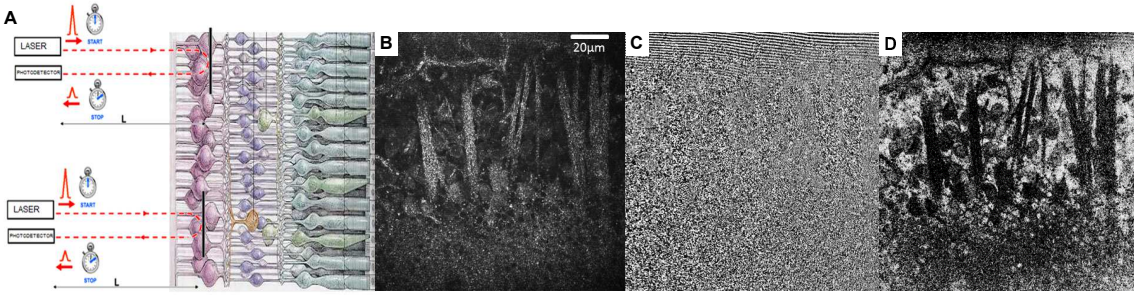

Figure 3.2 – Speckle-like maps in QPI tissue measurements. Panel A illustrates one origin of random phase images in reflection interferometers. Two objects can be within the same focus, but shifted of $\frac{\lambda}{4}$, which would correspond to a phase shift of $\frac{\pi}{2}$, changing the phase significantly between two adjacent pixels. **Panels B and C** present an example of an amplitude and phase image respectively in an *ex vivo* retina. They show that even if many structures can be captured in the amplitude image, the phase map appears random. Nevertheless, **panel D** highlights the temporal phase variation, which enables to find back many different structures, illustrating that the phase difference can therefore be calculated quantitatively. The contrast obtained in this image will be further described in chapter 5.

Out-of-focus phase changes

The last pitfall I want to discuss here concerns the localization of the phase changes one can expect to see in a reflection interferometer, which is quite critical if a quantitative phase is to be measured. Indeed, in biological tissues, because the light path can go through several complex layers before reaching the focal plane, one has to make sure that the acquired phase differences really come from a change at the plane of interest, and not at a random location between the sample surface and the imaging depth. This is a quite common issue in optical imaging and is often referred to as optical sectioning, *i.e.* the ability for an optical system to separate the contribution of the in-focus signal and the contribution of the out-of-focus noise. For example, in fluorescence, confocal microscopy, multiphoton microscopy or Structured Illumination Fluorescence Microscopy are systems providing optical sectioning in contrast to widefield fluorescence microscopy. These systems are almost mandatory to perform fluorescence measurements in scattering samples. Similarly, in interferometric measurements, optical sectioning is important to separate the interference signal coming from the sample plane, and the interference signal coming from out-of-focus structures. Optical sectioning in interferometric measurements is also a very common problem and has been thoroughly studied. It can be provided quite classically using low-coherence interferometry, that I will detail in the next section, since this a very vast topic. However, in a few words, low-coherence interferometry allows axial localization of interferences at a given plane, *i.e.* at a given depth, as the interference signal is blurred when the optical path difference exceeds a given length, generally

named the coherence length. Therefore, it becomes possible to filter the contribution coming from a given plane of interest, which corresponds to a given optical path difference with the reference arm from the contribution of different planes, or multiple scattering that has propagated for a shorter or longer time in the sample. In short, low-coherence interferometry enables to select a given arrival time of sample photons as illustrated in figure 3.3 A and C. Nevertheless, photons can undergo different scattering scenarios, as illustrated in figure 3.3 B and the photons arrival time is not sufficient to filter the contribution of multiply scattered photons. Nevertheless, the microscopy configuration emphasizes the contribution of ballistic photons at shallow depths and eliminates the high frequencies of phase variation caused by defocused multiply scattered photons. Additionally, most of the scattered photons can be spatially filtered using confocal pinholes as in standard OCT or using a low spatial coherence as in full-field OCT. I will provide further details on this matter in section 3.3, as I will describe the principle of Optical Coherence Tomography, based on low-coherence interferometry. We can also mention that it becomes a bit different when considering the effect of small temporal phases changes happening outside the focal plane, but I will address this issue in chapter 5.

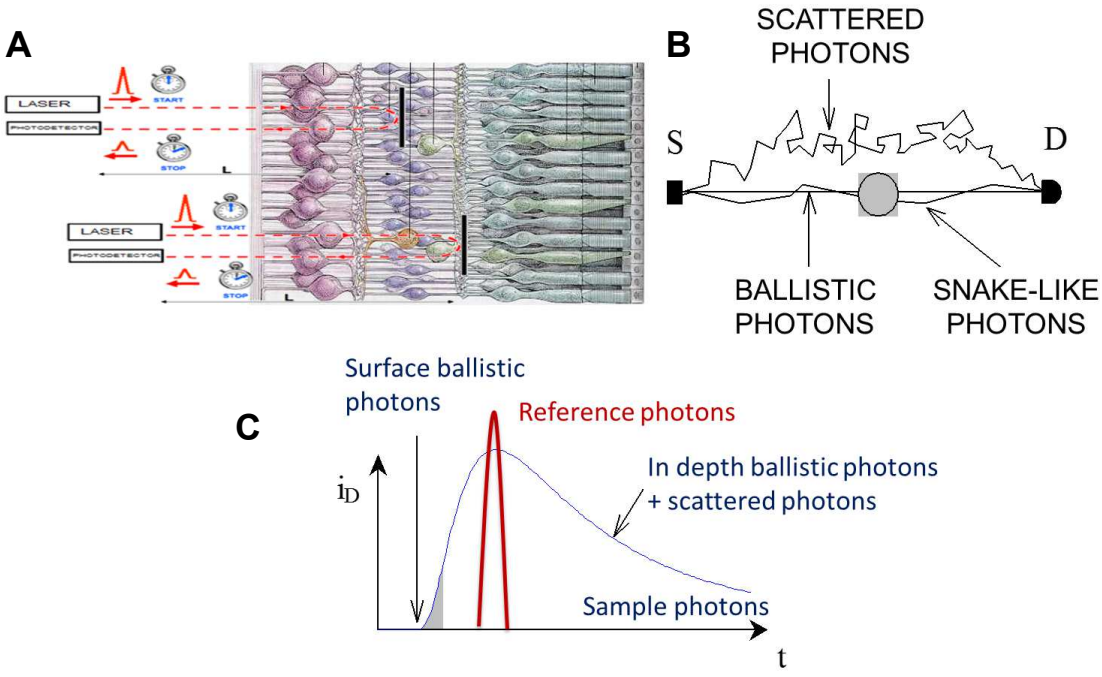

Figure 3.3 – Depth selection based on photons arrival time. Panel A and C illustrate the propagation time difference between two different depths inside a sample. A given depth can be chosen by adapting the length of the reference arm in low-coherence interferometry. **Panel B** shows different scattering regimes that a photon can encounter and illustrates the propagation time increase for scattered photons that arrive at a time larger than their depth would give with a ballistic propagation. These scattered photons are usually spatially filtered to be selective to a single depth.

3.1.2 Other 3-D phase imaging systems

Obviously, we are not the first team claiming that we are able to perform quantitative phase imaging inside scattering tissues, as it has been extensively studied in recent years. Apart from OCT techniques that I will voluntary forget here (as section 3.3 will be entirely dedicated to it) and that correspond to the large majority of reflection low-coherence interferometers, we can

mention a few other QPI strategies in transmission and transmission-like configurations that can provide 3-D information. A first strategy consists in imaging thin tissues (such as histology slides) in low-coherence transmission QPI microscopes, which can eventually integrate the phase from one surface to the other as it has been evoked in the previous chapter [48, 85]. A second strategy is based on phase gradient microscopy, also previously mentioned, in a low-coherence and transmission-like configuration. In these cases, the plane of interest can be illuminated by multiply scattered photons oriented to the sample surface [41] or by ballistic photons reflected by a strongly backscattering structure below the plane of interest [42]. In low-coherence phase gradient microscopy, all the measurable phase changes originate from the objective image plane [41].

3.2 Low-coherence interferometry

Low-coherence optical interferometry aims at using light with short coherence, either spatially or temporally, to produce a localization of the interference patterns in space along the light propagation direction. This localization is very important since it allows a 3-D microscopy by scanning the plane of localization, also named as coherence volume, in depth. If low-coherence interferometry has mainly started around 1990 to increase surface profiling performances [130,131] or to measure optical thickness of biological objects [19], it has become very popular from the 2000's with the development and popularization of OCT [20] and low-coherence QPI [48, 85, 132] to suppress coherent noise and enable 3-D localization. Even though the basic principle of low-coherence interferometry is quite simple and popular, the full characterization of the coherence effects in complex microscopy geometries is still a complex problem and is still being investigated [133]. In this section, I will briefly go through low-coherence interferometry, either from low temporal coherence systems or from low longitudinal coherence systems, trying to provide an intuitive notion of both cases rather than going into intense calculation and modeling. More accurate theories and calculations, as well as the coupling between low temporal and low spatial coherence can be found in an inspiring review from *Abdulhalim* [133] and articles cited herein. However, let's note that such theories are mainly developed in the case where the interferometer is operated with a flat mirror or any flat reflective surface, but I could hardly find complex modeling explaining the case of imaging a complex biological sample with a complex mix between Rayleigh or Mie scatterers.

3.2.1 Low temporal coherence

The first quite intuitive, and most popular, example of low-coherence concerns the low temporal coherence in a Michelson interferometer, which is a simple version of Michelson interferometer operated in white light, or any spectrally extended light source. The most simple case is to consider plane waves (only one single spatial frequency) interfering with a given optical path difference, and to analyze the effect of the spectral bandwidth on the interference pattern.

$$I = \frac{1}{2T}\int_{-T}^{T} E.E^{*}dt \tag{3.2}$$

with E the total electric field:

$$E(t) = \frac{1}{\Delta\omega}.\int_{\omega_{max}}^{\omega_{min}} E(\omega)e^{\backslash}i\omega t)d\omega \tag{3.3}$$

For the sake of simplicity, let's only consider two frequencies only of equal spectral irradiance,

to show that after sufficiently long temporal average, cross terms naturally disappear. Therefore, the intensities are summed:

$$I \propto \frac{1}{\Delta t}\int_0^{\Delta t}(\frac{(E_0.e^{i\omega_1 t}+E_0^*.e^{-i\omega_1 t})+(E_0.e^{i\omega_2 t}+E_0^*.e^{-i\omega_2 t})}{2}.C.C. \tag{3.4}$$

With *C.C.*, expressing the complex conjugate. The multiplication of two 4 terms quantities will generate 16 terms of which I only put a concatenated form:

$$I \propto \frac{1}{4}.\frac{1}{\Delta t}\int_0^{\Delta t}(2|E_0|^2.(2+e^{i(\omega_1-\omega_2)t+e^{i(\omega_2-\omega_1)t}}) + E_0.E_0^*(e^{2i\omega_1 t}+e^{-2i\omega_1 t}+e^{2i\omega_2 t}+e^{-2i\omega_2 t}+2(e^{i(\omega_1-\omega_2)t}+e^{i(\omega_2-\omega_1)t}))) \tag{3.5}$$

From equation 3.5, we can invoke similar arguments than in appendix A, taking advantage of the long response times of optical detectors with respect to the inverse of the optical frequencies to cancel all the terms in $e^{i\omega' t}$ for any ω'. In this case, the consequence is that the final intensity is only proportional to twice the intensity of the single wavelength intensity, while all the cross terms have canceled. We can easily generalize to the case where the spectral irradiance is no longer constant. In this case, we could show that total irradiance is the sum of the two spectral irradiances. Additionally, we can equally easily generalize this result to the case of multiple wavelengths. We would be able to show that the total irradiance is simply the integral of the spectral irradiance $I'(x,y,t,\lambda)$:

$$I(x,y,t)=\int_{\lambda_{min}}^{\lambda_{max}} I'(x,y,t,\lambda)d\lambda \tag{3.6}$$

This result is quite important when considering the temporal low-coherence interferometry because it states that we can consider each wavelength independently. It shows that the different spectral intensities do not interfere with each other. When using sources with extended spectral bandwidths S(ω), the total intensity can be written as:

$$\mathrm{I_{total}(x,y,t)}=\int_{-\infty}^{+\infty}\mathrm{I_{detector}(x,y,\omega,t).S(\omega)}\,d\omega \tag{3.7}$$

This form allows to interpret the white light spectrum as the convolution between a single wavelength interferogram and the source spectrum. Usually, the final spectrum is mainly controlled by the source spectrum, but one should also consider the attenuation by the different optical elements of the experimental setup, and the camera detection range. I(x,y,ω,t) can be expressed as the single wavelength interference intensity, similarly to equation 3.8:

$$\mathrm{I_{detector}(x,y,\omega,t)}=\mathrm{I_{inc}}+\mathrm{I_{coh}(x,y,\omega,t)}.cos(\frac{\omega.\delta_{\mathrm{sample}}(\mathrm{x,y,\omega,t})}{\mathrm{c_{light}}}) \tag{3.8}$$

From such equations, the effect of spectrally extended sources is quite straight forward, as the different wavelengths only are in constructive interference altogether when the path difference is equal to zero. When the optical path difference increases, all wavelengths present different states of interference, with some wavelength interfering constructively, and others interfering destructively, so that interferences are blurred, and the averaged intensity becomes simply equal to the sum of intensities.

If we neglect the spectral dependence of the backscattering coefficient, we can develop the

integral into:

$$\mathrm{I_{total}(x,y,t) = I_{inc} + I_{coh}(x,y,,t).} \int_{-\infty}^{+\infty} cos(\frac{\omega.\delta_{\mathrm{sample}}(\mathrm{x,y,}\omega\mathrm{,t})}{\mathrm{c_{light}}})d\omega \tag{3.9}$$

which we can easily calculate numerically, with the optical parameters of our experiments, as presented in figure 3.4.

Another way, to illustrate the effect of temporal low-coherence, that is more mathematical, but enables easier calculation of the final intensity, is to calculate the intensity coming onto the detector as a function of the time delay introduced between the two arms of the detector:

$$I(\tau) = <\mid E_{object}(t+\tau) + E^*_{ref}(t) \mid^2>_t \tag{3.10}$$

For similar arguments regarding the detector integration time, and spatial average, we obtain:

$$I(\tau) = I_{object} + I_{ref} + 2\sqrt{I_{Ref}.I_{object}}\Re(< \gamma_{RS}(\tau) >) \tag{3.11}$$

with $\gamma_{RS}(\tau)$, the temporal cross-correlation between the reference field and the sample field:

$$\gamma_{RS}(\tau) = \frac{< E_{object}(t+\tau)E^*_{ref}(t) >}{2\sqrt{I_{Ref}.I_{object}}} \tag{3.12}$$

From these 2 previous equations, and assuming that reference and sample arms reflectivities do no depend on the wavelength, we can invoke the Wiener Khinchin theorem that demonstrates the equality between the coherence function and the Fourier transform of the source:

$$\gamma_{RS}(\tau) = \int_{-\infty}^{+\infty} S(\omega)e^{i\omega\tau}d\omega \tag{3.13}$$

With $S(\omega)$, the source power spectral density. Therefore, the total intensity captured by the detector can be written as the sum of an incoherent intensity and a coherent intensity multiplied by the real part of the Fourier transform of the source power spectral density. We can add that at the end, this not only the source spectrum that matters but the entire system spectrum. It corresponds to the product between the source spectrum and the spectral transfer functions of all the optical elements in the light path, including the camera spectral response.

To illustrate it, we can choose the case of a single wavelength source:

$$S(\omega) = \delta(\omega_0) \tag{3.14}$$

So that the total intensity becomes:

$$I(\tau) = I_{object} + I_{ref} + 2 * \sqrt{I_{Ref}.I_{object}}\Re(e^{i\omega_0\tau}) \tag{3.15}$$

which corresponds to classical single wavelength interference equation:

$$I(\tau) = I_{object} + I_{ref} + 2 * \sqrt{I_{Ref}.I_{object}}cos(\omega_0\tau) \tag{3.16}$$

Another intuitive example is the case of a flat spectrum source on a region centered around ω_0 and of $\Delta\omega$ spectral bandwidth, which can be written as the convolution between a rectangular function of extension $\Delta\omega$ and a delta Dirac function centered at ω_0 :

$$S(\omega) = S_0(Rect(\Delta\omega) * \delta(\omega_0)) \tag{3.17}$$

Therefore, the Fourier transform of this convolution becoming the dot product of the Fourier

transforms of each term, and the Fourier transform of a rectangular function being a sinus cardinal, we can write the correlation function as:

$$\gamma_{RS}(\tau) = sinc(\frac{\Delta\omega\tau}{2}).e^{i\omega_0\tau} \tag{3.18}$$

Finally, the total intensity for a flat spectrum can be written:

$$I(\tau) = I_{object} + I_{ref} + 2 * \sqrt{I_{Ref}.I_{object}}cos(2\pi\tau).sinc(\frac{\Delta\omega\tau}{2}) \tag{3.19}$$

Interestingly, the interference term is modulated as a cosinus similarly to a single wavelength interference, but its amplitude decreases as a sinc function of the phase shift between the two arms. To estimate a coherence length, *i.e.* a length scale that describes the attenuation of the interference signal, we can choose this length to be the full-width at half maximum of this sinc function, and we can rewrite the above equation as a function of the optical path difference δ_{RS}, and of the main wavelengths λ_0 and $\Delta\lambda$:

$$I(\delta_{RS}) = I_{object} + I_{ref} + 2 * \sqrt{I_{Ref}.I_{object}}cos(\frac{2\pi}{\lambda_0}.\delta_{RS}).sinc(\pi.\delta_{RS}.\frac{\Delta\lambda}{\lambda_0^2 - \Delta\lambda^2}) \tag{3.20}$$

Finally, we can calculate the full-width half maximum of a sinc function to be $2.1.896 \simeq 3.79$, and then the coherence length l_c to be [1]:

$$l_c \simeq \frac{3.79}{\pi}.\frac{\lambda_0^2 - \Delta\lambda^2}{\Delta\lambda} \simeq 1.207.\frac{\lambda_0^2 - \Delta\lambda^2}{\Delta\lambda} \tag{3.21}$$

Similar calculations can be performed for several different source spectra [133], and we especially mention the gaussian source that gives a coherence length of $l_c = \frac{8ln(2)}{2\pi}.\frac{\lambda_0^2-\Delta\lambda^2}{\Delta\lambda} \simeq 0.88\frac{\lambda_0^2-\Delta\lambda^2}{\Delta\lambda}$, which is the general coherence length formula one can find in most of the articles describing low-coherence systems, even though the system spectrum is rarely gaussian. Here, $\Delta\lambda$ measures the wavelength difference at the full-width half maximum of the gaussian spectrum. We can also cite the case of Lorentzian-shaped sources that give coherence length $l_c \simeq 0.441\frac{\lambda_0^2-\Delta\lambda^2}{\Delta\lambda}$, about half of the Gaussian source for a similar spectral extension.

To conclude this subsection about temporal coherence, we have seen that it is possible to loose the interference signal for large phase shifts between the two interferometer arms by choosing spectrally extended light sources. The coherence length indicates a length scale after which the interference signal is lost. This coherence length is mainly proportional to the ratio between the central wavelength squared and the spectral bandwidth of the source. Nevertheless, one has to keep in mind that this coherence length is only a length scale, meaning that the interference signal is lost only after a few times of the coherence length. Additionally, one has also to pay attention to the values of coherence lengths that could be found in the literature, as the hypothesis of the Gaussian source is often chosen, without considering neither the actual spectrum shape nor the absorption caused by the different optical elements of the system. Interestingly, with a same spectral bandwidth, it should be possible to tune the coherence length by changing the spectrum shape captured by the camera. In figure 3.4, we illustrate the principle of temporal low-coherence and give some examples of different light spectra, and the theoretical interference pattern that should be obtained. In figure 3.4 E and F, we show the light spectrum, and theoretical interference pattern for the Full-Field OCT system I designed, and that I will describe in chapters 4 and 5.

[1] Note that $\Delta\lambda$ is generally considered as negligible with respect to λ_0 so that the coherence length is often written as proportional to $\frac{\lambda_0^2}{\Delta\lambda}$

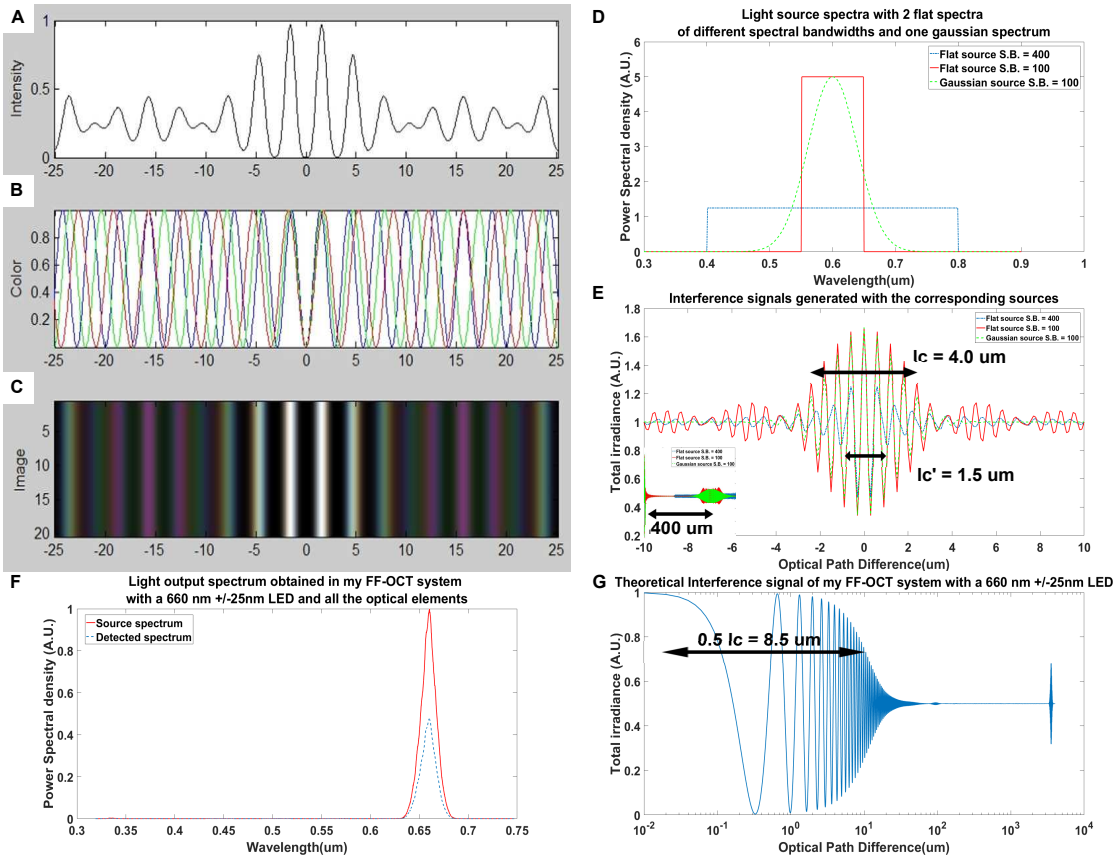

Figure 3.4 – Principle of temporal low-coherence interferometry. Panels A to C illustrate the principle of interference localization caused by the incoherent summation of the different wavelengths interferograms. Panel B presents three different spectral interferograms for respectively one blue, one green and one red wavelengths. At zero path difference, the interferograms are in phase, so that the total intensity (Panel A) looks like any spectral interferogram. As the path difference increases, the spectral interferograms become out-of-phase, up to a point where the red wavelength shows a maximum of intensity, while the blue wavelength shows a minimum of intensity so that the total intensity only corresponds to the green wavelength intensity. Panel C shows the iridescence generated by the white light interference. Close to the zero path difference, all wavelengths interference in phase, which creates black and white fringes. Further apart from the zero path difference, only a few wavelengths interfere constructively, leading to a local dominant color of the fringe pattern. **Panels D to G** are results of a simulation of different spectra, and the corresponding interference pattern. Panels D and E compare two different rectangular spectra of different bandwidths and a gaussian spectrum (Panel D), and their interference pattern close to the zero path difference. The small insert at the bottom left corner shows the first long-range rebound exhibiting a nonnegligible interference signal 400 μm away from the zero path difference. Panels F and G show a similar simulation that here takes into account all the optical elements in the light path (blue line), and not only the source spectrum (red line, panel F). Panel G shows the corresponding interference pattern in a semi-log scale that can nicely exhibit the zero path difference pattern and the first rebound.

3.2.2 Low Spatial Coherence

A more inconspicuous form of incoherence, although of large importance for Linnik interferometers or every configuration where the light beam is not collimated, is known as the longitudinal spatial coherence [133], which accounts for the interference signal attenuation in presence of defocus in one arm of the interferometer. Here again, the longitudinal spatial coherence can be understood in two ways, one phenomenological, and one using more intense calculation. Let's first consider a plane wave entering a Linnik interferometer. The effect of the imaging lens would be to create a

spherical wave focusing at the focal point, *i.e.* to create a phase law that transforms a plane wave into a spherical wave, generating wavevectors ranging from 0 to θ_{max}. The maximal angle θ_{max} depends on the imaging lens numerical aperture, with $NA = n_{medium}.sin(\theta_{max})$. If a reflective mirror is placed at the focal plane of the imaging lens, the same spherical wave is sent back to the lens, which recreates a plane wave at the system output. However, if the mirror is placed outside the focal plane, the reflected wave is going to be either converging or diverging when coming out the imaging lens, but will still be a spherical wave. Therefore, let's consider now the interference between the signal reflected by an in-focus reference mirror and the signal reflected by an out-of-focus sample mirror, or structure. As illustrated by figure 3.5 A, the output signal will be the interference between a plane wave and a spherical wave, the curvature of which being controlled by the importance of the defocus and by the imaging lens focal length and NA. Therefore, we can qualitatively imagine that interferences can only occur where the two wavefronts overlap so that the interference signal will be attenuated as the sample beam curvature increases, meaning that the defocus or the imaging lens NA increases.

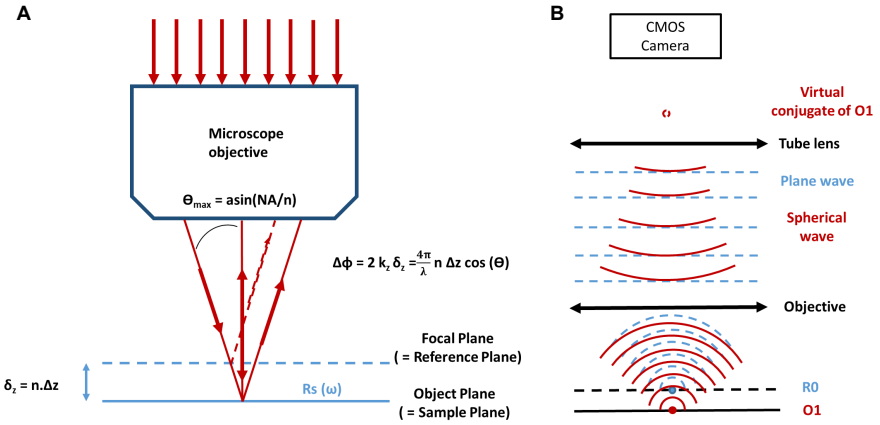

Figure 3.5 – Intuitive principle of spatial low-coherence interferometry. Panel A illustrates the phase shift caused by a defocus of the object with respect to the focal plane, virtually corresponding to the plane of the reference mirror. It simply corresponds to the phase shift associated with a double interface of thickness $n\delta z$. The phase shift depends on the incidence angle ranging from 0 to θ_{max}, and can therefore not be compensated for by adjusting the reference arm length. **Panel B** illustrates the interference term decrease associated with an axial defocus of an object. The reference mirror reflects the light in a spherical wave of curvature corresponding to the lens curvature so that the reference light comes out of the objective as a plane wave (blue dotted lines). On the contrary, a defocused object backscatters a spherical wave which curvature does not match the curvature of the lens anymore. Therefore, the sample light is still a spherical wave at the exit of the objective, trying to focus at the virtual point, placed here after the tube lens. The curvature of the spherical wave depends on the defocus, and on the objective numerical aperture. It shows that, due to the difference in curvature of the two-phase planes, the overlap is not optimal, which decreases the interference term accordingly to the curvature difference. For the sake of clarity, the light beams stop at the tube lens, even though the two curvatures that should be compared are the ones after the tube lens, at the focal point at the camera, but the principle is the same.

The mathematical expression of the effect of lateral spatial coherence can be found in several studies [131, 133, 134]. To understand this effect, we can realize that the presence of a defocus δz induces a phase shift that depends on the wavevector of the incident beam, as illustrated by figure 3.5 B:

$$\Delta\phi = 2k_z.\delta z \tag{3.22}$$

with k_z, the axial wavector, so that, under the assumption of rotational symmetry around the optical axis, we can write:

$$k = \sqrt{k_r^2 + k_z^2} = \frac{2\pi}{\lambda} \tag{3.23}$$

Finally, we can define θ, ranging between 0 and $\theta_{max} = asin(\frac{NA}{n_{medium}})$, the angle between the optical axis and the converging beam, so that we can write:

$$k_z = k.cos(\theta) \tag{3.24}$$

and

$$k_r = k.sin(\theta) \tag{3.25}$$

In the case of a monochromatic light, the wavevector $k = \frac{2\pi}{\lambda}$ is unique, and we can write the total intensity coming onto the detector as the integral of the intensity at a given angle over the angular distribution offered by the imaging lens:

$$I(\delta z) = I_{ref} + I_{sample} + 2\Re\int_{k_r=0}^{k_{max}} I(k_r)\sqrt{R_{ref}(k_r)R_{sample}(k_r)}e^{2ik_z\delta z}k_r.dk_r \tag{3.26}$$

From equation 3.25, we can change of variable inside the integral to write the interference term as an integral on the angle θ. Equation 3.26 therefore becomes:

$$I(\delta z) = I_{ref} + I_{sample} + 2\Re\int_{\theta=0}^{\theta_{max}} I(\theta)\sqrt{R_{ref}(\theta)R_{sample}(\theta)}e^{2ik\delta zcos(\theta)}k^2.cos(\theta)sin(\theta)d\theta \tag{3.27}$$

To simplify equation 3.27, we can postulate the independence of the Fresnel reflection coefficient with the incoming angle (which tends to fail at high angles [135]), and the independence of I_0 with the angle, which corresponds to having a homogeneous illumination of the imaging lens back focal plane. Therefore, and using the linearity of the real function, equation 3.27 reduces to:

$$I(\delta z) = I_{ref} + I_{sample} + 2\sqrt{I_{ref}I_{sample}}.\int_{\theta=0}^{\theta_{max}} cos(2k\delta zcos(\theta)).k^2.cos(\theta)sin(\theta)d\theta \tag{3.28}$$

Here again, we can directly use this integral formula in a numerical model to estimate the shape of the interference signal. Otherwise, we also recognize equation 3.26, as the expression of the Van Cittert Zernike theorem, which is equivalent to the Wiener-Kinchine theorem in the spatial domain [133] to relate the spatial coherence function to the Fourier transform of the light spatial distribution function $I(k_r)$. Similar to the case of temporal low-coherence, the interference fringes envelope will attenuate over a typical distance, hereby named spatial coherence length, and with a shape that depends on the angular distribution of intensity (instead of the spectral distribution). Similar to the previous section, if we still assume a constant spatial distribution function or an homogeneous filling of the imaging lens back aperture, we can write the interference term in equation 3.28 as a convolution between a rectangular function and a function that depends on θ. When inverse Fourier transformed, it gives a multiplication between a sinc function and a somehow cosinusoidal fast modulation. In a similar manner, we can easily imagine that if we fill the aperture with a Gaussian beam, we should have an interference term corresponding to the multiplication of a slowly varying Gaussian-shape envelope with a rapidly varying cosinusoidal modulation. Figures 3.6 C and 3.6 D illustrate the result of the theoretical calculation of the fringe pattern in the case of low spatial coherence, for different imaging lens NA's and for different illuminations of the back

focal plane. They show, likewise previous work on spatial coherence [133, 134], that interferences can be potentially strongly localized using high NA microscope objectives, even when using single wavelength illumination, with extremely high temporal and spatial coherence, such as laser beams. Figures 3.6 A and 3.6 B show the evolution of the longitudinal spatial coherence length versus the objective NA in the case of a laser illumination. We can finally add that, in order to perform a good simulation of our interferometers illuminated via a Kohler illumination, we should account for the spatial inhomogeneity at the back focal plane of the objective, since it is illuminated by the image of the LED. However, such a simulation would be a bit more difficult, as it breaks the rotational symmetry, and would require a reasonable measurement of the light intensity at the back focal plane in our systems, which we have never performed.

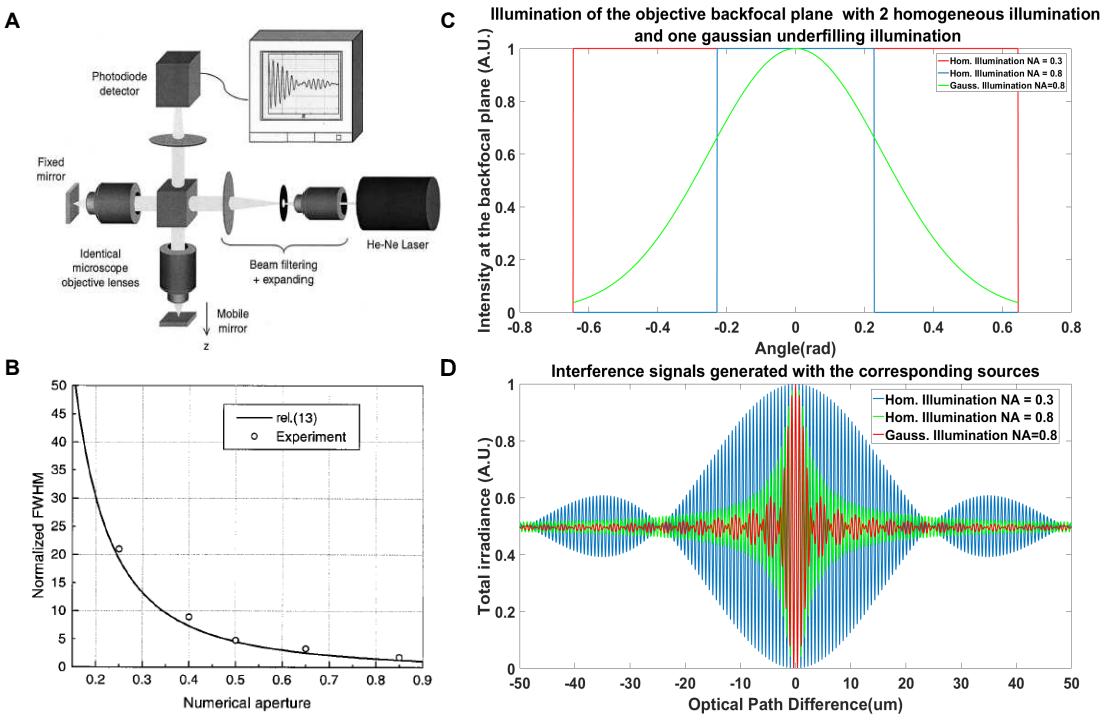

Figure 3.6 – Principle of spatial low-coherence interferometry. Panels A and B illustrate the principle of interference localization caused by the objectives wide aperture [134]. A Linnik interferometer is illuminated by a Helium-Neon laser, which is spatially and temporally coherent on very large coherence lengths (Panel A). Nevertheless, the angular distribution created by the microscope objectives might be important enough to localize the interference, with a full-width half maximum of the fringe envelope decrease with the numerical aperture, down to a few microns (Panel B). **Panels C and D** show the result of a simulation of a single wavelength interference signal generated as the two arms go trough microscope objectives of different NAs. The back focal plane of the objectives can be illuminated homogeneously for either 0.3 NA (blue curve), 0.8 NA (red curve), or with a gaussian illumination of a 0.8 NA objective (green curve). Different patterns of interference can be observed in panel D. Similarly to the temporal coherence, the homogeneous illumination creates several rebounds of small fringes, while the Gaussian illumination does not show similar feature.

A final form of spatial coherence is referred to as lateral spatial coherence, which often originates from a spatially inhomogeneous light sources, such as metallic filaments or LEDs. However, to my knowledge, lateral spatial coherence has never been directly used to axially localize the interferences. It can generate a long range correlation between different transverse points at a given axial position and can introduce a cross-talk noise in the interferograms. We will mainly discuss the interest of working with low lateral spatial coherence sources in the next chapter about Full Field OCT. However, we can mention that in low spatial lateral coherence systems, a lateral

mismatch obtained by translating one of the interferometer imaging lenses along its back focal plane can attenuate the measured interference pattern [133], as the mutual coherence decreases with the lateral mismatch. To my knowledge, it seems to be only considered as a drawback and has never been used as a source of fringes localization. However, it might explain an asymmetry of the fringe envelope, as it is sometimes observed in interferometers.

3.2.3 Combining low spatial and low temporal coherence

To conclude this part on low-coherence, we should add that understanding carefully the interference effects in high NA interferometers is even more difficult, as we often combine low temporal coherence and low spatial coherence. As we will see, all previous equations cannot therefore be simplified and, to my knowledge, there is no extended analytical solution to account for the coupling of these two coherence effects. What is often performed however, is the calculation of the smallest NA above which the low longitudinal spatial coherence should be taken into account for a given temporal coherence length [133], as illustrated in figure 3.7 A. Otherwise, the interference fringes pattern can still be calculated numerically, as I have performed it in figure 3.7 B and C for our different microscopes. Indeed, the difference starts from equation 3.26, where the wavevectors k_r not only depend on angle θ but also depend on the wavelength, which can be developed into:

$$I(\delta z) = I_{ref} + I_{sample} + 2\Re\int_{\lambda_{min}}^{\lambda_{max}}\int_{\theta=0}^{\theta_{max}} I(\theta,\lambda)\sqrt{R_{ref}(\theta,\lambda)R_{sample}(\theta,\lambda)}e^{\frac{4i\pi}{\lambda}.\delta z cos(\theta)}(\frac{2\pi}{\lambda})^2.cos(\theta)sin(\theta)d\theta d\lambda \quad (3.29)$$

Equation 3.29 might seem complicated and is analytically hardly calculable, but simply corresponds to a sum, that can be calculated numerically, even though it starts becoming computationally intense. In the case of the microscopes I used during my work, and that I will present in the next chapter, they mainly display extreme cases, in which the spatial coherence length is either dominant, with almost no influence of the temporal coherence, or almost negligible. However, in the case of the LightCT commercial FF-OCT setup operated with a high power red LED (figure 3.7 C), spatial coherence starts to have an influence on the interference pattern. Nevertheless, in an interferometer operated with a LED, such an interplay will mainly happen for intermediate NA objectives, from 0.3 to 0.7.

3.3 Optical Coherence Tomography (OCT)

Optical coherence tomography (OCT) is one of the most popular low-coherence interferometers among the biomedical imaging community and has been revolutionizing ophthalmology since its modern development in 1991 [20]. OCT is often cited as one the fastest examples of translational research to medicine with most of modern hospitals using OCT measurements for routine eye examination less than 25 years after its initial development. OCT is a reflection interferometer that can label-free and non-invasively measure backscattering coefficients in highly scattering samples with an extreme sensitivity (over 130 dB for current systems). Throughout the years, OCT has been declined in several different versions and is still an active field of research. In this section, I will review the two main families of OCT systems, namely time domain and Fourier domain OCT. A goldmine of information and references can be found in the book by *W. Drexler and J. G. Fujimoto* [21].

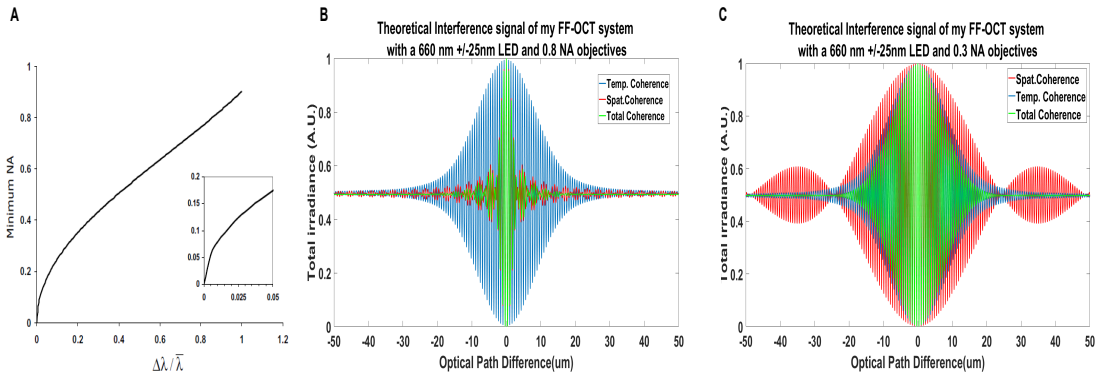

Figure 3.7 – Competition between spatial and temporal low-coherence in high NA interferometers. **Panel A** shows the evolution of the minimal NA value for the temporal coherence length not to be affected by the spatial coherence length [133]. **Panel B** presents the result of a simulation of the competition between temporal and spatial coherence with 0.8 NA objectives, and 625nm LED, similarly to my setup. The temporal coherence length of about 17 μm, the spatial coherence length is 3 μm, and the total coherence length is mainly imposed by the spatial coherence. **Panel C** presents the result of a similar simulation, but with microscope objectives of 0.3 NA, in a configuration close the LightCT commercial system (that will be described in the next chapter). Here, the spatial coherence length is of about 30 μm and is much larger than the temporal coherence length. However, the spatial coherence impacts the interference signal, reducing the total coherence length to 16 μm instead of the 18 μm of the temporal coherence length.

3.3.1 Principle of time domain Optical Coherence Tomography

Using the same extended metaphor of a pulse propagation timer, as we used for QPI description, the principle of OCT becomes fairly simple. The following explanation, and the associated figure 3.8A, are strongly inspired by J.Mertz's book [136]. When a short light pulse in sent onto a complex scattering medium, a part of the light will be naturally backscattered. Nevertheless, due to various axial positions of the scatterers, and due to multiple diffusion, the backscattered signal is temporally broadened. Interestingly, if we initially neglect multiple scattering, first photons to arrive at the detector are photons that have been backscattered at the surface of the tissue. And the longer time it takes for the photons to arrive at the photodetector, the deeper they have propagated inside the sample. Obviously, because light propagates so fast, there is no detector that could electronically select the arrival time of these photons. On the contrary, if the light pulse is reflected onto a mirror, its shape and temporal extension are globally conserved, as illustrated in the reference arm of the Michelson interferometer in figure 3.8 A. Therefore, when a light pulse comes onto such an interferometer, it is backscattered and temporally broadened in the sample arm, and is reflected while maintaining its short temporal extension in the reference arm. The light coming from both arms are recombined before reaching the detector. Finally, there is only a short time overlap between the two beams, when the reference arm length is adjusted to match sample arm length. The reference arm length can further be adjusted so that the reference light overlaps the sample light coming from a given depth. The longer the reference arm, the deeper the location of the backscattering event inside the sample it is. Obviously, interferences can only be detected if the two beams temporally overlap and, using phase-shifting algorithms as described in chapter 1, the interference term can be extracted over the noninterfering intensity. Only the light coming from the given depth corresponding to the reference arm optical path can be extracted.

Interestingly, it is not required to send such pulsed light, which would require very expensive and complicated lasers. Indeed, using low-coherence interferometry, it is equivalent, in terms of interferences generation, to send a short pulse or a continuous low coherent light. The continuous

light behaves, in terms of interference once again, like a successive generation of very short light pulses that can not interfere with each other. For a low-coherence light beam with a coherence length of 1 μm, it would correspond to the continuous successive emission of light pulses of temporal extension of 3.10^{-15} s that can not interfere with each other. Figure 3.8 B presents a more realistic scheme of a time domain OCT, as it can still be found in commercial systems. A spectrally extended light source is sent onto a fiber interferometer. The sample arm contains galvanometric scanning mirrors so that the transverse position inside the sample can be adjusted. Usually, a low NA objective, or imaging lens, focuses the light on the sample, in a large depth of field beam, scanning a substantial depth inside the sample. Therefore, the entire depth of the sample can be reconstructed by only scanning the reference arm length. We can add that higher NA objectives can be used to increase the transverse resolution but it requires to scan the sample in depth synchronously to the reference arm length or to use of Bessel beams to obtain a large depth of field with a short transverse extension [137]. Finally, so far, we have put aside the contribution of the multiple scattering. Indeed, at large depths, the time information is not sufficient to discriminate between deep ballistic photons, and surface multiply scattered photons. However, and particularly at low NA, the multiply scattered photons have mostly changed their directions, exhibiting wavevectors that are mostly different from the ballistic photons. Therefore, it becomes possible to spatially filter out most part of the multiply scattered photons, either directly from the NA limitation of the objective, or by adding a confocal pinhole at the detection. It should be noted that fiber-based OCT systems, such as the one presented in figure 3.8, use the fiber as the confocal pinhole as single mode fiber inner cores are usually below 10 μm of diameter.

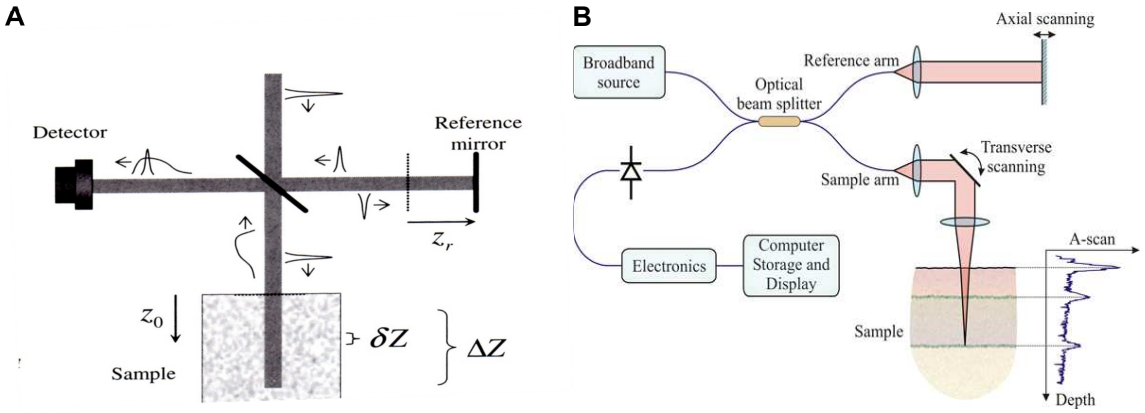

Figure 3.8 – Principle of time domain OCT. Panel A originates from J.Mertz book [136]. It illustrates the principle of time domain OCT using the metaphor of light pulses sent to the sample. Because light from the sample arm can be backscattered from multiple depths, the pulse is temporally broadened. However, the light captured by the detector is the sum of the light coming from the sample arm with some short pulse light coming from the reference, producing interferences only when the two beams temporally overlap. The interference can be selective of a given depth inside the sample by adjusting the length of the reference arm. **Panel B** has been taken from [138] and shows a practical implementation of a time domain OCT setup.

3.3.2 Spectral domain and swept-source OCT

OCT can also be performed in the Fourier or spectral domain. We will show that the interference signal spectrum is linked to the axial profile distribution of scatterers inside the sample arm. Therefore, from the measurement of the interference spectrum, it is possible to compute an axial profile of amplitude [139]. Interestingly, it allows the reconstruction of an axial profile without the

need of mechanical scanning of the reference arm, as the depth information is embedded in the interference spectrum. There are two main solutions to measure the spectrum, either by directly measuring it, using a spectrometer, or any spectral grating coupled to a line detector and using any white light source, or by using a swept source laser and by consecutively acquiring signal with small wavelength shifts. Spectral domain OCT (SD-OCT) axial performances are mainly controlled by two parameters. The first parameter is $\delta\lambda$, the smallest detectable spectral shift, controlled either by the spectrometer resolution or by the spectral extension of the swept source laser. It is inversely proportional to the scanning depth. The second parameter is the total extension of the spectrum $\Delta\lambda$, which imposes system optical sectioning, or axial resolution, similarly to time domain OCT. Each spectral interferogram has a very long coherence length controlled by $\delta\lambda$ and can measure interference signal from a large depth. However, the integration of all wavelengths permits to localize the origin of the different structures with good accuracy.

To explain SD-OCT, we will write the interference term as a function of λ, for a reflector at a single depth, corresponding to an optical path shift of $\delta(z)$ with the reference arm:

$$I(\lambda) = I_{ref}(\lambda) + I_{sample}(\lambda) + 2\sqrt{I_{ref}(\lambda)I_{ref}(\lambda)}cos(\frac{2\pi}{\lambda}\delta(z)) \tag{3.30}$$

A phase modulation allows the extraction of the complex interference term only:

$$C(\lambda) = \sqrt{I_{ref}(\lambda)I_{sample}(\delta(z),\lambda)}e^{\frac{2\pi}{\lambda}\delta(z)} \tag{3.31}$$

By calculating the inverse Fourier transform, we can find back the position of the scatterer:

$$I(z) = FT^{-1}(C(\lambda)) = \frac{1}{\Delta\lambda}\int_{\lambda_{min}}^{\lambda_{max}} \sqrt{I_{ref}(\lambda)I_{sample}(\lambda)}e^{\frac{2\pi}{\lambda}(\delta(z)-z)} \tag{3.32}$$

which, in the case of a single scatterer in $\delta(z)$, gives a single peak at $z = \delta(z)$ with an extension corresponding the source power spectral density.

Of course, a similar calculation can be performed in the case of multiple layers and continuous samples and can be found in an especially comprehensive form in *G.Hausler et. al.* [140]. In this article, they also explain an important feature of Fourier domain OCT that can even reconstruct an axial and phase profiles without the need for phase modulation of the reference arm. Indeed, when calculating the inverse Fourier transform of the total intensity (not only the complex interference term), it creates additional terms as expected, and creates ghost images. The ghost image corresponding to the conjugate of the complex interfering term is found in the negative optical path differences, while a DC term, corresponding to the source autocorrelation, can be found at the depth z=0, as illustrated in figure 3.9 D. This DC ghost image can be shifted away from the signal of interest by simply adding an offset of the reference plane to the sample surface.

The interest of using Fourier domain are two fold. First, as previously mentioned, it does not require any axial mechanical translation of the reference arm, which stabilizes the interferometer and therefore authorizes to acquire at faster speeds. Additionally, because the information but also noise is multiplexed on the N pixels of the spectrometer, it increases the SNR of a factor $\sqrt{N}$, which can be increased by up to 15 dB ($10.log(10^{1.5})$) for large line detectors, and up to 30 dB at important depths [141], as illustrated in figure 3.9 E and F [2]. In recent years, swept source OCT

[2]In spectral domain, the power is divided onto the N pixels of the detector but the exposure time is considered to be N times longer to reach similar A-line acquisition speed between spectral domain and time domain OCT. Therefore, the captured intensity is similar between both configurations but the noise is equally distributed over N pixels in spectral domain and not in timed domain OCT.

has taken advantage over spectrometer-based SD-OCT, mainly in terms of speed. It seems that swept source OCT offers higher scanning speeds with an A-line rate of up to 6 MHz [142], while spectrometer-based OCT seems to be limited to around 100 kHz, probably limited by technological features of line cameras in terms of speed and sensitivity.

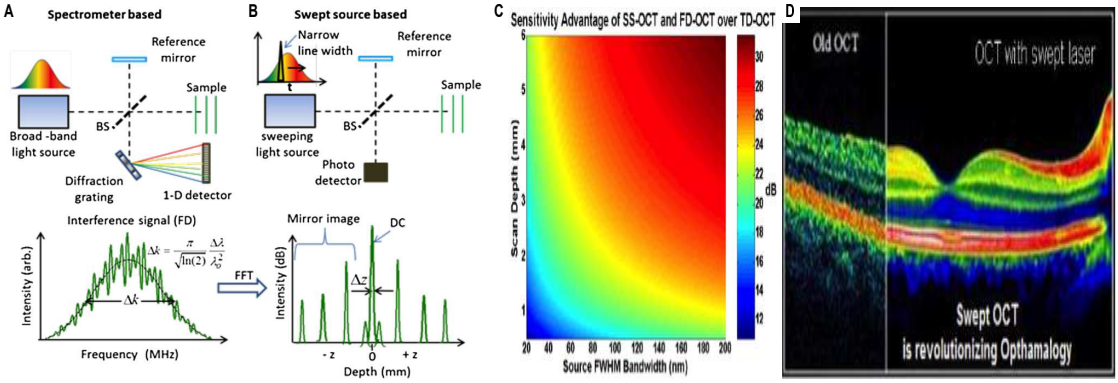

Figure 3.9 – Principle of Fourier domain OCT. Panel A to D originates from *W.Drexler et al.* review on OCT [139]. They illustrate the strategy of spectral domain OCT, using white light and a line spectrometer to measure the spectral interferograms in panel A, and the strategy of swept source OCT, successively recording the spectral interferogram of a sweeping frequency light source with a single detector, in panel B. **Panel C** shows a typical spectrum recorded by a Fourier domain OCT system, and **panel D** presents the result of the inverse Fourier transform enabling to recover the axial amplitude and phase profiles of the sample. To record a 3-D volume, a transverse scanning has finally to be performed. **Panel E** shows the sensitivity improvement offered by Fourier domain OCT versus time domain OCT, ranging from 10 dB to 30 dB, depending on the spectral bandwidth and the recorded depth [141]. **Panel F** illustrates the sensitivity gain by comparing two retinal OCT scans obtained either with a time domain on the left-hand side or with a Fourier domain OCT on the right-hand side [143].

3.4 Phase imaging using OCT

Similar to other tissue QPI systems, OCT is sensitive to sub-wavelength phase differences inside tissues depending on the backscattering strength of the structure of interest, as described in section 3.1. Moreover, as discussed in chapter 1 on the comparison between reflection and transmission-like configuration, the advantage of the reflection configuration displayed by OCT is that the phase change is likely to be a pure axial displacement, while a change in the refractive index difference would affect the backscattering amplitude. Therefore, OCT microscopes allow a sub-wavelength measurement of axial displacement inside tissues. In this section, I will present different OCT systems that take advantage of the phase sensitivity to provide a relevant and different contrast than the usual OCT backscattering contrast. I will first describe a small procedure that I started using during my PhD project to extract the phase difference information. Then, I will present two technologies, Doppler OCT and dynamic optical elastography OCT, that use phase difference information to measure blood flow and tissue mechanical properties respectively.

3.4.1 Recovery of quantitative phase differences

To be more exhaustive on the phase difference calculation, let me add that it can generally be calculated as long as the phase difference between the two successive phase maps is smaller than 2π, corresponding to an optical path difference of $\frac{\lambda}{2n}$ for all pixels. Therefore, the phase

can be locally reconstructed without ambiguity by 1-D phase unwrapping algorithms separately performed on each of the image pixels. To calculate accurate phase differences map, another option that we started to use in the lab after the suggestion of Michael Atlan was to calculate the product between one complex interference signal (without decoupling the amplitude and the phase), and the complex conjugate of the previously measured complex signal:

$$P(x,y,t) = (A(x,y,t+\Delta t)e^{i\phi(x,y,t+\Delta t)}).(A(x,y,t)e^{i\phi(x,y,t)})^* \tag{3.33}$$

with A the signal amplitude, and ϕ, the phase. Under the assumption that the amplitude is constant over a short period of time, we obtain:

$$P(x,y,t) \simeq |A(x,y,t|^2.e^{i\Delta\phi(x,y,t)} \tag{3.34}$$

From the complex number obtained in equation 3.34, we can calculate its modulus, giving access to the amplitude squared, and its angle, giving access to the phase difference. The main advantage of this calculation is that, as long as the phase difference is smaller than 2π, it directly creates a correct phase difference map, without the need of phase unwrapping algorithms. It is advantageous as phase unwrapping, even in 1-D, can fail in presence of noise, and can be computationally intense for large 2-D maps.

I chose not to illustrate the interest of this algorithm here, as I will discuss it later in chapter 5. I would like to insist here, though it is not intrinsically different than performing a 1-D temporal phase unwrapping algorithm along every single pixel, except that it seems to be less sensitive to noise, and faster to compute.

3.4.2 Doppler and Functional OCT

Thanks to its phase and frequency sensitivity, it is important to note that OCT is also able to measure flow-induced Doppler shift, similarly to functional ultrasounds [144]. Local measurement of blood flows is the main application of Doppler OCT since other biological fluids provide little backscattering. The optical resolution offered by OCT, and especially high-resolution OCT, are particularly interesting to reveal the many microcapillaries of the organism without the need to compromise between spatial resolution and temporal resolution to access these microcapillaries as in ultrasounds [145]

Doppler OCT principle is based on the frequency shift caused by the Doppler shift of the moving scatterer, which is equal to:

$$\delta\nu_z = 2k_z V_{s,z}(Z_{focus}) = 2\frac{2n}{\lambda_0}V_s(Z_{focus})cos(\alpha) \tag{3.35}$$

with $\delta\nu_z$, the frequency shift, k_z, the axial wavevector, nearly equal to $k_0 = \frac{2\pi}{\lambda_0}$ for low NA OCT systems (even more when a confocal pinhole is used in the detection path), n, the medium refractive index, V_s, the axial component of the scatterer velocity, and α, the angle between the OCT beam, and the direction of motion. The measurement of the frequency shift can be performed by calculating the Fourier transform of the temporal evolution of the interference signal at a given pixel, either measured with time domain [146, 147] or Fourier domain OCT [148]. The Doppler shift can also be calculated as a phase shift between two consecutive measurements [149]. At a given time and a given voxel, the interference signal difference can be expressed, as presented in equation3.33 to emphasize the phase shift:

$$P(x,y,z,t) = (A(x,y,t+\Delta t)e^{i\phi(x,y,t+\Delta t)}).(A(x,y,t)e^{i\phi(x,y,t)})^* \simeq |A(x,y,z,t)|^2 e^{\frac{2i\pi}{\lambda_0}.\delta\nu_z} \quad (3.36)$$

The axial component of the blood velocity can be computed as:

$$V_s(x,y,z,t) = \frac{\lambda_0}{4ncos(\alpha)}.arctan(P(x,y,z,t)) \quad (3.37)$$

Blood flow velocities ranging from 1 μm.s^{-1} to a few mm.s^{-1} can be measured, depending on the time scale of the measurements, accounting for the fact that flows that are too fast for the time resolution create a modulation higher than 2π, that can not be unambiguously calculated [150]. Only the axial component of the flow can be easily computed from phase measurements, but more complex schemes enable quantitative flow velocity measurement[3]. By either measuring the vessel angles in a 3-D data set, by measuring the Doppler spectrum standard deviation [151], or by measuring the temporal extension of the temporal autocorrelation function [152], as presented in figure 3.10. The blood flow can also be accurately measured by integrating the flow on the surface of the vessel [152]. An external measurement of the blood vessels dimensions with higher resolution techniques enables the computation of 3-D blood flows ranging from a few nanoliters per second to several microliters per second, as illustrated in figure 3.11.

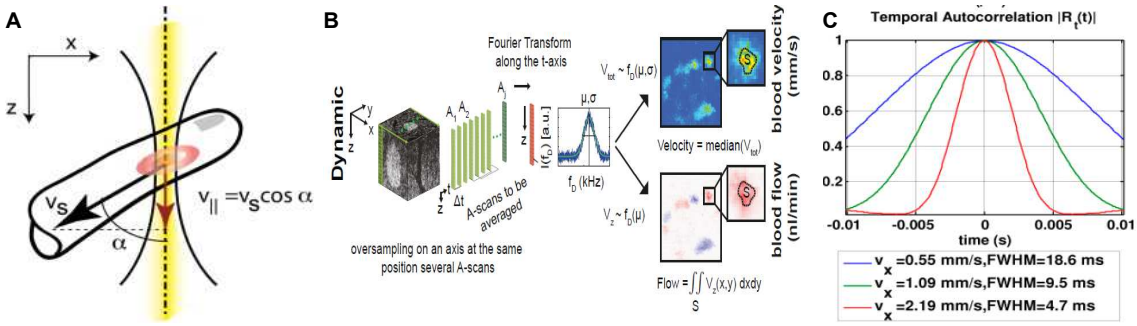

Figure 3.10 – Principle of Doppler Optical Coherence Tomography. Panel A illustrates the interaction between OCT beam and a blood flow. The phase shift only depends on the axial component of the velocity [150]. **Panel B** shows a possible calculation of the blood velocity and the blood flow using Doppler OCT [153]. From an axial versus time data set, a short time Fourier transform is applied on the time axis at a given depth, which gives the Doppler spectrum, from which the average frequency μ and the standard deviation σ. These two parameter values are used to compute the axial and transverse velocities, while the axial velocity can also be integrated on the transverse section of the capillary to quantify the blood flow. **Panel C** shows another way to extract the transverse velocity by measuring the full-width half maximum of the temporal autocorrelation function [152].

[3]Let's note that I could not find any report of time domain Doppler OCT measurements with high NA objectives. Nevertheless, it seems that due to the spatial spectral extension, a measurement sensitive to the transverse velocity is possible. From equation 3.26, we can write in presence of a flow:

$$I = I_{ref} + I_{sample} + 2\Re\int_{k_r=0}^{k_{max}} I(k_r)\sqrt{R_{ref}(k_r)R_{sample}(k_r)}e^{2i(k_z.v_{s,z}+k_r.v_{s,r})}k_r.dk_r \quad (3.38)$$

and,

$$I = I_{ref} + I_{sample} + 2\Re\int_{\alpha=0}^{\alpha_{max}} I(\alpha)\sqrt{R_{ref}(\alpha)R_{sample}(\alpha)}e^{2iv_s.cos(\alpha'-\alpha)}k^2d\alpha \quad (3.39)$$

with α', the angle between the optical axis and the capillary. We notice that it seems to create a phase shift that depends on the real velocity directly in contrast to low NA measurements.

Here, the phase sensitivity of OCT enables the quantitative label-free depth-resolved measurement of blood flows, giving access to a first functional contrast of *in vivo* tissues with OCT, that could successfully be used to detect several diseases, especially in the eye [150] or at the cortical surface [154]. Recent successful experiments could detect an additional functional contrast from this blood flow measurement, by assessing the local hemoglobin saturation level with visible light spectral domain OCT [155]. Surprisingly, if Doppler OCT can accurately quantify blood flows and hemoglobin content, it would seem possible to measure an even more interesting functional contrast that would take advantage of the BOLD (Blood-oxygen-level dependent) signal to measure a local neuronal activity, but it has yet never been reported in Doppler OCT to my knowledge. The BOLD signal corresponds to an increase of the blood flow (as measured in functional ultrasounds for example [144]), and a decrease in the hemoglobin content (as measured in functional MRI), linked with the neuronal activity. Nevertheless, the only few applications of functional Doppler OCT that seem to have been reported in the literature is the accurate following of flow changes associated with heart beat [153]. It might finally help to answer one of the key challenges in the understanding of the BOLD signal, which is to understand the link between the local single cell, or a single patch of cells activity and the associated change in the blood flow at the local scale. Thanks to its optical resolution, to its depth-resolved measurements, and to its high speed, Doppler OCT seems to be the perfect candidate to investigate such a local BOLD activity.

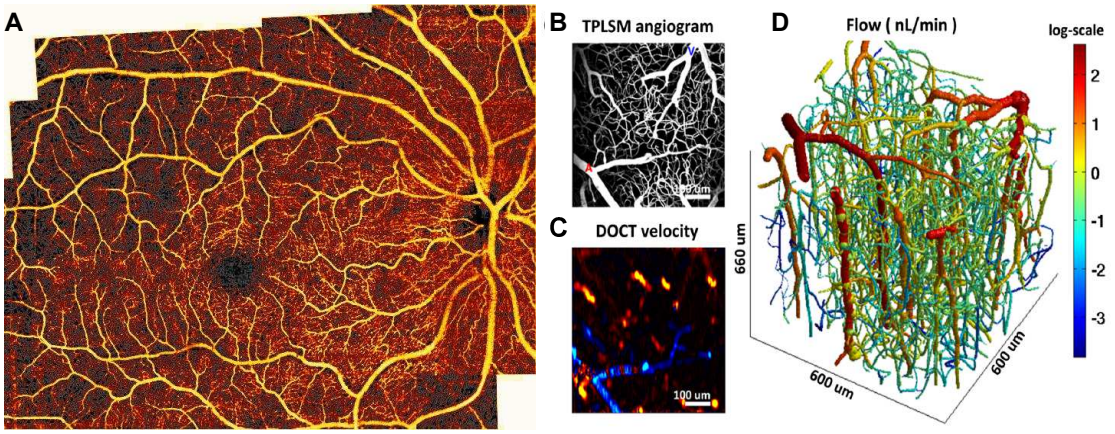

Figure 3.11 – Applications of Doppler Optical Coherence Tomography. Panel A shows a mosaic Doppler OCT angiogram of a human eye, acquired with a commercially available OCT device (Avanti, Optovue, Inc) [156]. **Panels B to D** present a 3-D quantitative reconstruction of blood flows in a mouse cortex [157] (panel D), calculated from a structural angiogram obtained with two-photon microscopy and the injection of FITC in the blood circulation (panel B) to accurately measure the blood vessels diameter, and from a Doppler-OCT map (panel C) to measure the blood mean velocity.

3.4.3 Optical elastography with OCT

Another important application of phase-sensitive OCT is undoubtedly optical coherence elastography that aims to measure mechanical parameters of a sample in 3-D with optical resolution. Quantitative phase measurements are important in this case since they allow to follow sub-micrometric mechanical deformations of a biological sample. The smaller the deformation, the less perturbative is the measurement, but more importantly it is important to stay within the elastic regime of deformations, within which the induced deformation is directly proportional to the mechanical strain applied to the sample. More details about the measurement of a mechanical contrast using optics can be found in appendix C. Nevertheless, as mentioned in this

manuscript introduction, the mechanical characterization of biological samples is not only complicated, but also of major interest for both the theoretical understanding of tissue development and for the mechanically-mediated biological activity. It can also be of interest as a diagnostics tool as discussed in appendix C. Optical elastography has the potential to bring these mechanical measurements at cellular level inside tissues, which might bring an entirely new perspective in the biomechanics field. In short, there are two main strategies to measure mechanical parameters inside a tissue, either in a quasi-static approach or in a dynamic time-resolved approach. The static approach can consist of applying a small deformation of the entire tissue and of measuring the 3-D phase variation map corresponding to the local deformation map to a given stress. Using the phase displacement map permits the detection of small deformations and to stay within the elastic regime. The stiffer the tissue, or some part of it, the less contracted it will be, and quantitative stiffness maps can be measured. Nevertheless, this approach can only work with fixed samples exhibiting no external phase fluctuation within a time frame of several seconds but it cannot account for dynamic mechanical changes. Moreover, it often fails at measuring a 3-D stiffness map with a good axial resolution, since a hard inclusion is likely to influence the deformability of the tissue above it. Otherwise, a second approach, presented in figure 3.12, consists in the dynamic measurement of externally induced shear waves inside the tissue. Phase measurements using OCT can easily detect transverse shear waves that propagate an axial mechanical deformation in the transverse plane. The shear wave can either be generated with an air puff, a vibrating mechanical-contacting probe [54] or by ultrasounds [158]. As discussed in appendix C, the local shear wave velocity being proportional to the local sample stiffness, OCT can access 3-D stiffness maps by measuring the local shear wave velocity. Nevertheless, these measurements can often be complicated in optics, as the shear waves propagate at speeds between 0.1 m.s^{-1} and 100 m.s^{-1}. It means that for small optical field of views (of a few millimeters at best), the acquisition speed has to be around 100 kHz to be able to follow their propagation. Scanning OCT, and especially Fourier-domain OCT for its superior speed, can interestingly follow the shear wave propagation with a good accuracy by synchronizing the shear wave emission with the camera detection, and can send multiple shear waves at progressively increasing time delays (similarly to a stroboscopic illumination).

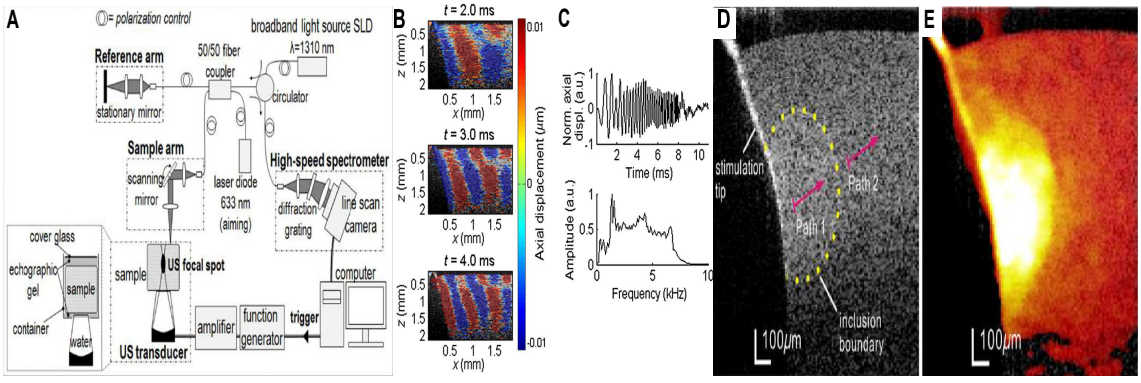

Figure 3.12 – Principle of Shear wave Optical Coherence Elastography. **Panel A** shows the setup scheme (a simple SD-OCT with an ultrasound generator), as used in *M.O'Donnell* lab [158]. **Panel B** illustrates the propagation of mechanical waves in the sample versus time, while **panel C** shows the evolution of the axial displacement in a single pixel versus time, as well as its quite broadband frequency content [54]. **Panels D and E** present the contrast enhancement of optical elastography(panel E) versus OCT (panel D) in an agarose phantom with a hard inclusion inside, which results in the local acceleration of the shear wave [159]).

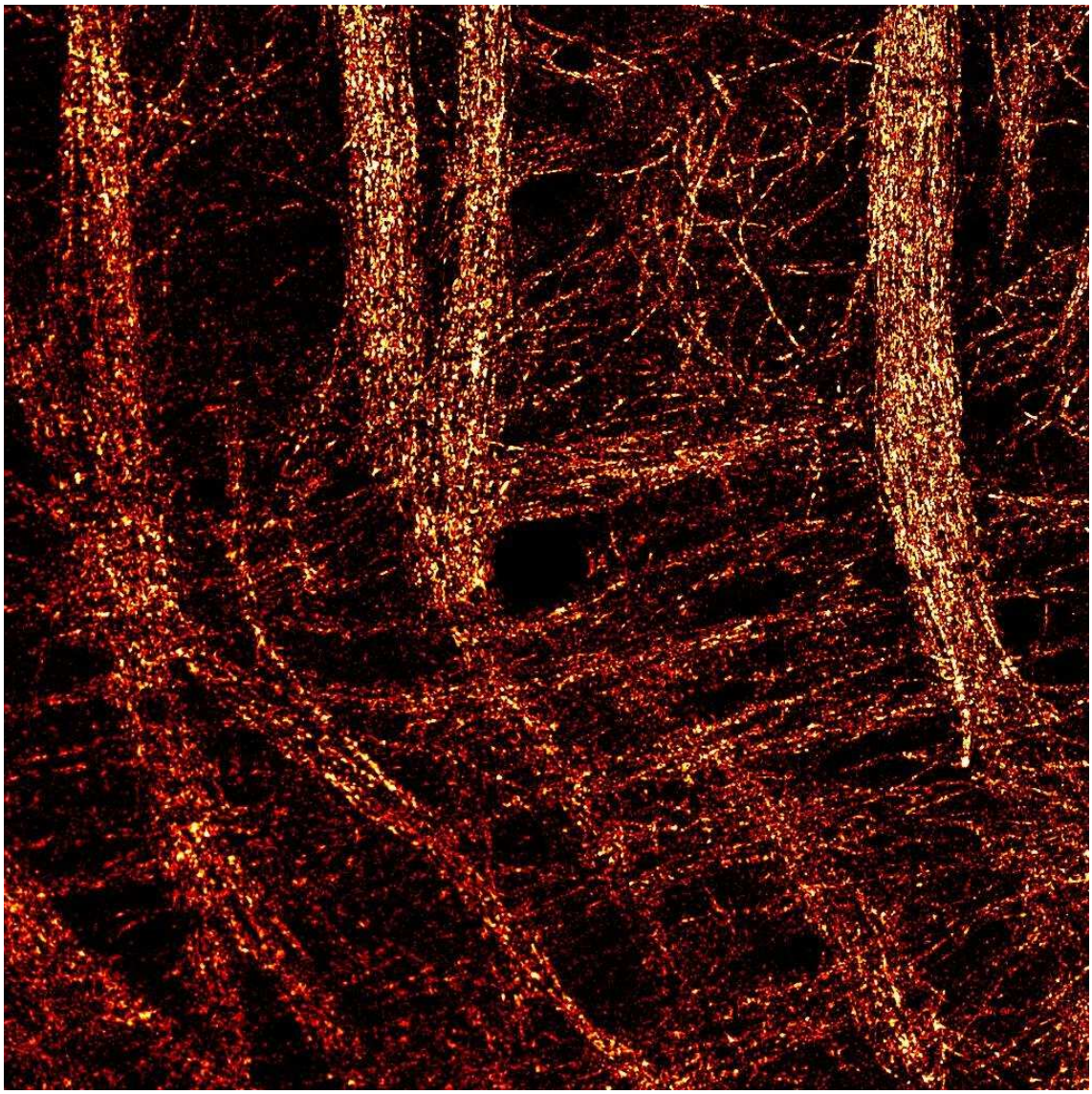

A brain on fire. *This image shows myelin fibers in a rat cortex as imaged with high-resolution full-field optical coherence tomography.*

CHAPTER 4

Full-Field Optical Coherence Tomography

Table of contents

4.1 Full-Field Optical Coherence Tomography **114**
4.1.1 Basic layout and interest 114
4.1.2 Layouts of our different systems 118
LightCT Scanner 118
Fast Full-Field OCT 120
My final home made design 121
4.2 Reasons for using a spatially incoherent illumination **122**
4.3 Full-Field OCT versus scanning OCT **123**
4.4 FF-OCT performance **124**
4.5 FF-OCT for histology **129**
4.6 A quick word about swept source FF-OCT **132**
4.7 Label-free *In situ* vesicle imaging in zebrafish larvae **133**

In this chapter, I will rapidly detail the principle of Full-Field OCT (FF-OCT). At this point, we have already introduced all main concepts in previous chapters. FF-OCT relies on the same Linnik interferometer presented in chapter 2 operated in low coherence conditions, mostly using spatially and temporally incoherent illumination. In this chapter, I will explain how to reconstruct an FF-OCT image, and present the different systems I used during my thesis. I will discuss Ff-OCT specific features and compare it with other standard techniques. I will notably show that FF-OCT can produce label-free and artifact-free images that resemble standard histology images, hence being a promising tool for medical diagnosis, especially when coupled with other modalities. In this chapter, I will mainly put aside the idea of phase imaging. As a matter of fact, the FF-OCT basic principle aims to detect the sample backscattering amplitude and reveal its 3-D microstructure organization. And even if FF-OCT is based on interferometry, the phase information has been rarely used so far as phase fluctuations are often averaged out to enhance the contrast of the amplitude maps. Nevertheless, we will have to wait until the following chapter, in which I will show that the phase information can be used in several ways to extract additional sub-wavelength axial information on the sample. I will show that phase sensitivity in tissues offered by FF-OCT is particularly important as it can provide mechanical and metabolic contrast at a given depth inside tissues.

4.1 Full-Field Optical Coherence Tomography

4.1.1 Basic layout and interest

Full-Field OCT is a modified version of OCT, in which *en face* images are directly obtained in contrast to scanning OCT that acquires single pixels, or single lines (A-lines). Images are obtained by a simple optical conjugation of the microscope objective focal plane with a 2-D detector, often a CMOS camera in our case. The optical sectioning ability comes from the low coherence interference with a reference arm of similar length. In practice, FF-OCT systems I have used are based on the Linnik interferometer presented in chapter 2, however operated in a low coherence configuration, as described in the previous chapter. Optical sectioning can be either controlled by the low temporal coherence, or by the low spatial coherence, depending on the system characteristics. From an OCT specialist point of view, FF-OCT can be understood as a time domain OCT system which uses an incoherent broadband illumination and a camera, instead of a scanning laser and a single detector. Further comparison between a full-field approach and a scanning approach will be performed in the next section.

I would like now to highlight FF-OCT benefits in a different approach that is possibly clearer for non-specialists of OCT, explained through figures 4.1 to 4.4. Let us first ignore the reference arm of FF-OCT microscope, therefore obtaining a simple widefield reflectance microscope, which is the most basic microscope one can find, simply recording images of the sample with a camera, and illumination coming from above. This configuration might even be more natural for imaging thick non-transparent samples compared to more commonly used transmission widefield microscopes. Furthemore, this configuration would be somehow equivalent to have a side illumination from external fiber sources, as could be found in some commercial microscopes. Figure 4.1 shows the

system layout, as well as a typical image that can be recorded with such microscope. Here, I have imaged a few millimeters thick brain coronal slice close to the surface, in a white matter region. I have successively imaged the same sample with the reference arm first being blocked out(figure 4.1), and then with the reference arm but without phase modulation (figure 4.2). Finally, I have imaged the sample with 2 phases (figure 4.3) and 4 phases modulation (figure 4.4). As a reminder, these procedures have been described in chapter 2 on quantitative phase imaging. I had chosen to image a white matter region of the brain since such regions are rich in highly myelinated fibers (due to the high refractive index of their myelin sheath, mainly composed of fat and proteins). Moreover, elongated structures such as myelin, tend to enhance backscattering in comparison to spherical scatterers (see appendix A), so the backscattered signal from white matter regions of the brain is usually quite important, and should be easily detectable with a reflectance microscope. However, even in such favorable conditions, we can see two limits of our widefield microscope, that will further be overcome by FF-OCT. The first limit is the relatively low backscattering that requires to increase the exposure time or increase the illumination intensity to work close to camera saturation (figure 4.1 B versus 4.1 C). Similarly to QPI measurements, working with as many photons as possible will increase the signal-to-noise ratio. The second limit of widefield microscopes is their absence of optical sectioning, which creates an important backscattering halo from out-of-focus structures and importantly reduces the signal-to-noise ratio. In practice, this halo can be partly eliminated by taking advantage of the fact that only in focus structures can exhibit high spatial frequencies. Therefore, a high-pass filter in the Fourier space can increase the SNR, as presented in figure 4.1D. In practice, it is also possible to increase the objective NA, or to use a confocal pinhole that will physically reject most of the out-of-focus light, to increase the SNR.

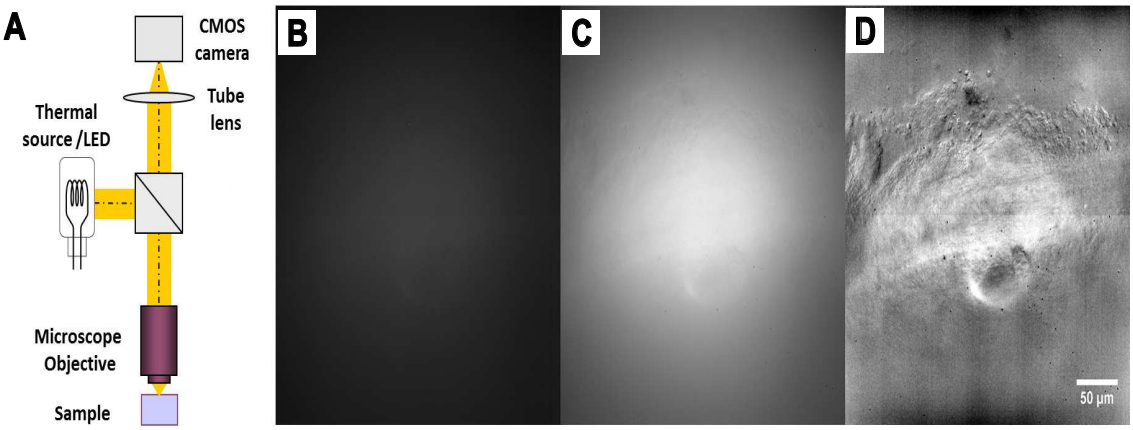

Figure 4.1 – Widefield reflectance microscope of a thick brain sample. A. Standard widefield reflectance microscope layout. It is composed of a simple light source, an imaging telecscope (combination of one microscope objective and one tube lens), and a camera. **B and C.** Widefield images of a brain coronal section acquired with 4 mW power, and exposure times of 10 ms and 35 ms respectively. Since the sample is highly scattering, a strong echo can be recorded on the camera, but echoes from different planes produce a strong background and prevent from imaging any structure. **D.** Panel C with a high-pass filter in the Fourier space to remove a part of the background and recover some of the sample structures.

In this case, FF-OCT provides another way to extract the signal coming from a given depth, as it is able to detect the localized interference between the backscattered light from the sample and a reference beam, simply reflected on a mirror placed in a second arm. Similarly to typical OCT's, the length of the reference arm should control the corresponding depth inside the sample.

However, in reality, because of spatial coherence, interferences can only be highly contrasted for in-focus beams. For relatively high NA objectives exhibiting a sharp depth of focus, the corresponding depth inside the sample is adjusted by translating the sample and eventually correcting for refractive index mismatch with the length of the reference arm.

In the configuration presented in figure 4.2 A, the sample and the reference beams are both transmitted once and reflected once by the central beamsplitter, so that the optical path difference does not depend on the beamsplitter characteristics. It also means that both sample and reference beam intensities only depend on the entrance intensity and on the respective reflectivities of each arm. Obviously, because the reference beam is reflected by a mirror, its intensity often dominates the total intensity captured by the detector. As a reminder, the measured intensity is:

$$I(x,y) = I_{ref}(x,y) + I_{sample}(x,y) + 2\sqrt{I_{ref}(x,y).I_{sample}(x,y)}.cos(\Delta\phi(x,y)) \tag{4.1}$$

with $I(x,y) \simeq I_{ref}(x,y)$, as illustrated in figure 4.2 B and C. We can make a further comment that the reference mirror reflectivity is chosen as a compromise between the ability to fill the camera close to saturation with reasonable power and exposure time, and the contrast optimization. Similar to QPI, the optimal contrast in FF-OCT is obtained when the camera is close to saturation and when the structure reflectivity is equal to the reference mirror reflectivity. However, because biological structures reflectivities are usually quite low, it wouldn't be enough to fill the pixel wells. Interferometry is interesting in that sense, as the interference term depends on $\sqrt{I_{ref}(x,y).I_{sample}(x,y)}$ so the signal from the sample is enhanced by the reference one and then becomes detectable.
In practice, in most of our systems, we have chosen to use flat silicon mirrors that provide a 23% reflection coefficient at the interface with water.

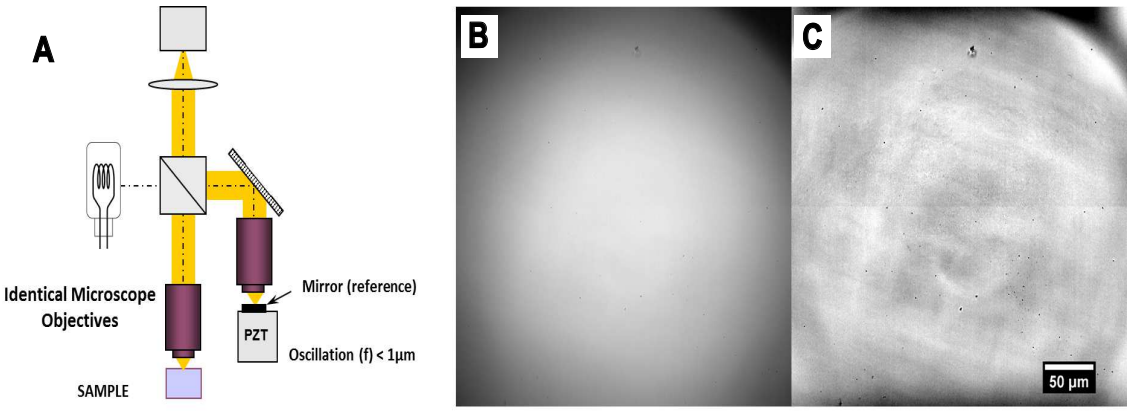

Figure 4.2 – Raw images of a thick brain sample acquired with an FF-OCT microscope. A.FF-OCT microscope layout. Compared with widefield reflectance microscope of figure 4.1, a reference arm has been mounted, in which light reflects on a silicon mirror. The respective length of the reference and sample arms have to be almost identical, with a difference below a few microns. **B.**Direct FF-OCT of the same brain coronal section, acquired with the same 4 mW power, and exposure time of 10ms. **C.** High-pass filtered image of panel B, like panel 4.1D. Here, the dominant signal comes from the reference arm, which is somehow homogeneous, and powerful enough to approach camera saturation.

As easily observable in figure 4.2, the direct image captured by the camera is not really interesting *per se*, as it mainly corresponds to the image of the reference mirror. The interfering signal is however hidden inside this signal and simply needs to be extracted. A first approach is to perform

2 phases modulation to get:

$$I_2(x,y) - I_1(x,y) = 4\sqrt{I_{ref}(x,y).I_{sample}(x,y)}.cos(\Delta\phi(x,y)) \tag{4.2}$$

which extracts only the interference term. However, in this case, a remaining coupling between the relevant amplitude signal $\sqrt{I_{sample}(x,y)}$ and an additional phase term tends to decrease the SNR by adding an apparently random fluctuation on the structures of interest, as it can be observed in figure 4.3C.

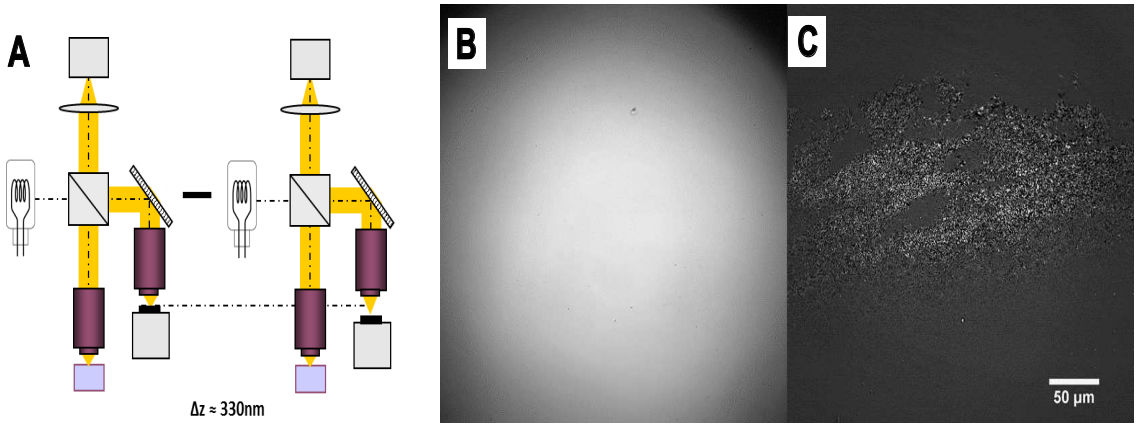

Figure 4.3 – 2 Phases FF-OCT image of a thick brain sample. A.2 Phases procedure. 2 successive images are acquired, while moving the piezo of about $\frac{\lambda}{2}$, corresponding to a phase shift of π. The two images are then subtracted to extract only the interference term.**B and C.** Corresponding raw image and two phases difference image of the same brain coronal section, acquired with 4mW power, and exposure time of 10 ms. In panel C, a few structures clearly appear, but the signal-to-noise ratio is lowered by speckle, *i.e.* the random phase distribution, as the backscattered amplitude is still coupled to the cosinus of the phase in the difference image.

Finally, in order to decouple the amplitude and the phase maps, at least one more image is required, and procedures like 3 phases, 4 phases up to N phases, as described in chapter 2, are applied to extract two independent amplitude and phase images. The more images are used for these procedures, the more accurate and resistant to the noise is the separation process. However, in the case of fresh tissues, amplitude and phase fluctuations can be relatively important over a few frames so that using as few frames as possible often produces a better outcome as it reduces motion and dynamic artifacts.Indeed, 4 phases modulation appears as a reasonable compromise in most of our experiments. In chapter 2, we have shown that 4 phases modulation allows to extract an amplitude and a phase map:

$$\sqrt{I_{sample}(x,y)} = \frac{\sqrt{(I_4(x,y) - I_2(x,y))^2 + (I_1(x,y) - I_3(x,y))^2}}{4\sqrt{I_{ref}(x,y)}} \tag{4.3}$$

$$\Delta\phi(x,y) = atan(\frac{(I_4(x,y) - I_2(x,y))}{(I_1(x,y) - I_3(x,y))} \tag{4.4}$$

Figure 4.4 presents the corresponding amplitude of phase images and demonstrates a much higher SNR on the amplitude image than what was obtained previously. The 4 phases amplitude image clearly reveals many of the sample structures at the given focal depth. Interestingly, the phase map shows its apparently random distribution, which explains the low SNR obtained in 2 phases modulation of figure 4.3.

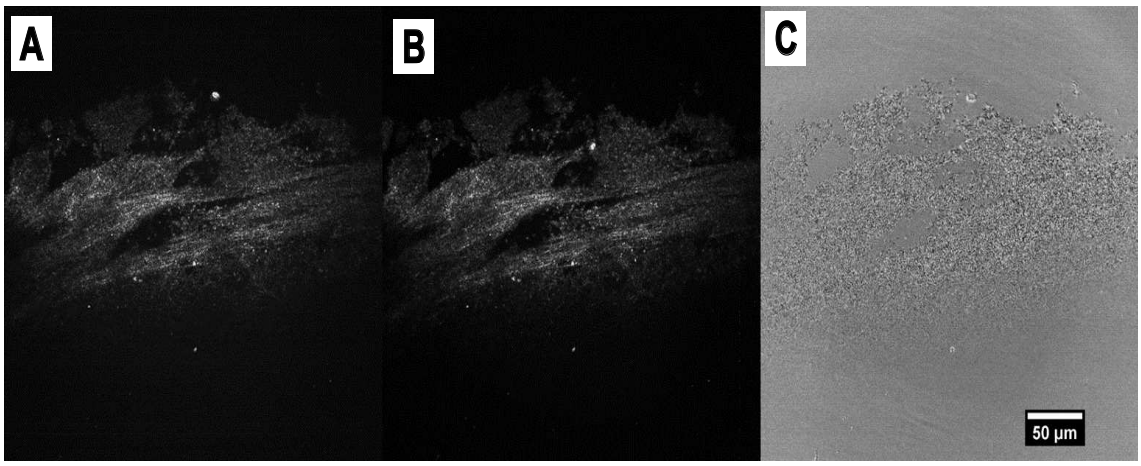

Figure 4.4 – 4 Phases amplitude and phase maps acquired with FF-OCT in a thick brain sample. The 4 phases procedure consists in acquiring 4 successive images with incremental reference piezo position shift of $\frac{\pi}{2}$. **A and B.** Backscattering amplitude maps of the same brain coronal section, acquired with 4 mW power, and exposure time of 10 ms. Panel A corresponds to the amplitude map computed from a single 4 phases iteration. Panel B has been computed from the average over 100 accumulations, and its signal-to-noise ratio should be 10 times higher than panel A. **C.** Corresponding phase image. A speckle map can be retrieved similarly to figure 4.1 C.

As an interim conclusion, we have demonstrated here the FF-OCT ability to reveal sample microstructures at a given depth, but an important advantage of OCT and FF-OCT lies in its tomographic performances, *i.e.* its ability to compute 3-D maps of the microstructural organization of the sample. The tomographic capability of FF-OCT is illustrated through figures 4.5 and 4.6. Figure 4.5 shows several planes acquired at successive depths in a neural ganglion of an *Aplysia punctata* exhibiting numerous large axons (at least 20 μm each).

Additionally, 3-D stacks can be visualized in cross sections, similarly to scanning OCT standard images. In figure 4.6, we demonstrate FF-OCT ability to image a 5 days post fertilization (dpf) zebrafish larva embedded in agar on the side, so that we imaged initial sagittal 2-D views of the larva, as shown in figure 4.6 A. Figure 4.6 B shows a reslice of the 3-D stack in the XZ plane associated with a maximum projection algorithm along the third dimension. It reveals the larva microstructure in a new coronal view.

4.1.2 Layouts of our different systems

During my thesis, I have mainly developed one FF-OCT system, which I have later used for most of my experiments. However, I have had the opportunity to use two other FF-OCT microscopes that are all based on the same principle but exhibit different technical characteristics that are described briefly in this subsection.

LightCT Scanner

The LightCT scanner [160] has been developed by LLTech, a start-up co-created by Claude Boccara to develop and commercialize FF-OCT systems, between 2009 and 2011 and has mainly kept its compact design since then. The system design is shown in figure 4.7, as well as typical images acquired by the system. This system presents all the advantages of a good commercial system, meaning that it can provide consistent and reproducible images of a given sample, is relatively easy to use, and has long range 3-D translations. Interestingly, the LightCT scanner has been installed in various hospitals, and benefit from a large atlas [161] and from clinician feedbacks. However,

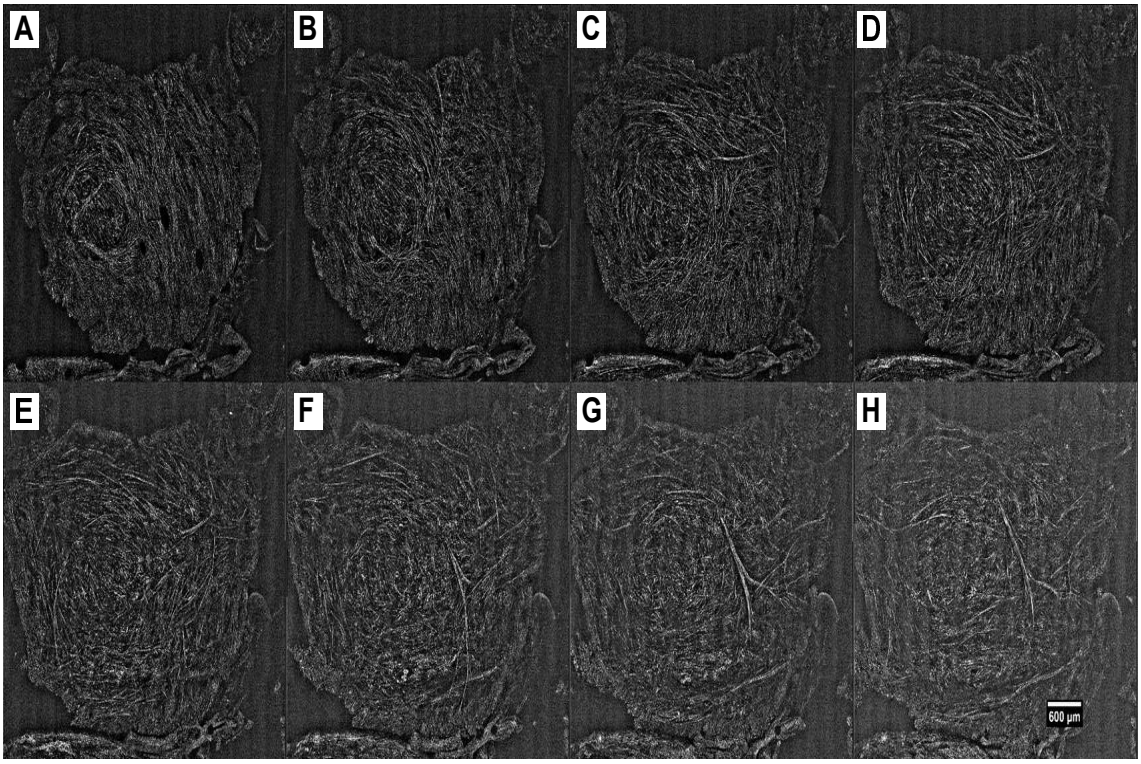

Figure 4.5 – 3-D FF-OCT imaging of an *Aplysia* ganglion. A to H. Successive transverse views of the ganglion with a 5 μm axial displacement between each frame. It clearly shows a change in the direction of the neurons between the different frames, illustrating FF-OCT ability to provide optical sectioning.

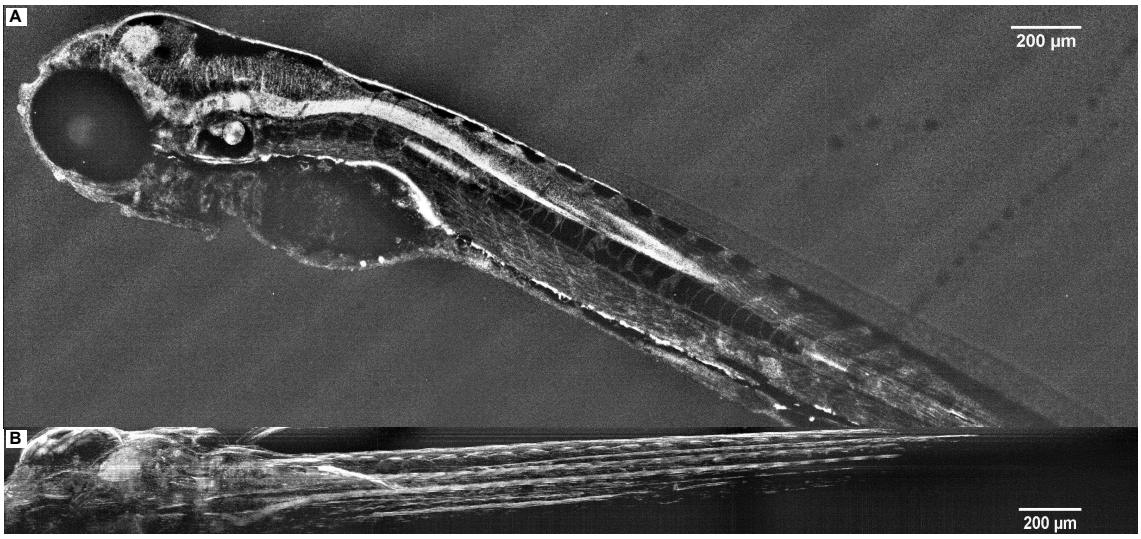

Figure 4.6 – 5dpf Zebrafish larva imaged in 3-D with FF-OCT. A. Initial 300 sagittal views of the larva are acquired from one of its sides to the other.**B.** These frames are combined to form a 3-D view of the entire animal. To demonstrate this on a 2-D format, we simply display another view of the larva, in the coronal plane.

its design is fixed, its software is only optimized for a small number of imaging conditions, and is not very robust to external mechanical noise, especially since the sample stays on a motorized platform that is mechanically decoupled from the rest of the setup. The sample is sandwiched between a thick silica coverslip and the bottom of the sample holder, which is not really sample-friendly, but presents the advantage of flattening the sample. This is quite important in order to image beautiful 2-D transverse views of the sample, and also reduces optical aberrations. Finally,

the LightCt scanner uses 10X, 0.3 NA objectives and a thermal source that gives an isotropic 3-D resolution of 1μm. Coupled to the long range motorized translations, it can acquire large field of views (1.2x1.2mm^2 single shot, and can be further extended by translating the sample and stitching the different frames). However, due to the relatively limited transverse resolution, and then backscattering collection, some intracellular features can be invisible with this setup.

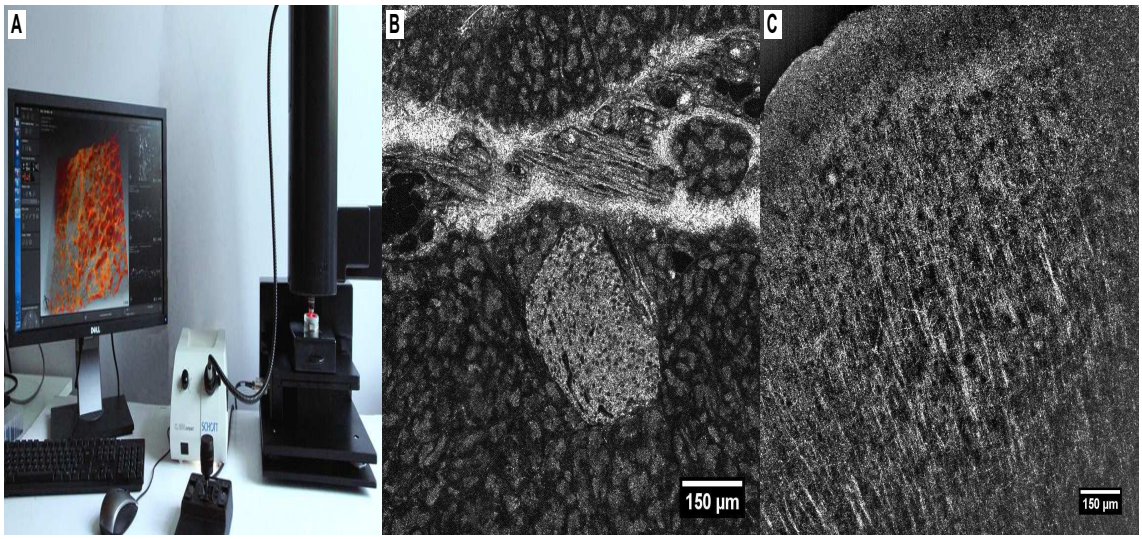

Figure 4.7 – LightCT Scanner. A. System compact design. **B.** Amplitude image of a pancreas. It can reveal morphological features in both the exocrine pancreas and the endocrine pancreas (inclusion of cells in the middle, corresponding to an islet of Langerhans). Note that the cells are particularly well contrasted in the islets thanks to the presence of numerous Zinc-Insulin nanoparticles (of 200 to 400 nm diameter) inside βcells [162].**C.** Amplitude image of a rat cortex coronal slice from the surface, and almost down to the bottom of the cortex. FF-OCT clearly reveals many myelinated fibers and their orientations in the cortex.

Fast Full-Field OCT

I have mainly used the fast FF-OCT system at the beginning of my thesis, before starting to develop my own system. This system was initially developed by Jean-Marie Chassot, an engineer from the Institut Langevin, a few years before I started my thesis. However, I had to remount the system from scratch a few times during my PhD, as it was not really stable over time, and was getting misaligned easily. The idea behind the setup is genuinely a *brute force* experiment: Because the FF-OCT frame rate is only limited by the camera framerate, it was proposed to buy the fastest camera that could be found at that time (Phantom V12.1). Interestingly, the camera could go at more than 30,000 frames per second on reduced fields of 512x512 pixels. The camera was going so fast, that the piezo modulation could not be performed in steps as usual, and a sinusoidal modulation had to be implemented to recover the amplitude image. This procedure is described in chapter 2. However, if the camera was able to image fast, its FWC was only of a few dozens of photoelectrons, meaning that the sensitivity of this system was only of about 50-60 dB and as a result, this system was able to only acquire poorly-contrasted images in depth for most samples. Nevertheless, I have mainly used this system on cell cultures, for which the SNR was less an issue. Figure 4.8 shows the system design and two images that were acquired with this system.

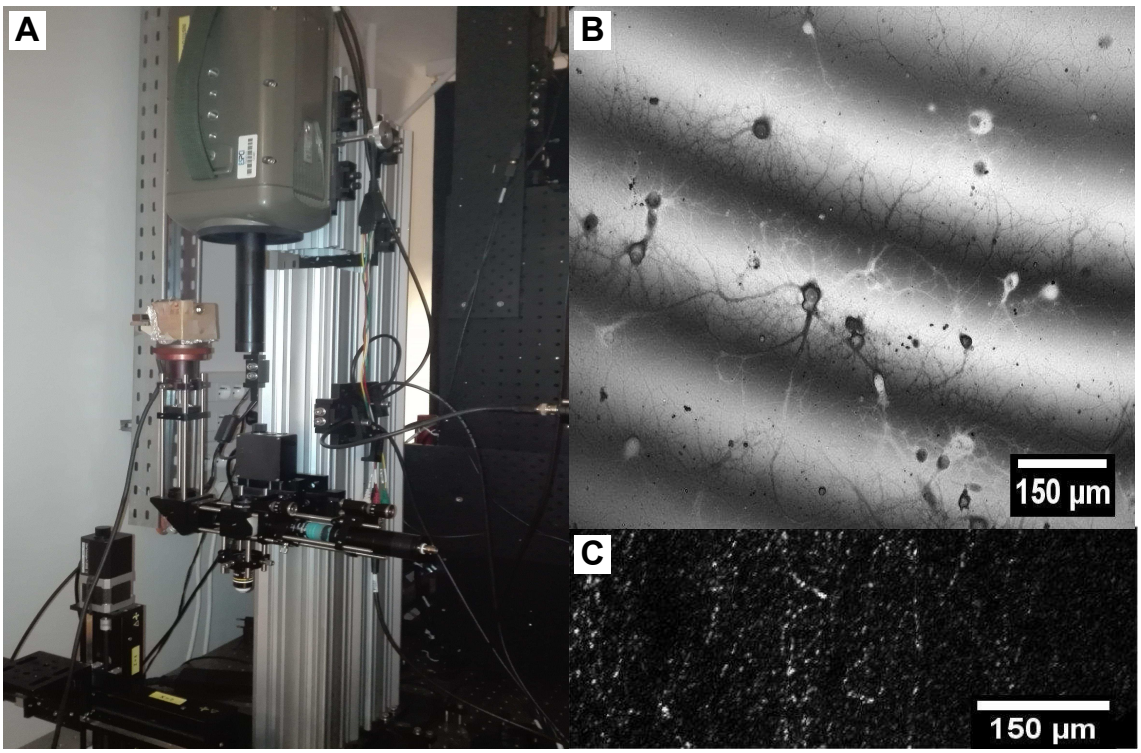

Figure 4.8 – Fast FF-OCT system. A. System design. The originality of this system lies in its camera, that can run at up to 30,000 frames per second for reduced fields. However, due to the camera low FWC, this setup was mainly useful for cell culture measurements, as illustrated in **panel B**.**Panel C.** FF-OCT Amplitude image in a rat brain coronal section that illustrates the low SNR provided by this system, especially compared with figures 4.7 C and 4.9 C.

My final home made design

I can now rapidly introduce the system I have designed during my work at the Institut Langevin. Because I have spent quite some time building it, unmounting it, and rebuilding it from scratch several times, I apologize in advance if I appear not quite objective at describing it! The final version of my system design results from many compromises (as it is probably for any microscope) that I will mainly explain in the next chapter. This system combines an FF-OCT path with a fluorescence path, and most of the choices I made were attempts to optimize both parts at the same time. On top of this parallel fluorescence path addition, its most significant difference relevant for this chapter lies with its high NA microscope objectives. I first mounted 30X, 1.05 NA oil objectives. For the (useless) record, this configuration provided the highest transverse resolution ever achieved in an OCT system to our knowledge. However, these oil objectives exhibit low working distance of 0.65 mm and require an additional glass coverslip of about 150 μm between the sample and the objective. To limit aberrations with such high NA objectives, it was moreover required to pass through oil for most of the path, and in practice, the sample had to be squeezed against the glass coverslip to reduce propagation in water. Nevertheless, even with such precautions, it was difficult to obtain an FF-OCT signal after 50 μm inside the sample, not to mention that these objectives were quite complicated to operate with. Therefore, we have decided to change these objectives for 40X, 0.8 NA objectives that work in water without coverslip. These objectives were an attempt to better preserve the sample without mechanically compressing it. However, I have soon realized that thin samples were rapidly floating in the medium without coverslip and that, surface heterogeneities were often drastically reducing the signal in depth or only allowed to see tilted views of the sample. As a consequence, I have often used thin transparent porous membranes (MILLICELL-CM, 0.4 μm) between the objective and the sample,

with a small weight on it to flatten and immobilize the sample. In the current system layout, the sample holder is mechanically coupled to the rest of the system, which reduces its sensitivity to external mechanical noise. Unfortunately, I couldn't find any 3 axis motorized translations that would fit in such design. Charles Edouard Leroux, a post doc in the lab, helped me to design my final translation stage, motorized in the Z axis and manual (with a 2 millimeters length course) along the X and Y axis. Finally, because I needed to interface and synchronize acquisitions from two cameras, I had to write my own acquisition software, a Matlab Graphical user interface of more than 15,000 lines of code, which I will not describe in this manuscript.

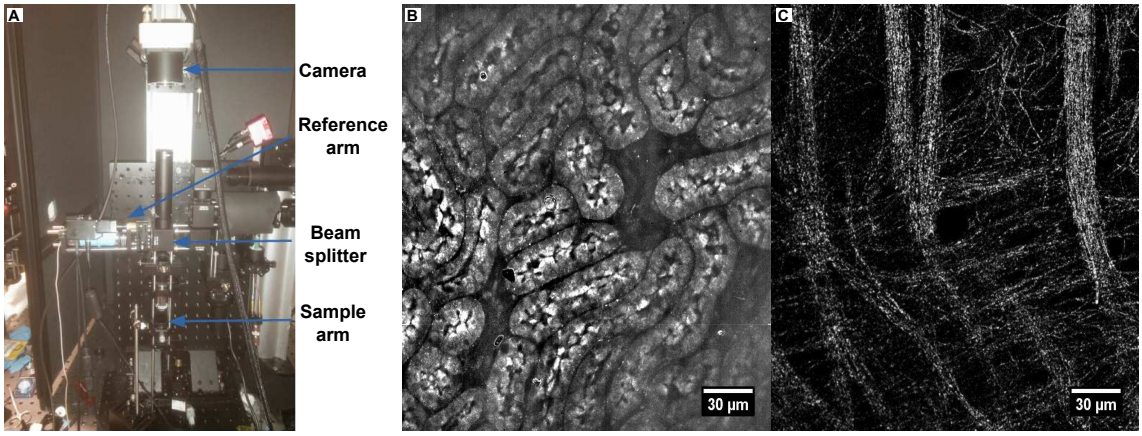

Figure 4.9 – Synchronous multimodal FF-OCT and fluorescence setup.A. System design. The corresponding setup scheme will be revealed in the next chapter. **B.** Amplitude Image of a kidney biopsy microstructure with 30X, 1.05 NA objectives, published in [163]. **C.** Amplitude image of a rat cortex coronal slice comparable to figures 4.7 C and 4.8 C. We can notably see how hard it is to find our position in the cortex. However, the higher NA allows the collection of more photons and enables to reveal many more myelinated fibers.

4.2 Reasons for using a spatially incoherent illumination

One advantage FF-OCT is its ability to work with light sources as simple (and cheap) as halogen lamps or LEDs. Despite their apparent simplicity, theses sources present a few other substantial features that enhance capabilities of FF-OCT. These sources are particular as they are highly incoherent both spatially and temporally. If thermal illumination (halogen lamps) was first used as a simple way to provide a white illumination that provides low temporal coherence, it was shown in 2004 that spatial incoherence was also important to suppress crosstalks, a coupling between adjacent pixels arising from multidiffusion, in the FF-OCT images [164]. Additionally, during my thesis, Peng Xiao from our team realized that these sources present yet another interest, as the widefield spatially incoherent illumination authorizes to perform FF-OCT amplitude images that are ultimately limited by the sharpest PSF between the two arms [165]. Advantageously, since the reference arm PSF is likely to have only a few aberrations, the final system PSF is almost insensitive to aberrations, at least low order aberrations, caused by the sample. Due to the tight mutual coherence in low spatial coherence system, the sides of the sample arm aberrated PSF do not interfere with the reference arm sharp PSF. Therefore, the interference term is only important on a size controlled by the sharpest PSF. Nevertheless, because some energy is spread to the sides of the sample arm aberrated PSF, the effect of aberrations is to decrease the interference contrast without affecting the transverse resolution. It makes FF-OCT (even more) worthwhile, as its high transverse resolution is preserved even at important depths inside a scattering sample,

even though it reduces the penetration depth due to aberrations. Figure 4.10 presents a few experimental pieces of evidence of this effect. Even in presence of important defocus (up to ten times the depth of field!), and even in the case where the transverse resolution of the direct image is significantly reduced, the amplitude image displays a much sharper and constant PSF, hence transverse resolution.

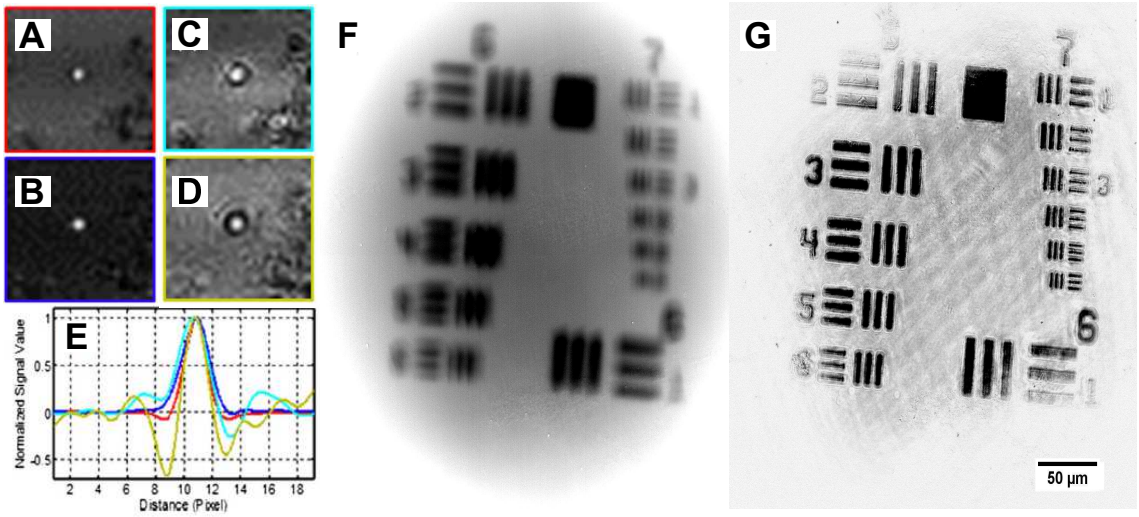

Figure 4.10 – Experimental validation of FF-OCT insensitivity to low order aberrations.A to D. FF-OCT amplitude image obtained on a sub-wavelength gold nanoparticle with a low NA objective (0.2 NA) in presence of additional incremental defocus of 0, 10, 20 and 30 μm, exhibiting similar PSF extension. **E.** Measured PSF with normalized maxima for the previous defocus. Even though side lobes can be observed for large defocus, the full-width at half maximum is almost constant for all measurements. The amplitude of the maxima is decreasing with increasing defocus, which is not displayed here for clarity. This figure has been taken and modified from [165] **F and G.** Corresponding direct and FF-OCT amplitude image of a USAF target, acquired with 40X, 0.8 NA objectives under a large defocus of 20μm, corresponding to about 6 times the depth of focus. **Panel F** shows the degradation of the sample arm PSF, as the smallest targets cannot be resolved anymore, while **Panel G** shows the PSF restoration due to spatially incoherent interference with an in-focus reference arm.

4.3 Full-Field OCT versus scanning OCT

The main difference between classical OCT and FF-OCT systems lies in the absence of transverse scanning. In OCT, or in optical coherence microscopy (OCM), an axial line (A-line) is captured with a single point [20, 21, 166] or with a line detection [167, 168] and further scanned in the transverse plane, to successively obtain 2-D planes (B-scan) and 3-D tomograms (C-scan). On the contrary, the full-field configuration captures a 2-D image at a single depth with a 2-D camera, and an axial scan enables the recording of a 3-D tomogram. In both configurations, the optical section is mostly controlled by the temporal coherence length, given by the inverse of the spectral bandwidth. Scanning in one dimension compared to two dimensions has several major consequences:

- Because it looks at a single depth at a time, FF-OCT can be performed with a small depth of field, and therefore with high numerical aperture (NA) objectives. This allows high transverse resolution to be obtained, below 1 μm for visible light. Other elegant OCT systems

have greatly increased their transverse resolution [21, 169–172], however, these techniques remain more complex and often have to sacrifice their temporal resolution.

- Moreover, scanning in two directions imposes a trade-off between exposure time and the field of view. In scanning OCT, each pixel is only illuminated for a few microseconds, while in FF-OCT, the entire field of view is usually evenly illuminated during a few milliseconds. It can make a difference in the light dose delivered to the sample, and the most rapid speckle fluctuations are often averaged out [173].

- The time required to get information from the sample is much longer in FF-OCT since it is limited by the camera frame rate, which is complicated to decrease below 1 ms, while some scanning OCT systems can now acquire lines at more than 100,000 lines per second [174]. The consequence is that FF-OCT is much more sensitive to sample motion, and is difficult to perform *in vivo*, other than on anesthetized animal or by pressing the sample against an imaging window [175].

- An important feature of scanning OCT is the spatial localization in both emission and detection on a single pixel. It allows the addition of a confocal pinhole in front of the photodetector, similarly to pinholes that can be found on confocal microscopes or spinning disks. It allows the rejection of most of out-of-focus and multiply scattered light. Even if this light is filtered out in the final FF-OCT amplitude image thanks to the low coherence, it might create an incoherent signal that can lower the effective FWC of FF-OCT detection and lower the FF-OCT SNR compared to scanning OCT SNR.

- A last important difference when looking at *en face* images either performed in scanning OCT or FF-OCT is that all pixels have been acquired at different times in OCT, while they are acquired at the same time in FF-OCT (if the camera is operated in global shutter mode), which can introduce some artifacts when looking at moving objects. On the other hand, all axial pixels are acquired simultaneously in OCT, while they are largely separated in time for FF-OCT. An important consequence is that the optical phase can be directly retrieved in OCT by subtracting two adjacent axial pixels [159] while FF-OCT requires multiple phase-shifted measurements to retrieve the optical phase.

4.4 FF-OCT performance

In this section, I will describe how to estimate most of the parameters to assess our systems performance, and attempt to give a few orders of magnitude for the previously described systems:

- **Transverse resolution:** The transverse resolution is directly controlled by the microscope objective numerical aperture (NA), giving the usual diffraction-limited resolution criterion: $\Delta_{XY} = 0.61\frac{\lambda_0}{NA}$. Note that transverse resolution depends on λ_0, the detected light central frequency, which partly explains the higher transverse resolution of our systems working mainly with visible light, compared with high NA scanning OCT systems rather operated in the near infrared. The other explanation comes from the under-filling of the objective back aperture, often required to enable efficient transverse scanning. We are usually working with a transverse resolution of 1.05μm with the 0.3 NA systems, and of 0.5 μm with the 0.8 NA system. In summary, we usually assert that the amplitude and phase map obtained with FF-OCT exhibit similar transverse resolutions than the direct image, since they are obtained from a set of direct images.

- **Axial resolution:** Axial resolution of FF-OCT is *a priori* given by the microscope depth of focus, controlled by the detection optical parameters, with the usual criterium: $\Delta_Z = \frac{\lambda.n}{NA^2} + \frac{n}{NA}.\frac{l_{pixel}}{M}$, where l_{pixel} is the physical camera pixel size and M is the system magnification. Therefore, the ratio $\frac{l_{pixel}}{M}$ represents the pixel size in the object plane. However, what is often called axial resolution in OCT is the axial sectioning ability, controlled by the system coherence length. As described previously in chapter 3, the sectioning ability can be defined as the smaller length between the temporal coherence length that depends on the system spectral bandwidth, and the lateral spatial coherence length, somehow controlled by the depth of focus. In practice, there are two main cases: The first one gathers most of OCT systems using low NA objectives, including the standard FF-OCT with 0.3 NA objectives. In this case, the sectioning ability takes over the depth of focus, and the axial resolution is given by the temporal coherence length, around 1 μm with a white thermal light, and up to 7.75μm with high-intensity LEDs. It means that the signal coming from the tail of the axial PSF does not interfere anymore with the reference signal. The second case appears for higher NA objectives, in which the depth of focus and the optical section are somehow equal [105, 133]. Figure 4.11 illustrates again this competition between temporal and coherence lengths for the sectioning ability in the case of our high NA FF-OCT systems.

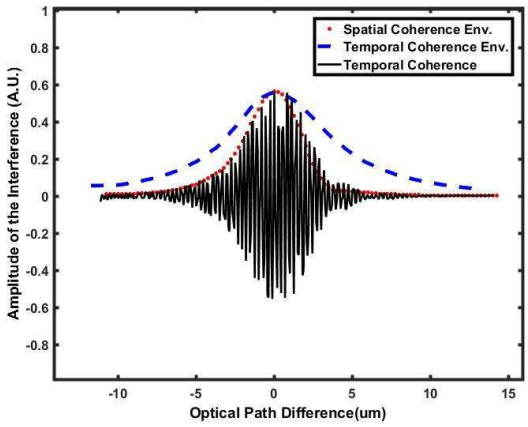

Figure 4.11 – Experimental competition between temporal and spatial coherence lengths. All curves are obtained by looking at interference fringes produced by placing similar silicon wafers in both arms of our high NA FF-OCT microscope [105]. The black and red dotted curves represent the intensity modulation and the fringe envelope respectively, obtained by changing the focus of the sample arm to probe the spatial coherence of the system. The dashed blue line represents the fringe envelope obtained by translating only the optical path difference, by changing the reference arm length. This probes the temporal coherence length that is only controlled by spectral characteristics of the source. The full width at half maximum of the envelopes, corresponding to the spatial and temporal optical sections, were measured to be 4.0 and 7.75 μm

- **Field of view:** It is intrinsically controlled by the number of pixels of the camera, by the system magnification and the field of view over which the objective is corrected. It can start from 300×300 μm^2 for the high NA system, to 1.4×1.4 mm^2 for the commercial system and even up to 3 $cm^2$for large field systems [69]. In practice, a tilted sample or a misaligned setup affects the field over which the interference signal is detectable and lowers the effective field of view. The sample tilt or flatness is usually controlled by pushing the sample against a glass window, or a transparent porous membrane I have described earlier

- **Imaging speed:** It is also mainly controlled by the camera frame rate. We can make a further comment that the frame rate of most cameras can be increased by reducing the field of view accordingly. However, one should note that for CMOS cameras, the frame rate increase with field reduction does not scale with the number of pixels squared, as it could be expected. Since CMOS reading process is done line by line (and often from dual opposite lines), the frame rate only depends on the number of lines of the image. Therefore, the camera frame rate will be similar for the same camera with reduced fields of respectively 128X1024 pixels and 128X128 pixels. Nevertheless, reducing the number of columns might reduce transfer and processing times. To acquire an FF-OCT amplitude image, 4 images are actually required, so that the FF-OCT frame rate should be considered 4 times lower than the camera frame rate. However, when looking at dynamic events, the limiting factor is ultimately the camera frame rate, as sliding windows and dynamic processing can be applied [176] as presented in chapter 2. The camera we are using in most of our systems can image 1 MPixels at up to 700 frames per second. The fast FF-OCT system described above is able to image at up to 30 kHz for 0.1 MPixels images.

- **Imaging depth:** The imaging depth is mainly controlled by three parameters. The first one is the extinction of the ballistic signal, which is the useful signal in FF-OCT, coming from absorption and scattering of the sample. It typically decays exponentially with the inverse of the extinction length (sum of the inverse of the absorption length and of the transport length), in the order of a few hundred microns up to one millimeter in most biological tissues. The attenuation also depends on the illumination wavelength and is particularly low in the *optical therapeutic window*, between 600 nm and 1.2 μm. In addition, multidiffusion [177] and aberrations [165] will respectively blur and lower the signal. Both effects strongly depend on the objective NA, and high NA systems effectively exhibit relatively low imaging depth of about 100 μm. We can add that FF-OCT is also more sensitive to multidiffusion than scanning OCT, due to the absence of a confocal pinhole that also rejects the out-of-focus light. If the multiple diffusion intensity does not interfere at the detector position, it is still captured on the detector, which limits the number of useful photons coming onto it, and decreases the SNR. Figure 4.12 from *A.Badon et al.* [177] shows the maximal imaging depths for different optical microscopes. We can note that OCT and FF-OCT can usually image at larger depths than widefield or confocal microscopy. I would say that FF-OCT can often image at depths similar to two-photon microscopy, ranging from 100 μm to 400μm in diverse biological samples, while scanning OCT can sometimes image down to 1 millimeter. Finally, we can add that, new techniques respectively named Dark-field FF-OCT [110] and smart-OCT [177], based on modified full-field versions of FF-OCT have recently been developed at the Institut Langevin to better filter out the multiple diffusion, either physically or numerically, and increase the imaging depth accordingly.

- **Amplitude sensitivity (dB):** The sensitivity in OCT (and in FF-OCT) is defined by the smallest backscattering coefficient detectable, giving an SNR of 1. As described in chapter 1, the SNR in low noise conditions (negligible multidiffusion, aberrations, and optics reflection in the light path) can be written as:

$$SNR = \frac{4.N_0.\sqrt{R_{ref}.R_{backscat}}}{\sqrt{FWC}} \tag{4.5}$$

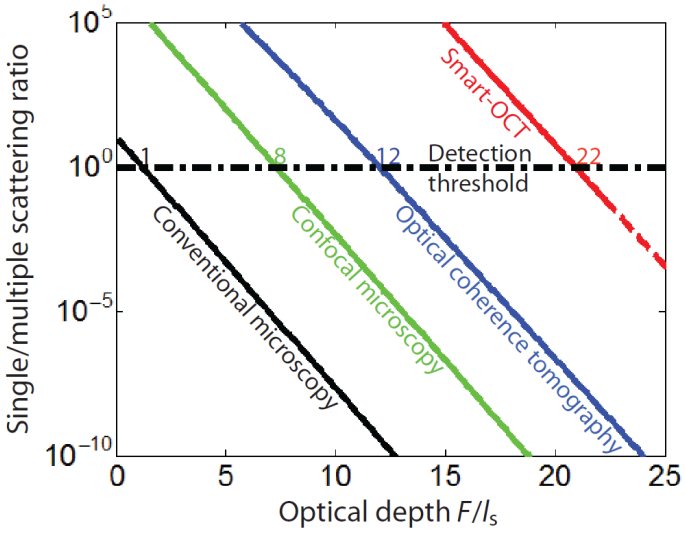

Figure 4.12 – Maximal imaging depth for different microscopes. This figure, extracted from [177], shows the evolution of the single to multiple scattering ratio (SMR) with the imaging depth, plotted as the ratio between the imaging depth F and the scattering length l_s. This evolution is plotted for widefield microscopy in black, confocal microscopy in green, OCT in blue and smart-OCT in red. The imaging depth corresponds to the crossing between such plots with the line corresponding to an SMR of 1, where the multiple scattering starts to become more important than single scattering. FF-OCT imaging depth would probably lie in between the confocal microscopy and the OCT imaging depths.

with N_0, the number of incoming photons, R_{ref} and $R_{backscat}$, the reflectivities of respectively the reference mirror and the considered object, and FWC the camera full well capacity. Generally, the camera is filled thanks to the photons coming from the reference arm (reflectivity R_{ref}) and from the incoherent photons originating from all out out-of-focus reflections (in the optical system or in the sample) and from the camera noise(and accounts for a total reflectivity R_{inc}), so that: $FWC = N_0(R_{ref} + R_{inc})$ and:

$$SNR = 4.\sqrt{FWC}.\frac{\sqrt{R_{ref}.R_{back}}}{R_{ref} + R_{inc}} \tag{4.6}$$

which is equal to 1 for $R_{back} = R_{min}$:

$$R_{min} = \frac{(R_{ref} + R_{inc})^2}{16.FWC.R_{ref}} \tag{4.7}$$

In most of our systems, we chose to use silicon wafers as reference mirror, which provides a reflection coefficient of 23.5% at the interface with water. In a typical sample, where the incoherent intensity corresponds to 10% of saturation of a CMOS Adimec camera (FWC of 1,6 Me^-), we obtain $R_{min} = 1.85.10^{-8}$, which corresponds to a 78 dB sensitivity.

- **Phase sensitivity:** Compared to QPI measurements on cell cultures, where sample and reference intensities were assumed to be equal, allowing optimal phase sensitivity computation, the structures that we observe in FF-OCT are much dimmer than the reference signal. From previous equations, it is easy to imagine that the sensitivity to phase changes depends on the structure reflectivity. Here, I will now try to estimate the phase sensitivity FF-OCT can provide for an average bright particle. Considerations about Rayleigh and Mie scattering can be found in appendix A and in figure 4.13. With both considerations, we can

estimate that FF-OCT can detect 200 nm vesicles of an 1.4 average refractive index that gives an apparent reflectivity R_{part} of 10^{-4}, far above the detection limit. To estimate the corresponding phase sensitivity, we now use the phase sensitivity derived in chapter 1. In the case of a shot noise limited measurement and a largely dominant reference signal (low contrast and negligible incoherent signal), the contrast becomes:

$$C = 2\sqrt{\frac{R_{part}}{R_{ref}}} \tag{4.8}$$

so that the phase sensitivity can be written as:

$$\sigma_\phi = \frac{1}{2\sqrt{2}.\sqrt{FWC}}.\sqrt{\frac{R_{ref}}{R_{part}}} \tag{4.9}$$

Finally, with the Adimec camera providing an FWC of about 10^6, and reflectivities of 23.5% and 10^{-4} respectively, we obtain a phase sensitivity of 0.02 radians, which is about twenty times worse than phase sensitivity in QPI. Nevertheless, it corresponds to axial displacements as small as 2 nm:

$$\sigma_\delta = \frac{\lambda}{4.\pi}.\sigma_\phi \simeq 1.72(\text{nm}) \tag{4.10}$$

This calculation shows that even for intermediate biological objects such as large vesicles, or organelles, FF-OCT is sensitive to their axial motions with a largely sub-wavelength accuracy thanks to its phase sensitivity. Note that the reflectivity coefficient depends on the particle radius at the power of 6 so that a 100 nm particle will give a contrast 8 times smaller and an axial sensitivity of 20 nm, which gets worse and worse as the particle size decreases. We will show in the next chapter that this important sensitivity to small axial displacements permitted us to follow a global activity-dependent motion in cells, which creates a new contrast that we revealed with Dynamic FF-OCT [178].

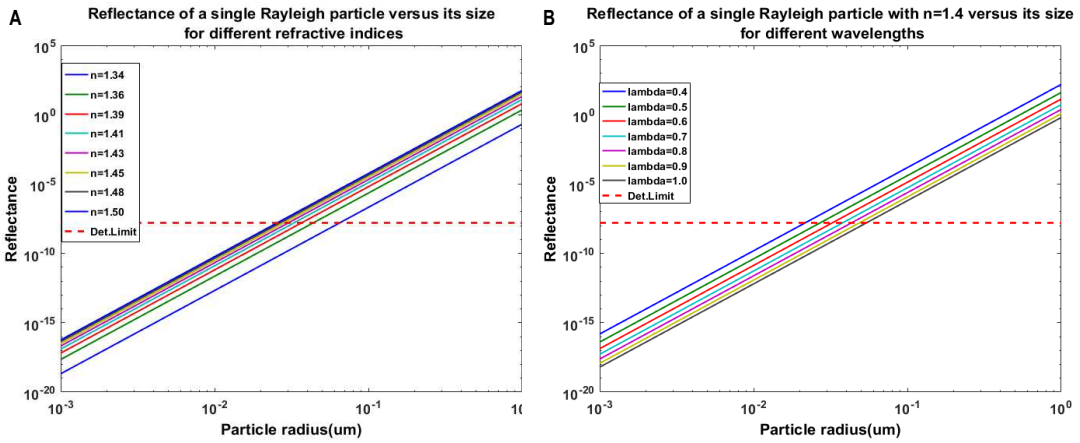

Figure 4.13 – Rayleigh scattering of single spherical particles. Simulation of apparent reflectivities of single spherical particles versus their radius and different parameters such as their refractive index (**panel A**) or the illumination wavelength (**panel B**). These curves show that FF-OCT can ultimately detect particles as small as 50 nm in a single amplitude image. When particles become bigger, Mie scattering has to be considered, and more complex calculations have to be performed, as introduced in chapter 3

4.5 FF-OCT for histology

FF-OCT has been successfully applied for non-invasive label-free *ex-vivo* pathology assessment in various tissues [179–186]. Thanks to its isotropic micrometric resolution, FF-OCT can often be compared to histology slices. In contrast to histology, FF-OCT does not require time for sample fixation, slicing, or labeling, and an histology-like image can be produced within a few minutes after tissue extraction. It also helps to reduce fixation and slicing artifacts, as FF-OCT does not necessarily require physical slicing and can image in depth, eventually far from a biopsy incision edges.

However, FF-OCT may suffer from its lack of specificity and sometimes fails to equal the diagnosis capability of gold standard histology. Yet, FF-OCT detection scores are above 80% for most pathologies in both sensitivity and specificity [107,185], and *Manu Jain and colleagues* could even report a 100% correct identification of tumors in *ex vivo* kidneys [163], obtaining similar results to histology, even though the tumor subtyping is still not 100%. In order to increase diagnosis scores, FF-OCT has therefore expanded to multimodal systems combining FF-OCT structural contrast with other pathology biomarkers inside a single microscope. The interest of such multimodal systems is to reduce the ambiguity in structure identification that can arise from sequential imaging with two different microscopes and to reduce operation time. Some FF-OCT multimodal systems have been reviewed in the recently published *Handbook of Full-Field Optical Coherence Microscopy*, edited by Arnaud Dubois [107]. We can non-exhaustively mention the multimodal combinations of FF-OCT with: fluorescence [187], photothermal imaging [188], elastography [189], polarization [190], multispectral and hyperspectral imaging [191–193]. Most of these multimodal systems have been inspired by similar systems developed in standard OCT, but they needed to be adapted and redesigned to fit FF-OCT's particular configuration.

In order to further compare histology and FF-OCT, we will describe histology contrast and procedures. It is commonly said that Marcello Malpighi is the precursor of modern histology, as he is the first scientist to carefully describe microanatomic features of plants and animal tissues by the end of the 17^{th} century with the first microscopes [194,195]. Since then, histology has continuously benefited from advances in chemical labeling and fixatives and has benefited from a better understanding of tissue nanostructures and organizations thanks to electron microscopy [196]. It now benefits from an extensive literature, and from digital atlases [197–199] enabling direct comparisons with normal or pathological slices of most tissues. However, the basic microscopy principles have mainly remained unchanged since the beginning of histology. It consists of imaging a thin slice of a sample with a simple transmission optical microscope. Since light absorption and scattering by biological structures exhibit a low contrast, histology commonly uses chemical agents to reveal specific contrasts of interest [200–202]. The most common staining uses two associated stains, Hematoxylin & Eosin (H & E), that respectively labels chromatin and chromosomes in blue, and cytoplasm in red. Hemoglobin usually appears orange, and collagen fibers appear pink. H & E staining is particularly versatile, as it can be used with a variety of fixatives. A wide range of different staining can be applied to a tissue slice. We can non-exhaustively mention Golgi staining that labels 1 to 2 % of neurons with silver that absorbs light to appear dark, Nissl staining that labels nucleic acids, or tetraoxide osmium that labels unsaturated lipids and lipoproteins.

If many subcellular structures can be selectively labeled, it is often difficult to combine different stains in a single slide. However, using specific labels imposes a prior knowledge of the tissue composition, and of the pathology, and some unlabeled biomarkers could be missed. Moreover, histology requires tissue fixation, performed either chemically or by freezing the sample, and

physical slicing of the tissue, usually performed by a microtome. The fixation first goal is to harden the sample to be able to cut it in thin sections. However, fixation can introduce strong artifacts, as it often removes lipidic structures, and can increase the tissue volume. The physical slicing can induce physical damage, notably in neuronal tissues, in which many axial neurites are usually cut, leading to neuronal death. Finally, these two steps are usually time-consuming and can lead to the physical destruction of the samples if not adequately performed. In the case of histopathology, the tissue is often fixated by replacing water by paraffin and is then sliced in 4 to 5 μm slices. For each slice, the dyes have then to diffuse through the paraffin scaffold. In total, these processes can last as long as a few days. In the case of intraoperative histology, the time allowed to the pathologist is usually not more than 15 to 30 minutes. To meet these time requirements, the sample is frozen, and directly sectioned and colored. However, many tissues, such as fat, brain, or retina, are not well suited for this process, and the number of available labeling is limited.

On the other hand, OCT was invented only 25 years ago, and its full-field version is 18 years old, so comparatively little literature and atlases can be found [161]. However, OCT and FF-OCT provide a label-free and optically sectioned imaging. This means that imaging can be performed right after tissue extraction, which then offers a very fast diagnosis, with the potential to provide an intraoperative diagnosis and to define efficiently a tumor margin during the surgery for example. The main advantage of OCT is its virtual sectioning ability, enabling imaging at a few hundred microns below the tissue surface, hence reasonably far from the sectioned surface if any section is even required [203]. To completely remove slicing artifacts and reach large depths, OCT systems have successfully been coupled to a vibratome, in a procedure where an entire volume is imaged before a physical slice smaller than the imaged volume is performed [204]. Additionally, OCT systems capture the light naturally backscattered by the sample, without using any label. Working label-free can be advantageous, as staining artifacts can be prevented, which significantly reduces the time prior to imaging. On the other hand, the recorded signal often lacks specificity. The obtained contrast is complicated to predict, as it is described by multi-scale complex theories, notably combining Rayleigh and Mie theories, depending on the scatterer size [205]. However, for a given tissue, the obtained contrast is highly reproducible, so that diagnosis performance could be increased only by simply characterizing better the typical contrast obtained for each tissue and for each condition. Quite typically, we can nevertheless emphasize the strong ability of FF-OCT to detect high refractive index (high lipid or high-fat content) fibers, such as collagen fibers [179], myelin fibers [129], and even some large unmyelinated axons in the retina [206]. Furthemore, the optical contrast accessible in backscattering configuration can differ substantially from the contrast obtained with a transmission configuration even in thick samples. However, it is reasonable to assume for thins samples that, compared to a transmission microscope, contrast in reflection is mainly the inverted contrast for scattering structures and the same contrast from absorbing structures . The OCT label-free ability has a final practical advantage as imaging can be performed prior to any tissue modification. It means that the same tissue can be further used for another procedure, including a standard histology procedure [179], or a fluorescence labeling. It is usually preferred to perform OCT imaging before any sample modification, as OCT signal alteration can occur after fixation, depending on the tissue content [206] (especially since fixatives often remove lipidic structures of the cells). Keeping this in mind, it is nevertheless possible to perform histology-like measurements in some fixed tissues [203].

To be impartial, we must acknowledge that scanning OCT has also been used successfully to perform histology-like measurements [203,207–209], and to detect tumor regions [210,211] through changes in the collagen content [88], inthe tissue microangiography and backscattering [212], or

in the tissue fractal dimension [86]. However, we believe that high resolution of FF-OCT can significantly improve the OCT diagnostic abilities [163, 179]. With higher numerical apertures, light collection is improved and helps revealing more structures and increase the signal to noise ratio for the calculation of backscattering coefficients or fractal dimensions [111, 213]. The signal coming from cell contours and from intracellular structures can also be detected. This will be described in chapter 5 in the Dynamic FF-OCT section. Finally, the En-Face view of the sample is quite natural for histologists, as it looks similar to histology slides. FF-OCT is also faster than scanning OCT to record a single *en face* image. Figure 4.14 finally shows a comparison between FF-OCT and a regular H & E histology in a breast sample which organization is altered by a Ductal Carcinoma In Situ. FF-OCT notably reveals normal adipocytes, normal and abnormal collagen fibers (based on their scattering strength), and enlarged ducts. These indicators are characteristics of Ductal Carcinoma In Situ (DCIS), that could be identified with 90% sensitivity and 75 % specificity in this case [185].

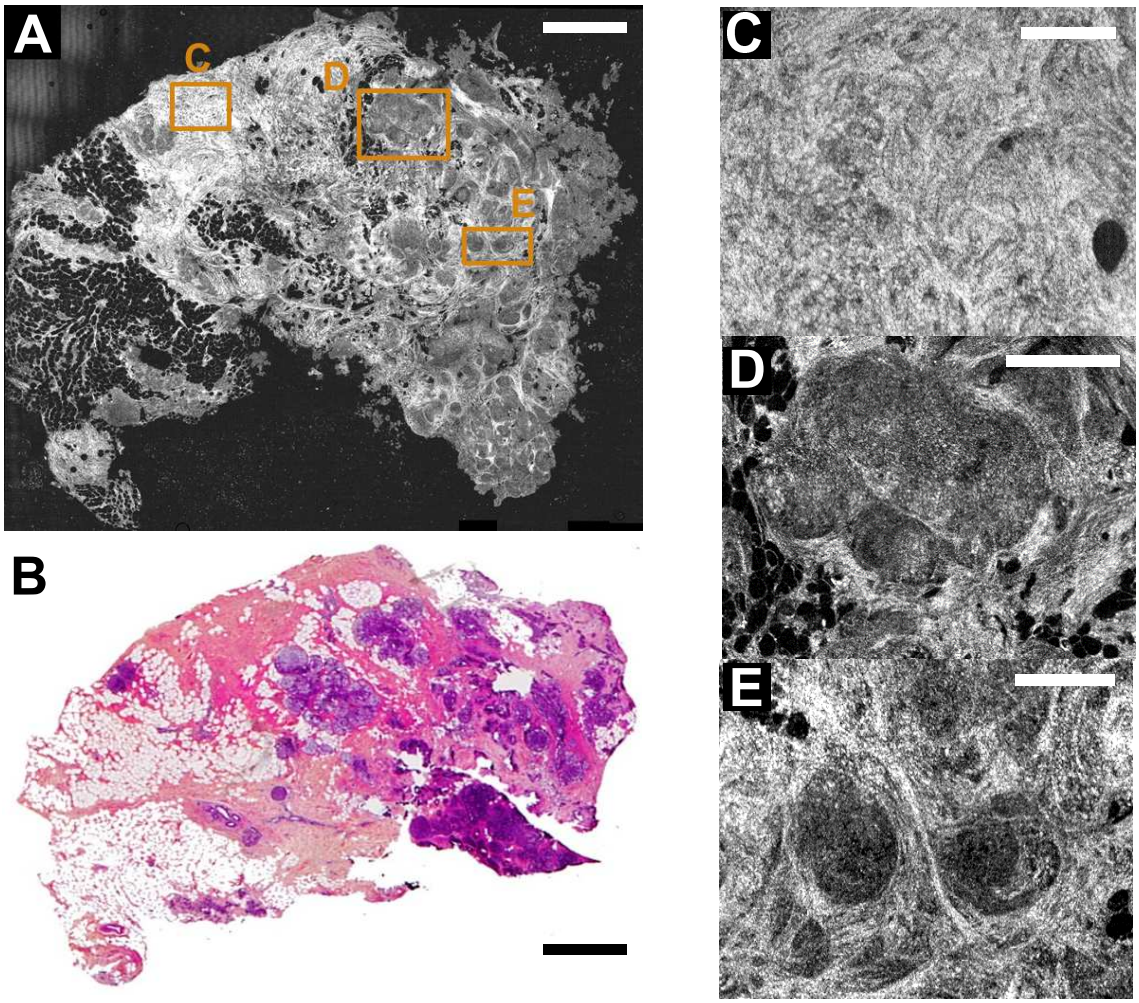

Figure 4.14 – Comparison between FF-OCT and Histology.A and B. Large field image of a breast sample affected by Ductal Carcinoma In Situ (DCIS) acquired with FF-OCT (**A**) and histology (H & E staining. **B.**). **C to E.** Zoom in from boxes represented in panel A, respectively showing normal fibrous tissue, enlarged ducts, and the collagen organization around the carcinomatous cells in a tumorous region [185]. These images have been acquired by LLTech, and have been published in *O. Thouvenin et al.* [214]. Scale bars in A and B represent 1 mm, and 200μm in C to E.

4.6 A quick word about swept source FF-OCT

In the previous chapter, I showed the interest of performing OCT in the Fourier space, which allows to increase the amplitude sensitivity [141] while preventing the need for mechanical axial scanning. If Fourier-domain Full-Field OCT has been demonstrated more than 10 years ago using swept source lasers [215], it has gained a new important interest these two past years with the development of fast cameras and synthetic aperture microscopy [172], and an insightful paper by *D. Hillman et. al.* [216]. I would like to shortly summarize this technique here, as it appears very promising, and will probably be the source of an increasing interest in the near future. Using a fast 2-D camera offering an acquisition rate of 60,000 0.35 MPixels frames per second, and a swept source laser scanning the wavelength by 50 nm in 500 steps, *D. Hillman* and its colleagues could acquire the equivalent of 38 million A-lines per second. Not only does this system exceed in speed the fastest scanning OCT ever reported (6.7 million A-lines per second with a dual beam, to my knowledge [142]) by almost an order of magnitude, it can also acquire 1,200 images in 20 ms, while most of the mechanical eye motions happen below 50 Hz [217,218]. Therefore, it is one of the first full-field OCT systems to enable volumetric acquisitions in the human eye. Likewise, this system can work at relatively high NA (up to 0.2, with a fully open eye pupil) in contrast to standard scanning OCT. To cope with the PSF degradation at out-of-focus planes, a numerical correction of aberrations is performed, by using a combination of interferometric synthetic aperture [172, 219], and volumetric motion correction [220] required for fastly moving samples. The motion correction can work efficiently only for fast acquisition rates with respect to the sample motion, which was made possible by the fast swept source FF-OCT system. Interestingly, as any Fourier domain OCT system, the phase variation at each pixel can be computed quite naturally, at a high frame rate in 3-D and *in vivo*. In another illuminating paper, *D. Hillman et. al.* could demonstrate and follow an optophysiological response of the photoreceptors [221], *i.e.*, a mechanical change in response to light, corresponding to a subwavelength axial motion of 50 nm extension with a rise time of 300 ms, and a decay time of a few seconds. Figure 4.15 presents the layout of the first swept source FF-OCT system [215] and the image reconstruction process. It also presents a volumetric reconstruction of an *in vivo* retina, and an example of optophysiological response of the retina.

I found this system useful to demonstrate the advantage of full-field techniques compared to scanning techniques. If it was theoretically known that FF-OCT could go faster than scanning OCT as it does not require physical transverse motion, the technological limitation of the cameras was still imposing similar pixel rates between both strategies. The articles from *D.Hillman and colleagues* illustrate that as soon as the technological barrier goes away, full-field techniques will enable faster acquisition rates but allow also to examine the fast propagation of phase changes in a transverse plane, which would be complicated in a scanning configuration, where all pixels are acquired separately. Nevertheless, this swept source FF-OCT system suffers from its low axial resolution coming from the limited bandwidth of the swept source laser. Additionally, as swept source lasers are spatially coherent, multiple scattering will reduce the contrast and create cross talks in the images, even though it seems to me that the numerical aberration correction might also lower down the impact of the multiple scattering.

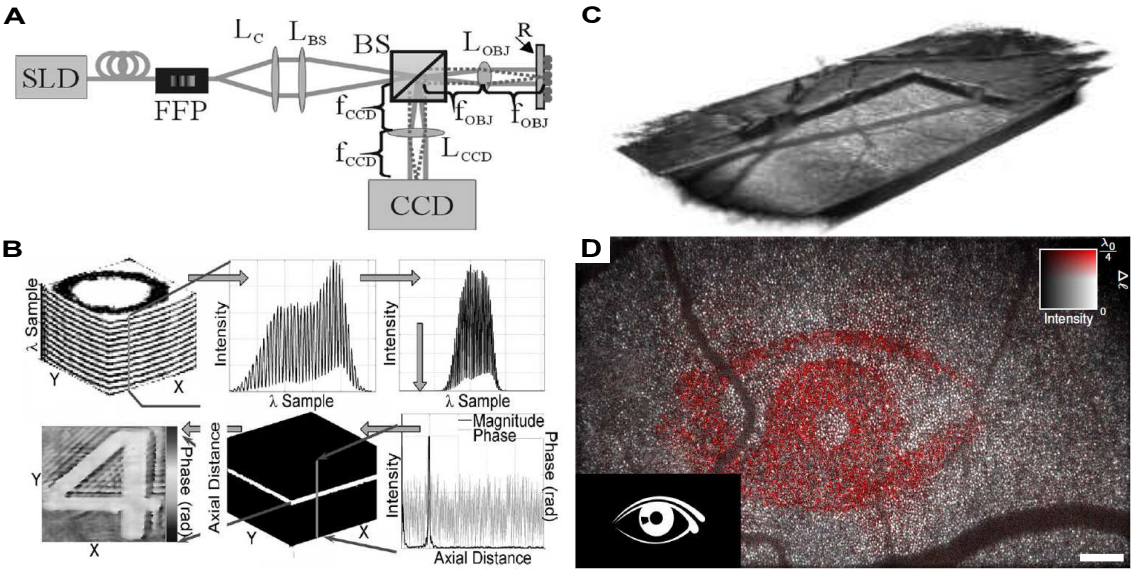

Figure 4.15 – Principle and application of Swept source FF-OCT. Panels A and B present the first swept source FF-OCT system described and the principle of data analysis its this configuration [215]. The system (Panel A) consists of a common path interferometer with the reference beam being reflected by the glass coverslip illuminating the camera as a large halo. The sample beam is focalized at the sample, and in the camera plane. It is equivalent to an *off-axis* holography system performed with a source of swept wavelength. Panel B shows the principle of the data acquisition. An interferogram is captured at each different wavelength. The individual spectra are then windowed and normalized, and then Fourier transformed to obtain an axial amplitude and phase scan at each pixel of the camera, obtaining a 3-D volume of interference signal amplitude. An *en face* view at a given depth can finally be extracted from this 3-D volume. **Panel C** gives an example of volumetric reconstruction of an *in vivo* human retina [216] after aberration correction. **Panel D** shows an example of optophysiological response of photoreceptors captured by swept source FF-OCT, and after white visible light illumination by an eye-shaped pattern (bottom right corner) [221]. The scale bar represents 200 μm, and the color bar corresponds to phase changes from 0 to 200 nm.

4.7 Label-free *In situ* vesicle imaging in zebrafish larvae

In this section, I will mention another FF-OCT advantage, without going too much into the details, as it is an ongoing project that I will probably pursue next year. After a number of discussions with Dr. Claire Wyart and her team at the Brain and Spine Institute (ICM) in Paris (including *Jena Sternberg* and *Yasmine Cantaut*), we have imaged a few living zebrafish larvae. We could show that high NA FF-OCT can successfully detect and track vesicles flowing in the central canal inside the cerebrospinal fluid (CSF). According to CSF composition, these vesicles are likely to be exosomes, vesicles of 30 to 130 nm that can be found in most vertebrates fluids and can be used as natural intercellular chemical cargos [222]. Even if we sometimes detect many vesicles, we are probably only sensitive to the largest exosomes, as presented in figure 4.13, even though particle movements sometimes allow us to extract them from the background noise allowing us to detect smaller particles.

Even though these results still have to be confirmed, vesicle tracking allows us to measure the CSF flow, showing a bidirectional flow, mainly imposed by motile cilia that seem to create vortices on one side of the central canal. We have also been able to exhibit a strong decrease in the vesicles number (which could simply be a decrease in their diameter so that they come below our detection limit) after the second day of development of the larva. Coincidence or not, a reduction of the

activity of the CSF-contacting neurons can also be observed after that time. Figure 4.16 presents one of the successful acquisition we have made on these 1-day old zebrafish larvae, with a quite large and flat central canal, which is one of the main obstacles of the experiment. Panel A will probably be easier to interpret after the presentation of Dynamic FF-OCT in the next chapter, but let's basically say that the interferometric signal allows us to reveal mainly cells in the larva, and to find the central canal. In this canal, a few sub-wavelength particles can be detected, even though it is quite hard to represent them in a static image, while many more particles can be detected dynamically. From these datasets, *Jena Sternberg* from the ICM performed tracking algorithms, which is quite difficult due to the low SNR of our measurements, although I will not detail these here. Instead, I have plotted two temporal profiles along different lines in the canal, exhibiting tilted propagating lines, corresponding to these vesicle movements, and from which we have been able to calculate an average velocity of 10 μm/s, corresponding to the values found in literature measured with fluorescent particles [223].

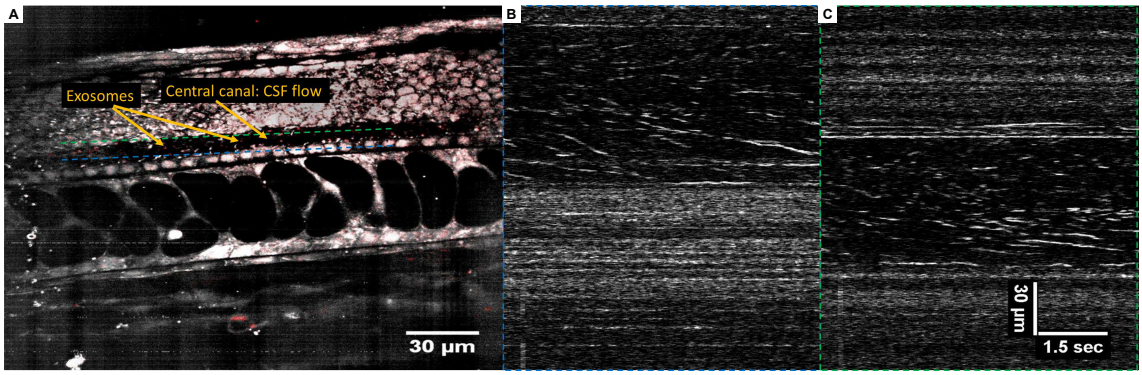

Figure 4.16 – Exosome detection and flow measurement. Panel A presents an FF-OCT imaging of a living 1-day old Zebrafish larva showing the central canal, in which the cerebrospinal fluid (CSF) flows. The CSF being mainly composed of water, it does not backscatter the light, but several subwavelength objects can be captured inside (red dots). These are most likely exosomes flowing in the canal. The image of panel A is the overlay between the standard deviation of the entire temporal stack of OCT image in gray scale and the standard deviation of 5 consecutive OCT amplitude frames. It helps enhancing the signal from the moving particles while being short enough not to lose the particle. **Panels B and C** present the temporal profile (Xt) along the blue (left bottom part of the canal) and green (right and upper part of the canal) lines of panel A respectively. Here again, these profiles present the temporal evolution of the standard deviation calculated from 5 consecutive OCT images. Patterns of flowing particles can be observed in these profiles, enabling to follow and measure an average CSF flow. The upper and bottom parts of the canal exhibit a bidirectional flow that can be captured in the two different profiles. In the lower part of the canal, particles flow toward the right-hand side. while particles flow inside the upper part of the canal is more chaotic, with some particles going toward the left-hand side of the image. Such flow could be explained by the rotation of a motile cilia attached to CSF-contacting neurons [223].

Finally, it is worth noting that FF-OCT ability to detect and track exosomes is quite appealing, as exosomes are likely to control many biological phenomena, while being hard to image with a limited number of fluorescence tools to label them, and being too small to generate a strong signal with most of label-free optical techniques. To my knowledge, I have heard about only two (still unpublished) optical systems that are able to follow exosomes inside tissues. The first one from a group in Nice uses a fluorescent specific label, and the second one from S.Boppart's group in the USA uses a very complex system that includes third harmonic generation and can only detect the largest exosomes. Otherwise, one has to use electron microscopy to detect such exosomes.

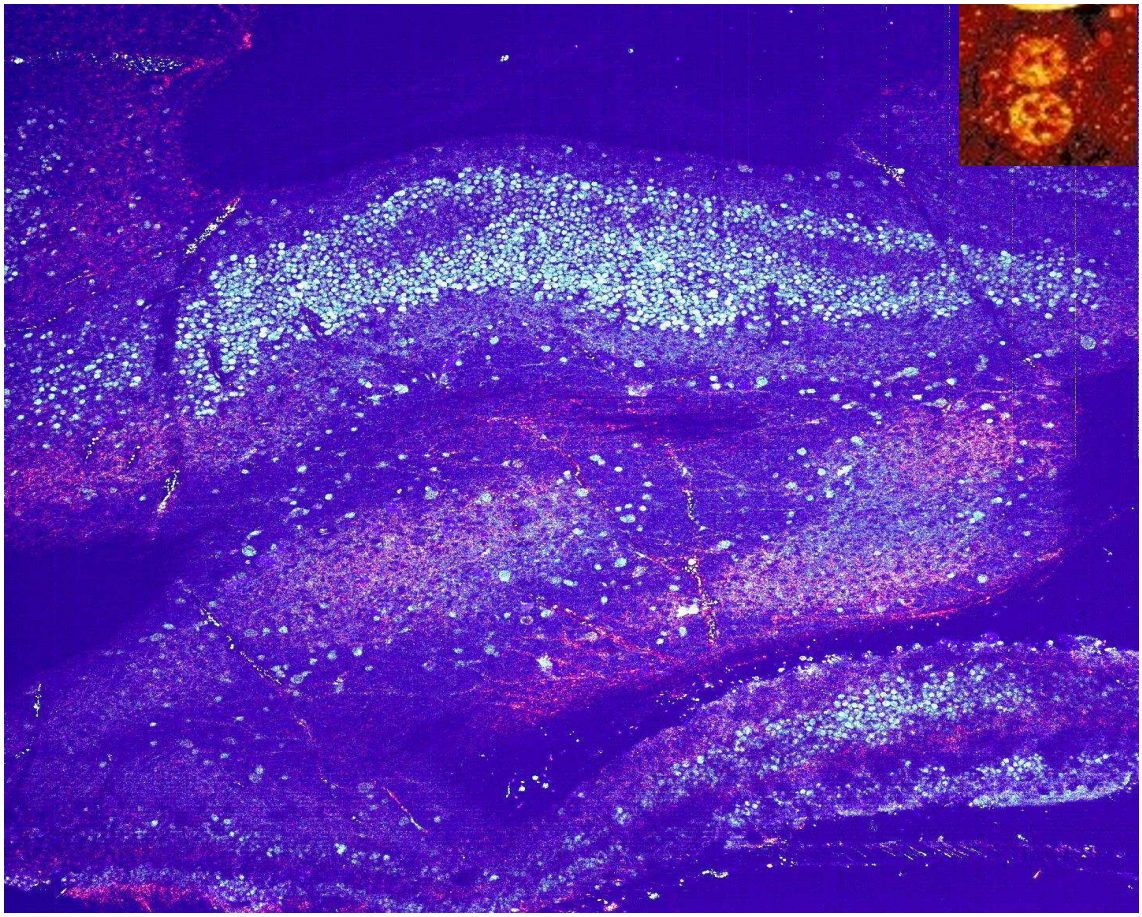

Imaging motility with dynamic FF-OCT. *The image at the top corresponds to a color-coded dynamic FF-OCT image of a macaque retina. The small insert shows angry nuclei captured in a rat liver.*

CHAPTER 5

Development of new multimodal Full-Field OCT systems

Table of contents

5.1 Simultaneous FF-OCT and SIM microscope **138**

5.1.1 Structured Illumination Fluorescence Microscopy 139

5.1.2 Multimodal system optical design 143

Full-Field Optical Coherence Tomography 144

Structured Illumination Fluorescence Microscopy 146

Optimization of the combination of the modalities 147

5.1.3 Static association of FF-OCT and SIM 148

5.1.4 Mechanical wave observation 149

5.2 Dynamic FF-OCT **152**

5.2.1 Principle of D-FF-OCT 152

5.2.2 Motility contrast in cells 156

5.2.3 Separation between amplitude and phase 158

5.2.4 Origin of the phase fluctuations and optical sectioning in D-FF-OCT . 161

5.2.5 Phase fluctuation signal analysis 164

Standard D-FF-OCT analysis and color coded D-FF-OCT 164

Display of the temporal characteristics of the phase fluctuations signal 165

Difference between the amplitude of fluctuations and the characteristic times 166

Singular Value Decomposition for signal extraction 167

5.2.6 D-FF-OCT for histology and to reveal various sample features 171

5.2.7 D-FF-OCT signal variation under different conditions 174

Effect of temperature 174

Effect of drugs 175

5.2.8 *In vivo* D-FF-OCT 177

In the previous chapter, we have seen the interest of FF-OCT to provide a noninvasive label-free tomographic microscope that captures images similar to standard histology images. Nevertheless, FF-OCT may suffer from its lack of specificity and sometimes fails to match the diagnostic capacity of gold standard histology. Yet, FF-OCT detection scores are above 80% for most pathologies in both sensitivity and specificity [107,185], and *Manu Jain and colleagues* have even been able to report a 100% correct identification of tumors in *ex vivo* kidneys [163], obtaining similar results to histology, even though the tumor subtyping is still not reaching 100%. In order to increase diagnosis scores, FF-OCT has therefore expanded to multimodal systems combining FF-OCT structural contrast with other pathology biomarkers inside a single microscope. The added value of such multimodal systems is to reduce the ambiguity in structure identification that can arise from sequential imaging with two different microscopes and to reduce operation time. Some FF-OCT multimodal systems have been reviewed in the recently published *Handbook of Full-Field Optical Coherence Microscopy*, edited by Arnaud Dubois [107]. We can non-exhaustively mention the multimodal combinations of FF-OCT with fluorescence [187], photothermal imaging [188], elastography [189], polarization [190], multispectral and hyperspectral imaging [191–193]. Most of these multimodal systems have been inspired by similar systems developed in standard OCT, but they needed to be adapted and redesigned to fit FF-OCT's particular configuration. If appendix C is dedicated to the description of an additional mechanical contrast that we have partly developed in the lab, this chapter aims at introducing two new modalities that we have developed and combined together with FF-OCT. First, I will (at last) describe the parallel combination of FF-OCT and structured illumination fluorescence microscopy (SIM) I have mentioned in chapter 2 and 4. I will explain the SIM principle, detail the advantage of adding a fluorescence contrast to FF-OCT and explain how I have optimized the simultaneous combination of these two techniques. Then, I will introduce Dynamic FF-OCT (D-FF-OCT), that has been developed in our group by several persons, including me, and that takes advantage of the higher intracellular phase fluctuations to reveal a specific contrast inside cells and tissue active structures. I will describe this new contrast as we currently understand it, and, most importantly, I will show that the amplitude of phase fluctuations depends on the metabolic activity of cells, and discuss D-FF-OCT ability to measure the effect of drugs on cell metabolic activity. I will illustrate that FF-OCT, Dynamic FF-OCT, and SIM can be combined in a single platform to increase the performance of these modalities. However, the main specific biological applications that we have been able to target using these systems will not be detailed in here but in the next chapters of part III.

5.1 Simultaneous FF-OCT and SIM microscope

If OCT and FF-OCT can access a label-free nonspecific microstructural contrast, fluorescence microscopy, on the other hand, can reveal a very specific molecular contrast using chemical dyes or genetically encoded proteins that can be attached to a specific structure of interest. It can also take advantage of dynamic fluorophores and observe fluorescence fluctuations caused by changes in the biochemical properties of the tissue. As mentioned in chapter 2, dynamic fluorescence probes can be as various as calcium indicators, voltage indicators, ATP or apoptosis indicators. Accurate fluorescence measurements can be performed inside biological tissues using optical techniques

that provide optical sectioning. Among them, structured illumination microscopy (SIM) can be described as a full-field version of confocal microscopy and can perform optical sections as thin as a few micrometers inside a tissue. Therefore, fluorescence and OCT techniques are quite complementary and multimodal systems combining both can help with diagnosis, as we will illustrate throughout this section. Many such multimodal setups have been developed with both scanning OCT approaches [224, 225] and full-field approaches. The latter are using either a flip mirror to switch from one modality to the other [187,226] or a simultaneous approach [227]. If all these multimodal approaches share a common interest, scanning OCT approaches are more easily combined with scanning fluorescence approaches, such as confocal or two-photon microscopies, whereas FF-OCT systems have been developed in combination with widefield fluorescence techniques, such as structured illumination microscopy (SIM).

Furthermore, usual histology staining and fluorescence techniques are quite similar in terms of contrast, except that fluorescence techniques use fluorescence probes instead of absorbing probes in histology. Some fluorescence techniques have been part of the histology toolkit for decades [228], such as immunofluorescence, which aims at detecting the interaction of a labeled antibody with a structure of interest [229] or Fluorescence In Situ Hybridization (FISH) [230,231, Chapter 6], which aims at detecting the interaction of a labeled nucleotide sequence with its specific complementary sequence in a cell. More recently, confocal microscopy [232] and two-photon microscopy [233] have been used in order to detect fluorescent probes in depth in tissues. Thanks to optical sectioning provided by these techniques, it has become possible to follow some fluorescent structures in *ex-vivo* tissues and *in-vivo* [234, 235]. However, fluorescence techniques still require fluorescent labels, that need to be injected into the tissue. It can take a long time before the label diffuses in depth inside a tissue. Moreover, similarly to classic histology stains, these labels only tag a few structures of interest and it might be hard to understand the organization of these structures inside their microenvironment. Multiple labeling can be used to tag several structures, but it increases the complexity and the cost of such experiments. We can also comment further that usually, confocal and two-photon microscopy can only access shallow depth inside a tissue, down to a few hundred μm at best. In contrast, OCT techniques can access deeper regions down to one millimeter considering the signal is often enhanced by the reference arm. Recently, clearing techniques [236, 237] with low tissue distortions have been developed in order to increase tissue transparency and to image through the entire tissue. OCT can also benefit from these approaches [238], even if we would expect the intrinsic signal to be reduced in OCT since clearing tends to remove lipid structures and to average out the refractive index fluctuations. However, it can help to detect exogenous OCT contrast agent at important depths, such as metallic nanoparticles. Here again, clearing processes are often time-consuming and can induce tissue distortions. All these concerns show both the interest of OCT and FF-OCT with respect to fluorescence microscopy and the potential for combining both in a single platform. In this section, I will first describe structured illumination fluorescence microscopy (SIM) and then demonstrate how it can be associated with FF-OCT in a synchronous manner. Finally, I will illustrate the advantage of this dual-modality platform for biomedical imaging.

5.1.1 Structured Illumination Fluorescence Microscopy

Structured Illumination Microscopy (SIM) can be understood as the widefield version of confocal microscopy (and as often in widefield microscopy, as a cheaper version!). This axially resolved fluorescence technique is convenient to associate with FF-OCT, because of its widefield configuration. This also means that the frame acquisition rate does not depend directly on the field size,

but depends only on a camera frame rate. It is notably faster for large fields and usually provides a higher number of "pixels" (1 pixel corresponds to a scanned position in scanning techniques). Especially, it allows working with higher exposure times for a similar acquisition time since all the pixels are illuminated at the same time. Widefield fluorescence systems are finally usually operated with sources that are more stable than lasers, which reduces the pixel-to-pixel variability and reduces the so-called *salt and pepper* noise that can be encountered in scanning fluorescence techniques. Nevertheless, widefield fluorescence microscopes can generate more photobleaching and phototoxicity because of the continuous illumination; They also do not allow for out-of-focus light rejection, which gives lower SNR and makes it complicated to perform in scattering tissues. The SIM basic principle can be easily understandable: In standard widefield fluorescence microscopy, only objects from the depth of field are conjugated to the camera. However, the camera detects the fluorescence from all fluorescent structures inside the sample. Light emitted or scattered from structures out of the depth of field thus create a fluorescence background in the entire field of view. This background can significantly decrease the signal-to-noise ratio. To isolate the light coming from the focal plane, the sample can be illuminated with a structured illumination [239–241]. The usual implementation is to add a grid, usually named Ronchi ruling, in a plane conjugated to the sample plane (and to the field diaphragm if there is any). The illumination pattern will modulate the light only around the sample plane. By scanning the illumination pattern in successive images, only a part of the light will be modulated. This corresponds to the light coming from an optical section around the focal plane, as illustrated in figure 5.1.

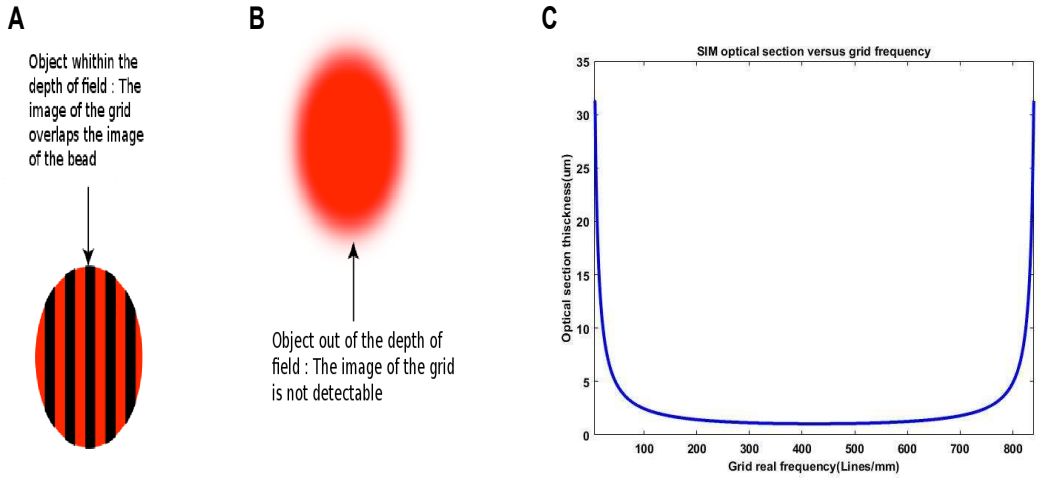

Figure 5.1 – Principle of Structured Illumination Microscopy. Panels A and B present two fluorescent beads illuminated by a structured illumination, using a grid pattern. Only one of the beads stays within the depth of field. As the grid is conjugated to the focal plane and, therefore, its image overlaps the image of objects that are inside the field of view. Here, the image of the first bead is modulated by the grid pattern, whereas the image of the second bead is not modified by the structured illumination. By changing the orientation of the grid pattern, it is later possible to reconstruct only the image of structures that are inside the depth of field and to remove the grid pattern from the images. This image has been taken from *F. Chasles* thesis manuscript [240]. **Panel C** shows the theoretical evolution of the SIM optical section with the grid frequency, calculated with our optical system parameters. A grid pattern of 100 lines/mm has been chosen, which should provide an optical section of 2.4 μm.

In SIM, the optical section thickness depends on the spatial frequency (or spatial frequencies in more complex patterns) of the illumination pattern and depends on the optical parameters of the

imaging path. It can be qualitatively understood. Due to the diffraction limit and because the imaging system does not have an infinite angle collection (*i.e.* maximal numerical aperture equal to the medium refractive index), the sample higher spatial frequencies are lost. And the longer distance to the focal plane is, the more high spatial frequencies are eliminated. To perform an efficient sectioning with structured illumination, the grid must be imaged in the focal plane and has to become blurred when the object moves away from the focal plane. The cut-off frequency is mainly defined by the diffraction limit. However, at such a spatial frequency, the grid is hardly detectable and, as a result, it is better to image lower spatial frequencies to provide a better contrast. To the contrary, with a lower spatial frequency, the grid will still be detectable at a larger distance from the focal plane and sectioning would then not be efficient. Therefore, we can understand why the minimal section thickness is obtained when the grid frequency in the sample plane (The grid is often magnified before the sample plane) is around $\frac{NA}{\lambda}$. In practice, as illustrated in figure 5.1 A, the optical section thickness, defined as the distance to the focal plane at which the intensity is halved, is symmetric and relatively flat around its minimal value. The latter is obtained when the grid frequency in the focal plane is equal to $\frac{NA}{\lambda}$. It is often preferred to choose imaged grid frequencies smaller than $\frac{NA}{\lambda}$ so that the grid pattern can be imaged on several pixels, which makes it more robust to PSF degradation due to aberrations. The full calculation of the relationship between the grid frequency and the SIM optical section can be found in [239,240,242] and gives:

$$I(\nu'_g, u) \propto |2.\frac{J_1(\nu'_g.u.(1-\frac{\nu'_g.u}{2}))}{\nu'_g.u.(1-\frac{\nu'_g.u}{2})}|^2 \tag{5.1}$$

with ν'_g, the normalized grid frequency in the sample arm and u, the axial distance from focus in optical coordinates. They are respectively related to the physical grid frequency f_{grid} (in lines/mm) and to the cartesian axial distance z by:

$$f_{grid} = 1000.M.\frac{\nu'_g.NA}{\lambda} \tag{5.2}$$

$$z = \frac{\lambda}{8\pi n_{medium}.sin(\frac{\alpha}{2})^2} \tag{5.3}$$

with $NA = n_{medium}sin(\alpha)$, the detection objective numerical aperture and M the illumination magnification, *i.e.* the yield between the focal length of the lens making the image of the grid and the focal length of the imaging objective. From equation 5.1, the size of the optical section can be computed by finding the axial position at which the intensity is divided by 2. Figure 5.1 C presents the evolution of the optical section versus the physical grid frequency for the optical characteristics of our system.

Furthermore, SIM can also slightly increase the transverse resolution and is more often used for its super resolution abilities than for its optical sectioning ability [243, 244]. This can be explained by the Moiré effect, illustrated in figure 5.1 B. When two patterns of two different spatial frequencies are superimposed, a third frequency appear, which is the difference between the two first frequencies. These so-called Moiré fringes can have a spatial frequency detectable by the microscope, whereas one of the two first two frequencies is not resolvable. In classical SIM experiments, the transverse resolution can be increased by a factor 2. It has also been demonstrated that other spatial frequencies can be added with a single frequency pattern by saturating the illumination. The more saturated the illumination is, the more spatial frequencies are created and the more the resolution improves. The transverse resolution has been improved

down to 50 nm in some cases [243, 244]. However, to achieve such resolution, a lot of power is required, which can increase photobleaching or sample damage while many images are also needed which also limits the actual frame rate.

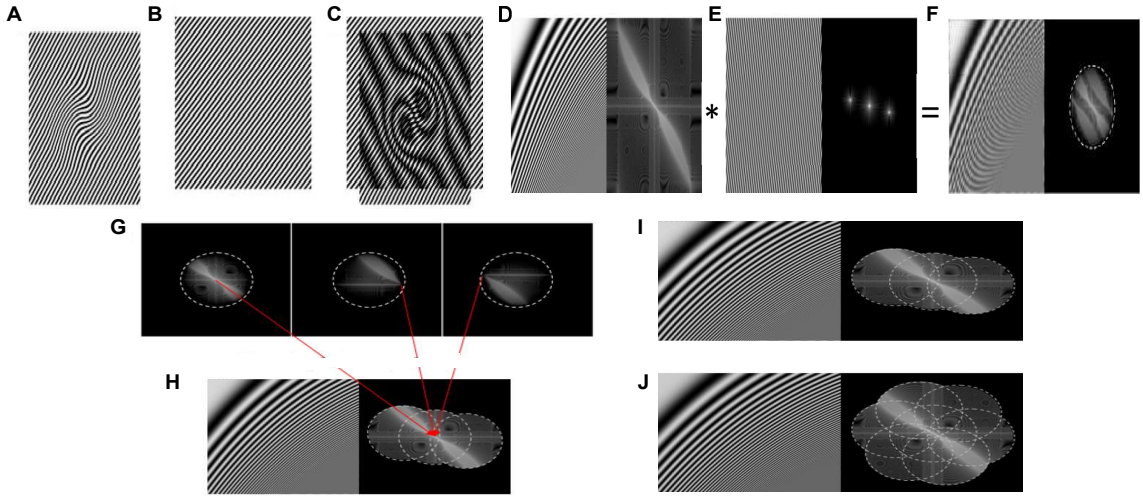

Figure 5.2 – Principle of the Moiré effect and resolution improvement using Structured Illumination microscopy. Panels A to C. illustrate the principle of the Moiréffect and are adapted from [243]. An unresolvable pattern is hidden in panel A and multiplied by a known regular illumination pattern (Panel B). It reveals a beat pattern (known as Moiré fringes) (Panel C) that corresponds to the difference between the spatial frequencies of the pattern frequency and each spatial frequency component of the sample structure and can be coarse enough to be revealed by a diffraction-limited microscope. **Panels D to J** present a more technical sequence leading to the transverse resolution improvement in SIM and are adapted from P.Vermeulen PhD manuscript [241]. Panels D to F show the initial images and their respective Fourier transform. The structured illumination will generate the product(Panel F) between the initial sample (Panel D) and the illumination pattern (Panel E), which corresponds to a convolution between the two images Fourier transform (Panel F on the right hand side). By shifting the grid pattern, it becomes possible to reconstruct 3 domains in the Fourier space (Panel G). These domains have a spectral extension that is limited by the microscope transverse resolution, *i.e.* the objective NA. They respectively correspond to the sample central frequencies, the frequencies centered around $+f_{pattern}$ and the frequencies centered around $-f_{pattern}$ from left to right, with $f_{pattern}$, the illumination pattern frequency. By numerically recombining these 3 spectra with respect to their corresponding shift (panel H), an image with super-resolution along one direction can be obtained (panel I). Finally, the illumination pattern can be further rotated to allow a better mapping of the Fourier space and obtain a fully 2D super-resolution image (Panel J) from 9 images (3 phases for each of the 3 illumination angles). A theoretically unlimited increase in resolution can further be obtained by reducing the illumination pattern frequency, by saturating the illumination pattern, or by illuminating with a rectangular pattern instead of a sinusoid pattern, which creates multiple-order spatial components in the Fourier space [243].

In figure 5.3, we present the imaging principle of SIM in cell cultures where the pattern can easily be detectable. The SIM reconstruction is performed by translating the Ronchi ruling in 4 successive steps, similarly to the 4 phase steps algorithms used for QPI and FF-OCT and presented in chapter 2.

Finally, one drawback of SIM is that this technique is quite sensitive to aberrations. Because the fringe pattern is chosen with a spatial frequency close to the diffraction limit, the visibility of the fringes and their sectioning ability can decrease significantly in presence of aberrations. It will especially become an issue in mammalian tissues source of much scattering and that create many

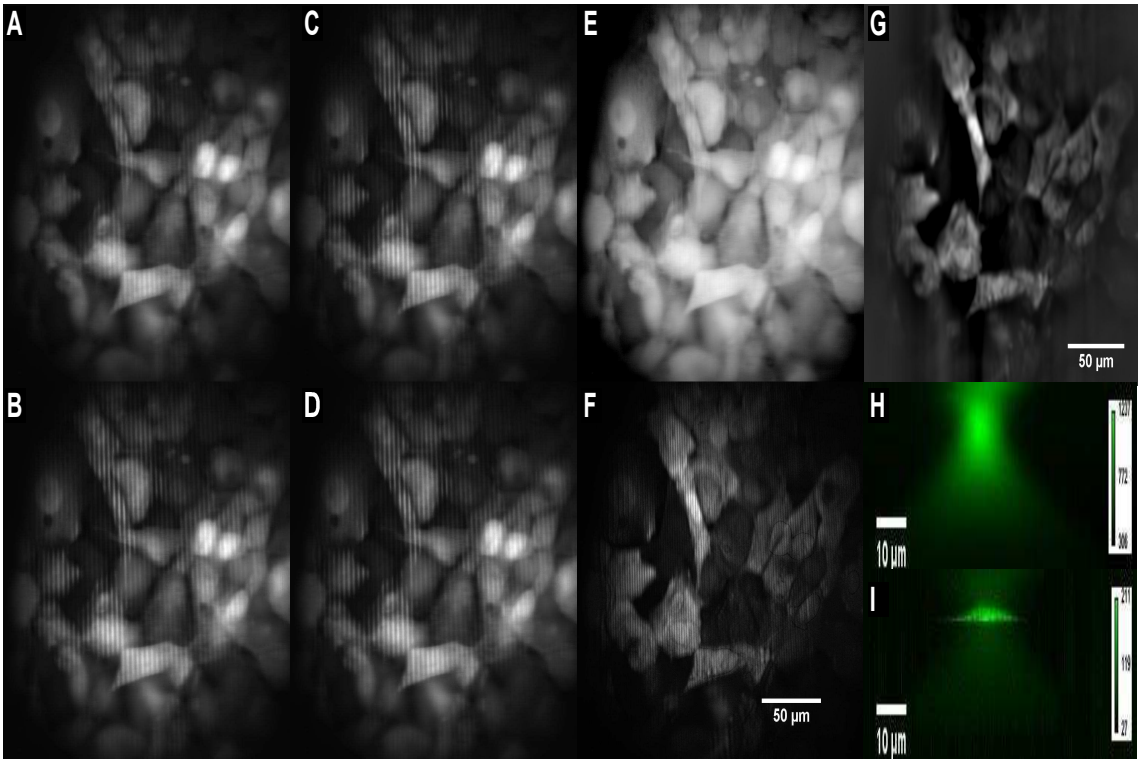

Figure 5.3 – Fluorescence and SIM in cells cultures. Panels A to G illustrate the principle of the SIM reconstruction in our fluorescence microscope in a dense 3t3 (one of the most common fibroblast cell line) cell culture, with cells growing on top of each other, forming two main cellular layers. **Panels A to D** show the 4 phases image while the illumination pattern is scanned. From these 4 images, we could compute the average (**Panel E**) image, that is equivalent to a widefield image and reveals most of the cells in the culture. We could also compute the SIM amplitude image (**Panel F**) that mainly reveals the cells of the upper layer. The SIM procedure fails at removing all traces of the illumination pattern, but a low-pass filter can help to filter out the remaining artifacts (**Panel G**). **Panels H and I** compare the axial sectioning of widefield (Panel H) and SIM images (Panel I). A rat hippocampal cultured neuron tagged with Fluo-4 is imaged and the axial profile of the average fluorescence collected on 10 μm is displayed. The smallest resolvable object in SIM is measured at 2.9 μm, which is supposedly larger than the smallest compartments of a neuron. Therefore, we can estimate the size of the SIM optical section in our system to be equal to 2.9 μ m.

optical aberrations. In such samples, the sectioning ability is usually lost after only 50 to 100 μm inside tissues. However, using adaptive optics or creating a structured illumination pattern with a DMD [245] or SLM enables fast modulation of the pattern and correction of aberrations to restore a sharp pattern in depth. Figure 5.4 illustrates the SIM limitation when imaging tissues of increasing scattering lengths. We can finally add that the out-of-focus fluorescence signal has a low spatial frequency so that the signal at a given depth can often be emphasized with a simple high-pass filter in a widefield fluorescence microscope. In scattering samples, such a strategy often performs better than SIM as illustrated in figure 5.4 B and G. It can be interesting to note that it is hard to find SIM images of structures embedded in scattering samples in the literature.

5.1.2 Multimodal system optical design

In this subsection, I will finally go into the details of the construction of my microscope, as promised in previous chapters. Our experimental setup is presented in figure 5.5 A and combines an FF-OCT path in red to a SIM path in blue. In the following subsections, I will first describe

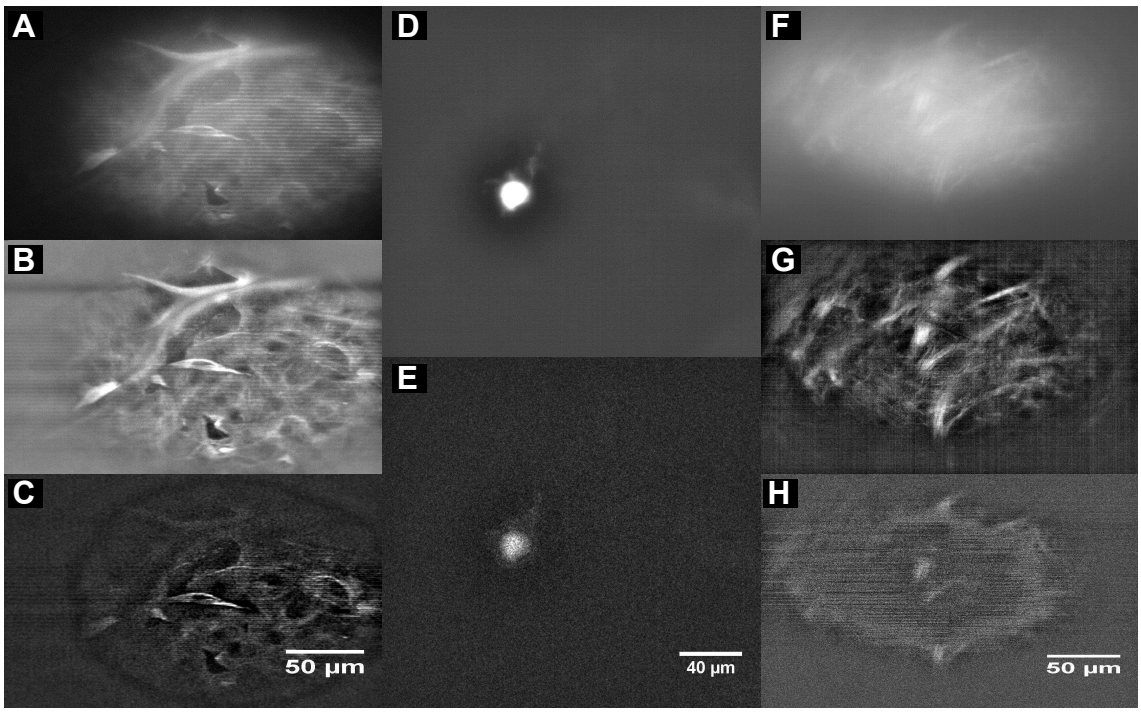

Figure 5.4 – Fluorescence and SIM images in tissues with various scattering properties. Panels A to C compare the fluorescence and SIM images in a rat cornea, which is almost transparent so that the fluorescence SNR is quite high. Panel A shows the direct fluorescence intensity in which the illumination pattern can be easily observed. Panel B is the average fluorescence intensity, corresponding to the widefield image, with an additional low pass filter to decrease the contribution of out-of-focus structures. Panel C shows the SIM image that gives a sharper optical sectioning mostly excluding the large fiber above the cell. **Panels D and E** are the corresponding fluorescence and SIM images of a ganglion cell inside a retina, which is a bit more scattering, with a lower SNR. In the SIM image, we can observe a single depth inside the cell, but the cell starts to become hardly visible. **Panels F to H** are the results of an imaging of a rat cortex with fluorescent myelin fibers. The cortex starts to be a quite highly scattering sample. Panel F shows the fluorescence image, where the illumination pattern is almost invisible since the contribution of the fluorescence signal coming from a single depth is weak. Panel G shows the low-pass filtered corresponding fluorescence image, reducing the contribution of the low-frequency background signal and revealing more fibers. Finally, panel H shows the SIM image that gives almost no signal from a single depth.

each path independently and then explain compromises we had to make when combining both paths.

Full-Field Optical Coherence Tomography

To perform FF-OCT measurements, a Linnik interference microscope is illuminated by a temporally and spatially incoherent light source. In practice, we use a high power red LED (Thorlabs M660L3, nominal wavelength: 660 nm, spectral bandwidth: 20 nm) mounted in a pseudo-Köhler configuration. In such arrangement, we use only one lens in the illumination path in order to collect more light and to build a more compact system. The aperture diaphragm is directly conjugated with the back focal plane of the objective, while the field diaphragm is at the focal plane of the lens and is therefore imaged at the focal plane. The source is mounted as close as possible to the aperture diaphragm. The light is split to sample and reference arms by a 90:10 visible cube beamsplitter. Each arm consists of an identical 40X water immersion microscope objective (Nikon CFI APO 40X Water NIR Objective, 0.8 Numerical Aperture, 3.5 mm Working Distance).

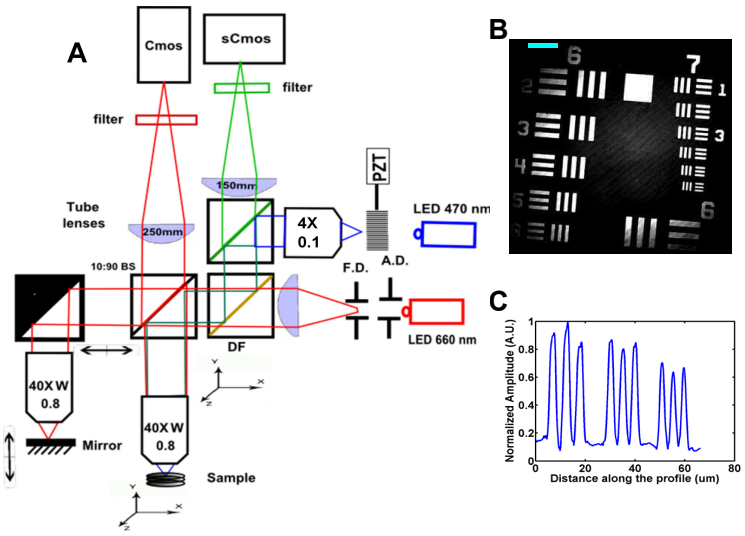

Figure 5.5 – Setup scheme and characterization. A. Synchronous multimodal setup associating Full-Field Optical Coherence Tomography and Structured Illumination microscopy. The light path presented in red is the FF-OCT path, which consists in a Linnik interferometer performed with a 90:10 beamsplitter, two 40X, 0.8 NA objectives and with a red LED (660 $\pm$10 nm), placed in a pseudo-Köhler illumination. F.D. and A.D. stand respectively for field and aperture diaphragms. A dichroic filter (DF) at 595 nm separates the FF-OCT path from the fluorescence part, represented in blue and green on the scheme. A blue LED (470 $\pm$13nm) shines onto a Ronchi ruling with a frequency of 100 lines per mm. The latter is imaged with a 4X, 0.1 NA objective and conjugated with the focal plane of the imaging objectives. Fluorescence from the sample arm is back-emitted, reflected by the interferometer beamsplitter and the dichroic filter. A second dichroic filter at 500nm finally separates excitation from emission light and fluorescence is finally imaged with an sCMOS camera. Tube lenses from FF-OCT and SIM paths are respectively 250 and 150 mm. **B and C.** Transverse resolution of the FF-OCT path. An USAF target is imaged to illustrate the high transverse resolution of the microscope. The blue scale bar in panel B represents 50 μm. The transverse resolution has been independently measured at 530 nm using subwavelength gold nanoparticles but is not displayed here.

In the reference arm, the light is focused onto a flat silicon wafer that provides a reflection coefficient of about 23.5 % at the interface with water. Such reflection is chosen as a compromise between having a large number of photons and having a reflection coefficient not too far from the sample's. Indeed, the signal-to-noise ratio depends on $\sqrt{N_{Photons}}$ and on $\sqrt{\frac{R_{Sample}}{R_{Ref}}}$, with $N_{Photons}$, the number of photoelectrons detected by a single pixel of the camera during one exposure, proportional to the full-well capacity of the camera. R_{Sample} and R_{Ref} are respectively the reflection coefficients in the sample and in the reference arms. Imaging a high number of photons also allows to reduce the importance of the camera noise with respect to the shot noise. The reference arm length can be adjusted using a motorized 1D translation stage. One manual XY translation stage is attached to the sample objective so that the two beams can be adjusted to be nearly co-linear. One final manual XY and one motorized Z translation stage are used to move the sample independently of the objective.

In the sample arm, FF-OCT detects any structure that could either reflect or backscatter the light. The backscattered and reflected coefficients are notably controlled by the refractive index, the size and the shape of the imaged structures [205]. Finally, the light back-reflected by the sample is recombined with the light reflected by the reference silicon mirror by the entrance beamsplitter. The two beams interfere only if the optical path length difference between both arms stays within the temporal coherence length of the system. At the output of the interferome-

ter, a highpass dichroic filter (cut-off wavelength of 595nm) transmits the FF-OCT beam. A final 25cm focal length achromatic doublet focuses the light to a high speed and high Full Well Capacity Cmos Camera (PhotonFocus, MV-D1024E-160-CL-12). The image focal plane is therefore conjugated with this camera. Complex Amplitude and phase images are obtained by modulating the optical path difference in 4 steps. Such modulation is performed via a piezo actuator that modulates the silicon mirror position along the optical axis. The entire interferometer is built as one mechanical block, in order to reduce mechanical vibrations. The transverse resolution and the depth of field are only constrained by the microscope objective. With the objectives we use, theoretical resolutions are 0.503 μm transversely and 1.31μm axially. We have measured our system experimental transverse resolution by looking at the signal backscattered from 50 nm gold beads and have measured a transverse resolution of 0.525 μm. The interferometer has also been built in such a way that changing objectives in both arms would preserve the optical path length difference. So, any microscope objective can be used, as long as the same objectives are used in each arm. Since we are using water in each arm, the dispersion is largely compensated, which preserves the FF-OCT signal.

Due to the temporal coherence length of the source, only light from a section of thickness 7.75 μm can interfere as seen in the previous chapters. To be able to measure a fluorescent light simultaneously, the source spectral bandwidth has to be limited meaning that the optical section has to be rather large. However, due to the high NA objective, the actual optical section is controlled by the spatial coherence length [133, 134], here equal to 4.0 μm. Finally, our camera can acquire 1440x1440 pixels images at up to 500 Hz and can acquire images at more than 1000 images/s for reduced fields of view.

Structured Illumination Fluorescence Microscopy

In the current microscope configuration, we use a high power blue LED (Thorlabs, M470L3, nominal wavelength: 470 nm, spectral bandwidth: 25nm) filtered with a bandpass filter centered at 480 nm to excite fluorophores. The LED shines onto a grid of 100 lines/mm imaged by a microscope air objective (Olympus 10X, 0.1 NA) and conjugated to the sample image plane. The light coming out the objective is made collinear with FF-OCT beam due to a dichroic mirror centered at 500 nm. The light then enters the interferometer, but fluorescence is only collected from the sample arm. Then, a long-pass dichroic filter centered at 595nm reflects the fluorescence signal onto an achromatic doublet of focal length 150 mm. The latter focuses the light on a high-speed low-noise sCMOS camera (PCO.edge 5.1). To reconstruct optically sectioned images, we have designed a structured illumination (SIM) by conjugating a physical grid (Ronchi ruling) with the sample plane and we have mounted the grid on a piezo-driven translation stage. Even though only 3 images are required to reconstruct a fluorescence image, we usually acquire 4 of them. It helps reducing grid artifacts, but more importantly, it permits to match SIM and FF-OCT acquisition rates, with similar exposure times between the modalities. The grid frequency is chosen to be 100 lines/mm, which is magnified by the telescope formed with the 10X Olympus objective and the 40X Nikon objective:

$$M_{Ill} = \frac{f_{tube_Olympus}}{M_{Olympus}} . \frac{M_{Nikon}}{f_{tube_Nikon}} = \frac{180}{10} . \frac{40}{200} = 3.6 \tag{5.4}$$

This telescope images the grid in the sample image plane and gives a spatial period of the grid in this plane of 2.78 μm. The fluorescence imaged pixel size being 0.216 μm, it means that one period of the grid is imaged on almost 13 pixels and corresponds to 6 times the system transverse

resolution. As a result, we should be able to image the grid even in presence of optical aberrations and PSF degradation. The corresponding optical section thickness (full width at half maximum) is 2.45 μm. Here again, a trade-off needs to be made between the thin optical section and the grid pattern visibility. The higher the grid frequency, the less visible is the grid in the sample plane, especially in thick tissues where aberrations can be significant. Transverse resolution and depth of field are imposed by the microscope objective and are supposed to be respectively 0.40 μm and 1.45 μm with the 40X 0.8 water objective.

Optimization of the combination of the modalities

Acquiring simultaneously an FF-OCT image and a SIM image imposes several constraints, but the current configuration has been developed in order to minimize such constraints. First, the use of high NA objectives provides two major advantages as it enhances the collection of fluorescent photons and enhances the size of the FF-OCT and fluorescence optical section, as described previously. The latter property is particularly useful as the spectral bandwidth of the FF-OCT is necessarily limited in such a configuration. Interestingly, our setup configuration can be adjusted to use any wavelength for FF-OCT or fluorescence sources, according to needs. With high NA objectives, even a quasi-monochromatic source can be used [246]. However, we have showed in chapter 4 that, even if a temporally coherent source can be used, it is more efficient to use a spatially incoherent illumination since cross talks are suppressed [164] and the transverse resolution becomes almost independent of aberrations in the sample arm [165]. To prevent any spectral overlap between the two modalities, additional band-pass filters are inserted in front of both cameras (respectively centered around 525 and 660 nm). We overlay the images of the camera by taking an image of the red illumination field diaphragm with both cameras and by removing the filter in front of the sCMOS camera. Synchronization between the two cameras, the OCT and SIM piezo actuators and eventually the illumination (to reduce illumination time and sample heating) is ensured by a DAQ card with a 10 μs precision.

We should add that having the dichroic filter separating FF-OCT and SIM out of the interferometer is not ideal since some of the fluorescence light is then lost. However, we have tried several configurations where a short-pass or long-pass dichroic filter was inserted into the sample arm, but we have never been able to observe a strong FF-OCT signal. Modeling and different failures let us believe that the reason comes from the fact that most dichroic filters have multiple coatings/reflection planes so that the optical path length takes multiple values. Imaging fringes on a mirror then gives a dozen of very low contrast rebounds, which reduce the contrast of the main fringe pattern. However, if a dichroic mirror having no effect on the FF-OCT signal is to be found, the optimal configuration would be to insert this dichroic in the sample arm only.

To minimize this issue, we have decided to use a 90:10 beamsplitter at the center of the interferometer and to mount the fluorescence detection part on the illumination side. Therefore, the illumination and fluorescence light are reflected at 90% by the beamsplitter so that 21% of the light used for fluorescence is lost instead of 75%. Because the light in each path of the interferometer in FF-OCT has been transmitted and reflected once by the beamsplitter, the ratio $\sqrt{\frac{R_{Sample}}{R_{Ref}}}$ is conserved. The drawback is that only 9% of the light can be collected instead of 25% as we could have with a 50:50 beamsplitter. However, we have chosen the 90:10 configuration, as we are much more often limited by the intensity in fluorescence than in FF-OCT, especially when using dynamical fluorescent probes.

Finally, our setup configuration requires 2 cameras, which increases its cost and complexity.

However, this is justified since FF-OCT and SIM require cameras with nearly opposite technical characteristics. FF-OCT requires fast cameras with large Full well capacities. To the contrary, fluorescence measurements require low-noise measurements, enabling the detection of a small number of photons.

5.1.3 Static association of FF-OCT and SIM

First, we are going to demonstrate the interest of our system for combining a structural information, captured with FF-OCT to a specific molecular contrast, captured by fluorescence microscopy. The static combination has already been demonstrated in previous work [187, 226, 227] and does not necessarily require that both modalities are acquired at the same time. A first advantage of combining static OCT with fluorescence is to identify structures that are captured in OCT, in order to better understand and characterize OCT contrast [206]. A second benefit is to use fluorescence to reveal some structures, proteins or ultimately any structure that cannot be captured by OCT. It can help to understand how a structure of interest integrates and evolves inside its microenvironment, such as neurons in the intestine [247] or to find the location of stem cells in the cornea [183], as we will illustrate it further in chapter 6.

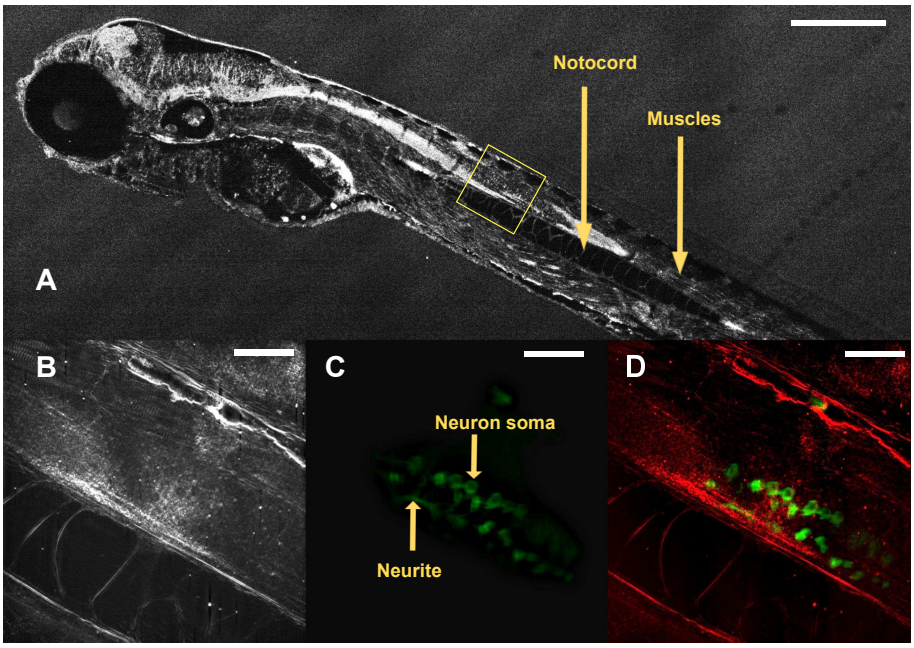

Figure 5.6 – Imaging of a Gal4^{s1020t}/UAS:GFP zebrafish larva. A. 10X wide field Full-Field OCT image of the larva 100 μm below the surface, first acquired with an FF-OCT commercial system, developed by LLTech [160]. The main functional microstructures of the zebrafish can be identified. The scale bar represents 300 μm. **B to D.** 40X 0.8 NA images of the same larva then acquired with our multimodal setup, right after the imaging with the other microscope. The imaged area roughly corresponds to the yellow box in panel A. Panel B is the FF-OCT image, panel C is the SIM image and panel D shows the overlay of panels B in red and C in green, illustrating the position of the larva motoneurons with respect to the notochord and spinal cord. All three scale bars represent 50 μm.

Figure 5.6 shows such a combination in 5 days post fertilization Zebrafish larvae with fluorescent motoneurons. Figures 5.6 A and 5.6 B show en face views of the structural contrast of a zebrafish larva at different magnifications. The main feature of the FF-OCT image is to image the microstructures of the zebrafish larva at a given depth. However, if the muscles and the notochord are clearly visible on the FF-OCT image, we can only suggest the presence of some cells corre-

sponding to small white round objects in the image. Among these cells, there is no information about their nature or their function. To identify the cells, we have imaged the same zebrafish, which is from transgenic line exhibiting GFP-fluorescent motoneurons along the larva spinal cord. Figure 5.6 C illustrates a SIM image obtained from a zebrafish larva, using the fluorescence part of our setup. Combining the two modalities allows us to see the organization of these motoneurons with respect to the surrounding tissue of the fish. In particular, we are able to see that some of these neurons have projections either onto the notochord or onto the spinal cord.

Additionally, figure 5.7 illustrates the benefit of the static association of FF-OCT and fluorescence in the context of histology measurements. Figure 5.7 shows the imaging of a tumorous intestine tissue, in which cell nuclei are labeled with fluorescence. It emphasizes the complementary contrast that can be obtained with both modalities. Additionally, with both sources of information, we can localize the cells on the contours of organized structures, named intestine villi, indicating that this field of view has been acquired in a healthy region of the cancerous tissue.

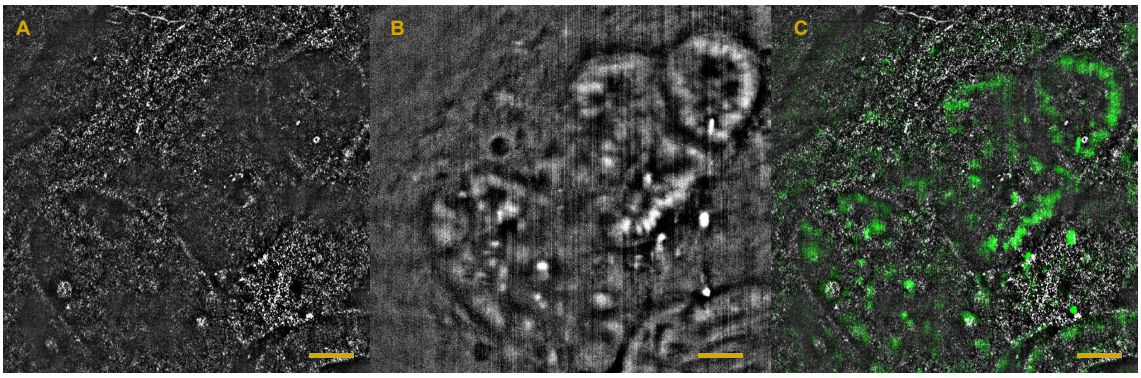

Figure 5.7 – Revealing cells in tumors with FF-OCT/SIM. A fixed tumorous tissue of intestine is imaged in FF-OCT (**A**), in Fluorescence (**B**) and the overlay is displayed in **panel C**. Fluorescence reveals cell nuclei in the tissue. These images show that the cells are located within a well-defined structure captured by FF-OCT, indicating that we are imaging in a healthy part of the tissue. The scale bars represent 40 μm.

5.1.4 Mechanical wave observation

Finally, we have imaged simultaneous dynamic processes in both FF-OCT and Fluorescence to illustrate the importance of synchronizing both modalities. Figure 5.8 presents the results of the imaging of a fresh beating rat heart interventricular septum. As expected in the literature, spontaneous uptakes of calcium should lead to fiber contractions, that further lead to heart beat [248]. In the atrioventricular node at the top of the interventricular septum, one can find pacemaker cells that spontaneously activate at a given frequency and regulate the calcium uptakes and heart beating rhythm [249]. Therefore, the interventricular septum is one of the only regions of the heart that is still beating and electrically active after dissection. If this region is labeled with a calcium fluorescent indicator, it is then possible to observe spontaneous calcium waves propagating inside the tissue, even several hours after the heart dissection. Similarly, as the calcium propagates inside the tissue, it causes fibers contraction, which creates a mechanical force inside the tissue that should be observable in FF-OCT or with other interferometric techniques.

Figure 5.8 shows one result of the imaging on such tissue [105]. More technically, we have represented the evolution of the standard deviation calculated on 5 direct images without piezo modulation. On the right-hand side, the evolution of the fluorescence signal is displayed. We can

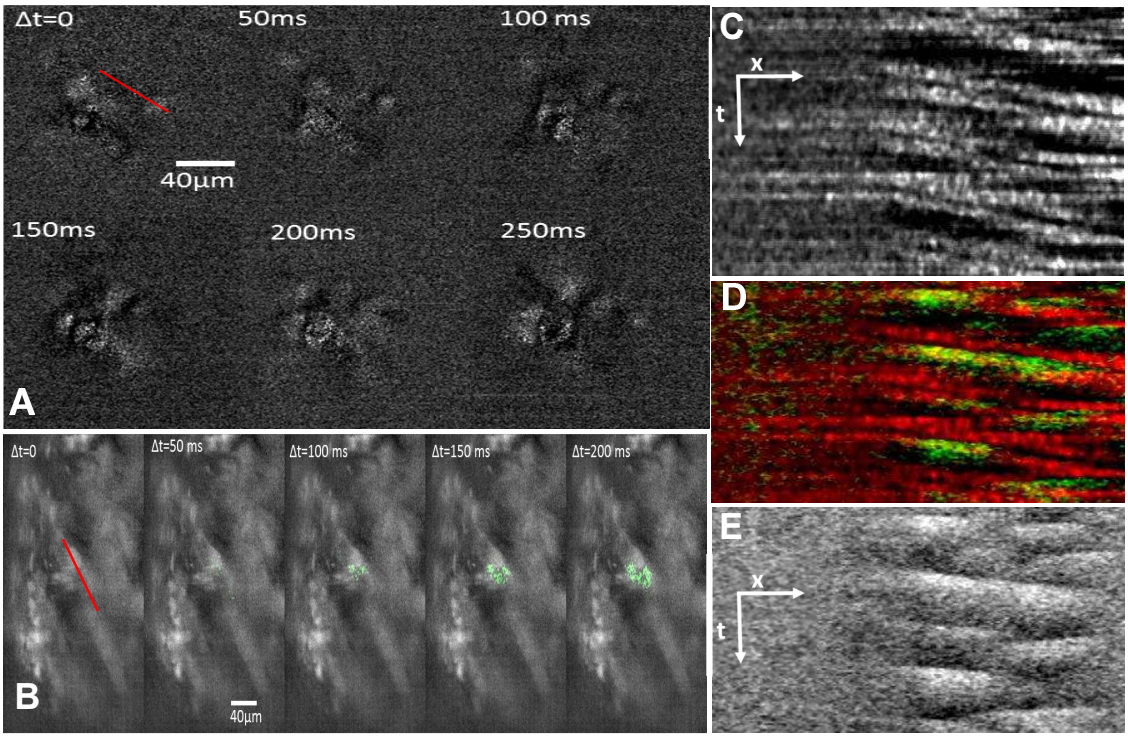

Figure 5.8 – Dynamic imaging of mechanical wave and calcium waves in a beating heart. All panels show the result of imaging a beating section of a rat heart using FF-OCT and fluorescence microscopy. The corresponding raw data movie can be found in *O.Thouvenin et al.* [105]. Panel A shows the propagation of a mechanical wave observed over time along a fiber. The corresponding fiber is masked with the red line in the first image. The images are the results of the standard deviation (STD) of 5 consecutive images to enhance the signal to noise ratio.The scale bar represents 40 μm. Panel C represents a temporal profile along the red line presented in panel A. This is the result of a sliding STD to keep the temporal resolution. On the right of the panel, the profile exhibits clear parallel tilted lines, characteristic of propagating waves. The scale bars represent 13 μm and 550 ms respectively. The slope of the lines can give us the wave propagation speed of about 100 μm.s^{-1}. Panel B shows the initiation and propagation of calcium waves imaged from the Fluo-4, a calcium fluorescent indicator, response. To enhance the signal-to-noise ratio, the fluorescence image has been superimposed on the fluorescence variation ΔF, in green, at different times. The scale bar represents 40 μm and is valid for all five images of the panel. Panel E represents the temporal profile along the red line of panel C. This fiber corresponds to the fiber along which the mechanical wave propagates, as illustrated in panels A and B. The profile represents the fluorescence difference ΔF across the fiber. Finally, panel D is the overlay of panels C and E.

identify mechanical wave and calcium waves propagating in the tissue. Figures 5.8 A and 5.8 B present the mechanical wave observed with FF-OCT, as we can see a propagating wavefront in panel A and stereotypic tilted lines in the spatiotemporal profile in panel B. This profile allows to calculate the wave speed, around 100 μm.s^{-1}, which is too slow to be a mechanical wave [250], especially in a stiff tissue like the heart. With the FF-OCT information only, it is therefore complicated to understand what this wave corresponds to. On the other hand, the fluorescence information shows slow calcium uptakes and slow calcium propagation, happening simultaneously to the mechanical waves. Figures 5.8 C and 5.8 D respectively show calcium propagation in the tissue and calcium fluctuations over time at a single position in the tissue, exhibiting a spontaneous excitation around 1 Hz. Interestingly, we have measured the propagation time of the calcium wave and have found a propagation speed also very close to 100 μm.s^{-1}. For this experiment, we used simple fluorescent measurement instead of SIM for two reasons: First, we have imaged at a depth

close to the tissue surface, so optical sectioning was less critical. More importantly, we had wanted to optimize the speed and the signal, while SIM would have required 4 images and would have reduced the excitation power due to the attenuation of the Ronchi ruling.

To conclude this subsection, our multimodal setup enables us to simultaneously acquire the propagation of a mechanical wave using FF-OCT and the propagation of a calcium wave using fluorescence. Because of the simultaneity of the measurements, we demonstrate that the mechanical waves propagating in the sample are linked to a biological activity of the tissue, *i.e.* the calcium wave, which is known to cause fibers contraction. It provides a potential mechanism explaining the initiation of mechanical waves observed. It is likely to be only the consequence of a sub-wavelength mechanical contraction of the muscle, rather than shear waves created by such deformation. We can further comment that the simultaneous acquisition was particularly critical in this experiment. Indeed, we have observed after a few minutes that the calcium uptakes have become more chaotic, which was probably the beginning of atrial fibrillation, which has led to the inactivation and destruction of the tissue. Therefore, with a switching multimodal system, by the time we take a movie with one modality, the activity may have stopped before switching to the other. And because, we are looking for waves, switching between modalities between each frame would significantly lower the acquisition speed and the wave propagation might become undetectable. Another insightful conclusion about this last experiment is that we have demonstrated the FF-OCT ability to detect mechanical waves propagation at high transverse resolution and sensitivity, in contrast to what was observed in *A.Nahas et al.* [251]. Even though these waves are too slow to be shear waves, it demonstrates that the only limit to perform dynamic optical elastography with FF-OCT is only a technological limit that could soon be overcome. If we could find a camera that could take up to 10,000 images per second with high FWC, we should thus be able to measure such waves propagation. We can add that with the new Adimec camera, the frame rate is already close to 700 frames/sec in full field. If we were to limit the number of lines to a few dozen, it might already be possible to follow a propagating wave along the columns direction at a maximal frame rate of 2 kHz (limited by the acquisition card and not the camera itself).

To conclude this section, I have reported on the development of a new multimodal system combining simultaneous FF-OCT and structured illumination fluorescence microscopy. I have illustrated the interest of this multimodal system to validate or enhance the contrast obtained with FF-OCT and its benefit in the context of histology. Finally, I would like to emphasize the importance of dynamic measurements with both fluorescence and FF-OCT. It also allowed us to combine fluorescence with dynamic FF-OCT, a phase-dependent FF-OCT signal giving us access to a metabolic contrast and revealing cells inside tissues, as I will present in the next section.

5.2 Dynamic FF-OCT

In this section, dynamic FF-OCT (D-FF-OCT) will be described in details, including available contrasts and structures that can be revealed. I will also introduce a few potential applications. Inspired by phase measurements in dynamic light scattering, OCT, and holography techniques, we have taken advantage of phase fluctuations of the FF-OCT signal to create a contrast that is significantly different from the usual static FF-OCT contrast. However, compared to the previously cited techniques, FF-OCT offers higher transverse resolution and offers widefield parallel acquisition of the phase fluctuations that reveals a contrast that is, for us, unique compared to what can be observed with other microscopes.

5.2.1 Principle of D-FF-OCT

We have developed dynamic full-field OCT (D-FF-OCT), inspired by the work on quasi elastic dynamic light scattering and other dynamic measurements to measure biological activity [173, 252–257]. We have therefore speculated whether intracellular movements and vibrations can be important enough to be able to modulate the optical path length of our interferometer by themselves, even without reference piezo modulation. Interestingly, we have found out that in fresh biological samples, calculating the standard deviation of the interferometric signal over time gives a substantially different contrast in comparison to the regular FF-OCT signal. To obtain a significant dynamic contrast, the sample has to be as fresh as possible. Usually, we have extracted organs directly after an animal sacrifice and image them as soon as possible. Hopefully, FF-OCT optical sectioning allows for minimal tissue preparation and be ready for imaging only a few minutes after the animal sacrifice. Tissues are usually kept in saline solution for transport and imaging or in complete solutions for more fragile tissues (as the brain or the eye). No dynamic contrast can be observed in tissues extracted several hours ago nor from fixed tissues. We have discovered later that this dynamic signal was somehow related to cellular metabolism [178]. Additionally, D-FF-OCT can access a motility contrast in 3-D, taking advantage of the FF-OCT low coherence to select mainly the phase variations at a given plane, as it will be detailed in section 5.2.4. Figure 5.9 presents the principle of D-FF-OCT and shows the intracellular contrast enhancement that is offered by the technique. It shows typical temporal evolution of interferometric signals at various locations inside a sample and their corresponding spectral evolution. It illustrates different dynamic features that can be revealed with D-FF-OCT, that will be detailed later in a specific section. Figures 5.9 B and E show that D-FF-OCT can reduce signal from static and potentially highly scattering structures down to the noise level and can also reveal cells that would normally be hidden by such static structures [1].

The new contrast revealed by D-FF-OCT originates from a different interpretation of the temporal fluctuations of the signal. In regular FF-OCT, temporal fluctuations are averaged out to increase the signal-to-noise ratio of strongly back scattering structures. To the contrary, in first versions of D-FF-OCT [178], we have emphasized the amplitude of fluctuations of the signal by calculating its standard deviation, as described previously. This amplitude of fluctuations not only depends on the backscattering strength, but also on the scatterers dynamics inside a given voxel. An interesting layout of D-FF-OCT is to remove the piezo modulation, since the incoherent light

[1] We can add that, due to its high phase sensitivity, FF-OCT and particularly D-FF-OCT, is very sensitive to sample motion artifacts and to mechanical vibrations. In presence of any external movements of amplitude on the order of the wavelength, the D-FF-OCT image tends to look like a blurred standard amplitude image that could be acquired with FF-OCT.

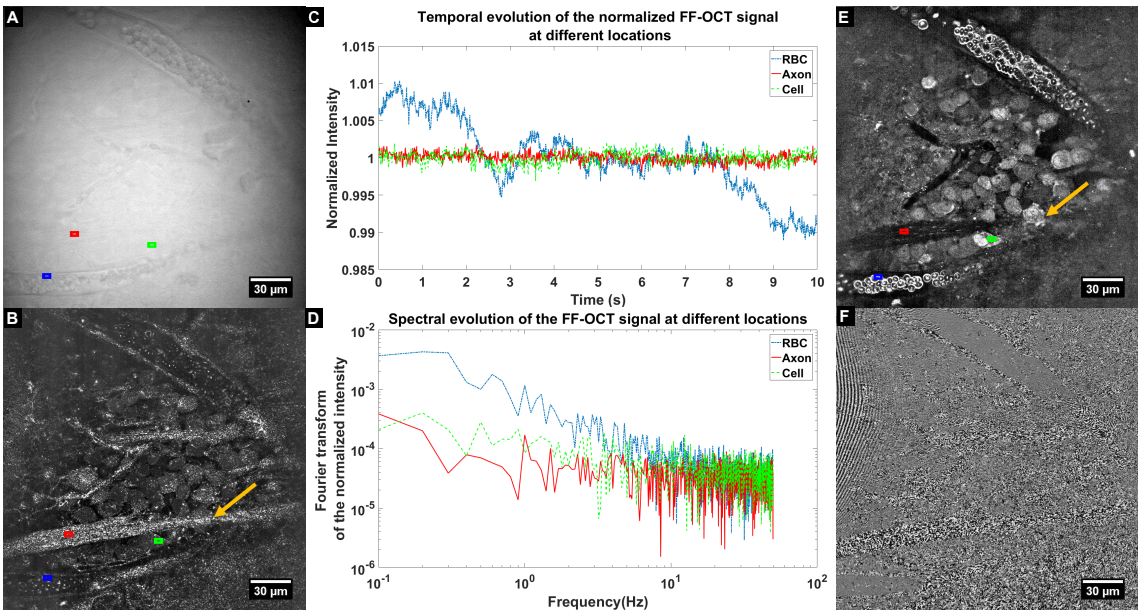

Figure 5.9 – Dynamic FF-OCT (D-FF-OCT) principle. Panel A shows the direct image of an *ex vivo* rat retina captured with our high NA FF-OCT system. If a few structures can directly be identified, the signal is dominated by the reference intensity. **Panel B** presents a classical FF-OCT amplitude image that would be obtained from a 4 phases scheme. The corresponding phase map is presented in **panel F**. In this static FF-OCT amplitude image, the dominant signal comes from large static fibers, such as large ganglion cell axons and capillary walls. Even though little differences can be found in either direct intensity signals or amplitude signals from the different regions in the image, **panel C** shows that the temporal evolution of the intensity at each region can exhibit significant differences. It illustrates the different temporal evolution of signals in either red blood cells (RBC) (blue box), axonal fiber (red box) or a cell (blue box). The RBC presents a strong variation due to its important membrane flickering, the cell presents an intermediate, but significant, fluctuation, while the signal from the axonal fiber is mainly shot-noise limited. **Panel D** presents the spectral evolution of the previous signals, which also present different specific characteristics. From these observations, we have developed D-FF-OCT, which consists in displaying a metric based on the interferometric signal temporal evolution. **Panel E** shows an average of temporal standard deviation maps calculated on a few direct images, which corresponds to the most basic D-FF-OCT scheme we use. D-FF-OCT reveals intracellular contrast, with the position of some cell nuclei. It also enhances the signal from RBC edges, highlighting their 3-D shapes. Finally, D-FF-OCT reduces the signal from static structures and is even able to reveal cells hidden below static but highly backscattering structures (yellow arrow).

varies less and more slowly than the interference term. In such a configuration, the backscattering amplitude and the phase fluctuation magnitude are coupled in the final image. In one of the next subsections, I will discuss the possibility to decouple these two pieces of information.

Now, what we generally name Dynamic FF-OCT is not only the calculation of the temporal standard deviation, but also a set of mathematical techniques that analyze the temporal fluctuations of the interferometric signal captured by FF-OCT. Through the following subsections, I will show that these fluctuations are mainly caused by phase fluctuations or movements of scatterers in the axial direction, to which OCT and FF-OCT are particularly sensitive. Trying to understand and quantify these fluctuations, we have been inspired and influenced by similar measurements performed with more standard OCT [258–261], other interferometric techniques [173, 255] or general dynamic techniques [262].

Finally, we can further comment that D-FF-OCT is attractive in terms of multimodality, as it

does not require any modification from a regular FF-OCT microscope. It can be associated with any other dual modality system to provide 3 different contrasts [105], as it will be pointed out in yet another subsection. D-FF-OCT is highly complementary to standard FF-OCT especially in fibrous environments, as fibers are highly backscattering structures and often hide cells entangled inside the matrix. However, fibers are usually still, while cells have an intracellular activity that produces a highly dynamic signal. Hence, D-FF-OCT can easily reveal these cells and suppress the stationary signal from the fibers.

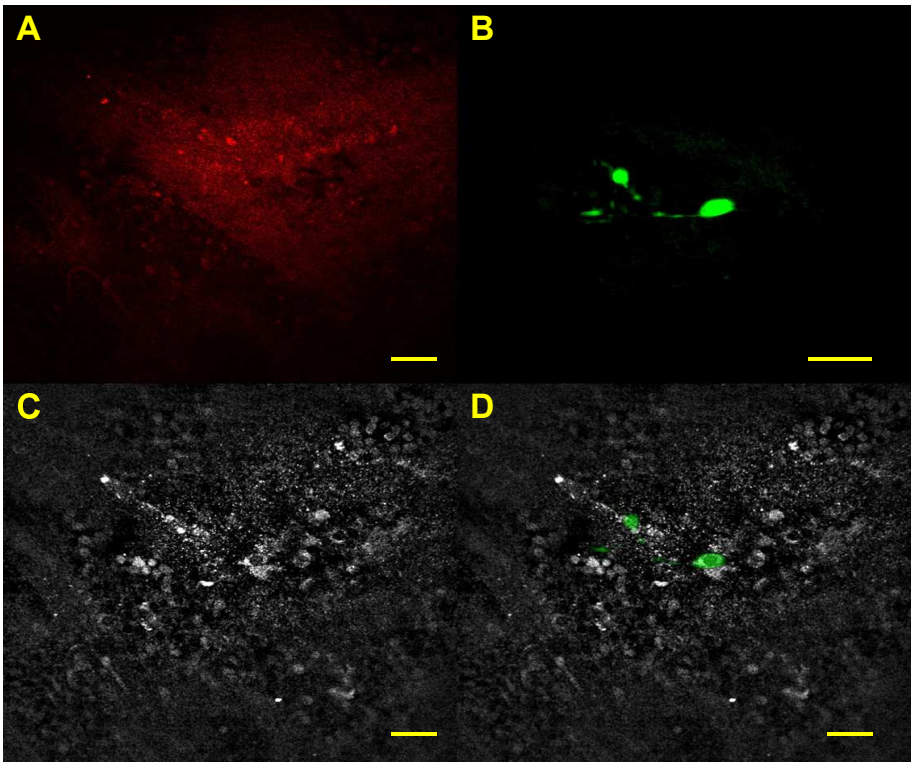

Figure 5.10 – Multimodal SIM/Dynamic FF-OCT of a macaque retina. The 4 panels show the ganglion cell layer of a fresh macaque retina revealed by 3 different modalities acquired simultaneously with our microscope. Panel A is the FF-OCT image and the signal from ganglion cells is masked by collagen signal. A sparse labeling of ganglion cells has been performed on this retina and the corresponding SIM image is displayed in panel B. Panel C shows the same field of view imaged with Dynamic FF-OCT, which removes the signal from the static collagen fibers to reveal several cells. The D-FF-OCT also reveals intracellular details. Finally, panel D is the overlay between the Dynamic FF-OCT image and the SIM image, revealing a perfect overlap between one of the ganglion cells and one cell revealed by Dynamic FF-OCT. All the scale bars represent 35 μm.

To further illustrate the benefit of our system to identify specific structures visible with dynamic-FF-OCT using fluorescence, we have imaged a macaque retina, labeled via gene gun to tag ganglion cells inside the retina. The gene gun technique produces a sparse labeling [263]. Thanks to fluorescence imaging, we were able to confirm that the cells we were imaging are indeed ganglion cells. Here, the imaging plane is in between the ganglion cell layer and the inner plexiform layer and strong signal from stationary fibers inside the inner plexiform layer dominates the static FF-OCT image, as illustrated in figure 6.3 A. However, using the temporal fluctuations of the signal, and displaying the average image over 10 standard deviation images calculated over 10 consecutive FF-OCT direct images, we could attenuate the signal from the collagen and reveal the cells at this depth, as illustrated in figure 6.3 C. However, two cell populations can be observed in the image, as expected, since the ganglion cell layer is mainly composed of ganglion cells and displaced

amacrine cells [264]. The overlay performed in figure 6.3 D shows that the ganglion cell labeled with fluorescence perfectly matches one of the cells at the center of the D-FF-OCT. In accordance with the literature describing ganglion cell morphology and distribution [264], we postulate that the dark central region corresponds to the nucleus, while the elongated bright surround is the cytoplasm. It appears that the axon hillock can also be observed in D-FF-OCT, as it matches the beginning of the ganglion cell axon labeled with fluorescence. The other rounded cells with lower intracellular contrast might then be amacrine cells. This is consistent with many more FF-OCT and D-FF-OCT images of the retinal ganglion cell layer, where the two same populations are observed [206]. In this figure, only one ganglion cell is labeled with fluorescence, due to the low success rate of the gene gun, producing a sparse labeling. The two smaller hot fluorescence spots are probably buddings along the ganglion cell neurites, which we don't necessarily see in D-FF-OCT. We can add that we are now trying to measure the ratio of ganglion cells that D-FF-OCT is able to reveal in the ganglion cell layer, but it is probably not 100%.

5.2.2 Motility contrast in cells

This initial phenomenological description of dynamic FF-OCT, as well as images laid out in figure 5.9, show that the display of the amplitude of fluctuations enhances the signal from cells while reducing the signal from stationary structures. Moreover, such contrast change had never been observed in fixed samples. Therefore, we have started to wonder whether these dynamic effects come from active processes inside cells or simply originate from passive confined Brownian motion. Indeed, as fixation can alter intracellular content, but can also modify refractive index difference distribution inside tissues, the absence of dynamic signal after fixation could originate from changes in the tissue optical properties. Similarly to D-FF-OCT contrast drop after fixation, we can observe a general decrease of the dynamic signal over time with a typical timescale of several hours for most tissues, even tough the tissue is kept at room temperature and in saline solution without proper pH or oxygen control. Nevertheless, we noted that tissues that are known to be highly energy-demanding, such as heart, brain or retina usually exhibit a faster decrease of their dynamic contrast. Figure 5.11 A illustrates such contrast decrease over time. This additional observation might help to believe that D-FF-OCT signal depends on active processes, but is still not completely convincing. Indeed, dying tissues undergoing apoptosis tend to change their volume, by first contracting and then expanding, meaning that cells inside tissues probably undergo similar volume changes, and concentrate, then dilute their intracellular material [55]. Additionally, apoptosis often pairs with an intracellular proteolysis [265], which would lead to further decrease of the cytosol refractive index. In any case, the decrease in the dynamic signal can originate from changes in the optical properties of the degrading tissue. More importantly and as reported in figure 5.11 B and C, as well as in *C.Apelian et al.* [178], we have used drugs to block the energy production inside cells and we have been able to monitor a corresponding decrease in the D-FF-OCT signal. *Clément Apelian* from our research group, have demonstrated that adding 2-deoxy-D-glucose to *ex vivo* liver samples rapidly kills all the dynamic signal (in less than an hour, compared to 27 hours with normal tissue degradation) from this tissue. It should be further noted that the injection of 2-deoxy-D-glucose is known to block glycolysis or anaerobic ATP production inside cells, but glycolysis also produces pyruvate, which is essential for aerobic ATP production of the cells. Therefore, the injection of 2-deoxy-D-glucose, without adding pyruvate, leads to a complete disruption of ATP production and to a complete stop of most active processes of the cells, including active transport.

This insightful experiment shows that signal fluctuations mostly depend on active processes inside cells and that confined Brownian diffusion does probably not create enough movements or enough movements heterogeneities to create a significant D-FF-OCT signal. However, we can discuss here the particular case of red blood cells, as illustrated in figure 5.9 E whose membrane produces a strong dynamic signal, as earlier explained in chapter 1.

But still, even with such an experiment, it is unclear whether D-FF-OCT signal comes from happily living cells or whether it is particularly enhanced in cells that are slowly entering in apoptosis, as it might enhance scatterers flow inside and outside the cell and could create such measured signal fluctuations. In order to further answer this concern, we have performed the following experiment, as illustrated in figure 5.12. It shows the result of the ClickIt TUNEL assay (from ThermoFisher Scientific [266]) on a fresh liver tissue. The ClickIt TUNEL directly probes the cell apoptotic state, even though the sample has to be fixed before. During this experiment, we have first and on purpose excised the tissue with a corner shape to elicit and follow the cell death propagation from the margin to the center of the tissue. After several minutes, the tissue has been imaged with FF-OCT and D-FF-OCT and an inactive region (dark region from the

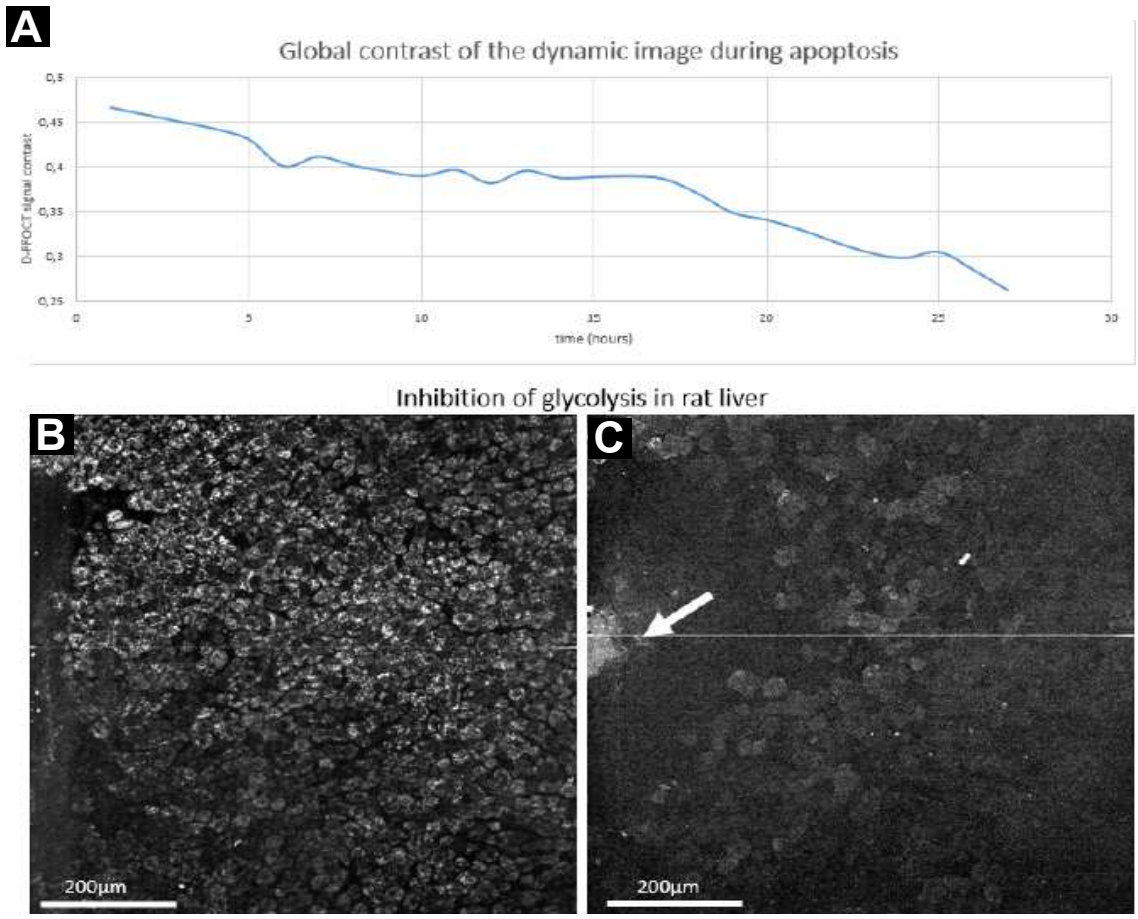

Figure 5.11 – Metabolic-dependent contrast of D-FF-OCT. Panel A presents the D-FF-OCT signal decrease over time in an excised rat liver, a particularly resistant organ. The liver sample is kept in the imaging chamber at room temperature, in a saline solution, without light exposure in between the experiments. Even if some signal can still be captured after 24 hours, the signal intensity has decreased by a factor of 2.25. The signal decreased below the noise level after 27 hours. **Panels B and C** show the evolution of dynamic FF-OCT signal after injection of 2-deoxy-D-glucose, a glycolysis and ATP production inhibitor. Panel B is the D-FF-OCT obtained right after the injection and panel C is the D-FF-OCT image at the same location after 1 hour. The white arrow points the injection site. Even though the image in panel C has been multiplied by a factor of 10, the D-FF-OCT signal looks clearly dimer and totally disappeared a few minutes afterward.

tissue margin) has been detected with D-FF-OCT (panels A to C). Directly after the imaging, the tissue has been fixed, in order to start the TUNEL assay and detect the apoptotic regions of this tissue. Unfortunately, this assay requires fixed tissues so that we were not able to overlay a D-FF-OCT and a fluorescence image. However, we have been able to detect that almost all cells in a 200 μm region from the tissue border were in apoptosis (panels D to F). The fluorescence signal started decreasing as we went further from the tissue margin and is almost equal to zero at the center of the tissue. Figure 5.12 tends to demonstrate that apoptotic cells do not produce dynamic contrast, at least for cells in apoptosis for a long time. Surprisingly, this indirect result is different from what was obtained with OCT measurements [267], where the authors have shown a decrease of the speckle decorrelation time (*i.e.*, an increase of the intracellular activity) in apoptotic cells. Explanations for this result may be the following: In contrast to *G.Farhat et al.* [267], we have used a *brute force* method to generate apoptosis, as we have physically cut the sample and have performed the imaging close to the tissue edge. It is likely that cells in the dark D-FF-OCT region

are in late stages of apoptosis. Furthermore, since cells in apoptosis tend to dilute and homogenize their intracellular material [268], it should lower the backscattered signal from the cell to a level that may be beneath our system detection limit, thus creating a dark D-FF-OCT image, even if dynamics have increased.

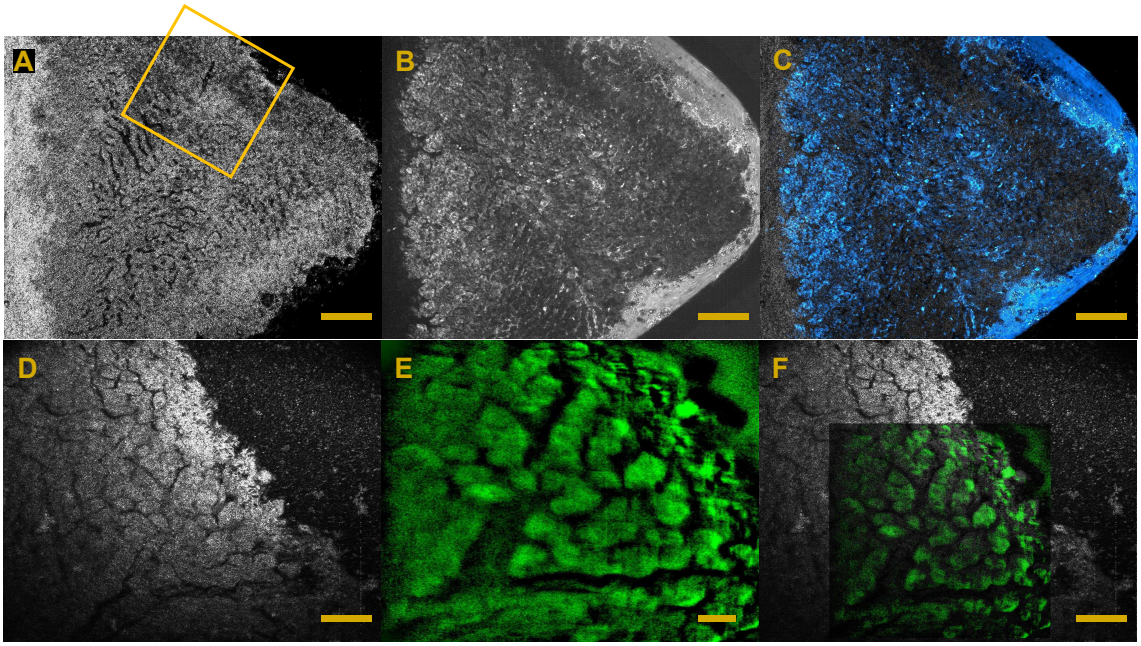

Figure 5.12 – Imaging apoptosis with multimodal FF-OCT systems. This figure presents the imaging of the edge of an *ex-vivo* liver. Here, the liver has been excised with a triangular edge to illustrate the propagation of cellular death from the excised edge. First, a large field FF-OCT and D-FF-OCT images have been acquired with the commercial LLTech system (**A,B and overlay in C**) 30 minutes after the excision. Then, the tissue has been fixed and labeled with ClickIt Plus TUNEL Alexa 488 assay (ThermoFisher) to reveal apoptotic cells. **Panels D, E and F** respectively show the FF-OCT and fluorescence signals (and the overlay) acquired from the part of the tissue in the yellow box in panel A. In this region close to the excised edge, almost all cells are apoptotic, as suggested by the low level of dynamic signal in panel B. Scale bars for panels A, B, and C represent 125 μm and scale bars in D to F represent 40 μm.

5.2.3 Separation between amplitude and phase

So far, we have mostly investigated dynamic signals from the interferometric signal variations and, therefore, we have been possibly sensitive to either amplitude or phase fluctuations (even though the phase sensitivity is supposedly much higher than amplitude sensitivity for most scatterers). Moreover, as pointed out in the two previous chapters, one of the key features of OCT technologies, and phase shifting techniques in general, is their ability to separate the amplitude and the phase information by shifting the phase in at least 3 positions. Therefore, we have naturally tried to perform similar dynamic analysis on either the amplitude or phase signals acquired from 4 phases measurements. Nevertheless, as illustrated in figure 5.13, the dynamic amplitude and phase images often look similar (with inverted contrast though) and give quite similar contrasts than what has already been observed without piezo modulation. But, more importantly, D-FF-OCT images without piezo modulation look sharper and highly scattering static structures seem to be more attenuated without piezo modulation, which seems to be counter-intuitive.

Even if we do not fully understand these observations, we will review here a few thoughts on this topic. First, figure 5.14 presents a quick and simple simulation showing that the separation

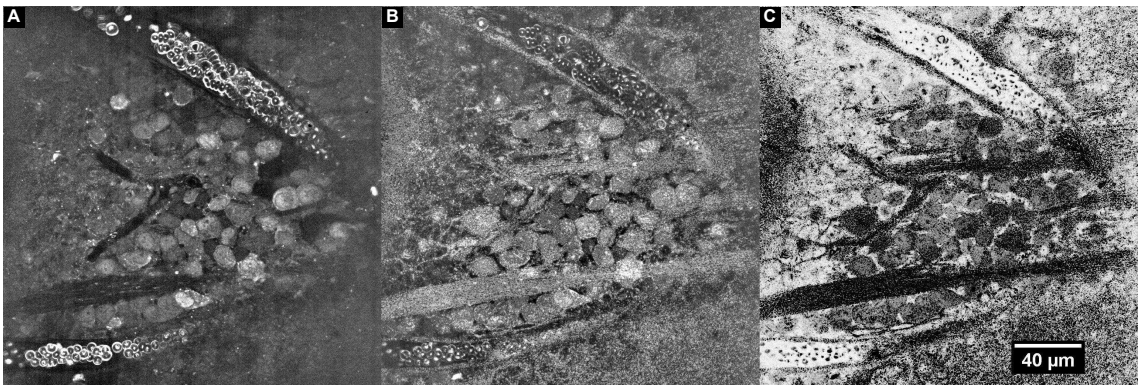

Figure 5.13 – D-FF-OCT images obtained from direct, amplitude and phase images. Panel A shows the same D-FF-OCT image of an *ex vivo* retina sample than figure 5.9 A. After acquiring direct images without piezo modulation, we have acquired the same number of images with 4 phases piezo modulation to calculate both amplitude and phase images over time. **Panels B and C** show the temporal standard deviation calculated from the amplitude and from the unwrapped phase images respectively. If the amplitude and phase fluctuations can enhance the contrast from the cells and the red blood cells, similarly to panel A, the images look less contrasted and the static structures are less excluded as well.

between amplitude and phase is in fact not really effective when the phase fluctuates more rapidly than the 4 phases process. Indeed, as mentioned in chapter 2 the 4 phases calculation of amplitude fails in presence of small additive random phase fluctuations. The calculated amplitude ultimately depends on the first order of the phase fluctuations amplitude. It might explain why the temporal STD of the amplitude gives a significant signal, and a signal similar to the temporal STD calculated either directly on the interferometric signal or on the phase image. Additionally, we might explain the loss of contrast in dynamic amplitude and phase images since the actual frame rate is divided by 4, and as a result, it might lower the sensitivity to fast phase fluctuations happening in cells. Finally, the contrast reduction might also be caused by piezo-induced movements, either axially then adding a random phase fluctuation on the entire image or laterally (a transverse piezoelectric effect can often be induced at large voltages [269]), which then would correlate neighboring pixel signals and decrease images sharpness.

Since the amplitude and phase can hardly be separated, we had to investigate some more complex signal analysis to access the different parameters of the phase signal only, as it will be described in the next subsection. Nevertheless, it shows that using 4 phases calculation might not be as important as it is for regular FF-OCT, which more or less justifies why we record direct images in most of our experiments.

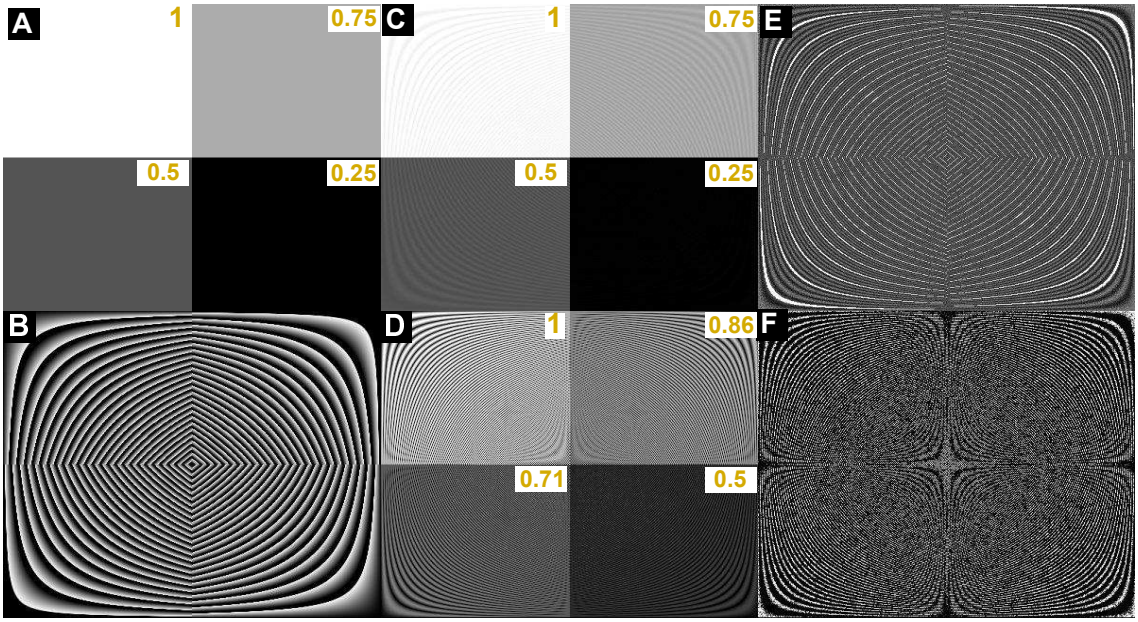

Figure 5.14 – Simulation of 4 phases reconstruction in presence of phase fluctuations. Panels A and B show the initial amplitude and phase maps respectively. For a given phase map, 4 different regions with variable contrasts (from 0.25 to 1) are computed. 1000 direct images are then calculated from these maps, with a $\frac{\pi}{2}$ phase shift and an additional random phase fluctuation (of ± 0.1 rad maximal extension) between each frame. The amplitude is constant over time. From 4 consecutive images, the respective amplitude and phase image are calculated. 250 images of each type are obtained. **Panel C.** The amplitude image shows that the phase fluctuations corrupt the amplitude reconstruction, while the temporal standard deviation (**Panel D**) of the amplitude image presents a coupling between the amplitude and the phase. On the other hand, **panels E and F** show the temporal standard deviation of the calculated phase images that do not depend on the amplitude. **Panel E** is the standard deviation map on the directly calculated phase map and shows highly varying regions that correspond to phase wrapping regions. Performing a 1D phase unwrapping prior to the STD calculation allows the reconstruction of the phase fluctuations map without artifacts (**Panel F**.

5.2.4 Origin of the phase fluctuations and optical sectioning in D-FF-OCT

We have not discussed yet the origin of the interferometric signal fluctuations, as we have never been able to find a fully indisputable unambiguous answer. In this subsection, I will discuss its origin and that, although we can not fully understand it, we can claim that we are much more sensitive to phase and corresponding axial displacements of scatterers. I will also show that we are in fact mostly sensitive to phase fluctuations caused by backscatterers that lie within the coherence volume. This will allow us to discuss the optical sectioning ability of D-FF-OCT.
The first comment to be made is that, as discussed with QPI measurements in chapter 1, the measured phase information is the spatial average of everything that backscatters the light within a voxel, that in this case corresponds to a diffraction-limited transverse pixel with a height corresponding to the coherence length. It means that the measured phase signal can either originate from the backscattering of a roughly micrometric size object (organelles, nuclei, large fibers, *etc*...) or from the complex backscattered interference between numerous nanometric scatterers (proteins, vesicles, cytoskeleton, *etc*...) and probably originates from a mix of both. If we have sometimes been able to see interference fringes on the myelin fibers [129] or on the nuclear envelopes, we have not been able to find any simple experiment to validate either of the hypotheses in the cell cytoplasm. In order to estimate the phase fluctuations depth origin and in order to estimate the optical sectioning ability of D-FF-OCT, I will take the example of a single scatterer, assuming that everything happens the same in the case of multiple small scatterers, since the collective interference signal might only produce a significant signal if all scatterers move with a net flow in a given direction. As food for thoughts, the schemes presented in figure 5.15 illustrate the interference intensity created by various displacements of a single scatterer. First, if the backscatters light comes from the moving scatterer, the particle axial motion will produce a sinusoidal modulation and require only a $\frac{\lambda}{8}$ (corresponding to a phase shift of $\frac{pi}{2}$ with the light feeling twice the displacement of the particle in backscattering) displacement to go from a maximum to the average value. On the other hand, the particle transverse motion creates an intensity modulation corresponding to the PSF decay, with a half width half maximum being equal to $\frac{0.61\lambda}{NA}$, which is about 2λ for a 0.3 NA objective and 0.75λ with the 0.8 NA objective. In both cases, the axial sensitivity is supposedly 5 to 16 times higher than sensitivity to transverse motion. More importantly, let's consider the case when the particle is outside the coherence volume, meaning that the detected interference signal necessarily originates from the backscattering by another particle. In this case, the phase at the focal plane could still be modified by phase changes happening above the coherence volume. Nevertheless, it should be noted that when the phase change happens outside the depth of focus (and outside the coherence volume), it is averaged on a section that can be much larger than a diffraction-limited spot and that corresponds to the section of the imaging cone at the particle depth. However, as illustrated in figure 5.15 D, axial motions from a particle outside the coherence volume do not create a significant phase fluctuation, as the light still passes trough the particle. Nonetheless, the phase at the focal plane can depend on the transverse flow of scatterers flowing through a section of the imaging cone above the coherence volume. As we previously noticed, we are more sensitive to axial motions so that we can most of the time neglect this transverse flow contribution, especially when particles are out-of-focus with their contributions being averaged out. Nevertheless, in the case of blood flow, which generates a large-scale net transverse flow, the phase fluctuation can be important enough to be detected several microns away from the capillary plane. Finally, because capillaries are generally large only along 1 dimension, phase fluctuations caused by the blood flow is geometrically attenuated as the coherence volume is set further apart

from the capillary. Finally, we can estimate that D-FF-OCT is able to provide optical sectioning, as it is mostly sensitive to axial phase fluctuations happening at the same coherence volume than standard FF-OCT, but keeping in mind that large phase fluctuations outside of this coherence volume can generate a significant D-FF-OCT signal.

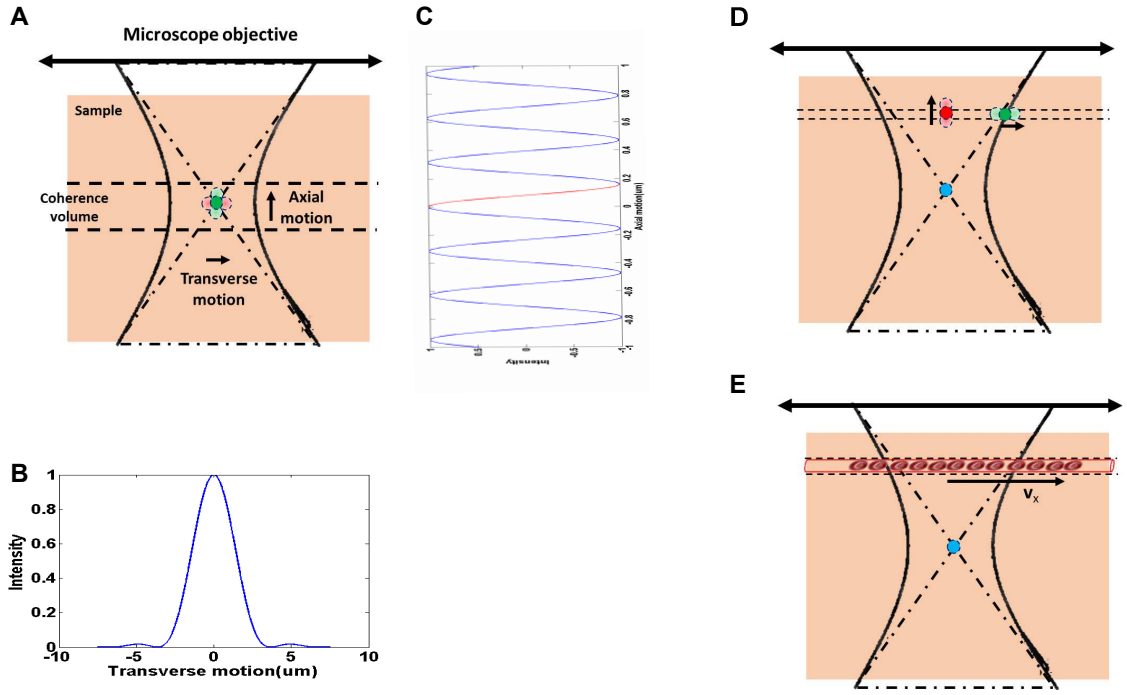

Figure 5.15 – Sensitivity to scatterers motion. Panels A to C illustrate the intensity modulation coming from a scatterer in focus and within the coherence volume. The effect of a transverse motion of the scatterer (red displacement in panel A) is governed by classical microscopy, with a signal intensity that will be attenuated as a jinc (first order Bessel function divided by its argument) function, as illustrated in panel B. Axial motion on the other hand (Panel C), will generate a sinusoidal modulation that will be attenuated as the scatterer goes out of the coherence volume. Note that, in the case of 10X 0.3NA objective and a 0.63 μm LED illumination, the scatterer has to move away from the pixel of more than 1 μm to generate a significant signal, while it requires only a 100 nm axial movement before the interference signal is divided by a factor 2. **Panel D** presents a similar scheme in the case where the scatterer is outside the coherence volume. In this case, the light goes through the scatterer instead of being reflected. Therefore, if the scatterer moves axially, the light still goes through. However, a small modulation can be obtained due to the geometrical tightening of the conical cross section. In this case, the interference signal is only sensitive to transverse motions, as a scatterer would leave the illumination path. However, the further away from the focal plane the scatterer is, the wider the cone cross section is, so the less sensitive to a single scatterer contribution the signal becomes. **Panel E** finally illustrates the case of an out-of-focus flow. If the flow goes through the entire cone cross section, the phase variation created by the flow can significantly modify the phase at the focal plane. However, this is only a 2D scheme, whereas the illumination path is a 3-D cone, while most of the biological flows are large only in one direction. The attenuation caused by the third dimension will decrease the phase coupling between the flow and the focal plane, as the flow goes further from the focal plane.

Even though the explanation might be too qualitative or a bit fuzzy, we have been able to demonstrate experimentally the D-FF-OCT ability to provide 3-D reconstructions of cells inside tissues, as illustrated in figure 5.16, with a sharp axial accuracy (hard to quantitatively estimate however). We can add that, to our knowledge, and except in the case of blood flows, we have never detected a D-FF-OCT signal from out-of-focus scatterers. As it will be discussed in the subsection on *in vivo* D-FF-OCT measurement, we have indeed been able to detect a D-FF-OCT

signal originating from a blood flow several microns away from the focus, but that eventually attenuates when going in depth away from the flow.

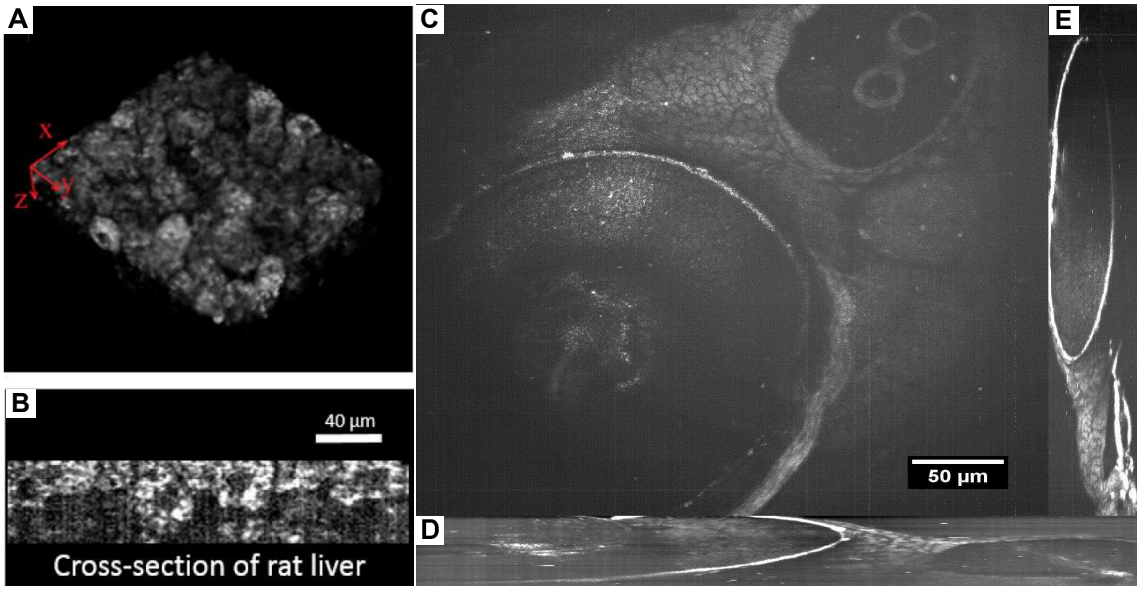

Figure 5.16 – 3-D performances of D-FF-OCT. Panel A and B are extracted from *Apelian et al.* [178] and show 3-D views of an *ex vivo* rat liver imaged with Dynamic FF-OCT with the LightCT commercial system. D-FF-OCT provides optical sectioning and allows a label-free 3-D reconstruction of the hepatocytes. **Panel A** shows a proper 3-D view of the entire sample, while **panel B** shows an X-Z projection of one line in the sample and highlights the position of nucleus inside hepatocytes. **Panel C, D, and E** show similar 3-D views of a 5 dpf zebrafish larva imaged with D-FF-OCT with our high NA microscope. **Panel C** shows a first transverse view of the larva and illustrates again D-FF-OCT ability to reveal otherwise transparent cells in complex tissues. 200 similar transverse planes have been acquired with a 1 μm step between each plane. **Panels D and E** present orthogonal slices obtained from this 3-D stack, respectively XZ slice and YZ slice.

5.2.5 Phase fluctuation signal analysis

We have already described several features that can be captured from the interferometric signal fluctuations, but so far, we have only used one component of these fluctuations, *i.e.* the magnitude of the fluctuations, while the signal is potentially much richer. Additionally, the amplitude of fluctuations that we calculate is also coupled to the FF-OCT signal amplitude, as we have seen in the previous subsection.
To extract more information from these dynamic signals, we have tried to run various analysis to properly emphasize not only the amplitude of fluctuations, but also the time scales of their variations. This subsection is dedicated to the description of these different analyses. I will present several of them, as well as a useful way for displaying all these pieces of information in a single 2D image. It will emphasize that two major different features can be extracted from these fluctuations, the amplitude of fluctuations, that is referred to as *motility metrics* [270] or *metabolic index* [271] on one hand and the time scales of fluctuations on the other hand. We have been able to demonstrate that these two features create two significantly different contrasts, as it will be illustrated in figure 5.19.

Standard D-FF-OCT analysis and color coded D-FF-OCT

Our initial treatment of the D-FF-OCT signal has consisted in calculating the temporal standard deviation on several consecutive images and then in averaging the computed sub-stack. If such treatment reveals the amplitude of fluctuations, we have also rapidly realized that it was possible on the size of the sub-stacks from which we calculate the standard deviation in order to get a first idea of the local temporal dynamics. For example, if we calculate the standard deviation on 5 to 10 images (corresponding to a total time of 100 ms), the standard deviation will be significant for rapidly-fluctuating structures, while slower structures will have almost no temporal variation, meaning that after average it will only emphasize fast scatterers. On the other hand, calculating the standard deviation on longer sub-stacks (100 images or 1 second) emphasizes both fast and slower scatterers. Usually, if the standard deviation is calculated on the entire stack, without averaging, the resulting image looks like the OCT image, which is probably caused by external motion artifacts. To extract intermediate dynamics, we can use a treatment consisting in starting to average on a few consecutive images to eliminate the fast phase fluctuations, then calculating the standard deviation on a few consecutive images of this first sub-stack and finally average the remaining images. From such a naive treatment, we have been able to generate 3 colors map to emphasize different temporal dynamics, as illustrated in figure 5.17 A, in which the blue color corresponds to the fast dynamics, the green color to intermediate dynamics and the red color to the slow dynamics, somehow comparable to the FF-OCT amplitude image. However, this requires to manually choose the color balance to emphasize a particular contrast, which obviously introduces a bias. Clément Apelian has therefore particularly worked on the computation of an automatic colormap that would be comparable between different data sets and would be user-independent. It is usually performed by using an HSV (hue-saturation-value) color space that permits to define the central wavelength, the color saturation and the pixel brightness independently, and that can finally be transformed to a more usual RGB color space so that it can be displayed in usual image formats. We can choose different metrics for the three different parameters, but a useful set of parameters is to choose the characteristic frequency that defines the exponential decay of the Fourier spectrum as the central wavelength (I will detail this frequency in the next paragraph), *i.e.* the hue, to have a fix saturation value of 0.9 and to choose the amplitude of fluctuations (standard

deviation on 100 images averaged 10 times for example) as the value. Such a user-independent color coded D-FF-OCT image is illustrated in figure 5.17 B.

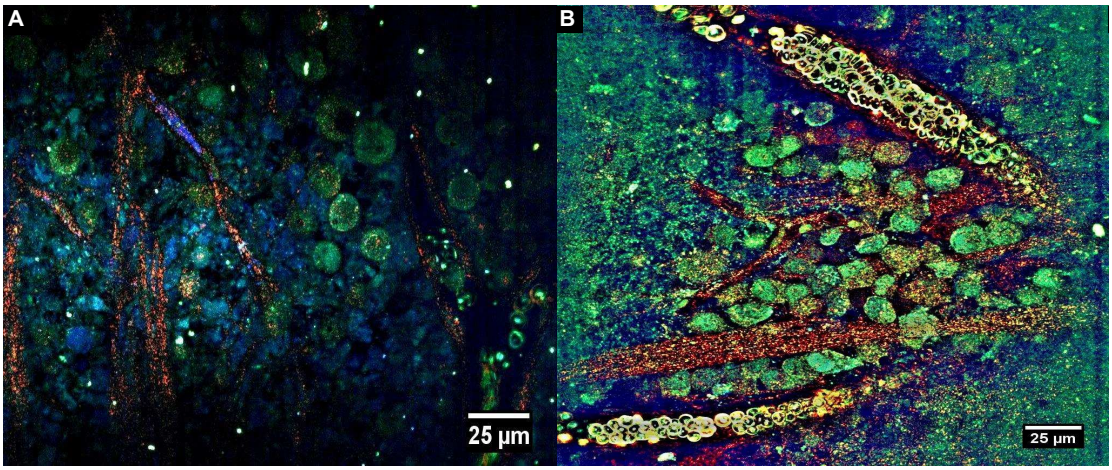

Figure 5.17 – Color coded D-FF-OCT. Panel A shows an RGB display of the D-FF-OCT signal obtained in a rat retinal ganglion cell layer. The red color corresponds to the amplitude FF-OCT image. The green color corresponds to a D-FF-OCT image computed by averaging 10 frames, calculating the STD on 10 images and averaging again 10 times. It eliminates the fast varying signals while emphasizing the intermediate dynamics. The blue color corresponds to the fast dynamics, obtained by calculating the STD on 10 images and averaging on the 100 calculated frames. If we can segregate a few different objects using either the shape or the color, the balance of colors has to be manually adjusted. **Panel B** presents a way to go around that by calculating a colormap depending on the signal characteristics. This image has been taken in another rat retina, also in the ganglion cell layer. It has been obtained by transforming an HSV color space into a regular RGB space. In the HSV color space, we used the characteristic temporal frequency as the hue, a fixed saturation of 0.9 and the amplitude of fluctuations as the value, calculated at each pixel of the image.

Display of the temporal characteristics of the phase fluctuations signal

To obtain an information about the temporal scales of variation of the phase fluctuations signal, we have tried several strategies that I will describe and compare. One of this strategy consists of fitting the slow part of the autocorrelation function as a bi-exponential; it has been mainly developed by Charles Edouard Leroux, a post doc of the team [111]. The autocorrelation function (ACF) is hereby defined as:

$$ACF_{ij}(\tau = m.dt) = \frac{1}{N-m} \sum_{k=0}^{N-1-m} OCT_{ij}(k).OCT_{ij}(k+m) \tag{5.5}$$

with m the number of shifted images, dt the acquisition frame time and OCT_{ij} the interference signal recorded at the pixel (i,j). The calculation of the autocorrelation function is computationally intensive on large data sets, but it provides useful information. First, the signal strength can be accurately estimated by the zero lag amplitude ACF (dt) of the autocorrelation function [111,260] so that the ratio $\frac{ACF(\tau)}{ACF(dt)}$ only bears the temporal evolution of the phase fluctuations signal. This ratio can ultimately be fitted by a biexponential function that is often used to model a continuous distribution of characteristics times:

$$\frac{ACF(\tau)}{ACF(dt)} = \alpha e^{-\frac{t}{T_1}} + (1-\alpha)e^{-\frac{t}{T_2}} \tag{5.6}$$

The model sorts the fluctuations into two populations of respective fractions α and $(1-\alpha)$ exhibiting either a fast decorrelation time T_1 or a slower decorrelation time T_2. In developing spheroids, T_1 is on the order of 0.5 to 1 second, T_2 of 3 to 10 seconds and α is typically around 0.3 [111]. This biexponential fit is supposedly advantageous since we can probably distinguish between an active transport component and a more passive subdiffusive component [111], which both are regulated by different molecular pathways. Nevertheless, both the autocorrelation function computation and the bi-exponential function are time-consuming calculation, especially when dealing with data sets of several Go and are also quite sensitive to noise. To increase the SNR and decrease computation time, we could either bin the spatially adjacent pixels, manually select region of interest, or corresponding elements matching together, or finally average pixels of similar signal strength, assuming that they originate from similar biological structures (see figure 6 in *C.E.Leroux et. al.* [111] for this last segregation strategy).

Alternatively, fluctuations timescales can also be estimated by calculating the Fourier transform of the time signal at a given pixel or a set of pixels. Then, two strategies are possible. It is first possible to select 3 frequency bands and associate them with one color of the RGB color space, as illustrated in figure 5.18 E and F, in a similar way to what was described in the previous subsection by changing the size of the sub-stack on which we calculate the standard deviation. A more subtle way of using the Fourier transform is to fit the interference signal power spectral density by an inverse power law function, similarly to what was performed in a paper from . *A.Oldenburg et al.* [260]. It appears to correspond to the estimation of a fractal dimension [272], as suggested by Clement Gastaud, an M2 intern in our group who has worked on these fluctuations signal analysis, which can be explained by the average contribution of scatterers with a continuous distribution of characteristic times [273]. The fractal dimension can arise from the automatic self-organization of dissipative dynamical systems with many temporal and spatial degrees of freedom [260, 274], which is likely to be a good estimation of our signal origin. Here, the computation of the fractal dimension is much faster than the autocorrelation, as it simply requires the calculation of the signal squared, its Fourier Transform, and to linearly fit its logarithm. However, in practice, the scales of variations of the fractal coefficient being quite narrow, it requires an accurate fit of the signal and, therefore, a good SNR. To reach a high enough SNR, we often have to bin the spatially adjacent pixels, similarly to what was performed for the autocorrelation function calculation.
Figure 5.18 illustrates some of the hereby described signal analysis strategies.

Difference between the amplitude of fluctuations and the characteristic times

Hopefully, I have not put all these previous different methods simply to show you how many of them we have tried, but because we can extract information that is significantly different than the usual amplitude of fluctuations we can obtain using the standard deviation and average process. I believe that figures 5.19 A and E, adapted from the work of C. Apelian [271] are of great importance, as they show that these different ways to analyze the D-FF-OCT signal produce significantly different contrasts. By combing them, it becomes possible to create clusters helping to segment the different pixels according to the cell type or even cell state they are corresponding to. Even in cases where the STD process was not accurate enough to separate the signal from the different cells. However, these results are still preliminary and need to be confirmed on a larger scale. At the end, the ultimate objective we are hoping to reach with these treatments would be to create a user-free automatic cell segmentation algorithm that would be able to automatically detect the number of cells corresponding to each cell type, compute cell density and the state of

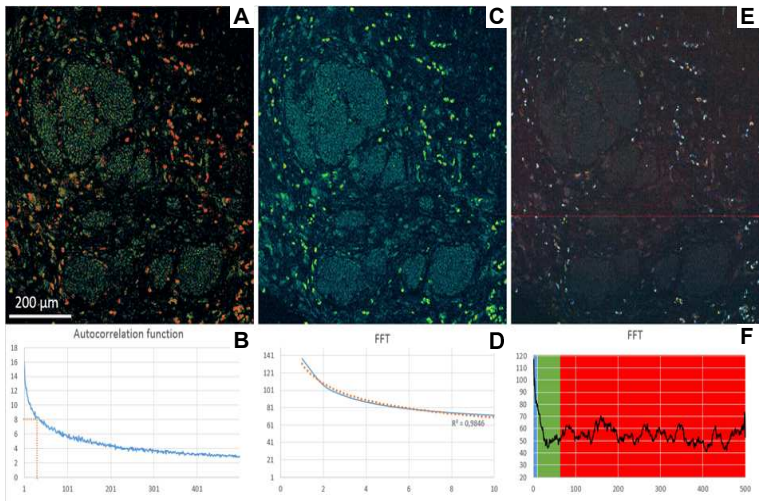

Figure 5.18 – Estimation of characteristic times of variation of the D-FF-OCT signal and corresponding color coded maps. All panels present several frequency-based analysis of the D-FF-OCT signal and are adapted from [271]. **Panel A** shows a D-FF-OCT image of a rat cancerous intestine with the color code based on the full width at half maximum of the individual pixels autocorrelation function. The color code is simply an LUT from Fiji. **Panel B** illustrates the mean autocorrelation function calculated on a few adjacent pixels in a cancerous region of panel A. **Panel C** shows a D-FF-OCT image of the same sample, with a color code calculated using an exponential fit of the power spectrum computed at each individual pixel. One of such fit is displayed in **panel D**. Here, the color code is given by the *Green Fire Blue* LUT from Fiji. **Panel E** shows yet another temporal analysis of the D-FF-OCT signal using the temporal Fourier transform calculated at each pixel. 3 frequency bands are then arbitrary chosen and associated with one color of the RGB space. **Panel F** shows the separation into 3 frequency bands at a given pixel.

the cells, leading to automatic diagnostics. This is the main objective of *Clément Apelian* thesis and these results show an important step forward towards that goal. Finally, the complexity of these signals should be emphasized, making such deep and complex multi-parametric analysis a pre-requisite to analyse fine motility changes in the future.

Singular Value Decomposition for signal extraction

Finally, both our group and *H. Ammari* 's [275] have also used singular value decomposition (SVD) to better separate large structures that are slowly varying from smaller structures that are varying more rapidly. SVD can also eliminate slow movements from the entire sample, in a similar way to what was obtained in ultrasounds [128]. SVD is the spatiotemporal equivalent of the more famous principal component analysis (PCA) and consists of finding an appropriate space to accurately describe the spatiotemporal evolution of the signal. To the contrary of Fourier transform, wavelet transforms and other metric-based transformations, SVD and PCA work in a metric that corresponds only to the corresponding data set and can not be directly interpreted in terms of spatial and temporal frequencies. However, because they use data-based metrics, they might better separate clusters of variations [276]. Both PCA and SVD are based on a matrix-based diagonalization of the initial spatiotemporal dataset. In the case of a 3-D or 4D time-space dataset, PCA aims at identifying spatial clusters of similar temporal evolution and outputs several eigenvectors, that are the corresponding spatial maps of those clusters. They are sorted in terms of their ability to better fit the entire dataset. On the other hand, SVD aims at identifying spatiotemporal clusters of similar spatiotemporal evolution. The difference lies in the ability of

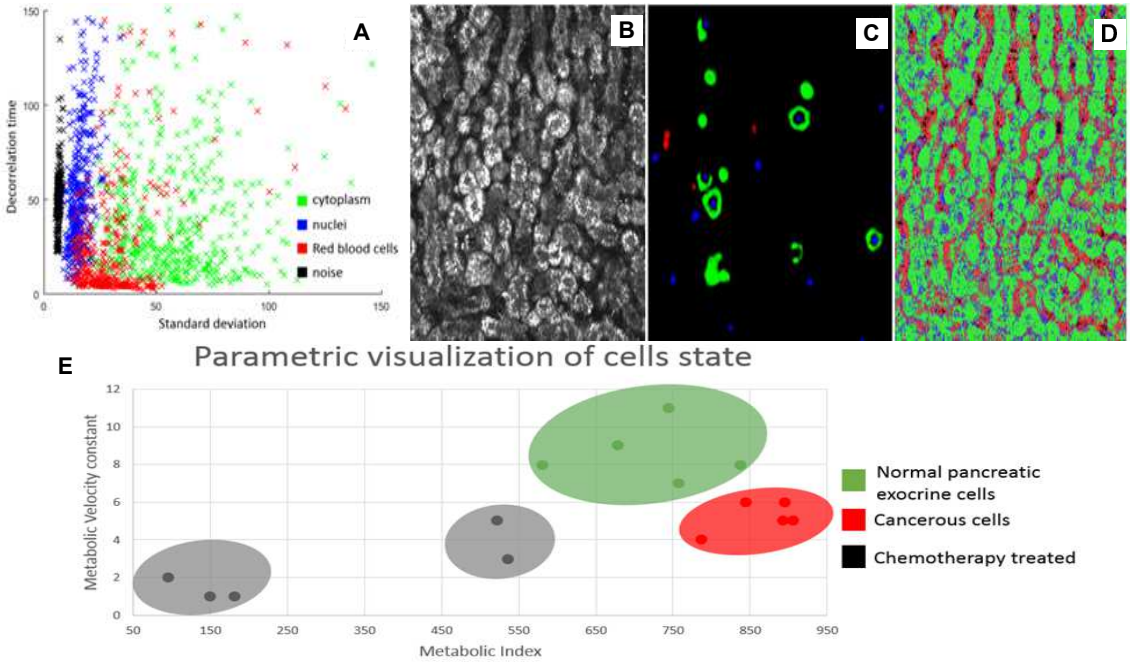

Figure 5.19 – Orthogonality between dynamic parameters and automatic segmentation using the full information of the D-FF-OCT signal. Panel A to D show a calculated segmentation. From a given D-FF-OCT image of a rat liver (panel B), pixels corresponding to cytoplasms (green), nuclei (blue), red blood cells (red), or noise (black) were manually selected (panel C).At each corresponding pixel, the standard deviation (in arbitrary units) over 100 consecutive images and averaged 10 times is calculated and plotted versus the decorrelation time (in ms) in panel A. Different clusters can be interestingly observed so that we can finally take all pixels of the first image, plot them on the same graph and give them a color corresponding to the cluster they most likely belong to. The result of this treatment is displayed in Panel D, showing a good agreement between the estimated and the observed cell types. **Panel E** presents preliminary results on a similar segmentation algorithm in healthy and cancerous human pancreas samples. We hope to be able to create four separable clusters that could either identify healthy cells, cancerous cells, efficiently treated cells and necrotic cells. All panels are adapted from [271].

SVD to extract a given pattern, not only spatially, but also temporally. SVD outputs a set of spatial eigenvectors, as well as a set of temporal eigenvectors, that corresponds to the specific temporal pattern followed by the corresponding spatial pattern. In brief, SVD imposes a coupling between the temporal and spatial evolution of the data and is supposedly efficient to filter out large scale slowly varying external mechanical vibrations and to filter out the shot noise, as it is supposed to vary independently from one pixel to the other and from one time frame to the other (then high temporal and spatial frequencies).

To describe the SVD mathematically, let's take a 3-D spatiotemporal data set M(x,y,t) of dimensions (N_x, N_y, N_t) and transform it into 2 dimensions by concatenating the two spatial dimensions into one:

$$M(x, y, t) = M'(s, t) \tag{5.7}$$

M' dimensions are $(N_x.N_y, N_t)$, that we will try to decompose using an SVD algorithm to create a set of spatial eigenvectors U, a set of temporal eigenvectors V and a diagonal matrix corresponding to the eigenvalues:

$$M' = UDV^* \tag{5.8}$$

Dimensions of U, D, and V respectively are $(N_x.N_y, N_x.N_y), (N_x.N_y, N_t)$ and (N_t, N_t), which is

problematic in our case. Indeed, for large N_x and N_y, the SVD calculation has to compute a matrix of size $(N_x.N_y)^2$ or 10^{12} in our case and would require having a computer with at least 1 To of RAM! An option would be to reduce the field of view, but, in the end, it is not very convenient to combine images as they are projected onto different eigenvectors. Additionally, when using SVD with rectangular matrices M', the maximal number of eigenvectors that we can compute at the end is limited by the smallest dimension, meaning that the D matrix is diagonal in its upper part of dimension (N_t, N_t) and there are zeros in the rest of the matrix. It also means that in the very large matrix U, there is plenty of useless information, as it will be multiplied by zeros when reprojected. Anyway, we calculate a tremendous amount of data, while only a fraction of them contains meaningful values.

Nevertheless, after a discussion with Amaury Badon and especially Charlie Demene from the Institut Langevin, we came out with a trick to reduce the computational cost of our SVDs. A similar scheme can exist somewhere else and is possibly not quite accurate from a mathematical point of view but it gives decent results in our case. First, we want to reduce the dimension of the matrix to the useful dimension so that we compute the matrix $(M')^*M$, which dimensions are (N_t, N_t) and to apply the SVD algorithm on this matrix:

$$(M')^*M = (UDV^*)^*.UDV^* = (VD^*U^*).UDV^* \tag{5.9}$$

Therefore, the large matrix U gives the identity and the diagonal matrix remains a diagonal matrix:

$$(M')^*M = VD^2V^* \tag{5.10}$$

Therefore, if we now apply an SVD algorithm to the matrix $(M')^*M$, it is possible to obtain a diagonal matrix with the matrix M eigenvalues squared, resulting in an computation of the diagonal matrix D, also enabling direct access to the matrix V, corresponding to the temporal eigenvectors. Finally, we can calculate a reduced matrix U, that we will call U', that corresponds to the useful part of the matrix U, of dimensions $(N_x.N_y, N_t)$ and that contains the spatial eigenvectors of M:

$$U' = MD^{-1}V \tag{5.11}$$

Finally, we have to reconstruct a 2D image from one eigenvector (A $(N_x.N_y)$ size column of U). In the end, this all procedure last only a few minutes, instead of one day that would be required if the SVD was performed on independent subspaces.

Figure 5.20 presents an example of a data set where the SVD was useful. In that case, there are 2 important artifacts that prevent us from getting a neat D-FF-OCT image. First, there are bubbles in the reference that create a strong noise and that can be seen on the D-FF-OCT. Additionally, the tissue is slowly sliding down, which blurs the D-FF-OCT image. By using an SVD, we can choose the eigenvectors corresponding only to the cell activity. Basically, the first eigenvector corresponds to the strong signal from the reference arm, including the bubble vibrations. It is also worth noting that the eigenvectors after rank 11 are mostly noise. However, the choice is quite arbitrary, even though we could attempt to give an arbitrary threshold on the energy. In *H.Ammari et. al.*, they have demonstrated that SVD should be able to separate static signals from fibers (low spatial and low temporal frequency) and dynamic signals from cells (high spatial and high temporal frequency) [275] but SVD does not seem to perform much better than D-FF-OCT with standard deviation. Finally, it would eventually make more sense to apply a PCA algorithm to our data sets in order to identify spatial clusters of identical temporal variations. Nevertheless, PCA only works on the spatial components and would compute the above mentioned U matrix

which requires more than 1 To of RAM but we couldn't find any solution to go around that nicely.

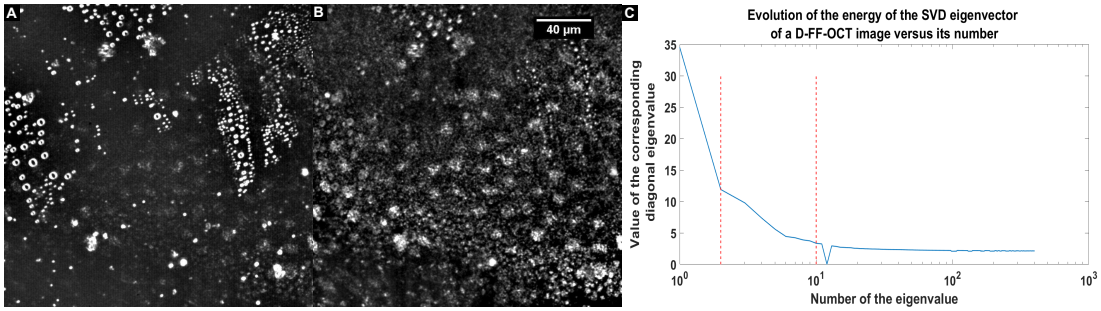

Figure 5.20 – D-FF-OCT with Singular Value Decomposition (SVD). Panel A shows a poorly contrasted D-FF-OCT image of a rat retina photoreceptor layer. Here, the poor contrast comes from moving structures in the reference arm that can hide some of the sample D-FF-OCT signal and from sample motions that blur the signal. **Panel B** shows the standard deviation calculated on 10 eigenvectors computed with an SVD.**Panel C** plots the singular value of the corresponding eigenvectors versus their rank and show the decrease of the singular value. To compute panel B, we exclude the first eigenvector that looks like the reference arm signal and exclude all the eigenvectors after rank 11 that mostly contain noise. The selected eigenvectors lie within the arbitrary region delimited by the red dotted lines of panel C.

5.2.6 D-FF-OCT for histology and to reveal various sample features

Although the location of cells bodies can often be inferred from the FF-OCT image in regions with low signal, D-FF-OCT can for example make the difference between a cell and a local oedema (which appears black in D-FF-OCT). It also gives a better precision of cell contours. In figure 5.21 and in the cortex region of coronal brain slices, the position of neuron somas can be inferred from the FF-OCT image, but the dynamic image can better reveal individual neuron shapes and sizes, from which the neuron type might be inferred (pyramidal or stellate neurons). Ultimately, identification of cortical layers can be performed *in situ*.

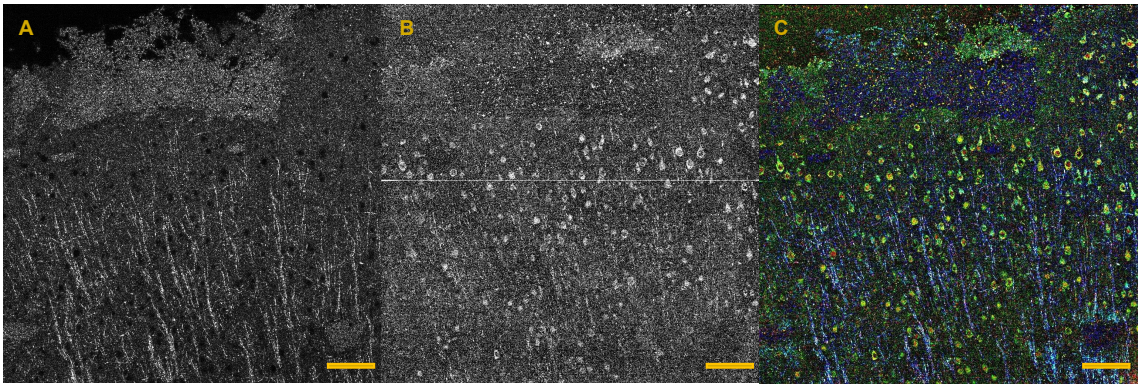

Figure 5.21 – D-FF-OCT as a histology tool for the brain. This figure presents a combination of FF-OCT (**P**anel A) and D-FF-OCT (**P**anel B) in a thick coronal section of fresh *ex-vivo* rat brain. This image has been acquired at a few dozen microns below the section surface and presents the first cellular layers of the cortex. It reveals myelinated axons in FF-OCT, as well as the neuronal cell bodies in D-FF-OCT. **P**anel C shows a frequency analysis performed in D-FF-OCT, which reveals highly dynamic nuclei in red, neuronal cytoplasms with intermediate dynamics (mostly in green) and mostly static myelin fibers in blue. The scale bar represents 60 μm.

In addition, D-FF-OCT may play an important role as a diagnostic tool since it can detect nuclei in large cells (Figures 5.22 E and F and figure 5.21). Nuclear size and shape is an important biomarker of cancer, with higher nuclear to cytoplasmic ratios in tumor cells [277, 278]. Nuclei mainly appear black in D-FF-OCT, even though the inner dynamics of the nuclei are significant and usually faster than cytoplasm dynamics [254]. Our hypothesis for the dark appearance of the nuclei is that they are more densely packed than cytoplasm and appear somehow homogeneous at a 1 μm resolution. Inside a homegenous nucleus, there should be no backscattering except on its contour and no dynamics to image, which may explain why nuclei appear black in both FF-OCT and D-FF-OCT. Interestingly, imaging cells with higher NA objectives and with a transverse resolution below 500 nm, allows us to recover some dynamic signal inside nuclei (See figure 5.22 F as an example).

Another useful D-FF-OCT feature for diagnosis is its ability to detect red blood cells and immune cells (See figure 5.22 B, D, and E). Indeed, in *ex-vivo* tissues, red blood cells are trapped inside capillaries and can be imaged even at low framerates. Due to their strong membrane fluctuations [53], they produce an intense and fast dynamic signal (See figure 5.22 E and G) on their edges. Similarly, immune cells are known for their intense motility as they are constantly exploring their environment and changing shapes, as their protrusions are looking for abnormal markers to suppress [279]. The nature of the immune cell might even be inferred from their motility coefficient [279]. Firstly, D-FF-OCT can therefore detect immune cells infiltration inside the tumors, which seems to be correlated with the tumor grade [280, 281]. Secondly, FF-OCT can

usually detect capillaries, but cannot make the difference between a blood vessel and a lymphatic vessel. Thanks to the additional information from D-FF-OCT and by detecting either red blood cells or lymphocytes in a vessel, a more accurate angiogram and lymphogram could be established in cancerous tissues. Furthermore, correlations between an increase in the blood vessel density and tumor grades have been well established for a long time ([282, 283] among many others). Similar results with the lymphangiogram have been obtained [284]. Quite generally, denser angiograms and lymphangiograms increase the risk of metastasis.

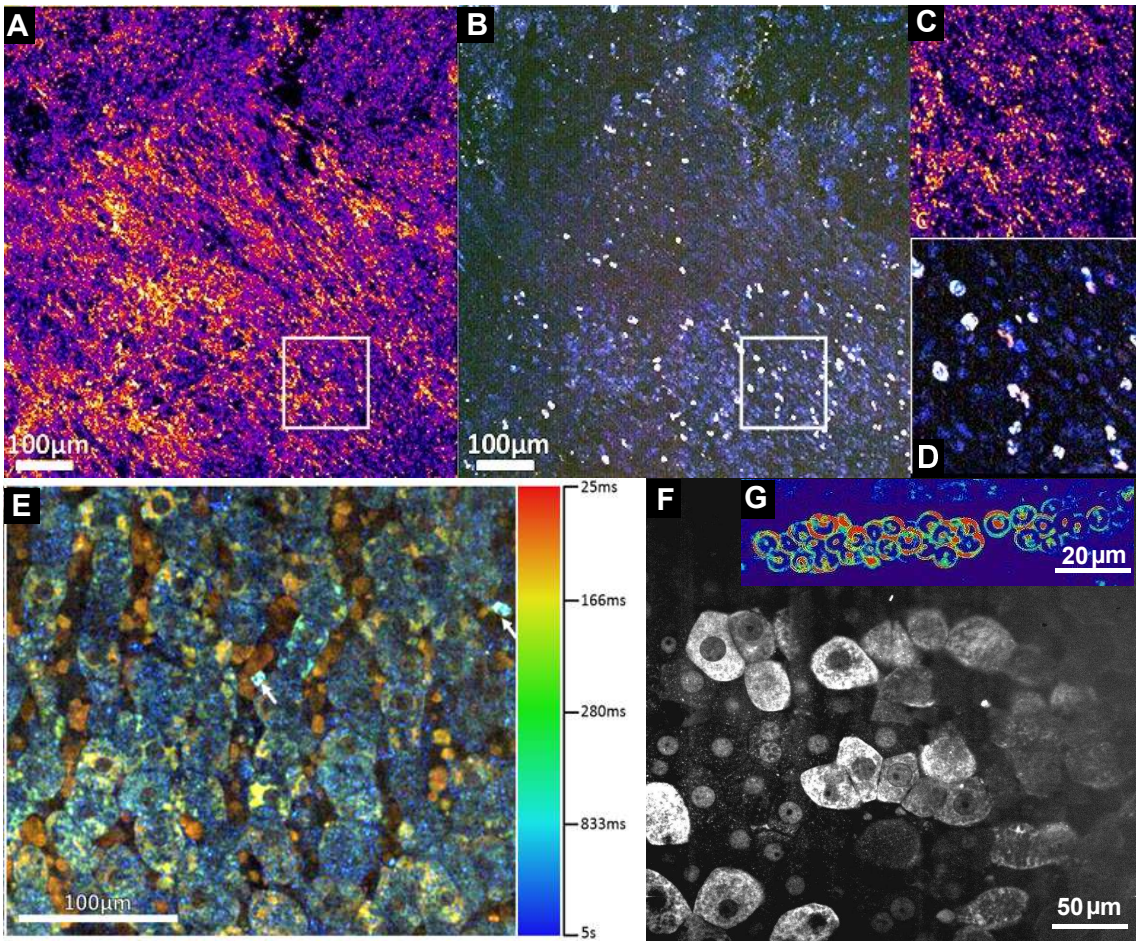

Figure 5.22 – Dynamic FF-OCT accessible contrasts. A and B. Same field of view of an *ex vivo* subcutaneous pancreatic tumor respectively with FF-OCT and D-FF-OCT. Panel A shows a fibrous environment dense in collagen fibers without specific cues of cancerous cells. On the other hand, panel B identifies slowly varying cell bodies (in blue) and rapidly varying immune cells (bright white cells). **C and D**. Zoom corresponding to the white areas of panels A and B respectively. **E**. D-FF-OCT image of a fresh rat liver with 10X 0.3 NA objectives, based on a frequency analysis to compute the color. D-FF-OCT can reveal hepatocyte cytoplasms and nuclei(black region at the center of cells), organized along stationary capillaries, characterized by the presence of rapidly varying red blood cells trapped inside. **F**. D-FF-OCT image of a similar fresh rat liver with 40X 0.8 NA objectives. The increased resolution allows to better capture intracellular dynamics and to capture some dynamic signal inside the nucleus. **G**. High-resolution image of red blood cells trapped in a capillary of a fresh rat retina, acquired with the 40X 0.8 objectives. The better resolution allows capturing the enhanced dynamics localized at the red blood cells membrane.

D-FF-OCT is promising, when compared with digital holography techniques [173], dynamic light scattering techniques [254] or quantitative phase imaging [94, 285, 286], as it provides optical sectioning and can access motility-based contrast in 3-D in scattering tissues with a subcellular

resolution. Additionally, compared with dynamic OCT techniques [153, 261], we take advantage of the higher spatial resolution to capture subcellular variations, which further permit the cells to be revealed. To our knowledge, the contrast revealed by D-FF-OCT is therefore quite unique. Similar dynamic measurements in OCT mainly focus on the blood flow velocity [150, 151, 261], even with high transverse resolution [287] similar to ours, but they never directly show dynamic signals coming from intracellular dynamics. We are wondering whether it comes from a loss in the signal collection due to the use of lower NA illumination, from a difference in the algorithms used (if only blood flow was expected), or from a difference in the exposure time per pixel.

5.2.7 D-FF-OCT signal variation under different conditions

So far, we have shown the D-FF-OCT ability to measure a metabolic contrast from intracellular motions inside tissues. However, it is quite surprising at first to obtain such a contrast while the *ex vivo* tissues we usually image are far from optimal operating conditions. In this subsection, we will first discuss the effect of temperature on D-FF-OCT contrast and on cells metabolic activity in general. Then, I will discuss the possibility to use D-FF-OCT not only to reveal different cells inside a tissue, but also to measure and compare cell motility, notably in presence of cytoskeleton inhibitors.

Effect of temperature

One fundamental effect we first wanted to investigate was the effect of temperature on D-FF-OCT. We have always been quite surprised to be able to monitor a metabolism-based contrast at room temperature in *ex vivo* tissues far from their optimal operating conditions. I will start this subsection, trying to justify why we did not perform many experiments at 37° C and then show that the D-FF-OCT contrast is not deeply modified by temperature but it tends to increase the proportion of faster dynamics in D-FF-OCT.

- **Of temperature control in FF-OCT.** We have first to admit that despite our initial intent to better control our measurements, environment control is rather complicated to perform in FF-OCT or in any dual arms interferometer, so we rather tried to get the most of our signal at 20° C instead. Indeed, as previously described, most of our systems have translation stages mechanically coupled to the interferometer through cage systems, but this limits the size of the sample stand and the most common sample heaters do not mechanically fit in our microscopes. Additionally, changing the environment in the sample arm only might change the air and other media refractive index, which creates phase changes that in turn generate noise in our measurements. The most reliable way to have an environment control in our microscopes would be to add a wide environmental chamber that would contain our entire microscope, but even in this case, the temperature-dependent refractive index might be able to change light scattering and might alter our measurements. However, these systems are quite expensive, especially if they have to fit custom microscope designs and tend to create significant mechanical noise that might also interfere with our measurements. We have considered many times building our own environmental control chamber, but, at the end, we have never taken the time to build it. I can add that I have designed plans to build a low-cost environmental chamber (estimated below 500$) controlled by an Arduino and inspired by complex environmental chambers used for soilless hydroponic agriculture [288,289]. I will try to build it and share it in future work.

  Charles Edouard Leroux was the main expert on temperature control in the team and he has performed most of the experiments we did at 37° C, mostly in spheroids [111]. He used a temperature controlled chamber (Delta T system, Bioptechs Inc.), which consists of a glass window with a conductive Indium Tin Oxide (ITO) coating, a thermocouple and a PIV (proportional integral derivative) regulator. These measurements were however quite complicated to perform as the temperature had to be homogenized for one to two hours prior to experiments to avoid phase fluctuations, not to mention that the sample had to be placed far above the conductive coating to avoid all rapid small temperature fluctuations. Finally, we have tried to install this temperature controller on the high NA FF-OCT microscope. We

have also tried to install a microfluidic perfusion chamber with a temperature control, but without great success for both measurements. In most experiments, we have finally worked at room temperature, in controlled osmolarity solutions, with HEPES, to control pH during long experiments.

- **Effect of temperature change.** In the end, the influence of temperature is not drastic on the D-FF-OCT contrast. When we first tried to simply compute the amplitude of fluctuations (by computing the average of short time standard deviation), we could not see any difference in the D-FF-OCT signal at 20° C and 37° C. However, when taking a closer look at the full phase fluctuation signal, by calculating the autocorrelation function, as described previously, we could exhibit a significant difference, as presented in *C.E.Leroux et al.* [111] and in figure 5.23. The effect of temperature seems to be mainly of increasing the speed of signal decorrelation while having almost no effect on the signal strength. Indeed, in figure 5.23, the near zero lag is not modified by the increased temperature, while the autocorrelation function decreases faster at 37° C. Additionally, after signal strength normalization, the bi-exponential fit of the autocorrelation function shows both an increase of α, the fraction of rapidly decorrelating events and the increase of both the T_1 and T_2 time constants, showing a global increase of high-frequency events in place of lower frequency events.

- **Biological discussion.** Once again, one of our early concern was to make sure that the D-FF-OCT signal originates from biological activity and not simply from Brownian motion, or from cellular death, or pathological activity. No temperature dependency would have been suspicious, as most of the cells, enzymes or proteins are supposed to function around 37° C. These results noticeably suggest that cells in tissues might be partly active even at lower temperature and do not necessarily stop their intracellular dynamics at room temperature, even though as expected, a more intense cell trafficking happen at body temperature. Nevertheless, such information is hard to correlate with literature, as I could hardly find papers describing temperature dependency on cellular motility, noting that such effect seems to be biologist-dependent and experience-dependent, with a few contradictory comments on the importance of temperature control for basic cell dynamics.

Effect of drugs

Probably one of the most important results obtained with D-FF-OCT was reported in *C.E.Leroux et. al.* [111] and is presented in figure 5.24. It shows the effect of drug injection on the D-FF-OCT signal and illustrates Dynamic FF-OCT ability to measure a functional intracellular contrast inside tissues. It paves the way for tumor characterization and drugs testing, in a similar way to what has been performed in OCT [260] or in digital holography [255, 290], but giving additional access to subcellular resolution. Here, the injected drug is blebbistatin, a myosin II inhibitor [291] and is known to accelerate cell migration and to lower cytoplasm viscoelasticity. It is therefore not so surprising to see an increase of the α coefficient that can be interpreted as the acceleration of some dynamic elements of the slower fraction of the signal. We can further note that we expect the high NA FF-OCT system to be more accurate in detecting such small changes in the intracellular dynamics, but the low field of view and the geometrical constraints have prevented us from performing reproducible high throughput measurements, especially in a thermalized 37° C environment. Finally, we have tested a few other cytoskeleton-specific drugs on fresh tissues on the high NA FF-OCT microscope at room temperature, but we have not been able to measure significant changes at this time.

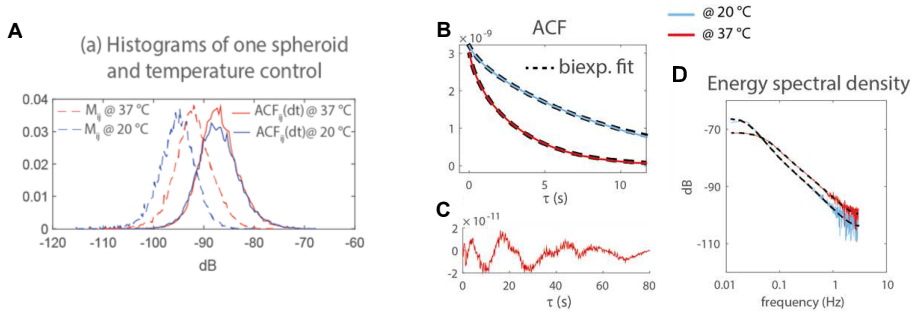

Figure 5.23 – Temperature dependence of the D-FF-OCT Signal. All panels illustrate the same aspect of temperature dependence of the D-FF-OCT signal in spheroids and have been adapted from *C.E.Leroux et. al.* [111]. **Panel A** shows two histograms of autocorrelation function (ACF) values at near zero lag (solid lines) and after 1 second (M_{ij}, dotted lines) at 20° C (blue lines) and 37° C (red lines). The near zero lag ACF value is not modified but the ACF value at 1 second shows an acceleration of the D-FF-OCT decorrelation at 37° C. **Panel B** directly displays autocorrelation functions at 20 ° C and 37° C, with an obvious faster decrease at higher temperature. **Panel C** plots the residuals of the biexponential fit of the autocorrelation function, showing the biexponential model accuracy. **Panel D** shows yet another evidence of the role of temperature on the D-FF-OCT in the frequency domain. The effect of temperature is to enhance high-frequency components over low-frequency.

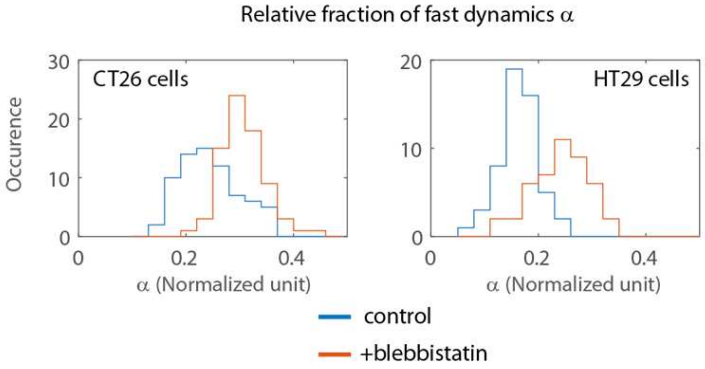

Figure 5.24 – Effect of blebbistatin on the D-FF-OCT Signal. Panel A shows the distribution of the α value, *i.e.* the fraction of rapidly varying elements, with or without the addition of blebbistatin, a Myosin II inhibitor, measured on 146 CT26 (undifferentiated colon carcinoma cell line) cells (71 control cells and 75 with blebbistatin). **Panel B** shows the same effect on another cell type, named HT29 (differentiated epithelial cells from a human colon carcinoma), on respectively 57 control cells and 47 with the blebbistatin addition. This figure has been reproduced from *C.E.Leroux et. al.* [111].

It should be noted that such analysis can be associated with drug testing and could be performed in the context of histology directly on biopsies, with the hope to increase the success rate of a potential treatment. Using D-FF-OCT signal, it has been possible to measure an overall decrease of intracellular dynamics speed of transport correlated with the spheroids age and potentially correlated with the spheroids growth rate [111].

5.2.8 *In vivo* D-FF-OCT

From all our concerns about D-FF-OCT and its potential imaging of slowly dying cells, we were highly motivated to demonstrate the feasibility of D-FF-OCT measurements *in vivo* to observe contrast that can be obtained with dynamic measurements. As previously mentioned in chapter 4, I had the chance to image numerous paralyzed *in vivo* zebrafish larvae mounted in agarose. The agarose mounting, as well as the use of neuromuscular blocking drugs, were important to prevent any sample motion that would destroy our D-FF-OCT contrast. However, for several hours, the larva is still living, with its heart beating and with almost functional brain activity [292]. In figure 5.25, I have illustrated our ability to obtain a subcellular contrast with D-FF-OCT *in vivo*, even in presence of blood flow. The dynamic signal is saturated above and below the blood vessels, but cells can be detected in between the vessels. Subcellular contrast, including nucleus position, has even been revealed in many similar experiments, as illustrated in figure 5.25 B. As the larva still lives and blood is running through its capillaries, it is unlikely that its cells would undergo apoptosis during the imaging. It is even less likely since the warm environments (about 25-27° C) of our experimental room is within typical comfort zones of zebrafish larvae. Therefore, being able to retrieve a similar contrast to what was observed in *ex vivo* samples is an additional proof of the ability of D-FF-OCT to provide motility-based contrast within normally behaving cells. Nevertheless, we agree that cells undergoing apoptosis might still generate a D-FF-OCT contrast for a short period of time and that further experiments should be conducted if we want to quantify the cell state from dynamic FF-OCT signatures. Finally, we hope that these *vivo* experiments will pave the way for the use of D-FF-OCT in larger animals and in patients. We acknowledge that the usual intracellular dynamics we have been probing are on the second timescale, which is usually longer than the mechanical vibrations timescales in humans. Nevertheless, we hope that using mechanical deflectors to correct dynamically the position and using phase-dependent motion correction algorithms [293], will allow the use of D-FF-OCT *in vivo* without paralytic measurements.

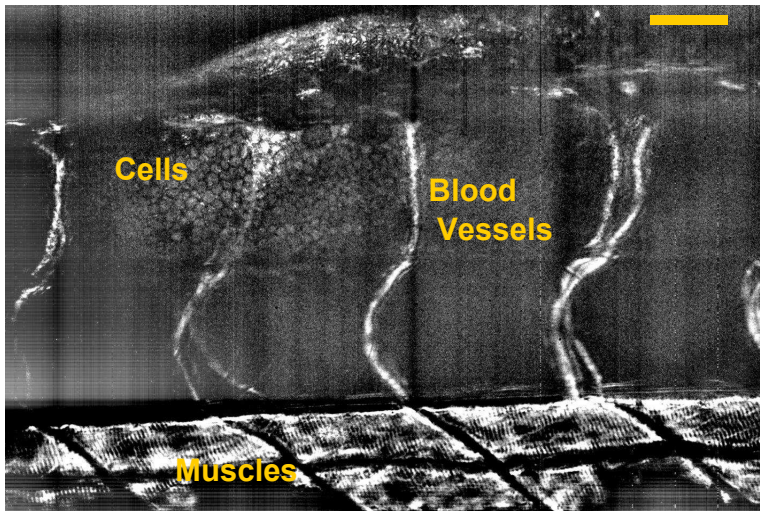

Figure 5.25 – *In vivo* **Dynamic FF-OCT in a 2 dpf zebrafish larva.** Despite strong phase variations caused by the blood flow, which generates a strong dynamic signal, some cells can still be revealed in between the capillaries. The scale bar represents 40 μm.

Intermediate conclusion

In this second part, I have first tried to illustrate that extending quantitative phase measurements inside scattering biological tissues is not trivial at all. Nevertheless, using low-coherence interferometry, smart optical microscopes have been developed to measure the localized interference term in 3-D in scattering samples and to amplify the weakly backscattering signals from biological samples. One set of techniques among these smart 3-D optical interferometers is known as optical coherence tomography (OCT) that has been described in chapter 3. From the interference term, OCT can extract either its amplitude that measures a structural map of the diverse tissue microstructures or a phase map that can be used to follow and track axial deformations inside samples. If the OCT signal amplitude allows the measurement of a structural contrast, the phase signal allows the recovering of diverse functional contrasts inside scattering samples. In chapter 3, I have emphasized two applications of the dynamic phase measurements allowed by OCT that can be used to measure blood flows (and ultimately functional activity of a tissue region) or to measure mechanical parameters of the sample. Over its 26 years of existence, OCT has been declined in many different configurations and has revolutionized several domains of biomedical imaging, especially ophthalmology, as it will be further discussed in chapter 6. One of these configurations is known as full-field OCT (FF-OCT) and has been developed at the ESPCI by Claude Boccara in 1999. FF-OCT is based on the same Linnik interferometer described in chapter 2 and authorizes to access submicrometric resolution deep inside a sample. In chapter 4, the different FF-OCT systems I have used or developed have been described and compared to OCT. FF-OCT main features are its cost and its transverse resolution. It enables to perform measurements similar to histology in terms of contrast and resolution but it can provide tomographic images each one being similar to an histology slide obtained with almost no tissue preparation. Furthermore, FF-OCT can reduce slicing, staining, and fixation artifacts known in histology and can significantly shorten the biopsy-to-diagnosis time down to a few minutes. Unfortunately, FF-OCT diagnosis scores are yet not 100% when compared with the histology gold standard. It raises the interest for multimodal platforms that combine the structural contrast of FF-OCT and as many other contrasts as possible. The aim of chapter 5 was to describe one such platform I have developed during my thesis, combining FF-OCT structural contrast with molecular contrast obtained with structured illumination fluorescence microscopy and a motility and metabolic contrast obtained by taking advantage of the local phase fluctuations of the dynamic FF-OCT signal. In chapter 5, we have reported on the new development of dynamic FF-OCT and discussed the available contrast and benefits. If many other characterizations could be further required, D-FF-OCT seems to be a very promising technology to provide both a label-free detection of most cell types inside a complex tissue, and a motility-based, and metabolic-driven, functional contrast in the same cells. In the next part, chapter 6 will be dedicated to the application of this multimodal platform to ophthalmology.

Beyond the scope of histology, we hope that the development of such multimodal platforms will increase the potential interest for FF-OCT, not only as an *ex vivo* diagnosis tool but also as a tool to answer complex biological questions. We have shown in this second part that FF-OCT reveals a label-free original contrast and can be used either in *ex vivo* tissues or *in vivo* in small animals. For example, in chapter 5, we have also reported on the first detection of sample-induced mechanical waves propagation inside *ex vivo* hearts, triggered by electrical activity using the phase sensitivity of FF-OCT. In chapter 4, I have also reported on the *in vivo* detection of extracellular vesicles that can hardly be tagged with fluorophores. In chapter 7, I will develop some ideas and experiment to use FF-OCT and D-FF-OCT to simultaneously record phase fluctuations and a biological

activity at relatively large depth inside biological samples. If scanning OCT techniques are now extensively used *in vivo* and in clinics, FF-OCT suffers from the slow speed of 2D detectors that do not allow dynamic correction of the sample motion, and is, therefore, challenging to implement *in vivo*, reducing the impact of FF-OCT. However, a few FF-OCT *in vivo* experiments have been successfully performed in paralyzed or anesthetized small animals [129, 175] and in human skins pressed against an imaging window. We recently successfully performed simultaneous FF-OCT, D-FF-OCT, and fluorescence measurements in living zebrafish larvae, as reported in 5. Additionally, an important effort is being made by *P. Xiao*, *V. Mazlin*, and *E. Auksorius* to enable FF-OCT measurements in patients, with the recent development of two adaptive optics FF-OCT systems [294, 295] for retina and cornea imaging, an FF-OCT system coupled with an OCT system to dynamically compensate for sample motion and a dark field FF-OCT system [110] to record internal fingerprints. Additionally, a group from the Institut Langevin recently developed an *en face* matrix based approach of OCT, which allows increasing the penetration depth by a factor 2 [177] and could be beneficial to compete with *in vivo* fluorescence experiments.

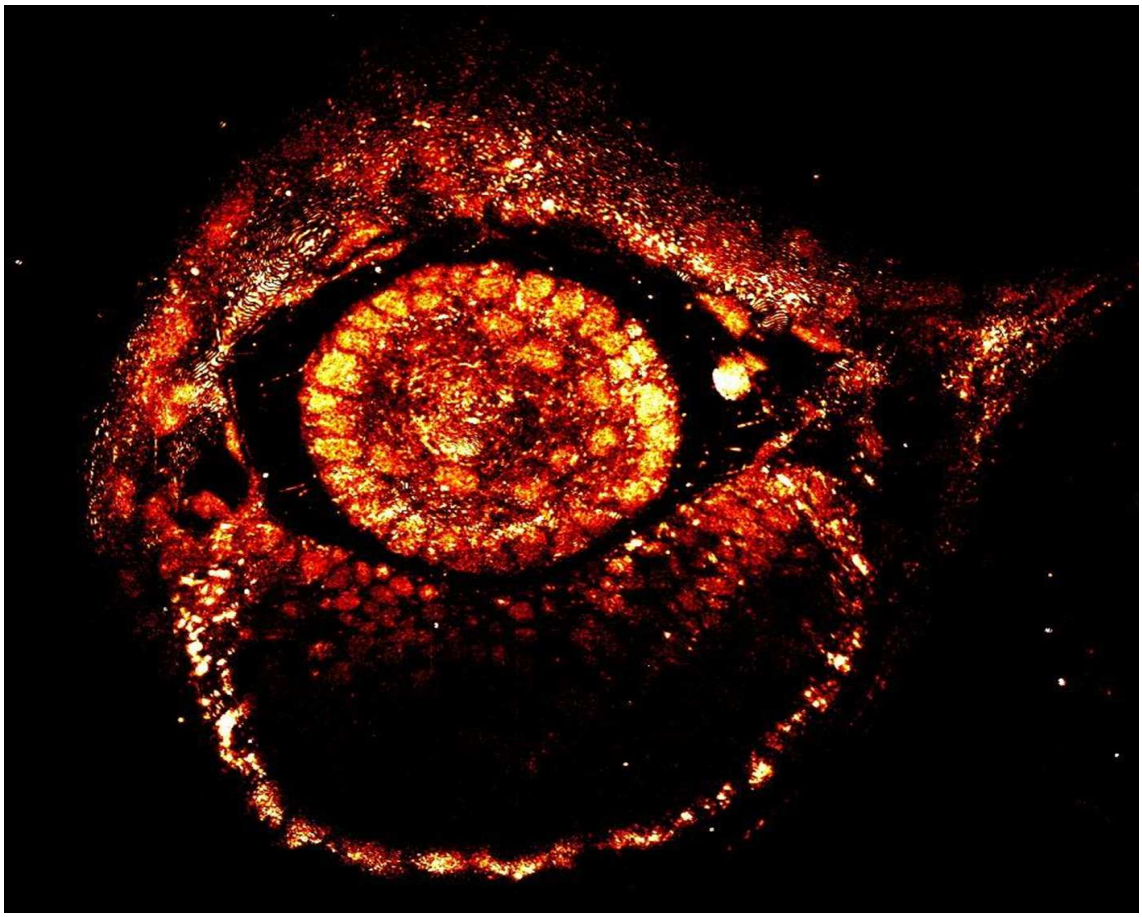

Big brother is watching you. *This image presents a dynamic FF-OCT image of the eye of a Zebrafish larva.*

Part III

Biological applications

If the two first parts of this manuscript have mainly focused on technological development, this part aims at describing some biological systems and at showing how dynamic phase imaging might help o understand and assess both their normal and abnormal functioning. In this part, most of the described measurements have been performed with the multimodal platform combining full-field OCT, dynamic full-field OCT, and structured illumination fluorescence microscopy I have presented in chapter 5. In this manuscript, two main biological applications are considered, keeping in mind that our ultimate goal was to image a neuronal functional activity. Chapter 6 will first focus on corneal and retinal imaging and on diverse application of dynamic phase imaging for Ophthalmology and vision investigation. Experiments towards both biological fundamental questions and clinical translational applications are described. The functioning of the retina is particularly emphasized especially since some of its cells behave similarly to cortical neurons. In this regards, the retina, often described as *an open window to the brain*, offers an optically-accessible brain region from which fundamental questions of neuroscience can be addressed and from which some neurological disorders could be detected. Similarly, more and more research projects aim at optically detecting diseases, such as diabete, invasive tumors (from the detection of circulating tumor cells), or blood diseases, and at doing so using a non-invasive external measurement of the retina. The optical accessibility is so convenient that a few research groups have even performed grafts of various pieces of some tissues (such as the pancreas) inside the ocular glob to externally and longitudinally study these tissues development. Nevertheless, if the optical accessibility is advantageous for optical imaging, the continuous eye displacements have forced optical systems to increase their speed and to produce a significant number of images between two motion artifacts. Because FF-OCT outputs data at a slower rate than standard OCT, FF-OCT has been little used for *in vivo* ophthalmologic measurements. As a consequence, most of the results presented in chapter 6 have been performed *ex vivo* although I will evoke the work of some of my colleagues who tried to push the FF-OCT speed further to perform *in vivo* experiments. Besides, the last chapter of this manuscript, chapter 7, focuses more direclty on Neurophotonics applications. It reviews the previous detection of fast intrinsic optical signals and discuss their potential origin. The potential detection of such activity-related intrinsic signals with our phase imaging systems is reported in both neuronal cultures and tissues. Chapter 7 also emphasizes some recent questioning of the standard model of electrical propagation in nerves and axons, known as the Hodgkin-Huxley model. It discusses the recent theories going beyond this standard model and that predict the existence of electromechanical waves to propagate neuronal information. It finally describes technological requirements to verify such theories and shows that they are probably yet too important to be met in a single optical system.

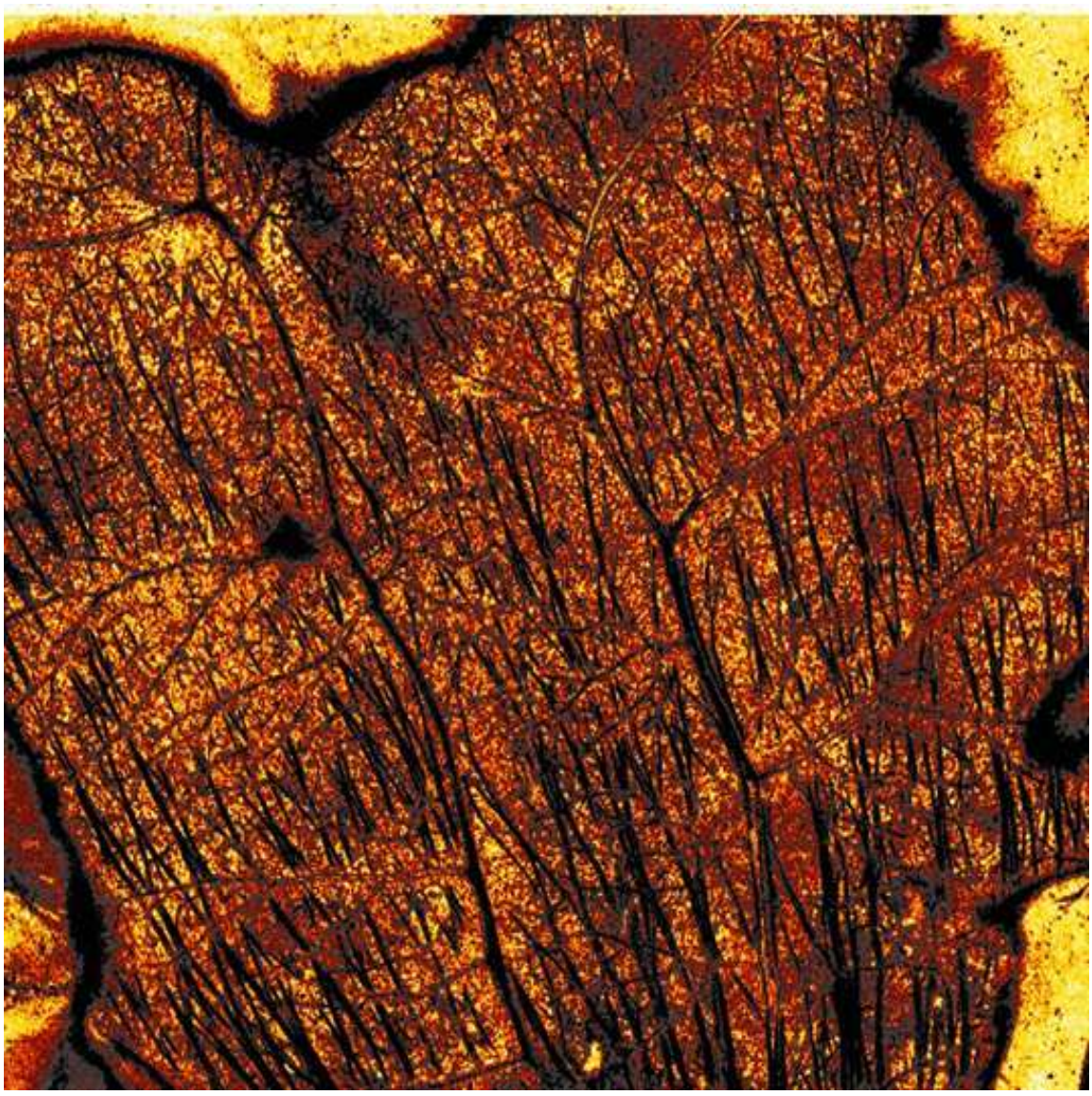

Autumn leaves. *The image shows an en face view of the retinal ganglion cell layer with static FF-OCT.*

CHAPTER 6

FF-OCT measurements in the eye

Table of contents

6.1 Organization of the eye **189**
6.1.1 Cellular organization of the cornea 190
6.1.2 Cellular organization of the retina 191
6.2 Static and dynamic FF-OCT imaging of the cornea **196**
6.2.1 Evidence of the stem cell niche in the cornea 196
6.2.2 Another interest for static FF-OCT and fluorescence in the cornea . . 197
6.2.3 Dynamic FF-OCT in the cornea 199
6.3 Static and dynamic FF-OCT imaging of the retina **199**
6.3.1 High-resolution imaging of the retina layer by layer 204
6.3.2 D-FF-OCT to assess local cell viability 207
6.4 Conclusion and future developments **207**

The aim of this chapter is to demonstrate that FF-OCT and the multimodal platform we have developed can be of interest for ophthalmology, both for the theoretical understanding of the functioning of the eye and for clinical applications. This chapter will mainly focus on the cornea and the retina, the organization of which will be presented in a first section. Then, a second section will focus on the imaging of the cornea with both FF-OCT and D-FF-OCT, while a third section will detail the imaging of the retina. Finally, a few potential further experiments to develop will be detailed in the last section. Most of our work on the eye has been led by *Kate Grieve*, a research associate at the *Institut de la Vision* in Paris and I have been involved when additional contrasts to FF-OCT were of interest to demonstrate some observed effects. Interestingly, this work has been one part of a larger collaboration between the *Institut Langevin* and the *Institut de la Vision*, for which an ERC Synergy Grant has been awarded and that aims to develop new tools, both in optics and in ultrasound, to improve the understanding of the functioning of the eye and to develop more accurate clinical tools. In the two previous chapters, we have seen that FF-OCT and its multimodal declinations were of particular interest to perform histology-like measurements and that OCT has revolutionized ophthalmology, and especially retinal imaging, thanks to its ability to measure the retinal layer organization non-invasively and without any label. Although OCT can access all the retinal layers, it usually provides a moderate axial resolution and a poor lateral resolution, while adaptive optics flood-illumination ophthalmoscopes [296, 297] can image the nerve fiber layer and the cone maps with good resolution, it can merely access other layers of the retina due to its low contrast. On the hand, FF-OCT can be of major interest as it can access subcellular details in all layers of both the cornea and the retina but has been limited to *ex-vivo* measurements so far. Unfortunately, full-thickness retinal biopsies [298] and corneal biopsies [299] are extremely invasive and complicated surgeries that are only performed for oncology and are not a routine examination as it could be for other organs, which obviously limits the potential impact of FF-OCT in ophthalmology for medical diagnosis. However, the increased need for label-free and non-invasive corneal graft assessment, as well as the development of recent FF-OCT systems for eye examination in our group [300, 301], will probably increase the interest of FF-OCT for ophthalmology diagnosis. Interestingly, usual histology procedures for the corneal and retinal typically observe axial sections of the samples, as both tissues are generaly too thin and too soft to be accurately cut without damage [1]. Moreover, both cornea and retina are highly organized structures, whose structure ensures their transparency [303]. Therefore, even slight structural changes that can be caused by fixation or slicing artifacts have a dramatic effect on the optical properties of these samples, as illustrated in *K.Grieve et al.* [206]. If the work presented in this chapter will focus on healthy *ex-vivo* eyes, we hope that it will be useful to demonstrate the interest of FF-OCT for a further *in-vivo* eye examination but also for increasing the fundamental understanding of the eye's function and dysfunctions in explanted retinas.

[1] Nevertheless, *en face* histology can be performed, especially in the cornea and more rarely in the retina [42,302]

6.1 Organization of the eye

This section aims to present the basic function of the eye and to introduce its complexity. Obviously, the eye is the fundamental organ that enables vision and is therefore dedicated to transforming an electromagnetic signal (visible light) into an electrical signal that can be understood and processed by the brain. The active transductive part of the eye consists of the photoreceptors that are located in a small layer of the retina, which is itself a thin structure compared to the eye size. The photoreceptor cells response to light does not look like a stereotypic train of action potentials. Transforming position and intensity information into trains of action potentials the firing rate of which encodes the signal amplitude requires subtle preprocessing, which is precisely the aim of the rest of the retina. The final preprocessed electrical signal is output by the ganglion cells that behave like usual neurons and is sent to the visual cortex in the brain through the optic nerve. Therefore, the retina can be thought of as a small, exposed, and optically-accessible part of the brain, and exhibits similar or even higher energy consumption rates than the brain [304]. Because the eye is exposed, its mechanics, osmolarity, and temperature have to be highly controlled and maintained, which is the aim of the larger parts of the eye. The sclera or white outer part of the eye plays the role of the supporting wall of the eyeball and controls the eye mechanics together with the vitreous humor, a gel-like viscous transparent liquid that presses against the retina to maintain it in place. Interestingly, the sclera is continuous with the cornea at its foremost section and with the dura in the brain. The aqueous humor is contained in the anterior and posterior chambers, respectively between the cornea and the iris, and between the iris and the crystalline lens. Together with the tears liquid, it controls the nutrient and oxygen (dissolved in the tears) diffusion in the cornea. The front part of the eye serves as a dynamic optical system that enables the formation of an image on the retina. It is composed of two lenses: the fixed cornea, of high curvature and that mostly controls the eye focal length, and the crystalline lens, the curvature of which can be controlled by the ciliary muscles to adapt from a vision at an infinite distance to a plane at a finite close distance, a process known as accommodation. The iris is a thin circular colored structure on top of the crystalline lens and contains a muscle that controls the size of the pupil (black region at the center of the eye). The pupil plays the equivalent role to a physical aperture placed in the back-focal plane of a lens and controls the amount of light coming onto the retina and controls the resolution. Nevertheless, in contrast to usual optical systems, the resolution is higher for smaller pupil sizes, where the eye's aberrations are limited. The eye blood supply is controlled by the choroid, a highly vascularized layer of particular importance since most of the parts of the eye have a minimal vascularization to optimize the eye transparency. Finally, the eye is constantly moving in its orbit and can extend over a visual field over 200°. The eye motion is controlled by the 7 extraocular muscles and is important to focus on parts of our visual field to conjugate them with the macula, the region of the retina with the highest photoreceptor cone density, which allows for the sharpest image formation. Ocular motion is also important to constantly modify the signal captured by a given photoreceptor and avoid a decay of excitability that is often associated with constant signals in neurons. The cellular structures of the cornea and the retina will be more extensively detailed in the next subsections before showing that FF-OCT and dynamic FF-OCT can reveal most of the details of these cellular structures in the two next sections.

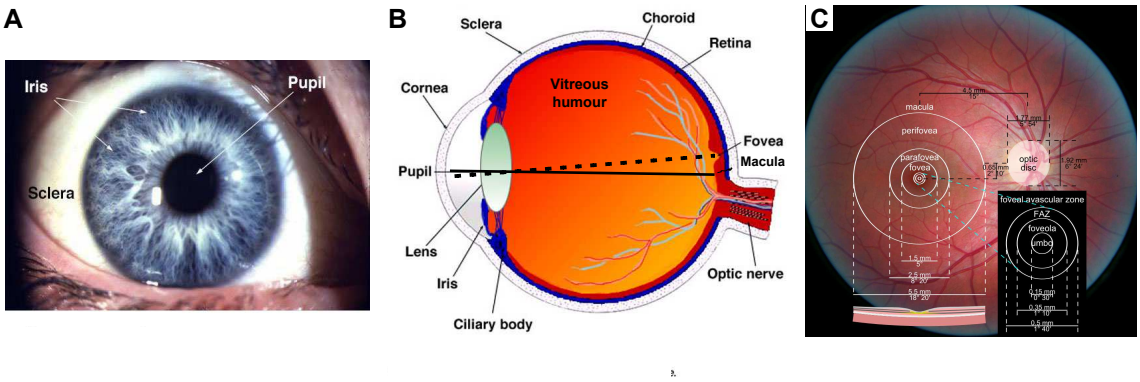

Figure 6.1 – Basic structure of the human eye. Panel A is a simple photograph of an eye, showing the white supporting wall of the eye, or *sclera*, the colored iris, which is mainly a colored aperture that controls the pupil (black region) size. **Panel B** shows a sagittal section schematics of a human eye that illustrates the function of an eye. A first fixed transparent membrane, named *cornea*, serves as a lens in conjunction with the eye *lens*, to focus the light on the retina. In contrast, the cornea, the *lens* focal length can be tuned thanks to the *ciliary bodies*. The *retina* is the active part of the eye that transforms the light into an electrical signal and sends it to the brain through the optical nerve. The *fovea* is the most accurate part of the retina, only composed of a compact pack of cone photoreceptors, the projection of which are shifted on the sides. The *fovea* lies at the center of the visual axis of the eye (dotted line), while the macula refers to a more extended region that includes the *fovea* and whose border is delimited by the optical axis of the eye (full line) that is defined as the center of the eye. The optical nerve defines a blind spot in the retina, which is shifted from the center of the eye. Both panels have been adapted from the Webvision book [264]. **Panel C** shows a typical retina photograph with a commercial ophthalmoscope, showing the eye vascularization and different characteristics of the retina [305].

6.1.1 Cellular organization of the cornea

The cornea is a mostly passive structure that protects the intraocular space from the outer world. The cornea has to preserve its curvature to keep a constant focal length, and has to be highly transparent [2] to allow an optimal light collection by the retina. The cornea accounts for about $\frac{2}{3}$ of the eye's converging power [3]. The cellular organization of the cornea is presented in figure 6.2 and mainly supports cornea function. The most important part of the cornea in terms of size is the corneal stroma composed of highly organized parallel packing of collagen fibers and interconnected large branched cells named keratocytes. The corneal stroma helps the cornea to keep its shape while the highly controlled organization ensures corneal transparency [303] despite its relatively high average refractive index of 1.376. The corneal stroma is protected and sandwiched between two layers each one being composed of a fibrous layer in contact with the stroma and a cellular layer. At the entrance of the cornea, the latter is first composed of a series of epithelial cells organized in six distinctive layers of increasing cell sizes. In contact with the external world, this epithelium is important to protect the cornea but also to control the diffusion of nutrient and oxygen present in the tears liquid. This epithelium can partly regenerate, as epithelial stem cells can be found in the corneoscleral limbus on the sides of the cornea [183]. At the bottom of the epithelium layer, the Bowman's layer is an acellular structure with several collagen fibers and contains most of the corneal nerve fibers. The Bowman's layer function is not fully understood and is thought to be absent in most nonprimates species. At the back surface of the cornea lies the

[2] which makes cornea difficult to image without any labeling!
[3] Eye disorders such as myopia are caused by abnormal eye length or cornea curvature.

Descemet's membrane and the endothelium. The endothelium is particularly important because it makes the link between the aqueous humor and the cornea and allows the leakage and diffusion of solutes and nutrients inside the cornea (since there is no blood vessel in the cornea to ensure its transparency). The endothelium also controls the flux of water from the cornea to the aqueous humor and prevents the hypotonic shock of corneal cells. The endothelium is also particularly precious because it does not regenerate. If a damage is caused and an endothelial cell is destroyed, its neighbors will grow in size to prevent the leakage. With successive damage, the endothelial cells density will decrease and the endothelial cells will grow up to a point when the cells are too big to extend more, which leads to the endothelium disruption (corneal edema) and cause blindness.

Nowadays, severe damage to the cornea affecting its transparency can not be treated. The only solution is to perform a corneal graft, which is in number the most frequent graft performed in the world with about 200,000 corneal transplants reported in the world in 2012 [306]. Nevertheless, there is still an important imbalance between corneal demand and supply, especially in developing countries mainly China, India, and Africa [306]. Moreover, the risk of corneal graft rejection is still on the order of 5% [307]. Therefore, there is an important research effort made to better predict the graft rejection and to design artificial corneas made of transparent collagen matrices injected with the patient stem cells [308].

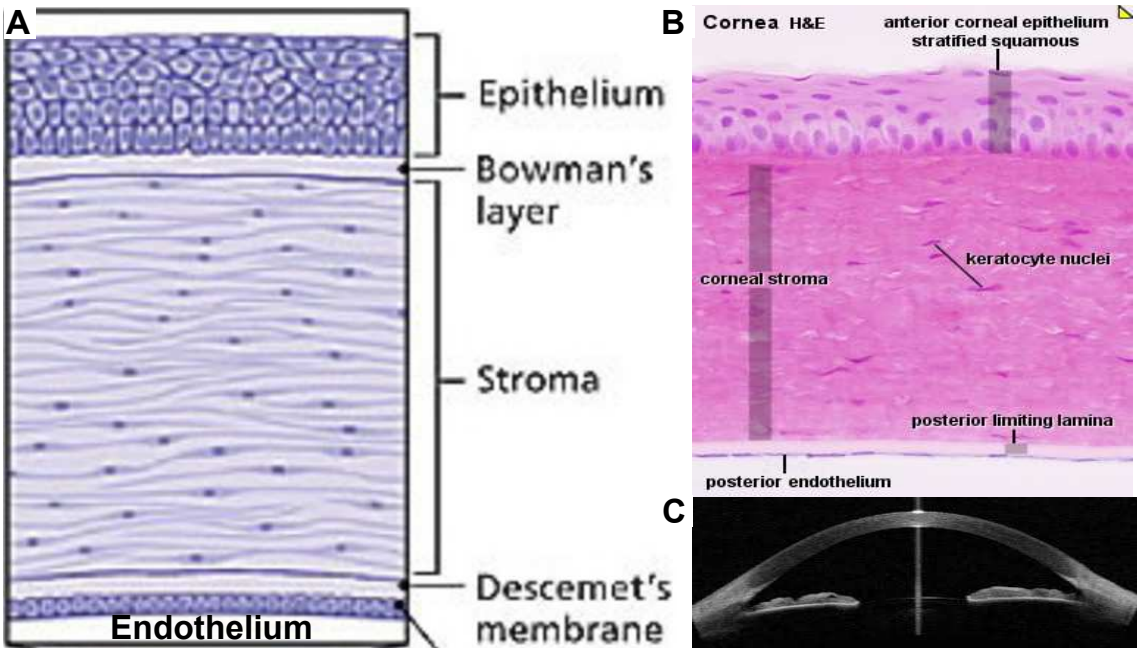

Figure 6.2 – Organization of the cornea. Panel A presents the different layers of the cornea, successively named epithelium (organized in 6 layers being composed of 3 epithelial cell types of decreasing sizes), Bowman's layer, stroma (highly organized parallel packing of collagen fibers and keratocytes), Descemet's membrane and endothelium. **Panels B and C** respectively present an H & E stained histology of the cornea and a typical OCT image of the cornea.

6.1.2 Cellular organization of the retina

The anatomy of a retina and the processing of the visual signal are presented in figure 6.3 and6.5 respectively. Here again, the retina layered organization supports its function, which is to transform a visual signal into an electrical signal that can be understood by the brain. In a quick glance, the retina is composed of three cellular (or nuclear) layers and two layers of neuronal synapses,

named plexiform layers. The cellular layers are layers that contain the retinal neuron cell bodies. The outer nuclear layer (ONL) packs the photoreceptors cell bodies that are the light-sensitive cells. On the other side of the retina, the ganglion cell layer (GCL) contains the final neurons that integrate the preprocessed signal captured by several photoreceptors inside a visual field and send this signal to the brain through their axons that are packed in the nerve fiber layer and directly form the fibers of the optic nerve. In between, the inner nuclear layer (INL) gathers bipolar cells, horizontal cells and amacrine cells that are interneurons used for the visual signal pre-processing. The bipolar cells have two major extensions, one forming synapses with the photoreceptors and the second forming synapses with the ganglion cells. The inner plexiform layer(IPL) is the area where the ganglion cells and the bipolar and amacrine cells form and develop their synaptic connections. The outer plexiform layer (OPL) is the equivalent connective layer between the INL and its bipolar and horizontal cells and the ONL and its photoreceptors. Finally, the active elements of the photoreceptors are contained in the outer segment (OS) of each individual photoreceptor cell while the inner segments serve as a supply unit to maintain the membrane voltage of the outer segment. The photoreceptors outer segments are maintained and supplied by the retinal pigmented epithelium (RPE) cells at the bottom of the retina. Below the RPE runs the choroid blood vessels that supply the photoreceptors in oxygen and represents 65% to 80% of the oxygen supply of the retina. The 20 to 30 % remaining oxygen supply is ensured by blood vessels running through transversely in the INL and the GCL. A surprising feature of the retina is that it seems to be mounted upside down since the light has to propagate through the all retina before reaching the photoreceptors. This organization can be explained by the high energetic and nutrient consumption of the photoreceptors, especially of the vitamin A, essential for the transformation of the opsin into rhodopsin the light-sensitive channel of the photoreceptor. The transport of oxygen and vitamin A is carefully controlled by the compact epithelial barrier of the RPE that would be too dense to allow for the synaptic connection between the photoreceptors and the other retinal neurons. Additionally, the RPE cells have developed a high concentration of melanin and absorb the remaining light not captured by the photoreceptors. It prevents the light to be backscattered by the choroid, which would create a blurred defocused second image on the retina. To emphasize the complexity of the retina, we can point out that primate retinas have 4 photoreceptors types, 1 to 4 types of horizontal cells, 11 types of bipolar cells, 22 to 30 types of amacrine cells and 20 types of ganglion cells [4]. More information about the retina organization and function can be found in several reviews or books [264, 309, 310] and the numerous references therein.

To go a bit further into the description of the retinal function, the functioning of the different retinal cells have to be investigated, as illustrated in figures 6.4 and 6.5. The opsins light-activatable channels are simple channels that can only hyperpolarize the photoreceptor cells with an hyperpolarization amplitude that increases linearly with the light intensity. The change of the membrane voltage is therefore quite different from a usual action potential. In the dark, the photoreceptor cells are in a depolarized state and are continuously releasing glutamate, the main neurotransmitter to which the bipolar cells react to. Under illumination, the photoreceptor cells membrane voltage decreases (hyperpolarization), which decreases the release of glutamate, which in turn affects the firing rate of the bipolar cells. On the contrary to usual neurons, photoreceptor cells sustain their hyperpolarized state as long as they are illuminated, which is controlled by active ion pumps that explain the extreme energy consumption of photoreceptors cells. In primates, there are 4 different types of photoreceptor cells: 3 cone photoreceptors sensitive to 3 wavelengths bands (blue, green and red cones) that are dedicated to daylight bright colored vision and exhibit

[4] The number varies depending on the primate species

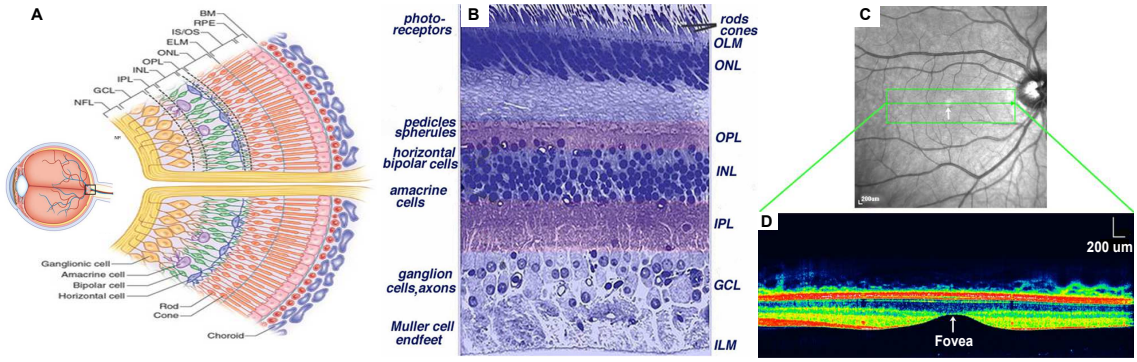

Figure 6.3 – Basic structure of the retina. Panel A presents a scheme of the retina organization. It is composed of five main distinct layers, respectively named ganglion cell layer (GCL), inner plexiform layer (IPL), inner nuclear layer (INL), outer plexiform layer (OPL), and the outer nuclear layer (ONL). The photoreceptor cell extremities are composed of an inner segment(IS) and of an outer segment (OS), which is the only light-sensitive part of the retina. The photoreceptor cells are attached to the cells of the retinal pigmented epithelium (RPE), which also controls the oxygen and nutrient flow (supplied by the highly vascularized choroid) to the photoreceptor layer. The ganglion cell axons form a last transverse layer named nerve fiber layer that directly forms the nerve fibers of the optic nerve. **Panel B** shows a typical histological vertical slice of the centered region of a human retina, which illustrates the layered organization. **Panel C** shows an eye fundus with the foveal pit (bright spot marked with a white arrow) and **panel D** shows an OCT scan of the profile marked in green in panel C. OCT scans can clearly identify the different layers of the retina based on their backscattering strength. The nerve fiber layer is particularly backscattering and the plexiform layers are often more backscattering than the nuclear layers.

a faster response to light fluctuations. A fourth photoreceptor, referred to as rods, exhibit an extreme light sensitivity (down to 3 to 5 photons) and possess its own processing pathway in the retina with specialized rod bipolar cells. The blue cone photoreceptors also exhibit a specialized processing pathway with specialized bipolar and ganglion cells. The macula exhibits a dense compact packing of cone photoreceptors with almost no rod photoreceptors, while the periphery areas are mainly composed of rod photoreceptors. Each individual photoreceptor has a very narrow receptive field that corresponds to the transverse extension of its external segment, while ganglion cells respond to larger visual fields by integrating the signal of many photoreceptors.

The bipolar cells integrate the signal from the photoreceptors thanks to glutamate receptors of various response speeds and nature specific to each type of bipolar cells. The main types of bipolar cells are ON cells that have inhibitory glutamate receptors (as the glutamate release is decreased in presence of light) and OFF cells that have excitatory glutamate receptors. Ganglion cells are also divided in these two ON and OFF responses. The ON pathway enables the detection of light images against a dark background, while the OFF pathway detects dark images against a bright background. The bipolar cells exhibit graded potentials, with a varying amplitude and temporal extension depending on the strength of the stimulus. While bipolar cells form synapses with only a few photoreceptors, the horizontal cells receive inputs from many cones and are connected to each other so that their effective receptive field is large. They give information on the global light exposure of a wider environment and are involved in the adaptive response to different light levels. Finally, ganglion cells have a receptive field organized as concentric circles, as illustrated in figure 6.5 with an on area and an off area and integrate color information and surrounding information thanks to a supplementary level of integration offered by the amacrine cells. Ganglion cells exhibit a normal neuronal response with the intensity of stimulus encoded in their firing rate. Ganglion cells also divide into sustained cells that keep firing during the entire stimulus or a transient type

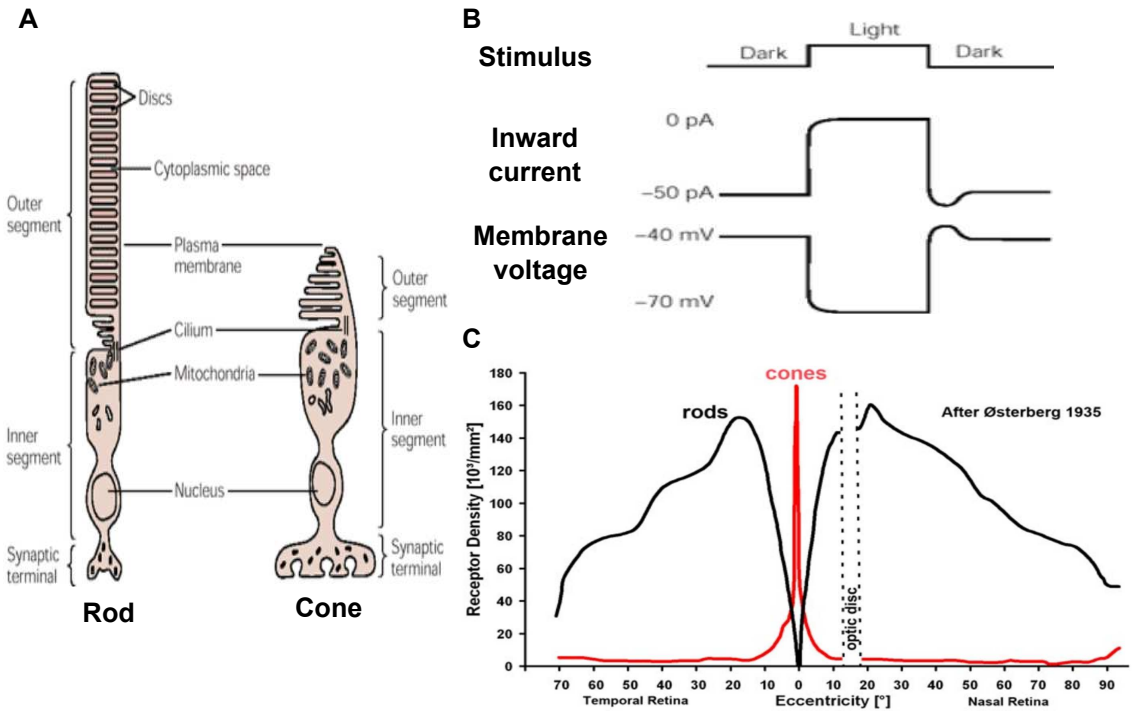

Figure 6.4 – Basic structure and functioning of photoreceptor cells. **Panel A** illustrates the anatomy of rod and cone photoreceptors. The outer segment consists of stacks of disks of cellular membrane to enhance the membrane total surface and hence, the number of rhodopsin light-sensitive transmembrane channels. The more extended outer segment in rods explains the higher light absorption and the better sensitivity to low light. Inner segments contain mitochondria and most of the machinery for protein synthesis. **Panel B** shows the basic functioning of photoreceptors cells under illumination. In the dark, photoreceptor cells are slightly depolarized around -40 mV but light stimuli close the sodium and calcium channels (cancels the negative inward current) and hyperpolarize the photoreceptors cells to bring the membrane voltage to about -70 mV. The different types of photoreceptors correspond to the nature of their rhodopsin light-sensitive channel that can be sensitive to a given spectral range and can respond with various speeds. **Panel C** illustrates the photoreceptor cell density in the retina versus the eccentricity. At the fovea (eccentricity of 0), the photoreceptor layer is composed of a high-density packing of cone photoreceptors exclusively (up to 10^5 cells per mm^2 while it is mostly composed of rod photoreceptors at the periphery with a cone density dropping to a few thousand per mm^2 for about ten to one hundred times more rods). Panels A and B are adapted from the book of *E. Kandel et al.* [310] and panel C from the Webvision book [264].

firing only at the beginning and the end of the stimulus depending on their nature.

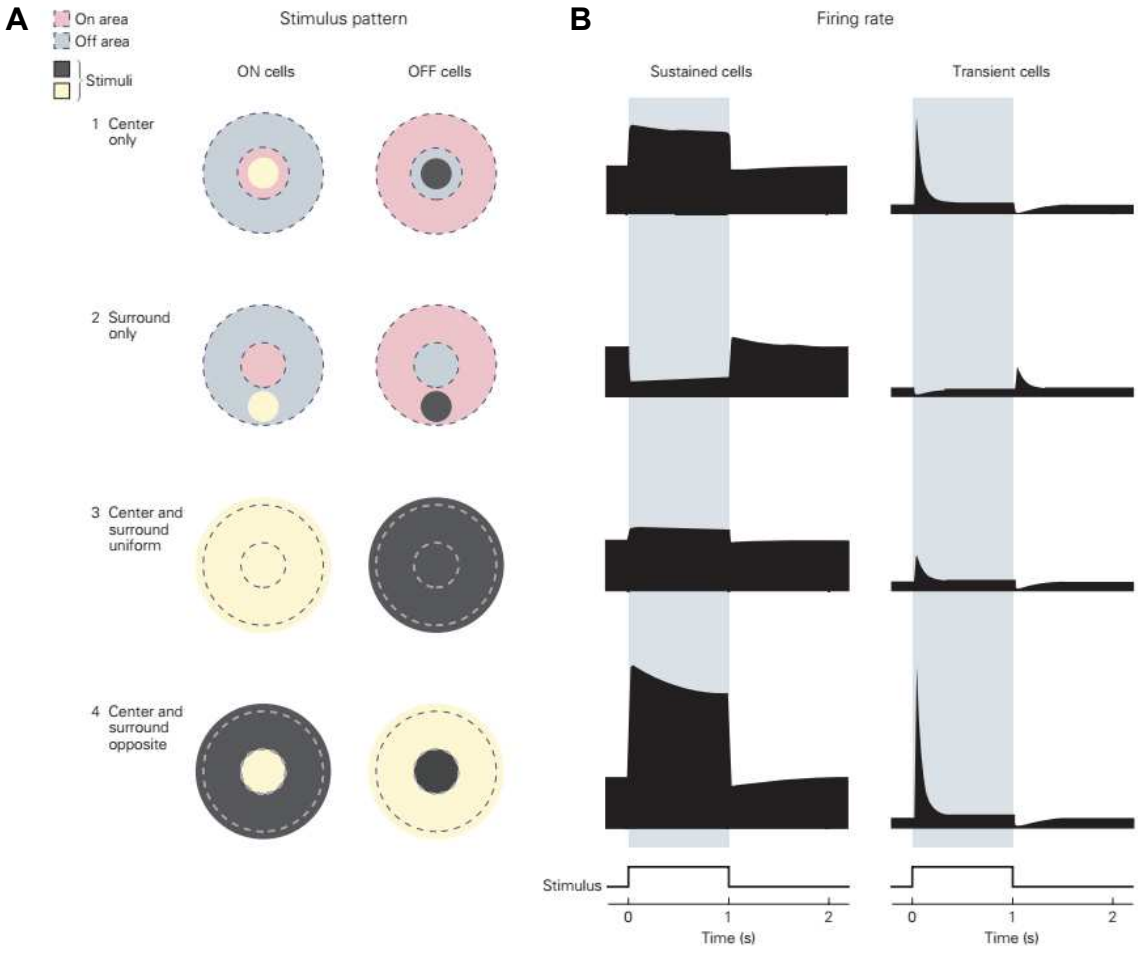

Figure 6.5 – Visual field of the retinal ganglion cells and their electrical response. Panel A shows different light stimuli, either bright or dark, to which ON ganglion cells and OFF ganglion cells would respond to in a similar way. If the diameter for the on and off areas are variable of the ganglion cell type and eccentricity, it usually ranges between 20 μm to 100μm, which corresponds to the integration of 20 to 200 photoreceptor cells. **Panel B** illustrates the corresponding electric response of sustained and transient ganglion cells in a thought experiment. Panel B represents various plots of the firing rate versus time during a corresponding light stimulus. This figure has been taken from *E. Kandel et al.* [310].

6.2 Static and dynamic FF-OCT imaging of the cornea

Due to its transparency, the cornea is quite difficult to image. If the usual slit lamp is traditionally used by the ophthalmologist to assess the corneal transparency, the investigation of a specific corneal layer requires the use of additional higher resolution techniques. They include the reflectance confocal laser scanning microscope and high axial resolution OCT that can both provide label-free imaging of the corneal layers. If reflectance confocal scanning microscopy displays high-resolution images of the cornea, it offers a limited field of view since increasing the field would increase the acquisition time or would need to work with lower transverse resolution but that would also lower the axial resolution and would prevent the detection of some corneal layers. It cannot reconstruct quantitative 3-D stacks of the cornea due to the eye motions. On the other hand, OCT can record low transverse resolution axial sections of almost the entire cornea. The interest of OCT is to decouple the axial sectioning from the transverse resolution that allows reduction of the resolution to image larger fields. Using lower NA objectives would also allow the use of long working distance objective and allow for noncontact techniques in contrast to scanning confocal microscopes, that are therefore less unpleasant for patients. FF-OCT would lie in between and is able to image the cornea in 3-D over a few mm^2 field of view with a cellular resolution. A large field of view noncontact FF-OCT microscope for clinical corneal imaging is currently being developed during the thesis of *Viacheslav Mazlin* [301]. FF-OCT is also being investigated to offer a quantitative assessment of corneal transparency to be used as a pre-marker of diseases [311]. Finally, OCT and FF-OCT can also advantageously image the corneoscleral ring, which is much more scattering than the cornea, while being of interest for corneal health assessment. If OCT can measure the layers disorganization to successfully identify several corneal diseases such as keratoconus, Fuch's endothelium dystrophy, or epithelium erosion [312], we expect that the cellular resolution offered by FF-OCT might help to detect similar diseases at the single cell level before the entire layer is disorganized. Figure 6.6 shows the imaging of a cornea with the LLTech commercial system. Epithelial and collagen fibers can be detected throughout the cornea. Endothelium organization can also be assessed, which is interesting as endothelial cell sizes and density are markers for the endothelium barrier disruption. Besides, I will show in this section several examples where FF-OCT and our multimodal platform has been or could be useful.

6.2.1 Evidence of the stem cell niche in the cornea

The fist study of the cornea using FF-OCT that I was involved in has demonstrated the ability of FF-OCT to investigate the 3-D structure and organization of the corneal limbus (at the frontier between the cornea and the sclera) and of the limbal crypts extending inside [183]. Such limbal crypts are of large interest as they provide a microenvironment that fosters the development of epithelial stem cells crucial for the renewal of the corneal epithelium [183, 313]. The corneal limbus is often referred to as a stem cell niche due to its highly-vascularized microenvironment with a dense innervation, high protection from light, and highly controlled biomechanics. FF-OCT enabled the 3-D investigation of the limbal crypts and to calculate their volumes. The multimodal FF-OCT and fluorescence microscope enabled us to demonstrate the presence of epithelial stem cells and differentiated corneal epithelial cells only inside these limbal crypts. Interestingly, a correlation was found between the mean crypt volume and the ability of the dissociated limbus to form epithelial cell colonies (which is an indicator of the health of the epithelial stem cells through their ability to divide and to differentiate). Using FFOCT as a screening tool to identify regions of limbus with dense, large limbal crypts could allow both the selection of limbal zones for graft

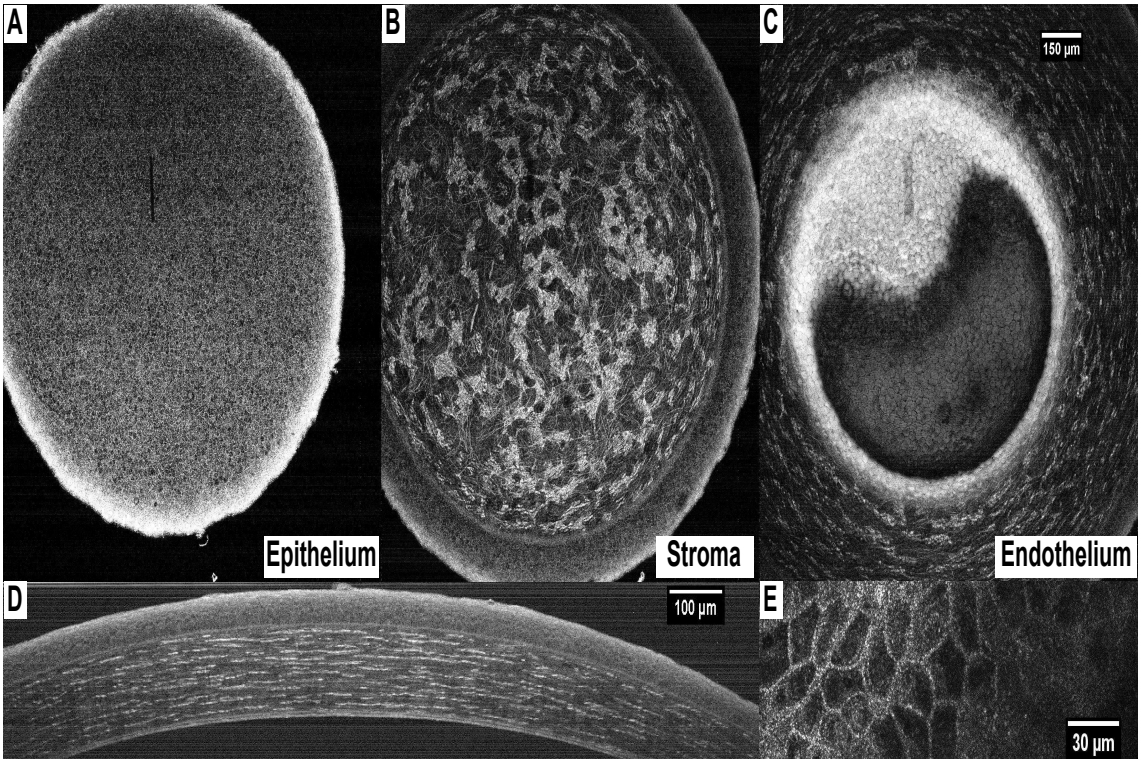

Figure 6.6 – Imaging mouse cornea with FF-OCT. Panels A to C show different amplitude OCT images (in log scale) obtained with the LLTech FF-OCT microscope at different depths and layers in the cornea, respectively epithelium, stroma, and endothelium. Compared to regular OCT, FF-OCT reveals the cellular contours of the epithelial and endothelial cells (Panels A and C), with a strong specular reflection visible on the top and bottom surfaces of the endothelial cells, and reveals collagen fibers as wells as keratocytes extensions. **Panel D** shows the corresponding axial profile that can be compared to OCT cornea images, as illustrated in figure 6.2 but displays a better resolution. **Panel E** shows a higher resolution image of the corneal epithelium to emphasize FF-OCT ability to reveal epithelial cell contours.

in limbal insufficiance patients and the identification of optimal zones of corneoscleral donor rims (left over after graft of central cornea) for cell culture in the development of artificial cornea [183].

6.2.2 Another interest for static FF-OCT and fluorescence in the cornea

Figure 6.8 illustrates another interest to combine FF-OCT and fluorescence imaging for cornea imaging. In this example, the 3-D organization of the cornea is measured thanks to FF-OCT while the fluorescence imaging specifically reveals nerves and nerve terminals in a mouse with fluorescently labeled nerves. In this example, FF-OCT can clearly identify the corresponding corneal layers and their associated structures that help to identify the position of the nerves with respect to the 3-D organization of the corneal layers. We could show that most of the thin sub-basal nerves in the cornea were located at the interface between the epithelium layer and the Bowman's layer, as expected from literature [314, 315]. We could identify some of the nerve terminals in the different layers of the epithelium layer and a few thicker nerve fiber at the top of the stroma. Interestingly, some of the thickest nerve fibers in the Bowman's layer can be detected with FF-OCT. However, FF-OCT fails to detect the thinner nerve fibers in the Bowman's layer, the nerve terminals, and the thicker stromal nerve fibers. Our ability to detect a few nerve fibers

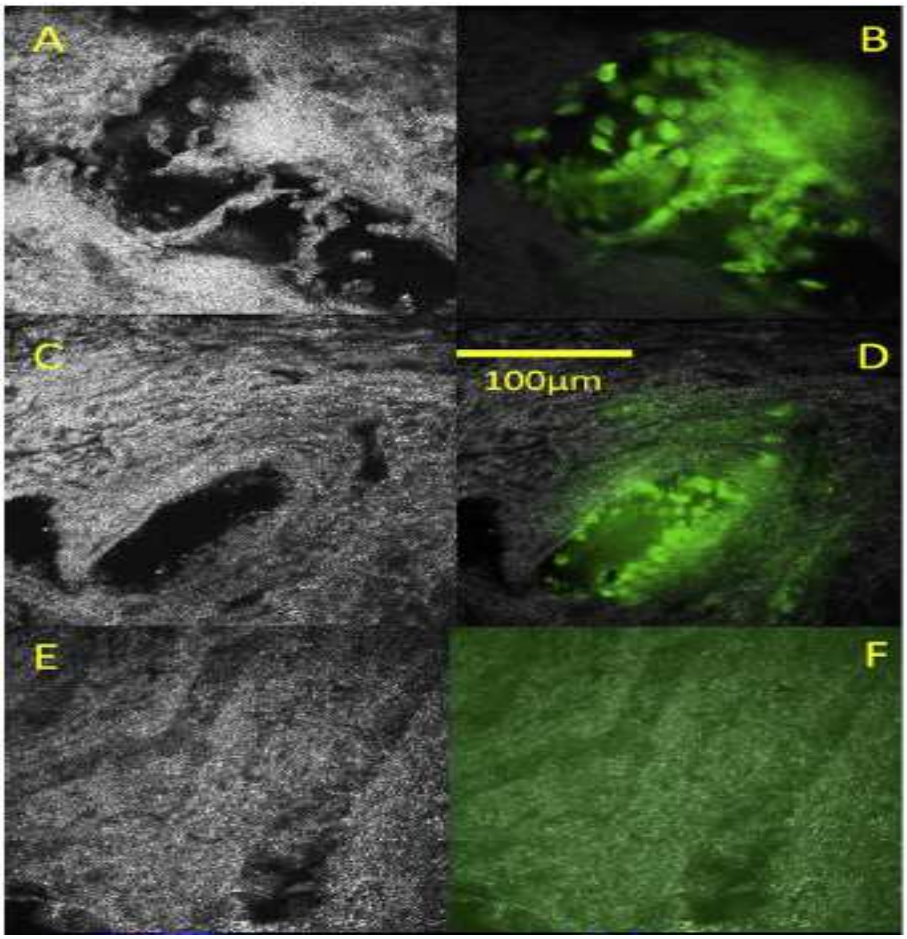

Figure 6.7 – Identification of the cellular content of limbal crypts using FF-OCT and fluorescence multimodal platform. Panels A to F show the corresponding FF-OCT and fluorescence images at different locations in the limbus. OCT amplitude images are displayed on the 3 left panels and fluorescence images overlaid with OCT on the 3 right panels. Panels A and B are taken near the limbal surface and show presence of epithelial cells (fluorescence is epithelial cell marker KC3). Panels C and D are taken at greater depth in the limbus, towards the crypt base, where stem cells are seen (fluorescence is stem cell marker p63alpha). E and F show that not all crypts contain stem cells (fluorescent marker p63alpha is used, but identifies no cells in this crypt). Stem cells are only present in a small percentage of crypts, but we found that crypt volume correlated with culture yield, meaning that zones with larger, denser crypts are more likely to contain stem cells and should therefore be targeted for efficient culture. These images have been reproduced from *K.Grieve et al.* [183].

suggests that FF-OCT could detect more fibers if the SNR were increased [5] but also highlights the importance of combining both FF-OCT and fluorescence contrasts. In this case, it could help to better understand the nerve formation or regeneration in different mouse models with the precise layer the nerve fiber is growing. In previous studies [314], the position of the nerve fibers with respect to the 3-D organization of the cornea could only be inferred with electron microscopy, which limits the available field of view, is quite complicated to obtain, and is not compatible with longitudinal studies.

[5] As a reminder, the SNR could be increased using cameras with higher full well capacities, objectives with higher NAs, or using accumulations.

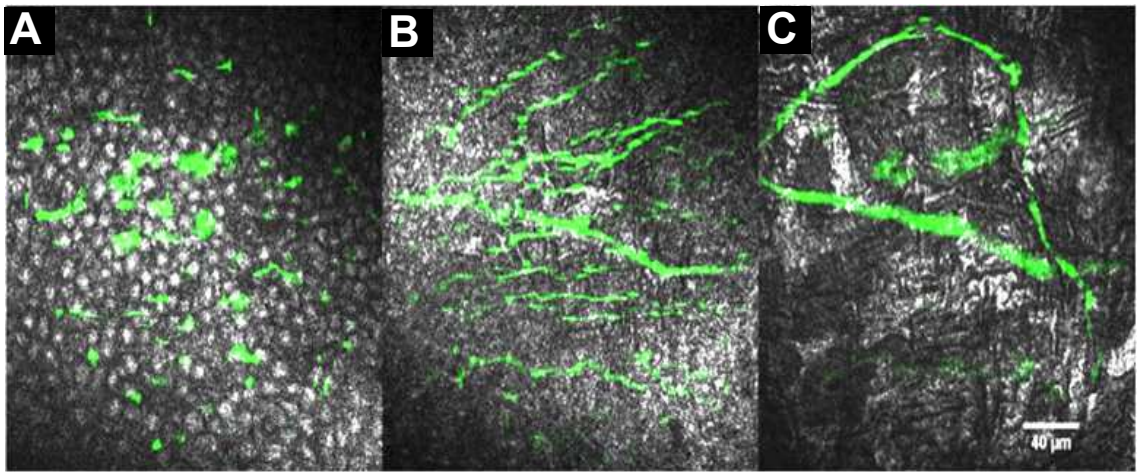

Figure 6.8 – Identification of nerve terminals in a mouse cornea with FF-OCT and fluorescence multimodal system. Panels A to C show the superimposition of an amplitude FF-OCT image (gray scale) with the corresponding fluorescence image (green channel) at three different depths around the Bowman's layer. Panel A shows nerve terminals projecting in the last epithelium cells layer. Panel B shows that most of the nerve fibers originate from the sides in the Bowman's layer, while panel C illustrate the presence of a few larger nerve fibers at the top of the Stromal layer of the cornea. Panel A is located 15 μm above the Bowman's layer (Panel B) and panel C is located 10 μm below.

6.2.3 Dynamic FF-OCT in the cornea

Similarly to other organs, Dynamic FF-OCT can be applied to corneal imaging to reveal cell bodies, as illustrated in figure 6.9. Especially, D-FF-OCT is particularly efficient at revealing epithelial cells, whereas FF-OCT can merely detect epithelial cell contours. As discussed in chapter 5, D-FF-OCT contrast is an indicator of cell motility and of the associated metabolism and can therefore be an indicator of the cell health. A dim dynamic FF-OCT signal can be detected in keratocytes but the obtained contrast is not necessarily different from static FF-OCT's. Finally, dynamic FF-OCT fails at detecting any metabolic activity inside the endothelial cells, while their surfaces are bright in both FF-OCT and D-FF-OCT. Indeed, there seems to be a strong specular reflection at the endothelial cell top and bottom surfaces so that interference fringes can be observed on these surfaces. Due to small motions (from either the sample or the surface itself) of these fringes, the intracellular D-FF-OCT signal is probably hindered [6]. Nevertheless, as previously suggested, endothelial cell sizes and density can be a good indicator of endothelium-impacting diseases. A last possible investigation enabled by D-FF-OCT is illustrated in figure 6.9 C. It consists in injecting stem cells in a cornea, or cornea-mimicking matrix in order to follow their migration and differentiation into keratocytes, as proposed and investigated by *Djida Ghoubay* at the *Institut de la vision* in order to design efficient rejection-free artificial corneas. If this could be followed by fluorescence imaging as well, the label-free ability of FF-OCT can be of interest to follow the correct migration of stem cells in explanted or artificial corneas prior to a cornea graft.

6.3 Static and dynamic FF-OCT imaging of the retina

The goal of this section is to show the potential interest of FF-OCT and dynamic FF-OCT for retinal imaging. Similarly to OCT systems, FF-OCT can image all the retinal layers but its

[6] We can add that dynamic signal from the endothelial cells might be detected by increasing the axial resolution (optical sectioning) down to 1 μm using white light sources instead of red LEDs.

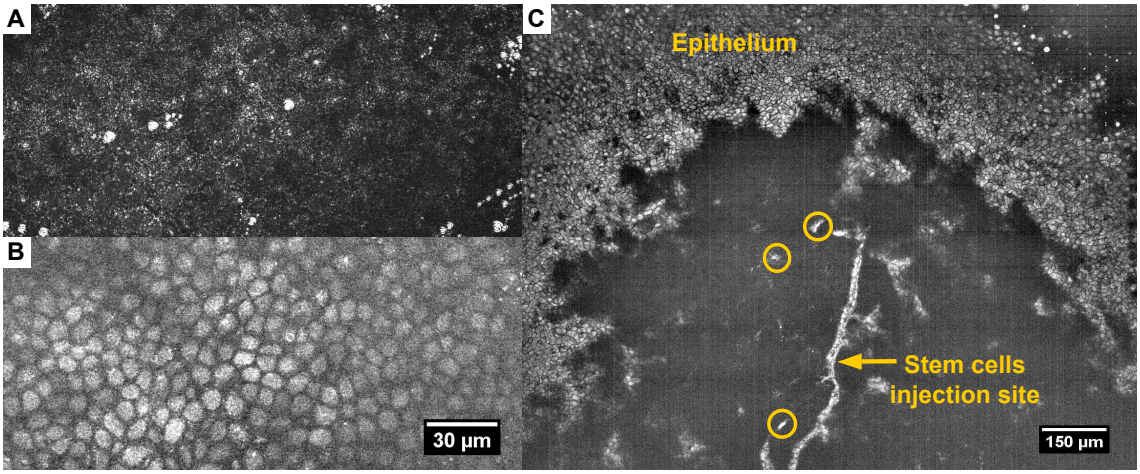

Figure 6.9 – Dynamic FF-OCT imaging in the cornea. Panels A and B compare the FF-OCT (Panel A) and dynamic FF-OCT (panel B) images of one of the first layers of a monkey corneal epithelium, illustrating the ability of D-FF-OCT to highlight the epithelium organization. **Panel C** presents a dynamic FF-OCT image acquired with the LLTech commercial system in a monkey cornea injected with stem cells. D-FF-OCT can reveal the epithelium organization (on the sides due to the curvature of the cornea) and the injection site as some stem cells are probably trapped inside. A few dynamic areas have been circled in yellow as they could be stems cells that have migrated in the stroma.

superior lateral resolution allows for the detection of cellular details of interest that are hidden in scanning OCT. These details include cellular contours, nerve fibers, or small capillaries, as illustrated in figure 6.10. The detection of the nerve fibers disruption in the top layer of the retina can be an indicator for a few diseases such as *retinitis pigmentosa* or glaucoma while an abnormal thinning of the nerve fiber layer is observed at the later stages of these diseases but that can be confused with the usual thinning of this layer with aging at the early stages of the disease. Interestingly, we suggest that FF-OCT could detect early stages of myelinated retinal nerve fiber layer, in which, not surprisingly, some of the ganglion cell axons become myelinated. Additionally, dynamic FF-OCT enabled us to reveal most of the retinal cells and to measure their metabolism and health over time, as illustrated in figure 6.11 that compares FF-OCT and D-FF-OCT contrasts in a macaque retina as imaged with the LLTech commercial microscope. The appearance of the retina with FF-OCT has been described in *K. Grieve et al.* and we are currently preparing another article describing the interest of D-FF-OCT for retinal imaging. Interestingly, and as will be discussed in the next subsection, Dynamic FF-OCT can identify most of the retinal cell populations and probably most of the retinal cells. High-resolution D-FF-OCT can additionally measure a cytoplasm-to-nucleus ratio that can further help to classify and identify the different cells based on morphological parameters.

Figures 6.10 and 6.11 present typical images of a retina acquired with FF-OCT and D-FF-OCT respectively and illustrate that D-FF-OCT enables the detection of a higher number of cells. They can be compared to the retina imaged with OCT presented in figure6.3, nevertheless keeping in mind that the OCT images are acquired *in vivo* in a moving eye. In the next subsection, high-resolution images of the different cellular layers of the retina will be described both in FF-OCT and D-FF-OCT. We imaged dozens of retinas from mice, rats, pigs, macaques, and even humans and can detect cellular activity in most of them, at least in the first retinal layers. FF-OCT can image the entire retina of rodents from the bottom to the top but fails at imaging deeper than the outer nuclear layer at the center of primate and pig retinas, where the density of fibers is important. This is probably due to aberrations and signal attenuation caused by the nerve fibers

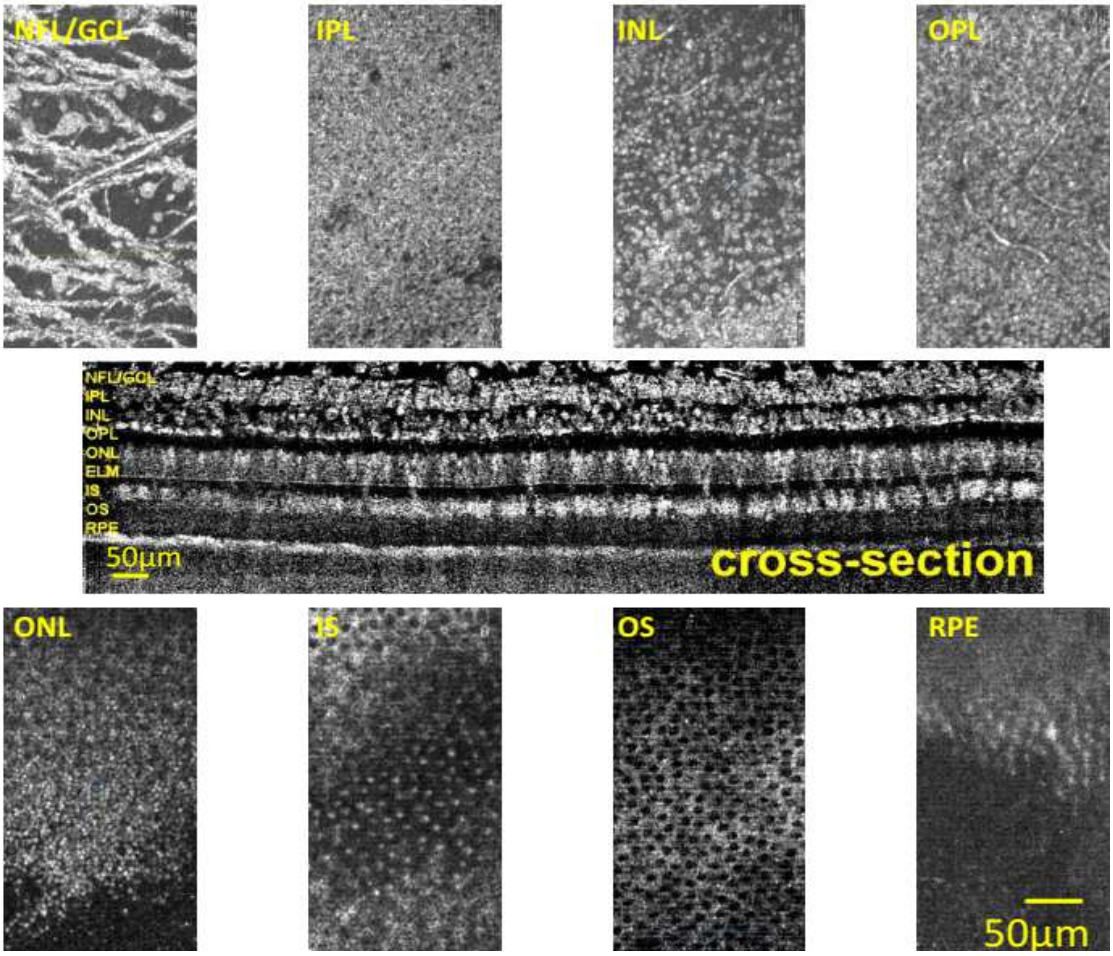

Figure 6.10 – Appearance of a macaque retina with FF-OCT acquired with the LLTech commercial system. The center image presents the cross-section of the retina, similarly to OCT or histological images, and the 8 small images present typical transverse views of the ganglion cell layer (GCL), the inner plexiform and nuclear layers (IPL and INL), the outer plexiform and nuclear layers (OPL and ONL), as well as the inner segments (IS) and outer segments(OS) of the photoreceptors and the retinal pigmented epithelium (RPE). FF-OCT can not only detect the different layers but can also detect cell somas in the GCL, the INL and the ONL. FF-OCT can additionally detect small blood capillaries and some of the photoreceptors. This image has been taken from *K. Grieve et al.* [206].

of the retina first layer. This decrease is especially important with the high-resolution system. In primates, we often image the periphery of the retina, where the fiber density and the cellular density is lower so that we could acquire images throughout the retina.

In order to validate the contrast obtained with dynamic FF-OCT, we used the multimodal fluorescence and FF-OCT platform with selective probes for ganglion cells, as illustrated in figure 6.12 and in figure 6.11 in the previous chapter. In figure 6.12, we could detect a few ganglion cells with dynamic FF-OCT and fluorescence, as well as two large cells with a large nucleus on one side of the cell and that are not labeled in fluorescence. Interestingly, these cells look like displaced starburst amacrine cells (see figure 37b (!) of the chapter on amacrine cells in the book Webvision [264]). With adequate labels, or specific genetic lines encoding for the (green) labeling of the different retinal cell populations, we could have theoretically validated D-FF-OCT for each cell population. For instance, we could also confirm the detection of amacrine cells at the bottom of the inner plexiform layer of the retina with a specific line (Choline acetyltransferase for amacrine starburst cells for example), the imaging of which is not displayed here. Nevertheless, this type of labeling is not common, is very specialized, and has variable success so that we could not image

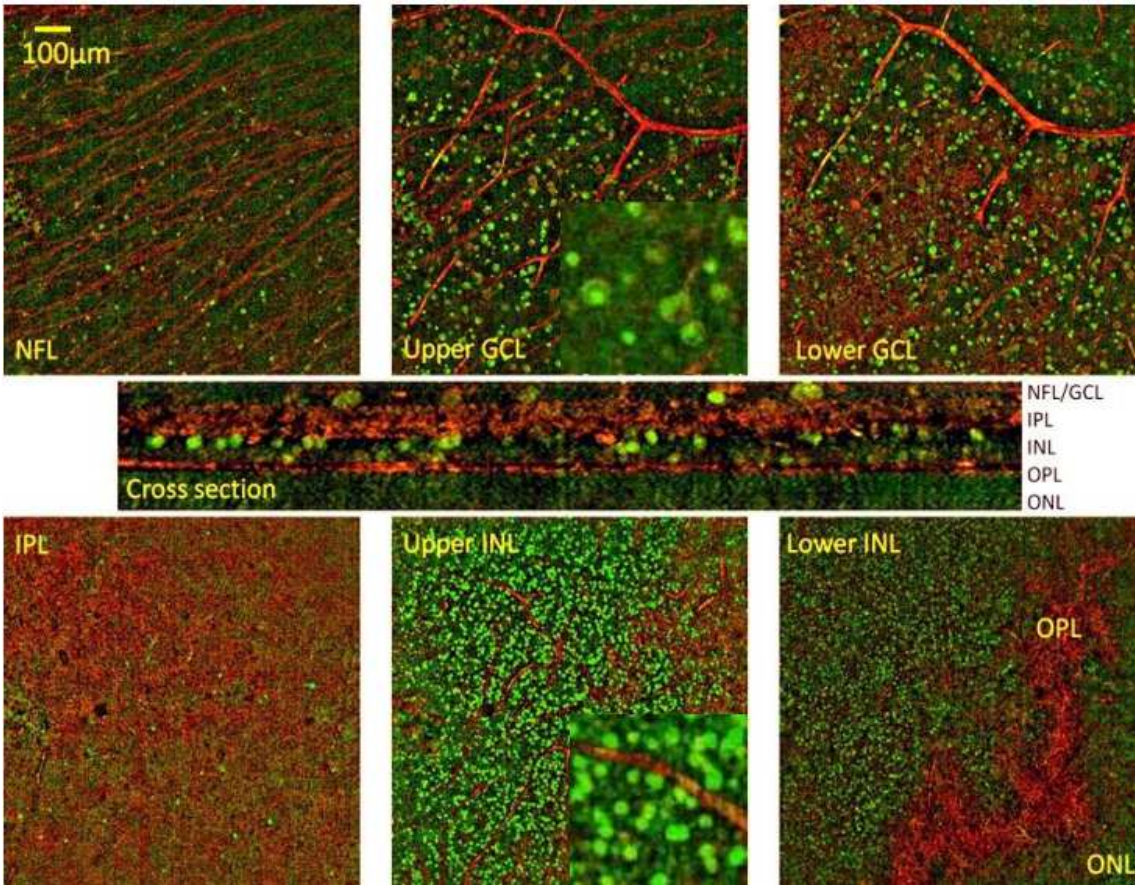

Figure 6.11 – Appearance of a macaque retina comparing FF-OCT and dynamic FF-OCT acquired with the LLTech commercial system. Similarly to figure 6.10, the red channels in all the panels present the FF-OCT view of the first layers of the retina. The green channel encodes the dynamic FF-OCT (calculated with the standard deviation and average). It illustrates D-FF-OCT ability to detect more cells than static FF-OCT as well as some intracellular contrast. These images also show that these retinal cells were still metabolically active at the time of the imaging.

many successfully labeled retinas and we mainly relied on the cellular positions and shapes to estimate their nature.

We can finally add that several fluorescently labeled cells exhibit strange shapes and intracellular contrasts, as illustrated in figure 6.12 on the right-hand side for instance while showing a more regular aspect in fluorescence. At this point, we could not conclude whether this comes from an artifact related to our microscope or a more generalized artifact due to fluorescence labeling. It might mean that some fluorescent labels significantly impact the intracellular dynamics, cell contour, and potentially function. Nevertheless, this might require further observations and require us to think about a smart protocol giving a positive contrast on the dynamics perturbation [7].

[7] Indeed, this is a recurrent problem with FF-OCT, and in microscopy in general I guess. If no signal is acquired, it is hard to know whether this comes from the microscope or from a real effect.

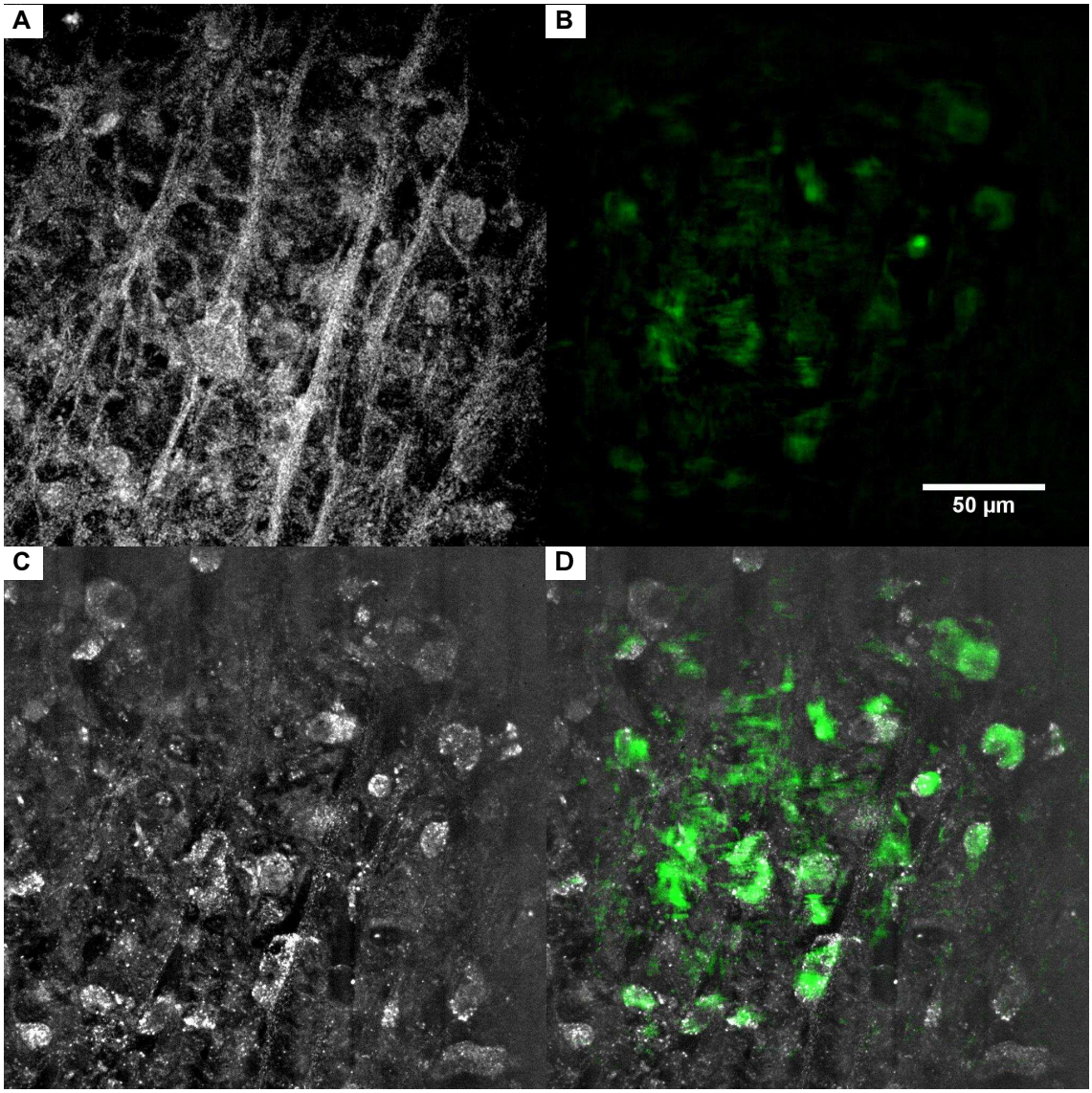

Figure 6.12 – Cellular identification using fluorescence microscopy and dynamic FF-OCT. A macaque retina with ganglion cells specifically labeled with gene gun [263] is imaged simultaneously with FF-OCT (**panel A**), fluorescence microscopy (**panel B**), and D-FF-OCT (**panel C**). An overlay between the fluorescence image and the dynamic FF-OCT image is presented in **panel D**. It shows that D-FF-OCT reveals all the cells labeled with fluorescence and even reveals two additional large cells with a large nucleus on the side of the cytoplasm. It can be due to the sparse labeling of the gene gun or might show that these cells are not ganglion cells but displaced amacrine cells.

6.3.1 High-resolution imaging of the retina layer by layer

In this subsection, I will illustrate typical images of some of the layers of the retina with high-resolution FF-OCT, D-FF-OCT, and color-coded D-FF-OCT (presented in the previous chapter). Even though such a detailed description can appear laborious, we emphasize the unique aspect of these images (to our knowledge) and believe these images can be of interest for eye specialists. Most of the electron microscopy and optical high-resolution images of the retina that are available in the literature were obtained on axial sections of the retina and do not account for the transverse organization of the retina inside the different layers. Besides, fluorescence transverse images of the retina often label only one cell population and can hardly account for the position of these cells with respect to the retinal 3-D organization. Therefore, these images are probably, the highest resolution label-free transverse sections of fresh retinas ever imaged. To be fair, we should add that imaging retinal explants is mandatory to obtain high-resolution images of the retina, since the eye equivalent NA is equal to 0.2 and cannot be increased without removing the cornea and the lens. We finally add that we recently discussed with the group of *Christophe Moser* in the EPFL in Switzerland who are currently publishing an article (available on Arxiv [42]) describing another technique allowing for *En face* views of the retina. Briefly, the technique consists of performing a transmission low coherence QPI imaging of the retina using an *oblique* illumination through the sclera and using the reflection on the retinal pigment epithelium (RPE) and choroid layers, which enables *in vivo* imaging of the retina [42]. They visibly also faced similar difficulties to ours in comparing their images but finally succeeded in performing transverse histology sections of the retina to compare to their images. Nevertheless, their system is ultimately limited by the eye NA, and to a transverse resolution around 1 μm and can only determine cell types from the cell shapes as they do not detect cell nuclei and cell metabolism, as offered by dynamic FF-OCT.

Figures 6.13 to 6.16 show FF-OCT and D-FF-OCT images respectively in the ganglion cell layer (GCL), inner nuclear layer(INL), outer nuclear layer(ONL) and photoreceptor layer (PRL). High-resolution FF-OCT enables detection of ganglion cell axons down to the single fiber and can image several cell bodies. Dynamic FF-OCT can emphasize the cell contours and detect cell nuclei. In the mouse retina presented in figure 6.13, D-FF-OCT detects at least two different cellular morphologies with small cells with a small nucleus and larger cells with a nucleus occupying about half the cell area. Both in terms of densities and morphology, these cells could be assimilated to displaced amacrine cells as revealed in the mouse retina thanks to their immunoreaction for GABA [316]. On average, D-FF-OCT measures cell densities in the ganglion cell layer between 1,500 (macaque at the periphery) and 4,000 (mouse retina closer to the retina center) cells per mm^2, which is in accordance with the ganglion cell density measured in pigs [8] [42, 318]. Interestingly, color-coded D-FF-OCT in the large cells emphasize fast dynamics in the cytoplasm and slower dynamics in the nucleus, while most of the small cells have intermediate dynamics. We also noticed that some of the small cells exhibit slower dynamics (blue color) than others, which suggests that it may be possible to distinguish different cell types according to their dynamics.

High-resolution dynamic FF-OCT is particularly spectacular in the inner nuclear layer, where FF-OCT can hardly detect cell contours, while D-FF-OCT can identify here again at least two different cellular morphologies, as illustrated in figure 6.14. A first patch of neurons exhibit a small size and a nucleus that takes almost the entire cellular space and a second are larger cells with higher cytoplasm-to-nucleus ratio. Some of the small cells seem to exhibit a faster dynamic

[8] The ganglion cell density that we measured is about 10 times lower than the value reported in *Ahmad et al.* [317] in macaque retinas. Nevertheless, this density has probably been obtained at the center of the retina, where the ganglion cell density is much higher compared to the periphery.

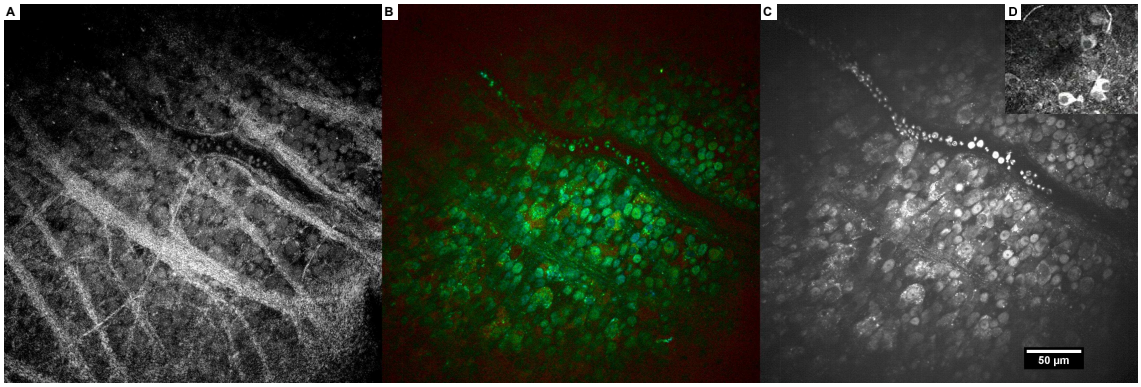

Figure 6.13 – Retinal ganglion cell layer. Panels A to C respectively show the amplitude FF-OCT (Log scale), dynamic FF-OCT image, and color-coded dynamic FF-OCT of a mouse retinal ganglion cell layer (GCL). **Panel D** is a small insert presenting a D-FF-OCT image in a monkey retinal GCL to emphasize D-FF-OCT ability to reveal ganglion cell axon hillocks.

signal than others. The cell density in the macaque INL is counted as 12,000 cells per mm^2 with the high-resolution system and 9,000 with the LLTech commercial system, also in accordance with the literature [42] for human retinas. Here again, we counted less cells than what was reported in the literature for macaque retinas [317] but this is probably due to the different eccentricity between our measurements. We can add that we also detected a few isolated cells in the IPL and a few cells with different morphologies at the top of the INL, that could possibly be amacrine cells based on their positions (Not displayed here). We could often detect two distinct layers in the INL but could not unambiguously assert that we detected horizontal cells on a criteria other than the cell positions in the depth of the INL.

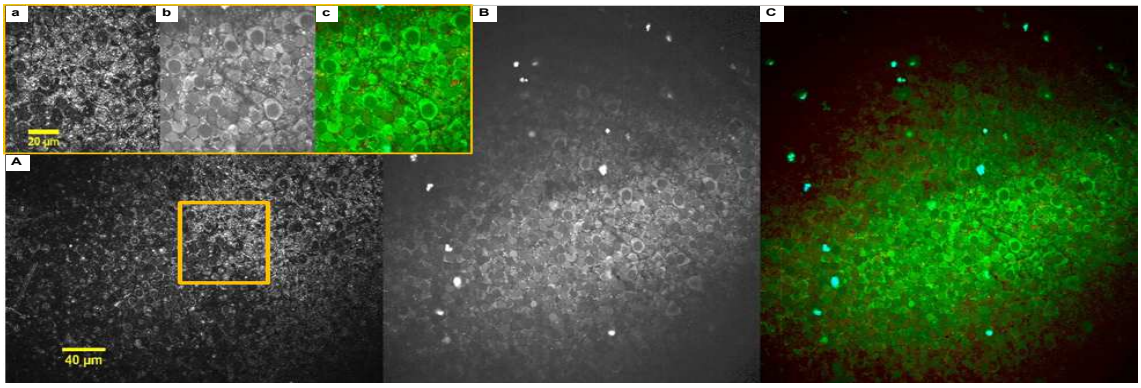

Figure 6.14 – Peripheral view of the inner nuclear layer (INL) of a macaque retina. Panels A to C respectively show the amplitude FF-OCT, dynamic FF-OCT, and color-coded dynamic FF-OCT image of a macaque inner nuclear layer (INL). **Panels a to c** present the corresponding zoom in at the same location of the 3 larger images. They emphasize the two different cell populations that can be identified with D-FF-OCT.

The frontier between the OPL and the ONL is interesting in both FF-OCT and D-FF-OCT, as illustrated in figure 6.15. FF-OCT can measure the fibrous layer of the OPL on the left of the image and can also image many small spheres, that we identified as the photoreceptor pedicle spherules, which are the synaptic endings of the photoreceptors that can be as large as 8μm for the cones spherules and 4 μm for the rods spherules. Dynamic FF-OCT can also detect theses structures but additionally detect photoreceptor cell bodies on the right-hand side of figure 6.15.

Finally, D-FF-OCT can nicely reveal photoreceptor inner segments, while the static FF-OCT corresponding image displays only low contrast. The larger cone inner segments can be easily

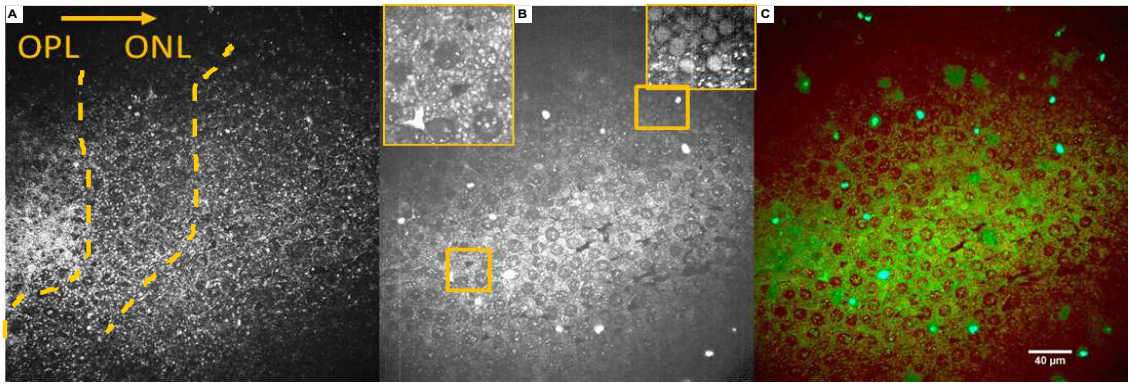

Figure 6.15 – Peripheral view of the outer nuclear layer (ONL) of a macaque retina. Panels A to C respectively show the amplitude FF-OCT, dynamic FF-OCT image, and color-coded dynamic FF-OCT of a region in between the outer plexiform layer (IPL) and the outer nuclear layer (ONL). Both layers can be seen in the field of view because the retina is tilted with respect to the coherence volume. In panel A, the OPL can be identified in the left region (hand-drawn line), pedicle spherules can be detected in the center region, while photoreceptor cell bodies can be guessed deeper inside the ONL (region at the right-hand side). The D-FF-OCT image in panel B can detect some activity in the photoreceptor cell bodies, as illustrated in the two additional zoom-in areas on the top corners (corresponding to the yellow boxes).

distinguished from the smaller rod inner segments. Both static and dynamic FF-OCT can detect the photoreceptor outer segments but D-FF-OCT enables emphasis of their contours. In the macaque retina presented in figure 6.16, we counted a density of cone cells of about 2,000 cells per mm^2 and of a density of rods around 50,000 cells per mm^2, which are reasonable values for the periphery of the primate retinas [319].

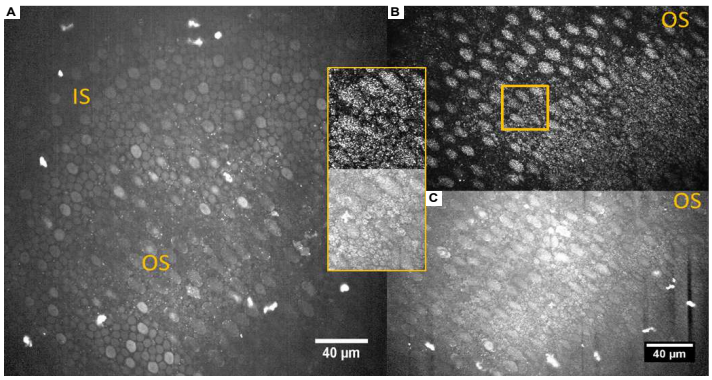

Figure 6.16 – Peripheral view of the photoreceptor layer (PRL) of a macaque retina. Panel A shows a dynamic FF-OCT image of the frontier between the inner segments(IS) and the outer segments (OS) of the photoreceptors cells, showing an increased dynamic activity in the inner segments. **Panels B and C** respectively show the static and dynamic FF-OCT image 10μm below panel A, in the outer segment layer. If the contrast is not significantly different, D-FF-OCT provides greater precision on the photoreceptor cell contours. The middle yellow inset present a zoom in of the yellow box presented in panel B in both static and dynamic FF-OCT. It seems that the center of the rod photoreceptors exhibits little dynamic activity.

In this description, we demonstrated D-FF-OCT ability to reveal most of the retinal cell types and most of the retinal cells as well, with cellular densities matching those reported in the literature. High-resolution FF-OCT is probably required for imaging the center of retinas and rodents retinas where the cells are smaller on average and the cell densities are higher, but is more sensitive to aberrations partly due to the high density of nerve fibers in the NFL. Nevertheless, our work is probably too preliminary to output an interesting information on retinal structure because we

faced the high complexity of the retina that has various subtypes of cells of various sizes and positions. To complexify it more, the structure and position depend on the location of the imaged area with respect to the fovea position and depend on the animal species. A careful investigation acquiring images at always the same location in the retina and with always the same imaging parameters might help to identify more retinal cell subpopulations based on their respective shapes, positions, and dynamics. We are now also trying to evaluate the potential interest for such cellular identification for ophthalmic diagnosis and the next step will be to image pathological retinas.

6.3.2 D-FF-OCT to assess local cell viability

As demonstrated in the previous chapter on a freshly excised liver, D-FF-OCT can also be interesting for its ability to assess and hopefully measure the cell metabolic state that is linked to the cell health. To illustrate this metabolic dependence, we tried to evaluate the dynamic FF-OCT signal decrease over time and found that D-FF-OCT was globally decreasing linearly while the static FF-OCT is constant over the same amount of time. Generally, the D-FF-OCT signal reaches the noise level after 5 to 6 hours in an HEPES (a pH buffering agent to replace a CO_2 controlled environment) neurobasal nonoxygenated medium at room temperature. Nevertheless, the cellular details are lost a few hours only after the tissue extraction. Figure 6.17 illustrates this loss of D-FF-OCT contrast after 3 hours of imaging. Similar measurements have been performed in the cornea, which might be a good indicator for corneal grafts and to ensure the retina maintenance in response to different chemicals, treatments, or stresses. We add that following the evolution of the D-FF-OCT signal in the cornea and the retina is quite complicated because explanted retinas and corneas undergo rapid swelling on the hour timescale that first dilates the tissue and then contracts it. To be sure the same cell can be imaged over long time periods, 3-D stacks should be acquired at every time period.

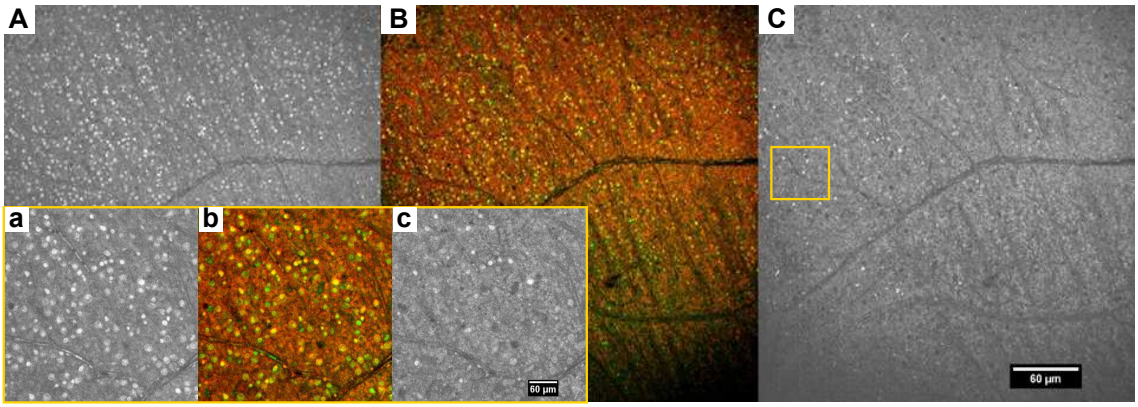

Figure 6.17 – D-FF-OCT contrast decay over time in macaque retinal INL. Panel A shows a typical INL image, as illustrated in figure 6.11 one hour after tissue extraction. **Panel C** shows the same region 4 hours after tissue extraction and illustrates the decay of the D-FF-OCT contrast over time. **Panel B** shows the overlay of panel A (green channel) and panel C (red channel) to emphasize the decay. **Panels a to c** correspond to the zoom in the yellow box region (displayed in panel C) for all the three larger panels.

6.4 Conclusion and future developments

In this chapter, we have seen the application of FF-OCT and dynamic FF-OCT to corneal and retinal imaging. We have demonstrated FF-OCT's ability to detect the layered structures and a

few cellular details in both tissues. Additionally, D-FF-OCT's ability to detect most of the cellular types in both cornea and retina and to potentially assess their metabolic state appears to be of particular interest. If our studies are mainly preliminary studies as we only imaged healthy retinas and we imaged retinas in a (probably too large) variety of experimental conditions (different animals, different eccentricity, different timing from extraction, *etc...*), D-FF-OCT appears to be a promising tool for early detection of retinal and corneal pathologies. The careful investigation of the retinal 3-D organization as well as the imaging of pathological retinas could be an interesting future step. We are now trying to convince medical doctors and biologists of the interest of (D-)FF-OCT and to find pathologies for which (D-)FF-OCT could bring insightful information. Ideally, FF-OCT might soon be available for clinical *in vivo* imaging as *Viacheslav Mazlin* is developing a contact-free corneal FF-OCT system and *Peng Xiao* is developing a similar system for retinal imaging. They are both about to submit a CPP (ethics) approval for both systems to allow for clinical trials. In the meantime, and as already discussed in previous chapters, we have demonstrated the feasibility to detect D-FF-OCT in living paralyzed zebrafish larvae and could reveal their corneal epithelium (See figure at the beginning of this chapter). Unfortunately, at such early stages of development, Zebrafish larvae do not have fully developed retinas with a layered structure, and retinal cells could not be detected unambiguously. Finally, I believe that D-FF-OCT can also detect a functional contrast in the retina from motility changes, as will be discussed in the next chapter. An interesting experiment might consist of detecting the dynamical activity of cone photoreceptor inner segments under illumination of different colors. It might allow for the label-free identification of the different types of cone photoreceptors (which have peak sensitivity at different wavelengths) from a change of the mitochondrial activity (a decrease of activity would be *a priori* observed), which has never been achieved by a label-free imaging technique to my knowledge. Dynamic changes under different illumination patterns could also be investigated using D-FF-OCT in the future.

A last perspective I would like to develop here is FF-OCT ability to measure red blood cell activity, dynamic phase fluctuations, and refractive index. As illustrated in figure 6.18, dynamic FF-OCT can reveal red blood cells trapped in retinal capillaries (since there is obviously no blood flow left in an excised retina) and can emphasize their shapes. As discussed in chapter 1, red blood cell membranes show rapid and relatively high amplitude fluctuations. It was also mentioned that red blood cell shapes and membrane fluctuations were accurate indicator (and pre-indicator) of several diseases. In terms of application, it is worth noticing that vascular diseases are one of the major pathologies in the retina and several techniques, including OCT angiography and Doppler OCT, aim to measure retinal blood flow. With FF-OCT, we can not only detect individual red blood cells, but also measure their membrane fluctuations and derive their refractive index. Obviously, these measurements have been performed in explanted retinas but a fast enough FF-OCT system would potentially allow the measurement of single red blood cells in retinal capillaries, and could even be able to measure their deformations under the blood flow. From such deformations, a mechanical index of the red blood cell might be computed.

Using explanted retinas, we have performed two types of measurements in red blood cells. The first one has been to acquire many phase images over time to perform similar measurements than the ones performed in quantitative phase imaging. At this time, we have been able to measure the time course of phase fluctuations at a red blood cell membrane in a few pieces of retina. If the phase signals show similar fluctuation amplitude and time scales than what we have been able to measure on red blood cells mounted on a glass plate, we are still trying to use similar algo-

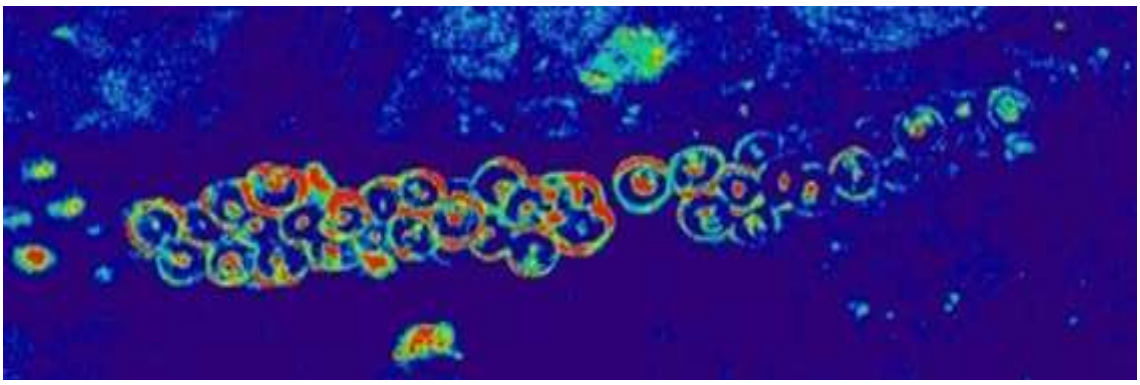

Figure 6.18 – Red blood cells dynamics. To our knowledge, this is the first time that an imaging technology can quantitatively measure red blood cells fluctuations in a tissue. Here, the red blood cells are trapped inside a capillary of an Ex vivo macaque retina. While several articles succeeded in forecasting blood diseases by measuring red blood cells fluctuations, our image paves the way of similar measurements in ex vivo tissues

rithms (as described in chapter 1 and in appendix C) to compute the red blood cell mechanical parameters. To our knowledge, it would be the first evidence of such measurement in red blood cells inside a thick tissue and would offer the possibility to run a bonus blood diagnosis during a biopsy evaluation (for other reasons).

Additionally, we have been able to estimate the refractive index of red blood cells inside the retina. As presented in chapter 1, the hemoglobin concentration in red blood cells can be estimated from their refractive index measurements. Furthermore, the blood oxygenation can be computed from a dual-wavelength refractive index measurement so that it can finally give a functional contrast associated with the BOLD signal. Interestingly enough, such a refractive index measurement can be performed with a limited number of images and might be considered for *in vivo* applications when FF-OCT will be ready to image *in vivo* retinas. The principle of this second measurement is to acquire a phase 3-D stack around a capillary. If the axial displacement between two successive measurements is small enough, axial 1-D phase unwrapping can be performed on each voxel of the data set. It allows to compute the optical path variation, from which the refractive index can be calculated as the physical displacement is known. Here, I have to admit that such a naive approach should not work in principle because it does not take into account the axial position of scatterers. and makes the strong hypothesis that the average phase moves continuously as we move in depth. Nonetheless, we have been able to measure reasonable values of refractive index in red blood cells and in the different layers of the retina. In fact, because biological tissues have a refractive index different than water, the induced refractive index dependent defocus (also mentioned in appendix B) has to be taken into account. In the low NA approximation, the optical axial shift Z inside the sample can be written as:

$$Z = Z_{mot}.\frac{n_M}{n_W} \tag{6.1}$$

with Z_{mot}, the tissue physical displacement, n_M, the medium refractive index and n_W the water refractive index. Therefore, when scanning axially, the phase difference becomes:

$$\Delta\phi = \frac{2\pi}{\lambda}.2.(n_M - n_W).Z_{mot}.\frac{n_M}{n_W} \tag{6.2}$$

It results in an equation of the second order:

$$\frac{4\pi}{\lambda}.Z_{mot}(\frac{n_M^2}{n_W} - n_M - \frac{\Delta\phi\lambda}{4\pi Z_{mot}}) = 0 \tag{6.3}$$

This equation admits only one solution with the sample refractive index above the water refractive index, which can be written as:

$$n_M = 0.5(n_W + n_W.\sqrt{1 + 4\frac{\Delta\phi}{n_W}\frac{\lambda}{4\pi Z_{mot}}}) \tag{6.4}$$

From this procedure, we have been able to measure continuous phase changes after a small spatial average (in the transverse direction), and to measure refractive index of red blood cells between 1.39 and 1.41, in accordance with values found in literature. We have also been able to measure the average refractive index of the first layers of the retina. Nevertheless, further experiments should be conducted to assess the reproducibility of these measurements and in order to try to understand what are the conditions under which they are valid.

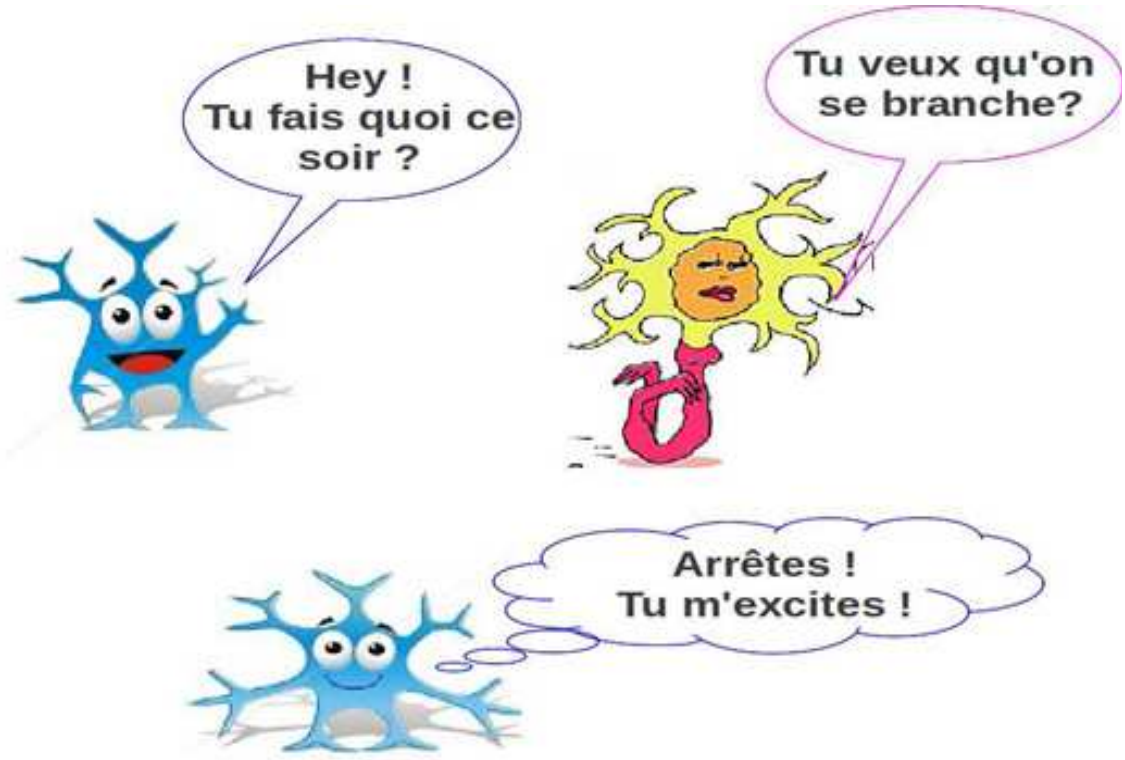

What if neurons could talk? *Illustration of a potential information transfer between neurons via mechanical waves, as postulated in a model described in chapter 7*

CHAPTER 7

Activity-dependent phase changes in neurons and electromechanical coupling

Table of contents

7.1 Classical theory of electrical activity propagation in neurons **214**

7.1.1 Brief history of the ionic hypothesis of action potentials 215

7.1.2 The passive properties of the cellular membrane 217

7.1.3 Ion channels and the cell resting potential 222

7.1.4 The Hodgkin & Huxley model 226

7.2 Beyond the Hodgkin & Huxley theory **231**

7.3 Alternative electrical models **236**

7.3.1 The pressure pulse model 237

7.3.2 The action waves model 238

7.3.3 The soliton model 240

7.4 Measurement of dynamic phase changes in neuron cultures **244**

7.5 Measurement of activity dependent phase changes in tissues **246**

In this last chapter of this manuscript, I will finally introduce what was our initial motivation to start this PhD project. We first wanted to detect phase changes related to electrical activity in cells. First, this might have a technological interest as it would enable label-free parallel but single cell detection of electrical activity in neuronal networks over large time scales, whereas existing technologies display several limitations. More importantly, if such activity-related phase changes have been extensively measured in giant [1] nerve fibers or neurites and are well accepted, they have never been measured in mammalian neurons and no consensus has ever been found to explain the origin of these phase changes. A mechanical deformation of the neurite following the shape of the action potential has been directly measured. If several hypotheses can eventually explain these observations, a few biophysical models have been recently proposed to complement the purely electrical model explaining the propagation of action potentials, known as the Hodgkin-Huxley model. In this chapter, I will first present the standard model of electrical activity propagation in neurons to emphasize that it is mainly phenomenological despite its good predictive abilities. Moreover, a few observations that can not be explained by such standard model will be detailed in a second section, including a mechanical and temperature change of a shape similar to the action potential. Either these observations are only epiphenomena of the action potential or can be an indicator that the Hodgkin & Huxley is incomplete, both possibilities will be considered in this manuscript. Three alternative models found in the literature that try to better explain the electrical propagation in neurons will be introduced and discussed. These models predict the existence of mechanical waves propagating along the action potential and that might have an impact on its propagation. Nevertheless, the detection of these predicted electromechanical waves is probably still unachievable with the current technologies in terms of speed and sensitivity. In the second part of this chapter, I will introduce a few other slower biophysical parameters that are impacted by the action potential and can more significantly modify the optical phase of active neurons. Finally, the two short last sections of this chapter will present our few potentially successful attempts to image electrical activity with our phase systems, first in cultures and then in tissues. Unfortunately, and as explained in the introduction, I could rarely image happily behaving neuronal cultures so that this chapter is mainly composed of theoretical considerations and of future experiment proposals. Nevertheless, it is eventually worth reading as it presents a short review of the electromechanical theory I have investigated througout my PhD project.

7.1 Classical theory of electrical activity propagation in neurons

With the development of relatively large animals, the propagation of information from one side to the other of the organism has become critical since random diffusion of chemicals and even directed active transport are not faster than a few microns per second. To put it in perspective, it would take about 3 months for a 1-meter human to react to a visual threat by moving away with his legs if the information was propagated with active transport and up to 10 years with passive diffusion. It

[1] For microscopists, let's note that giant diameters start from something around 100μm...

is obviously not a good strategy to survive and fight (or run away) against predators. To accelerate such reaction time from one side to the other of an organism, nature has evolved using electrical propagation to transmit information in most macroscopic organisms including plants [320, 321]. The use of electrical propagation has increased the conduction speed by 7 orders of magnitude compared to the motor-driven transport and up to 9 orders of magnitude compared to the diffusion transport so that we can react within a few hundred milliseconds only. Not surprisingly, the nature of the electrical conductance in biological systems is relatively different than the one developed by mankind, as organisms do no have the luxury to use important quantities of highly conductive materials such as copper or other metals. On the other hand, cells have developed specific ion channels to control the ionic chemical gradients flowing through their isolating membrane and creating an ionic flow to transmit an electrical current. In most animals, the electrical signal has been found to propagate in short pulses of conserved amplitude (along with the propagation and from one pulse to the other), known as action potentials. If many shapes and temporal extensions of action potentials can be measured, they all keep the same overall shape and always have the same shape for a given neuron. In this section, the main characteristics of cells to propagate electrical signals will be detailed, as well as the standard model of action potential generation and propagation, known as the Hodgkin-Huxley model. The latter is often described as one of the most important achievements of Biophysics. Unfortunately for this model, scientists usually like challenging successful models and the Hodgkin-Huxley model makes no exception. Several observations that can only be partly explained by the Hodgkin-Huxley model have been reported and a few alternative models have been proposed. If the alternatives to the Hodgkin-Huxley model will be developed in the next section, the description performed here will also illustrate some of its limitations. In order to emphasize the achievement of the Hodgkin-Huxley, a brief history of neuroscience that led to the development of this model is proposed in a first subsection.

7.1.1 Brief history of the ionic hypothesis of action potentials

The history of modern neuroscience has probably started in 1791 when *L. Galvani* discovered that muscle contraction could be triggered by connecting a muscle to a nerve fiber using a wire made of two different metals. If the electrical contraction of muscles were known for several years [2], *Galvani*'s experiment triggered a famous controversy between supporters of an animal electricity (the nerve fiber would have actively generated the electricity that contracted the muscle) defended by *Galvani* and supporters of a more passive vision of the biological tissues (that would only transmit the current, generated at the interface between the two metals) defended by *A. Volta*. This controversy was famous because it led *Volta* to investigate the current generation caused by the contact of two metals of different redox properties and led to the creation of batteries. This controversy also triggered numerous questions regarding the generation and conduction of electricity by animal bodies [3]. The next important development came from *H. Von Helmholtz* around 1860 who measured for the first time the conduction speed of nerve influxes and found that nerve conduction was fundamentally different than copper wires conduction. Whereas electricity is conducted at speeds close to the speed of light in metals but decays in amplitude over large distances, nerve conduction is relatively slow (about 25 meters per second in *Helmholtz*'s measurements) but provides a lossless propagation, suggesting an active mechanism for nerve propagation. In 1902, *J. Bernstein*, one of *Helmholtz*'s student, discovered and measured the resting potential in cells and

[2] At that time, the ancestor of modern capacitors, known as Leyde jars, were used to give electric shocks of several thousands volts to brave men in funfairs, which caused them strong muscle contractions and them to faint

[3] It also inspired the famous book *Frankenstein; or, The Modern Prometheus* by *M. Shelly*.

understood that the charge separation leading to this potential was performed by the isolating, but selectively permeable, cell membrane. From *Nernst*'s work in electrochemistry and from the measurements of the intracellular and extracellular ionic compositions, *Bernstein* showed that the membrane was permeable selectively to potassium ions, leading to a resting potential around -70 mV and postulated the existence of ion channels. *Bernstein*'s contribution was important since it raised the possibility for the nerve conduction to be regulated by ionic gradients. In his hypothesis, the selective nature of the cell membrane would shortly break down during an action potential and should lead to a charge balance and should bring the negative membrane potential to 0. On a parallel path, *E. D. Adrian* developed, in the 1920s, methods for the nerve electrical signal recording and amplification. He proposed a device coupling an electrode to an ink writer and to a loudspeaker to measure the activity. He discovered the stereotypical shape of nerve signals, later named action potentials, and could show that this shape is well conserved in all parts of the body. A striking founding showed that sensory (and motor) neurons all exhibit an electrical activity of similar shape so that the difference in signaling to explain vision or hearing could not originate from the produced electrical signal itself but requires a more complex processing. *Adrian* also demonstrated the encoding of a given stimulus with the electrical signal and showed that the strength of a stimulus is encoded by the frequency of spiking (ranging from 1 to 2 spikes per second to a few hundred spikes per second), while the duration of the stimulus was encoded by the duration of the electrical activity. The current understanding of the ionic origin of action potentials has also been made possible thanks to *J. Z. Young*'s discovery of the squid giant axon that is around one millimeter thick, about one thousand times larger in diameter than most mammalian axons. Interestingly, *Young* realized that squids, among the fastest swimmers of the seas, have probably evolved with such a large axon to increase their reaction time and escape better from predators. He also realized that such a large axon could be of major interest for neuroscience, as it would be easier to manipulate and to record signal from. Indeed, it allowed *A. Hodgkin* and *A. Huxley* to insert an electrode inside the axon while keeping another one outside and measure the axonal membrane voltage. They could redemonstrate axonal resting potential to be around -70 mV but also made the outstanding discovery that the action potential amplitude was around 110 mV, reaching a positive voltage during the peak of the action potential. It was incompatible with *Bernstein*'s theory of membrane breakdown during the action potential. A few years later, *A. Hodgkin* and *B. Katz* found out that the rise of the action potential was perturbed if the extracellular concentration of sodium was altered and that the action potential decrease was affected by a change in the concentration of potassium ions. This suggested that the cell membrane had to be partly selective to sodium ions during the rising phase of the action potential and to potassium ions in the decreasing phase. Finally, the last important building block has been brought by *K. Cole* and *G. Marmont* development of the voltage clamp technique in 1947 that allows forcing a constant voltage difference between intracellular and extracellular electrodes by using a third electrode and a feedback circuit to inject current inside the cell to compensate all the ionic leakages. It permitted the re-demonstration of the capacitive nature of the cell membrane (as illustrated in figure 7.2) but also and foremost the measurement of the voltage-dependent conductance of each ion channels. In a series of impressive papers between 1949 and 1952, *Hodgkin* and *Huxley* could measure the potassium and sodium channel conductances independently and showed the fast changes of these channels conductance. They postulated that such fast changes could only occur due to voltage changes and named these channels *voltage -gated ion channels*. In parallel to these two channels, they postulated the existence of a third channel, a *non-gated* (and therefore voltage-independent) ion channel that would help restore the resting potential. At the end of the action potential, sodium ions have flowed inside the cell and potassium ions

have flowed outside, ultimately changing the initial ionic concentrations balance. *Hodgkin* also postulated the existence of an active protein that would use energy to restore the initial ionic concentrations against the concentration gradient. Finally, *Hodgkin* and *Huxley* have developed an all-electrical model that explains the shape of the action potential and its propagation. The propagation is explained by the passive propagation of current to the next region of the axon, in which an action potential is therefore triggered, and so on so forth. This model is known as the Hodgkin-Huxley model, for which they shared a Nobel prize in 1963. Impressively, this model has been developed without any knowledge about the structure or nature of all these pumps and channels that have been later been identified as proteins and been characterized by crystallography. Obviously, such a simple model with only 4 proteins and two ions can not account for the complexity and variety of existing action potentials. More than a hundred ion channels have been discovered since then and a few other voltage-gated channels, such as the calcium channel, and ions have been demonstrated to play a more subtle role in the action potential generation and propagation. Nevertheless, the Hodgkin-Huxley model can be enriched with these other channels quite naturally and can take into account their respective influence. The Hodgkin-Huxley model proposes an equivalent model from which a large variety of action potential types can be explained simply by varying the concentration of diverse ion channels in the membrane. Through its many successes and predictions, the Hodgkin-Huxley model has become the absolute model of reference to explain the action potential propagation and have become hardly questionable by the neuroscientists' community. Nevertheless, the propagation of the ionic currents in the Hodgkin-Huxley model is quite phenomenological, and *Hodgkin* and *Huxley* themselves have always tried to question their model and to imagine a more general one. Additionally and despite its apparent simplicity, the Hodgkin and Huxley model describes a system of 5 coupled variables that does not admit any analytical solution. If several models, such as the *FitzHugh–Nagumo* or *Hindmarsh–Rose* models, have tried to simplify the Hodgkin-Huxley model to find an analytical solution or simplify the numerical calculations, the biological basis of such models has never been justified. More details about the history of neuroscience, and especially the biochemical basis of memory, can be found in *E. Kandel*'s autobiography [322], from which this subsection was partly inspired.

7.1.2 The passive properties of the cellular membrane

Going back to our current understanding of the cellular components, we can model the cell as an equivalent electrical circuit that will be described here. From such passive model, an electrical signal can diffuse along the cell but can not account for the wave-like propagation of the action potentials as it is observed. Nevertheless, this electrical model is interesting first to introduce the Hodgkin-Huxley model and to estimate the action potential speed. The cell intracellular medium is kept apart from the extracellular medium by a lipidic bilayer membrane 3 to 5 nanometers thick that separates the ions. Therefore, the membrane acts as a capacitor of surface capacitance $C_{M,surf}$ on the order of 1 μF.cm^{-2} [4].

Additionally, this membrane is not absolutely permeable and contain several specific ion channels that allow the ions to diffuse inside or outside the cell and that will be further described in the

[4] If the membrane is considered as a plane capacitor, the surface capacitance can be written:

$$C_{M,surf} = \frac{\epsilon_0.\epsilon_r.A}{e_M} \tag{7.1}$$

with ϵ, the permittivity and e_M, the membrane thickness. Surprisingly, assuming a membrane thickness of 4 nm and an optical index of the membrane of 1.5 (to calculate the permittivity), we can calculate a surface capacitance of 0.5 μF.cm^{-2}, very close to the experimentally measured values.

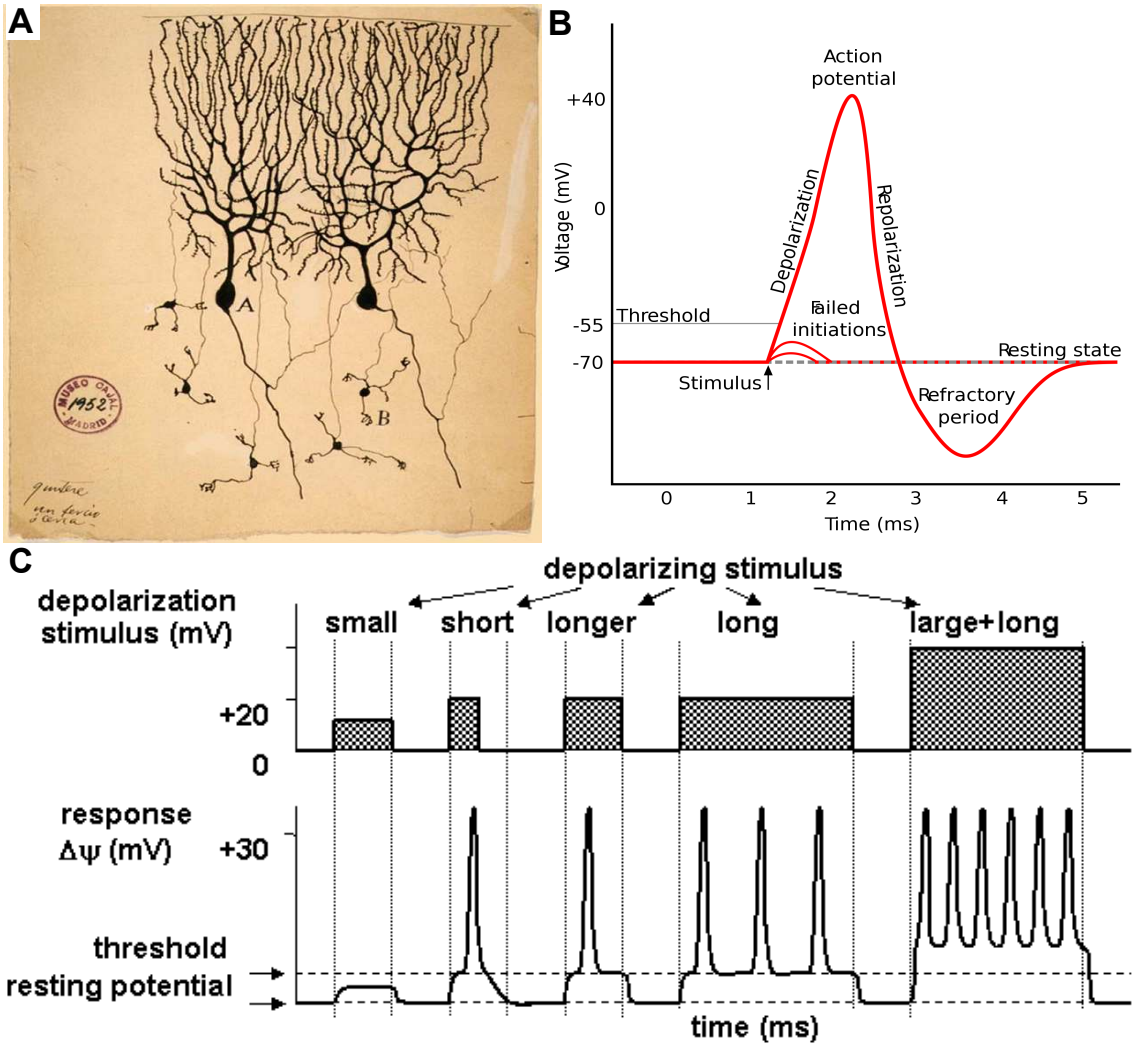

Figure 7.1 – The neural code. Panel A illustrates the diversity of neuronal morphologies with various soma diameters and various neurite sizes and numbers. Here, the large cells are Purkinje cells that integrate signal from a dense dendritic tree, while the small ones are granules cells that exhibit only a few main dendrites and send their signals upwards. Despite their different morphologies, both cell types transmit signal that has more or less the same shape as a train of action potentials. **Panel B** presents the stereotypical shape of an action potential. When excited above threshold (around -55 mV), neurons fire an action potential that begins with a fast depolarization of amplitude around +110 mV in 1 ms. Then, the membrane voltage decreases down to -90 mV within another ms. A final repolarization last for a few milliseconds during which the membrane voltage is lower than the resting potential and the cell is less excitable. **Panel C** illustrates the way neurons encodes signal despite their stereotypic response conserved in all neurons. Several voltage stimuli are applied to one neuron (upper trace), which answers to them with a train of action potentials (lower trace). The amplitude of the stimulus is coded in terms of action potential frequency, and the length of the stimulus is coded with the length of the neuronal response. Subthreshold excitation produces no effect and the length of a stimulus can be estimated within the time accuracy that can not exceed the length of an action potential. Panels A and B are reproduced from the web with authorization. Panel C is reproduced from the website of an online course of neurobiology [323].

next subsection. To account for this ionic *leakage*, a resistance R_M can be added in parallel to the capacitance. The porous cell membrane can therefore be associated with a a RC circuit that charges and discharges with a characteristic time $\tau = R_M.C_M$. This equivalence to an RC circuit is illustrated in figure 7.2 reproduced from *C. Kung and R. Eckert* [324] where a paramecium is

genetically modified to cancel the active properties of its membrane. Under voltage clamp and exposure to long depolarizing and hyperpolarizing currents, the membrane potential follows a typical exponential increase and decrease from which the characteristic time can be measured [5]. When considering the electrical signal propagation along an axon by applying a constant voltage at one location of the axon, it will propagate accordingly to the cable theory with negligible inductance. In short, the current change will propagate longitudinally at the interior of the cell that acts like a resistance R_{int} that depends on the axon radius and on the intrinsic resistivity of the intracellular medium. The resistance of the extracellular medium is neglected since it is supposed to be infinitely extended (infinite section) or to act as a voltage reservoir or reference. It can be understood as the medium is extended enough not to feel the influence of a few missing ions that have penetrated the cell and can be replaced without impacting the global concentration of the external solution. Additionally, a cylindrical symmetry is postulated to only consider the propagation along one dimension that we will call the x axis[6]. Therefore, the axon can be modeled by a series of small RC circuits linked by a series of resistances R_{int}, as illustrated in figure 7.2.

In this configuration, we can calculate the voltage change associated with a transient depolarization at one end of the axon. We can use the Kirchhoff's current law and the Ohm's law to write :

$$I(x+dx,t) - I(x,t) = I_{Membrane}(x,t) = \frac{V(x,t)}{R_M} + C_M \frac{\partial V}{\partial t}(x,t) \tag{7.2a}$$

$$V(x+dx,t) - V(x,t) = R_{int}.I(x,t) \tag{7.2b}$$

The local membrane resistance and the local axoplasm resistance can be estimated as a function of the the axonal radius r in a cylindrical geometry. The membrane conductance (inverse of resistance) can be calculated as the sum of all the individual channel conductances. Assuming here that all channels have the same conductance and that they are homogeneously distributed in the membrane, the membrane conductance is the product of a single channel conductance g_C by the surface density of ion channels d_C by the membrane surface. We can write:

$$R_M = \frac{1}{2 * \pi r \Delta x . g_C . d_C} \tag{7.3}$$

The axoplasm resistance can be estimated as a wire resistance with a locally homogeneous resistivity ρ_A, that ultimately depends on the ionic concentration of the cytoplasm:

$$R_{int} = \frac{\rho_A \Delta x}{\pi r^2} \tag{7.4}$$

Similarly, the membrane capacitance is the product of the membrane capacitance (that only depends on the membrane properties, as seen in equation 7.17) by the membrane surface:

[5]Note that the measurement of the membrane capacitance is a quite classical measurement in electrophysiology by first measuring the cell impedance to obtain the membrane resistance and then to measure the characteristic time of the exponential decay in response to a depolarizing current [325].

[6]The cylindrical symmetry originates from the cylindrical shape of the axon but probably also because the voltage clamp method was performed in the squid axon giant with an electrode placed at the center. Nevertheless, I would expect that a voltage depolarization using a patch clamp at the axonal membrane would propagate not only along the cylinder axis but also along the perimeter of the axon, especially for large axons. The consequence would be that a local excitation of the axon would generate an action potential that is delayed between the top and the bottom of the axon. Nevertheless, if the initial excitation is performed with a cylindrical symmetry, this symmetry should be conserved over the propagation (for a cylindrically-homogeneous membrane of course).

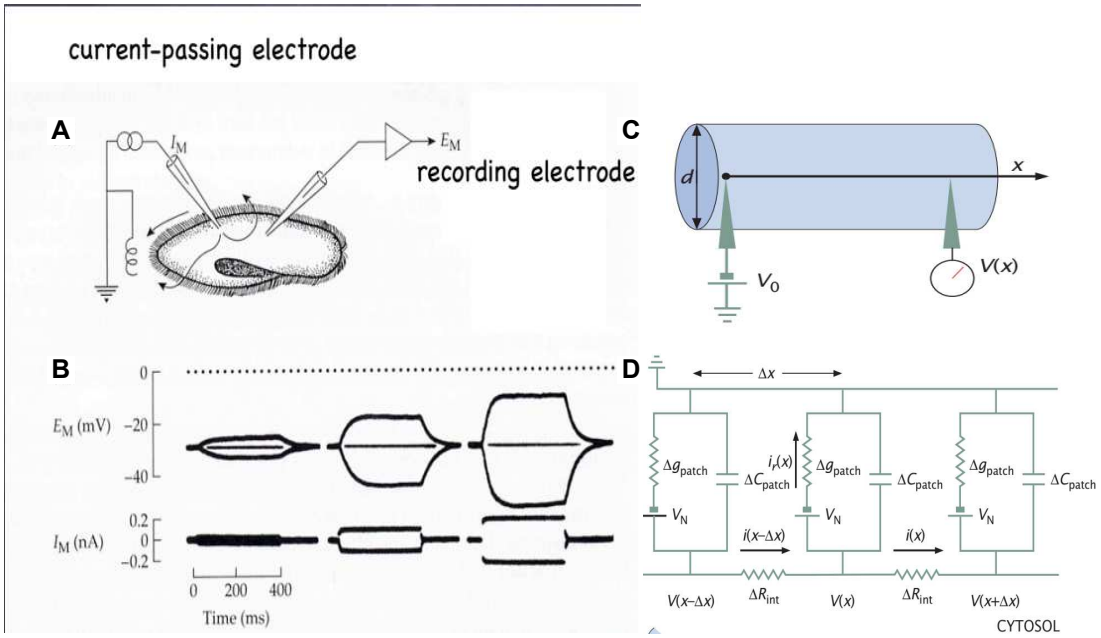

Figure 7.2 – Passive properties of the axonal membrane. Panels A and B present the measurement of the capacitive behavior of the cell membrane. A patch-clamp measurement was performed on a genetically-modified paramecium without ion channels canceling the active parts of its membrane (Panel A). Hyperpolarizing and depolarizing current of various amplitudes are applied to the paramecium and the voltage is measured and plotted in panel B. It shows the capacitive behavior of the membrane with the exponential increase and decays of the voltage versus time before reaching equilibrium. **Panels C and D** illustrate the equivalent passive electrical circuit that models the axonal membrane. Panel C illustrates the problem geometry with a cylindrical symmetry of the axon to allow for a 1-D problem consideration. Panel D shows the 1-D model of the passive membrane, similar to an electrical cable with negligible inductance. A unit cell is composed of a membrane resistance in parallel with a membrane capacitance. The resistor is coupled to a battery that accounts for the membrane resting potential. Two units cells are separated by an infinitesimal distance Δx and by a resistor corresponding to the axoplasm resistance. Panels A and B are reproduced from *C. Kung and R. Eckert* experiment [324] and panels C and D are reproduced from *Phillips*'s biophysics textbook ([326], chapter 17).

$$C_M = C_{Surf,M}.2\pi r\Delta x \tag{7.5}$$

Finally, by taking the Taylor expansion of equations 7.2a and 7.2b and by deriving equation 7.2b along the x-axis, we obtain:

$$\frac{\partial^2 V}{\partial x^2} - \frac{2\rho_A.g_C.d_C}{r}(V + \frac{C_{Surf,M}}{g_C.d_C}.\frac{\partial V}{\partial t}) = 0 \tag{7.6}$$

We recognize a 1-D diffusion equation, from which we can define a length constant λ and a time constant τ so that equation 7.6 becomes:

$$\lambda^2\frac{\partial^2 V}{\partial x^2} - \tau\frac{\partial V}{\partial t} - V = 0 \tag{7.7}$$

With λ and τ defined as:

$$\lambda = \sqrt{\frac{r}{2\rho_A g_C.d_C}} \tag{7.8}$$

$$\tau = \frac{C_{Surf,M}}{g_C.d_C} \tag{7.9}$$

The term $g_C.d_C$ is a surface conductance and corresponds to the product of a resistance by a surface, allowing the time constant to be expressed more classically as the product of a resistance by a capacitance. In a steady-state excitation, the passive properties of the axonal membrane would lead to a decay of the initial signal after a characteristic length λ that is measured to be around 9 mm for squid giant axons. Therefore, the passive properties of the axonal membrane only can not account for the lossless propagation of action potentials that is observed in neurons and therefore requires an active process to compensate the signal attenuation. Equation 7.7 could have been directly obtained by applying the cable theory with negligible inductance. Note that the absence of an inductance makes that the cable equation is no longer a wave equation but rather corresponds to a diffusion equation, that here again would fail to explain the wave-like propagation of action potentials. If the contribution of active ion channels will be detailed in the two next subsections, it is interesting to notice that the passive properties of the membrane set a boundary for the action potential speed. Indeed, the diffusion equation 7.7 obtained gives a maximal speed of energy propagation that corresponds to the diffuse wavefront speed that can be calculated as:

$$c_{AP} \sim \frac{\lambda}{\tau} \simeq \sqrt{\frac{g_C.d_C}{2\rho_A C_{surf,M}^2}}.\sqrt{r} \tag{7.10}$$

Equation 7.10 is interesting because it gives a feeling of the important parameters that can be controlled to increase the speed of action potential. The surface capacitance and axonal resistivity might be changed but are probably hardly controllable in the range of accessible material for the cells. The membrane conductance can be changed either transiently as will be the case during action potentials or to increase the permanent (or leakage) membrane conductance. Nevertheless, this would increase the leakage through the membrane and would increase the time constant so that the channel becomes less responsive to an abrupt voltage transient. Increasing the number of channels would have the same effect than increasing the conductance of each channel. Finally, the axonal radius r seems to be fairly easy to control and increase both the characteristic length (prevents the spatial decay) and the action potential speed. The latter should depend on the square root of the radius, which is in good agreements with experimental observations [327]. It has led to the development of giant axons in invertebrates including the squid giant axon to allow for a faster reaction time to escape predators.

Nevertheless, to go from a propagation speed of 1 meter per second to 10 meters per second, it requires an axon 100 times larger that would not only consume more energy but could also be damaged more easily. An alternative way to increase the action potential speed has developed in mammalian and consists in covering the axon with an additional insulating fat membrane called the myelin sheath. This capacitive layer consists in the extension of oligodendrocytes or Schwann's cells that wrap around the axon and provides a high-fat level layer to better insulate the neuron, as illustrated in figure 7.3. The myelin sheath acts as a capacitive layer of high resistance similarly to the membrane, although it is much thicker than the cell membrane and thus provide smaller capacitance (the charge separation distance is much longer) and of high resistance. According to previous equation 7.10, the capacitance drop should increase the action potential speed. Let's now try to quantify the propagation speed increase. In a first approximation, we now neglect the capacitance and resistance from the cell membrane and only consider the myelin characteristics. We note r_A, the axoplasm radius, and r_M, the myelin radius. The myelin sheath resistance can be calculated similarly to the axoplasm (or wire) resistance:

$$R_{Myelin} = \frac{\rho_M r_M}{2\pi(r_A + r_M)\Delta x} \tag{7.11}$$

And,

$$C_{Surf,Myelin} = \frac{\epsilon}{r_M} \tag{7.12}$$

Additionally, we use the experimental observation that the myelin thickness is linearly proportional to the axonal thickness [327]. According to these observations, we use a myelin thickness of 0.4 the axonal radius. We can therefore calculate:

$$\lambda_{Myelin} \simeq \sqrt{\frac{\rho_M}{7\rho_A}}.r_A \tag{7.13}$$

$$\tau_{Myelin} \simeq 0.29\epsilon\rho_M \tag{7.14}$$

And,

$$c_{Ap,Myelin} \sim \sqrt{\frac{1}{2.1\epsilon\rho_A}}.r_A \tag{7.15}$$

Equation 7.15 demonstrates that myelin allows for a linear scaling of the propagation speed with the axonal radius, as experimentally observed [328]. Nevertheless, the ion channels are small transmembrane proteins and could not run through the entire myelin sheath. As we have seen, the action potential passive propagation is a diffusion equation so that its amplitude should decay over large distances without ion channels to actively regenerate its amplitude. To preserve action potential amplitude, the myelin sheath is non-continuous and some holes are regularly spaced in the myelin. These holes are called nodes of Ranvier and present important concentrations of sodium and potassium channels. It enables to be highly sensitive to potential change (due to propagation) and to regenerate the action potential. The action potential conduction is said to jump from one node to the other and is therefore called saltatory conduction, as illustrated in figure 7.3. We can add that it was experimentally measured that the spacing between two nodes of Ranvier scales linearly with the axonal radius, which can be understood here since the decay length λ_{Myelin} also scales linearly with the axonal radius. Therefore, the action potential would have decayed of the same amount even with larger spacing between the nodes. Finally, a few degenerative diseases, such as multiple sclerosis, impact the myelin sheath and form holes in the membrane. It not only decrease the action potential propagation but can also lead to the attenuation of the action potential that can result in a loss of transmission. Indeed, the action potential in myelinated fibers can only be regenerated at the Nodes of Ranvier that are around 1 millimeter apart, which is close enough to prevent the action potential decay when the myelin sheath is here. But, the loss of myelin also impacts and lowers the decay length, and significant amplitude decay can be observed in demyelinated fibers.

7.1.3 Ion channels and the cell resting potential

To account for the experimentally measured active propagation and highly controlled membrane resting potential, neuroscientists have early predicted the existence of selective pores that might open and close to let specific ions go in or out the cell. During the past decades, more than a hundred of such selective pores called ion channels have been discovered and characterized. They can be either selective to a single ion or to a class of ions (all cations for example) and

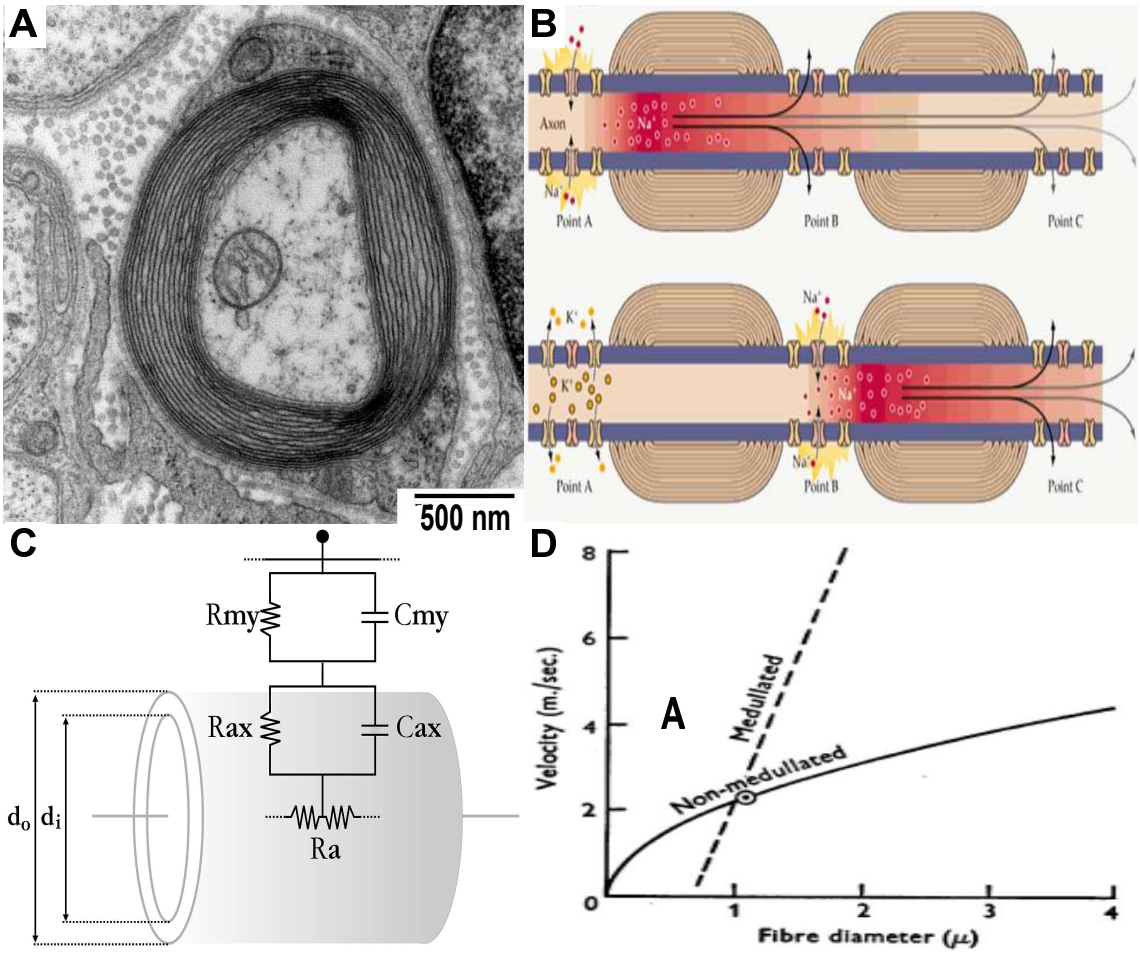

Figure 7.3 – Conduction speed increase with myelin. Panel A presents a transmission electron microscopy cross-section of a myelinated axon. The myelin sheath corresponds to the compact packing of several fatty cell membrane layers. **Panel B** illustrates the saltatory conduction observed in myelinated axons. Instead of depolarizing neighbor regions of the membrane, the action potential creates a significant voltage perturbation far from its location and excites a region without myelin called the nodes of Ranvier. The action potential is regenerated from one node of Ranvier to the other while almost no ion channels can be found in between the nodes. **Panel C** shows the equivalent passive electrical circuit that models the myelinated axon. The myelin can be modeled as a resistor mounted in parallel to a capacitor and is added in series with the membrane equivalent circuit. The myelin resistance is large due to its hydrophobicity and its capacitance is lower than the membrane capacitance since the myelin sheath (and the charge separation distance) is much larger. **Panel D** illustrates the conduction velocity dependency with the axonal radius and the global increase in the conduction velocity in myelinated fibers. Panel B is reproduced from the book *Principle of neuroscience* [310]. Panel D is reproduced from an article by *Rushton* [328].

can exhibit various sizes and specific conductances. Ion channels can be passive (always open), voltage-gated or triggered by physical or chemical signaling, such as light stimuli (in rhodopsin), calcium-activated channels, G-proteins channels, *etc.*.. In voltage-gated ion channels, the strength of the electric field acts on the channel folding that can ultimately stretch to adopt a structure in which a solvated ion can flow in. Mediated by electrostatic forces, the voltage-gated channels folding and unfolding (opening and closing) display a fast response time, especially in comparison to calcium-activated or G-proteins channels that have to wait for diffusion and chemical reaction rates to happen.

It is interesting to emphasize the impressive properties of some ion channels and of molecular engineering in general by taking the example of the potassium channel. The latter can specifically

select potassium ions and exclude sodium ions despite their smaller sizes and their radius difference of only 80 picometers. In fact, ion channels are selective to the solvated ions and the hydration shell has to be taken into account to consider the ion channels selectivity. The smaller radius of sodium ions makes them more tightly bound to water molecules with 6 of them are constantly surrounding the sodium cation. On the other hand, the potassium ions exhibit more flexible hydration shell that can more easily reorganize itself. When looking at the potassium channel structure in figure 7.4, we can see a central hole with 4 surrounding holes to let water molecules diffuse inside the channel as well. If the water molecules around the potassium ion can easily reorganize to fit the channel's structure, it is not the case for the sodium ion hydration shell, which prevents sodium to flow into the channel.
To account for the local membrane voltage response to a depolarization, two main classes of potassium channels are involved: a leakage potassium channel class that controls the membrane potential and a voltage-gated potassium channel type that opens during the action potential decay phase.

If selective ion channels are at the origin of a transmembrane charge separation and of the establishment of a membrane voltage, they can only be effective in the direction of their electrochemical gradients until they reach the cell Donnan equilibrium, which states a compromise between the transmembrane electric field and the relative concentration gradients of all ions. For each ion type taken independently, they try to reach their thermodynamic equilibrium, which is set by the famous *Nernst* equation:

$$V_i = \frac{RT}{zF} ln(\frac{C_{Out}}{C_{In}}) \tag{7.16}$$

With V_i, the Nernst potential for the ion type i, RT, the thermal energy, z, the number of charges carried by a single ion i, F, the Faraday's constant (Electric charge of one mole of electrons), and C_{Out} and C_{In} respectively the extracellular and intracellular ionic concentration. Taking into account the contribution of several ion types, the membrane voltage is set by a steady-state equilibrium set by the different Nernst potentials of each ion type and by and their respective permeability through the membrane. The equation integrating all these contributions is known as the *Goldman–Hodgkin–Katz* voltage equation. Interestingly enough, the Nernst equation and the *Goldman–Hodgkin–Katz* voltage equation both linearly depend on the temperature and can account for several temperature-dependent effects, as it shifts the membrane voltage resting state. For example, a fast cooling of a nerve to 0° C would create a voltage depolarization of about 10 mV and can eventually fire an action potential. Additionally, the importance of the concentration gradients would increase the responsiveness of the membrane exchange system since it is regulated by diffusion so that the number of ions exchanged is proportional to the concentration gradient.
In practice, the intracellular medium composition is significantly different from the extracellular composition as illustrated in figure 7.5, with a concentration ratio around 100 for sodium, potassium and chloride ions and a 10,000 concentration ratio for calcium ions. This extreme ratio coupled with an intracellular calcium concentration of a few nM (the cytoplasm is almost free of calcium ions) has a critical biological role. Indeed, calcium ions are involved in many triggerable events in biology such as muscle contraction, neurotransmitter release, adhesion, and many others. Several proteins can change their conformation when binding to calcium ions, the presence of which depends on the opening of calcium channels. The insignificant resting state intracellular concentration allows these proteins to be highly reactive to calcium and the extreme gradient with the extracellular medium allows for a fast and highly controlled calcium uptake and protein conformation change.

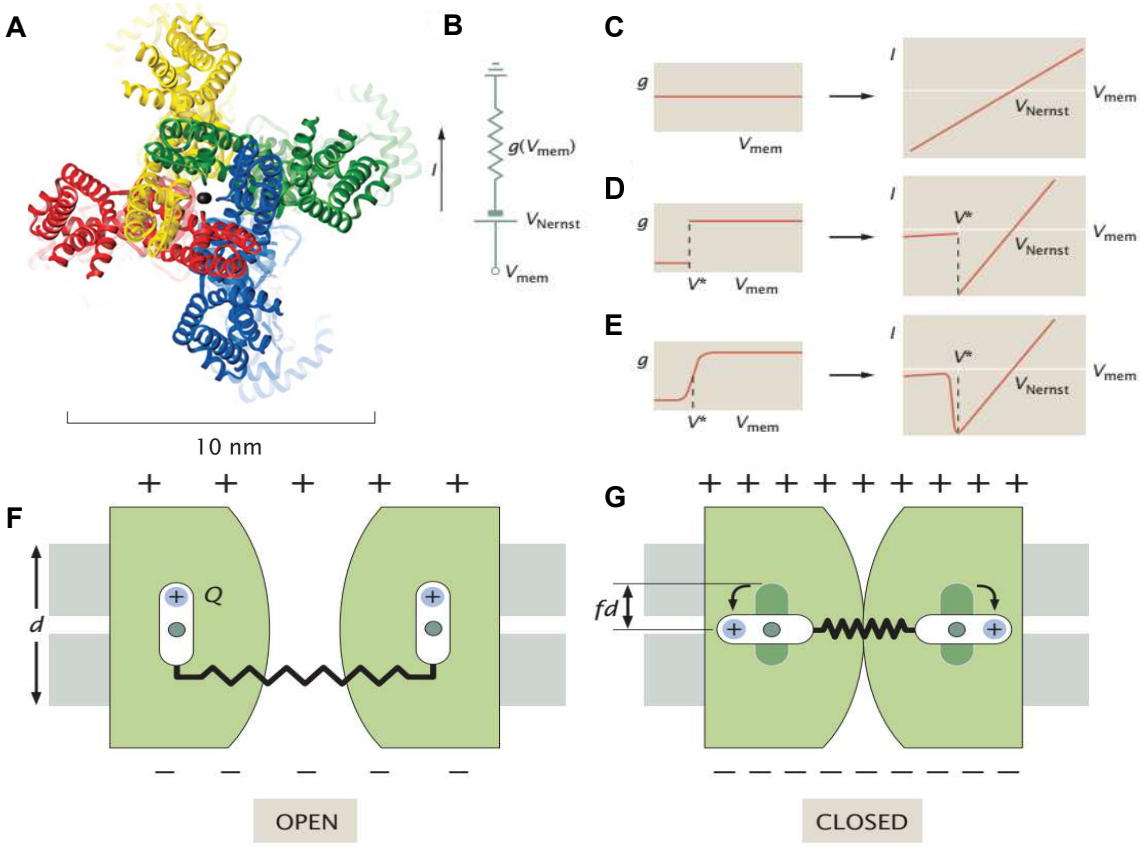

Figure 7.4 – Principle of voltage-gated ion channels. Panel A shows the structure of a voltage-gated potassium channel, illustrating the small hole at the middle to a solvated potassium ion to flow through. In presence of a voltage, the four subunits can rearrange themselves to either open or close the channel. **Panels B to E** present the electrical modeling of an ion channel. Ion channels are modeled as a varying resistor in series with a battery of potential equal to the ion Nernst potential (panel B) to account for the flow reversal when the voltage difference goes higher or lower than the Nernst potential. Panels C to E show different simple models of conductance and their associated intensity voltage curves. According to Ohm's law, a constant conductance gives a linear relationship between the intensity nd voltage (Panel C), while a sudden drop in conductance at a given voltage (switch from a closed state to an open state) generates two parts in the intensity-voltage curve (panel D). In order to smooth the transition around the switch voltage, a sigmoidal conductance model can be assumed leading to a smoother peak in the ionic current (panel E). The sigmoid conductance can be obtained by assuming a probabilistic model of ion channel opening (with a probability depending on the voltage difference with the switch voltage) for example. **Panels F and G** presents a two-state model of ion channels comparing the ion channel to an electrostatic spring that contracts and close the channel in presence of a high voltage (panel G). All these panels have been reproduced from a biophysics textbook ([326], chapter 17).

If the intracellular ion composition were only controlled by ion channels that allow the ions to flow in the direction of their electrochemical gradient, it could not be carefully controlled and every ion uptake would be hard to regulate to restore the initial ionic composition. Another class of proteins, called active ion pumps, are required to perform such a control. The ion pumps use chemical energy (of ATP consumption) to bring ions from one side of the membrane to the other in order to establish a concentration gradient. The most famous ion pump is the sodium-potassium ion pump that exchanges 2 sodium ions from the inside against 3 potassium ions from the outside by transforming an ATP molecule into ADP (equivalent to an H^+ exchange). This pump is the main responsible for the sodium and potassium gradients. With the conversion of ATP into ADP, the pump is electroneutral so that the membrane voltage can only be established in

presence of at least one selective ion channel, the most important of which is the *leaky* potassium channel. As illustrated in figure 7.5, the cell is constantly pumping potassium ions inside the cell while some holes (the ion channels) in the membrane permit the potassium to flow outside the cell. An entertaining analogy is to imagine someone trying to fill a pierced bucket with water constantly leaking out. By pursuing this analogy, the water content is controlled by the flow out (and directly proportional to the number of holes if they are all similar) and by the flow in (and directly proportional to the number of persons trying to fill the bucket if they are all working with the same efficiency). Additionally, the more water inside the bucket, the higher pressure around the holes, which increases the flow out and the energy required to compensate for the leakages. Similarly, the membrane voltage is set by the ratio between the potassium leakage channel number and the potassium-sodium ion pump number. The higher the resting state membrane voltage is (corresponding to a higher concentration ratio), the more energy the cell consumes to preserve its membrane potential. Keeping its resting potential and restoring it after an action potential represents most of a neuron energy consumption [329].

7.1.4 The Hodgkin & Huxley model

Now that the passive and active properties of the cell membrane have been reviewed, the Hodgkin-Huxley model consists in injecting the effect of the voltage-dependent channel into the cable equation 7.7. First, as *Hodgkin and Katz* demonstrated [330] the contribution of both potassium and sodium channels to form a normal action potential, it may be convenient to separate their contributions in the equivalent electrical circuit of the membrane. Therefore, the unitary cell of the cable line is modified in the H-H model, as illustrated in figure 7.6. The membrane resistance $R_{membrane}$ is now split into 3 branches that respectively represent the potassium channels, the sodium channels, and a voltage-independent leakage channel that accounts for chloride, other ions, and the potassium leakage channels. This separation allows using the voltage difference with each ion Nernst potential to account for the reversible ionic currents. The membrane conductance writes as the sum of the single conductances placed in a parallel configuration:

$$g_{membrane} = \sum_{k=ions} g_k = g_{Na}(V,t).(V(t) - V_{Na}) + g_K(V,t).(V(t) - V_K) + g_l.(V(t) - V_l) \qquad (7.17)$$

All the time and voltage dependency (and therefore the active part) of the membrane system is contained into $g_{Na}(V,t)$ and $g_K(V,t)$ and will be modeled in a second part. From above equation, we can additionally consider the conductance of all the channels of one type as the sum of all individual channels of this type in a local patch of the membrane, logically mounted in parallel as they represent gates mounted in the membrane the ones next to the others. The equivalent resistance of the channels is inversely proportional to the channel density, equal to about 20 potassium channels per micron squared of the membrane and about 60 sodium channels per micron squared of the membrane in the squid giant axon [331]. If the potassium channels density is always around a dozen of channels per micron squared, the sodium channels density can increase up to a few hundred in unmyelinated mammalian axons, and even a few thousands at the Nodes of Ranvier of myelinated axons [331–333]. Similarly, the contribution of additional channel types in more complex scenarios can easily be integrated by considering the leakage resistance as an equivalent resistance for these supplementary channel types. In the Hodgkin-Huxley model, the equivalent circuit equation is calculated as the sum of the passive circuit equation 7.7 with the more complex and voltage-dependent membrane conductance from equation 7.17:

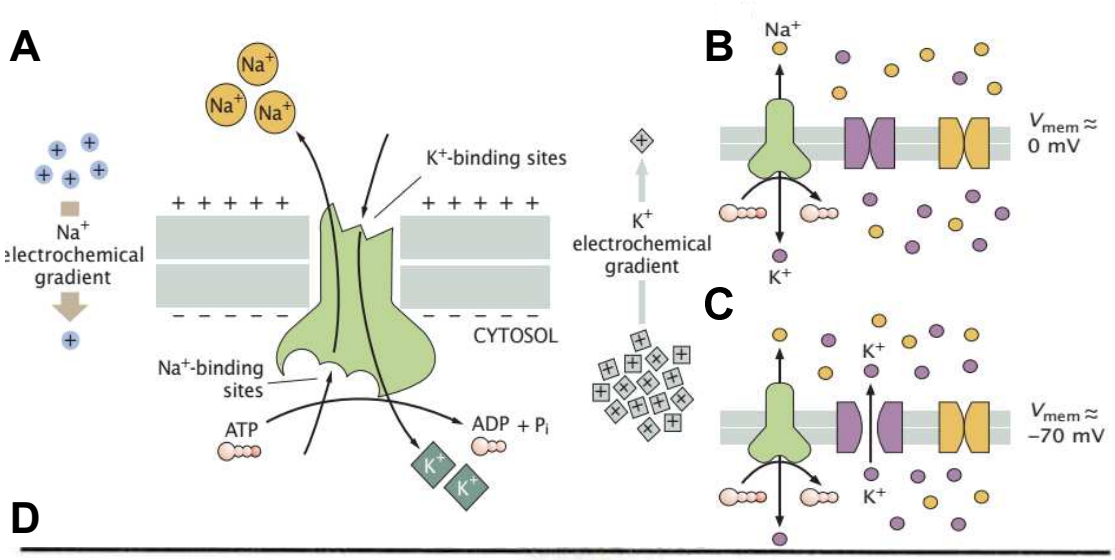

D

Ion	Extracellular concentration (mM)	Intracellular concentration (mM)	$\frac{[Ion]_o}{[Ion]_i}$	Equilibrium potential[a] (mV)
Na^+	145	12	12	+67
K^+	4	155	0.026	–98
Ca^{2+}	1.5	100 nM	15,000	+129
Cl^-	123	4.2[b]	29[b]	–90[b]

Figure 7.5 – Principle of the sodium-potassium ion pump and of the membrane resting potential. **Panel A** illustrates the principle of the sodium-potassium ion pump, which trades 3 sodium ions from the intracellular medium for 2 potassium ions from the extracellular medium and an H+ ion from the ATP hydrolysis. It allows generating a low concentration of sodium ions and a high concentration of potassium ions inside the cell against their respective electrochemical gradients. **Panels B and C** show how a resting potential can be established inside the cell. Because the sodium-potassium ion pump is electroneutral, there are as many charges on both sides of the cell membrane leading to a membrane voltage around 0 (panel B). The presence of an additional leakage potassium channel allows potassium ions to flow out the cell down their electrochemical gradient. Eventually, a steady-state equilibrium is reached around -70 mV. **Panel D** compares the ionic concentrations in the extracellular and intracellular media in a typical mammalian neuron and calculates the equilibrium potential for each ion separately. It suggests that similar ion pumps exist for calcium and chloride channels. The membrane resting potential is a steady-state equilibrium that balances all the ionic electrochemical gradients and permeabilities of the cell. All these panels have been reproduced from a biophysics textbook ([326], chapter 17).

$$\lambda^2 \frac{\partial^2 V}{\partial x^2} = C_M \frac{\partial V}{\partial x} + g_{Na}(V,t).(V(t) - V_{Na}) + g_K(V,t).(V(t) - V_K) + g_l.(V(t) - V_l) \qquad (7.18)$$

As previously mentioned, all the model complexity lies in the time and voltage-dependence of the sodium and potassium conductances. Thanks to their previous measurements [330, 334, 335] *Hodgkin*] and *Huxley* could fit sodium and potassium conductances to extract a few time-dependent only variables. The measured respective conductances are reproduced in figure 7.6.

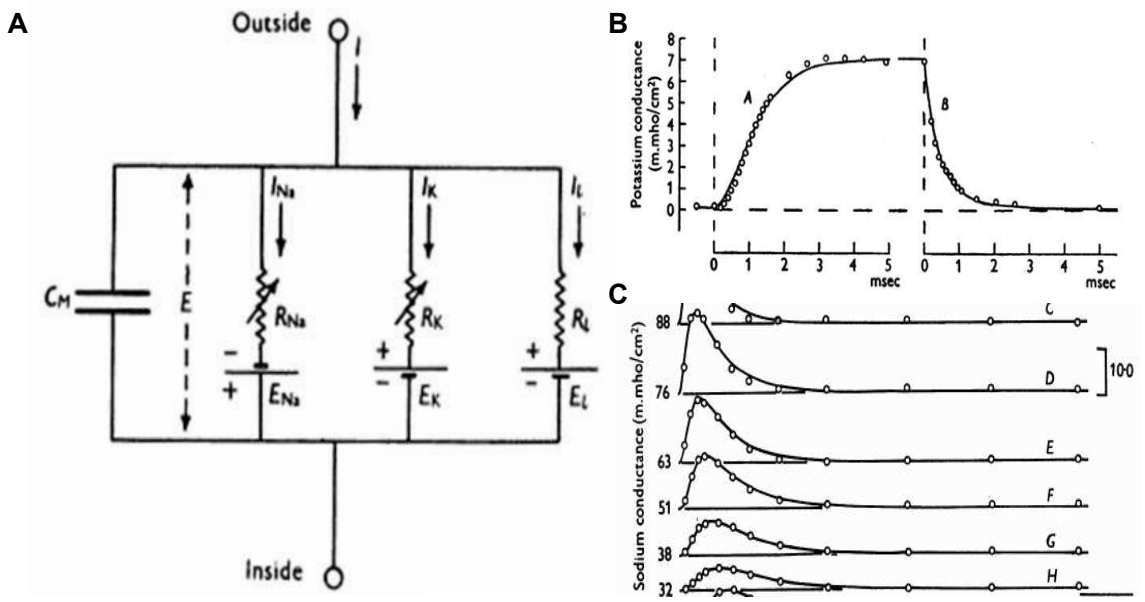

Figure 7.6 – Principle of the Hodgkin-Huxley model. Panel A presents the unit cell of the equivalent cable circuit proposed by *Hodgkin* and *Huxley*. Compared with the passive electrical model presented in figure 7.2, the unit cell separates the membrane resistance into the contribution of each ion channel type resistance. The sodium and potassium channels are modeled as resistances in series with a generator corresponding to their respective Nernst potentials. The orientation of the generator depends on the direction of the flow. The leakage channel corresponds to all other ion channels modeled as a constant resistor in series with a generator at the membrane resting potential. **Panels B and C** respectively show the potassium and sodium conductances in different voltage clamp experiments. Panel B shows the evolution of the potassium conductance in a low sodium experiment and by applying a 25 mV voltage increase during the 5 first milliseconds and by returning to the membrane resting potential in the second step. The potassium conductance roughly varies as an exponential with time. Panel C shows the sodium conductance in a low potassium experiment for a voltage increase of respectively +35, +38, +51, +63, and +76 mV (from the bottom trace to the upper trace), exhibiting an initial increase in conductance and a further decrease. This can be modeled by a second-order time equation or by the product of two exponentials varying in opposite directions with time. The three panels have been reproduced from *Hodgkin* and *Huxley* original article [336].

To account for the potassium conductance, *Hodgkin* and *Huxley* proposed an apparently simple fit of their experimental data, assuming it to be proportional to the fourth power of a variable that obeys a first order time equation [336]. The fourth power is the minimal power that correctly fits their experimental data but they acknowledge that a fifth or sixth power would fit them better but would complicate the numerical calculation. They defined:

$$g_K = \overline{g_K}.n^4 \tag{7.19}$$

with $\overline{g_K}$, a time constant that only depends on voltage and n an arbitrary function that verifies:

$$\frac{dn}{dt} = \alpha_n.(1-n) - \beta_n.n \tag{7.20}$$

α_n and β_n are other arbitrary rate constants that are time independent (but are voltage dependent). Therefore, the potassium conductance for a given imposed membrane voltage temporally evolves as:

$$g_K = \overline{g_K}.(\frac{\alpha_n}{\alpha_n + \beta_n})^4.(1 - (1 - \frac{g_{K,0}(\alpha_n + \beta_n)}{\alpha_n}).e^{-(\alpha_n+\beta_n)t})^4 \tag{7.21}$$

with $g_{K,0}$, the initial potassium conductance at the membrane resting potential, that is independent of both time and voltage. Finally, they fitted the potassium conductance change over time for many imposed membrane voltage so that they fit (again) the voltage-dependence of the rate constants α_n and β_n. To be exhaustive, their respective expressions are:

$$\alpha_n = 0.01\frac{V + 10}{e^{\frac{V+10}{10}} - 1} \tag{7.22}$$

$$\beta_n = 0.125.e^{\frac{V}{80}} \tag{7.23}$$

Not so surprisingly with so many arbitrary variables fitted from experimental data, they could accurately reproduce the potassium conductivity for any voltage and time.

Similarly, they estimated the sodium conductance change over time for several imposed membrane voltage. Nevertheless, the sodium conductance first increased similarly to the potassium conductance but experiences a latter decrease, as illustrated in figure 7.6. To account for such variations, two alternatives are offered. Either the sodium conductance is determined by a single variable that would obey a 2nd order time equation, or by two variables that would obey a first order time equation each but would have opposite effects on the sodium conductance. *Hodgkin* and *Huxley* decided to take the second option and define two arbitrary functions called m and h that respectively account for the sodium channel activation and for the sodium channel inactivation [336]. The sodium conductance is then given and described by:

$$g_{Na} = m^3.h.\overline{g_{Na}} \tag{7.24}$$

$$g_{Na} = \overline{g_{Na}}.(\frac{\alpha_m}{\alpha_m + \beta_m})^3.h_0(1 - e^{-(\alpha_m+\beta_m)t})^3.e^{-(\alpha_h+\beta_h)t} \tag{7.25}$$

with α_m, β_m, α_h, β_h, and h_0 are defined similarly to α_n, β_n, and $n_0 = \frac{g_{K,0}}{\overline{g_K}}$. As for these potassium variables, the evolution of all these sodium variables with the membrane voltage is fitted with an exponential voltage-dependence.

The leak channel conductance is thirdly supposed to be voltage-independent and to reach equilibrium at the resting membrane potential. Its contribution is essentially important to account for the restoration of the resting membrane potential after the hyperpolarization overshoot due to the voltage-gated potassium channels opening [336]. Finally, the last part of their main paper consists in the numerical recursive solving of the ten equations included in their model. These equations are the voltage equation 7.18, the 3 first-order time equation on n, m and h similar to equation 7.20 and the 6 voltage dependent equations on α_n, β_n, α_m, β_m, α_h and β_h similar to equation 7.23. If the propagation is first neglected, the Hodgkin-Huxley model can directly access the local evolution of the membrane voltage that nicely reproduce the shape of the action potential, can reproduce the time course of the sodium and potassium currents, can account for a voltage threshold above which an action potential is triggered and for a subthreshold response. It could also explain absolute and relative refractory periods and accurately predicted a voltage subthreshold oscillation during the recovering to the resting membrane potential [336, 337]. Finally, to account for the action potential propagation, equation 7.18 is transformed into a second order differential equation only dependent on time using a further assumption that the action potential

propagates as a wave so that:

$$\frac{\partial^2 V}{\partial x^2} = \frac{1}{c_{AP}^2} . \frac{\partial^2 V}{\partial t^2} \tag{7.26}$$

The membrane voltage temporal evolution was then calculated by guessing a value for the action potential propagation speed c_{AP}. It was found that the membrane potential diverges to $\pm\infty$ if the action propagation speed was guessed too small or too large [336], whereas the potential goes back to zero for a correct guess of the action potential propagation speed. Not only could they predict conduction velocities close the value measured experimentally but they could also estimate the action potential propagation speed from the passive properties of the axon and from a single time constant K that contains all the non-linearities due to the time and voltage dependence of the ion channels and that can be determined experimentally:

$$c_{AP} = \sqrt{\frac{K.r}{\rho_{axoplasm}.C_M}} \tag{7.27}$$

Therefore, the Hodgkin-Huxley model also predicts reasonable action potential propagation speeds and can account for the square root dependency of the speed with the axonal radius r. Equation 7.27 illustrates that the propagation speed is mainly controlled by the passive electrical properties of the axon but a correcting factor has to be applied to account for the active ion channels dynamics.

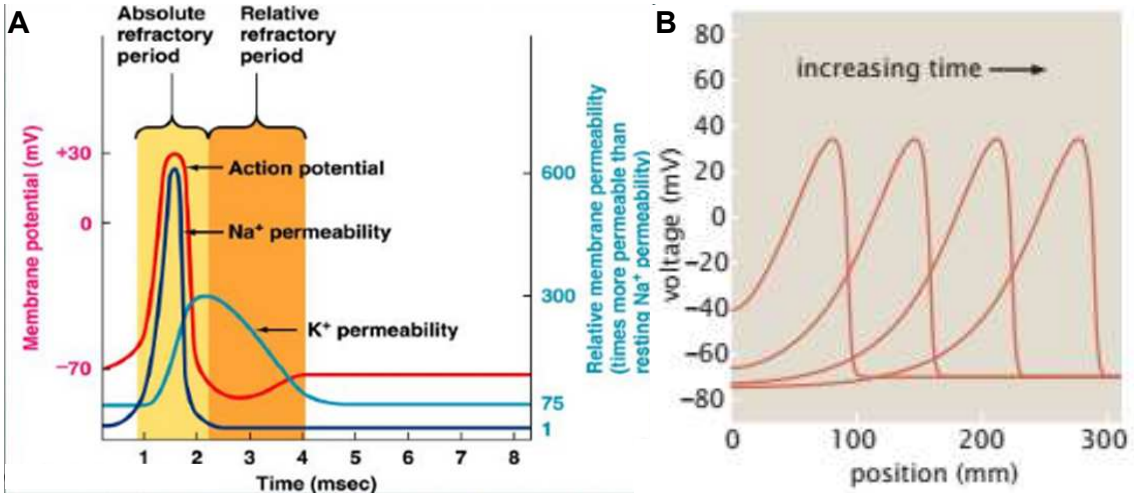

Figure 7.7 – Results from the Hodgkin-Huxley model. Panel A illustrates the local prediction of the model without considering the propagation. It could successfully reproduce the course of the membrane voltage (red curve), and predicts the time course of the sodium and potassium channels opening. Here, the sodium and potassium channels permeability (proportional to their conductances) is respectively plotted in blue and cyan. It allows the definition of an absolute refractory period during which the cell can not be reactivated since its sodium channels are already open. A second period called the relative refractory period corresponds to a membrane hyperpolarization during which the cell is less excitable but could be activated with a stronger current or voltage input. **Panel B** illustrates the spatial propagation of the action potential. Here, the change in voltage membrane is plotted versus distance for different times (corresponding to the different curves moving to the right with increasing time). It shows that a single action potential in the squid giant axon has a spatial extension of several centimeters and that the action potential plotted versus distance is the vertical symmetric of the action potential plotted versus time. The Hodgkin-Huxley model converges only for a given action potential propagation speed and predicts its propagation due to local circuit currents caused by the passive electrical properties of the axonal membrane.

To summarize this section in shorter terms, the cell membrane passively acts as an inductance-free line cable displaying a diffusion-like propagation of voltage, which controls the maximal speed of the wavefront propagation. The wave-like aspect of action potential propagation can only be explained by the active parts of the neuronal membrane, in which voltage-dependent ion channels open and close to compensate for the energy decay suggested by a passive diffusive model. To account for these active elements, the Hodgkin-Huxley model models the active elements of the cell membrane, *i.e.* the ion channels, with a time-dependent specific conductance for each channel type. A modeled conductance is arbitrarily fitted to match the experimentally measured conductances and lead to a complex, multiple variables, and non-linear model that can not be solved analytically. Nevertheless, using their model, *Hodgkin* and *Huxley* could numerically and recursively estimate the local shape of the membrane potential in response to a voltage clamp experiment. To account for the action potential propagation, the local transverse currents are assumed to depolarize the neighbor regions by diffusion. To solve it numerically, a wave-like solution is arbitrarily assumed to obtain a time-dependent only equation that converges only for a given range of action potential speeds. If this model is technically and conceptually impressive (especially in the early 1950s!), it requires the definition of a number of arbitrary variables that are fitted experimentally to converge towards a numerical solution. Nevertheless, this model large success can be explained by its highly predictive nature, while most of its prediction described above have been verified throughout the years.

7.2 Beyond the Hodgkin & Huxley theory

Despite its large success and its accurate predictions, the Hodgkin-Huxley model proposes a rather simple and qualitative version of the biological complexity of action potential propagation. It would not necessarily be an issue but several observations made over the six past decades can not be explained in this purely electrical framework The aim of this section is to review some of these unexplained observations that mainly include mechanical and thermal changes associated with action potentials and may justify the quest for more general theories to explain action potential propagation that will be considered in the next section. The following list of observations have been measured throughout the years and have been the object of recent criticisms of the Hodgkin-Huxley model [338, 339], even if some of them are not truly justified, as I will point it out:

- ***Reversible change of the optical and mechanical properties.*** One of the most consistent experimental evidence that would advocate for the development of a more generalized action potential framework is the change in the intrinsic optical properties, such as light scattering, birefringence, opacity, phase change, or absorption and quantum yield changes. More importantly, a reversible mechanical change has also been directly measured. Both the optical and mechanical response sharply follow the action potential and are probably too fast to be likely caused by biochemical response. The detecting of optical changes in neurons or nerves during activity has a quite long story, and is nicely summarized in *FangYen*'s review [340]. Over the years, several mechanistic explanation have been proposed and some papers have contradictory demonstrate that these fast optical changes are caused either by a change of refractive index, or by a physical displacement of the axon, or by both. All the studies are hardly comparable since they all used different nerves or axons and different preparations. I will try to review some of them here by sorting them by the mechanism they suggest. Before that, it may be interesting to emphasize that the changes in the electric field during an action potential are of the order of 2.10^7 V/m (which is higher

than the electric fields involved in lightnings(!), mainly because the distance on which the electrical field is created in cells is of a few nanometers only). More importantly, the electric field reverts during the course of the action potential. It would therefore not be surprising that the organization within the membrane (in which around 50% of the volume is occupied by locally charged proteins) is perturbed. It could lead to the physical remodeling of the membrane and can either stretch the membrane or change its local refractive index, both of each property affecting the optical properties around the membrane. Additionally, the water molecules from the ionic hydration shells diffusing inside and outside the cell could slightly impact the cell volume, especially during sustained neuronal activity. All these effects can impact the local optical properties of neurons and might be used as an intrinsic label-free signature of the action potential, even though their effects are probably still below the current systems detection limit. Interestingly, these effects can either simply be consequences of action potentials or can play an active role in the neuronal information processing and transmission.

We also emphasize that these fast intrinsic optical signals are fundamentally different from slower intrinsic signals detected at lower resolution, as in diffuse optical tomography and that rather correspond to a change in the spectral absorption of hemoglobin and are linked with the BOLD signal. Here, the fast intrinsic optical signals are associated with single nerve or axon without blood flow and show a response that follows the action potential.

The first evidence for such intrinsic optical changes was demonstrated in 1949 [341]. A change in opacity of a crab nerve under external stimulation was observed and was imputed to a reorganization of the nerve fibers, leading to a change in the refractive index. Then, the same group of authors published a lot of similar data in nerves from different species. They notably demonstrated that this was not only the opacity that changes but are also accompanied by a decrease in the nerve scattering and birefringence properties (about 5 times higher than the scattering) in unmyelinated nerves such as the squid giant axon or crab walking nerve [342]. The birefringence has been measured to change quadratically with the membrane voltage change, while the scattering change evolves linearly with the voltage difference in single neurons *Aplysia Californica* [343]. The fast birefringence change [344] and the angular-dependence of the scattering signals [343] advocated for a change in the refractive index during electrical activity [345]. Additionally, the quantum yield of fluorophores has been found to increase during the depolarizing phase of the action potential [346], which explains observations made in 1968 by *I.Tasaki et al.* that an intrinsic fluorescence signal (from a few different fluorescence probes) was following the action potential [347]. This result might indicate that the membrane becomes more rigidly oriented during action potentials or that the membrane becomes more hydrophilic during action potentials (without any selectivity and supposedly not directly the effect of the ion channels opening.) and let ions such as the fluorescent label to penetrate the membrane and find a more organized environment [346] [7]. In any case, these experiments advocate for an activity-related refractive index change.

Nevertheless, a change in the refractive index only could hardly account for the mechanical displacements experimentally measured with contacting probes (with AFM or with probes similar to AFM). Indeed, the group of *I. Tasaki* first reported such mechanical displacements in 1980 [349] in squid giant axon (around 1 nm displacement) and similar mechanical changes have been reported in mammalian and crustacean nerve terminal [350, 351] and in

[7] Interestingly, this higher-organized state associated with action potential might evoke the decrease fraction of the fast diffusion pool involved in diffusion MRI [348].

single cells [352]. It was proposed to be caused by cell swelling possibly associated with the ion channels opening. In 2007, *Foust et al.* demonstrated the role of interstitial swelling to account for the 90 degrees scattering change in nerves [344], which explained why the change in scattering was observed with a submillisecond delay. Millisecond optical transients have also been measured via Surface plasmon resonance in bulk brain tissue in response to an external electrical impulse [353]. A quantitative model has been developed and could explain the measured optical change dynamics with transient cellular volume changes. Nevertheless, surface plasmon resonance averages the signal over the entire field of view and no spatial information can be measured so that the measured swelling signal can either originate from the neuron cell bodies, from the neurites, or from glial cells. Additionally, *Jourdain* and its colleagues from the group of *Pierre Marquet* have measured a phase decrease in neuron cell bodies excited by diverse drugs and could link this phase decrease with the water uptake associated with the channels opening [70, 95, 96]. We emphasize that a cell swelling could both impact the cell thickness and refractive index, as reported in chapter 1. We also interestingly report a recent article that demonstrated a micron-scale mechanical deformation associated with action potentials in plant cells [354] even though the action potential and the cell membrane are quite different from mammalian characteristics.
Finally, a third mechanism has been suggested to explain the measured mechanical deformations. Surprisingly, *Tasaki et al.* have measured a volume extension in unmyelinated nerves that can not be associated with water uptake [355], as their exprimental tool measured a total volume of both the extracellular and intracellular medium. This last mechanism associates a natural mechanical displacement with a change in the membrane voltage as predicted by classical thermodynamics as the result of an effect called membrane electromotility. It accounts for the voltage-induced charge accumulation that modulates the surface tension and therefore the membrane tension, which itself controls the cell volume and shape. This effect has been invasively measured with atomic force microscopy (AFM) in HEK cells showing a 0.5 nm tip displacement associated with a 100 mV hyperpolarization of the HEK cell [352]. This suggests that changes in the membrane potential (hence possibly during action potentials) elicit changes in the membrane tension that can initiate membrane displacements and local pressure changes. Interestingly, this effect has also been unambiguously and non-invasively detected with diffraction phase microscopy [90] (a popular QPI system described in chapter 1) and a sinusoidal voltage change to enhance the sensitivity. As illustrated in figure 7.8, a linear relationship between the applied voltage and the measured phase change (and physical displacement in this case) has been measured and would associate a 50 pm membrane displacement (in terms of optical path that might roughly correspond to 1 nm physical displacement) to the rising phase of an action potential. Both papers reporting membrane electromotility have worked in HEK cells and suggest that the voltage-dependent membrane displacement can be a general property of cellular membrane and can not be restricted to neurons only. Nevertheless, a similar effect has never been reported in mammalian neurons that are more fragile to culture and that cannot be excited sinusoidally (as they would fire action potentials) or in any cell whose membrane voltage usually change over time. Whether or not membrane electromotility is conserved in neurons that are used to membrane voltage changes is still an open question.

We can also add that a few fast intrinsic optical signal measurements have already been performed with phase-sensitive OCT and offered a depth-resolved measurement of electrical

activity [356, 357]. More recently, several fast optical signals have been measured it in vivo in the human retina [221, 358, 359]. Nevertheless, due to the light-sensitivity of retina and to the amplitude of the observed signals, they probably originate from different mechanisms.

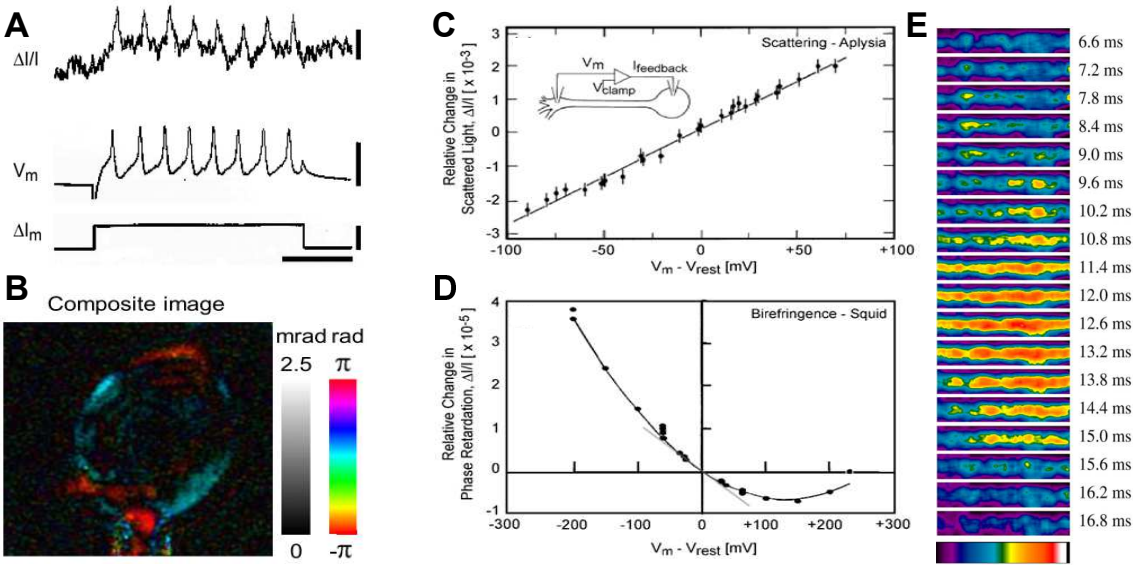

Figure 7.8 – Activity-dependent fast intrinsic optical signals. **Panel A** illustrates the activity-related (middle trace corresponds to the membrane voltage and the bottom trace to the associated current input) intensity scattering change in an *Aplysia* cultured neuron with dark field microscopy. The light scattering change follows the action potential shape with a small delay observable between the two signals. **Panel B** shows a phase change and associated time delay of an HEK cell surface in response to an external sinusoidal voltage excitation. **Panels C and D** illustrate the linear scaling of the light scattering change (panel C) with the membrane voltage difference, while the birefringence change(panel D) varies quadratically with the membrane voltage (on a larger voltage scale though). **Panel E** illustrates the light scattering change time propagation in a lobster leg nerve. The maximal amplitude of the light scattering change is 1.10^{-4}. Panels A, C, and D are reproduced from *Kleinfeld and Laporta* [345] who plotted data from different original articles [343, 360] . Panel B is reproduced from *S. Oh et al.* [90] and panel E from *Schei et al.* [361].

- ***Reversible thermal change*** Another important consistent observation has been the detection of reversible heat transfer the course of which was following the action potential evolution, as illustrated in figure 7.9. An initial release of energy accompanies the depolarizing phase of the action potential while a second energy uptake (heat absorption) almost compensates the initial heat increase [362, 363]. Overall, the heat transfer follows the action potential shape so that the temperature increase is quite mild at the end. Such heat transfer can hardly be explained in a purely passive electrical model in which case we would expect a continuous heat increase as $R_{membrane}.I^2$ during all the course of the action potential. It should also significantly increase the temperature at each neuronal excitation while the heat could only slowly diffuse away from the axon. The heat dissipation has been proven to be too fast to be ruled by diffusion only [363] and to be too important to be explained by the thermodynamic cooling associated with a capacitor charging [339]. We can add that this heat control might be of critical importance for the brain temperature control otherwise an intense activity of a compact neuronal network may significantly increase the local temperature and cause brain damage. We may imagine scenarios in which the excessive heat energy is absorbed and reused by endothermic chemical reactions that would open a part of the

potassium channels for example. Nevertheless, it is hard to imagine that this thermal energy can be used in a somehow selective precise reaction and would probably trigger several reactions and might therefore not appear as a good mechanism to control the energy excess.

- ***Propagation velocity versus axon radius.*** If the Hodgkin-Huxley model is often criticized for its non-predictive and non-analytical solution for the action potential speed in a given axon, we have previously seen that the passive properties of the membrane could account for an upper limit for this speed. More interestingly, it allows for the qualitative interpretation of the action potential speed dependence with the square root of the axon radius in unmyelinated axons and of the linear relationship between the speed and the axon radius in myelinated axons [328], as previously described and illustrated in figure 7.3.

- ***A general theory of anesthetics or Meyer-Overton correlation*** Despite their consistent use in hospitals, the effect of most of the general anesthetics (defined as a drug that causes a reversible loss of consciousness) is still not understood. Similar effects are obtained with simple and very different molecules and no specific target location has been found. Nevertheless, an intriguing relationship between the minimal concentration of these general anaesthetics molecules and their solubility in lipids (first experiments conducted in Olive oil!) has been observed in the 1890s and is known as the Meyer-Overton correlation [364] [8]. This correlation suggests that the general anesthetics solubilize in the axonal membrane and block the action potential transmission, which eventually leads to the loss of consciousness. If the cause of this signal transmission defect has never been demonstrated, its mechanical origin has been hypothesized in several articles [338,364,365]. On the other hand, the purely electrical and ionic hypothesis of the Hodgkin-Huxley has failed to explain this effect so far.

- ***Action potentials can collide without being without being affected.*** A few experiments in the 1950s had reported the annihilation of two counter-propagating action potentials [366]. Indeed, if the action potential propagation is unidirectional because of the refractory period following the action potential, there is no a priori preferential direction. It is likely that action potentials propagate from the soma to the axonal end because the action potential is generated in the soma. Nevertheless, if excited by patch clamp, it possible to propagate action potentials in both directions in a single axon. However, for similar reasons, two counter-propagating action potential are expected to block each other at the collision point because the respective ionic currents should cancel each other. Nevertheless, since 2014, *Gonzales* and colleagues have reported the penetration of counter-propagating action potentials in earthworm and lobster nerves [351, 367]. These experiments contradict the first observations and the theoretical explanation reported by Tasaki in the 1950s [366], even though it was not a recording from the same animal and nerve fiber. These intriguing experiments have been conducted by the group from *T. Heimburg* who developed the soliton theory of action potentials (that will be developed in the next section) that predicted the penetration of colliding action potentials. Nevertheless, these measurements have been discussed and questioned by several groups [368, 369] and they might be an artifact due to the presence of multiple axonal fibers inside the studied nerves so that action potentials could have propagated in different fibers. Waiting for a clear response to this controversy that may invalidate a part of the Hodgkin-Huxley local currents theory, I simply refer to these experiments here and will discuss them with the electromechanical models.

[8] Unfortunately, the original papers are in German but the associated Wikipedia page is particularly interesting [364] and additional information can be found in more recent articles [338, 365].

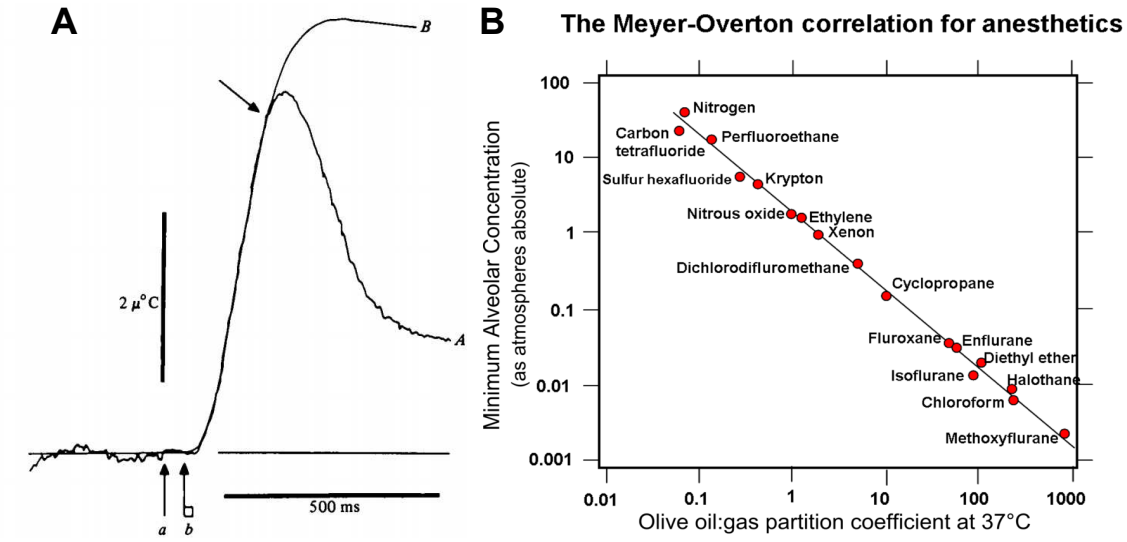

Figure 7.9 – Physical effects related with the action potential propagation. Panel A illustrates the temperature variation during an unmyelinated nerve electrical activity (trace A with a fast decay). The temperature variation is compared to the temperature decrease by diffusion (trace B) after heating with a pulsed laser in an hyperpolarized nerve. The temperature change is not completely reversible here but the heat loss is much faster in an electrically active nerve, showing the existence of an active phenomenon that controls the temperature. Panel A is reproduced from a paper of *Ritchie* and *Keynes* [363]. **Panel B** shows the Meyer-Overton correlation between the minimal concentration of a general anesthetics to asleep a patient versus the solubility of the anesthetics molecule in olive oil or other hydrophobic fluid. The higher the solubility, the lower the concentration needs to be for several anesthetics independently of their chemical reactivities. Panel B is reproduced with permission.

7.3 Alternative electrical models

Since the early 2000s, a few alternatives to the Hodgkin-Huxley model have been developed, including mechanics and thermodynamics considerations to the purely electrical modeling of the axon. The 3 models that will be considered in this section all postulate the existence and co-propagation of a mechanical wave explaining some of the previous unexplained observations. This coupling between a mechanical wave and the electrical activity of a neuron, also referred to as electromechanical waves, are proposed to be either a simple epiphenomenon of the action potential, or to play a role in the action potential propagation, or also to propagate an information faster than the action potential that might increase or decrease the cell excitability. As we have seen in the previous section, a local mechanical deformation is expected during the action potential. Such a mechanical deformation on a soft substrate is then supposed to propagate and decay throughout the medium, accordingly to the laws of Continuum Mechanics. Within neural tissues, a mechanical deformation should propagate at speeds around a few meters per second, and should significantly decay after hundreds of microns, similarly to the electrical activity. Therefore, it would not be so surprising that the mechanical and electrical waves couple, which was the basis of such electromechanical coupling and a legitimate starting point of investigation for more complex theories. Interestingly enough, these models resonate with recent yet unexplained observations that mechanical waves from ultrasounds can trigger an electrical local response [370] in single neurons [371] or in larger cortex areas [372] [9]. A local compression could originate from the

[9] For the sake of controlling the length of this manuscript, this exciting part of the bibliography will not be covered, even though it might play an important role in the understanding and the derivation of a future more complex vision of the neuronal functioning.

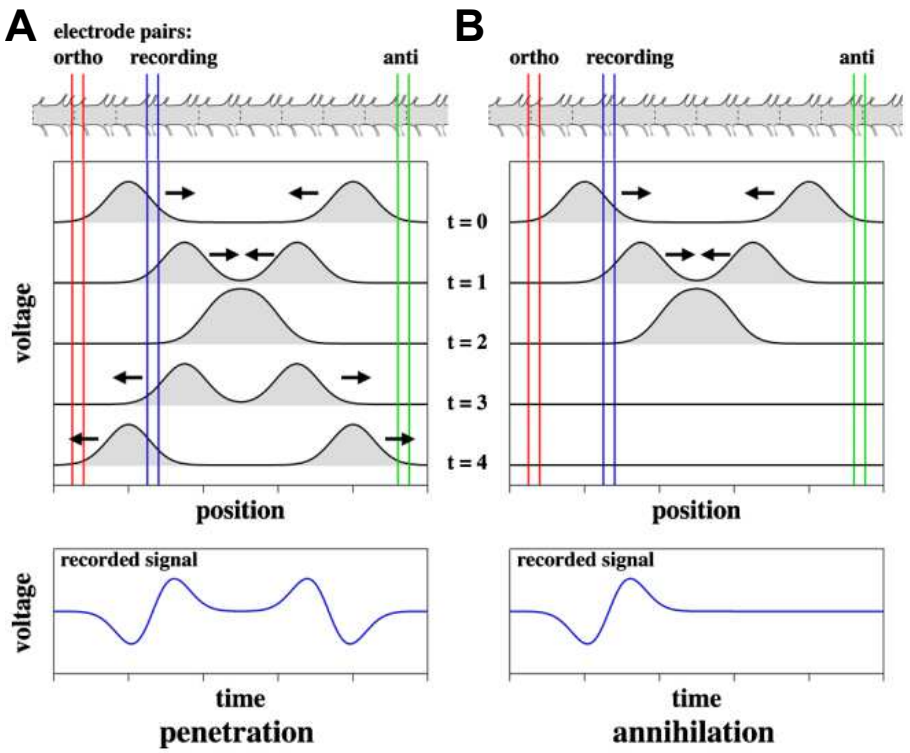

Figure 7.10 – Principle and simulation of an action potential collision. Panel A illustrates the principle of wave penetration when two action potentials are colliding. Two action potentials propagating in opposite directions are generated from both sides of a nerve so that they can collide around the center of the nerve. The time penetration scenario proposes that the two action potentials sum up at the collision point and the action potentials penetrate each other and continue their respective propagation. This view is supported by alternative models to the Hodgkin-Huxley and corresponds to a wave-like propagation. **Panel B** shows a similar experiment but in which the action potentials will annihilate, as predicted by the Hodgkin-Huxley theory. This figure has been reproduced from *Gonzales et al.* [367].

mechanical impedance change happening at the neuronal membrane and might trigger action potentials. In the following subsections, I will describe all the models, discuss their respective abilities to explain the above observations and propose a few experimental tests that might help to justify one model over the others.

7.3.1 The pressure pulse model

To my knowledge, the first electromechanical model of action potential propagation has been proposed by *M. Rvachev* in 2003 [373] and suggests that the action potential is driven by a mechanical pressure wave (more or less a mechanical shear wave trapped in the specific environment of the axoplasm). *Rvachev* pointed out that the transverse ionic current proposed in the Hodgkin-Huxley model to account for the action potential propagation has never been directly observed experimentally (only the local membrane voltage change and the fact that the action potential propagates have been) so that the action potential propagation might be driven by other different mechanisms. Furthermore, he considered the propagation of small amplitude axially-symmetric pressure pulses in a viscous compartment (cytoplasm) enclosed in a distensible membrane. The pressure pulse propagation is controlled by the viscoelastic cytoplasmic fluid and by the extendable membrane. It can propagate for short distances (around one millimeter) and with group velocities similar to the experimentally measured electrical pulse velocity. The pressure pulse velocity is supposed to increase linearly with the square root of the axonal radius in unmyelinated axons

and with the axonal radius in myelinated axons, similarly to the action potential propagation speed [338]. Nevertheless, because of viscosity, the mechanical pulse amplitude is expected to decay exponentially with a decay length of 180 μm in unmyelinated axons and of 15 mm in myelinated fibers (and would therefore decay of a few % in amplitude between two nodes of Ranvier). The viscosity also leads to frequency-dependent group velocity (or dispersion), which should lead to a broadening of the pulse, on the contrary to the action potential conservation. To compensate for the viscosity attenuation and to explain the electromechanical coupling, *Rvachev* postulated that the mechanical distortion would open the sodium channels and would therefore trigger a usual local action potential as predicted by the Hodgkin-Huxley model (and as verified experimentally). Additionally, he proposed a few mechanisms that could generate a radial compression that would amplify back the pressure pulse and prevents its decay and its broadening [338]. These possible mechanisms include a fast calcium-related contraction of actomyosin filaments anchored at the membrane [10], voltage-sensitive channels, or membrane electromotility (as presented in the previous section).
Despite this model does not provide any biological evidence for such electromechanical coupling, it is of interest for its relative simplicity and because it predicts the mechanical displacement of the membrane and suggests a mechanism for the Meyer-Overton correlation. Indeed, the lipid affinity of a given anesthetics could increase its solubility in the membrane and would decrease the membrane area expansion modulus. This would reduce the pressure wave velocity and its decay length and might lead to the pressure wave inhibition when the anesthetics are in sufficiently high concentration in the membrane [338]. If the observed reversible heat is not explained in *Rvachev* papers, the effect of temperature on the pressure wave velocity is similar to its effect on the action potential speed. Interestingly enough, the pressure waves have been hypothesized to induce elasticity changes that might cause a mechanical breakdown in damaged membranes. This might lead to the accumulation of axoplasmic fluid in the extracellular space and to the formation of plaques and tangles observed in Alzheimer's disease [374]. A few other neurological disorders might also be linked with mechanical changes in the extracellular medium [338,374]. Two pressure waves are expected to cross each other and might regenerate an action potential on the other side of the collision point. Nevertheless, due to the channels refractory period, the pressure wave might have significantly decayed before being able to generate another electrical pulse so that the pressure waves can either explain annihilation or penetration in collision experiments but should display two mechanical waves decaying from the collision point that can eventually regenerate after some distance.

7.3.2 The action waves model

A more recent electromechanical model of nerve activity propagations has been developed in 2015 by *A. El Hady* and *B. Machta* [375]. Similarly to the pressure pulse model, they postulated that a mechanical excitation might be generated by the change in membrane voltage. Nevertheless, they do not assume any reinforcement of the electrical activity by the mechanical wave. Therefore, their model does not question the Hodgkin-Huxley model but rather add a mechanical component to it. Whether the mechanical wave transports any useful information is voluntarily kept as an open question (mainly for *political* reasons) even though they suggest that it would be surprising that these two co-propagating pulses do not interact and would not carry additional information.

[10] Calcium-related effects usually display slower temporal dynamics but the calcium uptake begins from the start of the action potential and can have large consequences even at low concentrations so that there is no *a priori* unfeasibility of a fast calcium response.

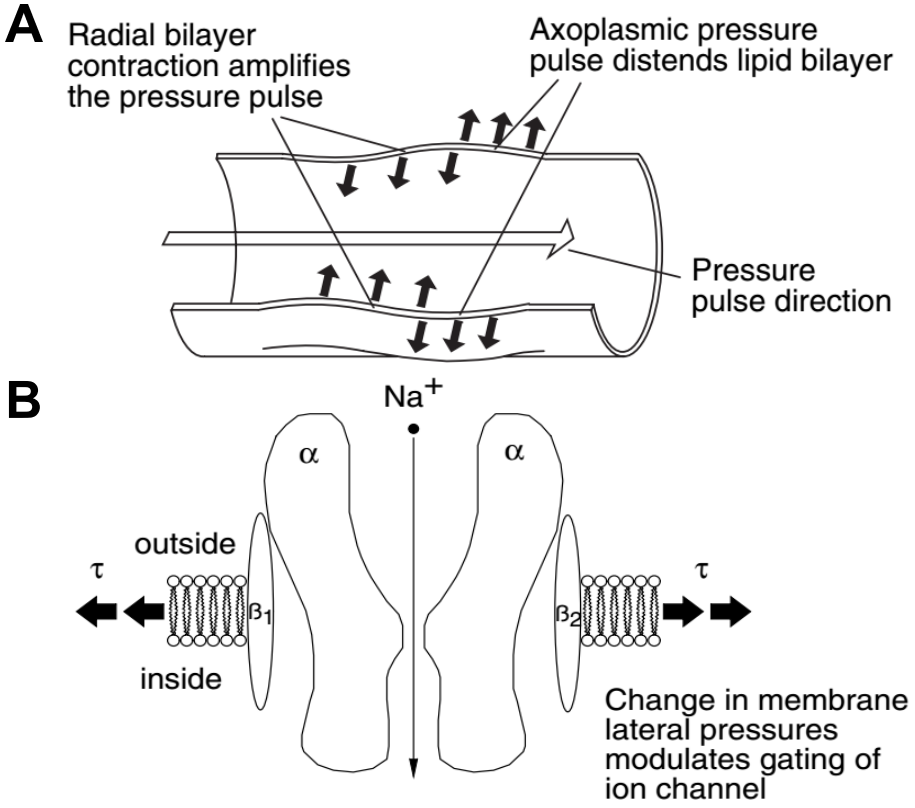

Figure 7.11 – Principle of the pressure pulse model. Panel A illustrates the shear pressure wave that propagates through the viscoelastic axoplasm and distends the membrane. **Panel B** illustrates the ability for sodium channels to open under a membrane distortion. The sodium inflow triggers an action potential as described by the Hodgkin-Huxley model. With the associated membrane voltage change, calcium ions flow inside the cell and can trigger a mechanical response that can create an axial displacement to compensate for the pressure pulse decay caused by viscosity. Both panels are reproduced from *Rvachev*'s paper [338].

Shortly, their model demonstrates the possible existence of mechanical surface modes in axons that could be excited by transferring a part of the electrical potential energy of the action potential to the elastic potential energy stored in the membrane that itself is coupled to the intracellular fluid kinetic energy. The propagation of the electrical activity continuously excites the surface modes leading to at least one mechanical wavefront propagating simultaneously to the action potential. The mechanical surface waves predicted by this model are called action waves. If the coupling between the membrane elastic potential energy and the axoplasmic kinetic energy is controlled by the laws of mechanics, the mechanism that couples the electric and elastic potential energies is not clearly defined [375]. Nevertheless, they suggest that electrostriction, a general property of all materials that can contract in presence of an electric field, can be involved [11]. This model advantageously predicts a reversible mechanical displacement (as the excitation of an axonal mechanical surface mode), a reversible heat change associated with the isothermal distortion of the membrane. It predicts a local radius increase of about 0.5 nanometers in squid giant axons and predicts a similar deformation in mammalian hippocampal axons of about 0.1 nanometers. Interestingly, this model also predicts a yet unobserved lateral displacement of the axoplasm simultaneously to the action potential that can be as large as -50 nm in amplitude in mammalian

[11] Electrostriction, and flexoelectricity in the case of curved materials, are more general properties of dielectric material similar to piezoelectricity in principle, meaning that an electric field can contract the material. On the contrary to piezoelectricity, these effects do not require any symmetry properties are a second order effect of the voltage [376]. Nevertheless, they do not display the reverse effect leading to a voltage change under compression as observed in piezoelectricity.

neurons. This lateral compression has only been predicted in this model and might be a selective way to test it. Indeed, if a longitudinal compression could also occur in the pressure wave model, it is expected to propagate much faster than the shear pressure wave and than the action potential. Nevertheless, a dynamic 50 nm amplitude lateral displacement is still challenging to measure since interferometry and AFM provide sub-wavelength measurements of axial displacements only. It might be easier to measure such lateral displacement with super-localization microscopy of a particle somehow attached in the axoplasm and the movement of which would be driven by the lateral compression. This model gives a mechanical wave propagation speed that depends on the temporal frequency that is not necessarily this of the electrical pulse [12]. In most cases, *El Hady* and *Machta* found the mechanical wave speed to be greater than the action potential propagation speed, although the mechanical characteristics of neurons have not been well characterized enough to provide very accurate predictions on the mechanical wave. With the continuous mechanical excitation provided by the action potential propagation, a faster mechanical wave will lead to the propagation of a first wavefront colocalized with the electrical pulse and a larger mechanical perturbation in front of this wavefront and which amplitude would decay with the distance of the electrical wavefront. Here again, this quite unique feature might give a good opportunity to test this model. This might also suggest that the mechanical wave can have a biological interest since it would give a way to transport information faster and might eventually rise or decrease the axonal end excitability. A square root dependence of the mechanical wave speed with the axonal radius is found but the case of myelinated axons is not considered. In this case also, the mechanical waves of two colliding pulses should penetrate each other but they should be unable to generate another action potential on the other side of the collision point. Finally, we can add that this model involuntarily demonstrates the membrane capacitance variation due to the longitudinal membrane distortion. In an equivalent RC circuit of the membrane at a constant voltage, the capacitance derivative should generate a depolarizing current. A rough estimation of the associated current would give around 3 pA in mammalian neurons whereas usual action potentials are usually triggered with currents of a few hundred pA. If this capacitive current is probably too small to trigger an electrical signal by itself, the summation of several such currents with the arrival of several mechanical waves might have a significant impact and trigger an action potential.

7.3.3 The soliton model

A thermodynamic theory of nerve pulse propagation has been proposed in 2005 by *T. Heimburg* and *A. D. Jackson* [377] from the postulate that solitons (non-linear self-reinforcing solitary wave packets) might be able to propagate inside the axonal membrane [339,377]. It originated from their observation that biological membranes (at least bi-lipidic membranes and bacterial membranes) are close to the transition temperature between a fluid state and a gel phase, in which the lipids become more ordered. It results in the coexistence of small portions of lipids in the gel phase inside a larger part of lipids in the fluid state. Under compression or cooling, the transition is facilitated and a larger part of the membrane turns into the gel phase. Another direct consequence is that lipidic membranes are close to their maximum of compressibility at body temperature while their compressibility decreases sharply in presence of a density or a pressure change, which gives the non-linear parameter that will be regulated during the soliton propagation [339]. Additionally, the compressibility being frequency-dependent and therefore dispersive, biological membranes seems to be adequate for the propagation of self-sustaining localized density pulses. If the soliton model

[12] For example, we can imagine a doubling frequency to account for the non-linearity of electrostriction.

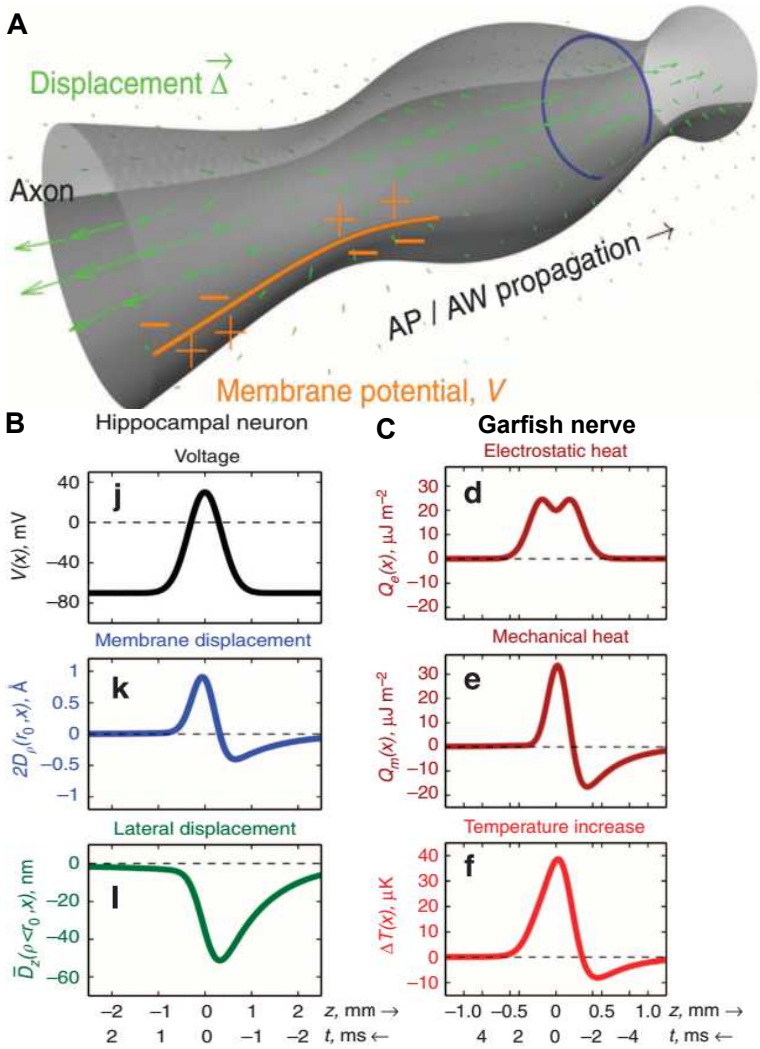

Figure 7.12 – Principle of the action waves model. Panel A illustrates the geometry of the model and its principle. The change in the electric potential energy due to the action potential is partly converted to the membrane elastic potential energy and generates a surface change. This elastic energy can also be converted to a kinetic energy and a physical displacement of the axoplasm fluid. **Panels B and C** present simulations and predictions obtained by the active waves model. Panel B shows the prediction of a sub-nanometric axial displacement of the axonal membrane (middle panel) and of a 50 nm amplitude lateral displacement of the axoplasm fluid (bottom panel) that should happen simultaneously to an action potential (top panel) in mammalian hippocampal axons. Panel C shows similar simulations in the olfactory garfish nerve that computes the electrostatic heat (top panel) and the mechanical heat (middle panel) associated respectively with the action potential and the action wave. The associated predictive temperature change due to both contributions (bottom panel) is reversible and returns to zero after the pulse. All figures are reproduced from the original paper of *A. El Hady* and *B. Machta* [375].

seems to have generated a rather large interest compared to the two other models and is able to account for a reversible heat change (as the transition energy between the gel phase and fluid phase) and a nanometric mechanical change (the axon should get thicker when the membrane is in the gel phase), it appears to be a more radical model than the two others and, therefore, a potentially less credible model. Indeed, if the soliton predicts a membrane voltage change around 100 mV due to the asymmetric charge distribution in the membrane [339], the membrane voltage change is considered as a simple consequence of the soliton propagation and the ion channels opening is not mentioned. It is also considered as incompatible with the Hodgkin-Huxley model [378]. The

soliton model is potentially valid only for the case of large nerves and myelinated axons in which the speed approaches 100 meters per second since solitonic solutions exhibit speeds that are on the order of the speed of sound in the bulk medium. Solitonic solutions do not account for the square root or linear dependence of the action potential speed with the axonal radius but can account for a refractory period and an hyperpolarized membrane state after its passage as a consequence of mass conservation [339]. The role of general anesthetics on the nerve activity can be considered within the soliton model, as the lipid transition would shift to a lower temperature in linear relation with the anesthetic concentration in the membrane [365]. To my knowledge, the soliton model fails at explaining the subthreshold membrane changes predicted by the Hodgkin-Huxley model. One of the key demonstration of the soliton model was the prediction of the penetration of action potentials when they cross each other, which was controversially demonstrated by the group of *T. Heimburg* as mentioned in the previous section. Nevertheless, such penetration, if confirmed, might also be explained by the two previously described models, and is not a specific proof of the soliton model.

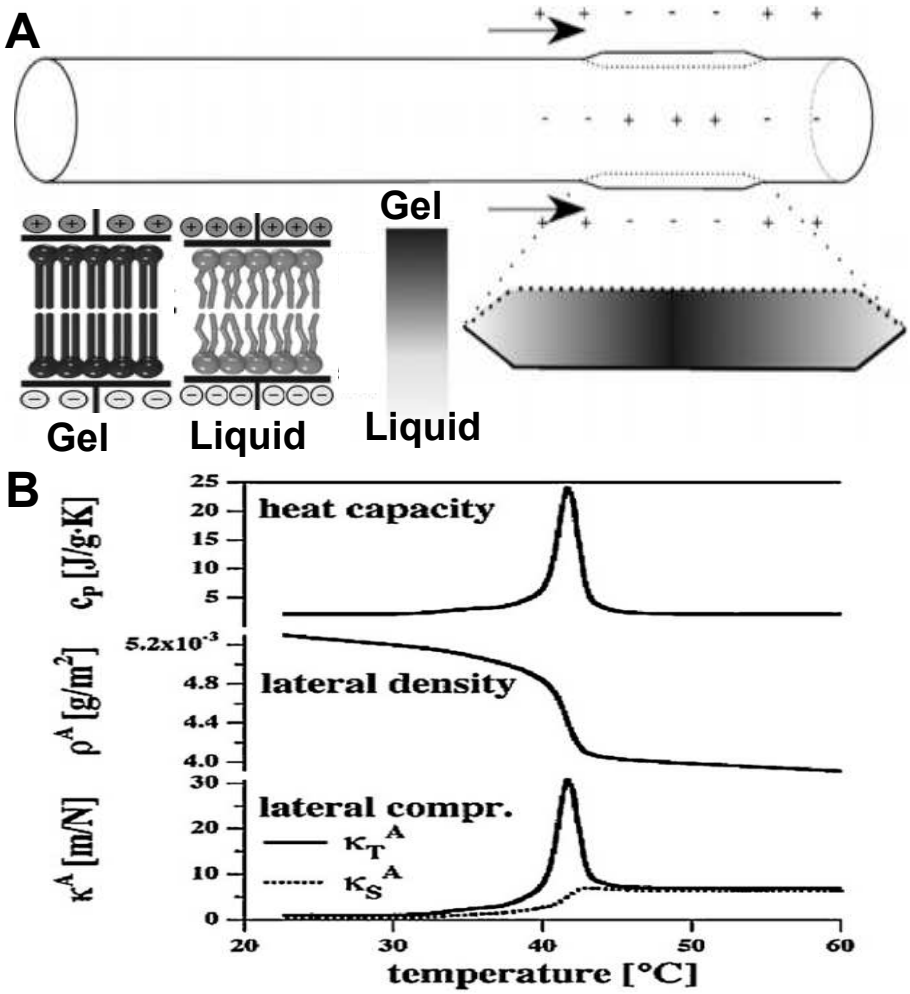

Figure 7.13 – Principle of the soliton model. Panel A illustrates the propagation of a soliton associated with a membrane thickening due to a forced phase transition (forced by the soliton compression) between the lipidic gel phase (more ordered and thicker membrane) and liquid phase. The Gouy-Chapman equation predicts that the change of surface area for a same number of charge will modify the membrane potential so that the gel phase that exhibits a lower surface area shows a higher membrane potential. **Panel B** illustrates the important non-linearities of a pure lipid bilayer membrane (DiPalmitoylPhosphatidylCholinein this case) heat capacity, one characteristic of the liquid-gel phase transition, around the body temperature. It leads to a non-linear compressibility of the lipid membranes in the vicinity of the transition, which, in addition to their dispersive properties (not shown), would be sufficient to self-sustain a compression pulse also called a soliton. The different panels have been adapted from two papers from *T. Heimburg*'s group [339, 379].

7.4 Measurement of dynamic phase changes in neuron cultures

If the electromechanical theories presented above are quite attracting, none of them have yet been demonstrated experimentally. Additionally, when looking at the numbers predicted by these theories of action potential propagation, the expected axial mechanical deformation is only of a few hundred picometers and should last for at most 2 millisecond. The worst part of it is that because of the small index mismatch between an axon and the extracellular medium, the expected associated phase variation should not be higher than 10 picometers! Even though the observation of a mechanical deformation in mammalian neurons is expected and would be interesting, the demonstration of any of the electromechanical theories would require an additional level of precision in order to observe variations of these mechanical deformations when adding drugs or different chemicals. Similarly, to be able to measure an eventual propagation delay between the two waves, an experimental system should be able to image first the mechanical wave propagation (even inside an unmyelinated axon, the action potentials usually propagate trough the entire field of view in less than 100 μs) and then small deviations from this speed. If we are still trying to see a mechanical wave propagating in large invertebrates axons with a high-speed large field of view holographic system (we might evoke it during the defense if results are obtained before), it seems to me that this imaging challenge still exceeds by one order of magnitude in both speed and sensitivity the current state of the art phase imaging systems. Nevertheless, we expect that, thanks to the large spatial extension of the action potential, we will be able to average the phase noise over the entire axonal length to increase the sensitivity. Unfortunately, due to physical and biological noise, we failed to produce a nice average over large distances in neuronal cultures so far.

In parallel to this long-end objective, we also tried to image activity-dependent phase changes that are expected to happen at larger scales. For example, if not looking at a single action potential but rather at a biologically-relevant activity displaying the usual train of action potentials, the signals can eventually sum up and produced a detectable signal. Briefly, it is expected that a sustained electrical activity and sustained membrane depolarizing would cause a significant and rather slow cell swelling. We also expect that a potential cell swelling might be more important at the soma than at the neurites. If we have thought of externally exciting the cultured neurons using optogenetically-modified neurons or external electrical pulses, we have also and mainly investigated spontaneous activity in hippocampal neuron networks. Not only is this supposed to be easier to experiment with, it would also be interesting since it is supposed to be the most complicated basic activity to detect. Essentially, we tried to image active neuronal cultures with our freshly developed quantitative phase imaging systems described in chapter 2, mainly with the Linnik interferometer coupled with a fluorescence path to measure calcium uptakes. We imaged both cortical and hippocampal rat cultures prepared successively by three different collaborators from 3 different research groups (successively *Pamela Rodriguez*, from *Alain Bessis* group at IBENS, *Celine Braini*, from *Catherine Villard* team at Curie Institute and finally *Julie Nguyen* from the group of *Diana Zala* at ESPCI). We will not detail the respective culture protocols here. To increase the signal-to-noise ratio of the phase measurements, we grew the neurons on silicon wafers on which cells can grow similarly than on glass [13]. Nevertheless, we faced several difficulties in integrating the silicon wafers into the culture protocols but also in the cell transport (around

[13]The silicon wafers exhibit a thin layer of Silicon dioxide at their surface similarly to the glass and hence have a similar chemical reactivity than glass.

10 to 15 minutes of transport every time) and in the neuronal survival in general. It seems that Fluo-4 soaking was also an important source of cellular death I will not go much further into the details of the many failed experiments but I want to emphasize that the two next sections will only show preliminary results with a few active cells every time. Even fewer labeled active cultures have been imaged so that the statistics of the experiments described below are obviously questionable.
We could basically image 2 types of neuronal activity, the first one consisting in a neuronal motility rather than in an electrical activity but could be indirectly related to neuronal intense peaks of activity as evoked in the previous section. In fact, neurons, and especially growing neurons, are highly dynamic structures at the second to minutes timescales exhibiting lots of protrusions moving around to feel the environment, vesicles flowing inside neurites to exchange proteins, or even neurites remodeling and displacements. Figure 7.14 illustrates a variety of neuronal objects we could detect and the dynamics of which could be investigated with our Linnik phase microscope. Extensively, we could image protrusions (as small as a few dozen nanometers) motions, vesicles and organelles trafficking, a few filament-like structures that we assimilated to microtubules, neurofilaments attachment and detachment, and growth cones propagation. In these cases, imaging such neuronal network dynamics has already been image both with fluorescence imaging and phase imaging and are good indicators of the health of the neuronal network. The mitochondrial transport is also expected to freeze during intense activity of the neuron as mentioned earlier [380]. All these motions exhibit changes of optical path variations around 10 nanometer and speeds between 1 second to several minutes and might be relatively easily further investigated under patch clamp or diverse electrical stimuli in a future work. If more carefully investigated, we can imagine that these effects can allow quantitative phase imaging systems including ours to evaluate and quantify without label an overall activity of a neuronal network to evaluate its health or its response to a given stimulus. Comparatively to fluorescence imaging, phase systems does not need any toxic and photobleachable external probes and exhibit less phototoxicity and could be of interest for longitudinal studies.

Additionally, we tried to push neuronal activity detection a bit further by imaging a phase response associated with the spontaneous activity of the network as illustrated in figure 7.15. We imaged the electrical activity with a calcium fluorescence reporter and can therefore only measure relatively important peaks of spontaneous activity. Nevertheless, our results, one of which being presented here, suggest the detection of an almost significant phase change during some of the calcium uptakes. If this decrease of a few hundred picometers in the optical path is yet close to the noise level and can simply be a phase signal statistical fluctuation, its good synchronicity with the calcium uptake is encouraging. These results are quite preliminary as they have been observed in a small number of neurons and a small number of events. In slightly noisier experiments, any phase change can be extracted out of the noise. Interestingly, similar initial phase decrease has been detected in response to glutamate that produces a strong cationic inward current using digital holography (Figure 2 (b1) in [70]). Similar results from the team of *Pierre Marquet* [95, 96] suggest that this phase decrease can be associated with a cell swelling associated with the water uptake caused by the calcium channel opening. Nevertheless, if these results happen to be accurate enough, it will be the first time, to my knowledge, that a phase decrease associated with the spontaneous activity of mammalian neurons is measured. These result finally suggest that a slightly more sensitive and more stable experiment would allow for an accurate label-free contact-free optical measurement of neuronal spontaneous activity, which here again would be of interest for the long term evaluation of neuronal networks. Finally, a few groups have recently

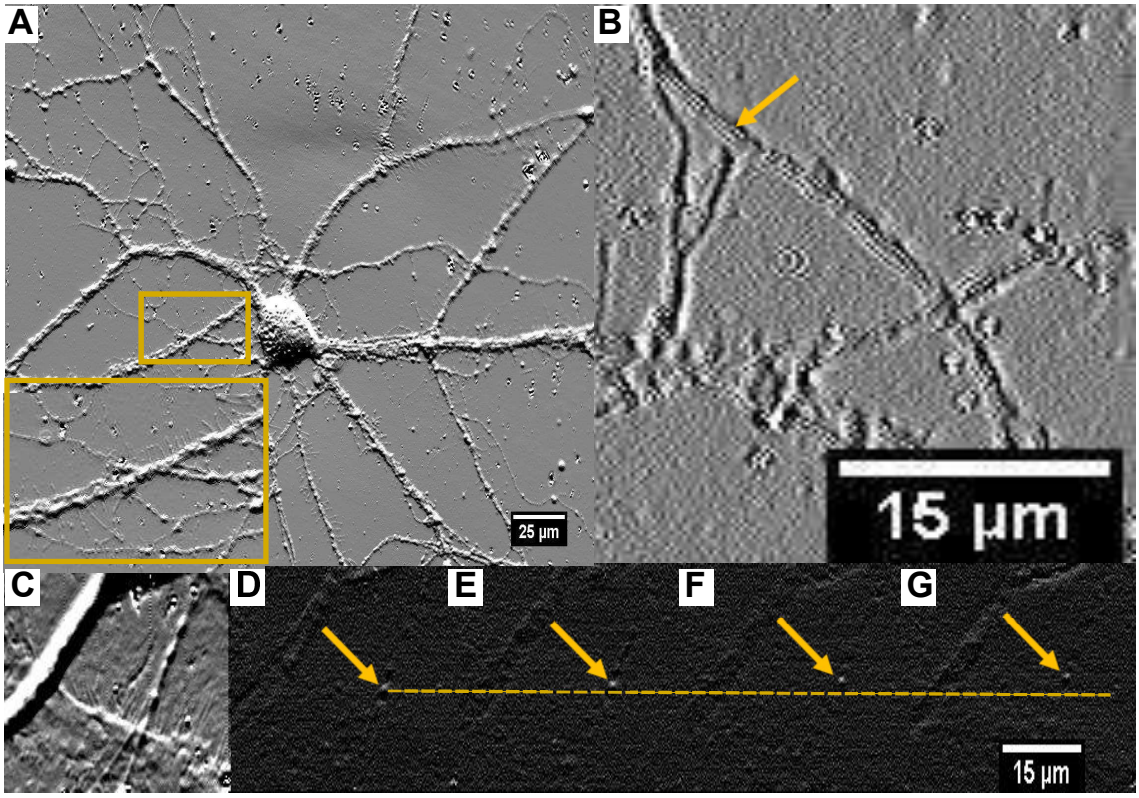

Figure 7.14 – Phase changes associated with neuronal motility. **Panel A** illustrates quantitative phase imaging ability to detect neuronal protrusions that are constantly remodeling and exploring the neuron close environment. It represents the phase gradient calculated along the vertical direction from a phase map measured with FF-OCT. **Panel B** shows the Laplacian of a phase map measured with FF-OCT in a 3 days old rat hippocampal neuron culture. The quite specific longitudinal structure emphasized with the yellow arrow can be consistently observed in many neurites, either at the center of the neurite or at its borders as shown in panel B. According to FF-OCT systems and the shape of these structures, these structures might be microtubule filaments parallel to the neurite direction. **Panels C to G** illustrates FF-OCT ability to detect subcellular transport along small neurites. Panel C shows the average phase gradient image calculated along the vertical dimension and panels D to G show 4 successive images corresponding to the phase difference between each phase map and the averaged phase map. The 4 images are separated by 5 seconds each, given a transport speed around 1 μ per second, which suggests that the scatterer detected here might be a single mitochondrion [380].

successfully reported a label-free signature of neuronal electrical activity at the single cell level, with either Raman spectroscopy [381] or quantitative phase imaging systems [382] (even though I am surprised by the high values of optical path changes they measured.) in presence of drugs or electrical stimulus.

7.5 Measurement of activity dependent phase changes in tissues

Finally, we were also attached to perform similar measurements in tissues especially since our Linnik interferometer can measure phase changes in both cultures and tissues. It is important to notice that if cells can easily swell and mechanically contract or expand, it is not obvious that they can do so in tissues in a more compact and softer environment. Nevertheless, in order to evaluate whether mechanical changes can play a role to transmit cellular-relevant information, it

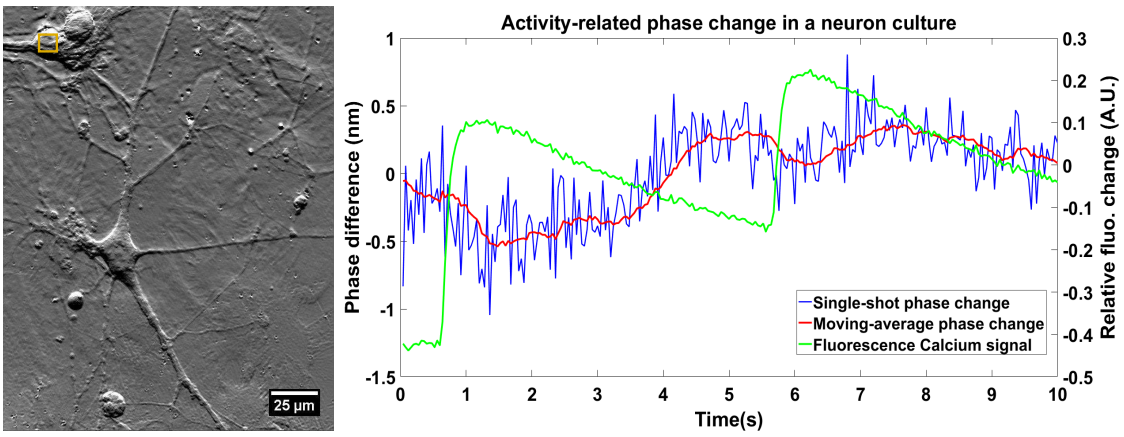

Figure 7.15 – Phase changes in mammalian hippocampal neuron cultures associated with calcium uptake. Panel A shows the gradient of the phase map measured in a 3 weeks old hippocampal neuron culture. The neurons are labeled with Fluo-4, a fluorescent calcium indicator. The temporal phase and fluorescence variations are measured and their spatial average on the pixels inside the yellow box is performed and plotted in **panel B**. The spontaneous activity of the corresponding cell as controlled with the fluorescence increase (green trace) is temporally correlated with a 0.5 nm phase decrease (blue trace with the red trace being the same data with a moving-average filter operated on 15 successive images), probably due to the cell swelling due to the calcium uptake.

would be critical to observe changes happening in tissues and not only in cell complex. Obviously, mechanical measurements in tissues are much more complex as the signal-to-noise ratio and the associated phase sensitivity is lower and the biological and mechanical noise is also expected to be more important. In a set of experiments, one result of which is presented in figure 7.16, we have imaged living 1-day post fertilization zebrafish larvae with their motor neurons genetically labeled with GCamp-5 (a green fluorescent calcium reporter). We imaged simultaneously the electrical activity of the motor neurons with fluorescence imaging and the dynamic FF-OCT signal, the fluctuations amplitude of which can reveal all the surrounding cells. In order to measure a dynamic signal variation over time, we only calculated the standard deviation of the high-pass filtered direct FF-OCT on small patches of 5 successive images taking advantage of the relatively slow dynamics of the calcium channels. In figure 7.16, we report on a small dynamic FF-OCT signal change potentially associated with the motor neuron activity. Here again, we only see a simple correlation between such decrease and the electrical activity that could be statistically random (and would require more samples), but here again, the synchronicity between the two events is quite striking. We have to emphasize that such a dynamic FF-OCT signal decrease is not necessarily associated with a mechanical change of the cell but could also be explained by a change in dynamics (expected to freeze during activity) or a change in the neuron reflectivity (For example, I was suggested that it might be related to a structural change in the Cytochrome-C oxidase due to increased mitochondrial activity to regenerate ATP and sustain the train of action potentials.). Nevertheless, if this result is later found to be significant and highly reproducible, it would demonstrate the possibility to use Dynamic FF-OCT as a functional tool to image neuronal activity in fresh tissues or *in vivo*. If similar activity-dependent fast intrinsic optical signal has already been reported a few years ago [353, 359, 381] in tissues, this would be the first intrinsic detection of neuronal activity at a cellular resolution in tissues, to my knowledge. Similarly to the case of neuronal cultures, we could enhance the signal-to-noise ratio of this technique by externally stimulating the neuron, using optogenetically modified motor neurons for example.

Such D-FF-OCT change related with electrical activity can be of interest for fundamental biology

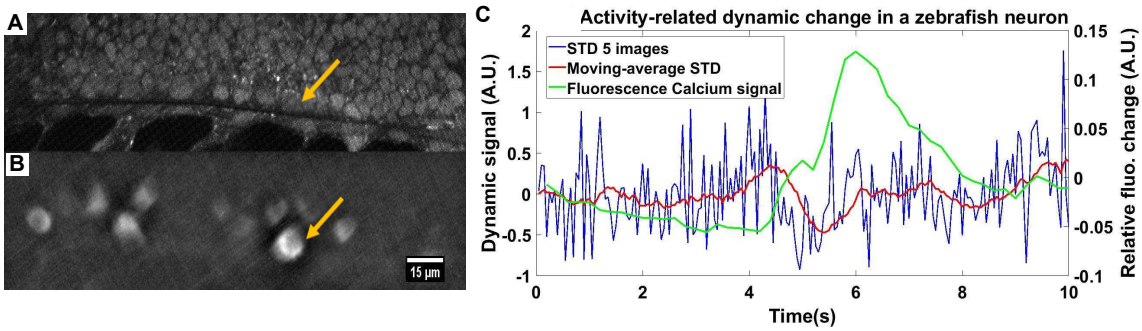

Figure 7.16 – Dynamic FF-OCT signal changes in a living Zebrafish larva correlate with its neuronal activity. Panel A shows the dynamic FF-OCT image of a one-day post fertilization Zebrafish larva spinal cord with various cells detectable. The dynamic FF-OCT image has been calculated by averaging 50 images of the standard deviation calculated on 10 direct images. **Panel B** shows the corresponding fluorescence image as the Zebrafish larva is genetically modified to express GCamp5 (green calcium indicator) in its motor neurons. The motor neuron pointed by the yellow arrows was electrically active during the acquisition and the fluorescence and dynamic FF-OCT signal spatially averaged on a 10 by 10 pixels region inside the neuron is plotted. **Panel C** is a plot of the temporal dynamic FF-OCT signal calculated as the standard deviation on 5 successive images without average (blue trace) and the corresponding signal with a moving average filter (on 15 images, red trace). It shows a dynamic signal decrease correlated with the beginning of the motor neuron calcium response.

and neuroscience. As an example, FF-OCT being also able to measure blood flows in small capillaries (similarly to OCT as reported in chapter 3) and would theoretically be able to measure simultaneously a blood flow increase associated with a local neuronal activity to better investigate the neurovascular coupling at the cellular level. Functional D-FF-OCT might also have another more straight forward clinical application in the future by studying the decay of β-cells in the pancreas of a diabetic patient. We happened to image several pieces of pancreas with *Clément Apelian* with both static and dynamic FF-OCT and we could show that the endocrine pancreas (especially the islets of Langerhans) that is responsible for the insulin production exhibit an important and specific signature in both FF-OCT and D-FF-OCT. Indeed, the high concentration of Zinc-insulin granules in β-cells probably cause these cells to be highly backscattering [162] and to produce a high dynamic FF-OCT signal associated with these granules displacements. Moreover, the insulin release is controlled by a characteristic electrical activity and a calcium uptake in the β-cells [383] that might be detected with D-FF-OCT. As a future work, it would be very interesting to try to detect such increased electrical activity in β-cells in a glucose-rich environment versus a low-glucose environment. We could additionally imagine that this activity might be altered in diabetes pancreas characterized by the defect of these β-cells. Additionally, D-FF-OCT ability to detect autoimmune cells around the islets of Langerhans could provide a supplementary biomarker to characterize (and/or predict) type I (or autoimmune) diabetes.

Chapter conclusion

This chapter has started from the very basics of Neuroscience and has reviewed the history and the main characteristics of the standard model of electrical activity propagation in neurons, the Hodgkin-Huxley model. In a second section, this chapter has given an overview of the dark side of this model and has described a number of experimental results that can not be explained by this standard model. One of these observations is the measurement of fast intrinsic optical signals that correspond to a change in the optical properties (such as phase or birefringence) of a

nerve or an axon experiencing electrical activity. If several models have developed to complement the Hodgkin-Huxley, this chapter describes three of them that take into account mechanics and thermodynamics to explain the nervous signal propagation. Unfortunately, the phase systems that we have built are yet not efficient enough to verify one of these models and we failed at detecting electromechanical waves so far. Nevertheless, the two last sections of this chapter have demonstrated our potential detection of fast intrinsic optical signal triggered by the spontaneous electrical activity of cultured neurons or motor neurons in a living Zebrafish larva. This opens the way for an all-optical, label-free, contact-free, intrinsic detection of relevant neuronal activity of both cultured neuronal networks and *ex vivo* neuronal tissues at the single cell level and shows the potential interest of the optical systems we have built to offer a less invasive and phototoxic alternative to electrophysiology and fluorescence imaging. However, our results still need to be confirmed and ideal filters are still to be invented to be able to sort a biological-relevant information from a random phase fluctuation, while we now require calcium imaging to make sure that the phase fluctuation we have measured indeed corresponded to electrical activity.

Conclusions and perspectives

Throughout this manuscript, we have seen a number of optical strategies to measure subcellular displacements in both cell cultures and diverse biological tissues. These displacements include active transport of organelles and vesicles, cellular membrane flickering, biological flows, and reversible compression induced by the propagation of a mechanical wave. This manuscript has highlighted our development of three novel and original optical microscopes that can detect sub-diffraction-limit displacements by transforming an unresolvable axial information into a detectable intensity difference. This manuscript has particularly emphasized the development of one of these systems, which consists of a multimodal platform combining depth-resolved interferometric imaging and depth-resolved fluorescence imaging. This system can simultaneously combine a label-free non-specific contrast and a motility-based contrast offered by interferometric imaging with a specific molecular and biochemical contrast obtained with fluorescence imaging. We have demonstrated full-field optical coherence tomography (FF-OCT) ability to measure subnanometric optical path changes over space and over time in cell cultures. More importantly, we have demonstrated FF-OCT ability to extend phase-sensitive measurements in thick scattering biological tissues. The subwavelength axial sensitivity phase measurements allows FF-OCT to measure the amplitude and timescale of an average motion of subcellular objects (between 100 nm and 1 μm approximatively) happening at a given position in a 3-D environment. It has led to the recent development of dynamic FF-OCT that takes advantage of the active transport based on displacements in active cells to provide a motility-related contrast in tissues and can reveal the living cells only. Dynamic FF-OCT can also compare different cell populations from their difference in the time course of their intracellular movements and from the detection of the cell nucleus position and size. This manuscript was also committed to provide biologically relevant examples in which our optical microscopes can bring an original information. We emphasized a first application in ophthalmology and especially retinal imaging where dynamic FF-OCT can measure the cell distribution in the different intact layers of the retina. Another potential application in neuroscience was considered where dynamic phase imaging could offer a label-free intrinsic detection of electrical activity. In both cases, our microscopes can be interesting both for clinical applications and for fundamental biology. Interestingly, a few electromechanical theoretical models that try to explain the neuronal signal propagation have finally been described. Dynamic phase imaging might soon help to verify or invalidate such models and are good candidate for such detection in any case. If one of this model is verified, it might have a critical impact in neuroscience as it would demonstrate the importance of biomechanical parameters to understand the brain functioning and possibly its abnormal functioning as well.

CHAPTER 8

Résumé substantiel (FR)

Table of contents

8.1 Objectifs, contexte, et organisation de la thèse **254**

8.2 Chapitre 1 : L'imagerie de phase quantitative et la détection de déformations axiales sub-longueur d'onde. **255**

8.3 Chapitre 2: Interféromètres développés au cours de cette thèse **256**

8.4 Chapitre 3 : Imagerie dans les tissus **259**

8.5 Chapitre 4 : Tomographie à cohérence optique plein champ **261**

8.6 Chapitre 5 : Approches multimodales de la tomographie à cohérence optique plein champ **261**

8.7 Chapitre 6 : Applications sur l'imagerie de l'oeil **265**

8.8 Chapitre 7 : Mesure de changements biophysiques de cellules actives électriquement **265**

Cette annexe est dédiée au résumé substantiel de la thèse en langue française, comme cela est demandé par les universités françaises. Je vais commencer par y décrire le contexte et les objectifs de la thèse d'une manière assez générale. Ensuite, je proposerai un résumé chapitre par chapitre, en mettant l'accent sur le résultat ou l'information le plus important de chaque chapitre. Autrement, je ne ferais que simplement décrire ce qui peut être trouvé dans le texte principal dans la langue de Shakespeare.

8.1 Objectifs, contexte, et organisation de la thèse

Cette thèse s'inscrit dans le contexte de l'imagerie optique intrinsèque d'objets biologiques visant la caractérisation de la structure et fonction de ces objets. Idéalement, la caractérisation la plus précise possible serait obtenue avec une préparation minimale des échantillons, en un temps et pour un coût minimaux, et de manière la moins invasive possible. L'objectif est alors la compréhension de nouveaux phénomènes biologiques, ou alors le suivi de tissus biologiques dans le contexte médical, dans le cas où une pathologie viendrait affecter la structure et la fonction d'un tissu. L'approche utilisée ici développe l'idée de microscopie interférométrique, permettant l'observation de déplacements d'objets biologiques avec une sensibilité largement sub-longueur d'onde, allant de quelques fractions de nanomètres en cultures, à 50 nm en profondeur dans les tissus. Cette sensibilité augmentée aux déplacements permet l'observation et le suivi de paramètres morphologiques (volume, masse, fluctuations de membrane) et fonctionnels (transport moléculaire, métabolisme, échanges d'eau,...) des cellules au sein de leur environnement, et ce, sans aucun marquage préalable. Au cours de cette thèse, nous avons développé 3 microscopes multimodaux différents permettant cette caractérisation d'objets biologiques sans marquage, et nous allons décrire dans ce résumé aussi bien les développements technologique sous-jacents à ces microscopes, la description des nouveaux contrastes observables avec nos microscopes, ainsi qu' un certain nombre d'applications biologiques.

Ce manuscrit de thèse est divisé en 3 parties relativement distinctes. La première partie propose une description des systèmes dits d'imagerie de phase quantitatifs, et présente aussi bien une revue détaillée des systèmes et applications principales de ces systèmes dans un premier chapitre, ainsi que les nouveaux systèmes que nous avons développé au cours de ce travail dans un second chapitre. La deuxième partie propose d'étendre ces mesures de phase dans le cas de tissus biologiques diffusants, pour lesquels les systèmes d'imagerie de phase usuels ne permettent pas la réalisation. Une description détaillée des problèmes émergents lors du passage d'une couche simple de cellules à un tissu complexe est proposé au chapitre 3, ainsi qu'un certain nombre de solutions pour y faire face. Le chapitre 4 met particulièrement l'accent sur une technique de microscopie développée au laboratoire il y a quelques années et qui permet la mesure de signaux optiques intrinsèques en profondeur dans les tissus, avec une résolution sub-micrométrique. Cette technique, appelée tomographie à cohérence optique plein champ (OCT plein champ ou FF-OCT), fût la base du microscope principal qui a vu le jour au cours de ma thèse. Le chapitre 5 en fait justement la description. Ce microscope consiste en une version à haute résolution de l'OCT plein champ, et est de plus couplé à deux autres modalités d'imagerie en parallèle. La première modalité est d'associer l'OCT plein champ à un microscope de fluorescence à illumination structurée, qui permet

l'observation de signaux biochimiques hautement spécifique à de faibles profondeurs dans les tissus. La particularité du montage développé est d'associer ces deux modalités en parallèle dans une configuration un peu particulière décrite dans la première partie du chapitre 5. Pour comprendre la seconde modalité additionnelle, il faut revenir à l'information de phase décrite dans les premiers chapitres dans les cultures. Au cours de cette thèse, nous avons pu démontrer que l'utilisation des fluctuations de phase locale nous permet d'obtenir un contraste inédit dans des tissus frais car il nous permet de détecter spécifiquement des cellules et leurs composants internes tout en réduisant la contribution des fibres et structures statiques dans les tissus. L'utilisation des fluctuations de phase permet de mettre l'accent sur les mouvements intracellulaires de diffuseurs de tailles intermédiaires comme des organelles ou des vésicules qui sont hautement contrôlés par la cellule et nécessitent de l'énergie pour avoir lieu. Nous avons notamment pu montrer que le blocage de la production d'énergie dans une cellule faisant disparaitre ce nouveau contraste accessible grâce aux fluctuations de phase. Il est donc dépendent, au moins indirectement du métabolisme cellulaire. La troisième et dernière partie de ce manuscrit s'attache à présenter les deux applications biologiques essentielles de ce travail. La première concerne l'ophtalmologie et notamment l'imagerie de rétines ex vivo, et est développé au cours du chapitre 6. L'utilisation du microscope haute résolution d'OCT plein champ associé aux nouvelles modalités de fluorescence et de l'activité métabolique nous a permis de mettre en évidence un certain nombre de caractéristiques morphologiques et fonctionnelles de la cornée et de la rétine, rarement, voire même jamais, observées optiquement sans marquage et en laissant ces organes intacts. Finalement, le chapitre 7 s'attache à montrer des applications potentielles de l'imagerie de phase dans le cadre des neurosciences. Je me suis attaché notamment à décrire un certain nombre de modèles théoriques prédisant l'existence d'un couplage entre le potentiel d'action d'un neurone et d'une onde mécanique qui se propagerait le long de son axone. Si nous n'avons pas pu faire l'observation directe de ces prédictions au cours de cette thèse, les contraintes expérimentales seront probablement déverrouillées dans les années à venir. Je montre toutefois que nous avons détecté un certain nombre de signaux optiques intrinsèques corrélés à l'activité spontanée de neurones en culture et in vivo, possiblement causés par un léger gonflement réversible des neurones associé à l'ouverture des canaux calciques à leurs surfaces.

8.2 Chapitre 1 : L'imagerie de phase quantitative et la détection de déformations axiales sub-longueur d'onde.

Ce chapitre est dédié à la description de l'histoire, du principe et des applications principales du domaine de recherche appelé imagerie de phase quantitative (QPI). D'une manière générale, les systèmes d'imagerie de phase utilisent le principe d'interférences optiques afin de transformer une information de différence de chemin optique (produit de la distance parcouru et de l'indice optique, qui n'est autre que le rapport entre la vitesse de la lumière dans le vide, et la vitesse de la lumière dans le milieu traversé.) en une information de différence d'intensité qui devient directement mesurable par des détecteurs optiques usuels. Il existe de nombreuses configurations de systèmes d'imagerie de phase, et les interférences détectées peuvent être produites entre une onde de référence et une onde venant scanner un objet, ou peuvent être produites entre la composante transmise d'un faisceau lumineux au travers d'un objet et la composante diffusée. La description de nombreux systèmes ainsi que la classification usuelle des systèmes de phase peut se trouver dans les deux premières sections du chapitre 1. Une revue de la littérature décrivant les principales applications biologiques de l'imagerie de phase est également réalisée dans ce chapitre. En deux mots, l'imagerie de phase autorise une mesure quantitative d'un certain nombre de paramètres

biologiques, tel que la masse sèche (masse protéine + lipides), la densité locale, l'élasticité de la cellule et de la membrane plasmique, ou encore les coefficients de diffusion moyen d'objets intracellulaires. Contrairement à la microscopie de fluorescence, la microscopie de phase ne nécessite aucune préparation préalable des échantillons et permet de détecter un mouvement global moyen en chaque endroit de la cellule. Le désavantage toutefois est que le signal est donc non-spécifique, et il est difficile d'en extraire une contribution d'un acteur unique. Dès le chapitre 1, je propose un certain nombre de développements personnels dans le cadre de l'imagerie de phase. Dans un premier temps, je développe un calcul original et se voulant aussi général que possible permettant d'estimer la sensibilité d'un système de phase quelque conque et je le compare avec succès à des simulations numériques réalisées pour l'occasion. Un second calcul développé dans la foulée permet de comparer les sensibilités relatives d'un système de phase en réflexion dans deux configurations différentes. Nous avons pu montrer que l'utilisation d'un système de phase ayant des intensités des signaux interferants équivalentes et de haute intensité permettent d'atteindre des sensibilités théoriques de l'ordre de 0,2 nm en une seule mesure. Nous avons utilisé une telle configuration dans les microscopes que nous avons développés au cours de cette thèse, car ils offrent le meilleur compromis possible entre haute sensibilité, imagerie d'un champ large et rapidité d'acquisition. Il est important de noter que la sensibilité ainsi obtenue est modulée par la résolution optique offerte par le microscope et limitée par la diffraction. La mesure de phase est une mesure moyenne sur une tache de diffraction optique, et l'augmentation de la résolution obtenue en augmentant l'ouverture numérique du système optique permet d'obtenir une mesure de phase et surtout des fluctuations de phase plus fine.

Enfin, dans ce chapitre 1, je me permets une petite (fausse) digression pour parler d'un projet annexe de ma thèse, qui a consisté dans le développement à la fois théorique et expérimental d'une nouvelle technique de microscopie, intitulée exclusion de fluorescence. Elle permet de mesurer des hauteurs ou des volumes d'objets à l'intérieur d'une chambre microfluidique remplie de fluorophores, grâce à la mesure de la diminution d'un signal de fluorescence en présence de cellules hermétiques à ces fluorophores et donc diminue le volume accessible à ces fluorophores. Il se trouve que, dans certaines conditions, il existe une relation de proportionnalité entre la hauteur locale d'un objet excluant la fluorescence et la diminution du signal de fluorescence, ce qui permet par inversion la mesure quantitative de la hauteur locale de l'objet. Si cette technique a été développée il y a déjà quelques années, nous avons pu développer au cours de cette thèse un modèle posant les limites de cette technique, permettant de calculer sa précision maximale, et offrant quelques pistes d'amélioration. Nous avons également associée cette méthode avec nos systèmes d'imagerie de phase, ce qui permet d'obtenir une mesure de hauteur et une mesure de phase indépendante et permet de reconstruire l'indice optique local de l'objet. Lien entre les deux !

8.3 Chapitre 2: Interféromètres développés au cours de cette thèse

Le chapitre 2 regroupe la description de deux interféromètres originaux développés au cours de ma thèse combinant simultanément une mesure d'imagerie de phase à une mesure de fluorescence. L'intérêt d'obtenir les deux mesures de manière synchrone est que l'on va pouvoir comparer des changements structurels intrinsèques (changement de volume, de densité, de transport, etc...) à des changements biochimiques à l'échelle de la cellule unique. Le chapitre 2 débute par la description du montage basé sur un interféromètre de Linnik, et décrit de manière détaillée les différentes étapes et traitements à effectuer, en les comparants à la fois théoriquement et expérimentalement,

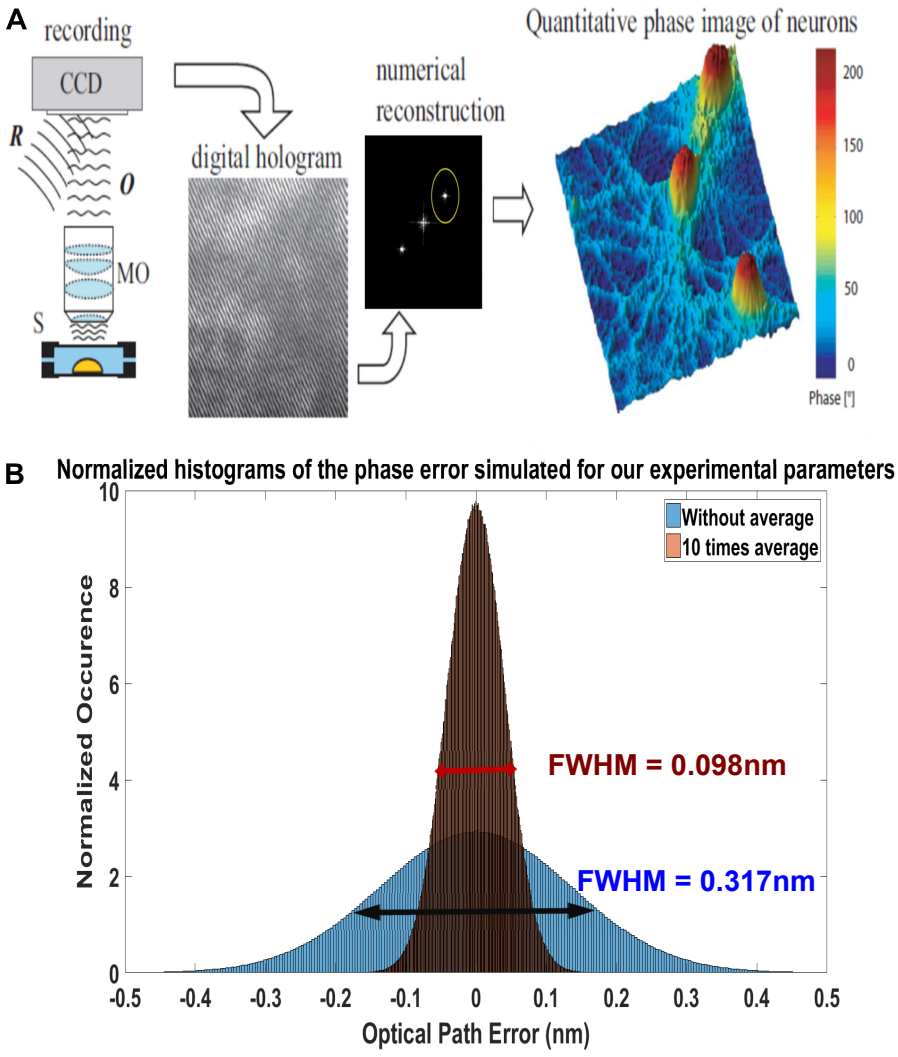

Figure 8.1 – Revue de l'imagerie de phase quantitative. La figure A présente le principe de l'imagerie holographique digitale pour mesurer la phase d'objets biologiques. Cette technique est une des premières et des plus importantes techniques d'imagerie de phase quantitative. Elle consiste à enregistrer la figure d'interférence entre la lumière traversant un objet et un faisceau de référence orienté de côté. Cet angle permet de venir isoler le terme d'interférence de manière spécifique dans l'espace de Fourier, et permet de reconstruire la phase de l'objet en prenant l'argument complexe de cette figure d'interférence dans l'espace de Fourier. **La figure B** présente un histogramme des valeurs de chemin optique calculées dans nos conditions expérimentales, et qui illustre donc la sensibilité attendue de l'imagerie de phase. Cette simulation est couplée avec un calcul théorique du bruit de photons, qui correspond bien aux simulations, et démontre la possibilité d'avoir une mesure sensible à quelques centaines de picomètres grâce à la mesure de phase.

pour obtenir une image de phase dans le cas général. Cette configuration a été choisie car elle permet de faire des mesures aussi bien dans des cultures de cellules (en imagerie de phase) que des mesures à l'intérieur d'un tissu diffusant, ce qui sera l'objet de la seconde partie du manuscrit. C'est pourquoi la description détaillée du montage n'est présentée qu'au cours du chapitre 4, dans la partie sur l'imagerie des tissus. Toutefois, ici, le système est brièvement décrit pour pouvoir introduire les mécanismes utiles à l'imagerie de phase, et pour introduire le second interféromètre que j'ai développé par la suite. En effet, au cours de ma thèse, nous nous sommes rendus compte que, si la première configuration en Linnik, présentait un certain nombre d'avantage dans le cadre de l'imagerie des tissus, elle était en fait plus limitée dans le cas des cultures, car cette configu-

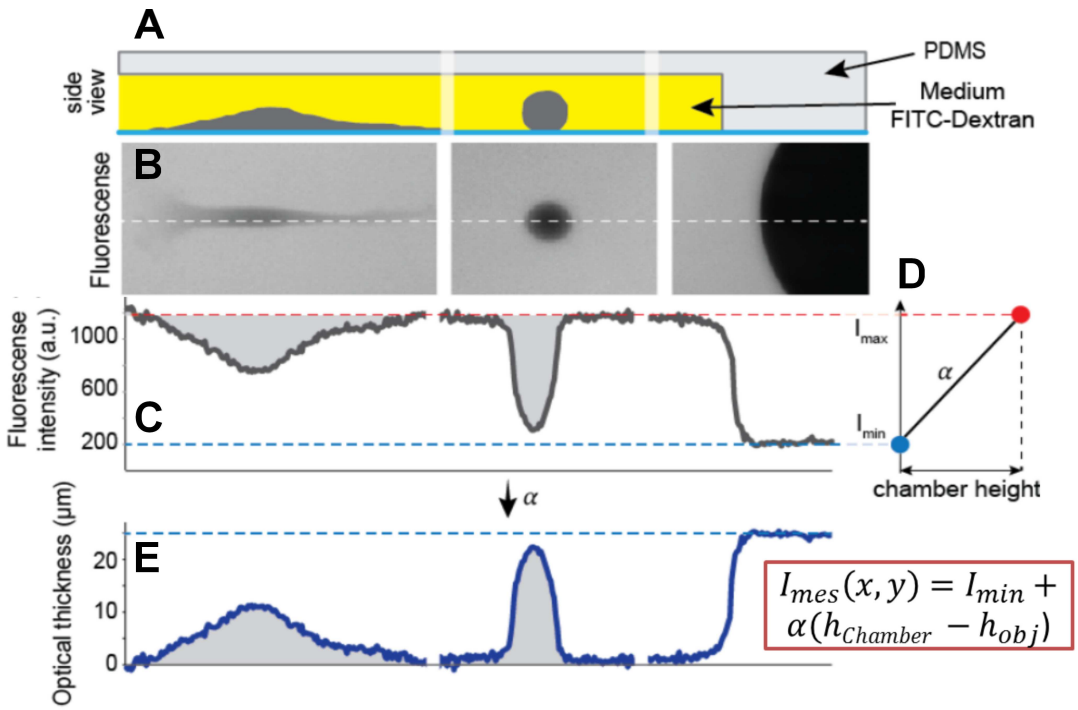

Figure 8.2 – Principe de l'exclusion de fluorescence. Cette technique permet d'encoder une information de hauteur de cellule en mesurant la décroissance du signal d'intensité de fluorescence en présence d'une cellule dans laquelle le fluorophore ne rentre pas. **La figure A** présente le dispositif expérimental qui consiste à confiner des cellules dans une chambre microfluidique de hauteur connue, et à injecter un fluorophore qui remplit la chambre, mais ne pénètre pas à l'intérieur des cellules. De la relation linéaire qu'il existe entre l'intensité locale de fluorescence et l'épaisseur locale de l'espace extracellulaire (hauteur de la chambre moins hauteur de la cellule), illustrée dans **les figures B, C, et D**, la hauteur locale de la cellule peut être reconstruite (**figure E**) à partir d'une image d'intensité. Cette mesure de hauteur peut être précise à quelques dizaines de nanomètre près, et peut aussi être couplée à l'imagerie de phase pour découpler l'information de hauteur et d'indice optique dans le signal de phase.

ration est plus sensible au bruit mécanique que certains autres microscopes d'imagerie de phase. En effet, la configuration Linnik impose la présence de deux bras dont la lumière va interférer au niveau de la caméra. La présence de ces deux bras de microscopie rend nécessairement la manip plus sensible aux bruits mécaniques et thermiques, car les deux bras ne sont physiquement pas au même endroit de la pièce.

C'est pourquoi nous avons développé une deuxième configuration de microscope, dans un montage appelé « common-path » ou de chemin partagé, dans lequel les deux bras de l'interféromètre sont physiquement confondus, ou presque. Dans la configuration que nous avons développée, l'interférence se produit entre les deux polarisations de la lumière que l'on décale de manière transverse d'une distance de quelques microns. Dans le cas où seulement un des deux faisceaux rencontre un objet alors que l'autre ne rencontre que de l'eau, il se créé donc une différence de chemin optique proportionnelle à la différence d'indice entre l'objet et le milieu environnant et à la hauteur de l'objet. Pour récupérer le terme d'interférence uniquement, nous avons pu utiliser un modulateur à cristaux liquides qui ne vient déphaser qu'une seule des deux polarisations de la lumière d'une valeur définie par la différence de potentiel électrique appliqué à l'appareil. Avec ce système, nous avons pu démontrer l'obtention de cartes quantitatives de phase, et pu démontrer que cette configuration permet bien de s'affranchir du bruit mécanique et thermique observé précédemment dans la configuration Linnik et permet de mesurer un bruit inférieur à 0,2 nm

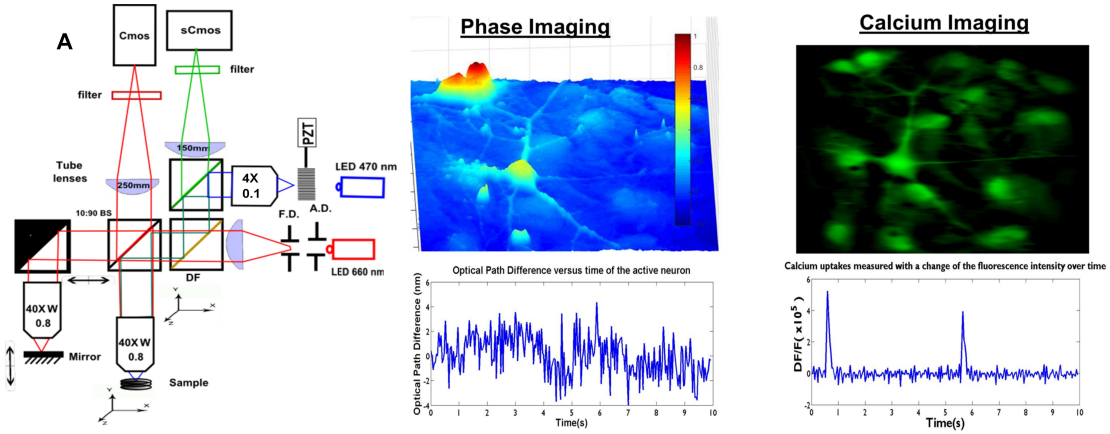

Figure 8.3 – Principe de l'interféromètre de Linnik. La figure A présente le schéma du montage principal développé au cours de la thèse. Il consiste en la combinaison d'un interféromètre de Linnik (chemin optique rouge) composé d'une lame séparatrice et de deux bras identiques contenant chacun un objectif de microscope identique. Ce montage permet de travailler sur des cultures de cellules montées sur du verre ou des lamelles de silicium (pour augmenter le contraste), et de mesurer l'évolution du signal de phase au cours du temps. Il permet aussi de venir mesurer de manière simultanée un signal de fluorescence, qui permet par exemple de venir mesurer l'activité calcique des neurones en même temps que le changement de phase associé.

entre deux acquisitions sur un pixel unique. Nous avons aussi pu démontrer que ce système se couplait efficacement avec une mesure de fluorescence simultanée. Cette nouvelle configuration de microscope rassemble la majorité des avantages observés dans les systèmes d'imagerie de phase décrits dans la littérature, mais impose un traitement numérique qui peut complexifier son implémentation et peut générer un certain nombre d'artéfacts.

8.4 Chapitre 3 : Imagerie dans les tissus

Dans le chapitre 3, nous partons de l'imagerie de phase dans les cellules pour progressivement se tourner à l'implémentation de ces mêmes techniques dans des tissus biologiques. L'objectif du chapitre 3 est d'effectuer doucement la transition entre les deux en venant présenter les différents effets physiques qui rendent l'imagerie dans les tissus un problème complexe. Il s'attache également à décrire les différentes configurations d'interférométrie à faible cohérence, technique requise pour l'imagerie de phase dans un volume. Je montre notamment, via des simulations personnelles que l'obtention d'un sectionnement optique peut se faire non pas seulement avec l'utilisation d'une source à large spectre fréquentiel (faible cohérence temporelle), comme utilisé jusqu'alors dans notre équipe, mais également en se servant d'un spectre angulaire important (faible cohérence spatiale), ce qui est notamment le cas lorsqu'on utilise des objectifs à haute ouverture numérique. Le chapitre 3 est finalement l'occasion d'introduire la tomographie à cohérence optique (TCO) et ses applications principales. Dans sa version commerciale la plus usuelle, la TCO permet l'acquisition d'une ligne dans la profondeur de la caméra qui mesure toutes les couches rétrodiffusantes d'un échantillon. Cette ligne peut ensuite être scannée dans les deux dimensions transverses afin d'obtenir la structure 3D de l'échantillon. Comme la TCO est une technique d'interférométrie, elle mesure soit l'amplitude du signal retrodiffusé à une profondeur donnée, soit la phase de la partie du signal retrodiffusée à cette profondeur. Et notamment, un certain nombre d'expériences mesurant des différences de phase par TCO pour mesurer le flux sanguin, et la propagation d'ondes mécaniques, sont présentées en fin du chapitre 3.

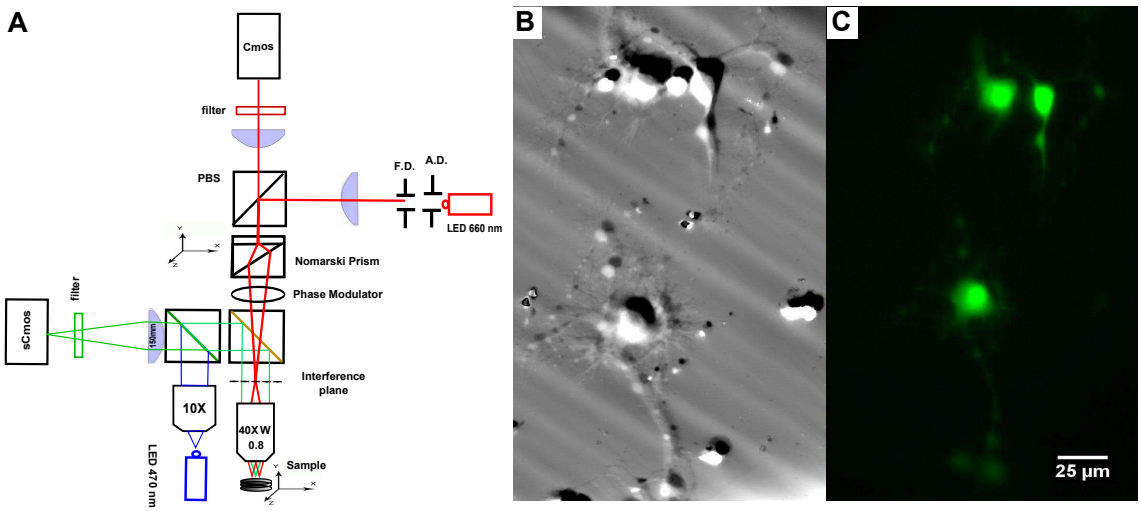

Figure 8.4 – Principe de l'interféromètre à contraste différentiel à large décalage. La figure A présente le schéma du montage expérimental développé au cours de cette thèse. L'intérêt de ce montage est sa configuration dite de *chemin partagée*, dans laquelle les deux faisceaux qui vont interférer pour permettre la reconstruction du signal de phase se propagent le long d'un chemin commun, ce qui permet de s'affranchir du bruit mécanique et thermique ressenti de la même manière dans les deux bras. Dans ce montage, l'interférence se produit entre les deux polarisations d'un même faisceau décalés spatialement d'environ 5μm par un prisme de Nomarski à large décalage. Il permet la reconstruction d'une image de phase dédoublée (une image est produite pour chaque polarisation), présentée en **figure B**. Comme le montage précédent, l'imagerie de phase est, ici aussi, couplée à une imagerie de fluorescence.

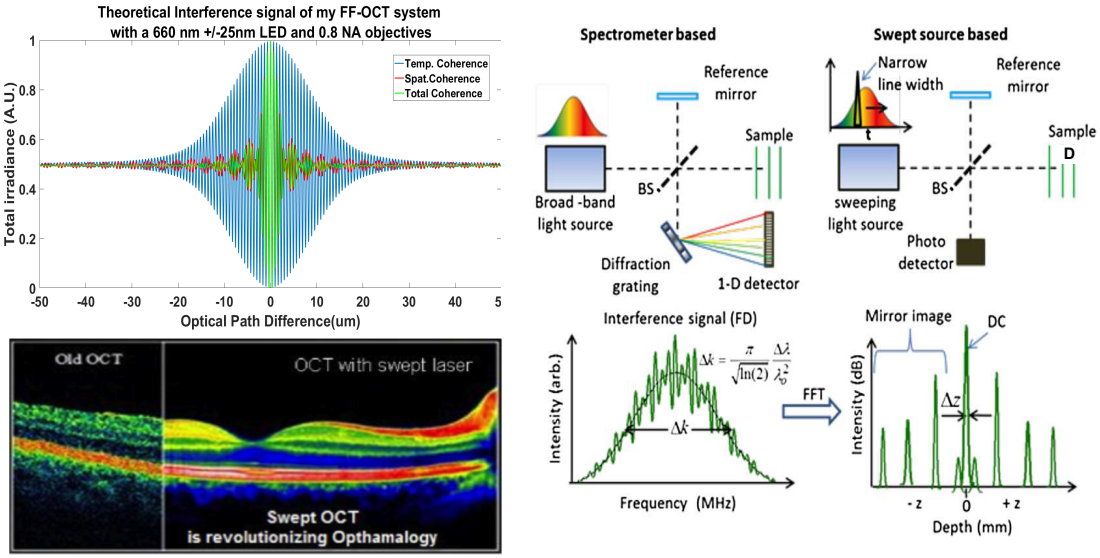

Figure 8.5 – Principe de la tomographie à cohérence optique. L'image de gauche montre le brouillage d'interférences dans le cas d'une illumination à faible cohérence, modélisé dans le cadre d'une simulation propre à notre montage expérimental et présentée dans le texte principal. Ce brouillage permet de sélectionner le signal venant d'une profondeur donnée dans l'échantillon. **L'image de droite** présente le principe d'un montage de tomographie à cohérence optique dans le domaine spectral, alors que la figure du bas (gauche) présente une image typique de rétine obtenue avec un tel appareil.

8.5 Chapitre 4 : Tomographie à cohérence optique plein champ

Ce chapitre est dédié à la présentation de la technique de tomographie à cohérence optique plein champ, version à haute résolution et à multiplexage spatial des systèmes précédents. Cette technique TCO plein champ a été développée par l'équipe de Claude Boccara au début des années 2000, bien avant mon arrivée au laboratoire. Dans ce chapitre, je décris les différentes étapes d'obtention d'une image avec cette technique et insiste sur les avantages et inconvénients de cet appareil par rapport aux versions plus standards de TCO, qui scannent un faisceau en 3 dimensions pour obtenir une image. La technique plein champ permet l'obtention d'images avec une résolution accrue d'un facteur 10 par rapport aux techniques classiques, et permet de mesurer tous les points d'un plan donné au même instant. Toutefois, la configuration en ligne plus usuelle permet une meilleure exclusion de la lumière parasite, et permet donc d'obtenir un meilleur contraste, et est plus facilement applicable in vivo, car chaque ligne de l'image est indépendante. J'explique également quelles sont les applications principales de cette technologie, comprenant essentiellement l'analyse histologique de tissus prélevés. Ce chapitre contient finalement deux découvertes récentes, dont une a été réalisée par mes soins, à propos de la TCO plein champ. La première, principalement développée par Peng Xiao de notre équipe, a montré que l'utilisation d'une lumière faiblement cohérente spatialement permet de préserver la résolution de l'image finale de TCO plein champ, même en présence d'aberrations. Cette caractéristique est assez spécifique à l'OCT plein champ, et permet de s'affranchir de l'utilisation d'un correcteur de front d'onde d'optique adaptative pour imager des structures fines, contrairement aux techniques de TCO classiques. La deuxième découverte a été l'observation in vivo de flux de vésicules natives (de l'ordre de 100 nm de diamètre) dans le liquide céphalo rachidien. Comme expliqué dans le texte principal, cette capacité d'observation d'aussi petites vésicules sans marquage est quasiment unique au monde, car nécessite des caractéristiques qui ne sont propres qu'au montage que j'ai développé pendant ma thèse.

8.6 Chapitre 5 : Approches multimodales de la tomographie à cohérence optique plein champ

Le chapitre 5 de ce manuscrit est sans doute le chapitre le plus important de la thèse et rassemble et explique le développement de deux nouvelles modalités que l'on a associées à la TCO plein champ au cours de ma thèse. Ce chapitre est divisé en deux sections principales décrivant chacune des modalités supplémentaires. Dans un premier temps, je décris (enfin) le système principal que j'ai développé au cours de ma thèse qui consiste à associer un microscope de TCO plein champ à très haute résolution transverse (0,48 μm, là où la plupart des systèmes de TCO commerciaux ont une résolution de l'ordre de 10 μm) avec une voie de fluorescence, permettant la mesure de signaux très spécifiques, aussi bien pour venir cibler une population de cellules en particulier, que pour sonder certains paramètres biochimiques des tissus. Afin de pouvoir fonctionner dans les tissus, cette voie de fluorescence est montée en illumination structurée, qui consiste à venir exciter les fluorophores avec une lumière structurée spatialement. Les hautes fréquences spatiales ne pouvant être résolues qu'au plan focal, cela permet, après reconstruction, d'isoler le signal venant du plan focal uniquement. La particularité principale du microscope que j'ai développé est de permettre une mesure simultanée à la fois de la fluorescence et du signal de TCO, ce qui permet de réaliser

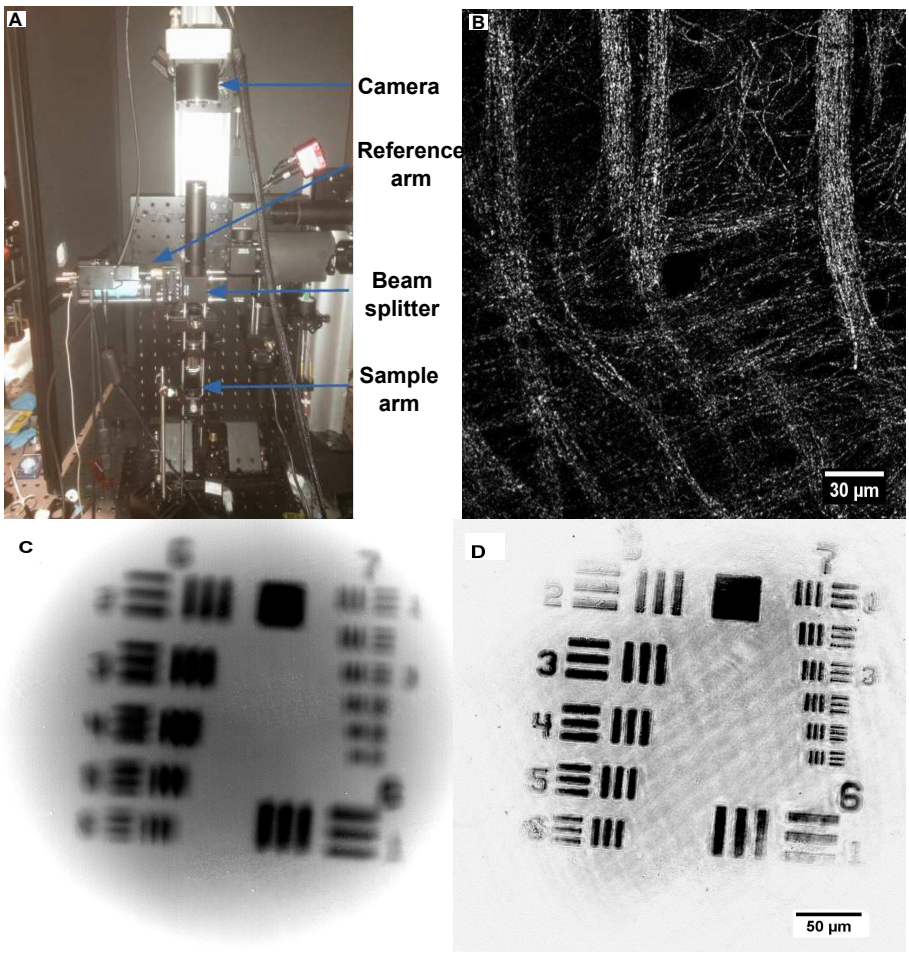

Figure 8.6 – Tomographie à cohérence optique (TCO) plein champ. La figure A montre une photo du montage expérimental correspondant au schéma de l'interféromètre de Linnik multimodal présenté dans la figure 8.3, mais opéré avec une lumière faiblement cohérente spatialement et temporellement. **La figure B** présente des fibres de myéline imagées en profondeur dans un échantillon de cortex grâce à ce montage. **Les figures C et D** illustrent l'indépendance aux aberrations du signal d'amplitude de la TCO plein champ. **La figure C** présente l'image directe d'une mire de résolution en présence d'un décalage de mise au point, montrant la présence d'une diminution largement visible de la résolution. Toutefois, le filtrage permis grâce au processus d'interférence à faible cohérence permet d'obtenir une image d'amplitude en **figure D** dont la résolution a été rétablie.

une corrélation de signaux transients entre les deux modalités. Pour démontrer l'intérêt d'obtenir ces signaux en parallèle, le couplage électromécanique cardiaque a été imagé dans un cœur ex vivo en train de battre. On peut voir une bonne corrélation entre la contraction du muscle, observé par TCO et l'influx calcique, mesuré en fluorescence et connu pour être à l'origine de cette contraction.

La deuxième modalité que nous avons ajoutée à ce microscope a été développée au laboratoire ces dernières années dans un effort conjoint entre plusieurs personnes. Comme expliqué précédemment, la TCO, et à fortiori, la TCO plein champ permet l'observation d'un contraste morphologique basé sur l'amplitude de rétrodiffusion des structures biologiques, mais permet également la mesure de différence de phases quantitatives, dont nous ne sommes pas servis jusqu'à maintenant. Comme vu en première partie, ces différences de phase vont nous permettre de suivre des déplacements axiaux inférieurs à la longueur d'onde optique, ou de suivre des changements de densité cellulaire au cours du temps. Au cours de ma thèse, nous avons réalisé qu'en utilisant cette dynamique des fluctuations de phase, nous pouvions obtenir un contraste très particulier et

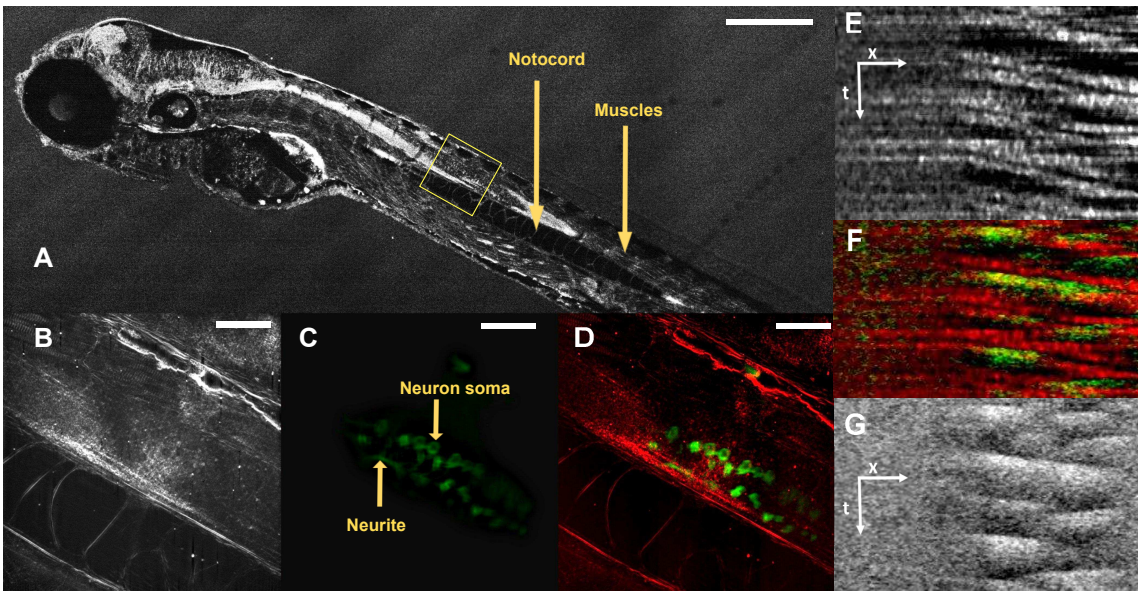

Figure 8.7 – Association du montage multimodal combinant TCO plein champ et fluorescence. Les images A à D présentent la combinaison des contrastes statiques obtenue avec ce montage. Si la TCO plein champ (**Figure A** prise avec un objectif 10X, et **figure B** avec un objectif 40X au niveau du carré jaune) permet la visualisation de la morphologie et de l'anatomie de la larve de poisson zèbre, le signal obtenu n'est pas spécifique et ne permet pas de voir les cellules individuelles. L'addition du contraste de fluorescence (**Figure C** et image combinée en **figure D**) permet de détecter spécifiquement les motoneurones le long de la moelle du poisson, et d'observer leur organisation par rapport à la morphologie du poisson. **Les figures E à G** montrent une application à une combinaison similaire, mais cette fois en dynamique. Le montage développé [105] permet ici de suivre de manière simultanée des ondes mécanique (**figure E**) générées par la contraction d'un coeur de rat, et des ondes calciques via le signal de fluorescence (**figure G, et F** pour la combinaison), qui permettent la contraction du coeur.

jamais reporté auparavant dans les tissus. De fait, la majorité des mouvements dans un tissu sont dus soit au flux sanguin soit à la motilité cellulaire au sens large. Cela rassemble des mouvements de la cellule entière, mais également le transport de matière intra ou intercellulaire. En étudiant les fluctuations temporelles de phase dans un tissu, nous nous sommes donc rendu compte que ces fluctuations sont bien plus importantes dans les cellules que dans la matrice extracellulaire environnante. Ces fluctuations nous permettent également d'identifier des compartiments intracellulaires tel que le noyau dont la densité plus importante nous empêche d'apprécier la dynamique réelle. Elles permettent également de suivre des fluctuations de membrane spécifiques de certains types de cellules, comme les globules rouges et les lymphocytes. Du coup, la TCO plein champ dynamique développée pendant ma thèse permet l'observation de cellules au préalable parfois cachées sous la matrice extracellulaire, ainsi que la structure subcellulaire de ces cellules, nous permettant ainsi leur identification. Mais encore plus important, nous avons pu montrer que ces fluctuations de phase sont directement reliées au métabolisme cellulaire dont dépend les moteurs moléculaires, et qu'ainsi le signal de TCO dynamique permettait également de s'assurer du métabolisme, et donc de la bonne santé des cellules observées. Grâce au montage que j'ai développé, nous avons pu observer des signaux de TCO dynamique plein champ à plus haute résolution, ce qui est un paramètre critique, car la résolution contrôle également la finesse des mouvements observables et permet l'identification de plus de structures sub-cellulaires. Le couplage avec la fluorescence est également assez naturel dans le montage, de telle sorte qu'un signal de TCO plein champ statique, un signal de TCO plein champ dynamique et qu'un signal de fluorescence peuvent être observés

simultanément. J'insiste également sur le fait que le signal de TCO dynamique est assez unique, car il nécessite une résolution suffisante pour ne pas moyenner tous les mouvements intracellulaires dans un seul pixel, et n'est probablement pas observable dans les montages de TCO commerciaux à plus faible résolution. Dans le manuscrit, je décris le développement de ce nouveau mode d'imagerie, et montre l'intérêt de le coupler à la fluorescence. J'ai également développé un certain nombre de simulations et de modèles prédictifs pour expliquer l'origine de ces fluctuations, diverses manières d'analyser ces fluctuations, et également pour montrer que nous ne pouvons observer que les fluctuations ayant pour origine des mouvements à l'intérieur du seul plan d'interférence, à condition que les fluctuations soient suffisamment faibles.

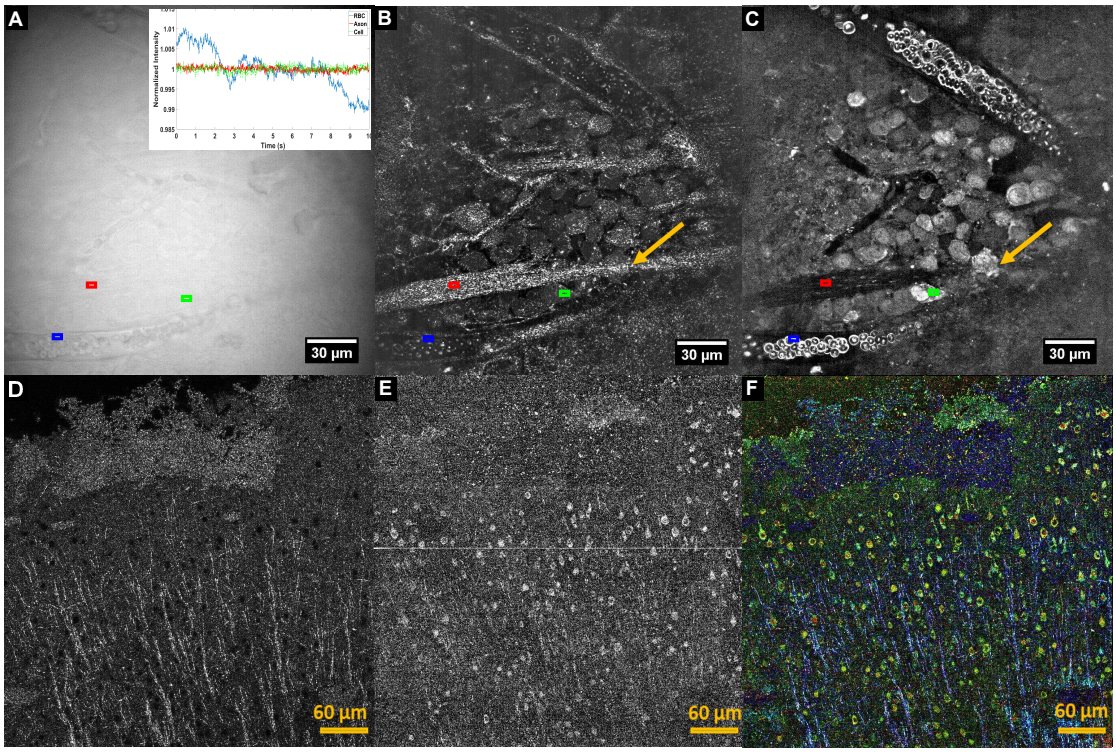

Figure 8.8 – Principe de la tomographie à cohérence optique plein champ dynamique, développée au cours de la thèse. **La figure A** représente l'image directe enregistrée par la caméra, après filtrage numérique spatial. Différentes structures sont observables, mais ne sont pas résolues dans la profondeur de l'échantillon. Néanmoins, on peut voir (graphe au dessus) que la fluctuation du signal d'intensité (d'interférences) varie localement d'un pixel à l'autre. Tandis que la TCO plein champ statique classique permet de reconstruire l'image présentée sur la **figure B**, la TCO plein champ dynamique consiste au calcul local de la fluctuation du signal d'interférence, et permet l'obtention d'un contraste significativement différent, tel que cela est présenté sur la **figure C**. L'analyse des fluctuations permet de mettre l'accent sur les fluctuations intracellulaires dépendant du métabolisme, et de réduire la contribution des signaux fixes correspondant aux fibres et à la matrice extracellulaire. **Les figure D à F** montrent une autre illustration de cette différence de contraste non plus dans la rétine, mais dans une tranche de cerveau. **L'image D** montre l'image de TCO plein champ statique, la **figure E**, l'image dynamique, et la **figure F** présente l'image dynamique enrichie d'un contraste temporel. Ce nouveau contraste consiste à ne plus seulement afficher l'amplitude des fluctuations du signal (comme en **figures B et E**), mais également d'encoder avec de la couleur le temps caractéristique des fluctuations (Bleu représente les dynamiques lentes, supérieures à la seconde jusqu'au rouge et ses dynamiques rapides, de l'ordre de quelques dizaines de millisecondes).

Fort de cette description technologique, nous pouvons maintenant aborder la troisième partie du manuscrit qui est dédiée à des applications biologiques que nous avons pu étudier grâce à ce

montage tri-modal.

8.7 Chapitre 6 : Applications sur l'imagerie de l'oeil

Le chapitre 6 de ce manuscrit est dédié à l'imagerie de diverses parties de l'œil, qui est la première application essentielle de mon travail de thèse. Dans la première partie de ce chapitre, je propose une description de la structure et de la fonction de l'œil, et notamment de la cornée et de la rétine. Un point important est que ces deux tissus sont extrêmement contrôlés dans leur organisation, car celle-ci assure leur transparence, critique pour la transmission de la lumière au fond de la rétine, là où la lumière est finalement captée. L'imagerie des différentes couches des tissus de l'œil est également l'application majoritaire de la TCO de manière générale. L'œil étant relativement transparent, optiquement accessible, et très organisé en couches successives, la TCO est donc particulièrement adaptée à son imagerie. Malheureusement, la cadence d'imagerie de la TCO plein champ est à l'heure actuelle trop limitée pour obtenir des images satisfaisantes chez l'homme. Par contre, elle obtient des images d'une rare qualité dans le cas de cornées ou rétines excisées auquel cas les mouvements oculaires sont évidemment évités. Nous avons notamment pu démontrer que la TCO plein champ dynamique permettait l'observation de la quasi-totalité de l'architecture et des cellules en trois dimensions, et ce aussi bien dans la cornée que dans la rétine. Nous avons pu démontrer que la résolution transverse supérieure de la TCO plein champ permet de visualiser les différentes fibres, terminaisons nerveuses, axones et capillaires de ces deux tissus. En combinant ces images statiques avec les images de TCO plein champ dynamique, nous pouvons désormais visualiser l'organisation et la morphologie des différentes cellules de ces tissus, et en étudier leur métabolisme. Là où la TCO usuelle ne peut détecter que des déformations à l'échelle de la couche rétinienne (et donc à priori à des stades avancées de maladies), la TCO plein champ dynamique permet d'observation des disfonctionnements à l'échelle de la cellule unique tout en étant toujours capable d'observer la structure de la couche entière. Le microscope que nous avons développé nous permet donc une meilleure caractérisation et visualisation de l'organisation tridimensionnelle des explants de cornées et de rétines, et la détection précoce de maladies impactant ces tissus.

La microscopie de fluorescence couplée à la TCO plein champ dans le microscope développé au cours de cette thèse nous a permis de valider les différentes structures visualisées sans marquage par la TCO plein champ. Pour finir, une observation intéressante est reportée à la fin du chapitre, et consiste en la mesure de deux paramètres physiques importants dans des globules rouges piégés dans des capillaires de la rétine. L'analyse des signaux de phase mesurés grâce à la TCO plein champ permet la mesure de l'amplitude de fluctuations de la membrane des globules d'une part, et la mesure de l'indice optique directement reliée à la concentration en hémoglobine d'autre part. Ces paramètres pourraient être utilisés dans des futures études afin de détecter préalablement un certain nombre de maladies sanguines comme cela a déjà été reporté dans des études in vitro. L'avantage est qu'ici, la mesure est effectuée in situ directement, c'est-à-dire directement à l'intérieur du tissu.

8.8 Chapitre 7 : Mesure de changements biophysiques de cellules actives électriquement

Le septième et dernier chapitre est dédié à la description d'applications potentielles en neurosciences. En effet, de nombreux modèles prédisent la possibilité d'une mesure de l'activité électrique des neurones, en utilisant des propriétés biophysiques intrinsèques dont le changement est

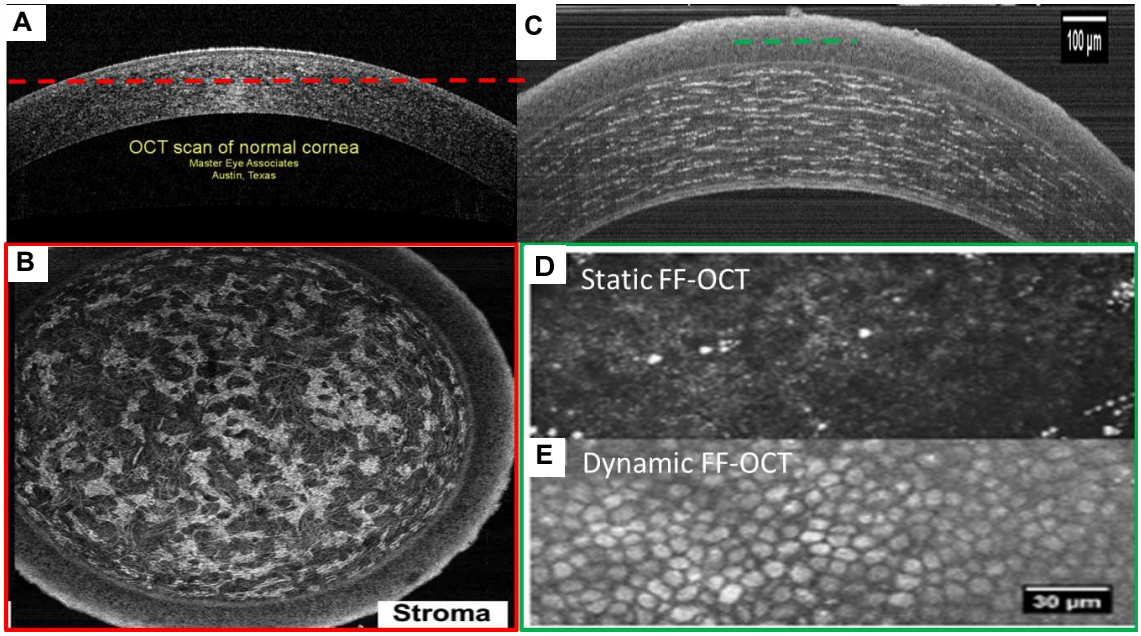

Figure 8.9 – Application de la TCO plein champ multimodale à l'imagerie de la cornée. La figure A présente une image classique de cornée obtenue avec un montage de TCO spectral, qui permet d'observer la courbure de la cornée, ainsi que d'éventuelles infiltrations d'eau, mais ne permet pas d'accéder aux structures cellulaires et subcellulaires. La résolution transverse supérieure de la TCO plein champ permet au contraire de mesurer de tels objets, comme les fibres de collagène et les keratocytes observés dans le stroma de la cornée en **figure B** (dans le plan suivant la ligne pointillée rouge), et sur la reconstruction axiale de la **figure C**. Si la TCO plein champ est efficace dans le stroma, elle ne permet pas naturellement de détecter l'organisation cellulaire dans les couches de l'épithélium (partie supérieure) de la cornée. En venant imager dans le plan suivant la ligne pointillée verte, la TCO plein champ statique (**figure D**) ne permet effectivement pas d'obtenir un bon contraste. Toutefois, l'ajout du contraste dynamique permet la reconstruction des différentes cellules de l'épithélium de la cornée, comme présenté en **figure E**.

attendu lors du changement de potentiel de membrane caractéristique du potentiel d'action. Ce n'est pas si surprenant, car, au cours d'un potentiel d'action, le champ électrique qui s'étend d'un côté à l'autre de la membrane plasmique change de polarité assez fortement. On peut donc logiquement s'attendre à une déstabilisation, et à une déformation, de la membrane, et autres structures composées de protéines, généralement négativement chargées. De plus, le potentiel d'action s'accompagne de flux relativement important d'ions à travers la membrane, flux qui s'accompagnent logiquement d'entrées et sorties d'eau. Là encore, on s'attend à un changement du volume du neurone au cours du potentiel d'action. Enfin, le changement de potentiel de membrane est probablement associé à un changement de la tension mécanique de la membrane du neurone, ce qui devrait s'accompagner d'un changement de forme (position d'équilibre différente) et possiblement de volume du neurone. A un autre niveau, il est également attendu l'activité soutenue d'un neurone perturbe la motilité globale du neurone, qui doit focaliser sa dépense énergétique pour rétablir son potentiel de membrane. Enfin bref, il existe un certain nombre de paramètres biophysiques associés au potentiel d'action, et dont nous pouvons tirer parti pour détecter l'activité électrique des neurones grâce à l'imagerie de phase de manière non invasive et sans marquage, qui est l'objet de ce chapitre. Celui-ci a un autre objectif plus large, qui est la description de modèles théoriques récents qui prédisent l'existence d'un couplage électromécanique, c'est-à-dire entre une onde mécanique qui se propagerait simultanément à l'onde électrique du

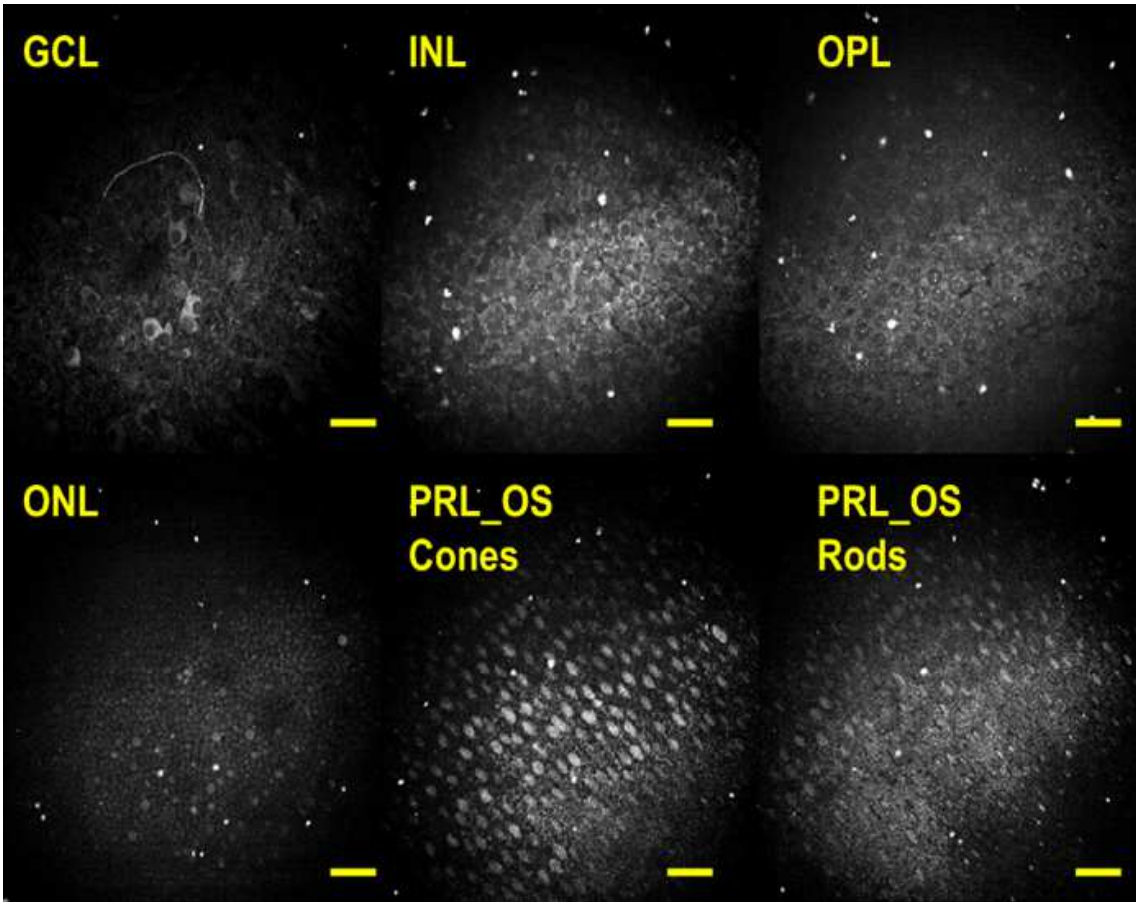

Figure 8.10 – Application de la TCO plein champ dynamique à l'imagerie rétinienne. Cette figure représente six couches cellulaires de la rétine, dans lesquelles la TCO plein champ dynamique permet l'obtention d'un contraste unique, permettant d'observer et de classer toutes les cellules de la rétine (*O. Thouvenin et al.*, IOVS, 2017). Les barres d'échelle représentent 40 μm.

potentiel d'action, pour assurer la bonne propagation du signal neuronal. A l'heure actuelle, ces modèles restent purement théoriques, mais s'ils sont vérifiés, cela pourrait correspondre à une véritable révolution en neurosciences. En effet, les paramètres mécaniques ne sont pour l'instant rarement, voire jamais, pris en compte pour comprendre le fonctionnement et éventuellement le dysfonctionnement de la transmission d'information dans le système nerveux. La validation expérimentale d'un de ces modèles était un des objectifs initiaux de ma thèse, malheureusement qui n'a pas abouti. Pourtant, dans ce chapitre 7, un certain nombre d'arguments pourront être trouvés et qui justifient l'utilisation de l'imagerie de phase quantitative plein champ, et un microscope proche de celui que nous avons utilisé, pour mesurer ce couplage électromécanique. Comme suggéré dans ce chapitre, il existe probablement encore une limite technologique d'un ordre de grandeur sur la vitesse et précision des caméras disponibles à l'heure actuelle, mais qui pourrait rapidement être surmontée.

Pour résumer, il existe un certain nombre de théories qui impliquent la prise en compte d'arguments biophysiques pour comprendre le fonctionnement des neurones et du cerveau plus généralement. Que ces paramètres soient simplement des conséquences passives du potentiel d'action (gonflement du neurone par entré d'eau par exemple), ou soient acteurs de la transmission d'information, l'imagerie de phase quantitative, aussi bien en cultures qu'en tissu, et entre autres les montages que nous avons développé au cours de ma thèse, promet de rendre possible la mesure de ces paramètres, et d'améliorer la compréhension du fonctionnement des neurones. Ce chapitre 7

débute par la description du modèle standard, purement électrique, dit d'Hodgkin-Huxley, qui décrit la formation et la propagation du potentiel d'action. La compréhension de ce modèle, pourtant largement accepté est essentielle pour réaliser qu'il ne décrit qu'une petite partie de ce qu'il se passe réellement dans un neurone actif. Notamment, si la réponse locale à une différence de potentielle est bien décrite, le mécanisme qui régit la propagation de la différence de potentiel n'est pas établit ou vérifiée par le modèle. Cela nous amène à nous intéresser dans une seconde section, à quelques expériences qui ne peuvent pas être expliquées par ce modèle purement électrique. Dans une troisième section, j'en arrive donc à décrire les modèles récents qui essayent de dépasser le modèle standard d'Hodgkin-Huxley pour inclure toutes les observations « anormales », décrites dans la partie précédente. Je décris trois modèles qui incluent tous une composante mécanique pour expliquer la propagation du potentiel d'action, et je les compare, et discute leur validité éventuelle, ainsi que propose des tests expérimentaux pour les distinguer. Enfin, les deux dernières sections décrivent quelques expériences préliminaires que nous avons réalisées au cours de ma thèse, et qui suggèrent que nous sommes capables de mesurer l'activité électrique de neurones en cultures et dans un tissu complexe, sans aucun marquage. Ces expériences consistent à mesurer simultanément la phase optique dans un neurone actif, et la mesure en fluorescence de la concentration en ions calcium, qui nous renseigne sur l'activité électrique de ces neurones. Dans des cultures de neurones, nous avons pu identifier une corrélation entre le signal de fluorescence et une diminution de la phase d'amplitude de l'ordre de 1 nm, possiblement associée à l'entrée d'eau causée par l'ouverture des canaux sodiques, comme discuté dans la section 4. De la même manière, des expériences similaires réalisées dans des larves de zebrafish in vivo, nous ont permis d'identifier une corrélation entre l'activité de motoneurones, avec une diminution de la fluctuation de phase, possiblement associée au ralentissement métabolique causé par l'activité électrique des neurones. Si ces mesures sont très intéressantes, elles restent à confirmer à une plus grande échelle et sur des nombres de neurones plus importants.

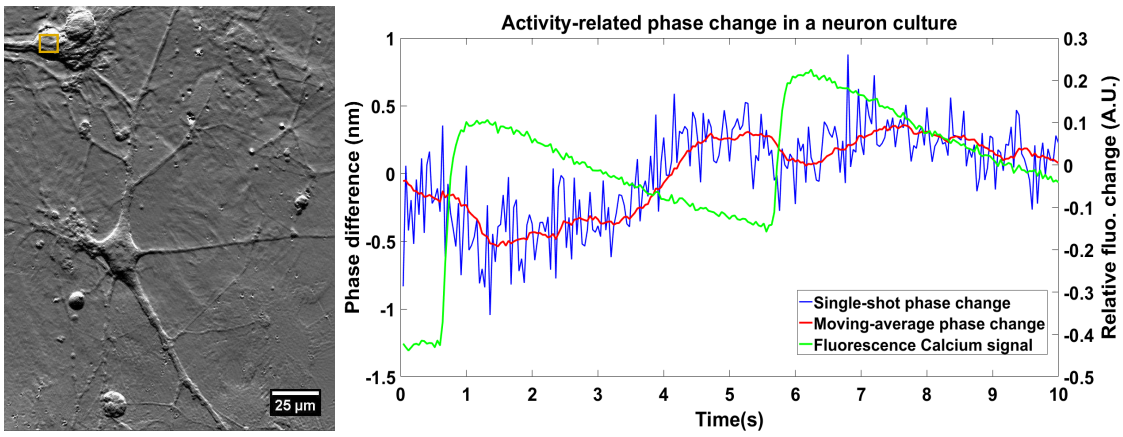

Figure 8.11 – Mesure d'un changement de phase associé à l'activité calcique spontanée d'une culture de neurones. La figure de gauche présente la carte de la dérivée de phase mesurée et calculée grâce au montage interférometrique de Linnik développé au cours de cette thèse. Le signal de phase et de fluorescence couplé correspondant à la zone entourée par le carré jaune est ensuite affiché sur la courbe de droite. On peut voir, ainsi que sur quelques autres expériences une faible décroissance du signal de phase, possiblement associée à l'entrée d'eau due à l'ouverture des canaux sodiques lors d'une activité électrique neuronale, effectivement corrélée avec la présence d'activité spontanée du neurone.

Conclusion

Au cours de cette thèse et de ce manuscrit, nous avons développé un certain nombre d'approches optiques pour mesurer des déplacements sub-cellulaires et sub-longueur d'onde d'objets biologiques à l'intérieur de cultures et tissus biologiques. Nous avons pu démontrer que ces mouvements actifs permettaient d'accéder à un certain nombre de paramètres d'importance pour la caractérisation des tissus biologiques, tels que la dureté mécanique, la motilité, le métabolisme et l'activité électrique. Un microscope multimodal combinant une approche interférométrique dite de tomographie à cohérence optique plein champ à la fois statique et dynamique, à une approche de fluorescence a été développé. Ce microscope permet la détection simultanée des contrastes morphologiques et fonctionnels décrits ci-dessus ainsi qu'un contraste biochimique spécifique associé à l'imagerie de fluorescence. Il a notamment permis de mettre en évidence la propagation conjointe d'une onde mécanique et d'une onde calcique lors de la contraction cardiaque, mécanisme bien caractérisé autrement. Ce microscope a permis l'observation de la structure de cornées et rétines ex vivo avec une résolution et un contraste jamais observés par ailleurs. Il a également permis de détecter des prémices de signaux morphologiques fonctionnels associés à une activité électrique neuronale, observés en cultures et in vivo. Nous espérons que cette approche interférométrique et multimodale permettra la détection d'ondes dites électromécaniques se propageant dans les neurones, et dont l"existence a été postulée par certains modèles théoriques pour expliquer la propagation de l'information neuronale. La détection, la compréhension, et la caractérisation de ces ondes permettrait d'envisager les neurosciences sous un aspect complètement nouveau, et dont la contribution mécanique serait essentielle pour comprendre le fonctionnement normal et anormal du cerveau.

APPENDIX A

Introduction to optical imaging in biological media

This appendix is still in progress... For now, you will find the introduction plus a small part on Rayleigh scattering to develop further the calculations performed in chapter 4. Anyway, sorry for the delay!

The aim of this appendix is to offer a brief general introduction of several basic notions of optical imaging that can be useful to keep in mind throughout the manuscript. Because this manuscript is yet long enough, I did not want to describe optical imaging in as many details as it might be needed from scratch, but I invite to read several textbooks or first chapters of other thesis to begin with [11, 126, 136]. This appendix is divided in several parts, the first of which being dedicated to the geometrical optics approximation. It gives some tricks and pitfalls in order to create an optical microscope and present a few notions developed throughout the manuscript. A second section aims to describe more carefully the optical response of such a microscope using wave optics to introduce the notion of Point spread function (PSF). Then, a small section will present optical detectors and the different sources of noise one can encounter with optical detectors. Finally, the two/three last sections aim to describe the optical endogeneous contrast, either based on absorption or on light scattering. I will try to give an insight on the main biological structures that can produce a significant optical signal.

A.1 A few principles of geometrical optics

A.2 Wave optics, diffraction limit and PSF

A.3 Optical detectors

A.4 Optical response: The complex refractive index

A.5 Light scattering

Rayleigh scattering: Let's consider a 200 nm spherical vesicle of average refractive index of 1.4 which would move in the axial direction. We want to estimate the phase sensitivity of FF-OCT,

meaning the minimal axial displacement that can be measured with FF-OCT. If we assume the vesicle to behave as a Rayleigh scatterer (In fact, we should consider Mie theory for 200 nm vesicles, as shown in figure 4.13, but we assume that the following estimated cross section is in the right order of magnitude, though a bit overestimated.):

$$R = \frac{I_s}{I_0} \simeq \frac{\Omega}{4\pi}.\frac{\sigma_s}{A_{diffraction}} \tag{A.1}$$

with Ω the detection solid angle depending on the objective NA, σ_s the Rayleigh scattering cross section, and $A_{diffraction}$, the smallest integration area limited by diffraction:

$$R_{part} \simeq \frac{1}{4(1-(\frac{NA}{n_{water}})^2)}.\frac{\frac{2*\pi^5}{3}.\frac{r_{part}^6}{\lambda_0}.(\frac{n_{part}^2-n_{water}^2}{n_{part}^2+2.n_{water}^2})^2}{\pi.(\frac{\lambda_0}{2.NA})^2} \tag{A.2}$$

in the Rayleigh regime, with r_{part} the particle radius, and n the refractive index of either the particle or the medium. Figure 4.13 shows the evolution of the apparent reflectivity of a spherical particle for different wavelengths and refractive index under the assumption of Rayleigh scattering. We note that the Rayleigh regime starts to become less valid for particles bigger than 100 nm, which will tend to constrain the apparent reflectivity of the particle (figure 4.13C). Additionally, Mie scattering becomes even more anisotropic with the particle size, with a more important contribution of the forward scattering. Therefore, the apparent reflectivity or backscattered intensity that FF-OCT can capture is even more reduced with particle size.

A.6 Imaging of cells

A.7 Imaging of tissues

APPENDIX B

Procedure for axial scanning in high NA FF-OCT

This appendix aims to describe a procedure for axial scans in tissues of variable refractive index with FF-OCT. The procedure allows both preserving signal in depth and calculating the average refractive index on a tissue slice. This procedure is adapted from the low NA procedure implemented in the software developed by LLTech and is available as follows in the Matlab user-defined interface software I have developed. As will be pointed out, this procedure uses a few approximations that might become invalid when higher NA objectives are used but performs a little better than the low NA procedure with 0.8 NA objectives. A more complex strategy with less error can be found in *J. Binding et al.* [384]. This appendix describes a procedure valid in the case where the sample is scanned up towards a glass coverslip or the microscope objective, as performed in the microscope we have develop during my thesis. One should note that in the current system configuration, it is better to perform axial scanning by lifting up the sample (and therfeore from the sample surface to the depth) because the translation stage is more precise and stable in this direction. If the system configuration is different, the following procedure has to be adapted. This appendix is organized in 6 different parts. A first section describes the procedure as it is implemented in the software without any formula demonstration. Then, a second section provides a brief reminder on numerical aperture that might be useful for the formula derivation. Section 3 and 4 develops the calculation of the sample and reference arm displacement. A fifth section aims to describe some reverse procedures that can be used to measure the refractive index, while a sixth one presents some of the procedure limitations.

B.1 Axial scanning procedure

To explain this procedure, we have chosen the example of an oil-immersion objective, in which the light penetrates through oil, a glass coverslip, and external medium before reaching the tissue. In the case where the tissue is lifted up, the oil and coverslip does not move and their contribution can be neglected for the rest of the procedure, as will be emphasized later. We also consider the external medium to have a refractive index close to the one of water (1.33), which is the case for PBS and relative media. (but can change with high glucose concentration for example). As the tissue is scanned up, the thickness of the external medium decreases so that the working distance remains somehow constant. In this section, the axial scanning procedure will be described without any justification of the formulas. The equations will be derived in the next sections. The axial

scanning procedure runs as follow:

- In a first place, we create a table with all the physical positions in the tissue we want to look at. The distance Z between two successive positions the microscope is capturing, can be either constant during all the axial scanning procedure, or can be user-defined. Similarly between two positions j and $j+1$, an average refractive index n_{j+1} is defined, either as a constant for the entire tissue, or can be user-defined for the various positions.

- Then, we calculate the associated displacement that the sample motor has to be moved in order to look at a position with an axial distance of Z from the following equation:

$$Z_{SampleMotor} = Z * \sqrt{\frac{n_W^2 - NA^2}{n_{j+1}^2 - NA^2}}, \tag{B.1}$$

- Then, the reference arm has to be scanned to match again the focal volume and the coherence volume. The reference motor has to be scanned of:

$$Z_{RefMotor} = n_{j+1}^2 \frac{Z}{\sqrt{n_{j+1}^2 - NA^2}} - n_W^2 \frac{Z_{SampleMotor}}{\sqrt{n_W^2 - NA^2}} \tag{B.2}$$

To be accurate in the case of a varying refractive index between two successive layers, all these formulas have to be computed layer by layer with Z, the displacement between each layer, and not the integrated displacement from the sample surface.

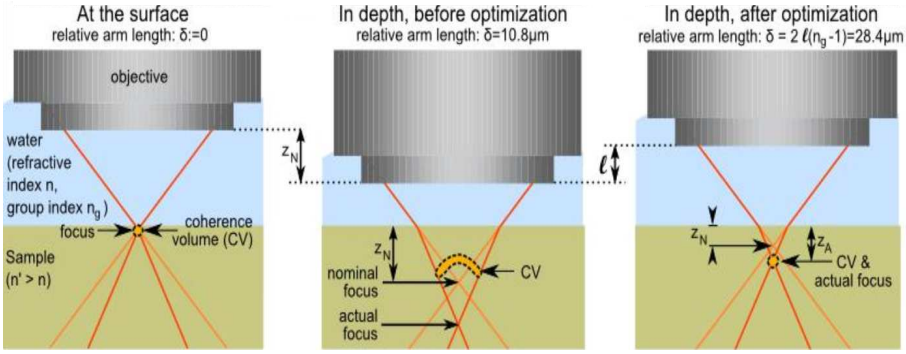

Figure B.1 – Principle and pitfalls of axial scanning in FF-OCT. Before scanning (left-hand side panel) the focus is made at the interface between the external medium and the sample. The objective being in this case optimized for water, the focus is sharp at the surface. After a given displacement (center image), light would focus at the nominal focus if the sample were of the same refractive index than water. Nevertheless, due to the refractive index difference, the actual focus of the maximum angle beam is different (deeper for a positive refractive index difference). Similarly, because the sample refractive index is higher than water, the coherence volume (area of zero-path difference with the reference arm) is closer to the surface than both the nominal and actual focus. To reach a given position inside the sample (right-hand side image), the sample arm has then to be moved of a smaller distance, and the reference arm length has to be adjusted to match the positions of the coherence and focal volumes. This figure has been reproduced from *J. Binding et al.* [384].

B.2 Reminder on numerical aperture

The numerical aperture of a microscope objective defines the maximal angle that can be sent onto a sample or that can be collected on the way back. It also accounts for the medium refractive index since the objective lens changes the angle according to Snell Descartes law. Additionally, inside the sample, for every change in refractive index, the angle also change so that we can write that at every interface the product refractive index by the maximal angle is constant. For the example of an oil-immersion objective, as illustrated in figure B.2, we obtain:

$$NA = n_{oil}sin(i_0) = n_{glass}sin(i_1) = n_W sin(i_2) = ... = n_j sin(i_j) \tag{B.3}$$

This relationship shows that the maximal angle penetrating a new layer of tissue with refractive index n_j only depends on the numerical aperture but not all previous layers light has encountered. Ultimately, the angular change only depends on the refractive index difference:

$$NA = n_j sin(i_j) = n_{j+1} sin(i_{j+1}). \tag{B.4}$$

It also shows that, in a procedure where the sample is progressively lifted up towards a glass coverslip, the only change comes from a reduction of the extracellular medium layer thickness, and from the changes inside the sample. Therefore, the case of oil-immersion objective and water-immersion can be considered identical in this case.

B.3 Calculation of the defocus

As previously stated, as we scan the sample motor in our setup configuration, the thickness of the external medium layer decreases of a distance $Z_{SampleMotor}$ while the light has propagated of $Z=Z_{Moteur1}+Z_{Defocus}$ inside the sample of refractive index n_{j+1}. The calculation will be run in two independent parts. The first part aims to calculate the defocus introduced in a sample of homogeneous refractive index. The second subsection performs a similar calculation in the case where the sample is composed of several layers of varying refractive index. The calculations can only be accurate if we neglect multiple diffusion, spatial transverse heterogeneities, and dispersion. Some of these issues are tackled in *J. Binding et al.* [384].

B.3.1 Defocus in a homogeneous sample

In a homogeneous sample, when the sample is scanned closer to the objective, the light travels through less water (corresponding optical path decreasing of $n_W.Z_{SampleMotor}$) and through more sample (corresponding optical path increasing of $n_j.Z$), with Z taking into account the defocus and is *a priori* larger than $Z_{SampleMotor}$. Additionally, if we consider the beam of maximal angle, we can define the lateral displacement of the beam for each layer. When propagating through less water, the associated lateral displacement decreases from d_{old} to a smaller d_{new}. Because the beam reaches the center of the lateral axis at the focus, this s and we can write:

$$\frac{D}{2} = d_{constant} + d_{old} + d = d_{constant} + d_{new} + d' \tag{B.5}$$

Where D/2 is the radius of the microscope objective pupil, d_{old} and d_{new} are the lateral displacements of the maximum angle beam encounters in the external medium respectively befora and after the motor displacement. $d_{constant}$ corresponds to the axial displacement the beam encounters

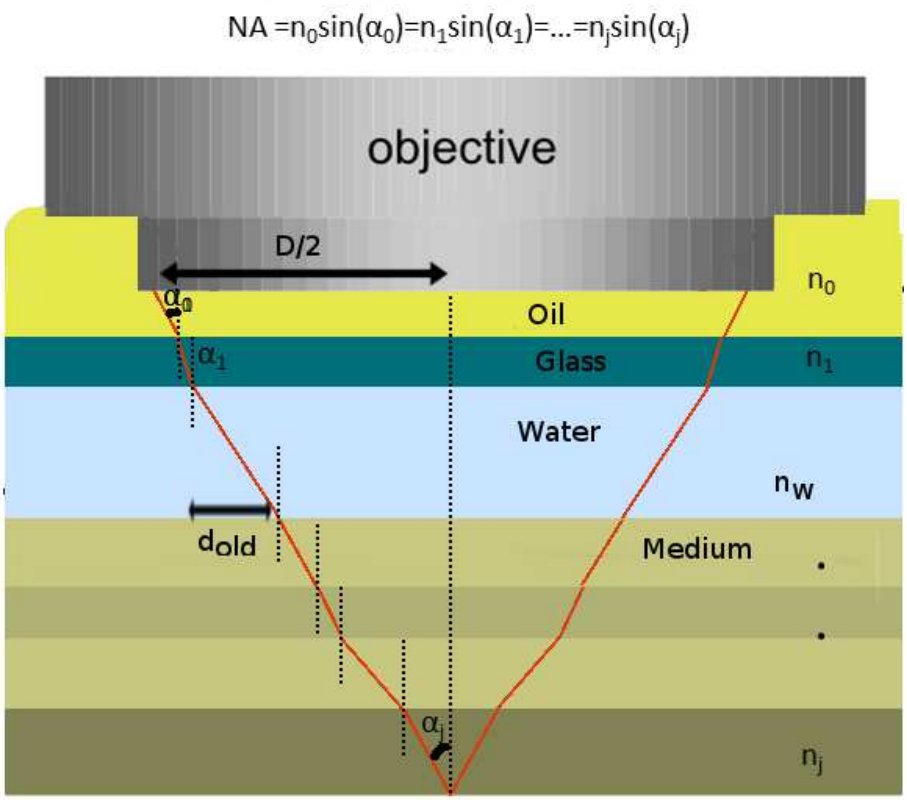

Figure B.2 – Experimental configuration for axial scanning. Before reaching the layer j inside the sample, light penetrates through several layers of various refractive index. In the case of an oil-immersion objective, two first layers of oil and glass are gone through, before going to water (or external medium) and the sample. At each interface, the maximum angle beam changes its angle with the axial line, which takes a value only controlled by the objective NA, and the layer refractive index. We also define d_i, the lateral displacement of the light in each layer $i = \{oil, glass, W, 1, ..j\}$, only controlled by the thickness of the layer i, its refractive index and the objective NA. The sum of all the lateral displacements gives $\frac{D}{2}$, the distance between the maximum angle beam and the center of the objective at its output, which is constant for a given objective (NA and focal distance).

inside the tissue before reaching the last imaged layer. The distance d and d' respectively correspond to the lateral distance in the last layer of the sample before and after the scan. Equation B.5 allows us to write:

$$d' - d = d_{old} - d_{new} = cste. \tag{B.6}$$

We now use the lateral displacements to estimate the vertical changes associated with the angles in each layer:

$$tan(i_W) = \frac{d_{new}}{t_W - Z_{SampleMotor}} = \frac{d_{old}}{t_W} \tag{B.7}$$

$$tan(i_j) = \frac{d'}{t_j + Z} = \frac{d}{t_j} \tag{B.8}$$

Where i_W and i_j correspond to the penetrating angle in the external medium layer and in the last tissue layer. t_W and t_j similarly correspond the external medium and the last tissue layer thickness before the scan. Equation B.7 permits the calculation of $d_{old} - d_{new}$:

$$d_{old} - d_{new} = d_{old}.(1 - \frac{t_W - Z_{SampleMotor}}{t_W}) = d_{old}.\frac{Z_{SampleMotor}}{t_W} \tag{B.9}$$

We then obtain:

$$d_{old} - d_{new} = tan(i_W) * Z_{SampleMotor} \tag{B.10}$$

In a similar manner from equation B.8, we can calculate:

$$d' - d = tan(i_j) * Z \tag{B.11}$$

We therefore obtain an expression of the displacement in the last layer accounting for the defocus that only depends on the motor displacement and on the penetration angle. To estimate these angles, we recall equation B.3 with the numerical aperture:

$$NA = n_j sin(i_j) = n_W sin(i_W) \tag{B.12}$$

Additionally, trigonometric considerations give that $\forall x \in [-1; 1]$:

$$tan(arcsin(x)) = \frac{x}{\sqrt{1 - x^2}} \tag{B.13}$$

Consequently, equations B.10 and B.11 being equal to the same constant (Equation B.6), we obtain:

$$Z * \frac{NA}{n_j * \sqrt{1 - (\frac{NA}{n_j})^2}} = Z_{SampleMotor} * \frac{NA}{n_W * \sqrt{1 - (\frac{NA}{n_W})^2}} \tag{B.14}$$

Finally,

$$Z_{SampleMotor} = Z * \frac{\sqrt{n_W^2 - NA^2}}{\sqrt{n_j^2 - NA^2}} \tag{B.15}$$

We can note that in the case where $n_j > n_W$, the defocus is positive corresponding to an increase of the focal distance as expected. Moreover, in the case of low NA objectives, we obtain the expected relationship:

$$Z_{SampleMotor} = Z * \frac{n_W}{n_j} \tag{B.16}$$

B.3.2 Defocus in a medium of varying refractive index

In this case, we will calculate the defocus light encounters taking into account the possibility for the medium to have a variable refractive index at the focal point. Once again, we recall that the axial heterogeneities of the refractive index distribution before the focal point does not impact the previous calculation. Nevertheless, a small difference exists in the case where the inital focus (before the motor displacement) is at an interface between two regions with different refractive index n_j and n_{j+1}. In a similar manner than what the previous subsection introduced, the propagation in only two media changes as the motor is scanned: the external medium and the

tissue layer "j+1". If the beam were not deflected by the last layer, it should focus at a distance Z of the interface (as calculated in equation B.15):

$$Z_{SampleMotor} = Z * \frac{\sqrt{n_W^2 - NA^2}}{\sqrt{n_j^2 - NA^2}} \tag{B.17}$$

Nevertheless, the actual focus is in Z' due to the change of refractive index. In the last layer $j+1$, we can estimate the tangent of the new angle i_{j+1}:

$$tan(i_{j+1}) = \frac{d_{j+1}}{Z'} \tag{B.18}$$

With d_{j+1} that is supposed to be the same whatever the refractive index of the last layer is. In particular, it can be calculated in the case where the refractive index is the same than the layer j, and where $i_j = i_{j+1}$. Therefore,

$$d_{j+1} = Z.tan(i_j) \tag{B.19}$$

$$tan(i_{j+1}) = \frac{Z.tan(i_j)}{Z'} \tag{B.20}$$

Then, the two tangents can be calculated using equation B.13 so that:

$$Z = Z' * \frac{\sqrt{n_j^2 - NA^2}}{\sqrt{n_{j+1}^2 - NA^2}} \tag{B.21}$$

Finally, we inject equation B.21 into equation B.17:

$$Z_{SampleMotor} = Z' * \frac{\sqrt{n_W^2 - NA^2}}{\sqrt{n_{j+1}^2 - NA^2}} \tag{B.22}$$

Which is very similar than equation B.15, with caution taken that Z' is the distance from the last interface between two layers of different refractive index. Similarly, the case of a sample with many layers of different refractive index can be processed by iteration by calculating a new distance at each interface, while the final depth is calculated by summing all the small distances in each layer.

B.4 Calculation of the reference arm correction

In this section, we are going to estimate the correction to be applied to the reference arm in order to re-optimize the signal. Here again, the only modifications of the optical path originate from the external medium layer and from the last sample layer. We also consider only the beam of maximal extension, supposed to account for the most part of the signal as discussed in the last section of this appendix. By considering the cosinus of this maximal angle and by comparing the distance before and after the motor displacement, we can calculate the optical path difference caused by the external medium compression:

$$\delta_1 = -n_W^2 \frac{Z_{SampleMotor}}{\sqrt{n_W^2 - NA^2}} \tag{B.23}$$

Similarly, the optical path difference caused by the longer propagation in the medium can be written as:

$$\delta_2 = n_{j+1}^2 \frac{Z}{\sqrt{n_{j+1}^2 - NA^2}} \tag{B.24}$$

To compensate for these two optical path changes (that are each felt twice due to the reflection configuration), the reference motor can be translated to stay match the focal volume and the coherence volume positions and maximize the signal. The reference arm length is adjusted in air and its displacement is also felt twice so that the optimal reference arm displacement is:

$$Z_{RefMotor} = n_{j+1}^2 \frac{Z}{\sqrt{n_{j+1}^2 - NA^2}} - n_W^2 \frac{Z_{SampleMotor}}{\sqrt{n_W^2 - NA^2}} \tag{B.25}$$

It can finally be further simplified using equation B.15:

$$Z_{RefMotor} = (n_{j+1}^2 - n_W^2).\frac{Z_{SampleMotor}}{\sqrt{n_W^2 - NA^2}} \tag{B.26}$$

B.5 Measurement of the refractive index

Additionally, the entire procedure can be reversed in order to measure the refractive index. In that case, the reference arm displacement required to re-optimize the interference signal after a given displacement is measured and the average medium refractive index can be inferred. In short, there are two ways to estimate the sample refractive index, one of which has been described at the end of chapter 6 and uses a phase measurement associated with an axial scanning. The advantage of this technique is that it is much faster since it only requires 4 frames (or 1 phase image) per axial position and is potentially a more local measurement. Nevertheless, as emphasized in chapter 6, the phase-based refractive index measurement might exhibit several artifacts and can only computed for small axial displacements to avoid phase unwrapping. The second technique uses the optimization of the FF-OCT contrast to calculate the refractive index and performs better for large axial displacements for which the coherence volume has moved significantly. Because of the current implementation of the FF-OCT signal optimization (average over the 1000 brighter pixels), this is not a local measurement in the transverse plane, but we can imagine changing the procedure to a more local measurement [1]. This second procedure is much longer as an entire scan of the reference arm length has to be performed for every axial position. In theory, only 3 measurements on both sides of the maximum have to be performed to estimate its position but does not seem accurate enough in our measurements. Once the maximum position has been measured, the refractive index is directly obtained by:

$$n_{j+1} = n_W . \sqrt{\frac{Z_{RefMotor} . \sqrt{n_W^2 - NA^2}}{Z_{SampleMotor}}} \tag{B.27}$$

B.6 Possible corrections

For all previous calculations, we have only used the maximum angle beam. In practice, in FF-OCT, the light beam is composed of many different angles belonging to the interval $\alpha \in [0\ \sin^{-1}($

[1] For example, if an amplitude image is saved during the entire displacement of the reference arm, the maximum can be estimated pixel by pixel.

$\frac{(}{N}A/n_{eau}))]$. For example, we can easily calculate the defocus and the optical path difference associated with the normal beam ($\alpha = 0$):

$$Z(\alpha = 0) = Z_{SampleMotor} * \frac{n_j}{n_W} \tag{B.28}$$

$$\delta(\alpha = 0) = (\frac{n_{j+1}^2}{n_W} - n_W).Z_{SampleMotor} \tag{B.29}$$

Therefore, the focal point has an axial extension that becomes larger and larger with the distance traveled inside the sample, and the coherence volume extends as well (without even accounting for dispersion)[2]. Nevertheless, if the objective back-focal is homogeneously illuminated, the energy corresponding to the maximum angle illumination is much larger than the energy corresponding to the normal beam. It can be easily understood since the energy corresponding to a given angle corresponds to the power sent onto the objective back-focal plane multiplied by the perimeter of the circle whose radius defines the illuminating angle [3]. In order to minimize the error, we should calculate the angle corresponding to the energy barycenter. A more complex model taking into account these considerations and dispersion is presented in *J. Binding et al.* [384].

[2]However, this effect is not so important. After 100μm of propagation in a sample of refractive index 1.38, the axial focus has extended of about 2μm with a 0.8 NA objective and of about 0.5 μm with a 0.3 NA objective. The extension of the coherence volume is of the same order of magnitude for both objectives. Nonetheless, we emphasize the critical importance to correct for the zero-order shift between the coherence volume and the focal volume, which in this case is around 15 μm!

[3]The signal attenuation due to the angular distribution might be decreased by illuminating the objective back-focal with a donut beam.

APPENDIX C

Mechanical contrast in optical phase systems

This appendix aims to describe the mechanical contrast that phase-sensitive optical systems (especially FF-OCT) can reveal, although I did not develop tools to assess biomechanical properties myself. Nevertheless, as mentioned in this manuscript introduction, phase-sensitive systems that can measure small displacements can assess as well biomechanics and motility. Indeed, mechanics studies how a material is deformed under an external displacement, while motility studies intracellular displacements.

This appendix first focuses on cellular mechanics accessible in QPI in cell cultures. It provides a contact-free measurement of cellular mechanics, is relatively easy to measure and require little sample preparation.

C.1 Cellular mechanics

The cellular mechanics controls membrane fluctuations and organelles transport. It can be involved in several mechanisms such as adhesion, mitosis or flow sensing. If several methods can measure the cell mechanics such as optical tweezers, Brillouin microscopy, micropillars, they usually are difficult to implement and allow only the recording of a few cells at a time. On the other hand, quantitative phase imaging can image either spontaneous fluctuations inside cells to infer a mechanical parameter or can be used in parallel to a controlled flow to measure the cell deformation and hence its Young's modulus. An example of mechanical calculation is given in *Popescu* 's book [7] on phase imaging. If the cell were only a microscopic water balloon, its membrane would highly fluctuate accordingly to a surface Brownian motion. Nevertheless, because of the cytoskeleton and the cell mechanical response, these fluctuations are lower and correlated between each other. For example, in red blood cells with little cytoskeleton, the fluctuations are of higher amplitude than in cells with higher cytoskeleton organization. It was somehow demonstrated that the shear modulus G of a cell was directly inversly proportional to the average amplitude of its membrane fluctuations [7]:

$$G = k_B T \frac{ln(\frac{S_{RBC}}{k_{min}})}{3\pi < \Delta h_t^2 >} \tag{C.1}$$

We can also add that phase imaging can perform measurements of cytoplasm viscosity by tracking the average motion of particles inside the cells, since the diffusion coefficient directly depends

on the viscosity. The effect of viscosity on mechanics is to damp the mechanical deformations.

C.2 Tissue Mechanics

Similarly, phase imaging in tissues using OCT technologies can also measure mechanical properties of a tissue, also named elastography in the case a tissue. Most of the techniques consist in applying a deformation and imaging how the deformation either propagates or decays. Another technique consists in taking advantage of the natural mechanical waves propagating in tissues, essentially due to the heart beat and capillaries pulsality. In this section, I will first describe the interest of the mechanical contrast as I have developed it in a review on multimodal FF-OCT systems [214] and the different measurable mechanical parameters will be described. In the review, we stress the differences and interests of static and dynamic elastography that won't be described here. Instead, I introduce here a new technique named passive elastography that has been developed in the lab, while I have slightly participated to its development.

C.2.1 Mechanical contrast: Elastography

Since the early beginning of medicine, palpation has been used to qualitatively assess abnormal tissue stiffness associated with several diseases. Palpation-based diagnosis of heart, abdomen, and wounds diseases or infections have been reported in many ancient cultures, like Greek, Egyptian, or Chinese medicine [385, 386]. The mechanical properties of tissues and cells are mostly related to their structure and function, and changes in a tissue's biomechanical properties can reveal its pathological state [3]. Notably, biomechanical changes can include the stiffness increase due to an extracellular matrix accumulation, including collagen accumulation, associated with liver fibrosis, and ultimately cirhosis [387, 388]. Moreover, tumor development significantly and progressively impacts the tissue biomechanics [389]. More importantly, the tumor stiffness actively increases its progression, and thus its malignancy, partly through a mechanically-induced molecular circuit, leading to the reduction in the number of tumor suppressors [390]. Therefore, tissue stiffness, but also stiffness anisotropy can be used as relevant diagnosis parameters.

In the 1980s', the thorough and quantitative measurement of tissue elasticity has been developed, giving access to stiffness in the approximation of purely elastic deformation of tissues. Elastography has been introduced in biomedical imaging with ultrasound and MRI elastography [391, 392], and has been proven to be a precious diagnosis biomarker for physicians since then [393, 394]. Here, we will only discuss here about tissue biomechanics in comparison to palpation-based diagnosis, and therefore at macroscopic and mesoscopic scales. However, we can add that cellular and molecular biomechanics can also be significant biomarkers of diseases, but they stay difficult to measure in tissues. To our knowledge, the most promising technique to study microscopic sub cellular biomechanics inside a tissue is fluorescent FRET sensors [395].

In OCT, mechanical contrast has been introduced by Schmitt in 1998 [396]. Since this pioneering work, many methods have been developed with success such as 2D, 3D, static or dynamic elastography [396–400].
In FF-OCT, our group adapted two similar approaches to measure mechanical contrast. The first approach is a static method based on a finite element 3D correlation algorithm that gives access to the 3D local strain tensor inside the samples [189], giving access to the local shear modulus, which is itself proportional to the tissue elasticity, or stiffness for soft tissues. The second approach is a quantitative dynamic method based on shear wave speed imaging, inspired by similar experiments

performed in ultrasounds developed in our lab. Using a fast FF-OCT system working at up to 30,000 frames per second, we could measure the local shear wave speed which is directly related to the local shear modulus [251].

In this section, we present a brief description of both methods and some results obtained on biological samples.

Description of the different mechanical parameters and approximations

Before describing how it is possible to optically measure tissue biomechanics, we briefly summarize here the numerous different mechanical parameters that can be found in the extensive literature on tissue biomechanics. We will emphasize the relationship between these parameters, and their relevance for diagnosis.

Most studies in MRI, as well as in ultrasound or optics, focus on the elastic properties of tissues, meaning the reversible linear deformation $\overline{\overline{\varepsilon}}$ caused by a small mechanical stress $\overline{\overline{\sigma}}$. In the elastic regime, and neglecting viscosity, the generalized Hooke's law gives:

$$\overline{\overline{\sigma}} = \overline{\overline{\overline{\overline{C}}}}.\overline{\overline{\varepsilon}} \tag{C.2}$$

Where $\overline{\overline{\overline{\overline{C}}}}$ is a fourth order tensor, named stiffness tensor, that depends on the mechanical parameters of the sample. All the other parameters that we will describe are elements of this fourth order tensor, and are usually obtained when the dimensions of the generalized problem are reduced. For example, Young's modulus E corresponds to the linear coefficient that relates a purely axial stress, and its associated deformation along the stress axis. In this case, the problem is reduced to a single dimension:

$$\mathrm{E} = \frac{\varepsilon}{\sigma} \tag{C.3}$$

We can add that Young's modulus is qualitatively the main measurement that is performed with manual palpation. Basically, the first information that one can get with manual palpation is how the tissue resists to an axial deformation or stress, which is given by the Young's modulus. From equation C.2, it is easy to realize that a given sample is not only deformed in the direction of the stress, but can also be deformed in the transverse direction, with preferential axis for anisotropic material.

In addition to these parameters, many mechanical measurements rely on shear wave speed measurement. The mechanical parameters on which depend the propagation of mechanical waves are simply defined as a result of the wave equation in a medium of a given stiffness. Inside biological media, two waves can propagate [401]: A longitudinal wave that corresponds to compression and traction of the medium with a mechanical displacement parallel to the direction of propagation. Additionally, shear waves can propagate, which correspond to perpendicular mechanical displacements with respect to the direction of propagation. The two waves propagate at speeds c_L and c_{shear} respectively that are controlled by the mechanical parameters of the medium. We can therefore define the bulk modulus K, and the shear modulus μ with:

$$\mathrm{c}_L = \sqrt{\frac{\mathrm{K}}{\rho}} \tag{C.4}$$

$$c_{shear} = \sqrt{\frac{\mu}{\rho}} \tag{C.5}$$

where ρ is the medium local density. These parameters are related to Young's modulus [401]:

$$E = \mu \frac{3K}{K + \frac{1}{3}.\mu} \tag{C.6}$$

Finally, for soft tissues, which represent most biological tissues, except bones, the bulk modulus is much larger than the shear modulus. Bulk moduli of biological samples range from 1 GPa to 10 GPa, while shear moduli range from 0.1 kPa in the brain to 0.1 GPa in epiderme and cartilage, and up to 10 GPa in bones [250]. When considering equation C.6 for soft tissues, the Young's modulus becomes dependent on the shear modulus only:

$$E \simeq 3.\mu \simeq 3\rho c_{shear}^2 \tag{C.7}$$

With such approximations, we have shown that it was possible to locally measure the Young's modulus by measuring the propagation speed of shear waves.

Static elastography based on digital volume correlation (DVC)

Transient elastography based on shear wave imaging

C.2.2 Towards passive elastography.

Finally, a promising technique, named passive elastography [402, 403], allows to measure dynamic mechanical parameters in the case where the product between sampling rate times the field of view is lower than the shear wave propagation speed. Optical passive elastography has recently been demonstrated with spectral domain OCT in our lab [404]. Passive elastography is well adapted to FF-OCT measurements, and we performed a few first attempts during my thesis.

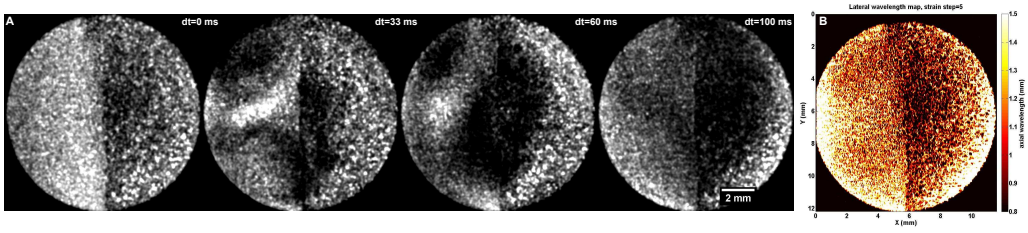

Figure C.1 – First results of FF-OCT passive elastography. Panel A shows mechanical waves propagation inside an agarose phantom, presenting two different stiffness. It can interestingly be seen than the spatial wavelength seems indeed shorter in the left hand side compartment. **Panel B** shows a probablby incorrect reconstruction of the .

To conclude this section, we have shown that FF-OCT can be coupled with elastography to measure the local mechanical parameters of a tissue. In terms of coupling with biomechanical contrast, FF-OCT and standard OCT measurements are not very different, since they rely on similar techniques to generate the mechanical contrast. Although FF-OCT-based mechanical measurements should theoretically have an isotropic 1μm resolution, we never could measure any relevant differences at this scale. Additionally, the mechanical models used to link local deformations with mechanical stiffness are mesoscopic models, whose validity can become questionable when decreasing the resolution below 10 μm.

We should add that as the deformation is applied along the optical axis, it seems more natural to look at its propagation in the transverse plane, especially when looking at shear waves. Therefore, FF-OCT, or any other *"En-Face"* OCT techniques should be well adapted for such dynamic mechanical measurements. However, mainly due to current technological limitations, these measurements are still difficult to perform in FF-OCT.

APPENDIX D

Scientific contributions

Papers

Grieve, Kate; Ghoubay, Djida; Georgeon, Cristina; **Thouvenin, Olivier**; Bouheraoua, Nacim; Paques, Michel; Borderie, VM ,"Three-dimensional structure of the mammalian limbal stem cell niche", Experimental eye research, 2015.

Jain, Manu; Robinson, Brian D; Salamoon, Bekheit; **Thouvenin, Olivier**; Boccara, Claude; Mukherjee, Sushmita , "Rapid evaluation of fresh ex vivo kidney tissue with full-field optical coherence tomography", Journal of pathology informatics, 2015.

Apelian, Clement; Harms, Fabrice; **Thouvenin, Olivier**; Boccara, A Claude , "Dynamic full field optical coherence tomography: subcellular metabolic contrast revealed in tissues by interferometric signals temporal analysis", Biomedical Optics Express, 2016.

Grieve, Kate; **Thouvenin, Olivier**; Sengupta, Abhishek; Borderie, Vincent M; Paques, Michel, "Appearance of the Retina With Full-Field Optical Coherence Tomography and the Retina", Investigative ophthalmology & visual science, 2016.

Leroux, Charles-Edouard; Bertillot, Fabien; **Thouvenin, Olivier**; Boccara, Albert-Claude, "Intracellular dynamics measurements with full field optical coherence tomography suggest hindering effect of actomyosin contractility on organelle transport", Biomedical Optics Express, 2016.

Cadart, C; Zlotek-Zlotkiewicz, E; Venkova, L; **Thouvenin, O**; Racine, V; Le Berre, M; Monnier, S; Piel, M, "Fluorescence eXclusion Measurement of volume in live cells", Methods in Cell Biology, 2017.

Thouvenin, Olivier; Grieve, Kate; Xiao, Peng; Apelian, Clement; Boccara, A Claude, "En face coherence microscopy [Invited]", Biomedical Optics Express, 2017.

Thouvenin, Olivier; Fink, Mathias; Boccara, Claude, "Dynamic multimodal full-field optical coherence tomography and fluorescence structured illumination microscopy", Journal of Biomedical Optics, 2017.

Thouvenin, Olivier; Apelian, Clement; Nahas, Amir; Fink, Mathias; Boccara, Claude, "Full-Field Optical Coherence Tomography as a Diagnosis Tool: Recent Progress with Multimodal Imaging", Applied Sciences, 2017.

Thouvenin, Olivier; Boccara, Claude; Fink, Mathias; Sahel, José; Paques, Michel, Grieve, Kate; "Cell motility as FF-OCT contrast agent in primate retinal", *Submitted to IOVS*.

Oral presentations as speaker

Thouvenin, Olivier ; Boccara, Claude; Fink, Mathias, "Non invasive label-free detection of action potentials", SPIE BiOS Photonics West, 2014.

Thouvenin, Olivier ; Boccara, Claude; Fink, Mathias, "Non invasive detection of action potentials from intrinsic electromechanical coupling in neurons", NEurosciences Workshop Saclay, 2014.

Thouvenin, Olivier; Fink, Mathias; Boccara, Claude, "Synchronous multimodal combination of full-field OCT and structured illumination fluorescence microscopy", SPIE BiOS Photonics West, 2016.

Thouvenin, Olivier; Fink, Mathias; Boccara, Claude, "Quantitative phase imaging technologies to assess neuronal activity", SPIE BiOS Photonics West, 2016.

Thouvenin, Olivier; Boccara, A Claude; Paques, Michel; Sahel, José-Alain; Fink, Mathias; Grieve, Kate F, "High resolution imaging of intracellular dynamics in explanted retinas with dynamic full-field OCT", SPIE BiOS Photonics West, 2017.

Thouvenin, Olivier; Fink, Mathias; Boccara, A Claude,"Fluorescence exclusion: A simple versatile technique to calculate cell volumes and local heights", SPIE BiOS Photonics West, 2017.

References

[1] Jeroen Eyckmans, Thomas Boudou, Xiang Yu, and Christopher S Chen. A hitchhiker's guide to mechanobiology. *Developmental cell*, 21(1):35–47, 2011.

[2] Gavin Low, Scott A Kruse, and David J Lomas. General review of magnetic resonance elastography. *World journal of radiology*, 8(1):59, 2016.

[3] Armen Sarvazyan. Shear acoustic properties of soft biological tissues in medical diagnostics. *The Journal of the Acoustical Society of America*, 93(4):2329–2330, 1993.

[4] Simon Henry Gage. Modern dark-field microscopy and the history of its development. 1920.

[5] Frits Zernike. Phase contrast, a new method for the microscopic observation of transparent objects. *Physica*, 9(7):686–698, 1942.

[6] H Köhler. On abbe's theory of image formation in the microscope. *Journal of Modern Optics*, 28(12):1691–1701, 1981.

[7] Gabriel Popescu. *Quantitative Phase Imaging of Cells and Tissues*. McGrawHill, New York, 2011.

[8] Douglas B Murphy and Michael W Davidson. Fundamentals of light microscopy. *Fundamentals of Light Microscopy and Electronic Imaging, Second Edition*, pages 1–19, 2001.

[9] MG Nomarski. Microinterféromètre différentiel à ondes polarisées. *Journal de Physique et le Radium*, 16:S9–S13, 1955.

[10] RD Allen and GB David. The zeiss-nomarski differential interference equipment for transmitted-light microscopy. *Zeitschrift fur wissenschaftliche Mikroskopie und mikroskopische Technik*, 69(4):193–221, 1969.

[11] Nikon microscopyu. `https://www.microscopyu.com/techniques/dic/de-s%C3%A9narmont-bias`

[12] Maurice Françon and Shamlal Mallick. Polarization interferometers. 1971.

[13] Dennis Gabor et al. A new microscopic principle. *Nature*, 161(4098):777–778, 1948.

[14] HG Davies and MHF Wilkins. Interference microscopy and mass determination. *Nature*, 169:541, 1952.

[15] R Barer. Interference microscopy and mass determination. *Nature*, 169:366–367, 1952.

[16] R Barer. Determination of dry mass, thickness, solid and water concentration in living cells. *Nature*, 172:1097–1098, 1953.

[17] Wikipedia page of newton's fringes. `https://fr.wikipedia.org/wiki/%C3%89chelle_des_teinte`

[18] Philippe Gleyzes. *Contribution à l'amélioration de la résolution en microscopie optique: Profilométrie différentielle picométrique et imagerie en champ proche*. PhD thesis, 1993.

[19] AF Fercher, K Mengedoht, and W Werner. Eye-length measurement by interferometry with partially coherent light. *Optics letters*, 13(3):186–188, 1988.

[20] David Huang, Eric A Swanson, Charles P Lin, Joel S Schuman, William G Stinson, Warren Chang, Michael R Hee, Thomas Flotte, Kenton Gregory, Carmen A Puliafito, et al. Optical coherence tomography. *Science (New York, NY)*, 254(5035):1178, 1991.

[21] Wolfgang Drexler and James G Fujimoto. *Optical coherence tomography: technology and applications*. Springer Science & Business Media, 2008.

[22] Michael A Choma, Audrey K Ellerbee, Changhuei Yang, Tony L Creazzo, and Joseph A Izatt. Spectral-domain phase microscopy. *Optics letters*, 30(10):1162–1164, 2005.

[23] Chulmin Joo, Taner Akkin, Barry Cense, Boris H Park, and Johannes F de Boer. Spectral-domain optical coherence phase microscopy for quantitative phase-contrast imaging. *Optics letters*, 30(16):2131–2133, 2005.

[24] ANTON Barty, KA Nugent, D Paganin, and A Roberts. Quantitative optical phase microscopy. *Optics Letters*, 23(11):817–819, 1998.

[25] Matthew R Arnison, Kieran G Larkin, Colin JR Sheppard, Nicholas I Smith, and Carol J Cogswell. Linear phase imaging using differential interference contrast microscopy. *Journal of microscopy*, 214(1):7–12, 2004.

[26] Pierre Marquet, Benjamin Rappaz, Pierre J Magistretti, Etienne Cuche, Yves Emery, Tristan Colomb, and Christian Depeursinge. Digital holographic microscopy: a noninvasive contrast imaging technique allowing quantitative visualization of living cells with subwavelength axial accuracy. *Optics letters*, 30(5):468–470, 2005.

[27] Gabriel Popescu, Lauren P Deflores, Joshua C Vaughan, Kamran Badizadegan, Hidenao Iwai, Ramachandra R Dasari, and Michael S Feld. Fourier phase microscopy for investigation of biological structures and dynamics. *Optics letters*, 29(21):2503–2505, 2004.

[28] N Verrier, M Atlan, and M Gross. Full field holographic vibrometry at ultimate limits. *New Techniques in Digital Holography (ed P. Picart), John Wiley & Sons, Inc., Hoboken, NJ, USA. doi*, 10:9781119091745, 2015.

[29] Takahiro Ikeda, Gabriel Popescu, Ramachandra R Dasari, and Michael S Feld. Hilbert phase microscopy for investigating fast dynamics in transparent systems. *Optics letters*, 30(10):1165–1167, 2005.

[30] Etienne Cuche, Pierre Marquet, and Christian Depeursinge. Simultaneous amplitude-contrast and quantitative phase-contrast microscopy by numerical reconstruction of fresnel off-axis holograms. *Applied optics*, 38(34):6994–7001, 1999.

[31] Yann Cotte, Fatih Toy, Pascal Jourdain, Nicolas Pavillon, Daniel Boss, Pierre Magistretti, Pierre Marquet, and Christian Depeursinge. Marker-free phase nanoscopy. *Nature Photonics*, 7(2):113–117, 2013.

[32] H Kadono, M Ogusu, and S Toyooka. Phase shifting common path interferometer using a liquid-crystal phase modulator. *Optics communications*, 110(3-4):391–400, 1994.

[33] YoonSeok Baek, KyeoReh Lee, Jonghee Yoon, Kyoohyun Kim, and YongKeun Park. White-light quantitative phase imaging unit. *Optics express*, 24(9):9308–9315, 2016.

[34] Gabriel Popescu, Takahiro Ikeda, Ramachandra R Dasari, and Michael S Feld. Diffraction phase microscopy for quantifying cell structure and dynamics. *Optics letters*, 31(6):775–777, 2006.

[35] Zhuo Wang, Larry Millet, Mustafa Mir, Huafeng Ding, Sakulsuk Unarunotai, John Rogers, Martha U Gillette, and Gabriel Popescu. Spatial light interference microscopy (slim). *Optics express*, 19(2):1016–1026, 2011.

[36] Basanta Bhaduri, Hoa Pham, Mustafa Mir, and Gabriel Popescu. Diffraction phase microscopy with white light. *Optics letters*, 37(6):1094–1096, 2012.

[37] Benjamin Rappaz. Cellular dynamics explored with digital holographic microscopy, 2008.

[38] Max Born and Emil Wolf. *Principles of optics: electromagnetic theory of propagation, interference and diffraction of light*. CUP Archive, 2000.

[39] Pierre Bon, Guillaume Maucort, Benoit Wattellier, and Serge Monneret. Quadriwave lateral shearing interferometry for quantitative phase microscopy of living cells. *Optics express*, 17(15):13080–13094, 2009.

[40] Ashwin B Parthasarathy, Kengyeh K Chu, Tim N Ford, and Jerome Mertz. Quantitative phase imaging using a partitioned detection aperture. *Optics letters*, 37(19):4062–4064, 2012.

[41] Tim N Ford, Kengyeh K Chu, and Jerome Mertz. Phase-gradient microscopy in thick tissue with oblique back-illumination. *Nature Methods*, 9(12):1195–1197, 2012.

[42] Timothé Laforest, Dino Carpentras, Laura Kowalczuk, Francine Behar-Cohen, and Christophe Moser. Quantitative phase imaging of retinal cells. *arXiv preprint arXiv:1701.08854*, 2017.

[43] Florian Charrière, Anca Marian, Frédéric Montfort, Jonas Kuehn, Tristan Colomb, Etienne Cuche, Pierre Marquet, and Christian Depeursinge. Cell refractive index tomography by digital holographic microscopy. *Optics letters*, 31(2):178–180, 2006.

[44] F Merola, L Miccio, P Memmolo, G Di Caprio, A Galli, R Puglisi, D Balduzzi, G Coppola, P Netti, and P Ferraro. Digital holography as a method for 3-d imaging and estimating the biovolume of motile cells. *Lab on a Chip*, 13(23):4512–4516, 2013.

[45] Wonshik Choi, Christopher Fang-Yen, Kamran Badizadegan, Seungeun Oh, Niyom Lue, Ramachandra R Dasari, and Michael S Feld. Tomographic phase microscopy. *Nature methods*, 4(9):717, 2007.

[46] Youngchan Kim, Hyoeun Shim, Kyoohyun Kim, HyunJoo Park, Ji Han Heo, Jonghee Yoon, Chulhee Choi, Seongsoo Jang, and YongKeun Park. Common-path diffraction optical tomography for investigation of three-dimensional structures and dynamics of biological cells. *Optics express*, 22(9):10398–10407, 2014.

[47] Yongjin Sung, Wonshik Choi, Christopher Fang-Yen, Kamran Badizadegan, Ramachandra R Dasari, and Michael S Feld. Optical diffraction tomography for high resolution live cell imaging. *Optics express*, 17(1):266–277, 2009.

[48] Sherazade Aknoun, Benoit Wattellier, Pierre Bon, and Serge Monneret. Tomographic incoherent phase imaging, a diffraction tomography alternative. *Biophysical Journal*, 106(2):603a, 2014.

[49] Poorya Hosseini, Renjie Zhou, Yang-Hyo Kim, Chiara Peres, Alberto Diaspro, Cuifang Kuang, Zahid Yaqoob, and Peter TC So. Pushing phase and amplitude sensitivity limits in interferometric microscopy. *Optics letters*, 41(7):1656–1659, 2016.

[50] P Gleyzes and AC Boccara. Interferometric polarization picometric profile. i. single detector approach. *Journal of Optics*, 25(5):207, 1994.

[51] Data analysis toolkit n.5 from j.w.kirchner, berkeley. `http://seismo.berkeley.edu/~kirchner/eps_120/EPSToolkits.htm`.

[52] Toyohiko Yamauchi, Hidenao Iwai, Mitsuharu Miwa, and Yutaka Yamashita. Low-coherent quantitative phase microscope for nanometer-scale measurement of living cells morphology. *Optics express*, 16(16):12227–12238, 2008.

[53] H Turlier, DA Fedosov, B Audoly, T Auth, NS Gov, C Sykes, J-F Joanny, G Gompper, and T Betz. Equilibrium physics breakdown reveals the active nature of red blood cell flickering. *Nature Physics*, 2016.

[54] Thu-Mai Nguyen, Shaozhen Song, Bastien Arnal, Emily Y Wong, Zhihong Huang, Ruikang K Wang, and Matthew O'Donnell. Shear wave pulse compression for dynamic elastography using phase-sensitive optical coherence tomography. *Journal of biomedical optics*, 19(1):016013–016013, 2014.

[55] Benjamin Rappaz, Pierre Marquet, Etienne Cuche, Yves Emery, Christian Depeursinge, and Pierre J Magistretti. Measurement of the integral refractive index and dynamic cell morphometry of living cells with digital holographic microscopy. *Optics express*, 13(23):9361–9373, 2005.

[56] Claire L Curl, Catherine J Bellair, Trudi Harris, Brendan E Allman, Peter J Harris, Alastair G Stewart, Ann Roberts, Keith A Nugent, and Lea Delbridge. Refractive index measurement in viable cells using quantitative phase-amplitude microscopy and confocal microscopy. *Cytometry Part A*, 65(1):88–92, 2005.

[57] Niyom Lue, Gabriel Popescu, Takahiro Ikeda, Ramachandra R Dasari, Kamran Badizadegan, and Michael S Feld. Live cell refractometry using microfluidic devices. *Optics letters*, 31(18):2759–2761, 2006.

[58] Benjamin Rappaz, Florian Charrière, Christian Depeursinge, Pierre J Magistretti, and Pierre Marquet. Simultaneous cell morphometry and refractive index measurement with dual-wavelength digital holographic microscopy and dye-enhanced dispersion of perfusion medium. *Optics letters*, 33(7):744–746, 2008.

[59] Some random website about commercial refractometer. `http://rudolphresearch.com/refractometers-use-selection/#.WMkaFqKmmUk`.

[60] Gabriel Popescu, YoungKeun Park, Niyom Lue, Catherine Best-Popescu, Lauren Deflores, Ramachandra R Dasari, Michael S Feld, and Kamran Badizadegan. Optical imaging of cell mass and growth dynamics. *American Journal of Physiology-Cell Physiology*, 295(2):C538–C544, 2008.

[61] Ewa Zlotek-Zlotkiewicz, Sylvain Monnier, Giovanni Cappello, Mael Le Berre, and Matthieu Piel. Optical volume and mass measurements show that mammalian cells swell during mitosis. *The Journal of cell biology*, 211(4):765–774, 2015.

[62] Thomas A Zangle and Michael A Teitell. Live-cell mass profiling: an emerging approach in quantitative biophysics. *Nature methods*, 11(12):1221–1228, 2014.

[63] Huaying Zhao, Patrick H Brown, and Peter Schuck. On the distribution of protein refractive index increments. *Biophysical journal*, 100(9):2309–2317, 2011.

[64] Charles Tanford et al. *Physical chemistry of macromolecules*. Wiley, 1961.

[65] R Barer. Determination of dry mass, thickness, solid and water concentration in living cells. *Nature*, 172:1097–1098, 1953.

[66] Mustafa Mir, Taewoo Kim, Anirban Majumder, Mike Xiang, Ru Wang, S Chris Liu, Martha U Gillette, Steven Stice, and Gabriel Popescu. Label-free characterization of emerging human neuronal networks. *Scientific reports*, 4:4434, 2014.

[67] Séverine Coquoz, Amir Nahas, Miguel Sison, Antonio Lopez, and Theo Lasser. High-speed phase-shifting common-path quantitative phase imaging with a piezoelectric actuator. *Journal of Biomedical Optics*, 21(12):126019–126019, 2016.

[68] Lei Tian and Laura Waller. 3-d intensity and phase imaging from light field measurements in an led array microscope. *Optica*, 2(2):104–111, 2015.

[69] Antoine Federici, Henrique S Gutierrez da Costa, Jonas Ogien, Audrey K Ellerbee, and Arnaud Dubois. Wide-field, full-field optical coherence microscopy for high-axial-resolution phase and amplitude imaging. *Applied optics*, 54(27):8212–8220, 2015.

[70] Pierre Marquet, Christian Depeursinge, and Pierre J Magistretti. Review of quantitative phase-digital holographic microscopy: promising novel imaging technique to resolve neuronal network activity and identify cellular biomarkers of psychiatric disorders. *Neurophotonics*, 1(2):020901–020901, 2014.

[71] KyeoReh Lee, Kyoohyun Kim, Jaehwang Jung, JiHan Heo, Sangyeon Cho, Sangyun Lee, Gyuyoung Chang, YoungJu Jo, Hyunjoo Park, and YongKeun Park. Quantitative phase imaging techniques for the study of cell pathophysiology: from principles to applications. *Sensors*, 13(4):4170–4191, 2013.

[72] Young Zoon Yoon, Jurij Kotar, Aidan T Brown, and Pietro Cicuta. Red blood cell dynamics: from spontaneous fluctuations to non-linear response. *Soft Matter*, 7(5):2042–2051, 2011.

[73] Roy B Tishler and Francis D Carlson. A study of the dynamic properties of the human red blood cell membrane using quasi-elastic light-scattering spectroscopy. *Biophysical journal*, 65(6):2586–2600, 1993.

[74] Alison M Forsyth, Jiandi Wan, Philip D Owrutsky, Manouk Abkarian, and Howard A Stone. Multiscale approach to link red blood cell dynamics, shear viscosity, and atp release. *Proceedings of the National Academy of Sciences*, 108(27):10986–10991, 2011.

[75] YongKeun Park, Catherine A Best, Kamran Badizadegan, Ramachandra R Dasari, Michael S Feld, Tatiana Kuriabova, Mark L Henle, Alex J Levine, and Gabriel Popescu. Measurement of red blood cell mechanics during morphological changes. *Proceedings of the National Academy of Sciences*, 107(15):6731–6736, 2010.

[76] YongKeun Park, Monica Diez-Silva, Gabriel Popescu, George Lykotrafitis, Wonshik Choi, Michael S Feld, and Subra Suresh. Refractive index maps and membrane dynamics of human red blood cells parasitized by plasmodium falciparum. *Proceedings of the National Academy of Sciences*, 105(37):13730–13735, 2008.

[77] Madalena Costa, Ionita Ghiran, C-K Peng, Anne Nicholson-Weller, and Ary L Goldberger. Complex dynamics of human red blood cell flickering: alterations with in vivo aging. *Physical Review E*, 78(2):020901, 2008.

[78] Natan T Shaked, Lisa L Satterwhite, Marilyn J Telen, George A Truskey, and Adam Wax. Quantitative microscopy and nanoscopy of sickle red blood cells performed by wide field digital interferometry. *Journal of biomedical optics*, 16(3):030506–030506, 2011.

[79] SangYun Lee, Hyunjoo Park, Seongsoo Jang, and Yongkeun Park. Refractive index tomograms and dynamic membrane fluctuations of red blood cells from patients with diabetes mellitus. *Biophysical Journal*, 112(3):218a–219a, 2017.

[80] Benjamin Rappaz, Elena Cano, Tristan Colomb, Jonas Kühn, Christian Depeursinge, Viesturs Simanis, Pierre J Magistretti, and Pierre Marquet. Noninvasive characterization of the fission yeast cell cycle by monitoring dry mass with digital holographic microscopy. *Journal of biomedical optics*, 14(3):034049–034049, 2009.

[81] Graham A Dunn and Daniel Zicha. Dynamics of fibroblast spreading. *Journal of Cell Science*, 108(3):1239–1249, 1995.

[82] Youngchan Kim, Hyoeun Shim, Kyoohyun Kim, HyunJoo Park, Seongsoo Jang, and YongKeun Park. Profiling individual human red blood cells using common-path diffraction optical tomography. *Scientific reports*, 4:6659, 2014.

[83] Jonghee Yoon, Kyoohyun Kim, HyunJoo Park, Chulhee Choi, Seongsoo Jang, and YongKeun Park. Label-free characterization of white blood cells by measuring 3-d refractive index maps. *Biomedical optics express*, 6(10):3865–3875, 2015.

[84] Kevin Gregory Phillips, Carmen Ruiz Velasco, Julia Li, Anand Kolatkar, Madelyn Luttgen, Kelly Bethel, Bridgette Duggan, Peter Kuhn, and Owen McCarty. Optical quantification of cellular mass, volume, and density of circulating tumor cells identified in an ovarian cancer patient. *Frontiers in oncology*, 2:72, 2012.

[85] Huafeng Ding, Zhuo Wang, Xing Liang, Stephen A Boppart, Krishna Tangella, and Gabriel Popescu. Measuring the scattering parameters of tissues from quantitative phase imaging of thin slices. *Optics letters*, 36(12):2281–2283, 2011.

[86] Amanda C Sullivan, John P Hunt, and Amy L Oldenburg. Fractal analysis for classification of breast carcinoma in optical coherence tomography. *Journal of biomedical optics*, 16(6):066010–066010, 2011.

[87] Changhuei Yang, Adam Wax, Irene Georgakoudi, Eugene B Hanlon, Kamran Badizadegan, Ramachandra R Dasari, and Michael S Feld. Interferometric phase-dispersion microscopy. *Optics Letters*, 25(20):1526–1528, 2000.

[88] Yi Yang, Tianheng Wang, Nrusingh C Biswal, Xiaohong Wang, Melinda Sanders, Molly Brewer, and Quing Zhu. Optical scattering coefficient estimated by optical coherence tomography correlates with collagen content in ovarian tissue. *Journal of biomedical optics*, 16(9):090504–090504, 2011.

[89] Ido Nitsan, Stavit Drori, Yair E Lewis, Shlomi Cohen, and Shelly Tzlil. Mechanical communication in cardiac cell synchronized beating. *Nature Physics*, 2016.

[90] Seungeun Oh, Christopher Fang-Yen, Wonshik Choi, Zahid Yaqoob, Dan Fu, YongKeun Park, Ramachandra R Dassari, and Michael S Feld. Label-free imaging of membrane potential using membrane electromotility. *Biophysical journal*, 103(1):11–18, 2012.

[91] Mikhail Eugene Kandel, Kai Wen Teng, Paul R Selvin, and Gabriel Popescu. Label-free imaging of single microtubule dynamics using spatial light interference microscopy. *ACS nano*, 2016.

[92] Sherazade Aknoun, Pierre Bon, Julien Savatier, Benoit Wattellier, and Serge Monneret. Quantitative retardance imaging of biological samples using quadriwave lateral shearing interferometry. *Optics express*, 23(12):16383–16406, 2015.

[93] Ru Wang, Zhuo Wang, Larry Millet, Martha U Gillette, AJ Levine, and Gabriel Popescu. Dispersion-relation phase spectroscopy of intracellular transport. *Optics Express*, 19(21):20571–20579, 2011.

[94] Lihong Ma, Gannavarpu Rajshekhar, Ru Wang, Basanta Bhaduri, Shamira Sridharan, Mustafa Mir, Arindam Chakraborty, Rajashekar Iyer, Supriya Prasanth, Larry Millet, et al. Phase correlation imaging of unlabeled cell dynamics. *Scientific Reports*, 6, 2016.

[95] Pascal Jourdain, Daniel Boss, Benjamin Rappaz, Corinne Moratal, Maria-Clemencia Hernandez, Christian Depeursinge, Pierre Julius Magistretti, and Pierre Marquet. Simultaneous optical recording in multiple cells by digital holographic microscopy of chloride current associated to activation of the ligand-gated chloride channel gaba a receptor. *PloS one*, 7(12):e51041, 2012.

[96] Pascal Jourdain, Nicolas Pavillon, Corinne Moratal, Daniel Boss, Benjamin Rappaz, Christian Depeursinge, Pierre Marquet, and Pierre J Magistretti. Determination of transmembrane water fluxes in neurons elicited by glutamate ionotropic receptors and by the cotransporters kcc2 and nkcc1: a digital holographic microscopy study. *Journal of Neuroscience*, 31(33):11846–11854, 2011.

[97] Céline Bottier, Chiara Gabella, Benoît Vianay, Lara Buscemi, Ivo F Sbalzarini, Jean-Jacques Meister, and Alexander B Verkhovsky. Dynamic measurement of the height and volume of migrating cells by a novel fluorescence microscopy technique. *Lab on a Chip*, 11(22):3855–3863, 2011.

[98] C Cadart, E Zlotek-Zlotkiewicz, L Venkova, O Thouvenin, V Racine, M Le Berre, S Monnier, and M Piel. Fluorescence exclusion measurement of volume in live cells. *Methods in Cell Biology*, 2016.

[99] Clotilde Cadart. *Cell size homeostasis in metazoan cells*. PhD thesis, Université Paris Saclay, 2017.

[100] Céline Braini. *Approche biophysique des formes neuronales*. PhD thesis, Université Grenoble Alpes, 2016.

[101] Hagai Kirshner, Franois Aguet, Daniel Sage, and Michael Unser. 3-d psf fitting for fluorescence microscopy: implementation and localization application. *Journal of microscopy*, 249(1):13–25, 2013.

[102] A Griffa, N Garin, and D Sage. Comparison of deconvolution software in 3-d microscopy: A user point of view—part 1. *GIT Imaging & Microscopy*, 12(EPFL-ARTICLE-163617):43–45, 2010.

[103] Psf generator website. `http://bigwww.epfl.ch/algorithms/psfgenerator/#usage`.

[104] Sarah Frisken Gibson and Frederick Lanni. Experimental test of an analytical model of aberration in an oil-immersion objective lens used in three-dimensional light microscopy. *JOSA A*, 9(1):154–166, 1992.

[105] Olivier Thouvenin, Fink Mathias, and Boccara Claude. Dynamic multimodal full-field optical coherence tomography and fluorescence structured illumination microscopy. *Journal of Biomedical Optics*, 2017.

[106] Jihoon Na, Woo June Choi, Eun Seo Choi, Seon Young Ryu, and Byeong Ha Lee. Image restoration method based on hilbert transform for full-field optical coherence tomography. *Applied optics*, 47(3):459–466, 2008.

[107] Handbook of Full-Field Optical Coherence Microscopy: Technology and Applications, 2016.

[108] Dan Fu, Seungeun Oh, Wonshik Choi, Toyohiko Yamauchi, August Dorn, Zahid Yaqoob, Ramachandra R Dasari, and Michael S Feld. Quantitative dic microscopy using an off-axis self-interference approach. *Optics letters*, 35(14):2370–2372, 2010.

[109] Pinhas Girshovitz and Natan T Shaked. Compact and portable low-coherence interferometer with off-axis geometry for quantitative phase microscopy and nanoscopy. *Optics express*, 21(5):5701–5714, 2013.

[110] Egidijus Auksorius and A Claude Boccara. Dark-field full-field optical coherence tomography. *Optics letters*, 40(14):3272–3275, 2015.

[111] Charles-Edouard Leroux, Fabien Bertillot, Olivier Thouvenin, and Albert-Claude Boccara. Intracellular dynamics measurements with full field optical coherence tomography suggest hindering effect of actomyosin contractility on organelle transport. *Biomedical Optics Express*, 7(11):4501–4513, 2016.

[112] William Cruz-Santos, Lourdes LÃ³pez-GarcÃa, and Arturo Redondo-Galvan. Improving the accuracy of phase-shifting techniques. *Optical Engineering*, 54(5):054102–054102, 2015.

[113] Zacarias Malacara and Manuel Servin. *Interferogram analysis for optical testing*, volume 84. CRC press, 2016.

[114] Emilie Benoit À La Guillaume. *Imagerie acousto-optique dans les milieux diffusants épais: de l'amélioration technique à l'application pré-clinique ex vivo*. PhD thesis, Université Pierre et Marie Curie-Paris VI, 2013.

[115] Arnaud Dubois. Phase-map measurements by interferometry with sinusoidal phase modulation and four integrating buckets. *JOSA A*, 18(8):1972–1979, 2001.

[116] Wikipedia page on analytic signal. `https://en.wikipedia.org/wiki/Analytic_signal`.

[117] Dennis Ghiglia and Mark Pritt. *Two-dimensional phase unwrapping theory, algorithms and applications*. John Wiley & Sons New York, NY, USA, 1998.

[118] Miguel Arevallilo Herráez, David R Burton, Michael J Lalor, and Munther A Gdeisat. Fast two-dimensional phase-unwrapping algorithm based on sorting by reliability following a noncontinuous path. *Applied Optics*, 41(35):7437–7444, 2002.

[119] Vyacheslav V Volkov and Yimei Zhu. Deterministic phase unwrapping in the presence of noise. *Optics letters*, 28(22):2156–2158, 2003.

[120] Tsai-Wen Chen, Trevor J. Wardill, Yi Sun, Stefan R. Pulver, Sabine L. Renninger, Amy Baohan, Eric R. Schreiter, Rex A. Kerr, Michael B. Orger, Vivek Jayaraman, Loren L. Looger, Karel Svoboda, and Douglas S. Kim. Ultrasensitive fluorescent proteins for imaging neuronal activity. *Nature*, 499(7458):295–300, 2013.

[121] K.R. Gee, K.A. Brown, W-N.U. Chen, J. Bishop-Stewart, D. Gray, and I. Johnson. Chemical and physiological characterization of fluo-4 Ca2+-indicator dyes. *Cell Calcium*, 27(2):97–106, February 2000.

[122] Micah S. Siegel and Ehud Y. Isacoff. A genetically encoded optical probe of membrane voltage. *Neuron*, 19(4):735–741, 1997.

[123] Hiromi Imamura, Kim P. Huynh Nhat, Hiroko Togawa, Kenta Saito, Ryota Iino, Yasuyuki Kato-Yamada, Takeharu Nagai, and Hiroyuki Noji. Visualization of ATP levels inside single living cells with fluorescence resonance energy transfer-based genetically encoded indicators. *Proceedings of the National Academy of Sciences*, 106(37):15651–15656, 2009.

[124] Mitotracker thermofisher. `https://www.thermofisher.com/order/catalog/product/M7514`.

[125] Robert S Shankland. Michelson-morley experiment. *American Journal of Physics*, 32(1):16–35, 1964.

[126] Dic description olympus website. `http://www.olympusmicro.com/primer/techniques/dic/dicov`

[127] Half-wave liquid crystal retarder. `https://www.thorlabs.com/newgrouppage9.cfm?objectgroup_`

[128] Charlie Demené. *Cartographie vasculaire et fonctionnelle du cerveau par échographie Doppler ultrarapide chez le petit animal et le nouveau-né*. PhD thesis, Paris 7, 2015.

[129] Juliette Ben Arous, Jonas Binding, Jean-François Léger, Mariano Casado, Piotr Topilko, Sylvain Gigan, A Claude Boccara, and Laurent Bourdieu. Single myelin fiber imaging in living rodents without labeling by deep optical coherence microscopy. *Journal of biomedical optics*, 16(11):116012–1160129, 2011.

[130] Mark Davidson, Kalman Kaufman, Isaac Mazor, and Felix Cohen. An application of interference microscopy to integrated circuit inspection and metrology. In *Microlithography Conference*, pages 233–249. International Society for Optics and Photonics, 1987.

[131] Gordon S Kino and Stanley SC Chim. Mirau correlation microscope. *Applied Optics*, 29(26):3775–3783, 1990.

[132] Zhuo Wang and Gabriel Popescu. Quantitative phase imaging with broadband fields. *Applied Physics Letters*, 96(5):051117, 2010.

[133] Ibrahim Abdulhalim. Spatial and temporal coherence effects in interference microscopy and full-field optical coherence tomography. *Annalen der Physik*, 524(12):787–804, 2012.

[134] Arnaud Dubois, Juliette Selb, Laurent Vabre, and Albert-Claude Boccara. Phase measurements with wide-aperture interferometers. *Applied optics*, 39(14):2326–2331, 2000.

[135] Antoine Morin. *Tomographie par cohérence optique spectroscopique en plein champ: application à l'analyse des pigments des couches picturales*. PhD thesis, Université Pierre et Marie Curie-Paris VI, 2012.

[136] Jerome Mertz. *Introduction to optical microscopy*, volume 138. CSIRO, 2010.

[137] RA Leitgeb, Martin Villiger, AH Bachmann, Lukas Steinmann, and Theo Lasser. Extended focus depth for fourier domain optical coherence microscopy. *Optics letters*, 31(16):2450–2452, 2006.

[138] Website of d.sampson's group. `http://obel.ee.uwa.edu.au/research/fundamentals/introduct`

[139] Wolfgang Drexler, Mengyang Liu, Abhishek Kumar, Tschackad Kamali, Angelika Unterhuber, and Rainer A Leitgeb. Optical coherence tomography today: speed, contrast, and multimodality. *Journal of biomedical optics*, 19(7):071412–071412, 2014.

[140] Gerd Hausler, Michael Walter Lindner, et al. " coherence radar" and" spectral radar"-new tools for dermatological diagnosis. *Journal of biomedical optics*, 3(1):21–31, 1998.

[141] Michael A Choma, Marinko V Sarunic, Changhuei Yang, and Joseph A Izatt. Sensitivity advantage of swept source and fourier domain optical coherence tomography. *Optics express*, 11(18):2183–2189, 2003.

[142] Thomas Klein, Wolfgang Wieser, Lukas Reznicek, Aljoscha Neubauer, Anselm Kampik, and Robert Huber. Multi-mhz retinal oct. *Biomedical optics express*, 4(10):1890–1908, 2013.

[143] Website of insight company. `http://www.sweptlaser.com/3-generations-of-OCT`.

[144] Emilie Macé, Gabriel Montaldo, Ivan Cohen, Michel Baulac, Mathias Fink, and Mickael Tanter. Functional ultrasound imaging of the brain. *Nature methods*, 8(8):662–664, 2011.

[145] Claudia Errico, Juliette Pierre, Sophie Pezet, Yann Desailly, Zsolt Lenkei, Olivier Couture, and Mickael Tanter. Ultrafast ultrasound localization microscopy for deep super-resolution vascular imaging. *Nature*, 527(7579):499–502, 2015.

[146] XJ Wang, TE Milner, and JS Nelson. Characterization of fluid flow velocity by optical doppler tomography. *Optics letters*, 20(11):1337–1339, 1995.

[147] Zhongping Chen, Thomas E Milner, Shyam Srinivas, Xiaojun Wang, Arash Malekafzali, Martin JC van Gemert, and J Stuart Nelson. Noninvasive imaging of in vivo blood flow velocity using optical doppler tomography. *Optics letters*, 22(14):1119–1121, 1997.

[148] Rainer Leitgeb, Leopold F Schmetterer, Maciej Wojtkowski, Christoph K Hitzenberger, Markus Sticker, and Adolf F Fercher. Flow velocity measurements by frequency domain short coherence interferometry. In *International Symposium on Biomedical Optics*, pages 16–21. International Society for Optics and Photonics, 2002.

[149] Yonghua Zhao, Zhongping Chen, Christopher Saxer, Shaohua Xiang, Johannes F de Boer, and J Stuart Nelson. Phase-resolved optical coherence tomography and optical doppler tomography for imaging blood flow in human skin with fast scanning speed and high velocity sensitivity. *Optics letters*, 25(2):114–116, 2000.

[150] Rainer A Leitgeb, René M Werkmeister, Cedric Blatter, and Leopold Schmetterer. Doppler optical coherence tomography. *Progress in retinal and eye research*, 41:26–43, 2014.

[151] Arno Bouwens, Daniel Szlag, Maciej Szkulmowski, Tristan Bolmont, Maciej Wojtkowski, and Theo Lasser. Quantitative lateral and axial flow imaging with optical coherence microscopy and tomography. *Optics express*, 21(15):17711–17729, 2013.

[152] Vivek J Srinivasan, Sava Sakadžić, Iwona Gorczynska, Svetlana Ruvinskaya, Weicheng Wu, James G Fujimoto, and David A Boas. Quantitative cerebral blood flow with optical coherence tomography. *Optics express*, 18(3):2477–2494, 2010.

[153] Corinne Berclaz, Daniel Szlag, David Nguyen, Jérôme Extermann, Arno Bouwens, Paul J Marchand, Julia Nilsson, Anja Schmidt-Christensen, Dan Holmberg, Anne Grapin-Botton, et al. Label-free fast 3-d coherent imaging reveals pancreatic islet microvascularization and dynamic blood flow. *Biomedical Optics Express*, 7(11):4569–4580, 2016.

[154] Vivek J Srinivasan, Emiri T Mandeville, Anil Can, Francesco Blasi, Mihail Climov, Ali Daneshmand, Jeong Hyun Lee, Esther Yu, Harsha Radhakrishnan, Eng H Lo, et al. Multiparametric, longitudinal optical coherence tomography imaging reveals acute injury and chronic recovery in experimental ischemic stroke. *PloS one*, 8(8):e71478, 2013.

[155] Shau Poh Chong, Conrad W Merkle, Conor Leahy, Harsha Radhakrishnan, and Vivek J Srinivasan. Quantitative microvascular hemoglobin mapping using visible light spectroscopic optical coherence tomography. *Biomedical optics express*, 6(4):1429–1450, 2015.

[156] Website of neec group on eye research. `http://www.neec.com/Pages/Services/Imaging/OCT.php`.

[157] Louis Gagnon, Sava Sakadžić, Fréderic Lesage, Emiri T Mandeville, Qianqian Fang, Mohammad A Yaseen, and David A Boas. Multimodal reconstruction of microvascular-flow distributions using combined two-photon microscopy and doppler optical coherence tomography. *Neurophotonics*, 2(1):015008–015008, 2015.

[158] Thu-Mai Nguyen, Bastien Arnal, Shaozhen Song, Zhihong Huang, Ruikang K Wang, and Matthew O'Donnell. Shear wave elastography using amplitude-modulated acoustic radiation force and phase-sensitive optical coherence tomography. *Journal of biomedical optics*, 20(1):016001–016001, 2015.

[159] Shaozhen Song, Zhihong Huang, Thu-Mai Nguyen, Emily Y Wong, Bastien Arnal, Matthew O'Donnell, and Ruikang K Wang. Shear modulus imaging by direct visualization of propagating shear waves with phase-sensitive optical coherence tomography. *Journal of biomedical optics*, 18(12):121509–121509, 2013.

[160] Commercial system lltech. `http://www.lltechimaging.com/products-applications/products/`

[161] Clinical atlas lltech. `http://www.lltechimaging.com/image-gallery/atlas-of-images/`.

[162] E Ilegems, PP Van Krieken, PK Edlund, A Dicker, T Alanentalo, Maria Eriksson, S Mandic, Ulf Ahlgren, and P-O Berggren. Light scattering as an intrinsic indicator for pancreatic islet cell mass and secretion. *Scientific reports*, 5:10740, 2015.

[163] Manu Jain, Brian D Robinson, Bekheit Salamoon, Olivier Thouvenin, Claude Boccara, and Sushmita Mukherjee. Rapid evaluation of fresh ex vivo kidney tissue with full-field optical coherence tomography. *Journal of pathology informatics*, 6, 2015.

[164] B Karamata, P Lambelet, M Laubscher, RP Salathé, and T Lasser. Spatially incoherent illumination as a mechanism for cross-talk suppression in wide-field optical coherence tomography. *Optics letters*, 29(7):736–738, 2004.

[165] Peng Xiao, Mathias Fink, and A Claude Boccara. Full-field spatially incoherent illumination interferometry: a spatial resolution almost insensitive to aberrations. *Optics Letters*, 41(17):3920–3923, 2016.

[166] Joseph A Izatt, Eric A Swanson, James G Fujimoto, Michael R Hee, and Gabrielle M Owen. Optical coherence microscopy in scattering media. *Optics letters*, 19(8):590–592, 1994.

[167] Adolph F Fercher, Ch K Hitzenberger, G Kamp, and Sy Y El-Zaiat. Measurement of intraocular distances by backscattering spectral interferometry. *Optics Communications*, 117(1):43–48, 1995.

[168] Johannes F De Boer, Barry Cense, B Hyle Park, Mark C Pierce, Guillermo J Tearney, and Brett E Bouma. Improved signal-to-noise ratio in spectral-domain compared with time-domain optical coherence tomography. *Optics letters*, 28(21):2067–2069, 2003.

[169] Michael Pircher, Erich Götzinger, and Christoph K Hitzenberger. Dynamic focus in optical coherence tomography for retinal imaging. *Journal of biomedical optics*, 11(5):054013–054013, 2006.

[170] Jon Holmes, Simon Hattersley, Nick Stone, Florian Bazant-Hegemark, and Hugh Barr. Multi-channel fourier domain oct system with superior lateral resolution for biomedical applications. In *Biomedical Optics (BiOS) 2008*, pages 68470O–68470O. International Society for Optics and Photonics, 2008.

[171] Zhihua Ding, Hongwu Ren, Yonghua Zhao, J Stuart Nelson, and Zhongping Chen. High-resolution optical coherence tomography over a large depth range with an axicon lens. *Optics Letters*, 27(4):243–245, 2002.

[172] Tyler S Ralston, Daniel L Marks, P Scott Carney, and Stephen A Boppart. Interferometric synthetic aperture microscopy. *Nature Physics*, 3(2):129–134, 2007.

[173] SM Shams Kazmi, Rebecca K Wu, and Andrew K Dunn. Evaluating multi-exposure speckle imaging estimates of absolute autocorrelation times. *Optics letters*, 40(15):3643–3646, 2015.

[174] Benjamin Potsaid, Iwona Gorczynska, Vivek J Srinivasan, Yueli Chen, James Jiang, Alex Cable, and James G Fujimoto. Ultrahigh speed spectral/fourier domain oct ophthalmic imaging at 70,000 to 312,500 axial scans per second. *Optics express*, 16(19):15149–15169, 2008.

[175] Kate Grieve, Arnaud Dubois, Manuel Simonutti, Michel Paques, José Sahel, Jean-François Le Gargasson, and Claude Boccara. In vivo anterior segment imaging in the rat eye with high speed white light full-field optical coherence tomography. *Optics express*, 13(16):6286–6295, 2005.

[176] Mafalda Correia, Jean Provost, Simon Chatelin, Olivier Villemain, Mickael Tanter, and Mathieu Pernot. Ultrafast harmonic coherent compound (uhcc) imaging for high frame rate echocardiography and shear-wave elastography. *IEEE transactions on ultrasonics, ferroelectrics, and frequency control*, 63(3):420–431, 2016.

[177] Amaury Badon, Dayan Li, Geoffroy Lerosey, A Claude Boccara, Mathias Fink, and Alexandre Aubry. Smart optical coherence tomography for ultra-deep imaging through highly scattering media. *Science Advances*, 2(11):e1600370, 2016.

[178] Clement Apelian, Fabrice Harms, Olivier Thouvenin, and A. Claude Boccara. Dynamic full field optical coherence tomography: subcellular metabolic contrast revealed in tissues by temporal analysis of interferometric signals. *arXiv preprint arXiv:1601.01208*, 2016.

[179] Manu Jain, Nidhi Shukla, Maryem Manzoor, Sylvie Nadolny, Sushmita Mukherjee, et al. Modified full-field optical coherence tomography: A novel tool for rapid histology of tissues. *Journal of pathology informatics*, 2(1):28, 2011.

[180] Kate Grieve, Karima Mouslim, Osnath Assayag, Eugénie Dalimier, Fabrice Harms, Alexis Bruhat, Claude Boccara, and Martine Antoine. Assessment of sentinel node biopsies with full-field optical coherence tomography. *Technology in cancer research & treatment*, 15(2):266–274, 2016.

[181] Frederic De Leeuw, Odile Casiraghi, Aïcha Ben Lakhdar, Muriel Abbaci, and Corinne Laplace-Builhé. Full-field oct for fast diagnostic of head and neck cancer. In *SPIE BiOS*, pages 93031Z–93031Z. International Society for Optics and Photonics, 2015.

[182] C Yang, R Ricco, A Sisk, A Duc, M Sibony, F Beuvon, E Dalimier, and N Barry Delongchamps. High efficiency for prostate biopsy qualification with full-field oct after training. In *SPIE BiOS*, pages 96891J–96891J. International Society for Optics and Photonics, 2016.

[183] Kate Grieve, Cristina Georgeon, Felipe Andreiuolo, Marie Borderie, Djida Ghoubay, Josette Rault, and Vincent M. Borderie. Imaging Microscopic Features of Keratoconic Corneal Morphology. *Cornea*, 35(12):1621, 2016.

[184] Osnath Assayag, Kate Grieve, Bertrand Devaux, Fabrice Harms, Johan Pallud, Fabrice Chretien, Claude Boccara, and Pascale Varlet. Imaging of non-tumorous and tumorous human brain tissues with full-field optical coherence tomography. *NeuroImage: Clinical*, 2:549–557, 2013.

[185] Osnath Assayag, Martine Antoine, Brigitte Sigal-Zafrani, Michael Riben, Fabrice Harms, Adriano Burcheri, Kate Grieve, Eugénie Dalimier, Bertrand Le Conte de Poly, and Claude Boccara. Large field, high resolution full-field optical coherence tomography: a pre-clinical study of human breast tissue and cancer assessment. *Technology in cancer research & treatment*, 13(5):455–468, 2014.

[186] Inge T. A. Peters, Paulien L. Stegehuis, Ronald Peek, Florine L. Boer, Erik W. van Zwet, Jeroen Eggermont, Johan R. Westphal, Peter J. K. Kuppen, J. Baptist M. Z. Trimbos, Carina G. J. M. Hilders, Boudewijn PF Lelieveldt, Cornelis J. H. van de Velde, Tjalling Bosse, Jouke Dijkstra, and Alexander L. Vahrmeijer. Non-invasive detection of metastases and follicle density in ovarian tissue using full-field optical coherence tomography. *Clinical Cancer Research*, page clincanres.0288.2016, 2016.

[187] Egidijus Auksorius, Yaron Bromberg, R?ta Motiej?nait?, Alberto Pieretti, Linbo Liu, Emmanuel Coron, Jorge Aranda, Allan M. Goldstein, Brett E. Bouma, Andrius Kazlauskas, and Guillermo J. Tearney. Dual-modality fluorescence and full-field optical coherence microscopy for biomedical imaging applications. *Biomedical Optics Express*, 3(3):661–666, 2012.

[188] Amir Nahas, Mariana Varna, Emmanuel Fort, and A Claude Boccara. Detection of plasmonic nanoparticles with full field-oct: optical and photothermal detection. *Biomedical optics express*, 5(10):3541–3546, 2014.

[189] Amir Nahas, Morgane Bauer, Stéphane Roux, and A Claude Boccara. 3-d static elastography at the micrometer scale using full field oct. *Biomedical optics express*, 4(10):2138–2149, 2013.

[190] Gael Moneron, Albert-Claude Boccara, and Arnaud Dubois. Polarization-sensitive full-field optical coherence tomography. *Optics letters*, 32(14):2058–2060, 2007.

[191] Lingfeng Yu and M Kim. Full-color three-dimensional microscopy by wide-field optical coherence tomography. *Optics express*, 12(26):6632–6641, 2004.

[192] Antoine Federici and Arnaud Dubois. Three-band, 1.9-μm axial resolution full-field optical coherence microscopy over a 530–1700 nm wavelength range using a single camera. *Optics letters*, 39(6):1374–1377, 2014.

[193] Arnaud Dubois, Julien Moreau, and Claude Boccara. Spectroscopic ultrahigh-resolution full-field optical coherence microscopy. *Optics express*, 16(21):17082–17091, 2008.

[194] Paolo Mandrioli and Annalisa Ariatti. Marcello malpighi, a pioneer of the experimental research in biology. *Aerobiologia*, 7(1):3–9, 1991.

[195] Rafael Romero Reverón. Marcello malpighi (1628-1694), founder of microanatomy. *Int. J. Morphol*, 29(2):399–402, 2011.

[196] M Arif Hayat et al. *Principles and techniques of scanning electron microscopy. Biological applications. Volume 1.* Van Nostrand Reinhold Company., 1974.

[197] Digital microscope. `http://www.histology.be/digital_microscope_histology_.html`.

[198] Histology guide: virtual histology lab. `http://histologyguide.org/index.html`.

[199] Katrin Amunts, Claude Lepage, Louis Borgeat, Hartmut Mohlberg, Timo Dickscheid, Marc-Étienne Rousseau, Sebastian Bludau, Pierre-Louis Bazin, Lindsay B Lewis, Ana-Maria Oros-Peusquens, et al. Bigbrain: an ultrahigh-resolution 3-d human brain model. *Science*, 340(6139):1472–1475, 2013.

[200] James L. Hiatt PhD Leslie P. Gartner PhD. *Color Atlas and Text of Histology*. Lippincott Williams and Wilkins, sixth, north american edition edition, 2013.

[201] Arthur Clarkson (Auth.). *A Text-Book of Histology. Descriptive and Practical. For the Use of Students*. Bristol: John Wright, London: Simpkin, Marshall, Hamilton, Kent, 1986.

[202] Patrice F. Spitalnik. *Histology Lab Manual*. Columbia University, 2015.

[203] Caroline Magnain, Jean C Augustinack, Ender Konukoglu, Matthew P Frosch, Sava Sakadžić, Ani Varjabedian, Nathalie Garcia, Van J Wedeen, David A , and Bruce Fischl. Optical coherence tomography visualizes neurons in human entorhinal cortex. *Neurophotonics*, 2(1):015004–015004, 2015.

[204] Hui Wang, Junfeng Zhu, and Taner Akkin. Serial optical coherence scanner for large-scale brain imaging at microscopic resolution. *Neuroimage*, 84:1007–1017, 2014.

[205] Michael Quinten. *Optical Properties of Nanoparticle Systems: Mie and Beyond*. John Wiley & Sons, 2010.

[206] Kate Grieve, Olivier Thouvenin, Abhishek Sengupta, Vincent M. Borderie, and Michel Paques. Appearance of the Retina With Full-Field Optical Coherence Tomography. *Investigative Opthalmology & Visual Science*, 57(9):OCT96, 2016.

[207] Shang Wang, Chih-Hao Liu, Valery P Zakharov, Alexander J Lazar, Raphael E Pollock, and Kirill V Larin. Three-dimensional computational analysis of optical coherence tomography images for the detection of soft tissue sarcomas. *Journal of biomedical optics*, 19(2):021102–021102, 2014.

[208] Stephen A Boppart, Wei Luo, Daniel L Marks, and Keith W Singletary. Optical coherence tomography: feasibility for basic research and image-guided surgery of breast cancer. *Breast cancer research and treatment*, 84(2):85–97, 2004.

[209] Robert A McLaughlin, Loretta Scolaro, Peter Robbins, Saud Hamza, Christobel Saunders, and David D Sampson. Imaging of human lymph nodes using optical coherence tomography: potential for staging cancer. *Cancer research*, 70(7):2579–2584, 2010.

[210] Benjamin J Vakoc, Dai Fukumura, Rakesh K Jain, and Brett E Bouma. Cancer imaging by optical coherence tomography: preclinical progress and clinical potential. *Nature Reviews Cancer*, 12(5):363–368, 2012.

[211] M Sharma, Y Verma, KD Rao, R Nair, and PK Gupta. Imaging growth dynamics of tumour spheroids using optical coherence tomography. *Biotechnology letters*, 29(2):273–278, 2007.

[212] Benjamin J Vakoc, Ryan M Lanning, James A Tyrrell, Timothy P Padera, Lisa A Bartlett, Triantafyllos Stylianopoulos, Lance L Munn, Guillermo J Tearney, Dai Fukumura, Rakesh K Jain, et al. Three-dimensional microscopy of the tumor microenvironment in vivo using optical frequency domain imaging. *Nature medicine*, 15(10):1219–1223, 2009.

[213] Wanrong Gao and Yue Zhu. Fractal analysis of en face tomographic images obtained with full field optical coherence tomography. *Annalen der Physik*, 2016.

[214] Olivier Thouvenin, Clement Apelian, Amir Nahas, Mathias Fink, and Claude Boccara. Full-field optical coherence tomography as a diagnosis tool: Recent progress with multimodal imaging. *Applied Sciences (2076-3417)*, 7(3), 2017.

[215] Marinko V Sarunic, Seth Weinberg, and Joseph A Izatt. Full-field swept-source phase microscopy. *Optics letters*, 31(10):1462–1464, 2006.

[216] Dierck Hillmann, Hendrik Spahr, Carola Hain, Helge Sudkamp, Gesa Franke, Clara Pfäffle, Christian Winter, and Gereon Hüttmann. Aberration-free volumetric high-speed imaging of in vivo retina. *Scientific reports*, 6, 2016.

[217] JM Findlay. Frequency analysis of human involuntary eye movement. *Biological Cybernetics*, 8(6):207–214, 1971.

[218] Roy de Kinkelder, Jeroen Kalkman, Dirk J Faber, Olaf Schraa, Pauline HB Kok, Frank D Verbraak, and Ton G van Leeuwen. Heartbeat-induced axial motion artifacts in optical coherence tomography measurements of the retina. *Investigative ophthalmology & visual science*, 52(6):3908–3913, 2011.

[219] Adeel Ahmad, Nathan D Shemonski, Steven G Adie, Hee-Seok Kim, Wen-Mei W Hwu, P Scott Carney, and Stephen A Boppart. Real-time in vivo computed optical interferometric tomography. *Nature photonics*, 7(6):444–448, 2013.

[220] Nathan D Shemonski, Fredrick A South, Yuan-Zhi Liu, Steven G Adie, P Scott Carney, and Stephen A Boppart. Computational high-resolution optical imaging of the living human retina. *Nature photonics*, 9(7):440–443, 2015.

[221] Dierck Hillmann, Hendrik Spahr, Clara Pfäffle, Helge Sudkamp, Gesa Franke, and Gereon Hüttmann. In vivo optical imaging of physiological responses to photostimulation in human photoreceptors. *Proceedings of the National Academy of Sciences*, page 201606428, 2016.

[222] Agata Abramowicz, Piotr Widlak, and Monika Pietrowska. Proteomic analysis of exosomal cargo: the challenge of high purity vesicle isolation. *Molecular BioSystems*, 12(5):1407–1419, 2016.

[223] Willy Supatto, Scott E Fraser, and Julien Vermot. An all-optical approach for probing microscopic flows in living embryos. *Biophysical journal*, 95(4):L29–L31, 2008.

[224] E Beaurepaire, L Moreaux, F Amblard, and J Mertz. Combined scanning optical coherence and two-photon-excited fluorescence microscopy. *Optics Letters*, 24(14):969–971, 1999.

[225] Shuai Yuan, Celeste A Roney, Jeremiah Wierwille, Chao-Wei Chen, Biying Xu, Gary Griffiths, James Jiang, Hongzhou Ma, Alex Cable, Ronald M Summers, et al. Co-registered optical coherence tomography and fluorescence molecular imaging for simultaneous morphological and molecular imaging. *Physics in medicine and biology*, 55(1):191, 2009.

[226] F. Harms, E. Dalimier, P. Vermeulen, A. Fragola, and A. C. Boccara. Multimodal full-field optical coherence tomography on biological tissue: toward all optical digital pathology. volume 8216, pages 821609–821609–8, 2012.

[227] Houssine Makhlouf, Karen Perronet, Guillaume Dupuis, Sandrine Lévêque-Fort, and Arnaud Dubois. Simultaneous optically sectioned fluorescence and optical coherence microscopy with full-field illumination. *Optics Letters*, 37(10):1613, May 2012.

[228] JD Hicks and E Matthaei. Fluorescence in histology. *The Journal of pathology and bacteriology*, 70(1):1–12, 1955.

[229] Marilyn Gamble John D. Bancroft. *Theory and practice of histological techniques*. Churchill Livingstone, 5 edition, 2002.

[230] Emanuela V Volpi and Joanna M Bridger. Fish glossary: an overview of the fluorescence in situ hybridization technique. *Biotechniques*, 45(4):385–386, 2008.

[231] Joseph E Roulston and John MS Bartlett. *Molecular diagnosis of cancer: methods and protocols*, volume 97. Springer Science & Business Media, 2004.

[232] Pietro Transidico, Marco Bianchi, Maria Capra, Pier Giuseppe Pelicci, and Mario Faretta. From cells to tissues: fluorescence confocal microscopy in the study of histological samples. *Microscopy research and technique*, 64(2):89–95, 2004.

[233] Rafael Yuste. Fluorescence microscopy today. *Nature methods*, 2(12):902–904, 2005.

[234] Juergen C Jung, Amit D Mehta, Emre Aksay, Raymond Stepnoski, and Mark J Schnitzer. In vivo mammalian brain imaging using one-and two-photon fluorescence microendoscopy. *Journal of neurophysiology*, 92(5):3121–3133, 2004.

[235] Benjamin A Flusberg, Eric D Cocker, Wibool Piyawattanametha, Juergen C Jung, Eunice LM Cheung, and Mark J Schnitzer. Fiber-optic fluorescence imaging. *Nature methods*, 2(12):941–950, 2005.

[236] Valery V Tuchin. Optical clearing of tissues and blood using the immersion method. *Journal of Physics D: Applied Physics*, 38(15):2497, 2005.

[237] Kwanghun Chung and Karl Deisseroth. Clarity for mapping the nervous system. *Nature methods*, 10(6):508–513, 2013.

[238] Kirill V Larin, Mohamad G Ghosn, Alexey N Bashkatov, Elina A Genina, Natalia A Trunina, and Valery V Tuchin. Optical clearing for oct image enhancement and in-depth monitoring of molecular diffusion. *IEEE Journal of Selected Topics in Quantum Electronics*, 18(3):1244–1259, 2012.

[239] MAA Neil, R Juskaitis, and T Wilson. Method of obtaining optical sectioning by using structured light in a conventional microscope. *Optics letters*, 22(24):1905–1907, 1997.

[240] Frédéric Chasles. *Méthodes de modulation pour la microscopie tridimensionnelle plein champ: applications à l'imagerie d'échantillons biologiques*. PhD thesis, Paris 6, 2007.

[241] Pierre Vermeulen. *Microscopie à illumination structurée et optique adaptative pour l'imagerie de fluorescence 3-D dynamique*. PhD thesis, Université Paris-Diderot-Paris VII, 2012.

[242] Per A Stokseth. Properties of a defocused optical system. *JOSA*, 59(10):1314–1321, 1969.

[243] Mats GL Gustafsson. Nonlinear structured-illumination microscopy: wide-field fluorescence imaging with theoretically unlimited resolution. *Proceedings of the National Academy of Sciences of the United States of America*, 102(37):13081–13086, 2005.

[244] Bi-Chang Chen, Wesley R Legant, Kai Wang, Lin Shao, Daniel E Milkie, Michael W Davidson, Chris Janetopoulos, Xufeng S Wu, John A Hammer, Zhe Liu, et al. Lattice light-sheet microscopy: Imaging molecules to embryos at high spatiotemporal resolution. *Science*, 346(6208):1257998, 2014.

[245] Dan Dan, Ming Lei, Baoli Yao, Wen Wang, Martin Winterhalder, Andreas Zumbusch, Yujiao Qi, Liang Xia, Shaohui Yan, Yanlong Yang, et al. Dmd-based led-illumination super-resolution and optical sectioning microscopy. *Scientific reports*, 3:1116, 2013.

[246] Avner Safrani and Ibrahim Abdulhalim. Ultrahigh-resolution full-field optical coherence tomography using spatial coherence gating and quasi-monochromatic illumination. *Optics letters*, 37(4):458–460, 2012.

[247] E Coron, E Auksorius, A Pieretti, MM Mahé, L Liu, C Steiger, Y Bromberg, B Bouma, G Tearney, M Neunlist, et al. Full-field optical coherence microscopy is a novel technique for imaging enteric ganglia in the gastrointestinal tract. *Neurogastroenterology & Motility*, 24(12):e611–e621, 2012.

[248] Jeremy Pinnell, Simon Turner, and Simon Howell. Cardiac muscle physiology. *Continuing Education in Anaesthesia, Critical Care & Pain*, 7(3):85–88, June 2007.

[249] A. B. Arrenberg, D. Y. R. Stainier, H. Baier, and J. Huisken. Optogenetic Control of Cardiac Function. *Science*, 330(6006):971–974, November 2010.

[250] Armen P Sarvazyan, Oleg V Rudenko, Scott D Swanson, J Brian Fowlkes, and Stanislav Y Emelianov. Shear wave elasticity imaging: a new ultrasonic technology of medical diagnostics. *Ultrasound in medicine & biology*, 24(9):1419–1435, 1998.

[251] Amir Nahas, MickaÃĢl Tanter, Thu-Mai Nguyen, Jean-Marie Chassot, Mathias Fink, and A Claude Boccara. From supersonic shear wave imaging to full-field optical coherence shear wave elastography. *Journal of biomedical optics*, 18(12):121514–121514, 2013.

[252] Robert Pecora. *Dynamic light scattering: applications of photon correlation spectroscopy*. Springer Science & Business Media, 2013.

[253] Michaël Suissa, Christophe Place, E Goillot, Bruno Berge, and E Freyssingeas. Dynamic light scattering as an investigating tool to study the global internal dynamics of a living cell nucleus. *EPL (Europhysics Letters)*, 78(3):38005, 2007.

[254] Michaël Suissa, Christophe Place, Evelyne Goillot, and Eric Freyssingeas. Internal dynamics of a living cell nucleus investigated by dynamic light scattering. *The European Physical Journal E*, 26(4):435–448, 2008.

[255] Kwan Jeong, John J Turek, and David D Nolte. Volumetric motility-contrast imaging of tissue response to cytoskeletal anti-cancer drugs. *Optics Express*, 15(21):14057–14064, 2007.

[256] David D Nolte, Ran An, John Turek, and Kwan Jeong. Tissue dynamics spectroscopy for phenotypic profiling of drug effects in three-dimensional culture. *Biomedical optics express*, 3(11):2825–2841, 2012.

[257] Ran An, Chunmin Wang, John Turek, Zoltan Machaty, and David D Nolte. Biodynamic imaging of live porcine oocytes, zygotes and blastocysts for viability assessment in assisted reproductive technologies. *Biomedical optics express*, 6(3):963–976, 2015.

[258] Amy L Oldenburg, Raghav K Chhetri, Jason M Cooper, Wei-Chen Wu, Melissa A Troester, and Joseph B Tracy. Motility-, autocorrelation-, and polarization-sensitive optical coherence tomography discriminates cells and gold nanorods within 3-d tissue cultures. *Optics letters*, 38(15):2923–2926, 2013.

[259] Wei Tan, Amy L Oldenburg, James J Norman, Tejal A Desai, and Stephen A Boppart. Optical coherence tomography of cell dynamics in three-dimensional tissue models. *Optics Express*, 14(16):7159–7171, 2006.

[260] Amy L Oldenburg, Xiao Yu, Thomas Gilliss, Oluwafemi Alabi, Russell M Taylor, and Melissa A Troester. Inverse-power-law behavior of cellular motility reveals stromal–epithelial cell interactions in 3-d co-culture by oct fluctuation spectroscopy. *Optica*, 2(10):877–885, 2015.

[261] Jonghwan Lee, Weicheng Wu, James Y Jiang, Bo Zhu, and David A Boas. Dynamic light scattering optical coherence tomography. *Optics express*, 20(20):22262–22277, 2012.

[262] Huimin Chen, Elaine R Farkas, and Watt W Webb. In vivo applications of fluorescence correlation spectroscopy. *Methods in cell biology*, 89:3–35, 2008.

[263] Satoru Moritoh, Yusuke Komatsu, Tetsuo Yamamori, and Amane Koizumi. Diversity of retinal ganglion cells identified by transient gfp transfection in organotypic tissue culture of adult marmoset monkey retina. *PloS one*, 8(1):e54667, 2013.

[264] Michael Kalloniatis and Charles Luu. Visual Acuity. In Helga Kolb, Eduardo Fernandez, and Ralph Nelson, editors, *Webvision: The Organization of the Retina and Visual System*. University of Utah Health Sciences Center, Salt Lake City (UT), 1995.

[265] Seamus J Martin and Douglas R Green. Protease activation during apoptosis: death by a thousand cuts? *Cell*, 82(3):349–352, 1995.

[266] Kit for apoptosis detection from thermofisher scientific. `https://www.thermofisher.com/order/catalog/product/C10617`.

[267] Golnaz Farhat, Adrian Mariampillai, Victor XD Yang, Gregory J Czarnota, and Michael C Kolios. Detecting apoptosis using dynamic light scattering with optical coherence tomography. *Journal of biomedical optics*, 16(7):070505–070505, 2011.

[268] Benjamin Rappaz, Pierre Marquet, Etienne Cuche, Yves Emery, Christian Depeursinge, and Pierre Magistretti. Measurement of the integral refractive index and dynamic cell morphometry of living cells with digital holographic microscopy. *Optics express*, 13(23):9361–9373, 2005.

[269] Lateral displacements in piezos (website from pi, a piezoelectric manufacturer). `https://www.piceramic.com/en/piezo-technology/properties-piezo-actuators/displaceme`

[270] Daniel Merrill, Ran An, Hao Sun, Bakhtiyor Yakubov, Daniela Matei, John Turek, and David Nolte. Intracellular doppler signatures of platinum sensitivity captured by biodynamic profiling in ovarian xenografts. *Scientific reports*, 6, 2016.

[271] Clément Apelian, Clément Gastaud, and A Claude Boccara. Extracting relevant information for cancer diagnosis from dynamic full field oct through image processing and learning. In *Proc. of SPIE Vol*, volume 10053, pages 100531H–1, 2017.

[272] Ignacio Izeddin, Vincent Récamier, Lana Bosanac, Ibrahim I Cissé, Lydia Boudarene, Claire Dugast-Darzacq, Florence Proux, Olivier Bénichou, Raphaël Voituriez, Olivier Bensaude, et al. Single-molecule tracking in live cells reveals distinct target-search strategies of transcription factors in the nucleus. *Elife*, 3:e02230, 2014.

[273] Aldert Van Der Ziel. On the noise spectra of semi-conductor noise and of flicker effect. *Physica*, 16(4):359–372, 1950.

[274] Per Bak, Chao Tang, and Kurt Wiesenfeld. Self-organized criticality. *Physical review A*, 38(1):364, 1988.

[275] Habib Ammari, Francisco Romero, and Cong Shi. A signal separation technique for sub-cellular imaging using dynamic optical coherence tomography. *arXiv preprint arXiv:1608.04382*, 2016.

[276] H Björnsson and SA Venegas. A manual for eof and svd analyses of climatic data. *CCGCR Report*, 97(1):112–134, 1997.

[277] Daniele Zink, Andrew H Fischer, and Jeffrey A Nickerson. Nuclear structure in cancer cells. *Nature reviews cancer*, 4(9):677–687, 2004.

[278] DN Slater, S Rice, R Stewart, SE Melling, EM Hewer, and JHF Smith. Proposed sheffield quantitative criteria in cervical cytology to assist the grading of squamous cell dyskaryosis, as the british society for clinical cytology definitions require amendment. *Cytopathology*, 16(4):179–192, 2005.

[279] Mark J Miller, Sindy H Wei, Ian Parker, and Michael D Cahalan. Two-photon imaging of lymphocyte motility and antigen response in intact lymph node. *Science*, 296(5574):1869–1873, 2002.

[280] Eiichi Sato, Sara H Olson, Jiyoung Ahn, Brian Bundy, Hiroyoshi Nishikawa, Feng Qian, Achim A Jungbluth, Denise Frosina, Sacha Gnjatic, Christine Ambrosone, et al. Intraepithelial cd8+ tumor-infiltrating lymphocytes and a high cd8+/regulatory t cell ratio are associated with favorable prognosis in ovarian cancer. *Proceedings of the National Academy of Sciences of the United States of America*, 102(51):18538–18543, 2005.

[281] Sahar MA Mahmoud, Emma Claire Paish, Desmond G Powe, R Douglas Macmillan, Matthew J Grainge, Andrew HS Lee, Ian O Ellis, and Andrew R Green. Tumor-infiltrating cd8+ lymphocytes predict clinical outcome in breast cancer. *Journal of Clinical Oncology*, 29(15):1949–1955, 2011.

[282] Noel Weidner, PR Carroll, J Flax, W Blumenfeld, and J Folkman. Tumor angiogenesis correlates with metastasis in invasive prostate carcinoma. *The American journal of pathology*, 143(2):401, 1993.

[283] Noel Weidner. Current pathologic methods for measuring intratumoral microvessel density within breast carcinoma and other solid tumors. *Breast cancer research and treatment*, 36(2):169–180, 1995.

[284] JOHN G MAIER and DEAN T SCHAMBER. The role of lymphangiography in the diagnosis and treatment of malignant testicular tumors. *American Journal of Roentgenology*, 114(3):482–491, 1972.

[285] Gabriel Popescu, YoungKeun Park, Wonshik Choi, Ramachandra R. Dasari, Michael S. Feld, and Kamran Badizadegan. Imaging red blood cell dynamics by quantitative phase microscopy. *Blood Cells, Molecules, and Diseases*, 41(1):10–16, 2008.

[286] Natan T Shaked, Matthew T Rinehart, and Adam Wax. Quantitative phase microscopy of biological cell dynamics by wide-field digital interferometry. In *Coherent Light Microscopy*, pages 169–198. Springer, 2011.

[287] Arno Bouwens, Tristan Bolmont, Daniel Szlag, Corinne Berclaz, and Theo Lasser. Quantitative cerebral blood flow imaging with extended-focus optical coherence microscopy. *Optics letters*, 39(1):37–40, 2014.

[288] Caleb Harper and Mario Siller. Openag: a globally distributed network of food computing. *IEEE Pervasive Computing*, 14(4):24–27, 2015.

[289] Open agriculture initiative by caleb harper. http://openag.media.mit.edu/.

[290] Hao Sun, Daniel Merrill, John Turek, and David Nolte. Biodynamic profiling of three-dimensional tissue growth techniques. In *SPIE BiOS*, pages 97070S–97070S. International Society for Optics and Photonics, 2016.

[291] Mihály Kovács, Judit Tóth, Csaba Hetényi, András Málnási-Csizmadia, and James R Sellers. Mechanism of blebbistatin inhibition of myosin ii. *Journal of Biological Chemistry*, 279(34):35557–35563, 2004.

[292] To be published.

[293] Vincent Hingot, Claudia Errico, Mickael Tanter, and Olivier Couture. Subwavelength motion-correction for ultrafast ultrasound localization microscopy. *Ultrasonics*, 77:17–21, 2017.

[294] Jinyu Wang, Jean-François Léger, Jonas Binding, A Claude Boccara, Sylvain Gigan, and Laurent Bourdieu. Measuring aberrations in the rat brain by coherence-gated wavefront sensing using a linnik interferometer. *Biomedical optics express*, 3(10):2510–2525, 2012.

[295] Peng Xiao, Mathias Fink, and Albert Claude Boccara. Adaptive optics full-field optical coherence tomography. *Journal of Biomedical Optics*, 21(12):121505–121505, 2016.

[296] Junzhong Liang, David R Williams, and Donald T Miller. Supernormal vision and high-resolution retinal imaging through adaptive optics. *JOSA A*, 14(11):2884–2892, 1997.

[297] Jungtae Rha, Ravi S Jonnal, Karen E Thorn, Junle Qu, Yan Zhang, and Donald T Miller. Adaptive optics flood-illumination camera for high speed retinal imaging. *Optics express*, 14(10):4552–4569, 2006.

[298] Lyndell L Lim MBBS FRANZCO and David J Wilson. The role of choroidal and retinal biopsies in the diagnosis and management of atypical presentations of uveitis. *Trans Am Ophthalmol Soc*, 103:84–92, 2005.

[299] Paul Lee and W Richard Green. Corneal biopsy: Indications, techniques, and a report of a series of 87 cases. *Ophthalmology*, 97(6):718–721, 1990.

[300] Peng Xiao, Mathias Fink, and A Claude Boccara. Retinal imaging with adaptive optics full-field oct. In *Proc. of SPIE Vol*, volume 10053, pages 100530K–1, 2017.

[301] Viacheslav Mazlin, Eugénie Dalimier, Kate Grieve, Kristina Irsch, José Sahel, Mathias Fink, and Claude Boccara. Non-contact full-field optical coherence tomography: A step towards in-vivo cellular-level imaging of the human cornea. In *Imaging Systems and Applications*, pages IM3F–3. Optical Society of America, 2016.

[302] EH Polley and C Walsh. A technique for flat embedding and en face sectioning of the mammalian retina for autoradiography. *Journal of neuroscience methods*, 12(1):57–64, 1984.

[303] Keith M Meek and Carlo Knupp. Corneal structure and transparency. *Progress in retinal and eye research*, 49:1–16, 2015.

[304] Margaret TT Wong-Riley. Energy metabolism of the visual system. *Eye and brain*, 2:99, 2010.

[305] Wikipedia page on the fovea. https://en.wikipedia.org/wiki/Fovea_centralis.

[306] Philippe Gain, Rémy Jullienne, Zhiguo He, Mansour Aldossary, Sophie Acquart, Fabrice Cognasse, and Gilles Thuret. Global survey of corneal transplantation and eye banking. *JAMA ophthalmology*, 134(2):167–173, 2016.

[307] Gustavo Souto Maior Figueiredo, Mark Neville Arthur Jones, Yamini Krishna, Francisco Carlos D'Amorim Figueiredo, Daniel Frank P Larkin, Stephen Bruce Kaye, National Health Service Blood, Transplant Ocular Tissue Advisory Group, and OTAG Audit Study. Transplant rejection following endothelial keratoplasty and penetrating keratoplasty in the united kingdom: incidence and survival. *American journal of ophthalmology*, 160(3):416–421, 2015.

[308] Aurélien Tidu, Djida Ghoubay-Benallaoua, Barbara Lynch, Bernard Haye, Corinne Illoul, Jean-Marc Allain, Vincent M Borderie, and Gervaise Mosser. Development of human corneal epithelium on organized fibrillated transparent collagen matrices synthesized at high concentration. *Acta biomaterialia*, 22:50–58, 2015.

[309] Helga Kolb. How the retina works. *American scientist*, 91(1):28–35, 2003.

[310] Eric R Kandel, James H Schwartz, Thomas M Jessell, Steven A Siegelbaum, and A James Hudspeth. *Principles of neural science*, volume 4. McGraw-hill New York, 2000.

[311] Kristina Irsch, Marie Borderie, Kate Grieve, Karsten Plamann, Laurent Laroche, and Vincent M Borderie. Objective analysis of stromal light backscattering with full-field optical coherence tomographic microscopy shows potential to quantify corneal transparency. In *Frontiers in Optics*, pages FW6A–6. Optical Society of America, 2015.

[312] René M Werkmeister, Sabina Sapeta, Doreen Schmidl, Gerhard Garhöfer, Gerald Schmidinger, Valentin Aranha dos Santos, Gerold C Aschinger, Isabella Baumgartner, Niklas Pircher, Florian Schwarzhans, et al. Ultrahigh-resolution oct imaging of the human cornea. *Biomedical Optics Express*, 8(2):1221–1239, 2017.

[313] Philipp Eberwein and Thomas Reinhard. Concise reviews: the role of biomechanics in the limbal stem cell niche: new insights for our understanding of this structure. *Stem Cells*, 33(3):916–924, 2015.

[314] Linda J Müller, Carl F Marfurt, Friedrich Kruse, and Timo MT Tervo. Corneal nerves: structure, contents and function. *Experimental eye research*, 76(5):521–542, 2003.

[315] Andrew J Rozsa and Roger W Beuerman. Density and organization of free nerve endings in the corneal epithelium of the rabbit. *Pain*, 14(2):105–120, 1982.

[316] Luis Pérez De Sevilla Müller, Jennifer Shelley, and Reto Weiler. Displaced amacrine cells of the mouse retina. *Journal of Comparative Neurology*, 505(2):177–189, 2007.

[317] KAREEM M AHMAD, KARL KLUG, STEVE HERR, PETER STERLING, and STAN SCHEIN. Cell density ratios in a foveal patch in macaque retina. *Visual neuroscience*, 20(02):189–209, 2003.

[318] Mónica Garcá, Javier Ruiz-Ederra, Henesto Hernández-Barbáchano, and Elena Vecino. Topography of pig retinal ganglion cells. *Journal of Comparative Neurology*, 486(4):361–372, 2005.

[319] Kenneth C Wikler and Pasko Rakic. Distribution of photoreceptor subtypes in the retina of diurnal and nocturnal primates. *Journal of Neuroscience*, 10(10):3390–3401, 1990.

[320] Andrej Pavlovič and Stefano Mancuso. Electrical signaling and photosynthesis: Can they co-exist together? *Plant signaling & behavior*, 6(6):840–842, 2011.

[321] Plant electrophysiology by backyardbrains. https://backyardbrains.com/experiments/Plants.

[322] Eric R Kandel. *In search of memory: The emergence of a new science of mind*. WW Norton & Company, 2007.

[323] Lecture on neurobiology. http://psych.lf1.cuni.cz/bpen/neurobiology.htm.

[324] Ching Kung and Roger Eckert. Genetic modification of electric properties in an excitable membrane. *Proceedings of the National Academy of Sciences*, 69(1):93–97, 1972.

[325] Luc J Gentet, Greg J Stuart, and John D Clements. Direct measurement of specific membrane capacitance in neurons. *Biophysical journal*, 79(1):314–320, 2000.

[326] Rob Phillips, Jane Kondev, Julie Theriot, and Hernan Garcia. *Physical biology of the cell*. Garland Science, 2012.

[327] MJ Gillespie and RB Stein. The relationship between axon diameter, myelin thickness and conduction velocity during atrophy of mammalian peripheral nerves. *Brain research*, 259(1):41–56, 1983.

[328] WAH Rushton. A theory of the effects of fibre size in medullated nerve. *The Journal of physiology*, 115(1):101, 1951.

[329] Simon B Laughlin, Rob R de Ruyter van Steveninck, and John C Anderson. The metabolic cost of neural information. *Nature neuroscience*, 1(1):36–41, 1998.

[330] Alan L Hodgkin and Bernard Katz. The effect of sodium ions on the electrical activity of the giant axon of the squid. *The Journal of physiology*, 108(1):37, 1949.

[331] Bertil Hille et al. *Ion channels of excitable membranes*, volume 507. Sinauer Sunderland, MA, 2001.

[332] Harvey Lodish, Arnold Berk, S Lawrence Zipursky, Paul Matsudaira, David Baltimore, and James Darnell. The action potential and conduction of electric impulses. 2000.

[333] Shangyou Zeng. *Spatial distribution and function of ion channels on neural axon*. PhD thesis, Ohio University, 2005.

[334] Allan L Hodgkin and Andrew F Huxley. Currents carried by sodium and potassium ions through the membrane of the giant axon of loligo. *The Journal of physiology*, 116(4):449, 1952.

[335] AL Hodgkin and AF Huxley. The components of membrane conductance in the giant axon of loligo. *The Journal of physiology*, 116(4):473–496, 1952.

[336] Alan L Hodgkin and Andrew F Huxley. A quantitative description of membrane current and its application to conduction and excitation in nerve. *The Journal of physiology*, 117(4):500, 1952.

[337] Introduction to bioelectricity. course by pedro irazoqui on youtube and edx. https://www.youtube.com/watch?v=iEZPTBMU4Rc.

[338] Marat M Rvachev. On axoplasmic pressure waves and their possible role in nerve impulse propagation. *Biophysical Reviews and Letters*, 5(02):73–88, 2010.

[339] Søren SL Andersen, Andrew D Jackson, and Thomas Heimburg. Towards a thermodynamic theory of nerve pulse propagation. *Progress in neurobiology*, 88(2):104–113, 2009.

[340] Christopher Fang-Yen and Michael S Feld. Intrinsic optical signals in neural tissues: measurements, mechanisms, and applications. ACS Publications, 2007.

[341] DK Hill and RD Keynes. Opacity changes in stimulated nerve. *The Journal of Physiology*, 108(3):278, 1949.

[342] LB Cohen, RD Keynes, and Bertil Hille. Light scattering and birefringence changes during nerve activity. *Nature*, 218(5140):438–441, 1968.

[343] RA Stepnoski, A LaPorta, F Raccuia-Behling, GE Blonder, RE Slusher, and D Kleinfeld. Noninvasive detection of changes in membrane potential in cultured neurons by light scattering. *Proceedings of the National Academy of Sciences*, 88(21):9382–9386, 1991.

[344] Amanda J Foust and David M Rector. Optically teasing apart neural swelling and depolarization. *Neuroscience*, 145(3):887–899, 2007.

[345] David Kleinfeld and Arthur LaPorta. Detection of action potentials in vitro by changes in refractive index. *Light Scattering Imaging of Neural Tissue Function. Humana Press, Totowa, New Jersey*, 2003.

[346] I Tasaki, A Watanabe, and M Hallett. Fluorescence of squid axon membrane labelled with hydrophobic probes. *Journal of Membrane Biology*, 8(1):109–132, 1972.

[347] I Tasaki, A Watanabe, R Sandlin, and L Carnay. Changes in fluorescence, turbidity, and birefringence associated with nerve excitation. *Proceedings of the National Academy of Sciences*, 61(3):883–888, 1968.

[348] Denis Le Bihan. The 'wet mind': water and functional neuroimaging. *Physics in medicine and biology*, 52(7):R57, 2007.

[349] K Iwasa and I Tasaki. Mechanical changes in squid giant axons associated with production of action potentials. *Biochemical and biophysical research communications*, 95(3):1328–1331, 1980.

[350] GH Kim, P Kosterin, AL Obaid, and BM Salzberg. A mechanical spike accompanies the action potential in mammalian nerve terminals. *Biophysical journal*, 92(9):3122–3129, 2007.

[351] Alfredo Gonzalez-Perez, Lars D Mosgaard, Rima Budvytyte, Edgar Villagran-Vargas, Andrew D Jackson, and Thomas Heimburg. Solitary electromechanical pulses in lobster neurons. *Biophysical Chemistry*, 216:51–59, 2016.

[352] Ping-Cheng Zhang, Asbed M Keleshian, and Frederick Sachs. Voltage-induced membrane movement. *Nature*, 413(6854):428–432, 2001.

[353] Jonghwan Lee and Sung June Kim. Spectrum measurement of fast optical signal of neural activity in brain tissue and its theoretical origin. *Neuroimage*, 51(2):713–722, 2010.

[354] Christian Fillafer, Matan Mussel, Julia Muchowski, and Matthias F Schneider. On cell surface deformation during an action potential. *arXiv preprint arXiv:1703.04608*, 2017.

[355] I Tasaki and PM Byrne. Volume expansion of nonmyelinated nerve fibers during impulse conduction. *Biophysical journal*, 57(3):633–635, 1990.

[356] Taner Akkin, Digant P Davé, Thomas E Milner, and H Grady Rylander III. Detection of neural activity using phase-sensitive optical low-coherence reflectometry. *Optics Express*, 12(11):2377–2386, 2004.

[357] Benedikt W Graf, Tyler S Ralston, Han-Jo Ko, and Stephen A Boppart. Detecting intrinsic scattering changes correlated to neuron action potentials using optical coherence imaging. *Optics express*, 17(16):13447–13457, 2009.

[358] VJ Srinivasan, Y Chen, JS Duker, and JG Fujimoto. In vivo functional imaging of intrinsic scattering changes in the human retina with high-speed ultrahigh resolution oct. *Optics express*, 17(5):3861–3877, 2009.

[359] K Bizheva, Renate Pflug, Boris Hermann, Boris Považay, H Sattmann, P Qiu, E Anger, H Reitsamer, Sergei Popov, JR Taylor, et al. Optophysiology: depth-resolved probing of retinal physiology with functional ultrahigh-resolution optical coherence tomography. *Proceedings of the National Academy of Sciences of the United States of America*, 103(13):5066–5071, 2006.

[360] LB Cohen, RD Keynes, and D Landowne. Changes in light scattering that accompany the action potential in squid giant axons: potential-dependent components. *The Journal of physiology*, 224(3):701, 1972.

[361] Jennifer L Schei, Matthew D McCluskey, Amanda J Foust, Xin-Cheng Yao, and David M Rector. Action potential propagation imaged with high temporal resolution near-infrared video microscopy and polarized light. *Neuroimage*, 40(3):1034–1043, 2008.

[362] Ichiji Tasaki and Paul M Byrne. Heat production associated with a propagated impulse in bullfrog myelinated nerve fibers. *The Japanese journal of physiology*, 42(5):805–813, 1992.

[363] JM Ritchie and RD Keynes. The production and absorption of heat associated with electrical activity in nerve and electric organ. *Quarterly reviews of biophysics*, 18(4):451–476, 1985.

[364] A very nice wikipedia page where the action of general anaesthetic is discussed. `https://en.wikipedia.org/wiki/Theories_of_general_anaesthetic_action`.

[365] Thomas Heimburg and Andrew D Jackson. On the action potential as a propagating density pulse and the role of anesthetics. *Biophysical Reviews and Letters*, 2(01):57–78, 2007.

[366] Ichiji Tasaki. Collision of two nerve impulses in the nerve fibre. *Biochimica et biophysica acta*, 3:494–497, 1949.

[367] Alfredo Gonzalez-Perez, Rima Budvytyte, Lars D Mosgaard, Søren Nissen, and Thomas Heimburg. Penetration of action potentials during collision in the median and lateral giant axons of invertebrates. *Physical Review X*, 4(3):031047, 2014.

[368] Rosangela Follmann, Epaminondas Rosa Jr, and Wolfgang Stein. Dynamics of signal propagation and collision in axons. *Physical Review E*, 92(3):032707, 2015.

[369] Christian Fillafer, Anne Paeger, and Matthias F Schneider. Collision of two action potentials in a single excitable cell. *arXiv preprint arXiv:1704.00118*, 2017.

[370] Jerel K Mueller and William J Tyler. A quantitative overview of biophysical forces impinging on neural function. *Physical biology*, 11(5):051001, 2014.

[371] Stuart Ibsen, Ada Tong, Carolyn Schutt, Sadik Esener, and Sreekanth H Chalasani. Sonogenetics is a non-invasive approach to activating neurons in caenorhabditis elegans. *Nature communications*, 6, 2015.

[372] William J Tyler, Yusuf Tufail, Michael Finsterwald, Monica L Tauchmann, Emily J Olson, and Cassondra Majestic. Remote excitation of neuronal circuits using low-intensity, low-frequency ultrasound. *PloS one*, 3(10):e3511, 2008.

[373] Marat M Rvachev. Alternative model of propagation of spikes along neurons. *arXiv preprint physics/0301063*, 2003.

[374] Helmut Barz and Ulrich Barz. Pressure waves in neurons and their relationship to tangled neurons and plaques. *Medical hypotheses*, 82(5):563–566, 2014.

[375] Ahmed El Hady and Benjamin B Machta. Mechanical surface waves accompany action potential propagation. *Nature communications*, 6, 2015.

[376] Lars D Mosgaard, Karis A Zecchi, and Thomas Heimburg. Mechano-capacitive properties of polarized membranes. *Soft matter*, 11(40):7899–7910, 2015.

[377] Thomas Heimburg and Andrew D Jackson. On soliton propagation in biomembranes and nerves. *Proceedings of the National Academy of Sciences of the United States of America*, 102(28):9790–9795, 2005.

[378] Revathi Appali, Ursula van Rienen, and Thomas Heimburg. A comparison of the hodgkin-huxley model and the soliton theory for the action potential in nerves. *Advances in planar lipid bilayers and liposomes*, 16:275–299, 2012.

[379] T Heimburg, A Blicher, LD Mosgaard, and K Zecchi. Electromechanical properties of biomembranes and nerves. In *Journal of Physics: Conference Series*, volume 558, page 012018. IOP Publishing, 2014.

[380] Andrew F MacAskill and Josef T Kittler. Control of mitochondrial transport and localization in neurons. *Trends in cell biology*, 20(2):102–112, 2010.

[381] Hyeon Jeong Lee, Delong Zhang, Ying Jiang, Xiangbing Wu, Pei-Yu Shih, Chien-Sheng Liao, Brittani Bungart, Xiao-Ming Xu, Ryan M Drenan, Edward Bartlett, et al. Label-free vibrational spectroscopic imaging of neuronal membrane potential. *The Journal of Physical Chemistry Letters*, 2017.

[382] Subrata Batabyal, Sarmishtha Satpathy, Loan Bui, Young-Tae Kim, Samarendra K Mohanty, and Digant P Davé. Label-free optical detection of action potential in mammalian neurons (conference presentation). In *SPIE BiOS*, pages 1005205–1005205. International Society for Optics and Photonics, 2017.

[383] Leonard Best, Peter D Brown, Abdullah Sener, and Willy J Malaisse. Electrical activity in pancreatic islet cells: the vrac hypothesis. *Islets*, 2(2):59–64, 2010.

[384] Jonas Binding, Juliette Ben Arous, Jean-François Léger, Sylvain Gigan, Claude Boccara, and Laurent Bourdieu. Brain refractive index measured in vivo with high-na defocus-corrected full-field oct and consequences for two-photon microscopy. *Optics express*, 19(6):4833–4847, 2011.

[385] Malcolm Nicolson. The art of diagnosis: Medicine and the five senses. In W.F. Bynum and Roy Porter, editors, *Companion encyclopedia of the history of medicine, vol.02*, pages 801–825. Routledge, London, 1997.

[386] Medical diagnosis in egyptian world. `http://www.arabworldbooks.com/articles8.htm`.

[387] Ramón Bataller and David A Brenner. Liver fibrosis. *The Journal of clinical investigation*, 115(2):209–218, 2005.

[388] Sebastian Mueller and Laurent Sandrin. Liver stiffness: a novel parameter for the diagnosis of liver disease. *Hepat Med*, 2:49–67, 2010.

[389] Sanjay Kumar and Valerie M Weaver. Mechanics, malignancy, and metastasis: the force journey of a tumor cell. *Cancer and Metastasis Reviews*, 28(1-2):113–127, 2009.

[390] Janna K Mouw, Yoshihiro Yui, Laura Damiano, Russell O Bainer, Johnathan N Lakins, Irene Acerbi, Guanqing Ou, Amanda C Wijekoon, Kandice R Levental, Penney M Gilbert, et al. Tissue mechanics modulate microrna-dependent pten expression to regulate malignant progression. *Nature medicine*, 20(4):360, 2014.

[391] J Ophir, I Cespedes, Hm Ponnekanti, Y Yazdi, and Xin Li. Elastography: a quantitative method for imaging the elasticity of biological tissues. *Ultrasonic imaging*, 13(2):111–134, 1991.

[392] R Muthupillai, DJ Lomas, PJ Rossman, James F Greenleaf, et al. Magnetic resonance elastography by direct visualization of propagating acoustic strain waves. *Science*, 269(5232):1854, 1995.

[393] Yogesh K Mariappan, Kevin J Glaser, and Richard L Ehman. Magnetic resonance elastography: a review. *Clinical anatomy*, 23(5):497–511, 2010.

[394] Mickael Tanter, Jeremy Bercoff, Alexandra Athanasiou, Thomas Deffieux, Jean-Luc Gennisson, Gabriel Montaldo, Marie Muller, Anne Tardivon, and Mathias Fink. Quantitative assessment of breast lesion viscoelasticity: initial clinical results using supersonic shear imaging. *Ultrasound in medicine & biology*, 34(9):1373–1386, 2008.

[395] Charlène Gayrard and Nicolas Borghi. Fret-based molecular tension microscopy. *Methods*, 94:33–42, 2016.

[396] Joseph M Schmitt. Oct elastography: imaging microscopic deformation and strain of tissue. *Optics express*, 3(6):199–211, 1998.

[397] Ruikang K Wang, Zhenhe Ma, and Sean J Kirkpatrick. Tissue doppler optical coherence elastography for real time strain rate and strain mapping of soft tissue. *Applied Physics Letters*, 89(14):144103, 2006.

[398] Brendan F Kennedy, Kelsey M Kennedy, and David D Sampson. A review of optical coherence elastography: fundamentals, techniques and prospects. *Ieee Journal of Selected Topics in Quantum Electronics*, 20(2):272–288, 2014.

[399] Shang Wang and Kirill V Larin. Optical coherence elastography for tissue characterization: a review. *Journal of biophotonics*, 8(4):279–302, 2015.

[400] Jeffrey A Mulligan, Gavrielle R Untracht, Sri Nivas Chandrasekaran, Cory N Brown, and Steven G Adie. Emerging approaches for high-resolution imaging of tissue biomechanics with optical coherence elastography. *IEEE Journal of Selected Topics in Quantum Electronics*, 22(3):1–20, 2016.

[401] Daniel Royer and Eugène Dieulesaint. *Elastic Waves in Solids I: Free and Guided Propagation, translated by DP Morgan*. 2000.

[402] S Catheline, R Souchon, M Rupin, J Brum, AH Dinh, and J-Y Chapelon. Tomography from diffuse waves: Passive shear wave imaging using low frame rate scanners. *Applied Physics Letters*, 103(1):014101, 2013.

[403] Ali Zorgani, Rémi Souchon, Au-Hoang Dinh, Jean-Yves Chapelon, Jean-Michel Ménager, Samir Lounis, Olivier Rouvière, and Stefan Catheline. Brain palpation from physiological vibrations using mri. *Proceedings of the National Academy of Sciences*, 112(42):12917–12921, 2015.

[404] Thu-Mai Nguyen, Ali Zorgani, Maxime Lescanne, Claude Boccara, Mathias Fink, and Stefan Catheline. Diffuse shear wave imaging: toward passive elastography using low-frame rate spectral-domain optical coherence tomography. *Journal of Biomedical Optics*, 21(12):126013–126013, 2016.

Biblio.bib